

**THESE DE DOCTORAT DE L'UNIVERSITE PARIS-SACLAY**

préparée à

**L'UNIVERSITE PARIS SUD**

**ÉCOLE DOCTORALE No.575 : Physique et ingénierie : électrons, photons, sciences du vivant  
(EOBE)**

**Spécialité de doctorat : Physique**

par

**Mitradeep SARKAR**

**Hybrid surface plasmon modes in metallic nanostructures:  
Theory, numerical analysis and application to bio-sensing.**

**Thèse présentée et soutenue à Palaiseau, le 18 décembre 2015**

**Composition du jury**

<i>Président du jury :</i>	Paul CHARETTE	Professeur (Université de Sherbrooke)
<i>Rapporteurs :</i>	Anne SENTENAC	Directeur de Recherche (Institut Fresnel-UMR 7249)
	Dominique BARCHIESI	Professeur (GAMMA3-Université de Technologie de Troyes)
<i>Examineurs :</i>	Anatole LUPU	Chargé de recherche (Institut d'Électronique Fondamentale (IEF))
	Stéphane COLLIN	Chargé de recherche (Laboratoire de Photonique et de Nanostructures (LPN))
<i>Directeur de thèse :</i>	Michael CANVA	Directeur de Recherche (Laboratoire Charles Fabry, Institut d'Optique Graduate School)
<i>Encadrant :</i>	Julien MOREAU	Maître de conférences (Laboratoire Charles Fabry, Institut d'Optique Graduate School)



**To Mitanti**



---

# Contents

---

<b>General introduction</b>	<b>11</b>
Outline of the manuscript . . . . .	11
<b>I Introduction to plasmonics : Theoretical Foundations</b>	<b>13</b>
<b>1 Electromagnetic properties of metals</b>	<b>15</b>
1.1 Electromagnetic wave propagation . . . . .	15
1.1.1 Fields and matter . . . . .	15
1.1.2 Time harmonic fields . . . . .	16
1.2 The complex dielectric function of metals . . . . .	17
1.2.1 Drude-Sommerfeld model of free electron gas . . . . .	17
1.2.2 Interband transitions in real metals . . . . .	18
1.3 Some typical values for bulk gold . . . . .	18
<b>2 Excitation of surface plasmon polaritons in metals</b>	<b>21</b>
2.1 Surface plasmon polariton on planar surfaces . . . . .	21
2.1.1 The plasmon polariton . . . . .	21
2.1.2 The plasmon polariton surface waves . . . . .	22
2.1.3 Dispersion of the plasmon polariton . . . . .	23
2.1.4 Some typical length scales of the PSP . . . . .	25
2.2 Plasmon modes in metallic nanoparticles . . . . .	26
2.2.1 Theoretical models for LSP . . . . .	26
2.2.2 Typical LSP resonance in metallic sphere . . . . .	27
<b>Conclusion of Part I</b>	<b>29</b>
<b>II Application of plasmonics for biosensing</b>	<b>31</b>
<b>Introduction to plasmonic biosensors</b>	<b>33</b>
<b>3 Surface plasmon resonance detectors</b>	<b>35</b>
3.1 Coupling of incident photons to plasmons . . . . .	35

3.2	Practical realization of SPR detectors . . . . .	37
3.2.1	Interrogation methods for SPR detectors . . . . .	40
3.3	Molecular detection using SPR detectors . . . . .	41
<b>4</b>	<b>Detectors using particle plasmons</b>	<b>47</b>
4.1	Detection based on localized plasmon resonance . . . . .	47
4.1.1	Synthesis and functionalization of metal nano-particles . . . . .	49
4.1.2	LSPR detector configurations . . . . .	50
4.2	Surface enhanced Raman scattering . . . . .	53
4.2.1	Role of surface plasmons in SERS . . . . .	54
4.2.2	Instrumentation for SERS . . . . .	55
<b>5</b>	<b>Biochip and nano-structuration</b>	<b>59</b>
5.1	Limitations of conventional detection systems . . . . .	59
5.1.1	Limitation of SPR detectors . . . . .	59
5.1.2	Limitation of detector systems using particle plasmons . . . . .	61
5.2	Structure fabrication techniques . . . . .	62
5.3	Detection using Nano-structured bio-chip . . . . .	65
5.4	ANR PIRANEX project . . . . .	70
	<b>Conclusion of Part II</b>	<b>73</b>
	<b>III Numerical methods for electromagnetic modeling</b>	<b>75</b>
	<b>Computational electromagnetics</b>	<b>77</b>
<b>6</b>	<b>Introduction to the numerical formulations</b>	<b>81</b>
6.1	Generalized Rouard method . . . . .	81
6.2	Fourier modal method (FMM) . . . . .	84
6.2.1	Formulation in Fourier space for 1D array . . . . .	85
6.2.2	Formulation in Fourier space for 2D array . . . . .	88
6.2.3	Generalized Matrix formulation for 1D and 2D arrays . . . . .	90
6.3	Finite element method (FEM) . . . . .	92
6.3.1	The elements of Whitney . . . . .	92
6.3.2	FEM formulation for 1D array . . . . .	94
6.3.3	FEM formulation for 2D array . . . . .	95
<b>7</b>	<b>Hybrid model for complex structures</b>	<b>97</b>
7.1	Formulations used for the hybrid numerical model . . . . .	98
7.1.1	Developing the G-matrix for the meshed domain . . . . .	100
7.2	Conclusion . . . . .	101

<b>IV Plasmonics of Nano-structures</b>	<b>103</b>
<b>8 The concept of plasmonic mode</b>	<b>105</b>
8.1 Uniform metallic film: the basic plasmonic mode . . . . .	105
<b>9 Plasmonics of a metallic grating on glass substrate</b>	<b>111</b>
9.1 Plasmonic modes for binary metallic grating . . . . .	111
9.1.1 The Wood-Rayleigh anomaly (WRA) . . . . .	112
9.1.2 Far and near field characteristics of the WRAs . . . . .	114
9.1.3 Plasmonic Band Gaps in periodic structures . . . . .	120
9.2 Plasmonic modes in periodic metallic strips . . . . .	122
9.2.1 The Confined Propagating Plasmons (CPP) . . . . .	124
9.2.2 Near-field and Far-field properties of the CPP . . . . .	125
<b>10 Plasmonics of nano-particles on glass substrate: The LSP resonance</b>	<b>133</b>
10.1 The LSP resonance condition . . . . .	133
10.1.1 Theoretical models for LSP resonance . . . . .	133
10.1.2 Effect of particle dimensions on LSPR . . . . .	137
10.1.3 Effect of substrate on LSPR . . . . .	140
10.2 LSPR condition for metallic nano-cylinders . . . . .	142
10.3 Array of metallic cylinders on a glass substrate . . . . .	145
<b>11 Plasmonics of a metallic array on metallic film</b>	<b>149</b>
11.1 Metallic grating on gold substrate . . . . .	149
11.1.1 The Bragg Modes . . . . .	151
11.2 The hybrid plasmonic modes: Basic introduction . . . . .	153
11.2.1 Mode coupling in plasmonic systems: Fano resonance or not? . . . . .	157
<b>12 The Hybrid lattice plasmon (HLP)</b>	<b>165</b>
12.1 Array of metallic cylinders on gold substrate . . . . .	165
12.2 Far field characteristics of the HLP . . . . .	168
12.3 Near field characteristics of the HLP . . . . .	171
<b>Conclusion of Part IV: Structures and Modes</b>	<b>175</b>
<b>V Plasmonic modes for biodetection</b>	<b>177</b>
<b>13 Intrinsic sensitivity of plasmonic modes for bulk refractive index changes</b>	<b>179</b>
13.1 Bulk index sensitivity for the PSP . . . . .	180
13.2 Bulk index sensitivity for the WRAs . . . . .	181
13.3 Bulk index sensitivity for the CPP modes . . . . .	182
13.4 Sensitivity of metallic array on metallic film to bulk index changes: BM and HLP . . . . .	184
<b>14 Enhancing detection limit for affinity biodetection</b>	<b>187</b>
14.1 Sensitivity enhancement factor (SEF) for affinity biosensors . . . . .	190

14.2	Increasing SEF by selective target localization . . . . .	191
14.2.1	The CPP modes for increasing SEF . . . . .	192
14.2.2	Increasing SEF using the HLP mode . . . . .	196
<b>15</b>	<b>Experimental excitation of the modes in Kretschmann configuration</b>	<b>203</b>
15.1	Experimental characterization of the CPP modes . . . . .	206
15.1.1	Measurement of bulk index sensitivity of CPP . . . . .	208
15.1.2	Measurement of bio-molecular sensitivity of CPP . . . . .	209
15.2	Experimental characterization of the HLP and the BM modes . . . . .	212
15.2.1	Sensitivity measurements for the HLP . . . . .	215
<b>16</b>	<b>Nano-structures for SERS detection</b>	<b>221</b>
16.1	SERS enhancement by localized surface plasmons . . . . .	223
16.2	SERS enhancement due to the Bragg Modes . . . . .	226
16.2.1	Directional SERS intensity due to the Bragg modes . . . . .	228
	<b>General conclusion and perspectives</b>	<b>235</b>
	What has been done in this work : Conclusions . . . . .	235
	What can be done : Perspectives . . . . .	237
	<b>Appendix</b>	<b>241</b>
<b>A</b>	<b>LSPR condition for metallic strips</b>	<b>241</b>
<b>B</b>	<b>Dispersion maps for array of metallic cylinders on metallic film</b>	<b>243</b>
<b>C</b>	<b>Sensitivity of gold film for bio-sensing</b>	<b>247</b>
	<b>Bibliography</b>	<b>251</b>
	<b>Epilogue</b>	<b>273</b>
	<b>Acknowledgments</b>	<b>275</b>
	<b>Abstract</b>	<b>280</b>
	<b>List of publications</b>	<b>284</b>



# **General introduction**



## Outline of the manuscript

This work is aimed at understanding the various plasmonic modes that can be supported by metallic structures. The application of such plasmonic modes for bio-sensing has been demonstrated. The essence of surface plasmons can be described by the fact that metallic structures undergo a resonance in absorption of EM radiation. When such resonance condition is satisfied, the EM field is confined within sub-wavelength distances from the metallic surfaces. The basic understanding of surface plasmons thus lies in explaining or rather predicting this resonance condition.

- The condition obviously depends on the type of metal which in turn is mathematically expressed as the dielectric function of the metal. The first chapter of this work (Chapter 1) is focussed on the different models currently available to describe the complex dielectric function.

- The condition also depends on the geometry of the metallic structures. However till date, analytical solutions for such conditions are available only for a handful of geometries. The second chapter (Chapter 2) describes the two types of surface plasmons that are excited in metallic structures. The very basic geometry is a metal-dielectric interface and the surface plasmons are known to propagate along such a interface. The second type of surface plasmon can be supported by isolated particles with dimensions much smaller than the wavelength of light. The excitation of such plasmons lead to strong localized EM fields around the surface of the metallic particles.

- Furthermore, the resonance condition depends on the dielectric medium surrounding the metal surface. This factor is used for the purpose of molecular detection. The basic governing principle for Surface plasmon resonance (SPR) detectors are described in Chapter 3. Another type of plasmonic detection technique, the Surface Enhanced Raman Scattering (SERS) described in Chapter 4, relies on the actual EM field intensity confined around the metallic nano-particles.

- In Chapter 5 the limitations of conventional SPR detectors and the various types of nano-structured biochips used in order to overcome such limitations are discussed. A major portion of this work was done as a part of ANR project «PIRANEX» which aims at developing a novel instrument combining SERS and SPR detection. The project is described in section 5.4.

It is important to understand the mechanism of surface plasmon excitation in nano-structures for their application to biosensing. The EM properties can be calculated by solving the Maxwell's equations by numerical methods. A brief introduction to various such numerical models is presented in Chapter 6. In this work, numerical simulations were carried out to evaluate the near and far field characteristics of various metallic structures.

- The numerical model used for this work is a combination of two well-known methods namely the Fourier modal method (FMM) and the finite element methods (FEM). This hybrid model described in Chapter 7 can be used for different complex geometries involving metal and is shown in this work to give accurate results which are verified by experiments.

Having described the purpose of this work and the numerical tool used for it, we have then described the excitation of various types of surface plasmons in a number of periodic geometries. To our knowledge such a complete description of the mechanisms behind the plasmon excitation in metallic structures have never been published. Along with novel explanations for already observed types of surface plasmons, in this work we have also introduced some new types of surface plasmons that can be excited in periodic

structures. These are covered in Part IV of this work.

- To explain the mechanism for the excitation of different types of surface plasmons in metallic structures, we have classified them in terms of «Plasmonic modes». The concept of plasmonic modes was described in Chapter 8. The basic fundamental plasmonic mode called the Propagating surface plasmon (PSP) can be excited at a metal-dielectric interface.

- In nano-structures depending on its geometry, the PSP can manifest itself to give rise to various other plasmonic modes. For metallic gratings on a glass substrate, owing to its periodicity, the Wood-Rayleigh anomaly (WRA) are excited when the incident photon lies along the axis perpendicular to the gratings. The EM properties of these modes are described in details in section 9.1 of Chapter 9. When the photon is incident parallel to the grating ridges, the PSP can propagate along the length of the ridges. However owing the finite width of the grating, the Confined Propagating plasmon (CPP) modes can be excited. These modes are described in section 9.2 of Chapter 9.

- Another fundamental plasmonic mode is excited in nano-particles with dimensions much smaller than the wavelength of light. These modes are called the Localized plasmon modes (LSP) and are strongly confined within a few tens of nanometers from the metal surface. In this work we have introduced a simple analytical model called the  $\chi$  formulation to calculate the resonance condition for the LSP and is described in Chapter 10.

- For arrays of metallic nano-particles with an underlying metallic film, a mode similar to the WRA, called the Bragg modes (BM) are excited. These modes are excited due to the diffraction of the PSP of the metallic film by the array of metallic particles. They are described in Chapter 11. In such a structure, the LSP of the nano-particles can also couple to the PSP of the metallic film, to give rise to a new plasmonic mode, called the Hybrid Lattice Plasmon (HLP). In section 11.2.1, we have offered a complete description of the coupling mechanism of the LSP and the PSP.

- This model along with the EM properties of the HLP is discussed in Chapter 12 for a 3D array of metallic nano-cylinders on a metallic film. Appropriate analytical formulation is introduced in this work which can accurately predict the resonance condition of all the plasmonic modes that are excited in such types of nano-structures.

Finally in Part V, the plasmonic modes were studied for their application in bio-detection.

- First the sensitivity of the various modes to bulk refractive index change of the surrounding medium was calculated by numerical methods. Appropriate analytical formulations for the same are also derived and shown in Chapter 13.

- In Chapter 14, the sensitivity of the different modes for affinity biosensing is calculated by numerical methods. The effect of localization of the target molecules at areas where the EM field intensity is enhanced due to excitation of the plasmonic modes, is also calculated. To quantify this for plasmonic modes a figure of merit called the Sensitivity Enhancement factor (SEF) is introduced.

- Different nano-structures are fabricated by e-beam lithography to validate the numerical results. A SPR imaging system, based on a spectral scanning modality is used to experimentally excite the plasmonic modes in different nano-structures. This is covered in chapter 15. The plasmonic modes for applications in SERS is also experimentally studied and calculations to quantify the electromagnetic contribution for the SERS intensity enhancement were shown in chapter 16.

## **Part I**

# **Introduction to plasmonics : Theoretical Foundations**



---

# Electromagnetic properties of metals

---

The evidence for describing light as waves was well established by the turn of the last century. The photo-electric effect confirmed that light can also manifest itself as a particle. The long wavelength radiation (microwaves, radiowaves) is described mainly by the wave theory while short wavelength radiation (X-rays) mainly exhibit particle properties. In the optical regime the wave-particle duality is most pronounced. However for nano-optics we can describe most of the observed phenomenon by adopting the wave theory.

## 1.1 Electromagnetic wave propagation

### 1.1.1 Fields and matter

The starting point to describe the optical phenomenon in nano-scale would be the classical field theory based on the macroscopic Maxwell's equations. The equations in differential form and in SI units can be written as

$$\begin{aligned}\nabla \cdot \mathbf{D}(\mathbf{r}, t) &= \rho(\mathbf{r}, t) \\ \nabla \cdot \mathbf{B}(\mathbf{r}, t) &= 0 \\ \nabla \times \mathbf{E}(\mathbf{r}, t) &= -\frac{\partial \mathbf{B}(\mathbf{r}, t)}{\partial t} \\ \nabla \times \mathbf{H}(\mathbf{r}, t) &= \mathbf{J}(\mathbf{r}, t) + \frac{\partial \mathbf{D}(\mathbf{r}, t)}{\partial t}\end{aligned}\tag{1.1}$$

where the four macroscopic fields  $\mathbf{D}$  (the dielectric displacement),  $\mathbf{E}$  (the electric field),  $\mathbf{H}$  (the magnetic field) and  $\mathbf{B}$  (the magnetic induction) are related to the external charge and current densities,  $\rho(\mathbf{r}, t)$  and  $\mathbf{J}(\mathbf{r}, t)$  respectively. It should be noted that the total charge and current densities are given as the sum of the internal and external charge and current densities respectively ( $\rho_{tot} = \rho + \rho_{int}$  and  $\mathbf{J}_{tot} = \mathbf{J} + \mathbf{J}_{int}$ ). The external charges and currents excite the system while the internal set represents the response of the material system to external excitations [1].

The first equation relates the distribution of electric charge to the resulting electric field while the second equation considers the basic entity for magnetism to be the magnetic dipole. These two basic

electromagnetic Gauss's laws do not contain enough essential information for our purpose of developing the fundamental base for explaining electromagnetic wave propagation. However the conservation of charge is contained in these equations and by rearranging them, we can write

$$\nabla \cdot \mathbf{J}_{int}(\mathbf{r}, t) + \frac{\partial \rho_{int}(\mathbf{r}, t)}{\partial t} = 0 \quad (1.2)$$

The third and fourth equations which stem from the Faraday's law of induction and Ampere's circuital law respectively will be used extensively to develop the in-homogeneous wave equations. But the macroscopic equations do not include the microscopic nature of matter. In other words apart from these equations we also need relations that describe the behavior of matter under the influence of the fields defined by the Maxwell's equations. The electromagnetic properties of a medium are described by the macroscopic polarization  $\mathbf{P}$  and magnetization  $\mathbf{M}$  given by

$$\begin{aligned} \mathbf{D}(\mathbf{r}, t) &= \epsilon_0 \mathbf{E}(\mathbf{r}, t) + \mathbf{P}(\mathbf{r}, t) \\ \mathbf{H}(\mathbf{r}, t) &= \frac{\mathbf{B}(\mathbf{r}, t)}{\mu_0} - \mathbf{M}(\mathbf{r}, t) \end{aligned} \quad (1.3)$$

where  $\epsilon_0$  and  $\mu_0$  are the permittivity and permeability of vacuum respectively. In a non-dispersive, linear and isotropic medium these material equations (also called the constitutive relations) have the form

$$\begin{aligned} \mathbf{D}(\mathbf{r}, t) &= \epsilon_0 \epsilon \mathbf{E}(\mathbf{r}, t) \\ \mathbf{P} &= \epsilon_0 \chi_e \mathbf{E}(\mathbf{r}, t) \\ \mathbf{B}(\mathbf{r}, t) &= \mu_0 \mu \mathbf{H}(\mathbf{r}, t) \\ \mathbf{M} &= \chi_m \mathbf{H}(\mathbf{r}, t) \end{aligned} \quad (1.4)$$

where  $\chi_e$  and  $\chi_m$  are the electric and magnetic susceptibility respectively. In an anisotropic medium the tensorial form of  $\epsilon$  and  $\mu$  must be used. The last important constitutive linear relationship is between the internal current density  $\mathbf{J}_{int}$  and the electric field  $\mathbf{E}$  defined by the conductivity  $\sigma$  given as

$$\mathbf{J}_{int}(\mathbf{r}, t) = \sigma \mathbf{E}(\mathbf{r}, t) \quad (1.5)$$

The Maxwell's equations show a duality between the electric and the magnetic fields and from Equation (1.1) we see that a variable electric field can generate a variable magnetic field and vice-versa. This causes a flow of energy in the form of an electromagnetic wave. Substituting equation (1.4) in (1.1) we obtain the vectorial wave equation given by

$$\begin{aligned} \nabla \times \nabla \times \mathbf{E}(\mathbf{r}, t) + \frac{1}{c^2} \frac{\partial^2 \mathbf{E}(\mathbf{r}, t)}{\partial t^2} &= -\mu_0 \frac{\partial}{\partial t} \left( \mathbf{J}(\mathbf{r}, t) + \frac{\partial \mathbf{P}(\mathbf{r}, t)}{\partial t} + \nabla \times \mathbf{M}(\mathbf{r}, t) \right) \\ \nabla \times \nabla \times \mathbf{H}(\mathbf{r}, t) + \frac{1}{c^2} \frac{\partial^2 \mathbf{H}(\mathbf{r}, t)}{\partial t^2} &= \nabla \times \mathbf{J}(\mathbf{r}, t) + \nabla \times \frac{\partial \mathbf{P}(\mathbf{r}, t)}{\partial t} + \mu_0 \frac{\partial \mathbf{M}(\mathbf{r}, t)}{\partial t} \end{aligned} \quad (1.6)$$

### 1.1.2 Time harmonic fields

The time dependence of the fields can be expressed as a harmonic variation with a frequency  $\omega$ . It is thus possible to use a complex representation of the fields for the temporal sinusoidal variation. Thus the electric and the magnetic fields can be written as



$$\begin{aligned} \mathbf{E}(\mathbf{r}, t) &= \text{Re} \left| \mathbf{E}(\mathbf{r}) e^{-i\omega t} \right| \\ \mathbf{H}(\mathbf{r}, t) &= \text{Re} \left| \mathbf{H}(\mathbf{r}) e^{-i\omega t} \right| \end{aligned} \quad (1.7)$$

The last two Maxwell's equations of (1.1) can now be written as

$$\begin{aligned} \nabla \times \mathbf{E}(\mathbf{r}) &= i\omega \mathbf{B}(\mathbf{r}) \\ \nabla \times \mathbf{H}(\mathbf{r}) &= -i\omega \mathbf{D}(\mathbf{r}) + \mathbf{J}(\mathbf{r}) \end{aligned} \quad (1.8)$$

Combining the two time harmonic equations we can derive the wave equation for the complex fields given by

$$\nabla \times \frac{1}{\mu} \nabla \times \mathbf{E}(\mathbf{r}) - \frac{\omega^2}{c^2} [\epsilon + i\sigma / (\omega\epsilon)] \mathbf{E}(\mathbf{r}) = i\omega\mu_0 \mathbf{J}(\mathbf{r}) \quad (1.9)$$

In absence of external charge and current densities and by substituting  $[\epsilon + i\sigma/\omega\epsilon]$  by  $\epsilon$ , the complex dielectric constant, we can simplify equation (1.9) to have the Helmholtz equation which describes how the electromagnetic wave propagates in space with wave-vector  $\mathbf{k}_0 = \omega/c$

$$\nabla \times \frac{1}{\mu} \nabla \times \mathbf{E}(\mathbf{r}) - k_0^2 \epsilon \mathbf{E}(\mathbf{r}) = \mathbf{0} \quad (1.10)$$

A similar equation can be written for the magnetic field as  $\nabla \times \frac{1}{\epsilon} \nabla \times \mathbf{H}(\mathbf{r}) - k_0^2 \mu \mathbf{H}(\mathbf{r}) = \mathbf{0}$  and for situations when the relative permeability  $\mu$  is discontinuous, this equation cannot be defined. However such situations will not be considered for this work, as all the materials under study are considered to be non-magnetic with  $\mu = 1$ .

Depending on the geometry we can describe most of the optical phenomenon of electromagnetic wave propagation using the basic concepts introduced in this section. We will now proceed to describe the material properties and then to the propagation of plasmons in the material.

## 1.2 The complex dielectric function of metals

The optical properties of a material can be best described by using the complex dielectric function as shown in equation (1.10). It gives a complete picture of the material which a simple dielectric constant fails to provide. In 1900, Paul Drude proposed a simple model to describe the properties of a free electron gas [2]. This was later modified by Arnold Sommerfeld by combining it with quantum mechanical Fermi-Dirac statistics. This model of free electron gas can give accurate approximations for the complex dielectric function of metals for longer wavelengths. However for visible wavelengths the effect of bound electrons must be considered. The various models to calculate the dielectric complex function of metals and their accuracy will be discussed.

### 1.2.1 Drude-Sommerfeld model of free electron gas

The Drude model considers electrons as free particles moving in a constant background potential. Sommerfeld modified the model by treating the electrons as fermions and used Pauli principle to distribute them in the available energy states. Applying the Drude-Sommerfeld model for the free electron gas we can write the equation of motion as

$$m \frac{\partial^2 r}{\partial t^2} + m\Gamma \frac{\partial r}{\partial t} = eE_0 e^{-i\omega t} \quad (1.11)$$

where  $m$  and  $e$  are the mass and charge of electron respectively and  $E_0 e^{-i\omega t}$  is the applied electric field with the frequency  $\omega$ . The damping term  $\Gamma$  is related to the Fermi velocity  $v_f$  and electron mean free path  $l_e$  as  $\Gamma = v_f/l_e$ .  $\tau = 1/\Gamma$  is known as the relaxation time of the free electron gas and has typical values of the order of 10fs. Solving equation (1.11) we can derive the complex dielectric function of metals as a function of the frequency of the applied electric field as

$$\epsilon_{d-s}(\omega) = 1 - \frac{\omega_p^2}{\omega^2 + \Gamma^2} + i \frac{\Gamma \omega_p^2}{\omega (\omega^2 + \Gamma^2)} \quad (1.12)$$

where  $\omega_p^2 = ne^2/(m\epsilon_0)$  is the plasma frequency of the free electron gas with  $n$  being the density of electrons. The implications of the result and some typical values and its relation to the propagation of light in a metal will be discussed shortly. However for more accurate results we must consider the effect of bound electrons in a metal.

## 1.2.2 Interband transitions in real metals

In the visible range of the spectrum, higher energy photons can excite electrons lying in the lower shells of the metal atom to the conduction band. This phenomenon can be described as the oscillations of the bound electrons. We can write the equation of motion similar to equation (1.11) with an additional term which results from the contribution of the bound electron with resonance frequency  $\omega_0$ .

$$m \frac{\partial^2 r}{\partial t^2} + m\Gamma \frac{\partial r}{\partial t} + m\omega_0^2 r = eE_0 e^{-i\omega t} \quad (1.13)$$

The resulting contribution of the interband transitions to the complex dielectric function of metals can be written as

$$\epsilon_{ibt}(\omega) = 1 + \frac{\omega_p^2 (\omega_0^2 - \omega^2)}{(\omega_0^2 - \omega^2)^2 + \Gamma^2 \omega^2} + i \frac{\Gamma \omega_p^2 \omega}{(\omega_0^2 - \omega^2)^2 + \Gamma^2 \omega^2} \quad (1.14)$$

A number of equations of the form of equation (1.13) must be solved for each contribution of the bound electrons and then added to the free electron result to have a more accurate model for the dielectric function of metals.

## 1.3 Some typical values for bulk gold

The complex refractive index  $n = \sqrt{\epsilon}$  can be written as  $n + ik$ . In 1972, P. B. Johnson and R. W. Christy in their article [3] calculated the optical constants  $n$  and  $k$  for gold from reflection and transmission measurements on vacuum-evaporated thin films at room temperature. The volume plasma frequency ( $\omega_p$ ) and the relaxation time of electrons ( $\tau$ ) were then calculated by fitting the measured results to the models of the complex dielectric function described in the last section. The typical values are given in Table 1.1.

The calculated values for the complex dielectric function of gold from equation (1.12) and equation (1.14) using the constants given in Table 1.1 are shown in figure 1.1. The values of the parameters for the interband transition model (contribution of a single interband transition was accounted for) were taken as  $\omega_p = 45 \times 10^{14} s^{-1}$ ,  $\Gamma = 9 \times 10^{14} s^{-1}$  and  $\omega_0 = 2\pi c/\lambda$  with  $\lambda = 450nm$ .

Table 1.1: Optical mass, plasma frequency, Fermi velocity and relaxation time of gold

$m$	$\omega_p$	$v_f$	$\tau$
$0.99 m_e$	$13.4 \times 10^{15} s^{-1}$	$1.39 \times 10^6 m/s$	$9.3 \times 10^{-15} s$

In figure 1.1,  $\epsilon$  is plotted as a function of the wavelength of the applied field  $\lambda = 2\pi c/\omega$ . The figure also shows the values of  $\epsilon$  as obtained by Johnson and Christy. The imaginary part of  $\epsilon$  below  $\lambda = 650nm$  clearly shows that the interband transitions become important in this regime.

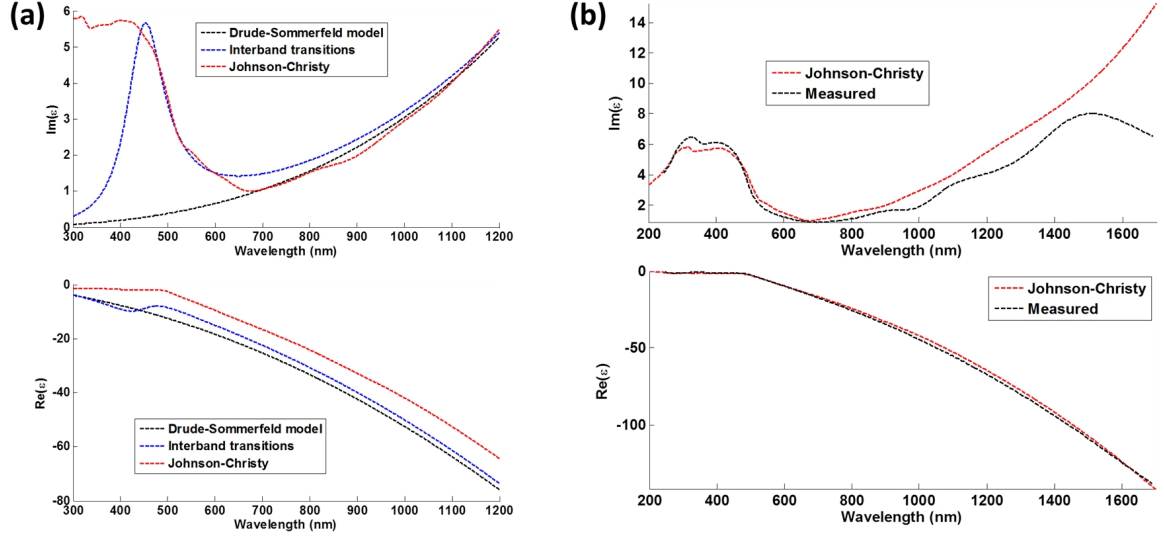


Figure 1.1: (a)Dielectric function of gold  $\epsilon$  calculated using the Drude model, considering the effect of interband transitions and the values obtained by Johnson-Christy.(b)The measured values of  $\epsilon$  is shown along with those found by Johnson-Christy.

The gold used for fabrication of all structures used in this work was characterized using ellipsometry on a thin gold film of 200nm. As shown in figure 1.1(b), the dielectric function of the gold used follows closely that of the values found by Johnson-Christy. There are different methods of fit used to model the dielectric function of metals based on the values of Johnson-Christy [4, 5]. For this work we have used a table of values calculated from the dielectric function of Johnson-Christy, for all the theoretical and numerical calculations. As can be seen from figure 1.1(b), we do not expect strong deviations between the numerical calculations and experimental results due to the variation of the refractive index of gold in the visible. However slight deviations can be expected for wavelengths greater than 1100nm.

Another point that must be mentioned for the property of bulk gold is the depth of penetration of electromagnetic field in metal. We can derive from equation (1.10) the electric field of a propagating wave to be proportional to  $e^{-ik_0nr}$ . Applying Beer's law of absorption according to which the field in a material falls off as  $e^{-\alpha r/2}$  we can find the absorption coefficient ( $\alpha$ ) and the corresponding skin depth ( $\delta = 2/\alpha$ ) as

$$\alpha = 2 \times k_0 Im(n) = 2 \frac{\omega}{c} Im(n) \quad (1.15)$$

The skin depth as a function of wavelength for the measured values of the refractive index of gold

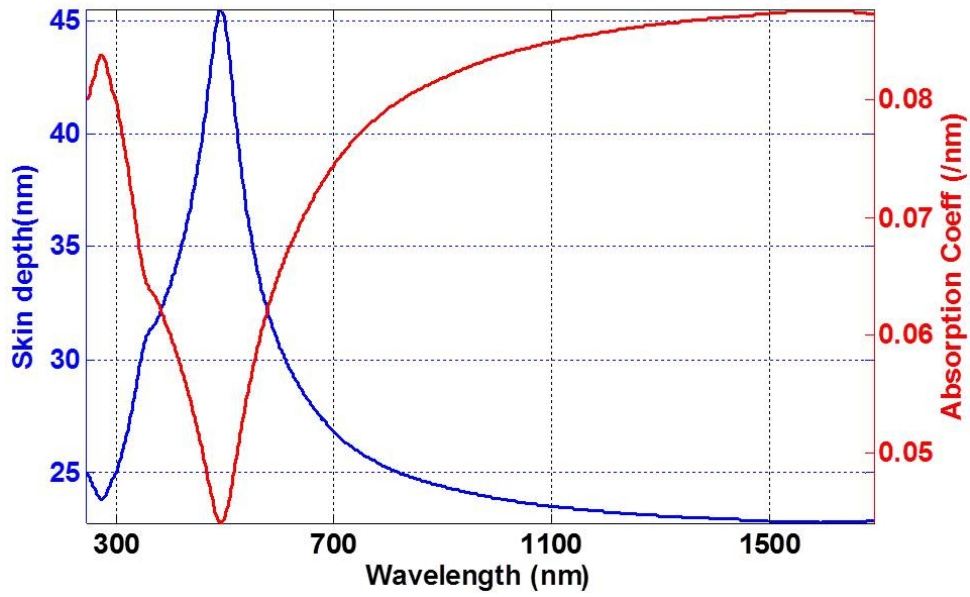


Figure 1.2: The skin depth( $\delta$ )and the absorption coefficient( $\alpha$ )of gold.

was calculated and is shown in figure 1.2. The values of skin depth is of the order of 20-40nm and this plays a very important role in nano-optics where structures and thin films of metal used may have similar dimensions.

# Excitation of surface plasmon polaritons in metals

---

In 1902, while working with optical gratings Robert Wood observed that spectra obtained with a continuous light source "drop from maximum illumination to minimum, a drop certainly of from 10 to 1, occurred within a range of wavelengths not greater than the distance between the sodium lines" [6]. This finding followed decades of work to explain the so-called 'Wood's anomaly' starting with the hypothesis of Rayleigh based on classical grating theories [7] and Fano with his breakthrough theory based on "leaky waves" supported by gratings [8]. In the same decade as Wood, J.C. Maxwell-Garnett observed colors in metal doped glasses [9, 10] and in 1908, Gustav Mie proposed his theory on the scattering of light by metallic nano-particles [11]. These observations reported at the beginning of the last century over the years has developed into a new branch of science and consequent development has resulted in what we know today as nano-plasmonics [12]. However most of the study on nano-plasmonics can be traced back to the two types of phenomenon namely the surface waves in metallic films and scattering of light from metal particles [1]. In the following sections the two pillars of plasmonics will be explained in details.

## 2.1 Surface plasmon polariton on planar surfaces

To start this section we must first describe the concept of a polariton. An electromagnetic wave (photon) polarizes the material through which it propagates causing a collective oscillation of the material constituents. The strong coupling of the photon with these collective oscillations of the material constituents excites a polariton. The coupling of photons and the electron-hole pair oscillations (excitons) when the photon propagates through a semi-conductor gives rise to exciton polaritons. The coupling of the same with mechanical oscillations of atoms or molecules in condensed matter (phonons) excite the phonon polaritons. For materials that can support free electrons, like metals, the coupling of photons with the collective oscillations of the electron gas results in the plasmon polaritons, to which this work is purely dedicated.

### 2.1.1 The plasmon polariton

The concept of oscillations of the electron gas in metals was introduced in section 1.2. We have shown that a free electron gas has the oscillation frequency at  $\omega_p = \sqrt{ne^2/(m\epsilon_0)}$ . The incoming photon can

be considered as an oscillation at frequency  $\omega = k_0 c$ . From equation 1.12 and neglecting the damping of the electrons we see that for values of  $\omega > \omega_p$  the real part of the dielectric function of metals is positive and the metal behaves mostly as a dielectric from the optical point of view. For  $\omega < \omega_p$  the metal retains its optical 'metallic' properties with a negative dielectric constant. At the transition between the two regimes the dielectric constant  $\epsilon(\omega) = 0$  (almost zero but for damping and interband transitions as explained before). For the wave equation (1.10) in Fourier space, the electric fields for transverse waves obey  $\mathbf{k} \cdot \epsilon \mathbf{E} = 0$ . However for the condition  $\epsilon = 0$  we may have longitudinal solutions of the wave equation with  $\mathbf{k} \cdot \mathbf{E} \neq 0$ . From the point of view of harmonic coupling between two oscillator, the solution of the coupled system has oscillation frequencies which are different from both  $\omega$  and  $\omega_p$  and this new oscillation frequency of the coupled system (mode) is the plasmon polariton. The plasmon polariton propagating in a bulk medium is thus a longitudinal electromagnetic mode. But for applications and realization of the plasmon polariton we are more interested in the transverse waves propagating at the surfaces of metals. The approach will be the same, to search for transverse solutions of the wave equation at the surfaces of metals. This will be explained in brief in the next section.

### 2.1.2 The plasmon polariton surface waves

Surface waves can be described as the energy flow along an interface of two media with the field decaying in the direction normal to the interface. Considering the interface in the x-y plane as shown in figure 2.1 the solution of the Helmholtz equation (1.10) must have a decaying term along z and a propagating term along x in medium 1. Such a solution does not exist for s-polarization (transverse electric or TE) and the solution for p-polarization (transverse magnetic or TM) for the electric field components (x and z) can be written as

$$\begin{aligned} z < 0 & \left\{ \begin{aligned} E_x(z) &= E_0 e^{i k_x x} e^{-k_z z} \\ E_z(z) &= E_0 e^{i k_x x} e^{-k_z z} \end{aligned} \right\} \\ z > 0 & \left\{ \begin{aligned} E_x(z) &= E_0 e^{i k_x x} e^{k_z z} \\ E_z(z) &= E_0 e^{i k_x x} e^{k_z z} \end{aligned} \right\} \end{aligned} \quad (2.1)$$

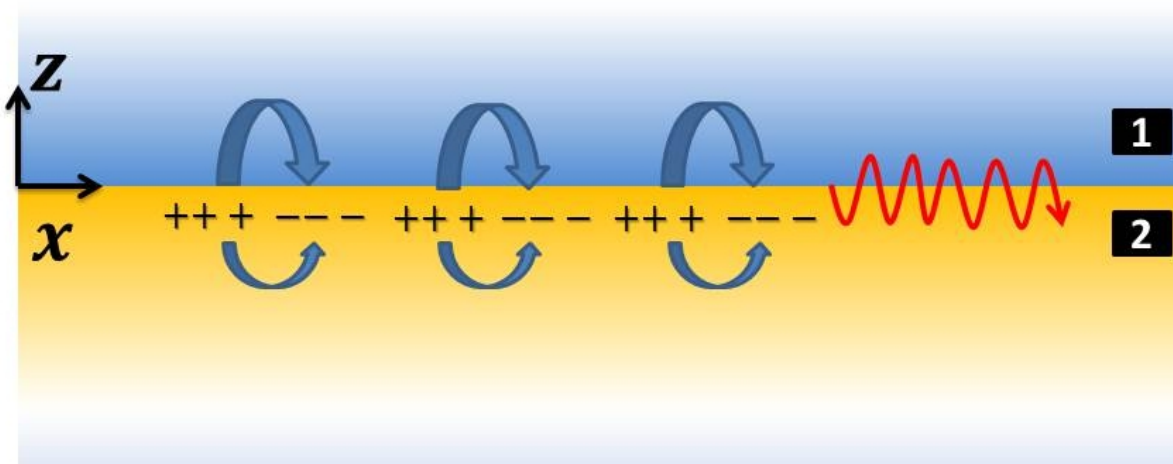


Figure 2.1: Geometry of the metal(2)-dielectric(1) interface illustrating the surface charge and the field lines of the surface plasmon polariton.

Applying the boundary conditions and continuity of H and E to equation 2.1 at the interface we obtain

$$\frac{k_{z1}}{k_{z2}} = -\frac{\epsilon_1}{\epsilon_2} \quad (2.2)$$

where  $\epsilon_1$  and  $\epsilon_2$  are the dielectric constants of medium 1 and 2 respectively. This result implies that surface transverse wave solutions of the Maxwell's equations are possible at the interface of two materials only if

a) the dielectric constant of one of the media is negative in which case the surface waves are called Fano waves. The phase velocity ( $v_p = \omega/k$ ) for the Fano waves is less than the velocity of light.

b) or has a nonzero imaginary part in which case they are called the Zenneck waves and their phase velocity is more than the velocity of light. In fact the concept of surface waves was first proposed by Zenneck in 1907 which was further developed by Sommerfeld and observed much later in the late 1980s. For optical frequencies Zenneck waves have not really been observed [13]. A detailed description of the Zenneck waves can be found in Chapter 2 and Chapter 6 of reference [1].

### 2.1.3 Dispersion of the plasmon polariton

To understand the phenomenon of surface waves for metals which is the main focus of this work, we need to look at the dispersion of the surface waves (dependence of the solutions (modes of the system) for the surface waves of frequency  $\omega$  and wave-vector  $k$ ). The surface waves have a decaying z component but a propagating x component. The values of  $k_x$  would give the wave-vector ( $k_{sp}(\omega)$ ) of the propagating surface wave along x. By squaring equation 2.2 and solving for  $k_x$  we can derive one of the central conditions for surface wave dispersion.

$$k_{sp}^2(\omega) = k_0^2 \left[ \frac{n_d^2 n_m^2}{n_d^2 + n_m^2} \right] \quad (2.3)$$

where  $\epsilon_1 = n_d^2$  and  $\epsilon_2 = n_m^2$  as medium 1 will be considered a dielectric and medium 2 as metal henceforth and  $n_d$  and  $n_m$  are their refractive indices respectively. In this case, the dielectric constant is both negative and has a non-zero imaginary part depending on the frequency. So we can excite the surface waves of both the Fano or Zenneck type.

The physical mechanism of the surface wave at a metal-dielectric interface can be explained by the fact that the z-component of the electric field creates a surface charge at the metal interface. So the surface wave can be seen as a propagation of surface charge density along x. To have continuous field lines in the dielectric we must have a field component in the dielectric close to the surface charge density. This is the origin of the propagating surface plasmon (PSP) polariton.

The dispersion curve was calculated using the values of the dielectric constant for gold calculated by the Drude-Sommerfeld model (section 1.2) and as found by Johnson-Christy mentioned in section 1.3. An interesting characteristic of the dispersion curve must be mentioned here [14].

For equation 2.3, when considering losses in the metal, the term  $n_{PSP} = \frac{n_d^2 n_m^2}{n_d^2 + n_m^2}$  is a complex term and thus the equation needs to be solved with complex  $k$  and complex  $\omega$ . In figure 2.2 the dispersion of the PSP is plotted for a plane interface between gold and air ( $n_d = 1$ ). Please note that the axes were normalized by  $k_p = \omega_p/c$  where  $\omega_p = 13.4 \times 10^{15} s^{-1}$ . We see that the solution has two branches. For real values of  $n_{PSP}$ , the lower  $\omega$  branch is an asymptote to  $\omega_p/\sqrt{2}$ . This is because for an interface,

when the thickness of metal tends to infinity, the charge density builds up only on one surface instead of two. So the oscillation frequency of the electron gas at the interface is  $\omega_p/\sqrt{2}$  instead of  $\omega_p$ .

The dispersion curve is also an asymptote to the light-line ( $k_0 = \omega/c$ ). This behavior is similar to the characteristic frequencies of a coupled system of two harmonic oscillators. Thus we can consider the PSP as a result of the harmonic coupling of a photon with oscillation frequency  $\omega$  and the electron gas cloud with oscillation frequency of  $\omega_p/\sqrt{2}$ . This asymptotic behavior of the PSP dispersion is also observed if we solve equation 2.3 for complex roots of  $\omega$ .

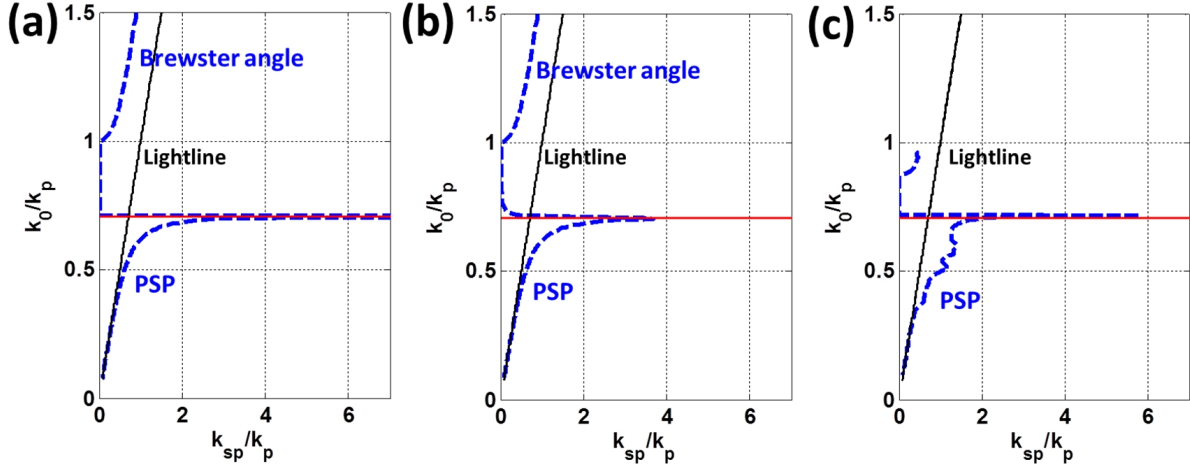


Figure 2.2: a)Dispersion of the PSP calculated for real values of  $n_{PSP}$ . b)The same for complex values of  $n_{PSP}$ . c)The dispersion of PSP considering the values of Johnson-Christy. The axes are normalized by  $k_p = \omega_p/c$ . The lightline ( $k_0 = \omega/c$ ) is also shown (data for Johnson-Christy is restricted to values of wavelength  $\lambda > 150nm$  ( $k_0/k_p < 0.93$ )).

However if we take into account the losses (mathematically represented by the complex refractive index of metals ( $n_m = n + ik$ ) and thus complex values of  $n_{PSP}$ ) we see a back bending of the dispersion curve [15]. This phenomenon is quite well know and first observed by Arakawa et al in 1973 [16]. Quoting from the article "In the vicinity of the surface plasmon energy the dispersion curve was found to bend back toward the light line instead of increasing asymptotically to the surface plasmon energy at infinite momentum. We conclude that surface plasmon interactions must be characterized by a complete response-function surface rather than by a single dispersion curve." This backbending is also observed is we solve equation 2.3 for complex roots of  $k_{sp}$ . So one must be careful when studying the dispersion characteristic of a PSP, close to the oscillation frequencies of electron gas. We must mention here that for values of  $\omega > \omega_p$  the upper  $\omega$  branch of the solution of equation 2.3 is not a surface wave as the metal behaves as a dielectric. In fact, equation 2.3 which was solved by squaring equation 2.2, is also a solution of  $\frac{k_{z1}}{k_{z2}} = \frac{\epsilon_1}{\epsilon_2}$  which is simply the Brewster's angle for which the p-polarized light has zero reflection [13, 17].

The dispersion of the PSP with values of the dielectric constant of Jhonson-Christy is also shown in figure 2.2. We see that the dispersion matches closely in the region  $\omega < \omega_p/2$  which corresponds roughly to wavelengths greater than 300nm. However some bumps are observed in the dispersion curve which results from the interband transitions in gold as mentioned in section 1.2. As this work is mainly dedicated to bio-sensing it will be focused on the visible and near infrared region of the EM spectra. In this domain, the surface plasmon dispersion lies close to the lightline and to the right of it. Therefore, the



PSP cannot be excited at a simple interface of a metal and a dielectric. The method for excitation of PSP in this region of the spectrum will be described in chapter 3.

### 2.1.4 Some typical length scales of the PSP

From the previous section we can conclude that PSP is a surface wave which exists at the surface of a metal and the electric field decays exponentially from the surface. We can also see that the PSP has finite values of  $k_x$  which signify that they are waves propagating along the metal-dielectric interface. This work is dedicated to applying surface plasmon polaritons for biodetection. For this application the electric field confined to the metal surface due to the excitation of the plasmon polaritons plays a very important role.

The evanescent field due to the plasmon polaritons at the metal-dielectric interface guides the energy of the incident light along the surface of the metal. However due to absorption in the metal the PSP has a finite propagation length which can be directly calculated from the imaginary part of the wave-vector  $k_x$ . From equation 2.1 we see that the electric field at the interface varies as  $e^{ik_x x}$  so the propagation length ( $L_x$ ) of the field intensity can be written as

$$L_x = \frac{1}{2\text{Im}(k_{sp}(\omega))} \quad (2.4)$$

The decay length of the electric field into the dielectric is called the penetration depth ( $\delta_z$ ) of the PSP and is given by  $\frac{1}{2\text{Im}(k_z(\omega))}$ . The wave-vector  $k_z$  is related to  $k_{sp}$  by the relation

$$k_z^2 + k_{sp}^2 = k_0^2 \quad (2.5)$$

The values of  $L_x$  and  $\delta_z$  are shown in figure 2.3 as a function of excitation wavelength for a gold-water interface. We see that the values of  $L_x$  is around  $10\mu m - 20\mu m$  and  $\delta_z$  is around  $100nm - 200nm$  in the visible part of the spectrum.

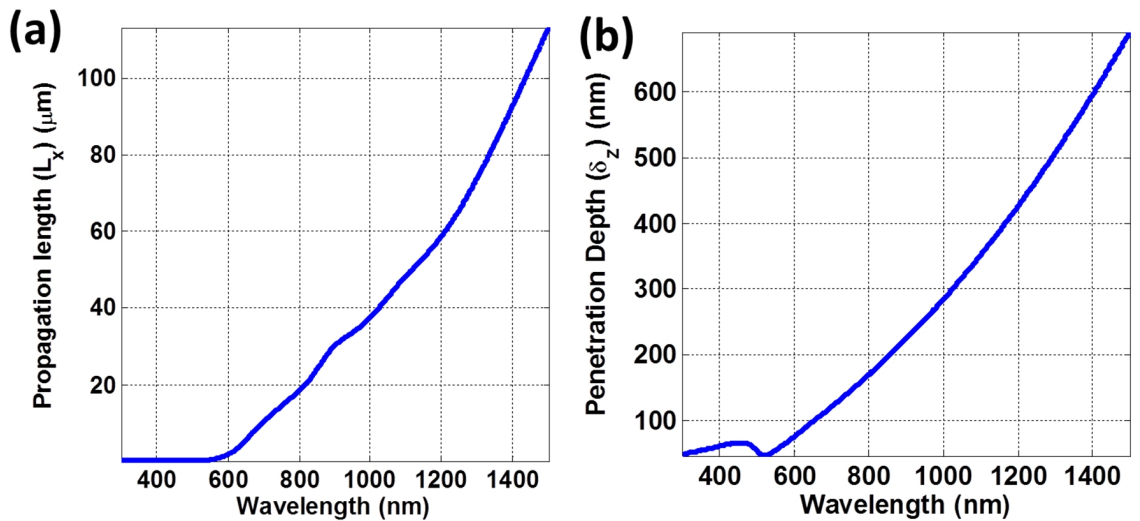


Figure 2.3: a)The propagation length of the PSP as a function of wavelength b)The penetration depth of the PSP as a function of wavelength. The values were calculated for a gold-water interface which is typical for bio-detection experiments.

## 2.2 Plasmon modes in metallic nanoparticles

In the previous section we have described the propagating, dispersive electromagnetic wave caused by the electron plasma at a metal-dielectric interface. The second fundamental type of plasmon polariton occurs when the incoming photon energy couples to the localized oscillation of the electron charge density at the surface of metallic nano-structures. The oscillating field of the incident light causes a polarization of the electronic charges in metal nanoparticles. We will consider the case where dimensions of the particles are much smaller than the wavelength ( $\lambda$ ) of the incident light. The approximation on the particle dimensions much smaller than  $\lambda$  is only to assume a quasi-static condition where the polarization charge does not have retardation effects. However the same effect can take place for much larger particles and the consecutive theories for them have been developed. The curved surface of the particle offers a restoring force to the developed charge density resulting in a depolarization field. This depolarization field is strongly localized to the particle surface with typical decay lengths of some tens of nanometers [18, 19]. The magnitude of the depolarization field undergoes a resonance at certain frequencies of the exciting light which depends on the particle shape, the dielectric function and the distribution of charge densities in the particle. This resonance is called the localized surface plasmon (LSP) resonance [20, 21, 22, 23].

### 2.2.1 Theoretical models for LSP

Most theories on the LSP are based on the solutions of a scattering problem of a particle brought into a electromagnetic field  $E_0(r)$  [24]. The polarization of the particle present in the incident field is proportional to the depolarization field ( $E_d(r)$ ) created by  $E_0(r)$ . We can assume the relation between  $E_0(r)$  and  $E_d(r)$  to be linear and thus the polarization can be written as (equation 1.4)

$$p = \epsilon_0 \alpha E_0(r) \quad (2.6)$$

where  $\alpha$  is the microscopic polarizability of the particle and is similar to the macroscopic susceptibility ( $\chi_e$ ) of a medium. Given that the scattering and absorption cross-section are proportional to  $\alpha^2$  and  $Im(\alpha)$  respectively, the starting point of most theories to evaluate the resonance condition of the LSP rests on the calculation of  $\alpha$ . The earliest evaluation of  $\alpha$  dates back to the 1870s when the Clausius-Mossotti formula was developed to show that the polarizability of a substance with dielectric constant  $\epsilon$  in air is proportional to  $(\epsilon - 1)/(\epsilon - 2)$ . In an electrostatic approach, solving the Laplace equation for the potential ( $\nabla^2 \Phi = 0$ ), we can derive the polarizability of a spherical metallic particle of diameter  $d$ , with dielectric constant  $\epsilon_m$  in a medium  $\epsilon_d$  as

$$\alpha = 4\pi d^3 \frac{\epsilon_m - \epsilon_d}{\epsilon_m + 2\epsilon_d} \quad (2.7)$$

From this, the Frohlich condition for resonance of the LSP is given by  $Re(\epsilon_m(\omega)) = -2\epsilon_d$ . For non-spherical particles the solution of the scattering problem is a lot more demanding. However it has been shown that a general equation can be derived of the form

$$\alpha \propto \frac{\epsilon_m - \epsilon_d}{\epsilon_d + \chi(\epsilon_m - \epsilon_d)} \quad (2.8)$$

where  $\chi$  is the depolarization factor which depends on the shape and size of the particles (not to be confused with the susceptibility which is written in this manuscript as  $\chi_e$  or  $\chi_m$ ). the evaluation of  $\chi$  for

different nano-particles and modification of equation 2.8 depending on the particle type and environment will be discussed later and constitutes a major portion of this work.

We must mention here that the above equation assumes a quasi-static approach where the nano-particle is treated as a radiating dipole. For larger particle dimensions a rigorous electrodynamic treatment of the scattering problem was proposed by Mie in 1908 [11]. The Mie theory takes into account the radiation damping and retardation of the polarization caused by the larger size of the particle. We will come back to this theory and will also use rigorous solutions for the Maxwell's equation to arrive at similar results for the resonance of LSP for larger particle dimensions. Such methods are explained in chapter 10.

## 2.2.2 Typical LSP resonance in metallic sphere

The depolarization factor for a metallic sphere can be taken as  $1/3$  and the resonance frequency for it was evaluated using equation 2.8. The extinction spectrum (proportional to  $\alpha$ ) of a metallic sphere in water ( $n_d = 1.333$ ) is shown in figure 2.4. At resonance, the depolarization field of the LSP is in phase with the incident electric field. This causes an enhancement of the local electric field at the position of the charge density induced by the incident field. As seen in section 2.1.4 the decay length of the PSP is of the order of hundreds of nanometers. For the LSP as seen in figure 2.4 the decay length is a few tens of nanometers. This is very useful for certain bio-detection applications which will be presented in this work. We can also see from figure 2.4 that the field distribution of the LSP is directional and is parallel to the polarization of the incident field. In general,  $\alpha$  is a tensor and thus the depolarization field may or may not be parallel to the incident field depending on the shape and size of the particle. Thus playing with the polarization of the incident field, the shape and size of the particles we can have multiple LSP modes in a system. This will be described in details in the following chapters.

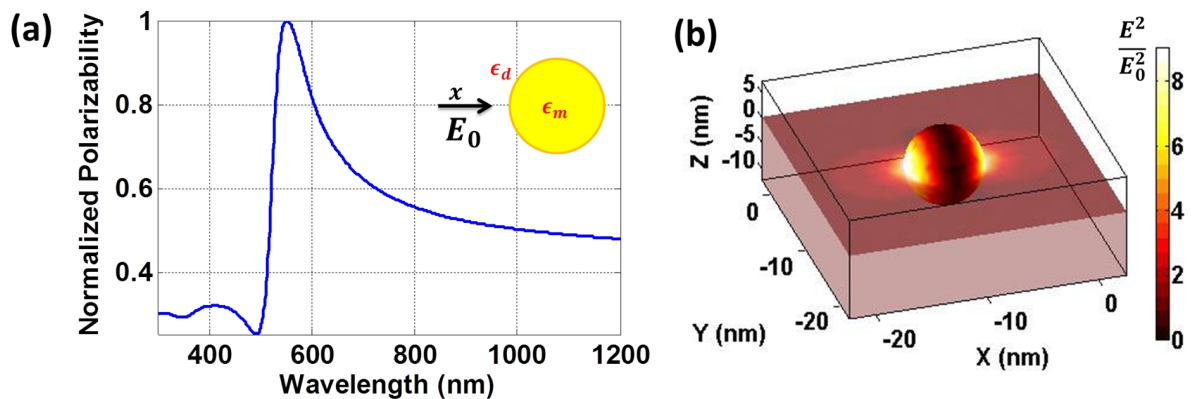


Figure 2.4: (a) The calculated normalized polarizability ( $\alpha$ ) for a sphere in water (b) The electric field intensity ( $E^2$ ) normalized to the incident intensity ( $E_0^2$ ) calculated at 540 nm (at the position of resonance). The incident field is polarized along  $x$ .



---

# Conclusion of Part I

---

In this part we have shown the mechanism of excitation of surface waves in metal-dielectric interfaces. We have seen that due to the presence of conduction electrons in metals we can have a resonance for the oscillation frequencies of the charge densities of the electron cloud. The coupling of a photon to such plasma oscillations give rise to plasmon polaritons.

We can broadly classify the plasmon polaritons into two families. The coupling of an incident photon to the electron charge density oscillations at uniform metal-dielectric interfaces result in the propagating surface plasmon (PSP). The resonance frequencies of the PSP can be calculated from a eigenvalue problem and they are simply the transverse wave solutions of the Maxwell's equations at the interface. These waves propagate along the interface and decay exponentially in the direction normal to the interface. The propagation length is of a orders of a few tens of micrometers while the penetration depth into the dielectric is of the order of few hundreds of nano-meters for the visible part of the spectrum.

The second type of plasmon polaritons are supported by curved metal surfaces and thus by metal nano-particles. The electric field caused by these plasmon polaritons are strongly localized close to the metal surface. The mechanism of excitation of the localized surface plasmons (LSP) is similar to the PSP and the modes that can be supported by the particles can be calculated by solving the scattering problem of the particle brought into a electromagnetic field. The LSP modes are non-propagating and the decay length of the electric field into the dielectric, at resonance, is of the order a few tens of nanometers.

With these two fundamental types of plasmon polaritons we can play with the structure geometries to have various other modes of the complete system. Such modes which result from intra or inter coupling of PSP and LSP have certain properties in terms of electric field enhancement or field confinement which can prove to be useful for various applications. The focus of this work is to use such hybrid modes of complex plasmonic structures to enhance detection capabilities of bio-sensors. Such plasmonic biosensors and their advantages and limitations will be discussed in Part II.

The basic approach to optimize structures for applications is to first understand the mechanism of excitation of the different modes in a complex structure. For this we need various numerical methods to solve the modes of the system. In Part III we will discuss the numerical methods that we have used in this work.



## **Part II**

# **Application of plasmonics for biosensing**





---

# Introduction to plasmonic biosensors

---

Biosensors comprise of two principle components: the bio-receptor and the transducer. The bio-receptor is a bio-chemical part of the biosensor which helps to recognize the analyte under study. The analyte may consist of the biomolecular species such as DNA, antibody, enzymes, living components such as cells or tissues or biomimetic materials such as synthetic bioreceptors. A probe layer which offers high degree of selectivity to the target analyte is used for the recognition by various interaction mechanisms such as nucleic acid interactions, antibody-antigen interactions, enzymatic interactions and so on. The transducer helps to convert such bio-chemical interactions into measurable signals which can be analyzed. Transduction process can follow various methods such as optical detection, electro-chemical detection or mass based methods. Each method has its own type of output signal which give an insight on the bio-chemical process under study. This work is dedicated mainly to the transduction part of the bio-sensor and more specifically the method of optical transduction based on surface plasmons.

Majority of the optical transduction techniques depend on various methods of spectroscopies to measure the spectrochemical properties of the analyte. This offers a direct insight into the type of chemical species under study. Fluorescence spectroscopy is widely used and depends on the fluorescence emission process of either the molecule itself (intrinsic fluorophores) or fluorescent labels attached to the bio-molecules. Depending on the optical detection procedure used such methods can be used to detect individual bio-chemical species or chemical interaction kinetics. However the main drawback of fluorescence spectroscopy lies in the availability of appropriate intrinsic fluorophores or other fluorescent dyes. Photo-bleaching (temporal delay between the excitation and emission of fluorescence) and fluorescence quenching (any process which decreases the fluorescence intensity of a given substance such as its proximity to a metal surface) are other challenges faced by fluorescence detection methods.

Raman spectroscopy is a label-free technique that has been used for chemical analysis because of its capability to offer molecular fingerprint of the analyte and thus identify specific chemical groups. However the low scattering cross-section of the Raman emission process deterred its used until the development of Surface Enhanced Raman scattering (SERS). SERS is based on the excitation of particle plasmons as introduced in section 2.2 and this detection technique will be discussed in details in chapter 4. Another commonly used label free optical bio-detection method is the surface plasmon resonance (SPR) detection which mainly depends on propagating plasmons as introduced in section 2.1.2 and will be discussed in chapter 3. This work is purely based on these two detection techniques namely SPR and SERS.



---

# Surface plasmon resonance detectors

---

Surface plasmon resonance (SPR) detectors are based on the detection of refractive index changes that occur due to various bio-chemical interactions. Since such detectors directly measure the refractive changes, they do not require labeling of the chemical species and thus simplifies the chemical processes involved in data collection. Conventional SPR detectors are based on a simple metal-dielectric interface which can support the PSP. As shown in figure 2.3 the penetration depth of the PSP is around a few hundred nanometers. The SPR detectors can thus probe local refractive index changes within a few hundreds of nanometers from the metal surface. This makes it possible to detect molecular binding processes which induce a change in the local refractive index. With advanced SPR detection systems, minute refractive changes up to the order of  $10^{-6}$  can be measured with very high precision. In this work we will focus on the detection limit of SPR detectors with respect to analyte molecular concentrations which has already been shown to be as low as a few nano-molar.

The dispersion of the PSP was discussed in section 2.1.3. From equation 2.3, we see that the dispersion of the PSP depends on the refractive index of the dielectric medium ( $n_d$ ) at the metal-dielectric interface. Thus a change in the refractive index translates to a shift in the resonance condition of the PSP. This shift in the resonance condition with  $n_d$  forms the basis of almost all SPR detectors. However as can be seen from figure 2.2, for a simple metal-dielectric interface the wave-vector of the PSP ( $k_{sp}$ ) is greater than the wave-vector of light in the dielectric ( $k_0$ ). Thus the propagating plasmon cannot be excited in a simple metal-dielectric interface. To excite the PSP certain coupling schemes must be employed. The most common method conventionally used for coupling the incident photons to surface plasmons was introduced by Otto in 1968 and another similar coupling method was demonstrated by Kretschmann and Raether in the same year.

## 3.1 Coupling of incident photons to plasmons

To excite the surface plasmons in an uniform metallic film we need to match the incident photon momentum (or wave-vector  $k_{inc_x}$ ) to the wave-vector of the propagating surface wave of the PSP ( $k_{sp}$ ). The wave-vector for a plane wave incident at an angle  $\theta$  from a medium with refractive index  $n_g$  can be written as  $k_{inc_x} = k_0 n_g \sin(\theta)$ . For the configuration shown in figure 3.1 the condition for coupling the wave-vectors of the incident light to the PSP using equation 2.3 is given by

$$k_{inc_x}/k_0 = n_g \sin(\theta) = \sqrt{\frac{n_d^2 n_m^2}{n_d^2 + n_m^2}} \quad (3.1)$$

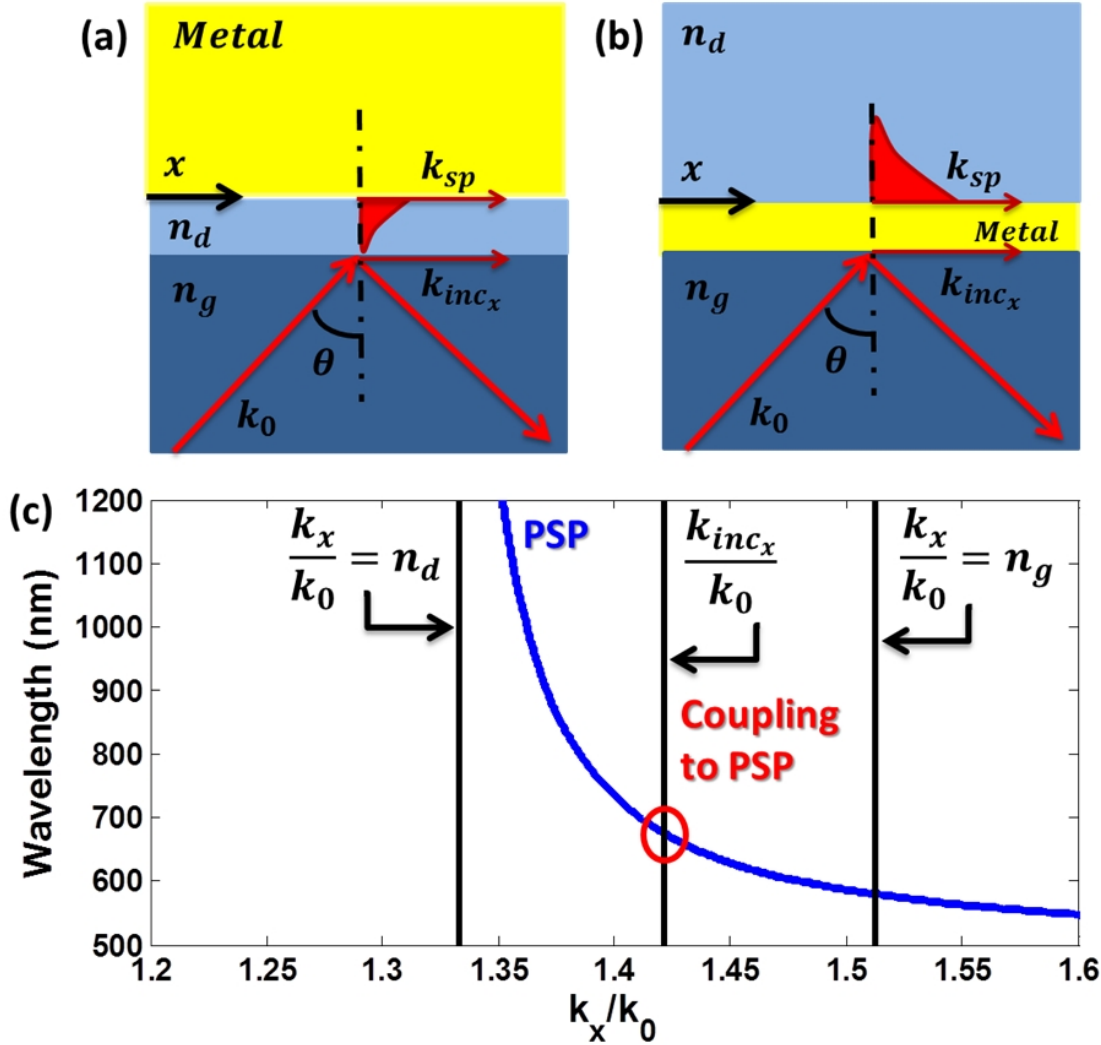


Figure 3.1: Coupling of incident light to surface plasmons by (a) the Otto configuration (b) the Kretschmann configuration. The incident field is TM polarized with incident wavelength  $\lambda$  and thus wave-vector  $k_0 = 2\pi/\lambda$  (c) The coupling of incident wave-vector  $k_{inc_x}$  to the wave-vector of the PSP ( $k_{sp}$ ) with  $\theta = 70^\circ$ .

We see that the coupling condition cannot be satisfied with  $n_g = n_d$ . To match the wave-vectors Otto proposed the configuration shown in figure 3.1(a) where a thin layer of dielectric with refractive index  $n_d$  was sandwiched between the metal and another dielectric with index  $n_g > n_d$ . However the configuration is not very adaptable for practical reasons. The configuration shown in figure 3.1(b) was proposed by Kretschmann and Raether [25], uses a thin metal film (of a few 10s of nms in thickness) between two dielectric layers of refractive indices  $n_g > n_d$  where the coupling condition can be satisfied for the metal- $n_d$  interface [26]. The dispersion of the PSP in terms of wavelength ( $\lambda$ ) and  $k_x/k_0$  is shown in figure 3.1(c) with  $n_d = 1.333$  and  $n_g = 1.513$ . We see that for metal- $n_d$  interface the PSP is excited for values of  $k_x/k_0 > n_d$ . This was also seen in figure 2.2. With the angle of incidence  $\theta$  and incidence medium with index  $n_g$  we can have access to the values of  $k_x/k_0$  from  $0 - n_g$ . The value of

$k_x/k_0 = n_d$  denotes the critical angle for the  $n_g - n_d$  interface. Thus without the gold film we expect total internal reflection (TIR) for values of  $k_x/k_0 > n_d$ . For certain values of wavelength ( $\lambda$ ) and angle  $\theta$  the coupling condition is satisfied as shown in figure 3.1(c) for  $\theta = 70^\circ$  and the PSP can be excited at that particular  $\lambda$  and  $\theta$ . When light passes through a high refractive index ( $n_g$ ) medium and is totally reflected at the the medium of index  $n_d$  it gives rise to an evanescent wave which can penetrate the metal film given its thickness is of a few tens of nms. This evanescent wave propagates along the interface ( $x$ ) with the propagation constant  $k_{inc_x}$  and if its value matches the wave-vector of the PSP it couples to the surface plasmons at the metal- $n_d$  interface generating the PSP.

For SPR detectors the Kretschmann configuration is conventionally used to couple the incident photons to the plasmons. Other methods such as matching the PSP wave-vectors to that of diffraction orders from a grating or the wave-vectors of propagating modes of a waveguide have also been used. However such methods have not proved to be as convenient as the Kretschmann configuration owing to the inherent simplicity of the later. Here in this work we will focus on the SPR detectors using the Kretschmann coupling configuration.

## 3.2 Practical realization of SPR detectors

SPR detectors using the Kretschmann coupling configuration are generally realized using a prism for the high refractive index medium ( $n_g$ ). The scheme of a conventional SPR detector is shown in figure 3.3. The fluidic cell generally contains water (or other solvent used to dissolve the analyte) and has a refractive index lower than that of the prism used (generally BK7 glass, index 1.513 or flint SF10 glass, index 1.712). Light with wavelength ( $\lambda$ ) and internal angle of incidence (angle at the prism-biochip interface)  $\theta$  is totally reflected at the prism-fluidic cell interface and the reflectivity is measured by the detector. We will consider the biochip as a uniform thin metallic film, which is conventionally used for SPR detectors. The aim of this work is to develop new generations of structured bio-chips which we will explain in details in part IV. For the wavelengths and internal angle at which the PSP, is excited the energy of the incident photons is coupled to the PSP and thus we have a fall in reflectivity measured by the detector. Thus by scanning over  $\lambda$  or  $\theta$  and measuring the reflectivity we can virtually follow the resonance condition given by equation 3.1. This resonance condition is strongly dependent on the refractive index of the medium in the fluidic cell ( $n_d$ ) and thus any change in the index will manifest as a shift in the resonance condition in both  $\lambda$  and  $\theta$ . This is the basic principle of all SPR detectors and most of them are used to probe bulk refractive index changes around the bio-chip surface.

Some examples of currently used SPR detection systems is shown in figure 3.2. All the SPR detectors shown use the same principle, which is to follow the satisfaction of the coupling condition in either  $\lambda$  or  $\theta$ . Some of the setups use a broad band source and use a monochromator or diffraction grating for wavelength scanning. Others use narrow band sources such as LED or laser diodes and thus the coupling condition is matched by tuning the angle of incidence.

The SPR configuration used for this work is based on a spectro-angular modality shown in figure 3.4 [35]. The source is a halogen lamp and thus have a broad range of wavelengths. A monochromator is used to scan the wavelengths for interrogation. Light from the monochromator is collected by a multi-mode fiber and then collimated and linearly polarized using a polarizer. The angle of incidence is chosen by a motorized platform. The reflected light from the bio-chip surface is imaged by a CCD camera. Using this

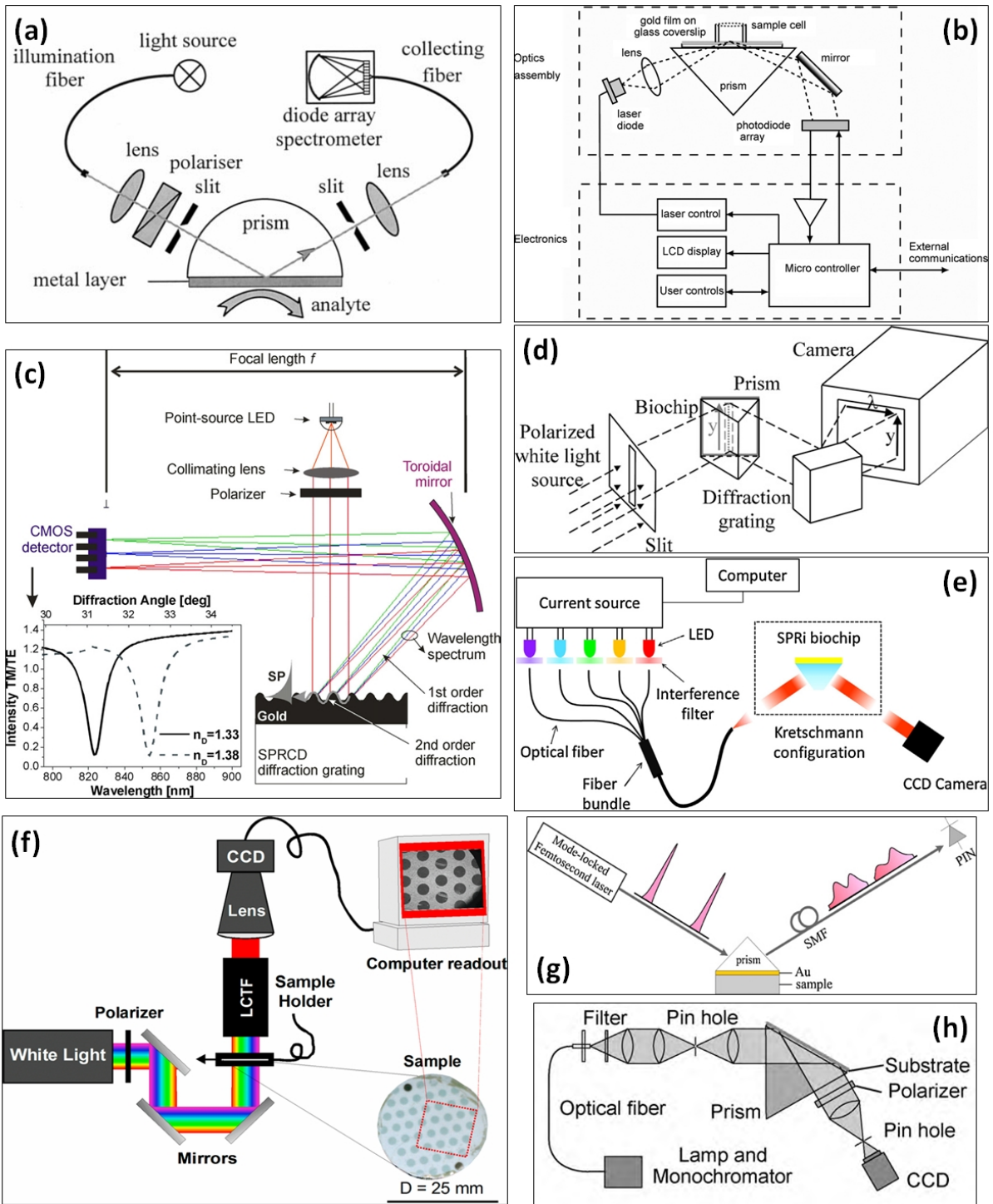


Figure 3.2: Different SPR detectors: (a) I.Stemmler et al (1999)[27] uses illumination and collecting fibers to couple the photons to the plasmons and collect the reflected light. A diode array spectrometer was used to study the reflectivity spectrum. (b) B.N. Feltis et al (2008) [28] constructed a compact hand held SPR biosensor (c) M.Piliarik et al (2009) [29] used a special diffraction grating structure which coupled the incident light to the plasmons and the same was used to diffract the light for spectral readout of SPR signal. (d) F.Bardin et al (2009) [30] used a diffraction grating at the output to study the reflectivity spectrum (e) A.Sereda et al (2015) [31] used a compact 5-LED illumination system for spectral interrogation in SPR imaging. (f) J.A.Ruemmele et al (2013) [32] using a collimated white light source and spectroscopic read out using a liquid crystal tunable filter (g) Z. Zheng et al (2008) [33] using an ultrafast laser and dispersive element for spectral analysis (h) S. Otsuki et al (2010) [34] used a broadband lamp as the source and a monochromator for spectral scanning.

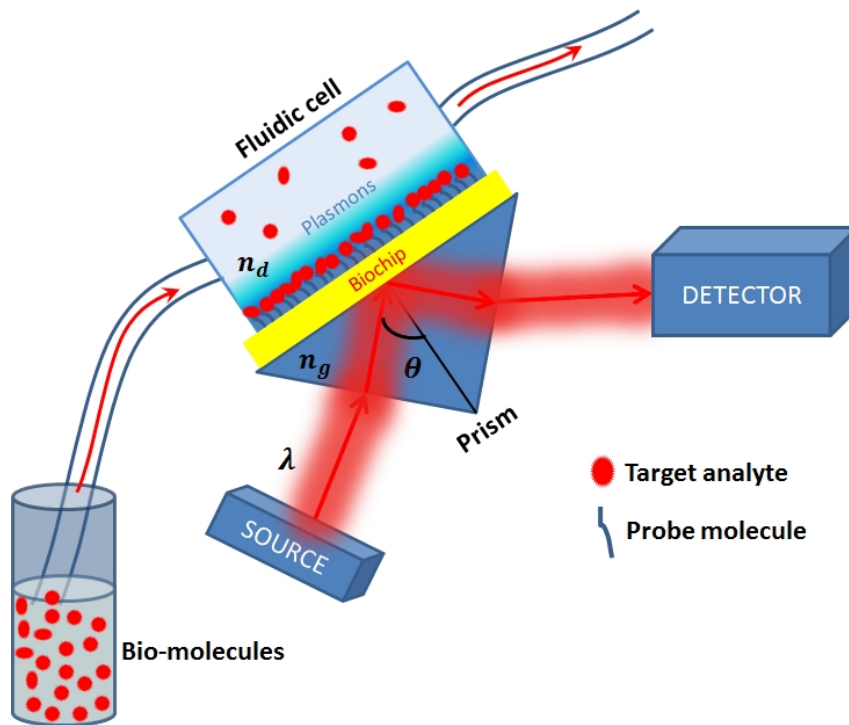


Figure 3.3: The scheme of a conventional SPR detector using a prism to couple the incident light to the PSP. The source is generally tuned over a range of wavelengths ( $\lambda$ ). The detector is used to measure the reflectivity from the biochip-prism surface. The bio-chip is functionalized with the probe molecules and the target analyte is introduced in the fluidic cell. The SPR detector can study the interaction between the probe molecules and the target analyte.

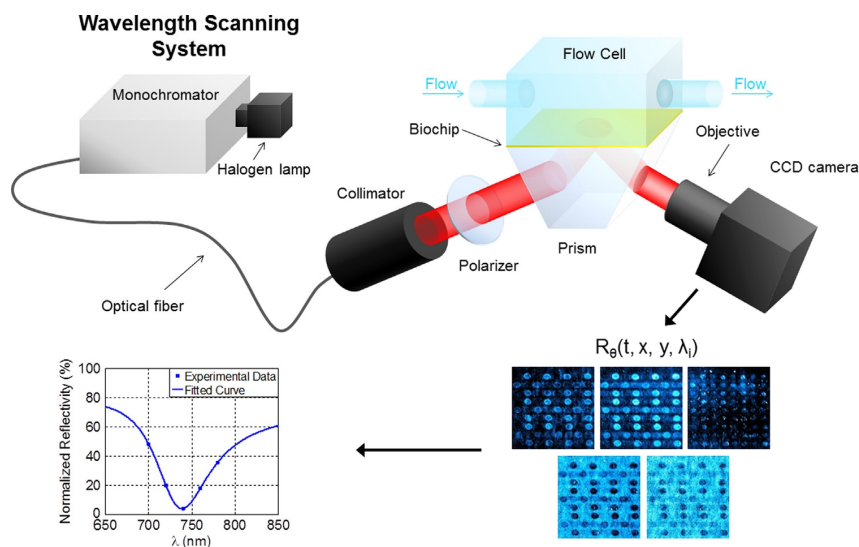


Figure 3.4: A.Sereda et al (2014) [35]: SPR imaging setup in Kretschmann configuration. The source is a halogen lamp with a monochromator to choose the wavelength of interrogation. A polarizer is used to choose the polarization of the incident collimated beam. A motorized platform is used to scan the angle of incidence. A CCD camera records the reflection from the bio-chip surface at different wavelength and internal angle. Using this configuration we can extract the complete image of each point of the biochip surface.

configuration we can image the entire bio-chip surface and thus have complete access to the reflectivity coefficients for all wavelength and internal angle at each point.

A complete spectro-angular map of the reflectivity can be extracted using the setup described above. For a simple bio-chip comprising of a 50nm gold film the variation of the reflectivity as a function of wavelength and  $k_x/k_0 = n_g \sin(\theta)$  is shown in figure 3.5. The value of refractive index of the BK7 prism used was taken as 1.513. This was verified by ellipsometric measurements. Henceforth we will write  $k_x/k_0 = (k_{//}/k_0)$  following the notation commonly used for waveguides. The details and benefits of this notation will be explained in later sections. We see a drop in reflectivity at certain wavelengths and internal angle( $k_{//}/k_0$ ) which correspond to the dispersion of the PSP as given by equation 3.1. This is the direct demonstration of the excitation of plasmonic modes in an experimental setup. The complete reflectivity variation as a function of wavelength and ( $k_{//}/k_0$ ) can be considered directly to be the dispersion map of the plasmonic modes present in the system. This work consists of such detailed dispersion maps of different structures and the understanding of the plasmonic modes that can be identified in such a map.

### 3.2.1 Interrogation methods for SPR detectors

On the aspect of bio-sensing as mentioned earlier, a change in the local refractive index manifest in a shift of the resonance condition of the PSP and thus a shift in the position of reflectivity minimum in the dispersion map. In figure 3.6 we have shown the variation of reflectivity as a function of wavelength and ( $k_{//}/k_0$ ). The measurement was done with water injected into the fluidic cell. Then a sucrose solution was injected in the fluidic cell which manifests a change in refractive index of the medium (a change of around  $2 \times 10^{-3}$  RIU is expected). We see that the position of the reflectivity minimum shifts with a change in refractive index of the medium in the fluidic cell. This offers three different methods of interrogations for SPR detectors

**(a) Reflectivity interrogation:** Due to the shift of the PSP dispersion condition in wavelength and internal angle, there is a change in the absolute reflectivity close to the resonance position. This reflectivity change ( $\Delta R$ ) is proportional to the changes in refractive index of the surrounding medium. With present available SPR detectors a refractive index variation as low as  $10^{-6}$  RIU can be measured. The advantage of reflectivity interrogation method is that it does not require a scan over the wavelength or angle of incidence and thus can be used to measure real time refractive index changes. An image with a digital camera, of the biochip surface at a given wavelength and internal angle (close to the resonance position) is sufficient to measure  $\Delta R$ . However the main disadvantage of this method is the dispersion of the absolute reflectivity, due to the inhomogeneity of the dielectric above the metallic film. This is caused by different experimental conditions and inhomogeneity of the biochip functionalization method. Thus this method is not very robust to detect really small refractive index changes.

**(b) Spectral interrogation:** The shift in the resonance wavelength ( $\Delta \lambda$ ) at a fixed internal angle can also be used to probe refractive index changes in the fluidic cell. This method is more robust than the reflectivity interrogation as  $\Delta \lambda$  does not depend on the inhomogeneity over the biochip surface and is also less sensitive to noise in the light source used. However it is not possible to extract  $\Delta \lambda$  in real time and have SPR imaging capabilities at the same time. Measurement of  $\Delta \lambda$  requires post processing by spectroscopic measurements. Thus real time spectral interrogation can be carried out using a spectrometer coupled to the camera, but a complete image of the biochip surface cannot be recorded.



For a conventional biochip which comprises of a thin gold film, the reflectivity dip can be fitted to a Lorentzian distribution and the spectral position of the minimum reflectivity can be calculated directly to evaluate  $\Delta\lambda$ . This however may not be adapted, when studying nano-structured biochips, where a simple Lorentzian distribution to fit the reflectivity spectra is no longer applicable. This will be treated elsewhere in this work.

**(c) Angular interrogation:** This is similar to the spectral interrogation and thus the advantages and drawbacks of the method is same as those of spectral interrogation. The incident wavelength is fixed and the shift in the internal angle ( $\Delta\theta$ ) satisfying the resonance condition is measured. In figure 3.6 we have shown the shift in  $(k_{//}/k_0)$  at a fixed wavelength. This is proportional to the shift in internal angle as  $(k_{//}/k_0) = n_g \sin(\theta)$ . It has been shown that resolutions upto  $10^{-7}$  RIU can be achieved by SPR detectors using spectral or angular interrogation.

Recent works have also demonstrated SPR detection with phase modulation. The reflection at an interface is generally associated with phase shift of the reflected field. In case of a flat metal surface, the phase of the reflected field in TM configuration undergoes an abrupt phase shift of upto  $2\pi$  when the PSP is excited. This has inspired researchers to use interferometric configurations to measure the phase shift ( $\Delta\Phi$ ) associated with the excitation of surface plasmons. In such configurations the shift in phase is observed as spatial displacement of the interference fringes. In figure 3.7 we have shown the calculated reflectivity and the phase of the reflected field for a thin gold film of 50nm in the configuration similar to that shown in figure 3.5. The calculation was done by the Rouard method described in section 6.1. We see that the phase jump is rather sharper compared to the SPR reflectivity dip width in spectral or angular interrogation. This has proved to enhance the detection limit of SPR sensors and resolutions of upto  $10^{-8}$  RIU has been obtained using phase interrogation. However due to the sharp nature of the phase jump, such a detection method is vulnerable to temperature and index fluctuations of the fluidic cell and has a very limited dynamic range of detection. For this work we will not use the phase interrogation method.

### 3.3 Molecular detection using SPR detectors

So far we have introduced the basic principle of SPR detectors and the various methods for detection of refractive index changes in the medium surrounding the bio-chip. The inherent detection limit of the conventional bio-chip using a thin metallic film and structuration of the bio-chip surface is the motivation for this work and will be described in details in part IV. However the main application of this work is not to detect bulk refractive index changes around the bio-chip surface but detection of specific molecular interactions close to the bio-chip surface. In this section we will present some of such bio-molecular interaction which SPR detectors are capable of sensing.

Depending on the method of interrogation used, the signal of a SPR detector is a the change in reflectivity ( $\Delta R$ ), shift in resonance wavelength ( $\Delta\lambda$  measured in nm) or shift in angle of incidence ( $\Delta\theta$  measured in  $^\circ$ ). The signal can be normalized to the change in refractive index (RIU) and the sensitivity used to characterize the sensor is generally expressed in terms of  $/RIU$  such as  $nm/RIU$  for spectral shift or  $^\circ/RIU$  for angular shift.

Another major application of the SPR detection systems is SPR affinity biosensing, which studies the interaction of a biorecognition element with a specific analyte [36, 37]. The binding occurs within a thin layer of a few nanometers above the bio-chip surface. The signal for such applications is normalized to the size of the analyte bound to the biochip surface. Thus the sensitivity used to characterize such detection is

generally expressed in terms of analyte thickness (in nm) such as  $nm/nm$  for spectral shift or  $^{\circ}/nm$  for angular shift.

For SPR affinity detection, one of the molecules is generally immobilized on the bio-chip surface. We will call this the probe molecule. The analyte (or target) molecule is generally prepared in a liquid solution and injected into the fluidic cell. The choice of the target and probe molecules and the immobilization of the probe on the biochip surface plays a critical role in the performance of SPR affinity biosensors. Thus such systems require an additional step of surface functionalization to immobilize the probe. Such detection offers binding kinetics measurement and real time monitoring of biomolecular recognition.

The main advantage of using SPR for affinity detection, lies in the fact that SPR detection is sensitive only within a few hundreds of nanometers from the biochip surface, depending on the penetration depth of the electric field into the dielectric as shown in section 2.1.4. Thus such detection is not affected by the inhomogeneity or fluctuations in the bulk medium of the fluidic cell. However any molecule binding to the biochip surface can cause a variation in the signal measured. Thus the biochip surface must be functionalized to maximize the specific binding of the analyte molecules on the sensor surface and at the same time prevent the binding of non-specific molecules which may cause a spurious signal.

Four main types of detection schemes that govern affinity bio-sensing are shown in figure 3.8.

**(a) Direct detection:** For this method the probes are immobilized such that the entire biochip surface can be covered, thus inhibiting non-specific binding of other molecules. The binding target is introduced in the fluidic cell and they are directly captured by the probe molecules. This method applies when the probes are such that they specifically bind to the analyte molecules and repel other non-specific molecules. Once binding occurs the analyte comes within the evanescent field of the plasmons and thus cause a detectable signal.

**(b) Indirect detection:** This method may involve two types of probe molecules, one that can bind to the target molecules and the other that undergoes modification in their chemical structure and thus have decreased biomolecular affinity to the analyte. Sometimes specific probe molecules are not available for the analyte molecule and thus the probes used can capture all types of molecules present in the solution. To solve for non-specific binding a second step of detection process is involved where the probe molecules of the same type or different, are reintroduced into the fluidic cell and the binding of probe-analyte-probe is followed to measure the bio-molecular interactions.

**(c) Detection by competition:** This method is used when the analyte molecules have very low molecular mass and thus the signal caused by their binding to the probe is below the detection limit of the system. In this case another molecule with higher molecular mass ( $M$ ) which binds specifically to the analyte is introduced and the binding event of probe-analyte- $M$  is studied. The presence of the molecule with higher molecular mass assures a signal above the detection limit of the system.

**(d) Detection by inhibition:** This method like the previous one is used for analyte molecules which cause signals lower than the limit of detection during the binding event. In this case if possible the analyte is directly functionalized on the bio-chip surface and probe molecules with larger molecular mass is introduced in the fluidic and the binding of analyte-probe is measured.

SPR affinity biosensors have been implemented for the detection of various bio-molecule groups such as DNA, RNA and peptides, proteins, immunoassays and cell studies. Chemical functionalization plays a major role in such detection techniques and involves specific choice of probe molecules for each measured analyte. Rigorous steps are also involved in passivation of the metallic surface to avoid non-specific

binding. This work is not directly involved in the surface chemistry used for such detection and details of the chemical methods used will be avoided. However one example of probe immobilization on a gold biochip surface as presented by J. Spadavecchia et al [38] is shown in figure 3.9 and will be briefly described.

The aim of such surface chemistry is

(a) passivation of the metallic surface to prevent non specific absorption of target molecules on the surface.

(b) to facilitate the specific absorption of probe molecules on the surface

(c) prevent modifications (as much as possible) of the bio-molecular interaction process of the probe and the analyte

(d) in some cases, help the regeneration of the unbound target molecules.

The various steps in surface chemistry (as per the example shown in figure 3.9) are described below.

(1) The first step is to functionalize a SAM (self-assembled monolayer) on the metallic surface, in this case the thiol (HS). This layer helps in the passivation of the metallic surface and facilitates the binding of a reactive chemical group (in this case  $-NH_2$ ). In the cited example this is done by binding a short chain of -mercaptoethylamine (cysteamine) to the gold.

(2) The next step is to activate the chemical group ( $-NH_2$ ), in this example done by covalent attachment of cross-linked 1,4 phenylenediisothiocyanate (PDC).

(3) The final step of surface chemistry is to bind the probe molecules to the activated chemical group. For the example this is done by a neutravidin layer that allows binding of the biotinylated probes.

Such surface chemistry is a long process and generally takes more than a day of preparation time. However the process is robust in terms of reproducibility and can be used for various bio-molecular binding processes.

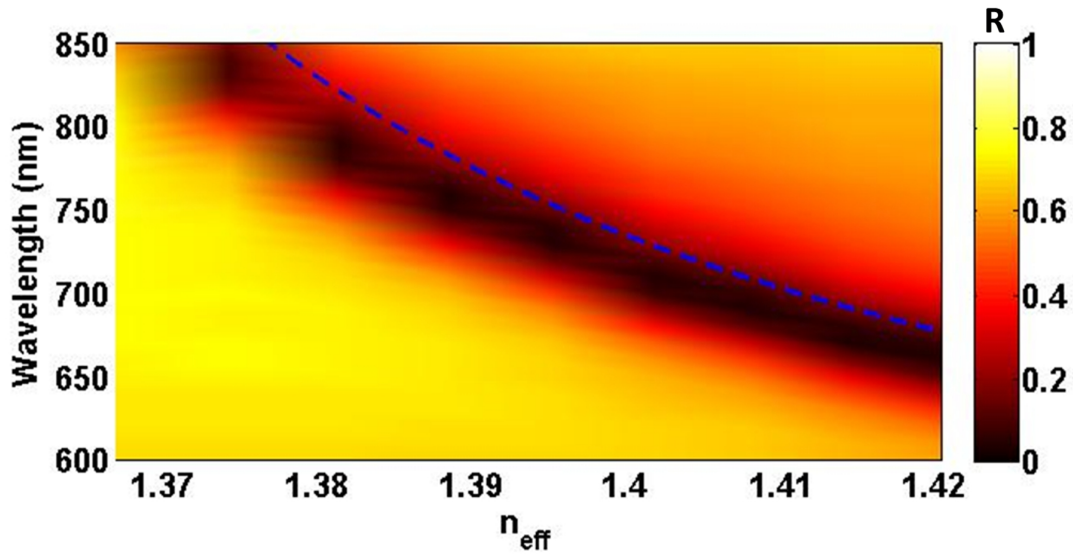


Figure 3.5: The measured reflectivity ( $R$ ) of a 50nm thin gold film with wavelength and  $(k_{//}/k_0) = n_g \sin(\theta)$  as obtained by the SPR imaging setup. The prism is of BK7 glass and the medium in the fluidic cell is water. We see a drop in reflectivity at certain values of wavelength and internal angle ( $(k_{//}/k_0)$ ) which correspond to the dispersion of the PSP as given by equation 3.1 (blue dashed).

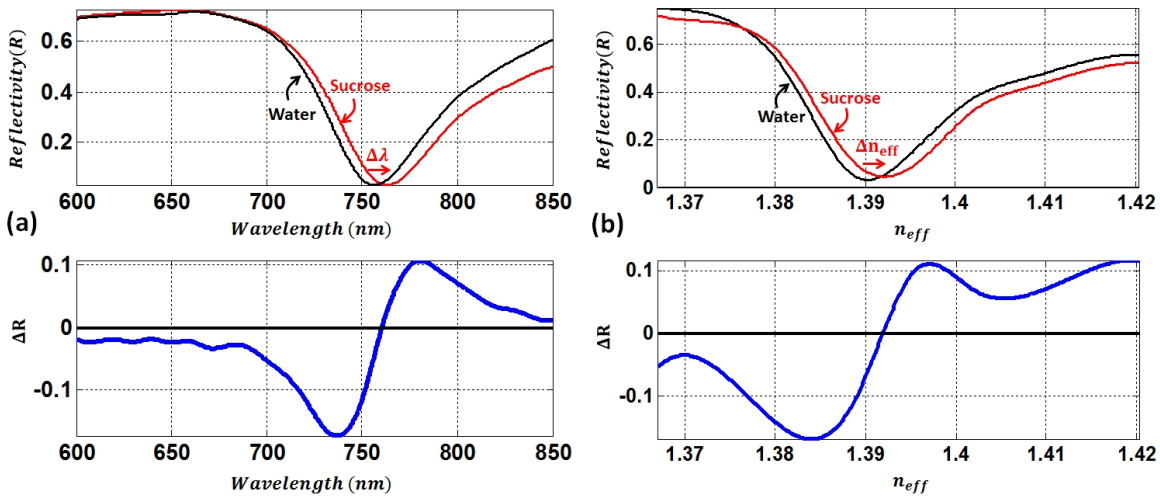


Figure 3.6: The various interrogation methods for SPR detection: (a) The variation of reflectivity as a function of wavelength ( $\lambda$ ) for  $(k_{//}/k_0) = 1.39$  ( $\theta = 66.6^\circ$ ) for the fluidic cell containing water (black) and the same containing sucrose (red). An expected refractive index change between water and sucrose is  $2 \times 10^{-3}$  RIU. The reflectivity difference ( $\Delta R$ ) for water and sucrose solution as a function of wavelength is also shown (blue). (b) The variation of reflectivity as a function of  $(k_{//}/k_0)$  ( $n_g \sin(\theta)$ ) for  $\lambda = 750\text{nm}$  for the fluidic cell containing water (black) and the same containing sucrose (red). The reflectivity difference ( $\Delta R$ ) for water and sucrose solution as a function of  $(k_{//}/k_0)$  is also shown (blue).

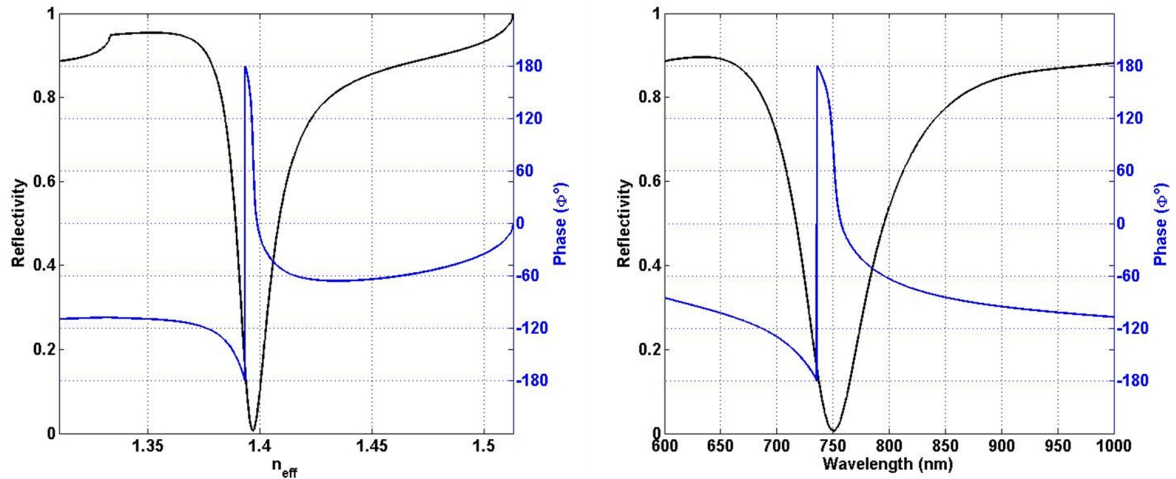


Figure 3.7: The calculated reflectivity (R)(black) and phase of the reflected field (blue) of a 50nm gold film as a function of  $(k_{//}/k_0)$  for incident wavelength of 750nm (left). The same as a function of wavelength for angle of incidence of  $67^\circ$  ( $(k_{//}/k_0) = 1.39$ ) (right).

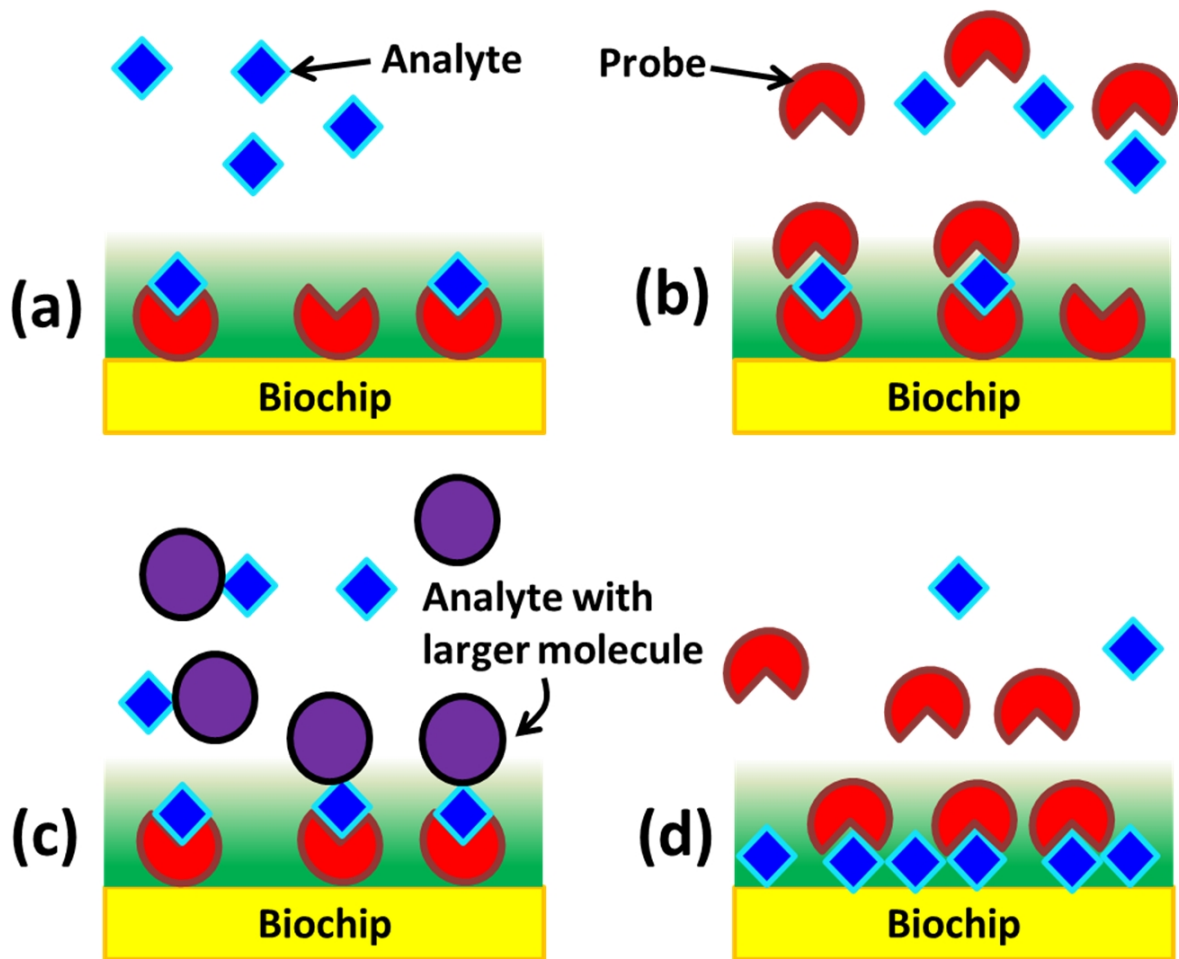


Figure 3.8: The four main types of detection formats in SPR affinity biosensors: (a) Direct detection (b) Indirect detection (c) Detection by competition (d) Detection by inhibition. The green background represents the decaying evanescent field caused by the plasmon mode.

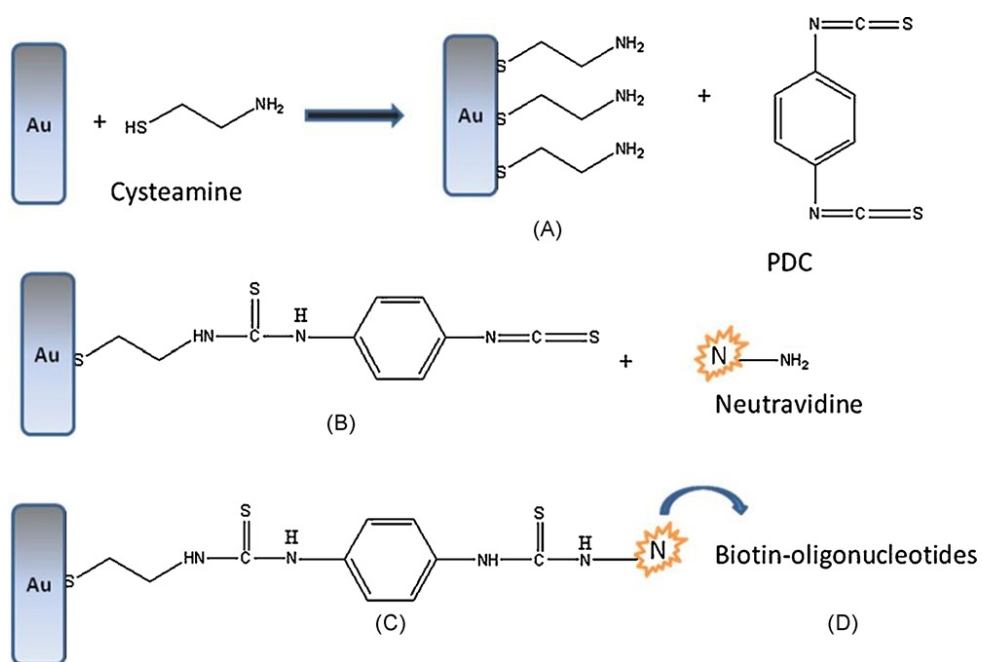


Figure 3.9: J. Spadavecchia et al (2009)[38]: Structural reaction mechanism for the covalent attachment of neutravidin to a gold surface.

## Detectors using particle plasmons

---

Localized plasmon mode was introduced in section 2.2. Photon coupling to the localized oscillation of electron charge density at the surface of metallic particles induce a strong electromagnetic field on the surface that decay within a few nano-meters into the dielectric medium surrounding the particle. This LSP mode like the PSP can be used to measure refractive index variations of the surrounding medium. Coupling of the incident light to the LSP modes in metallic particles can be achieved directly and do not need specific coupling configurations like in the case of the PSP. However the dispersion and the resonance frequencies of the LSP can be sometimes complicated to calculate and depend largely on the metallic particle size, shape and distribution. In this chapter we will present some examples of bio-detectors that use the phenomenon of photon-LSP coupling and the consequent optical approach used to realize them.

### 4.1 Detection based on localized plasmon resonance

Single nano-particle based nano-probes have found various applications in sensing local chemical changes within nanometric scales such as molecular-binding events, gas detection, catalytic reactions, in vivo imaging, therapy monitoring and so on [39, 40, 41, 42, 43, 44]. The main advantage of nano-particles is the strong confinement of the evanescent field induced by the plasmon resonance. They are almost insensitive to bulk drift that occur beyond the penetration depth of the evanescent field. The absorption and scattering cross-sections of metallic nano-particles can be enhanced up to a million times compared to the fluorescence cross-section of a fluorescein molecule. Moreover the fact that metallic nano-particles do not undergo photo-bleaching makes them more attractive for spectroscopy based bio-detections.

Most of the localized plasmon resonance (LSPR) detectors are based on spectroscopic measurements which probe the extinction spectra (absorption or scattering peaks in the spectrum) of an incoming light beam. The resonance frequency shift in such an extinction spectra can give insight on molecular events occurring in the medium surrounding the nano-particles. Various particle sizes ranging from a few nano-meters to 100s of nano-meters, various shapes starting from a simple sphere to even weird particle geometries and materials such a noble metals, heavy metals and alloys have been fabricated for this purpose [45, 46, 47, 48]. Silver nanoparticles exhibit the strongest absorption and scattering characteristics among all metals. However oxidization of silver makes it less attractive when chemical functionalization of the nano-particles are involved. Gold given its bio-compatibility and the possibility of thiol-Au functionalization and other types of bio-chemical conjugations, makes it the most common metal

for LSPR based biosensors.

Y.Wang et al [49] in a recent review presented an overview of various nano-particles fabricated for surface enhanced raman scattering (SERS) detection. SERS will be explained in the following section (4.2). Figure 4.1 taken from the above mentioned review gives an idea of the range of nano-particle types which has been under research and the diversity of the extinction spectra that can be observed in such nano-particles.

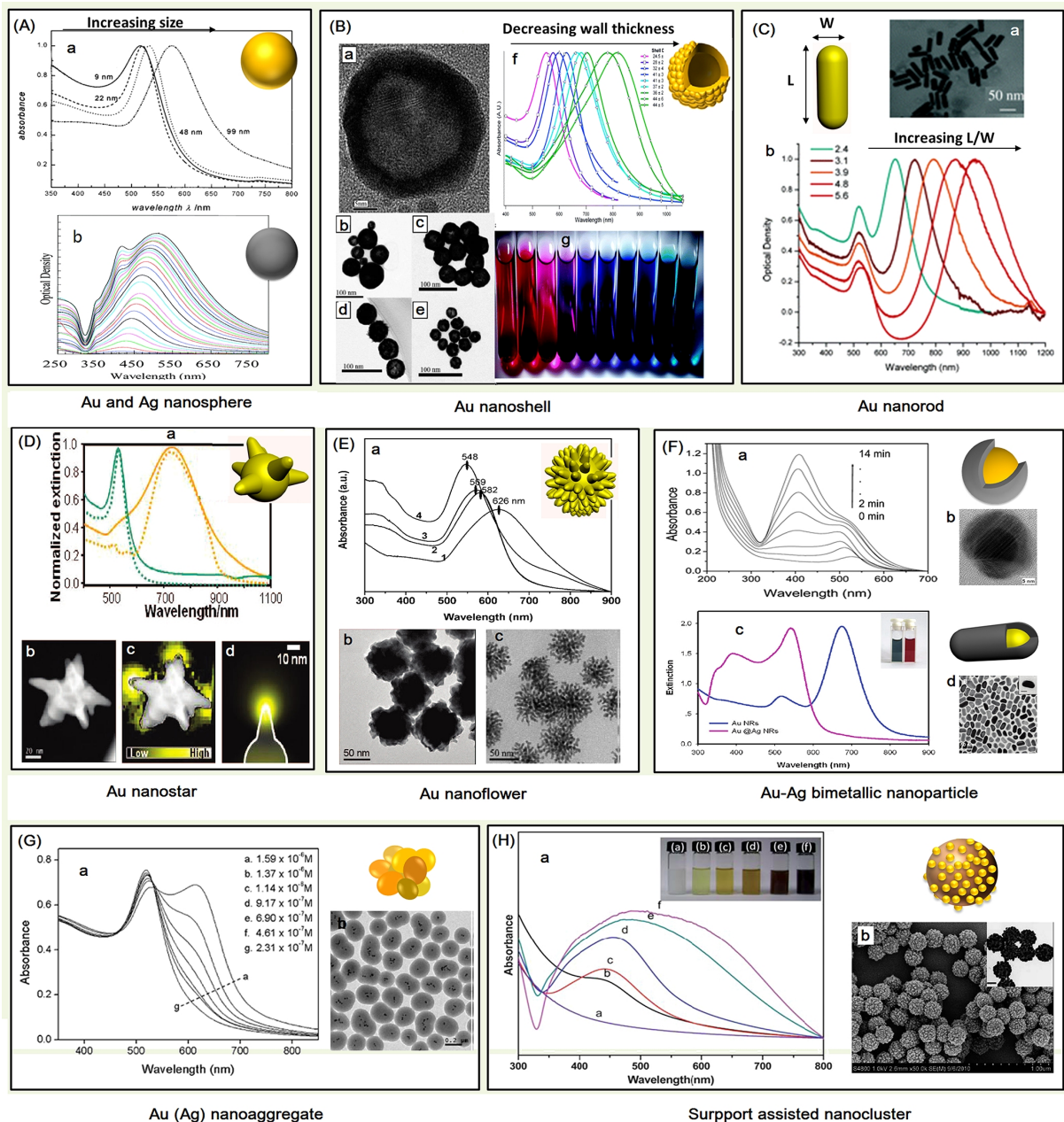


Figure 4.1: Y.Wang et al (2013)[49]: Nano-substrates for synthesis of SERS tags and their extinction spectra (absorbance).



### 4.1.1 Synthesis and functionalization of metal nano-particles

The most common chemical process to synthesize colloidal gold nano-particles was introduced by J. Turkevich et al. in 1951 [50] and further developed by G. Frens in the 1970s [51, 52]. The process follows the reduction of chloroauric acid by sodium citrate to form Au ions. The citrate acts both as a reducing agent and a capping agent which inhibits the gold nano-particles to aggregate into larger particles. The process also offers stability and quasi-spherical nano-particles ranging from 8-120nm in size can be synthesized by varying the citrate/Au ratio. With increasing demand of metal nano-particles in sensing applications various other chemical methods have been developed by which colloidal nano-particles can be synthesized with controlled homogeneity in shape, size and surface properties. Physical processes such as lithography, vapor deposition, laser ablation and so on have also been used for the purpose.

For biochemical applications the nano-particles thus synthesized needs to be functionalized. Different methods of functionalization for gold nano-particles was presented in the review by R.A.Sperling et al (2008) [53] and further discussed by G.Doria et al (2012) [54]. Table 4.1 taken from the later review shows the various types of conjugations between bio-molecules and metallic nano-particles and their respective advantages and drawbacks.

Table 4.1: G.Doria et al (2012) [54]: Types of nano-particle functionalizations and their respective advantages and drawbacks.

Type of conjugation	Advantage	Drawbacks
Electrostatic interactions (e.g., adsorption of negative charged DNA to positive charged gold NP)	- Very simple and straightforward to perform	Restricted to opposite charged biomolecules and NPs; - Very sensitive to environmental properties (e.g., pH, ionic strength, etc.); - Weak functionalization.
Chemisorption (e.g., quasi-covalent binding of thiolfunctionalized biomolecule to gold NP)	- Allows oriented functionalization; - Very robust functionalization.	- Requires NPs with capping agents with weaker adsorption than the derivatization moiety; - Usually requires modification of the biomolecule; - Subject to interference by other chemical groups available for adsorption within the biomolecule; - Affected by chemical degradation and surface oxidation of some NPs (e.g., silver).
Affinity-based (e.g., His-tag protein binding to Ni-NTA derivatized gold NP)	- Allows oriented functionalization; - Very straightforward binding between affinity pairs.	- Requires modification of both NPs and biomolecules with an affinity pair; - Limited to availability of suitable binding affinity pairs.

### 4.1.2 LSPR detector configurations

As mentioned earlier LSPR detectors are based on direct spectroscopic measurements of the absorption or scattering by the functionalized nano-particles. Gold or silver nano-particles undergo LSPR in the near UV to visible part of the spectrum. Thus the colloidal solutions of such nano-particles are generally colored depending on the absorption band, and can help in direct colorimetry measurements. In figure 4.2 the extinction spectrum of silver nano-disks and nano-prisms are shown with different sizes to give an idea of the range over which the LSPR resonance frequencies can be tuned for such nano-particles. Generally for single nano-particles as can be seen from equation 2.8 the size dependence of the resonance frequency stems from the depolarization factor  $\chi$ . It has been widely reported that resonance frequencies of symmetrical nano-particles undergo a red-shift with an increase in size. However for particles with unsymmetrical geometries the tendency depends on the aspect ratio of the particles and the polarization of the incident light. We will describe the various phenomenon which affect the resonance frequencies of nano-particles in details in part IV and it forms an important part of this work.

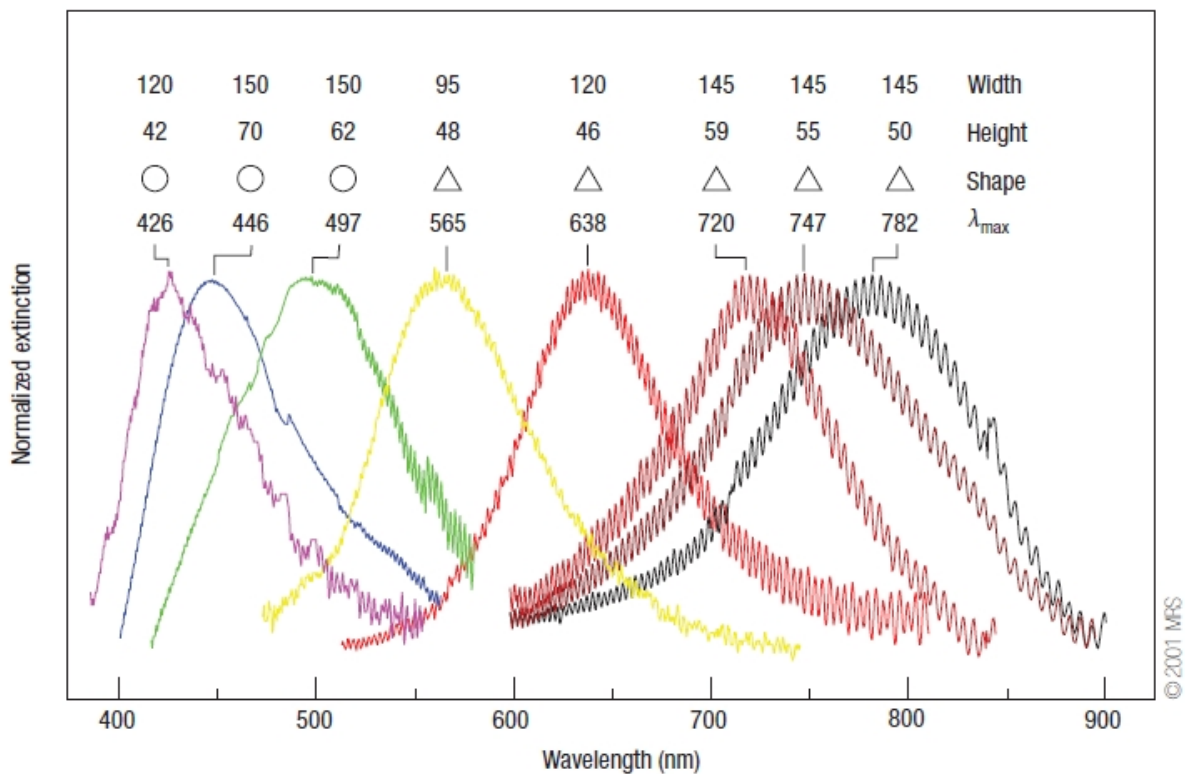


Figure 4.2: J.N.Anker et al (2008) [55]: The LSPR extinction spectrum of silver nano-disks and nano-prisms of different sizes.

In most detectors (apart from in-vivo measurements) the colloidal nano-particles are deposited on a substrate on which spectral measurements are carried out. Different optical instrumentation geometries have been tried for this purpose. Most optical instruments consist of a broad band light source, the sample holder and a detector. For transparent samples the direct transmission spectra are recorded. For opaque samples however, optical geometries to record the reflection spectra are used. Mostly bright field microscopy techniques are used to record the reflection or transmission spectra. Dark-field scattering microscopy techniques are used when only a small portion of the sample is needed to be studied. In

such configurations only the scattered field from the sample is received for spectroscopic measurements. Figure 4.3 shows the four different types of instrumentation and optical geometries commonly used for LSPR detectors. Apart from them, different groups have also tried illuminating the nano-particles using waveguides or optical fibers and then recording the scattered field using dark-field microscopy techniques.

Various research groups have reported different bio-molecule detection techniques [56, 57, 58, 59]. LSPR can be used to detect bulk refractive index changes of the medium surrounding the nano-particles by recording the shift in resonance wavelength [60, 61]. However this technique is much less sensitive for this purpose as compared to the SPR technique mentioned in chapter 3. In fact the bulk index sensitivity of metal nano-particles using LSPR is atleast 3 times smaller as compared to that of an uniform metallic film using the PSP. This can be attributed to the fact that the penetration depth of the PSP is much larger than the LSP. This will be discussed in details in part IV. However this very principle is useful when using LSPR detectors for affinity based biosensors as introduced in section 3.3 as they offer robust detection almost insensitive to bulk refractive index or temperature drifts in the bulk solution. In table 4.2 we have given a brief overview of different reported research using LSPR for affinity detection.

Table 4.2: Various LSPR affinity biosensors and the type of detection carried out.

Type of detection	Optical Configuration and nano-particle geometry	Reference
Immunoassay: Antibody-Antigen	Transmission bright field mode : Gold Nanorods with average length of 50nm and 15nm in diameter	K.M. Mayer et al (2008)[62]
SAM formation on single nano-particles with zepto-mole sensitivity	Dark field microscopy: Silver nano-spheres, nano-triangles and nano-rods.	A.D.McFarland et al (2003) [63]
Length of DNA measured with subnanometre axial resolution	Dark field microscopy in transmission mode: DNA conjugated to gold nano-particles; LSPR shift is proportional to DNA length	G.L.Liu et al (2006) [64]
Demonstrated Al as a potential nanoplasmonic material in UV-Visible part of the spectrum	UV Dark-Field Microspectroscopy with Al nano-disks ranging from 70-180nm. Also studied the effect of Al native oxide formation on the plasmonic behavior.	M.W. Knight et al (2014) [65]
Sequence-specific DNA sensor: detection of DNA molecules complementary to a ssDNA oligonucleotide probe	Dark field optical microscopy in transmission mode with gold nano-triangles of average size of 100nm and thickness of 17nm.	L.Soares et al (2014) [66]
Tracking individual gold nanoparticles in live cells	Bright field transmission microscopy used to track 5nm gold nano-particles in living cells	D.Lasne et al (2006) [67]

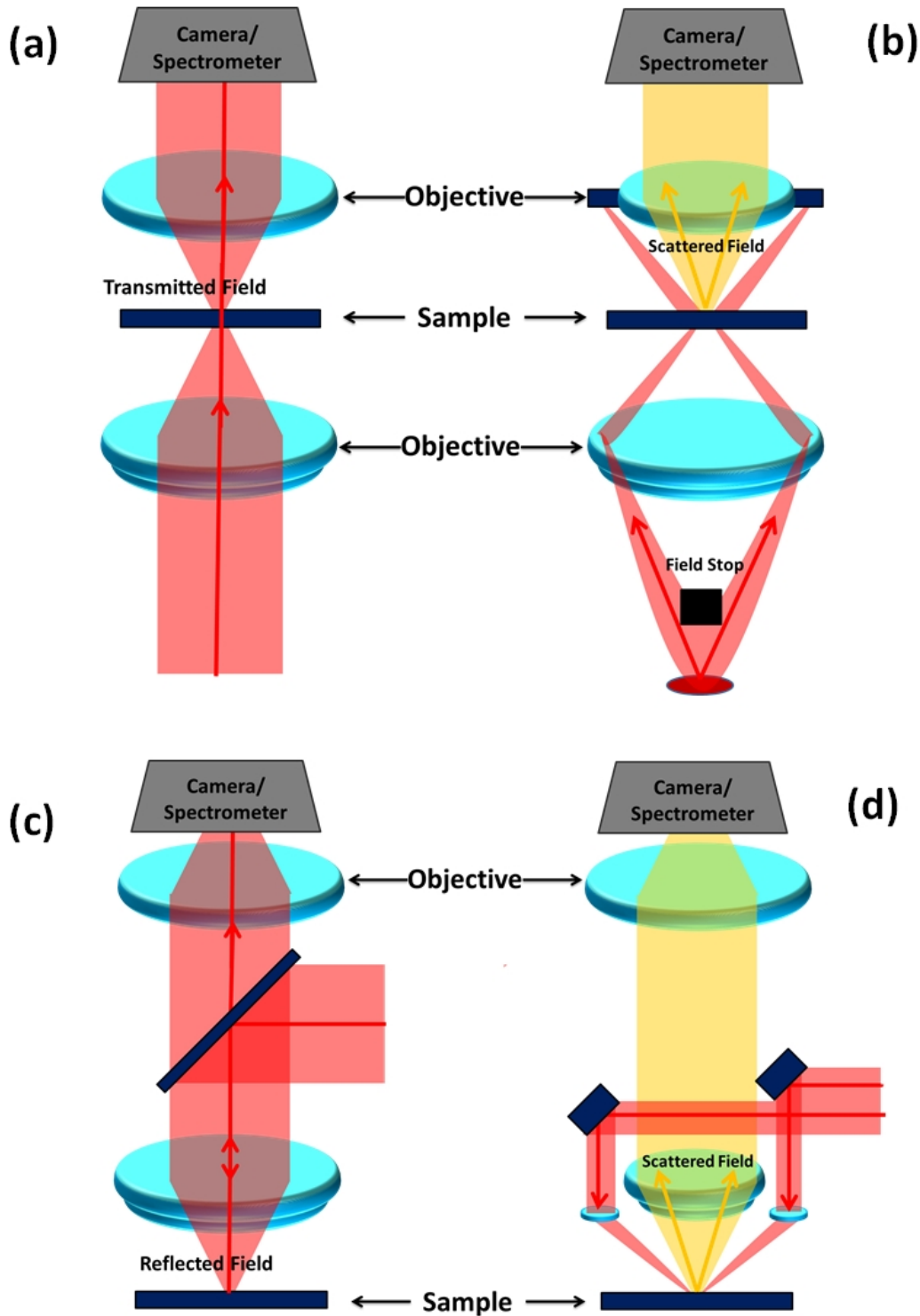


Figure 4.3: Optical geometries used for LSPR detection: (a) Bright field transmission mode using a broad band source and an objective to illuminate the sample. Light scattered from the sample is recorded by a spectrometer to obtain the extinction spectra. (b) Dark field microscopy in transmission mode where only the scattered field transmitted by the sample is recorded. (c) Bright field reflection mode where the same objective is used to illuminate the sample and collect the reflected field. (d) Dark field microscopy in the reflection mode where the same objective is used to illuminate the sample and collect the scattered field reflected from the sample.

## 4.2 Surface enhanced Raman scattering

Inelastic scattering of light by matter was predicted by Adolf Smekal in 1923 [68]. In 1928, C.V.Raman [69] and K. S. Krishnan (and independently by G.Landsberg and L.Mandelstam [70]) experimentally demonstrated that a small portion of white light changes frequency when scattered by a fluid and for this work, C.V.Raman received the Nobel Prize in Physics in 1930. Ever since this first demonstration, the phenomenon which takes his name has been reported widely and used in spectroscopy to identify molecules by their unique Raman spectral fingerprint.

For elastic scattering (called Rayleigh scattering) of photons by particles smaller than the wavelength of light, there is no shift in the frequency of the incoming photon. The Raman effect is caused by the inelastic scattering of a photon by the molecule owing to a vibrational or rotational mode of the later. In such an inelastic scattering the energy of the fundamental vibration ( $h\nu_m$ ) is transferred to the photon and thus the incoming photon undergoes a change in energy and a consequent shift in frequency. There are two types of scattering process that can take place when a photon with energy  $h\nu_p$  is incident on the molecule. Firstly the photon can excite a vibrational mode of the molecule and thus loosing energy ( $h\nu_p - h\nu_m$ ). This process is called the Stokes scattering. The second possibility occurs if the photon gains energy ( $h\nu_p + h\nu_m$ ) owing to the de-excitation of a vibrational mode of the molecule. This is called the anti-Stokes scattering. The two possible Raman scattered frequencies are therefore  $\nu_s = \nu_p - \nu_m$  and  $\nu_{as} = \nu_p + \nu_m$  for Stokes and anti-Stokes scattering respectively. The energy diagram of a molecule undergoing Raman scattering is shown in figure 4.4.

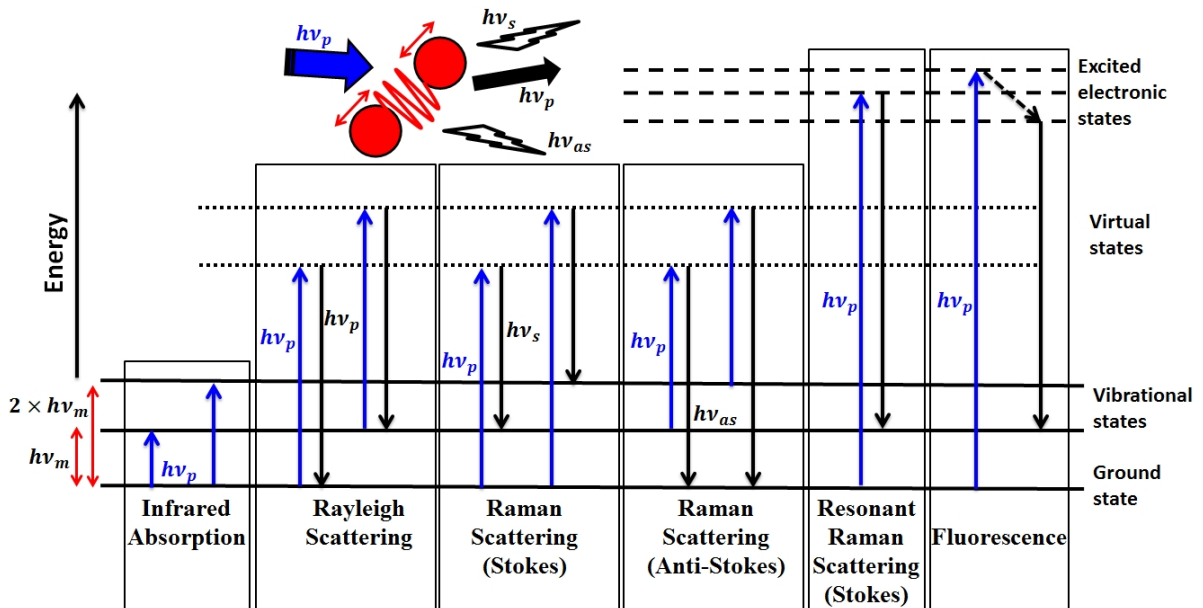


Figure 4.4: The Jablonski energy diagram of a molecule showing different scattering processes. For simple IR absorption a photon with energy  $h\nu_p$  is absorbed. For the Rayleigh scattering the photon undergoes elastic scattering without a shift in frequency. For Raman scattering there is a shift in frequency, proportional to the energy of the vibrational band ( $h\nu_m$ ). Resonant Raman scattering occurs when the molecule is excited to one of the electronic states, followed by an inelastic scattering process. The process of fluorescence is also shown.

The schematic of the fluorescence process is also shown in figure 4.4. Due to the non-elastic electron relaxation process in the case of fluorescence, the spectrum is relatively broad as compared to the sharp

spectrum of Raman scattering. This thus offers a much detailed analysis of the molecule under study. Raman spectroscopy is also more robust compared to IR absorption as the shift in frequency is not affected by background absorption. However the Raman process occurs through transitions between the vibrational states and virtual states of the molecule and thus is not a resonant process. Thus the efficiency of Raman scattering is much lower as compared to fluorescence [71]. This is even true for resonant Raman scattering which takes place via electronic transition states. Therefore with a scattering cross-section in the order of  $10^{-28} - 10^{-30} \text{cm}^{-2}$  per molecule per steradian, Raman scattering have not really been useful for molecular detection till the 1970s.

In 1974 Fleischmann et al [73] reported a huge increase of the Raman signal while studying pyridine molecule using rough silver electrodes. This was followed by a series of publications which reported the enhancement of Raman scattering efficiency when the molecules under study were adsorbed on roughened metallic surfaces [74, 75]. One such spectrum is shown in figure 4.5. An enhancement of the order of  $10^5$  was reported and thus paved way for the research of Surface Enhanced Raman Scattering (SERS) [76, 77]. Later similar enhancements were observed for metal nano-particles and soon the effect was attributed to the possibility of plasmon resonance in metallic particles [78, 79]. Thus Raman effect which is somewhat a chemical phenomenon depending on molecular properties, now became a research interest in the field of photonics and optical properties of metals. In the next section we will discuss briefly the known causes for the enhancement of Raman scattering by metallic surfaces.

#### 4.2.1 Role of surface plasmons in SERS

Surface enhanced Raman scattering (SERS) is a powerful tool used to identify molecular species using their Raman fingerprint [80, 81]. Recent development in the domain has reported an enhancement of the Raman response of molecules by a factor of up to  $10^7$  when they in the vicinity of rough metallic surfaces [82, 83, 84, 85]. A complete understanding of this enhancement is still eluding [86, 87]. However researches have pointed out that such enhancements may be related to local chemical effects due to the interaction of the analyte with metal surfaces [88, 89]. This chemical enhancement is mainly due to the modification of the electronic structure of the molecule by complex charge transfer between the molecule and the metal. Chemical enhancement can also be a result of the modification of the polarizability of the molecule and thus modifying its Raman response. Such effects though reported and studied over sometime, cannot attribute to an enhancement factor of more than  $10^2$  [90, 91].

A more prominent reason for SERS has been found to be the enhancement of the local electromagnetic field close to the metallic structures which in turn enhance the Raman response of the molecules [92, 93, 94]. This process can be explained in two steps as shown in figure 4.6.

The incident electromagnetic field ( $E_{inc}$ ) is enhanced by the metallic structure owing to the excitation of surface plasmon resonance modes. This enhancement ( $M(\nu_i)$ ) depends of the localized plasmon mode excited and thus on the type of metallic structure. However as commonly known for LSP, the enhancement is generally larger at sharp edges and with surfaces with roughness. This enhancement also depends on the incident frequency  $\nu_i$  and its proximity to the LSP resonance frequency. This enhanced field ( $E_l$ ) is scattered by the molecule at the Raman shifted frequency  $\nu_s$ . The scattered field is re-radiated by the metallic structure and it also undergoes an enhancement owing to the plasmon resonance, however this time at the Raman shifted frequency ( $M(\nu_s)$ ). The field is then emitted to the far field and the SERS intensity recorded ( $I_{SERS}$ ) is enhanced by a factor roughly proportional to  $M(\nu_i)^2 M(\nu_s)^2$ .

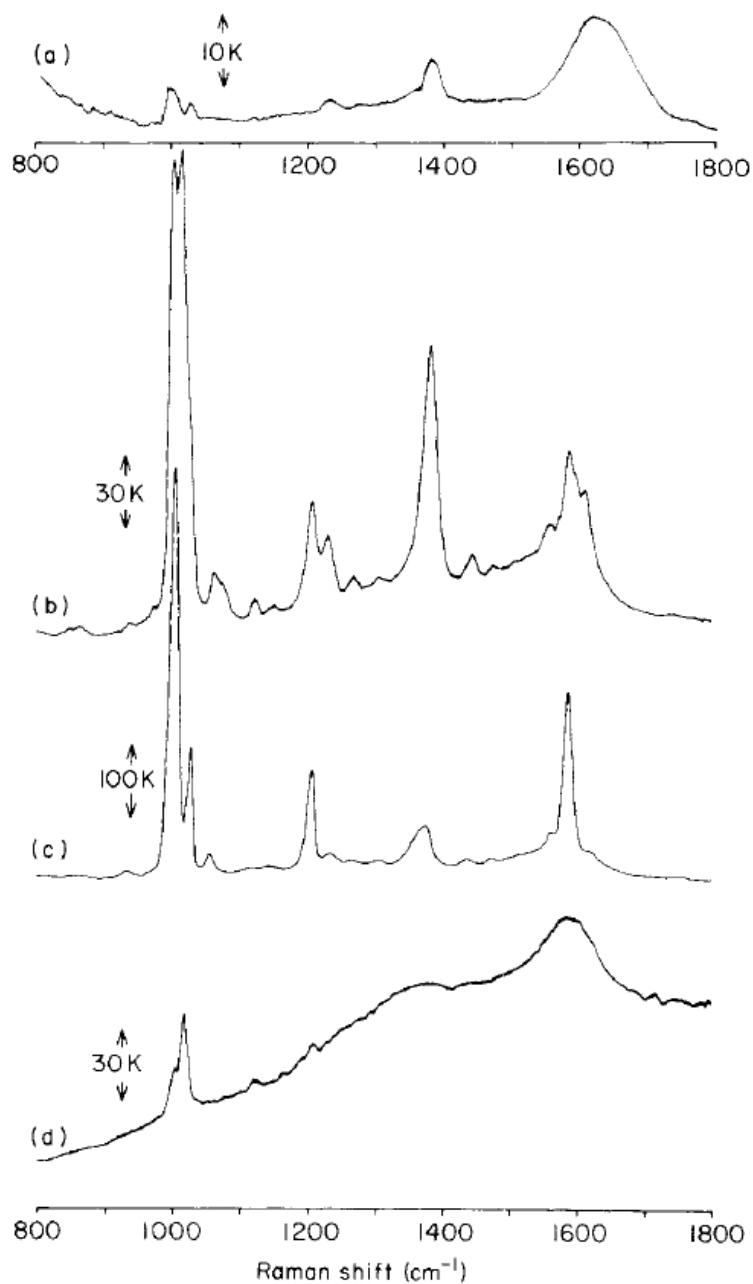


Figure 4.5: M.W.Howard et al(1980) [72]: The Raman spectra of pyridine at silver electrode interfaces. (a)The pyridine applied to electrode surface at a potential of -0.2V but before the anodic cycle. (b) after anodic cycle (c) at a electrode potential of -0.6V (d) the signal from a dry electrode 3 days after the potential control was removed at -0.2V.

The detailed mathematical formulation for the EM enhancement in SERS will be treated in part V and forms an important application of this work.

#### 4.2.2 Instrumentation for SERS

Raman spectroscopy is based on the detection of Raman shift in frequency of an incident illumination owing to the molecular vibrations of the analyte [95, 96]. This shift is much smaller than the incident frequency ( $\nu_i$ ) and is generally calculated in terms of wave-number given as  $\Delta S_{Raman} = [\nu_s - \nu_i] / c$ .

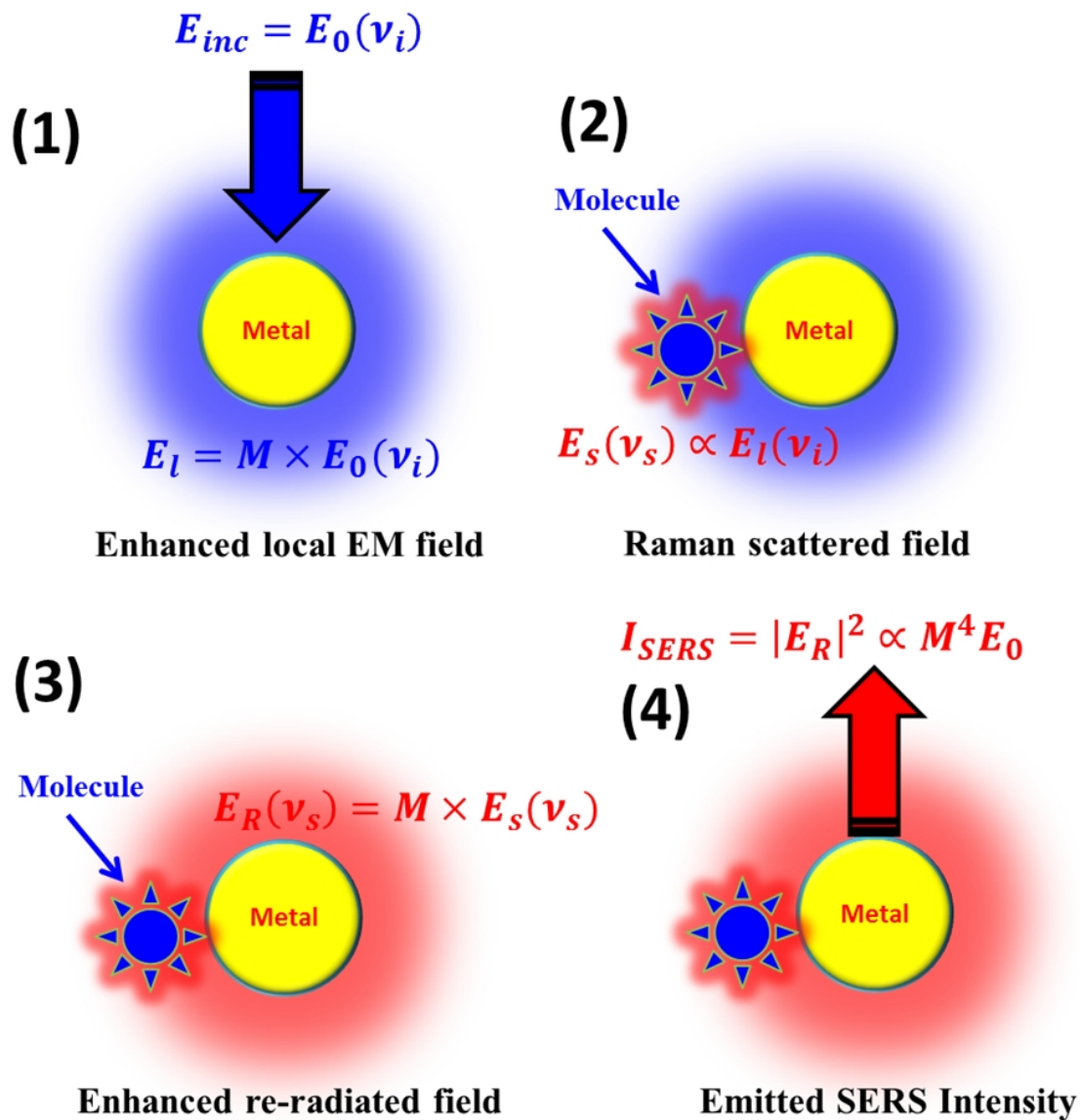


Figure 4.6: Process of electromagnetic enhancement in SERS: 1) The local electromagnetic field around the metallic structure is enhanced at the incident frequency  $\nu_i$ . 2) This enhanced field is scattered by the molecule to give the Raman scattered field  $E_s$  at Raman shifted frequency  $\nu_s$ . 3) The scattered field is re-enhanced by the metal structure ( $E_R$ ). 4) This re-radiated field at the Raman shifted frequency is emitted to the far field with intensity  $I_{SERS}$ .

The recorded signal in Raman spectrometers is the scattered intensity as a function of this shift  $\Delta S_{Raman}$  in units of  $cm^{-1}$ . Because of the low shift in frequencies, Raman spectroscopy requires a source with well defined excitation frequency with a very low spectral width. Thus almost all Raman spectroscopes use lasers as source. The Raman shift is generally independent of the excitation wavelength ( $\lambda_i = c/\nu_i$ ) and depends purely on the type of molecule and its vibration states.

A normal microscopic configuration is used to record the scattering event from the molecules and then spectroscopic measurements are done on the recorded intensity. To have higher spatial resolution Raman microscopy generally uses a confocal configuration. This also assures excitation of specific zone of the sample and thus reduces background scattering and fluorescent events from effecting the Raman



spectrum. A notch filter is also used to block the light at the incident wavelength and thus filtering the Rayleigh scattered intensity.

Recent development has also paved way for Raman imaging where the confocal microscope is scanned over the sample to obtain a 2D (and even 3D) profile of Raman spectra [97, 98]. In this case a complete spectrum is acquired at each and every pixel of the image, and then interrogated to produce a false color image of the Raman spectra over the entire sample surface. Another method of detection of molecules by enhanced Raman spectrometry is by introducing a metallic tip and scanning the sample. The method called Tip enhanced Raman scattering (TERS) follows the same principle as SERS but with a much higher spatial resolution (down to a few tens of nanometers) [99, 100]. Figure 4.7 shows an example of a commercial Raman microscope from Horiba scientific and this is one of the instruments used for the Raman spectra presented in this work.

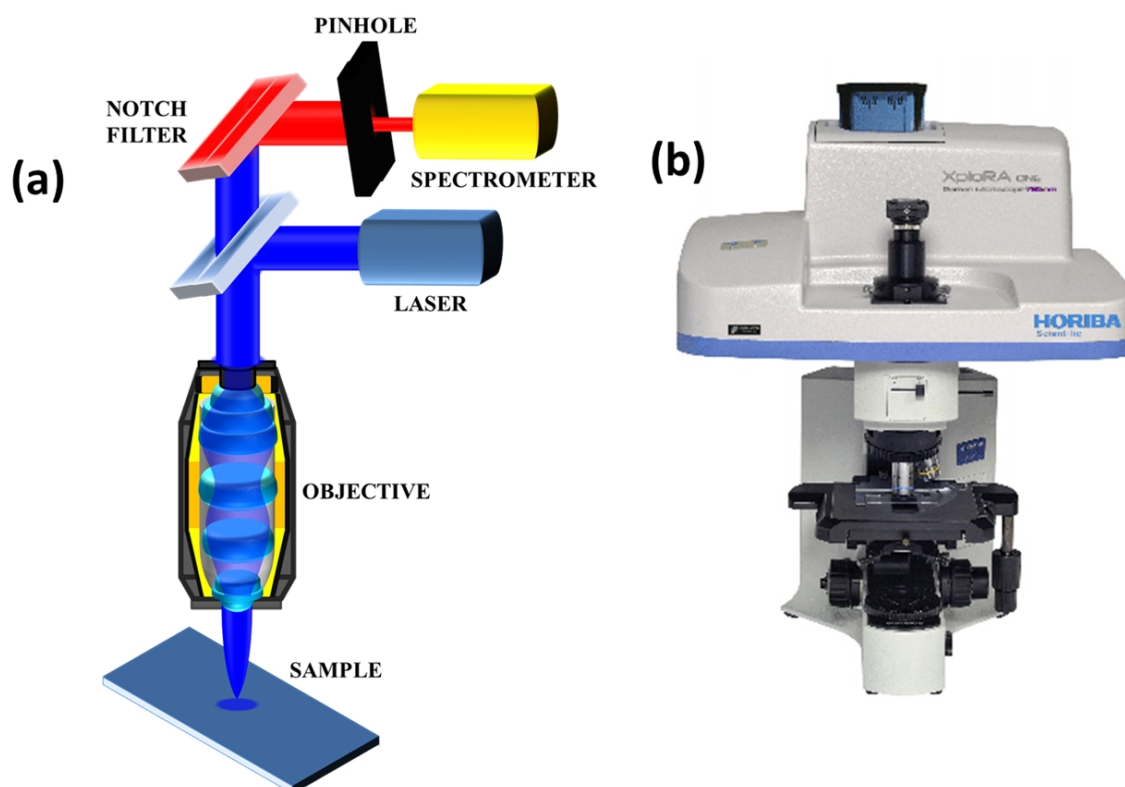


Figure 4.7: (a) Schematic of confocal microscopy configuration for Raman spectroscopy. A laser is generally used as the source and a microscope objective to illuminate the sample. The same objective is used to collect the Raman scattered field which is then passed through a notch filter to eliminate the Rayleigh scattered field at the frequency of incidence. The Raman scattered field is then processed by a spectrometer to obtain the Raman spectra. (b) Commercial Raman microscope XploRA ONE <sup>TM</sup> from Horiba Scientific.



---

# Biochip and nano-structuration

---

We have introduced the different methods of bio-sensing using surface plasmon resonance. Broadly we can classify the detectors in two categories. Firstly the ones that use propagating surface plasmons to detect bulk refractive index changes or local molecular binding kinetics. These were described in chapter 3. The other category of plasmonic bio-sensors use localized plasmon resonance of metallic nano-particles and can be used to probe individual molecular interaction events or to specifically identify the molecules by their Raman fingerprint. These were described in chapter 4. However both these categories of detectors have one thing in common: they depend on the electromagnetic field confined at metallic surfaces. Thus a complete understanding of this phenomenon is very important to enhance the performance of these detectors. Apart from the fluctuations and drifts causes by various noises introduced inherently by the instrumentation used in the detectors, plasmonic detectors also have inherent limit of detection (LOD) owing to the very physical properties of the plasmons. Thus to surpass the LOD we cannot purely rely on the PSP or the LSP and recent research and this work is concentrated on combining both types of plasmonic modes in various hybrid configurations. This paves the way for nano-structuration of the metallic surface which we will discuss in this chapter.

## 5.1 Limitations of conventional detection systems

### 5.1.1 Limitation of SPR detectors

Conventional SPR detectors use a thin metal film with the PSP excited at the metal-dielectric interface for bio-sensing. M.Piliarik and J.Homola in their publication in 2009 [101] calculated the ultimate performance of such SPR detectors. In the article they have shown that the resolution of a SPR detector to changes in refractive index depends primarily on three factors

1) The noise factor of the detector which depends on the instrumentation used and the method of data processing.

2) The coupling factor which depends on the coupling of the incident light to the surface plasmons and depends on the coupling methods used such as the Kretschmann configuration or grating coupling.

3) The material factor which was shown to be equal to  $\left[\frac{d(k_{sp}/k_0)}{dn}\right]^{-1}$  where  $k_{sp}$  can be calculated by equation 2.3 and  $n$  is the refractive index of the medium.

Thus the total refractive index resolution was shown to be

$$\sigma_R = \left[ \frac{Kr}{\sqrt{N}} \right] \left[ \frac{(C+1)^3}{C^2} \right] \left[ \frac{d(k_{sp}/k_0)}{dn} \right]^{-1} [\sigma_I/I_0] \quad (5.1)$$

where  $K$  is the noise distribution factor (shot noise value of 6% of light intensity),  $r$  the noise correlation factor (ideal value 1),  $N$  the total number of averaged values in the measurement (around  $4 \times 10^4$ ).  $C$  characterizes the coupling strength between the incident light and the plasmons with values between 1 and 2.  $\sigma_I$  is the standard deviation of the incident intensity  $I_0$ .  $\left[ \frac{d(k_{sp}/k_0)}{dn} \right]^{-1}$  was calculated to be  $\frac{\epsilon'_m n_d^3}{2(\epsilon'_m)^2}$  where the permittivity of metal is  $\epsilon'_m + i\epsilon''_m$  and the refractive index of the dielectric medium is  $n_d$ .

The first two factors can be reduced depending on the available materials, optical components and data processing methods. It was shown back in 2009 that developments in instrumentation have helped to achieve a resolution very close to the calculated "ultimate resolution" as shown in figure 5.1.

So the future of SPR detectors depends on the improvement of the 3rd factor  $\left[ \frac{d(k_{sp}/k_0)}{dn} \right]^{-1}$  and thus changing the very dispersion characteristic of the plasmon mode used. Recent research have tried to overcome this barrier by replacing the thin metal film by structured bio-chips and developments in fabrication technology have helped enormously in this aspect.

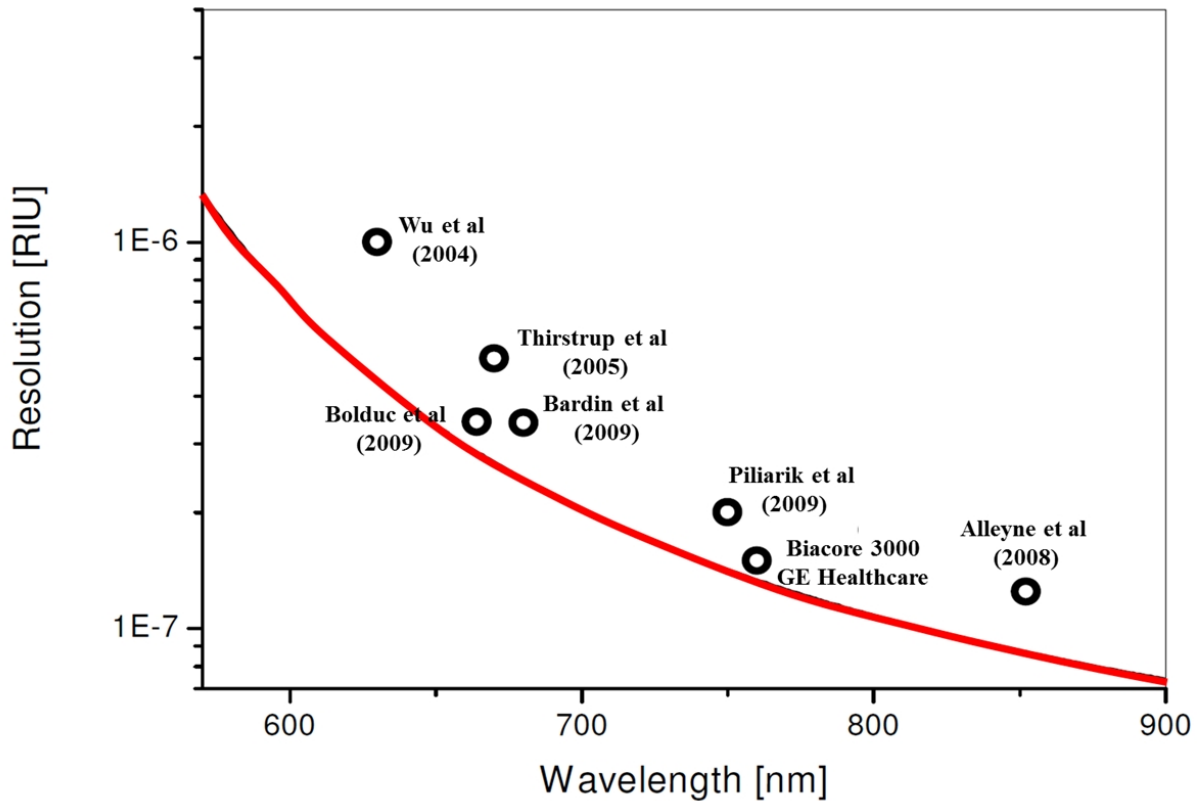


Figure 5.1: Adapted from M.Piliarik et al (2009) [101] showing the calculated ultimate resolution of SPR detectors using a thin metallic film and different reported resolutions: Wu et al [102], Thirstrup et al [103], Bolduc et al [104], Bardin et al [30], Piliarik et al [105], Alleyne et al [106].

### 5.1.2 Limitation of detector systems using particle plasmons

For detectors based on particle plasmon resonance, the LSP mode characteristics strongly depend on the nano-particle shape and geometry [107, 108]. Recent research in this domain is far from realizing an ultimate resolution of detection limit as still no consensus has been reached to understand and validate an optimum nano-particle. This is mainly because the frequency, line width and line-shape of resonance is completely different for particles with different shape, roughness and edge rounding. Such detections also depend largely on the localization of the analyte molecules and the homogeneity of molecular species attached to the particles. It is now known and as mentioned earlier, the LSPR mode has a high field confinement close to sharp edges of the particle and decay rapidly (within 10s of nm) into the medium. This is what makes LSPR an attractive phenomenon for detectors, but the very same characteristics make it difficult to develop a theoretical model to predict the behaviour of the nano-particles.

Thus to understand the resonance feature of a nano-particle it is of utmost importance to be able to develop an analytical theory that can somewhat predict its performance. Recent development in computational electrodynamics can help this in certain aspect but rigorous numerical calculations of spectra do not help to understand the physical mechanisms involved in such resonances.

The resonances of isolated particles are easier to model though presently all analytical models work for spherical or quasi-spherical or ellipsoidal particles. It is also easier to study molecular localizations for single nano-particle detection. However such methods are not really applicable for practical biosensing given their low throughput. Also detecting single nano-particles require narrow field of view and thus not suitable for detection of large number of functionalized nano-particles. Such methods also are not applicable for bio-chip based detections and nano-particle mobility pose addition detection issues.

Colloidal nanoparticles solve the problem of low throughput. However a colloidal solution with random distribution of nano-particles makes it impossible to predict detector performance. The fundamental principle governing multi-particle detection is the possibility of coupling between the plasmonic modes of adjacent particles or an array of particles. The plasmon resonance of individual particles are generally treated as oscillating dipoles. If two particles are brought in close proximity with gaps less than the wavelength of incident light, the respective dipoles can interfere coherently giving rise to new plasmonic modes. Such new modes generally have an enhancement of the local electromagnetic field compared to that for isolated nano-particles. In figure 5.2 we have shown a calculated electric field distribution ( $\frac{E^2}{E_0^2}$  with  $E_0$  being the incident field) in logarithmic scale for a gold nano-sphere when approaching a thin gold film. The field is incident from the side of the film and thus similar to the Kretschmann configuration. For the film the field confinement results from the PSP while for the sphere it results from the LSP. We see that the field intensity is enhancement almost by a factor of  $10^6$  when the separation between the film and the particle is 5nm. This enhancement is due to the coupling of the LSP and the PSP and the main aim of this work is to understand and characterize this phenomenon.

Though refractometric measurements depend mainly on the dispersion characteristics of the plasmonic mode as shown in the previous section (equation 5.1), measurements such as SERS depend mostly on field enhancement caused by the metallic particle. In this respect such coupled structure geometries are more beneficial than single particles. But such field enhancement vary strongly with the distance and distribution of the interacting particles and this is impossible to predict in random colloidal nano-particles. Thus the results often obtained are not reproducible and characterization of such substrates for bio-detection is difficult. Thus for a systematic understanding of the working of particle plasmon detectors we need to

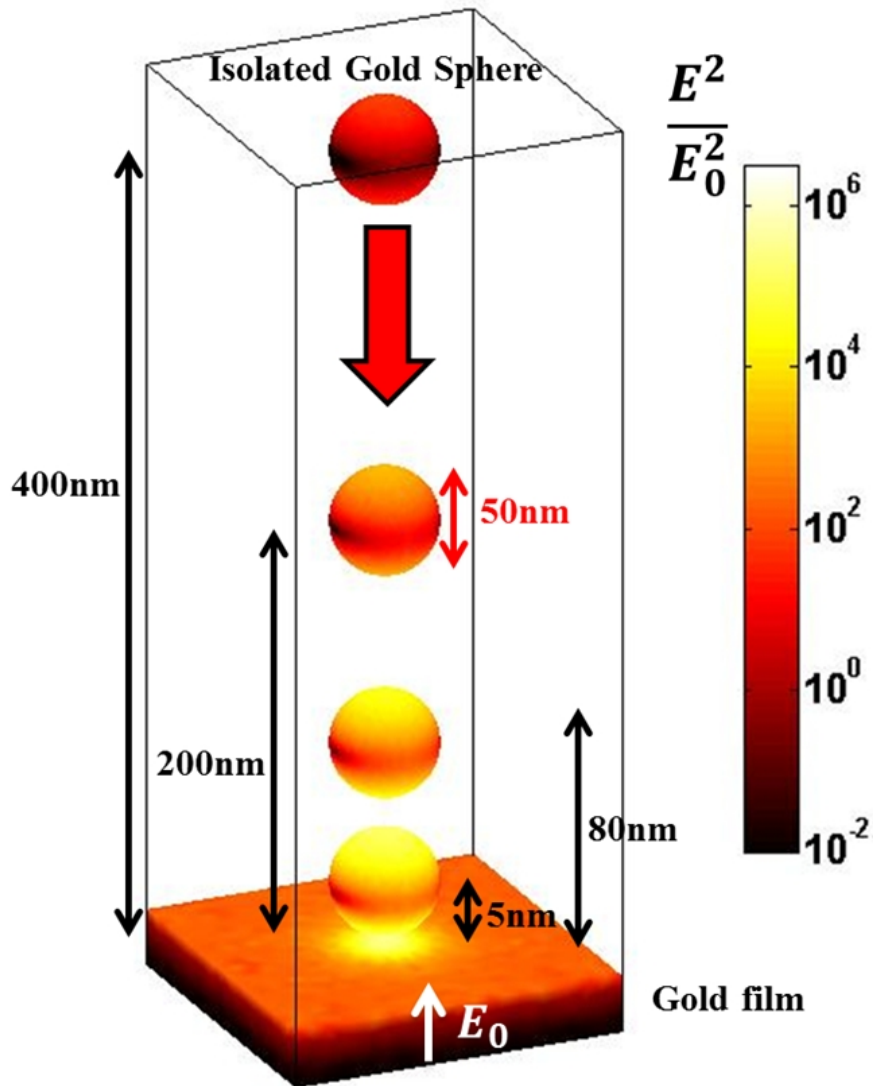


Figure 5.2: Electric field intensity distribution in logarithmic scale for a gold sphere of 50nm with separations of 5nm,80nm,200nm and 400nm from a thin gold film.

focus on ordered arrays of nano-particles. Understanding the very physical aspect of SERS is another research problem and this work will aim to explain some of physical phenomenon relating the SERS effect to plasmonic modes in an arrayed substrate.

## 5.2 Structure fabrication techniques

Gold nano-particles have been synthesized for the last 2000 years with a famous example of its use being the 4th century Roman Lycurgus Cup. But only recently have they found interest in scientific research and thus methods to control precisely the tailored shape and size have been developed. One such method was described in section 4.1.1. For ordered structures a greater control on the structure geometry over larger surfaces is required.

A biochip surface consists of different zones each dedicated to a specific functionalization and read-out depending on the type of detection carried out. For detections based on confocal imaging such as

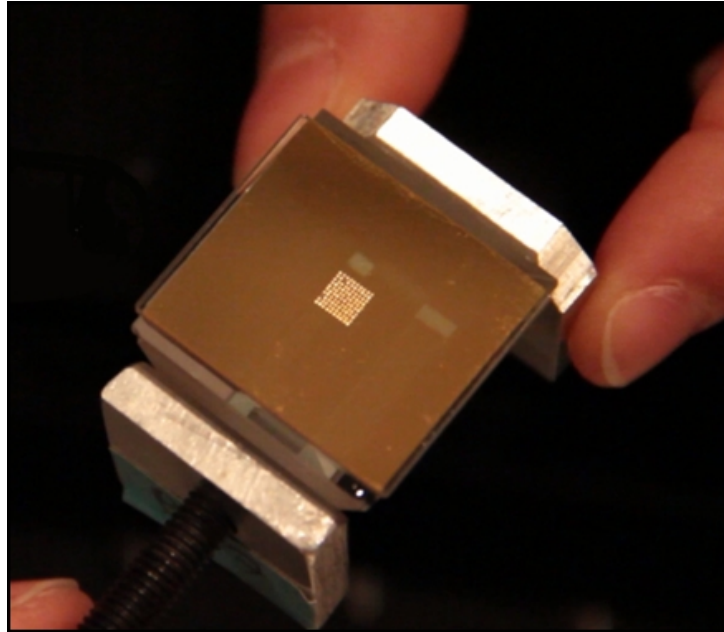


Figure 5.3: A structured biochip placed on a glass prism, used for SPR imaging. The biochip consists of a thin gold film and a nano-structured zone in the center.

absorption spectroscopy or SERS a small portion (up to a few micrometers) of the biochip surface is studied. However for detections based on imaging such as SPR or Raman imaging a large area of the biochip surface is imaged for data processing. In the case of SPR detection using propagating plasmons a homogeneous structured zone larger than the propagation length of the plasmons (around a few tens of micrometers) is required. For periodic structures a stable control over the periodicity and structure roughness must be maintained for the entire zone under study.

The fabrication techniques currently available are broadly classified into two categories, the top-down or bottom-up methods. The bottom-up method generally relies on a seed mediated growth. In such a process the atoms or molecules are deposited one by one to form the desired structure. The structure geometry is controlled by the initial seed growth on the substrate and then by chemical precipitation of metal, oxides or alloy ions on the substrate. Certain defects or faults of the initial seed allow preferential growth directions of the nano-structures. Self assembly of nano-particles or molecules or electro-chemical deposition is also used to fabricate plasmonic structures. Another technique used in this domain is called the Glancing Angle Deposition (GLAD) where the atoms or molecules are deposited on the substrate at an oblique angle in a vacuum which results in a columnar deposition [109, 110]. The angle of incidence controls the tilt of the columns and affects the degree of shadowing. This has been used to fabricate structures such as nano-pillars, nano-spirals etc.

For this work the structures that have been used were fabricated using the top-down method. In this method a bulk material is removed step by step to form the desired structures in nanometric scale. Some common techniques used in this method are electron beam lithography (EBL) [111, 112], plasma etching or nano-imprint lithography (NIL) [113, 114].

EBL and NIL are shown in figure 5.4. In EBL, an electron sensitive photoresist, commonly poly(methyl methacrylate) PMMA, is deposited by spin coating on the substrate. Then the desired pattern is obtained on the resist by exposing it to e-beam and a step of chemical development commonly with methyl isobutyl

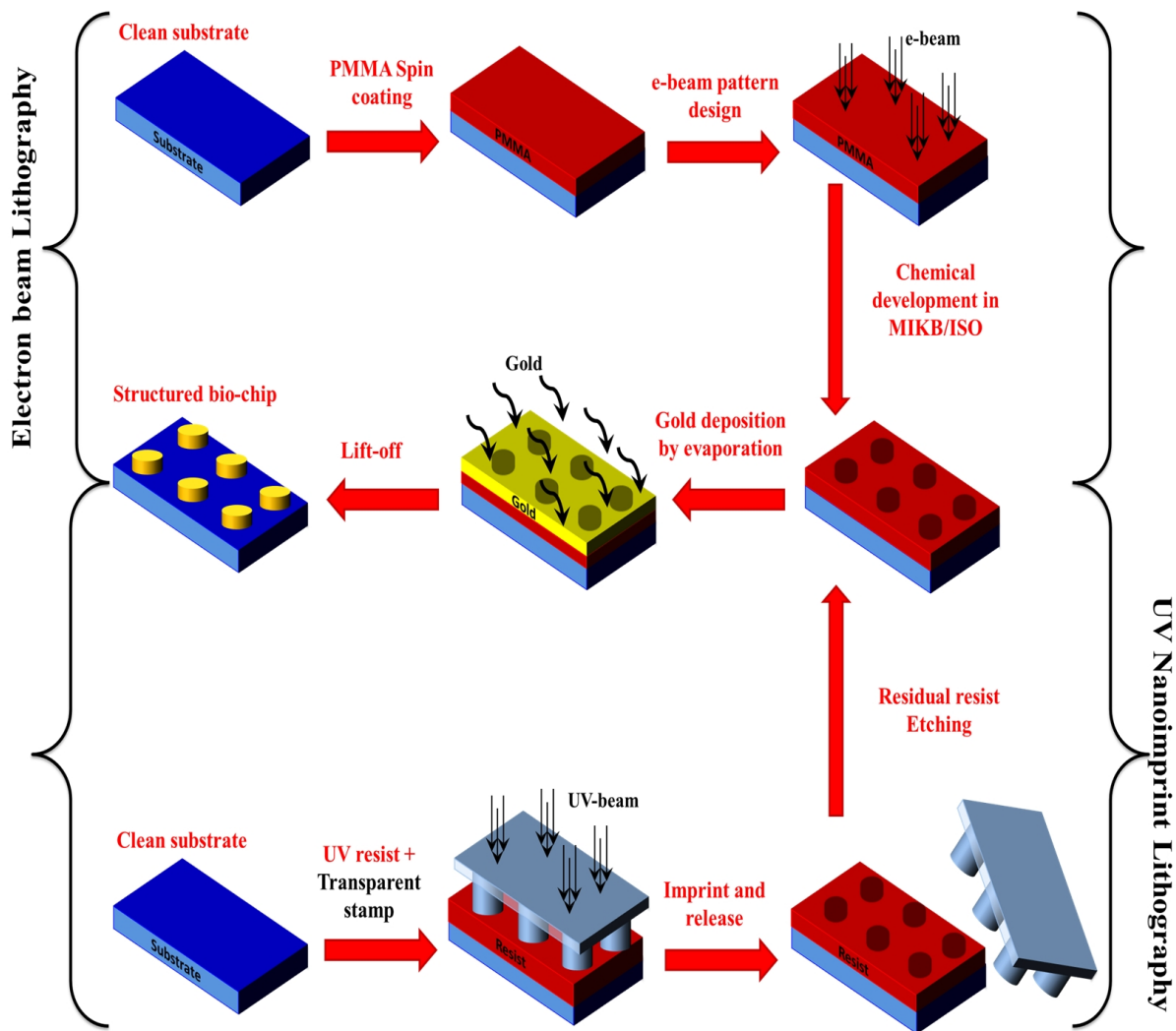


Figure 5.4: Top-down fabrication techniques: Electron beam lithography (top) and UV nanoimprint lithography (bottom).

ketone (MIBK) and isopropyl alcohol (ISO). This process allows precise control of shape, size and spatial distribution with a high resolution of less than a hundred nano-meters. The resolution of the process depends on the wavelength of the radiation source in this case the wavelength and thus the energy of the electron beam. However e-beam patterning of the PMMA is a time-consuming process and has low throughput for larger surfaces.

For such larger zones (around a few millimeters) requiring less precision the NIL is more suitable. NIL is based on patterning the resist using mechanical molding of the PMMA by a transparent mold or stamp. The mold is pre-fabricated and the resolution of process depends on the dimensions of the stamp used. This process allows control of geometrical parameters comparable to e-beam lithography at a much faster fabrication rate and thus is useful for mass-production of bio-chip substrates for commercial use.

Metal is deposited on the patterned substrate after EBL or NIL, by thermal evaporation and then the resist along with the excess metal is removed by a lift-off process by dipping it in acetone. This leaves behind the desired structured bio-chip.

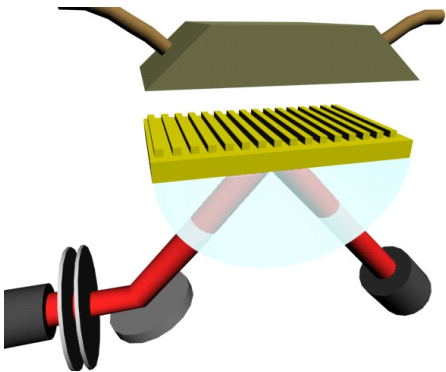
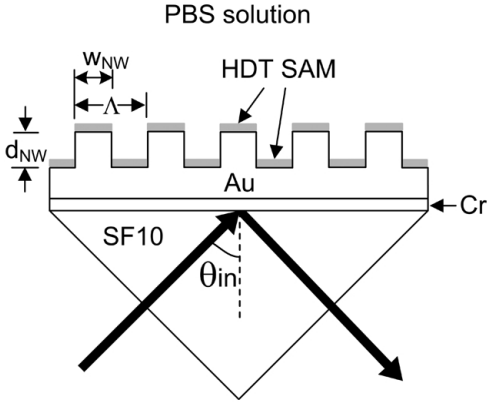
Other techniques used for nano-fabrication are laser ablation, electrolytic deposition or other electro-chemical processes [115, 116, 117, 118]. The main factors governing the choice of technique are the



reliability and reproducibility requirements for the substrates.

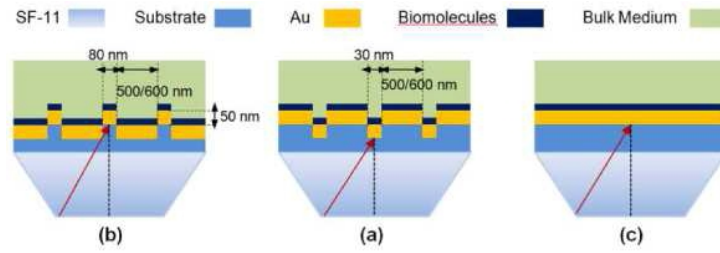
### 5.3 Detection using Nano-structured bio-chip

Structured biochips can help in bio-detection owing to different plasmonic modes that such structures can support either by coupling the PSP and the LSP or by other optical phenomenon which rise due to the periodicity of the structure. This has been used successfully and reported by various groups where such structures help to increase the detection performance of the respective biosensor. Table 5.1 shows the various bio-detector configurations reported in the literature which uses such structured biochips.

Type of detection	Structure geometry
<p>K.Kim et al (2009) [119]: SAM formation; DNA Hybridization; Ethanol ambience</p>	<p>Gold gratings of height 10/15nm and periodicity 200/300nm on a uniform gold film of height 40/55nm.</p> 
<p>K.M.Byun et al (2008) [120]: SPR imaging to monitor SAM formation</p>	<p>Gold nano-wires of height 20nm and periodicity 50/100/200nm on a thin gold film.</p> 

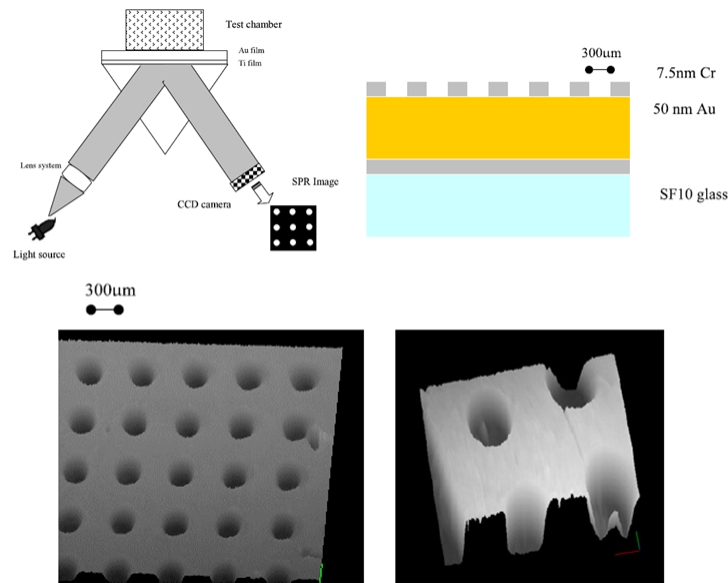
L.Malic et al (2009) [121]: SPR imaging to monitor refractive index changes, DNA immobilization and DNA hybridization events

Nano-gratings and Nano-grooves fabricated using NIL of periods 500/600nm and widths 30/80nm.



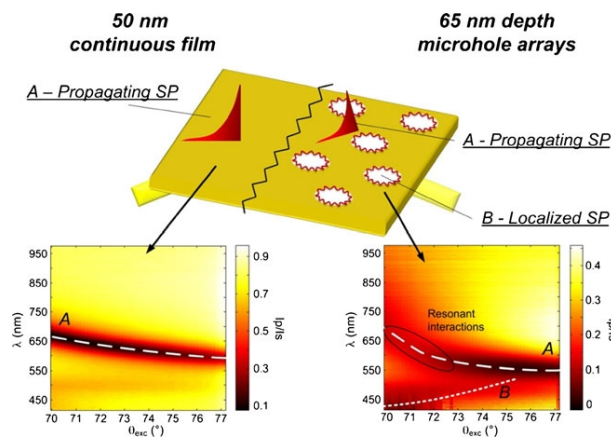
M.G.Manera et al (2009) [122]: SPR imaging to study the hybridization process of ssDNA carbonarius probes.

Gold film of 50nm with patterned chromium layer of diameter  $300\mu m$



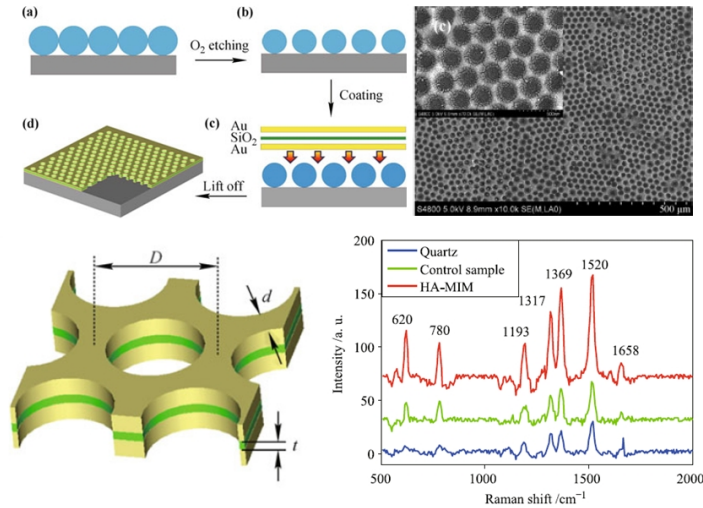
L.S.Live et al (2012) [123]: SPR sensitivity enhanced by a factor of 3 to five times compared to continuous films; order of magnitude lower detection limit of IgG biodetection; the potential for surface-enhanced spectroscopy.

Microhole array of depth 65nm and hole diameter of  $1.8\mu m$  and period  $3.2\mu m$  fabricated by nanosphere lithography



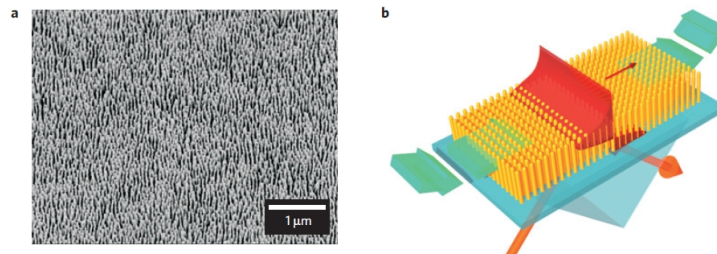
L.P. Xia et al (2014) [124]: Enhancement of Raman scattering spectrum of rhodamine 6G (R6G) upto 3.85 times

Hole arrayed metal-insulator-metal (HA-MIM) structure with  $SiO_2$  used as the insulator with thickness of around 20nm. Diameter of holes around 400nm and separation of holes around 20nm. Structure fabricated by etching and then lifting off polystyrene (PS) spheres



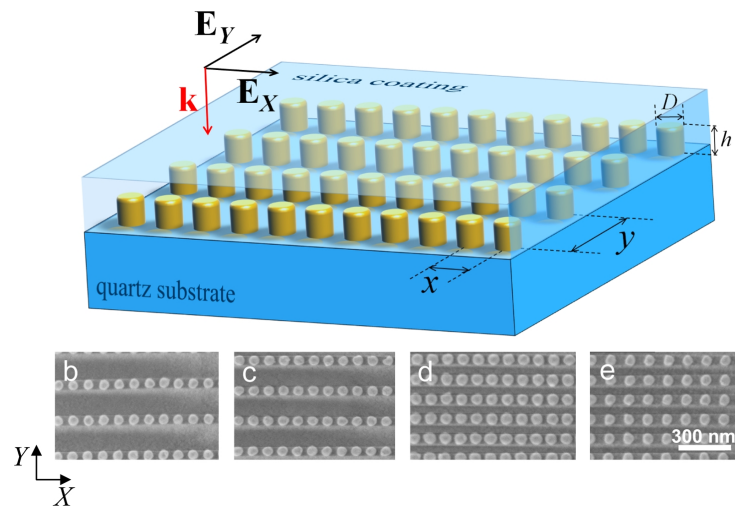
A. V. Kabashin et al (2009) [125]: Enhanced sensitivity to refractive-index variations up to 30000nm per refractive-index unit.

Metamaterial consisting of an assembly of Au nanorods electrochemically grown into a substrate. The range of rod lengths between 20 and 700 nm, rod diameter 10-50nm and separation from 40 to 70 nm.



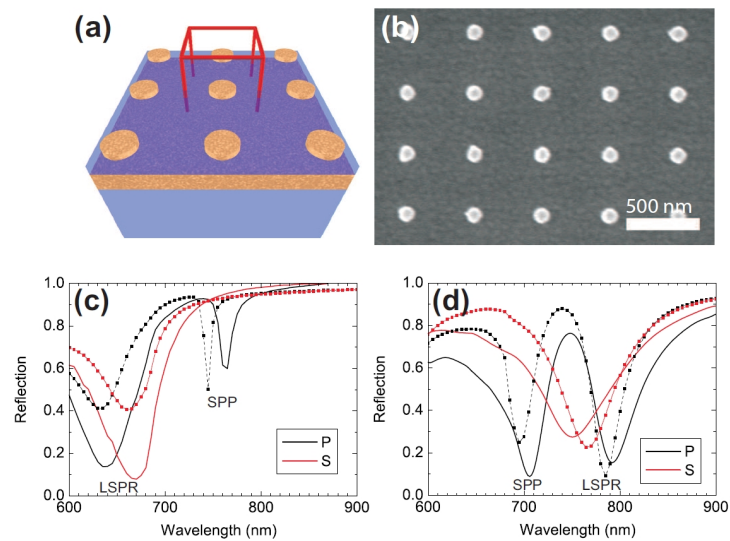
X.Wang et al (2012) [126]: Understanding plasmon coupling between nano-particles to optimize them for chemical and biological sensing.

50nm gold nano-particle array of period ranging from 80-170nm and varying periodicity along two axes. Structure array fabricated by EBL on a quartz substrate



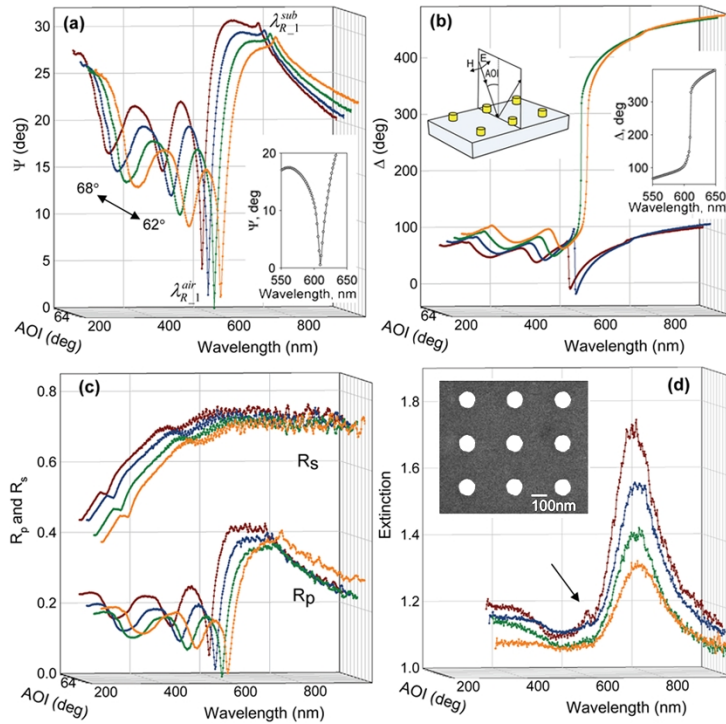
K.Lodewijks et al (2012) [127]: Study of LSP and PSP coupling using phase sensitive spectroscopic ellipsometry. Dramatic increase of refractive index sensitivity of LSP modes.

Gold nano-disks of periodicity 400nm and diameter 100/140nm.



V. G. Kravets et al (2008) [128]: Extremely narrow plasmon resonances with half-width of just several nanometers in regular arrays of metallic nanoparticles.

Gold nano-pillars of period 320nm, diameter 100nm and height 90nm.



W.D.Li et al (2011) [129]: High area-average SERS enhancement ( $1.2 \times 10^9$ ).

Dense three-dimensional cavity nanoantenna array, through nano-gaps, with dense plasmonic nanodots; new nanofabrication that combines nanoimprint, guided self-assembly and self-alignment.

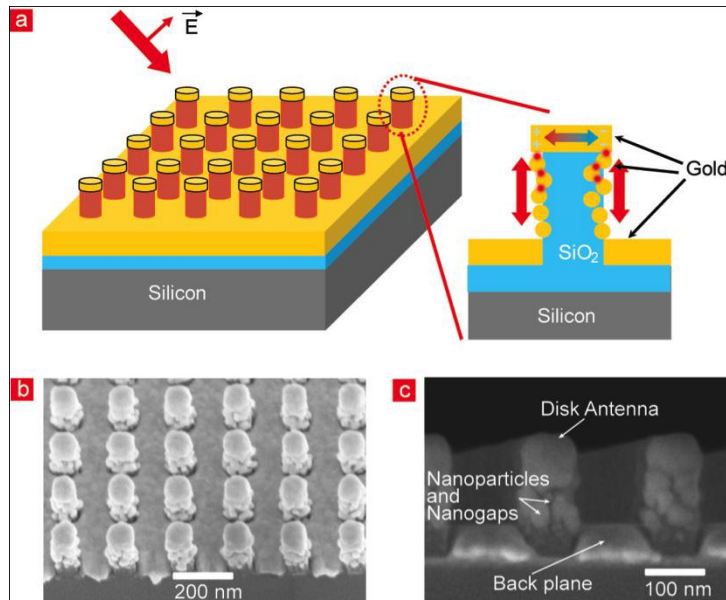


Table 5.1: Detection using structured bio-chips

Apart from the above mentioned reports there are other numerous articles in the literature where use of structured bio-chip has helped to enhance the performance of SPR or SERS detectors. In this work we

would present the principle of coupling between various plasmonic modes which helps in such enhanced performance.

## 5.4 ANR PIRANEX project

This work was partially done as a part of the ANR project «PIRANEX». The project focuses on developing a bimodal instrument which combines SERS and SPRI detection. SPRI provides parallel imaging capabilities and label free detection to probe bio-molecular binding events and real time molecular interaction kinetics. SERS helps in unique identification of the binding molecules owing to the Raman spectral signatures of the molecules at the binding locations. Such bimodal detection techniques have been proposed in the literature [130, 131, 132]. Piranex project however aims to develop the bimodal instrument using the same biochip. Thus an optimized nano-structuration of the bio-chip surface is required to assure high throughput for both local refractive index changes using SPRI and high Raman enhancement for SERS. An in-laboratory made code is developed for this purpose to model the plasmonic modes of various structures and have a better understanding of the role played by each mode in molecular sensitivity. With a detailed understanding of the electromagnetic aspects of plasmonic nano-structures, one of the aims of the project is to provide various bio-chip surfaces adapted to various sensing requirements of the bimodal instrument thus developed.

The structures were initially produced by EBL for experimental validation of the numerical methods used and the electromagnetic model developed. Such structures were also used to demonstrate biochemical detection procedures. Chemical functionalizations were developed to utilize such structures as bio-chips. Some applications of the system developed by Piranex are in the domain of bio-marker detection for cancer, cardio-vascular pathologies and other medical diagnostics or detection of food containments. Then the optimized nano-structures would be fabricated by NIL techniques to have large areas (millimetric scales) at low cost and less fabrication time for industrial use. The schematic of PIRANEX project is shown in figure 5.5.

Here in this work we will use the numerical models developed to characterize the plasmonic nano-structures and present a detailed understanding of the electromagnetic properties of the structures in terms of the confined EM field intensity and refractive index sensibility. Various structure geometries are studied for this purpose in different configurations for their use in SERS and SPRI. Some geometries with huge enhancement of sensitivity will be described and experimental results have been used to validate the numerical results. Using new hybrid plasmonic modes which result from inter-coupling of different fundamental modes, we can help to increase the throughput of the bimodal instrument and lower its limit of detection.

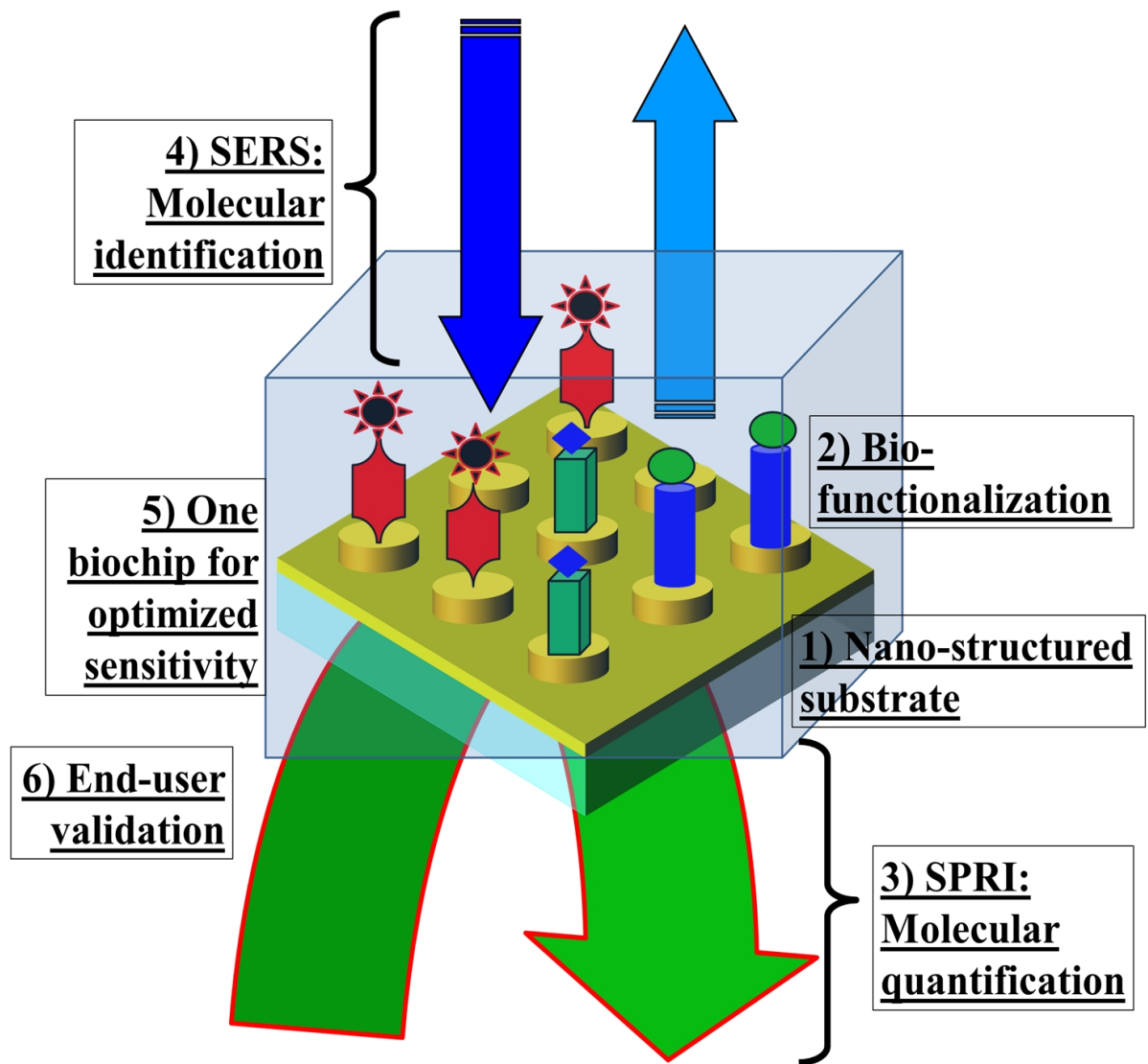


Figure 5.5: Schematic of PIRANEX project showing the bimodal instrument for simultaneous SERS and SPRI detection.





---

## Conclusion of Part II

---

In this part we have introduced the different types of plasmonic bio-sensors which are currently available. In chapter 3 we have explained the basic principle of surface plasmon resonance detectors. Such detectors use propagating plasmon mode (PSP) which has a penetration depth of a few hundreds of nano-meters and is sensitive to refractive index changes within the decay length of the evanescent field. Conventional SPR detectors use an uniform metallic film to probe refractive index changes in the bulk medium. This can also be used for affinity based detectors which probe molecular binding events. For this, a confined evanescent field is necessary which is more sensitive to local index changes and almost inert to refractive index drift of the bulk medium.

In chapter 4 we have described the various detectors that use metal nano-particles for bio-sensing. These detectors conventionally use the Localized plasmon (LSP) mode which have strong confinement of the electromagnetic field within a few tens of nano-meters from the metallic surface. The various configurations used for such detectors were also shown. Metal surfaces with roughness has proved to be useful to enhance the Raman signal of molecules and this has opened a new arena in biosensing using raman spectroscopy, the surface enhanced raman scattering (SERS). The basic mechanism of SERS was described in section 4.2. To optimize the SERS substrates a complete understanding of the plasmonic modes of the metallic system is required.

SPR detectors using an uniform metallic film has a fundamental limit of detection resolution and to surpass that limit we need to develop new structured bio-chips and harness the potential of coupling different plasmonic modes. The fabrication techniques currently used to synthesize such structured bio-chips was shown in chapter 5. We have also presented some of the reports in the literature which use such structured bio-chips for enhanced sensitivity of bio-detection. Recent research has also focused on combining SERS and SPR imaging using the same substrate. This will help in studying molecular binding events using SPRI and at the same time identify the molecules involved in such a event using SERS. This is one of the aims of the ANR project Piranex and a part of this work is dedicated in that respect.

This work will focus on the development of structured bio-chips to enhance the detection sensitivity of SPR detectors. At the same time we will explain the physical phenomenon involved in the excitation of various plasmonic modes in hybrid structures and such an understanding can help to optimize the structures for SERS detection.



## **Part III**

# **Numerical methods for electromagnetic modeling**



---

# Computational electromagnetics

---

The basis of this work is to study the various plasmon polariton modes present in structures with complex geometries and then optimizing the modes for applications in bio-detection. Such bio-detectors was discussed in part II and structures will be described in part IV. But first we need to study the electromagnetic phenomenon of light interacting with materials and the dependence of the same on the geometry of the material. Generally such phenomenon is treated by electromagnetic field theories by studying the interaction between electric charges at rest and electric currents.

Such interactions are well described by the Maxwell's equations as shown in section 1.1. By treating the Maxwell's equations as an eigenvalue problem, the solutions thus obtained, give the modes of the system. Such a treatment for an planar metal-dielectric interface was shown in section 2.1.2. The scattering problem as shown in section 2.2 is yet another example of such treatment. However analytical solutions for most real life situations are not possible mainly when considering complex geometries and advanced applications. Applying certain crude approximations can help to arrive at a relatively acceptable analytical solution.

However with advanced computers at our disposal, we can solve electromagnetic problems that require large amount of computations. The branch of electromagnetic that deals with such computational methods is called Computational electromagnetics (CEM). Using CEM, the partial differential equations that arise from relating the charges and currents in a system to the electromagnetic flux and field in a system can be broken down into discrete sets of equations. Such discretized differential equations can be solved by well known numerical methods. Such methods can treat a variety of real life electromagnetic problems using simple computer algorithms and programs. In table 5.2 we would introduce a few of the many different methods of CEM that have been used to characterize plasmonic modes in metallic systems.

Method used	Studied EM problem	Remarks	References
Mode solver based on density of states (DOS) formulation.	Study of dielectric-loaded surface-plasmon-polariton waveguide (DLSPPW) with 100nm thick gold film and strips of PMMA of height and thickness of 600nm.	Numerically investigated both leaky and bound (lossy) modes supported by dielectric-loaded surface-plasmon-polariton waveguides	G. Colas des Francs et al (2009) [133]
B-spline modal method (BMM)	Applied to a 1D metallic grating structure	Resolution of Maxwell and constitutive equations with a B-spline approximation. Method compared to Rigorous Coupled Wave Analysis (RCWA) method.	P.Bouchon et al (2010) [134]
Multipole expansion (ME) and FEM (COMSOL software).	Studied dimers of 20nm and separation of 5nm consisting for solid spheres and shells.	Comparison between ME and FEM; 1D triangular nanowires also studied as SERS substrate.	C.G. Khoury et al (2010) [135]
An ab initio theory for Fano resonances using the Feshbach formalism	Applied to dolmen type plasmonic structures	Verified the theory with numerical results ; analogy to mechanical coupling of two harmonic oscillators with losses.	B.Gallinet et al (2011) [136]
Zubarev's Green functions method	Metallic particle of few 10s of nm and a quantum emitter in its vicinity; for modeling the optical response of plasmons interacting with quantum emitters	studied coupled plasmon-exciton system that supports plexitons;	A. Manjavacas et al (2011) [137]
Method of Moments (MoM)	Gold V-shaped antennas of length $1.2\mu\text{m}$ and thickness 100-200nm.	Compared result to FDTD simulations.	R. Blanchard et al (2012) [138]
RCWA modal method	Gold grating of width 200nm and height 100nm deposited on free standing silicon nitride membrane of 650nm thickness for use as transmission band pass filters.	Structure studied in 1D and 2D for periodicities of 2-3 micrometers.	E.Sakat et al (2012) [139]

2D Finite Difference Time Domain (FDTD)	Double layered silver nano strips of thickness 20nm and widths ranging from 50-90nm separated by PMMA layer.	Structure applied to sensing applications; Refractive index sensitivity and SERS enhancement factor evaluated numerically.	Z.Kang et al (2013) [140]
A self-consistent electromagnetic treatment of the local density of states	Study of coupling between dipoles emitters and dissipative nano-resonators	Method verified by vectorial numerical results obtained for plasmonic nanoantennas made of gold nanorods.	C. Sauvan et al (2013) [141]
Green tensor formulation	Calculation of electric field in metallic nano particles; Optimizing particle dimensions for complete absorption of electromagnetic radiation.	Rapid and simple analytical method to optimize nanoparticle dimensions for total absorption of incident light.	A.Sentenac et al (2013) [142]
3D Fourier Modal Method	Applied to plasmonic waveguide called the hybrid dielectric-plasmonic slot waveguide (HDPSW)	Capable of efficient 3D vector modelling	J.Ctyroky et al (2013) [143]
Extended coupled oscillator (ECO) model	Study of highly tunable Fano resonant nano-structure consisting of 4 interacting nano-rods.	In contrast to Conventional coupled oscillator (CCO) model, for ECO the damping characteristics of the hybridized modes are calculated and not set a priori.	A.Lovera et al (2013) [144]
A general theory to describe scattering electromagnetic interactions of resonator networks for arbitrary multipolar orders.	Application of the method for single and binary metallic particle arrays dispersed in regular hexagonal lattices	Results verified by Finite element method (FEM).	M.Langlais et al (2014) [145]

Table 5.2: Numerical methods to characterize metal nano-structures and some examples of the application of the method.





# Introduction to the numerical formulations

---

In this work we would study the different plasmonic modes present in structures with complex geometries. As mentioned in chapter 2 the two fundamental types of plasmon polaritons are the propagating surface plasmons (PSP) and the localized surface plasmons (LSP). The PSP can be excited in flat surfaces and the analytical solution for such a flat surface was already shown in section 2.1.2. However we are also interested in calculating the reflectivity and transmission of such an uniform metallic surface. The generalized Rouard method offers an analytical solution to such problems consisting of uniform layers of various materials. We will discuss this method in section 6.1. However for more complex structures as mentioned earlier, analytical solutions are not possible and we have used a hybrid model for modeling the optical responses of the systems. The hybrid model described in details in chapter 7 combines two popular numerical methods namely the Fourier modal method (FMM) and finite element method (FEM) which have been described in sections 6.2 and 6.3 respectively of this chapter.

## 6.1 Generalized Rouard method

Treating Maxwell's equation as matrix formulation was first proposed by Abeles [146] and later developed by P. Yeh [147]. Such matrix formulation was further developed and is used in most CEM techniques which will be described in later sections. However in 1937 M.P. Rouard proposed a method for calculating the reflectivity for multiple stacks of thin films [148]. His method accounted for the light that may reflect back and forth between the interfaces, thus affecting the effective reflective properties of the stack. The method was developed by an infinite mathematical series to sum the response of these multiple reflections. The result of this infinite series formulation gives a single coefficient to represent the effective reflection of the complete stack. However his method was limited to non-absorbing materials and applying it to absorbing materials such as metals generally lead to convoluted expressions. In 2006, Lecaruyer et al developed a general formulation of the Rouard method for an absorbing thin film stack [149]. This is the method which we will describe in brief and have used for this work.

The Rouard method stems from the basic Fresnel coefficients for reflection ( $r$ ) and transmission ( $t$ ) at an interface ( $mn$ ) which are given by

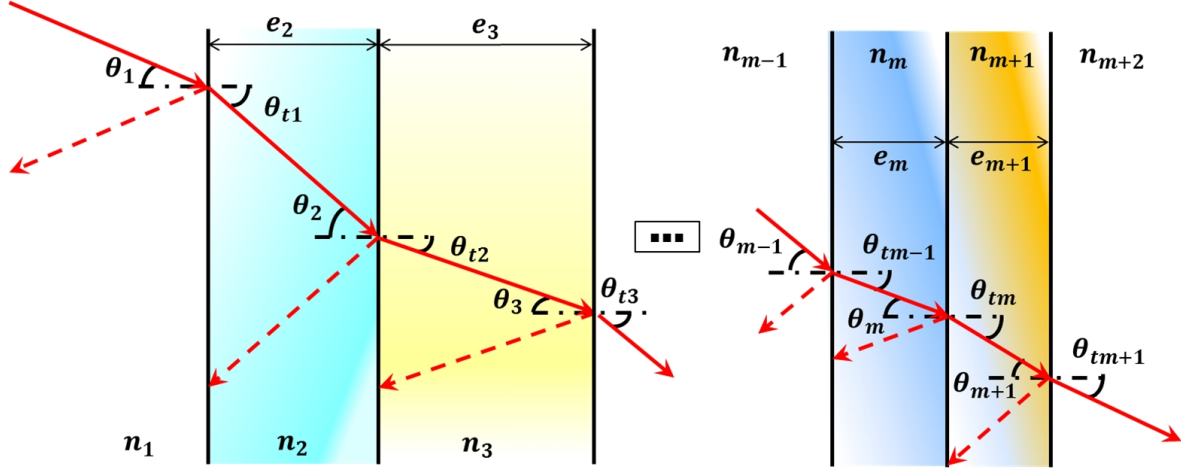


Figure 6.1: A stack of multiple thin films with refractive index  $n_m$  and thickness  $e_m$  for the  $m$ th layer. The angle of incidence and angle of refraction at the interface  $m \rightarrow m + 1$  is taken to be  $\theta_m$  and  $\theta_{tm}$  respectively.

$$TE \left\{ \begin{array}{l} r_{s:m \rightarrow n} = \frac{n_m \cos \theta_m - n_n \cos \theta_{tm}}{n_m \cos \theta_m + n_n \cos \theta_{tm}} \\ t_{s:m \rightarrow n} = \frac{2n_m \cos \theta_m}{n_m \cos \theta_m + n_n \cos \theta_{tm}} \end{array} \right\} \quad (6.1)$$

$$TM \left\{ \begin{array}{l} r_{p:m \rightarrow n} = \frac{n_m \cos \theta_{tm} - n_n \cos \theta_m}{n_m \cos \theta_{tm} + n_n \cos \theta_m} \\ t_{p:m \rightarrow n} = \frac{2n_m \cos \theta_{tm}}{n_m \cos \theta_{tm} + n_n \cos \theta_m} \end{array} \right\}$$

for TE and TM polarization respectively, where  $\theta_m$  and  $\theta_{tm}$  are the angle of incidence and angle of refraction respectively. A schematic of reflection and transmission in a stack of multiple thin films is shown in figure 6.1. By a simple summation of all the reflection and transmission coefficients at an interface  $m \rightarrow (m + 1)$  we can write the total reflectivity of interface  $m$  as

$$\begin{aligned} r_m &= r_{m-1 \rightarrow m} + t_{m-1 \rightarrow m} e^{-i\phi_m} r_{m \rightarrow m+1} e^{-i\phi_m} t_{m \rightarrow m-1} \\ &\quad + t_{m-1 \rightarrow m} e^{-i\phi_m} r_{m \rightarrow m+1} e^{-i\phi_m} r_{m \rightarrow m-1} \\ &\quad e^{-i\phi_m} r_{m \rightarrow m+1} e^{-i\phi_m} t_{m \rightarrow m-1} + \dots \\ &= r_{m-1 \rightarrow m} + \frac{t_{m-1 \rightarrow m} r_{m \rightarrow m+1} t_{m \rightarrow m-1} e^{-2i\phi_m}}{1 - r_{m \rightarrow m-1} r_{m \rightarrow m+1} e^{-2i\phi_m}} \end{aligned} \quad (6.2)$$

The phase change for propagation in layer  $m$  is given as  $\phi_m = \frac{2\pi}{\lambda} n_m e_m \cos \theta_m$  where  $\lambda$  is the wavelength of light,  $e_m$  the layer thickness and  $n_m$  the refractive index of the layer. The equation can be simplified considering that the Fresnel coefficients are related to each other in the manner  $t_{m-1 \rightarrow m} t_{m \rightarrow m-1} = 1 - r_{m-1 \rightarrow m}^2$  as

$$r_m = \frac{r_{m-1 \rightarrow m} \times r_{m+1} e^{-2i\phi_m}}{1 + r_{m-1 \rightarrow m} \times r_{m+1} e^{-2i\phi_m}} \quad (6.3)$$

For a multiple thin film stack the contribution of each layer must be summed to have the total reflection coefficient of the stack. For the metallic layers the complex refractive index for equation 6.1 can be written as  $n_m = n + ik$  as shown in section 1.3. We have developed an in-lab program using Matlab to calculate the total reflectivity ( $R = rr^*$ ) of a multilayer stack at each incident wavelength and angle of incidence ( $\theta_1$  for figure 6.1) to give a complete dispersion map (variation of reflectivity with  $\lambda = 2\pi c/\omega = 2\pi/k_0$  and  $k_x = n_m k_0 \sin\theta_m$ )

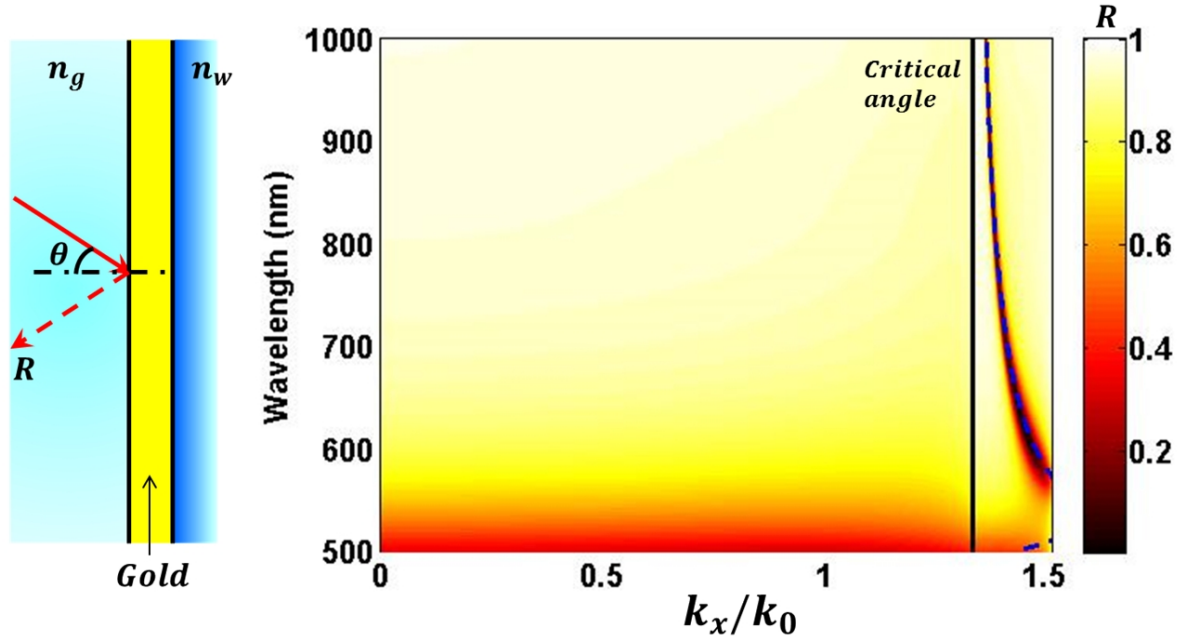


Figure 6.2: The calculated reflectivity ( $R$ ) for a gold film of 50nm as a function of wavelength ( $\lambda$ ) and  $k_x/k_0$ . Light is TM polarized and incident from a homogeneous medium of refractive index  $n_g = 1.513$ . The refractive index of the medium on the other side of the gold film is  $n_w = 1.333$ . The condition for  $k_x = k_{sp}$  is also shown (blue dotted)

In figure 6.2 we have shown the calculation of total reflectivity ( $R$ ) dispersion map for a thin gold film of 50nm with homogeneous media of refractive index  $n_w = 1.333$  and  $n_g = 1.513$  on either side. Light is considered to be TM polarized and incident at an angle  $\theta$  from the medium of index  $n_g$ . The map is plotted with respect to the incident wavelength  $\lambda$  and  $k_x/k_0 = n_g \sin\theta$  where  $k_x$  is the wave-vector of the incident light in the plane of the interface along the direction of propagation. We see that the reflectivity is close to 1 for most of the map which is expected with a metal film. The critical angle for the  $n_g \rightarrow n_w$  interface is given by  $\theta_c = \sin^{-1}(n_w/n_g)$  thus for  $k_x/k_0 = n_w$ . This also defines the light line in the medium  $n_w$ . We see an abrupt drop in reflectivity at certain wavelengths and internal angles which correspond to  $k_x = k_{sp}$  where  $k_{sp}$  is given by equation 2.3 with the index of the dielectric taken as  $n_w = 1.333$ . This drop is due to the excitation of the PSP at the gold- $n_w$  interface which was explained in section 2.1.2. The physical interpretation of this in practical conditions and the different methods for the excitation of the PSP was shown in chapter 3. The other drop of reflectivity below  $550nm$  is due to high absorption of gold for lower wavelengths (figure 1.2) and not due to plasmon excitation.

## 6.2 Fourier modal method (FMM)

The Rouard method is suitable to calculate the reflection of a stack of thin films but is limited to only planar surfaces. Another fundamental problem in CEM is that of a periodic diffraction grating. As mentioned in the beginning of chapter 2 the research in plasmonics originated somewhat from Wood's anomaly in optical gratings and Rayleigh's hypothesis based in classical grating theories. For a long time, different theories to define perfectly the orders of diffraction, reflection and transmission from a grating has been proposed and formulated.

The well known grating equation for a periodicity of  $\Lambda$  written as

$$k_{xm} = k_{xi} + mK_B \quad (6.4)$$

gives precisely the direction of diffracted orders with  $k_{xi}$  being the wave-vector of the incident field in the plane parallel to the grating and  $k_{xm}$ , the same for the diffracted order  $m$ .  $K_B = 2\pi/\Lambda$  is a constant and depends only on the period of the grating and is generally considered as the 'wave-vector' of the grating. We will call it the Bragg wave-vector in reference to the work by William Lawrence Bragg and William Henry Bragg in 1913 where they formulated the theory to explain diffraction of X-rays from the periodic lattice of crystalline solids [150]. However the grating equation does not give any information on the energy distribution in the different orders.

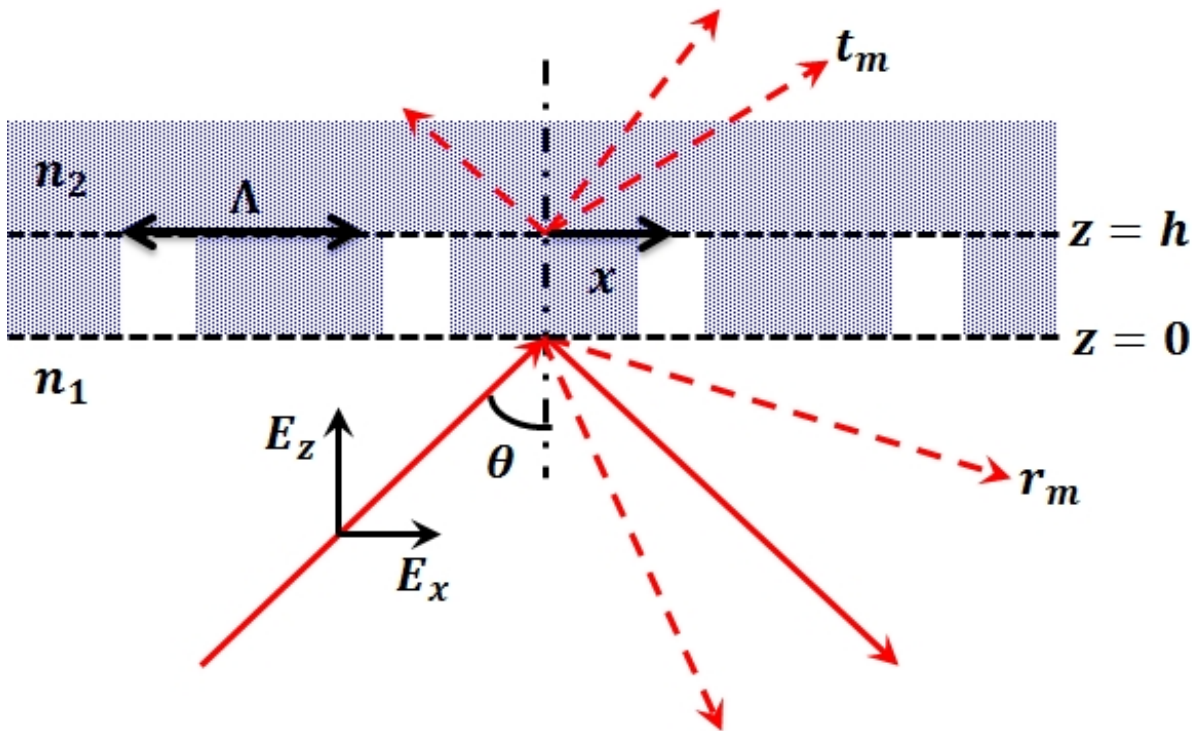


Figure 6.3: Geometry for the binary rectangular-groove grating diffraction problem. The period of the grating is  $\Lambda$ . The refractive index of the incident medium is  $n_1$  and that on the other side is taken as  $n_2$ .

The earliest known method to derive the distribution of energy in different diffraction orders was by the Rayleigh expansion method which states that the total field can be represented by a series expansion

of plane waves. In the space on either side of the grating (shown in figure 6.3) the electric field can be written in the form of Rayleigh expansion as

$$\begin{aligned}
 z < 0 & \left\{ E_R(\mathbf{x}, z) = \sum_{m=-\infty}^{\infty} r_m e^{ik_{xm} + ik_{zm}} \right\} \\
 z > h & \left\{ E_T(\mathbf{x}, z) = \sum_{m=-\infty}^{\infty} t_m e^{ik_{xm} + ik_{zm}} \right\}
 \end{aligned} \tag{6.5}$$

where  $r_m$  and  $t_m$  are the reflection and transmission coefficients that are to be determined to solve for the energy distributed in each order  $m$  with wave-vectors  $k_{xm}$  and  $k_{zm}$  in  $x$  and  $z$  direction respectively. This expansion directly stems from the wave condition and the Helmholtz equation (equation 1.10) and can be solved using suitable boundary conditions. This holds in the upper and lower halfspace however fails to give precise results inside the grating grooves. This is because the complex dielectric constant ( $\epsilon$ ) of the grooves is not constant but a function of  $x$  and  $z$  and thus a well defined solution is not possible directly. The method also fails to take into account the polarization of the incident light. A more accurate approach to the problem is to solve the set of Maxwell's equations.

To solve for the field in the grating grooves two methods were introduced in the early 1980s. One method called the C-method was introduced by Chandezon et al [151, 152]. The method is based on the fact that the Rayleigh expansion would work if the interface was planar and thus the method introduces a new coordinate system to map the corrugated grating surfaces to planar surfaces.

The other method is to write the solution in the grooves as a Fourier expansion and was introduced by Knop et al [153] and further developed by Moharam and Gaylord [154, 155]. This method, called the Fourier modal method (FMM) or historically called the rigorous coupled wave analysis (RCWA), eliminates the  $z$ -dependency of  $\epsilon$  by slicing up the grating such that at each slice,  $\epsilon$  only depends on  $x$ . Then applying suitable boundary condition at the slice edges we can resolve the Maxwell's equations into a matrix eigenvalue problem. In this section we would describe in details the basics of FMM and the formulation that we have used for this work in the case of 1D and 2D arrays.

### 6.2.1 Formulation in Fourier space for 1D array

The two Maxwell's equations 1.8 when considering no external charges or currents can be written as

$$\begin{aligned}
 \nabla \times \mathcal{E}(\mathbf{r}) &= i\omega\boldsymbol{\mu}\boldsymbol{\mu}_0\mathcal{H}(\mathbf{r}) \\
 \nabla \times \mathcal{H}(\mathbf{r}) &= -i\omega\epsilon\epsilon_0\mathcal{E}(\mathbf{r})
 \end{aligned} \tag{6.6}$$

where  $\boldsymbol{\mu}$  and  $\epsilon$  are symmetric tensors and we define  $\mathbf{Z}_0 = \sqrt{\frac{\boldsymbol{\mu}_0}{\epsilon_0}} = c\boldsymbol{\mu}_0$ . By dividing the first equation by  $\sqrt{(\mathbf{Z}_0)}$  and multiplying the second equation by  $i\sqrt{(\mathbf{Z}_0)}$ , we can have the symmetric Maxwell's equations of the form

$$\begin{aligned}
 \nabla \times \mathbf{E} &= k_0\boldsymbol{\mu}\mathbf{H} \\
 \nabla \times \mathbf{H} &= k_0\epsilon\mathbf{E}
 \end{aligned} \tag{6.7}$$

This provides the advantage of solving for either  $\mathcal{E}$  or  $\mathcal{H}$  and then obtaining the other just by permuting the tensors  $\epsilon$  or  $\mu$  with the fields  $\mathbf{E}$  and  $\mathbf{H}$ .

The wave equation (equation 1.9) can now be written as

$$\nabla \times \frac{1}{q} \nabla \times \vec{u} - k_0^2 p \vec{u} = 0 \quad (6.8)$$

where for the electric field formulation  $p = \epsilon$ ,  $q = \mu$  and  $\vec{u} = \mathbf{E} = \mathcal{E}(r)/\sqrt{Z_0}$  while for the magnetic field formulation  $p = \mu$ ,  $q = \epsilon$  and  $\vec{u} = \mathbf{H} = i\mathcal{H}(r)\sqrt{Z_0}$ .

Considering the geometry of figure 6.3 for TE and TM polarization, we can write the equation 6.7 as

$$TE \left\{ \begin{array}{l} \frac{\partial E^y}{\partial z} = -k_0 \mu^x(x) H^x \\ \frac{\partial E^y}{\partial x} = k_0 \mu^z(x) H^z \\ \frac{\partial H^z}{\partial x} - \frac{\partial H^x}{\partial z} = k_0 \epsilon^y(x) E^y \end{array} \right\} \quad (6.9)$$

$$TM \left\{ \begin{array}{l} \frac{\partial H^y}{\partial z} = -k_0 \epsilon^x(x) E^x \\ \frac{\partial H^y}{\partial x} = k_0 \epsilon^z(x) E^z \\ \frac{\partial E^z}{\partial x} - \frac{\partial E^x}{\partial z} = k_0 \mu^y(x) H^y \end{array} \right\}$$

To solve in the grating grooves (we will consider here the incident field to be TE polarized, similar treatment can be shown for TM polarization), the system of equations can be written within a slice along  $x$  in terms of the field components continuous in  $x$  (considering  $\epsilon$  and  $\mu$  to be functions of  $x$ ) as

$$TE \left\{ \begin{array}{l} \frac{\partial E^y}{\partial z} = -k_0 B^x \\ \frac{\partial H^x}{\partial z} = \frac{\partial H^z}{\partial x} - k_0 \epsilon^z(x) E^y \end{array} \right\} \text{ with } \left\{ \begin{array}{l} H^z = B^z / \mu^x(x) \\ B^x = \mu^x(x) H^x \\ k_0 B^z = \frac{\partial E^y}{\partial x} \end{array} \right\} \quad (6.10)$$

By applying the Floquet theory to the above set of equations we can write the fields in terms of a Floquet-Fourier series with period  $\Lambda$  as

$$\left\{ \begin{array}{l} E^y(x, z) = \sum_{m=1}^N \hat{E}_m^y(z) e^{i\beta_m x} \\ H^x(x, z) = \sum_{m=1}^N \hat{H}_m^x(z) e^{i\beta_m x} \\ H^z(x, z) = \sum_{m=1}^N \hat{H}_m^z(z) e^{i\beta_m x} \end{array} \right\} \left\{ \begin{array}{l} D^y(x, z) = \sum_{m=1}^N \hat{D}_m^y(z) e^{i\beta_m x} \\ B^x(x, z) = \sum_{m=1}^N \hat{B}_m^x(z) e^{i\beta_m x} \\ B^z(x, z) = \sum_{m=1}^N \hat{B}_m^z(z) e^{i\beta_m x} \end{array} \right\} \quad (6.11)$$

while the dielectric constants can be expressed in terms of a Fourier series as

$$\left\{ \begin{array}{l} \epsilon^y(x) = \sum_{m=-N}^N \hat{\epsilon}_m^y e^{imK_B x} \\ \frac{1}{\mu^x(x)} = \sum_{m=-N}^N \left[ \frac{\hat{1}}{\mu_m^x} \right] e^{imK_B x} \\ \mu^z(x) = \sum_{m=-N}^N \hat{\mu}_m^z e^{imK_B x} \end{array} \right\} \quad (6.12)$$

where we define  $\beta_m = \beta_0 + mK_B$  with  $\beta_0 = n_1 k_0 \sin\theta$ , a constant determined by the incident plane wave.  $\hat{E}_m^y, \hat{H}_m^x, \hat{H}_m^z, \hat{D}_m^y, \hat{B}_m^x$  and  $\hat{B}_m^z$  are the Fourier coefficients (for convenience we will refer to both Fourier and Floquet-Fourier coefficients as Fourier coefficients). We must note that  $E^y, H^z$  and  $B^x$  are continuous in  $x$  and thus we can reduce the number of Fourier coefficients by using the relation between them similar to equation 6.9. We can also write the dielectric constants in form of Toeplitz matrix. We should also note that for equations of the form  $\vec{E}^y(x, z) = \sum_{m=1}^N \hat{E}_m^y(z) e^{i\beta_m x}$  and  $\frac{\partial \vec{E}^y}{\partial x} = k_0 \vec{B}^z(x, z) \Rightarrow k_0 \sum_{m=1}^N \hat{B}_m^z(z) e^{i\beta_m x}$ , we can write for the coefficients in matrix form as  $k_0 \hat{B}^z = i\beta \hat{E}^y$  where  $\beta$  is a diagonal matrix of size  $N \times N$ . Thus equation 6.9 can be simplified in terms of Fourier coefficient matrices as

$$\left\{ \begin{array}{l} \frac{\partial \hat{E}^y}{\partial z} = -k_0 \hat{B}^x \\ \frac{\partial \hat{H}^x}{\partial z} = i\beta \hat{H}^z - k_0 \hat{D}^y \end{array} \right\} \text{with} \left\{ \begin{array}{l} \hat{H}^z = [\mu^z]^{-1} \hat{B}^z \\ \hat{B}^x = \left[ \frac{1}{\mu^x} \right]^{-1} \hat{H}^x \\ \hat{D}^y = [\epsilon^y] \hat{E}^y \end{array} \right\}$$

$$\text{with } [\epsilon^j] = \begin{pmatrix} \hat{\epsilon}_0 & \hat{\epsilon}_{-1} & \dots & \hat{\epsilon}_{-N} \\ \hat{\epsilon}_1 & \hat{\epsilon}_0 & \dots & \dots \\ \dots & \dots & \dots & \dots \\ \hat{\epsilon}_N & \dots & \dots & \hat{\epsilon}_0 \end{pmatrix} \quad (6.13)$$

$$\text{and } [\mu^j] = \begin{pmatrix} \hat{\mu}_0 & \hat{\mu}_{-1} & \dots & \hat{\mu}_{-N} \\ \hat{\mu}_1 & \hat{\mu}_0 & \dots & \dots \\ \dots & \dots & \dots & \dots \\ \hat{\mu}_N & \dots & \dots & \hat{\mu}_0 \end{pmatrix}$$

$$j = x, y, z$$

where  $[\epsilon^j]$  and  $[\mu^j]$  are in the form of Toeplitz matrix (diagonal-constant matrix).

In equation 6.13 we have a symmetric form of the Maxwell's equation in terms of Fourier coefficients. The equations can be expressed as matrices which are purely functions of  $z$  as

$$\left\{ \begin{array}{l} \frac{d\hat{E}^y}{dz} = -k_0 \left[ \frac{1}{\hat{\mu}^x} \right]^{-1} \hat{H}^x \\ \frac{d\hat{H}^x}{dz} = \frac{1}{k_0} \beta [\hat{\mu}^z]^{-1} \beta \hat{E}^y - k_0 [\hat{\epsilon}^y] \hat{E}^y \end{array} \right\}$$

or

$$(6.14)$$

$$\frac{d}{dz} \begin{pmatrix} \hat{E}^y \\ \hat{H}^x \end{pmatrix} = \begin{pmatrix} 0 & A \\ B & 0 \end{pmatrix} \begin{pmatrix} \hat{E}^y \\ \hat{H}^x \end{pmatrix} = M \times \begin{pmatrix} \hat{E}^y \\ \hat{H}^x \end{pmatrix}$$

where  $A$  and  $B$  are constant matrices of dimension  $N \times N$  given by

$$A = -k_0 \left[ \frac{1}{\hat{\mu}^x} \right]^{-1} \quad (6.15)$$

$$B = \frac{1}{k_0} \beta [\hat{\mu}^z]^{-1} \beta - k_0 [\hat{\epsilon}^y]$$

The solution of equation 6.14 for initial value  $z = z_0$  and final value  $z = z_h = z_0 + h$  can be written as

$$\begin{pmatrix} \hat{E}_{z_h}^y \\ \hat{H}_{z_h}^x \end{pmatrix} = e^{M \times h} \begin{pmatrix} \hat{E}_{z_0}^y \\ \hat{H}_{z_0}^x \end{pmatrix} = T \times \begin{pmatrix} \hat{E}_{z_0}^y \\ \hat{H}_{z_0}^x \end{pmatrix} \quad (6.16)$$

Where  $T$  is called the transfer matrix and relates the fields at  $z = z_0$  and  $z = z_0 + h$ . To solve for each slice along  $z$  (figure 6.4) as a function of  $x$  we need to find the values of the matrix  $T = e^{M \times h}$ .

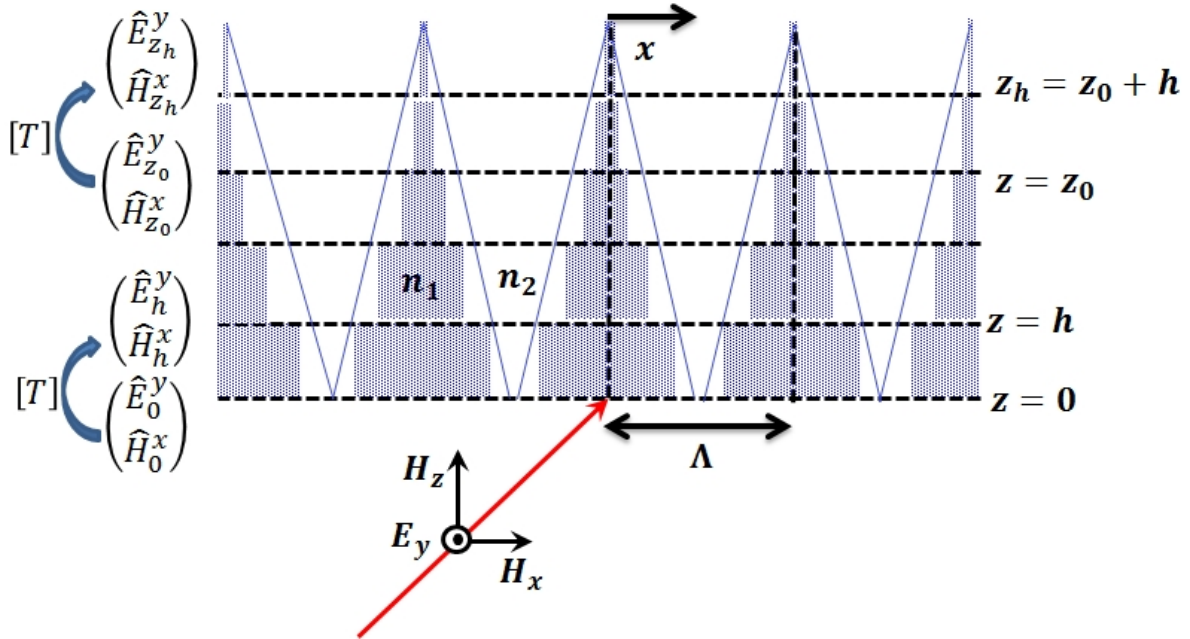


Figure 6.4: Geometry for the binary triangular-grating diffraction problem with transfer matrix ( $T$ ) formulation with slices along  $z$  for 1D array. The period of the grating is  $\Lambda$ .

## 6.2.2 Formulation in Fourier space for 2D array

For the 2D array we will follow the same approach as explained for the 1D case in the last section. We can write the relation for the fields, similar to equation 6.9 but now in terms of all the 6 field components



$E^x, E^y, E^z, H^x, H^y$  and  $H^z$  as

$$\left\{ \begin{array}{l} \frac{\partial E^x}{\partial z} = \mu^y H^y + \frac{\partial E^z}{\partial x} \\ \frac{\partial E^y}{\partial z} = -\mu^x H^x + \frac{\partial E^z}{\partial y} \\ H^z = \frac{1}{\mu^z} \left( \frac{\partial E^y}{\partial x} - \frac{\partial E^x}{\partial y} \right) \\ E^z = \frac{1}{\epsilon^z} \left( \frac{\partial H^y}{\partial x} - \frac{\partial H^x}{\partial y} \right) \end{array} \right\} \quad (6.17)$$

Substituting the last equation in the first two of equation 6.17 we can write

$$\left\{ \begin{array}{l} \frac{\partial E^x}{\partial z} = \mu^y H^y + \frac{\partial}{\partial x} \left[ \frac{1}{\epsilon^z} \left( \frac{\partial H^y}{\partial x} - \frac{\partial H^x}{\partial y} \right) \right] \\ \frac{\partial E^y}{\partial z} = -\mu^x H^x + \frac{\partial}{\partial y} \left[ \frac{1}{\epsilon^z} \left( \frac{\partial H^y}{\partial x} - \frac{\partial H^x}{\partial y} \right) \right] \end{array} \right\} \quad (6.18)$$

By decomposition of the fields in terms of Floquet-Fourier series with periodicity along  $x$  and  $y$  being  $\Lambda^x$  and  $\Lambda^y$  respectively, we can write the field components similar to equation 6.11 as

$$E^x(x, y, z) = \sum_{m_x=1}^{N_x} \sum_{m_y=1}^{N_y} \hat{E}_{m_x, m_y}^x(z) e^{i(\beta_{m_x}^x x + \beta_{m_y}^y y)} \quad (6.19)$$

*etc...*

where  $\beta_m^x = \beta_0^x + (m - m_0^x)K_{B_x}$  and  $\beta_m^y = \beta_0^y + (m - m_0^y)K_{B_y}$  with  $K_{B_x} = 2\pi/\Lambda_x$  and  $K_{B_y} = 2\pi/\Lambda_y$  for each value of  $m$ . The dielectric constants can also be expressed in terms of a Fourier series similar to equation 6.12 as

$$\epsilon^x(x, y) = \sum_{m_x=1}^{N_x} \sum_{m_y=1}^{N_y} \hat{\epsilon}_{m_x, m_y}^x e^{i(m_x K_{B_x} x + m_y K_{B_y} y)} \quad (6.20)$$

*etc...*

Considering  $\hat{E}^x$  to be the column vector with the Fourier coefficients  $\hat{E}_{m_x, m_y}^x(z)$  as the elements, we can write the relation between the coefficients of field in matrix form as

$$\left\{ \begin{array}{l} \frac{\partial \hat{E}^x}{\partial z} = [\hat{\mu}^y] \hat{H}^y - \beta^x \left[ \frac{1}{\hat{\epsilon}^z} \right] (\beta^x \hat{H}^y - \beta^y \hat{H}^x) \\ \frac{\partial \hat{E}^y}{\partial z} = -[\hat{\mu}^x] \hat{H}^x - \beta^y \left[ \frac{1}{\hat{\epsilon}^z} \right] (\beta^x \hat{H}^y - \beta^y \hat{H}^x) \end{array} \right\} \quad (6.21)$$

*with*

$$\hat{E}^z = \left[ \frac{1}{\hat{\epsilon}^z} \right]^{x,y} (\beta^x \hat{H}^y - \beta^y \hat{H}^x)$$

Treating the above equations in a form similar to equation 6.14 we can write the coefficients in matrix form as

$$\frac{d}{dz} \begin{pmatrix} \hat{E}^x \\ \hat{E}^y \\ \hat{H}^x \\ \hat{H}^y \end{pmatrix} = \begin{pmatrix} \mathbf{0} & \mathbf{A} \\ \mathbf{B} & \mathbf{0} \end{pmatrix} \begin{pmatrix} \hat{E}^x \\ \hat{E}^y \\ \hat{H}^x \\ \hat{H}^y \end{pmatrix} = \mathbf{M} \times \begin{pmatrix} \hat{E}^x \\ \hat{E}^y \\ \hat{H}^x \\ \hat{H}^y \end{pmatrix} \quad (6.22)$$

where  $\mathbf{A}$  and  $\mathbf{B}$  are constant matrices given by

$$\mathbf{A} = \begin{pmatrix} \beta^x \left[ \frac{1}{\hat{\epsilon}^z} \right] \beta^y & [\hat{\mu}^y] - \beta^x \left[ \frac{1}{\hat{\epsilon}^z} \right] \beta^x \\ -[\hat{\mu}^x] + \beta^y \left[ \frac{1}{\hat{\epsilon}^z} \right] \beta^y & -\beta^y \left[ \frac{1}{\hat{\epsilon}^z} \right] \beta^x \end{pmatrix}$$

$$\mathbf{B} = \begin{pmatrix} \beta^x \left[ \frac{1}{\hat{\mu}^z} \right] \beta^y & [\hat{\epsilon}^y] - \beta^x \left[ \frac{1}{\hat{\mu}^z} \right] \beta^x \\ -[\hat{\epsilon}^x] + \beta^y \left[ \frac{1}{\hat{\mu}^z} \right] \beta^y & -\beta^y \left[ \frac{1}{\hat{\mu}^z} \right] \beta^x \end{pmatrix} \quad (6.23)$$

Generalizing equation 6.14 for 1D array and equation 6.22 for 2D array we can write the general relation in the form of transfer matrix  $\mathbf{T}$  as

$$\begin{pmatrix} \hat{E}_{z_h} \\ \hat{H}_{z_h} \end{pmatrix} = e^{\mathbf{M} \times h} \begin{pmatrix} \hat{E}_{z_0} \\ \hat{H}_{z_0} \end{pmatrix} = \mathbf{T} \times \begin{pmatrix} \hat{E}_{z_0} \\ \hat{H}_{z_0} \end{pmatrix} \quad (6.24)$$

where  $\hat{E}_{z_h} = \hat{E}_{z_h}^y$  and  $\hat{H}_{z_h} = \hat{H}_{z_h}^x$  for the 1D array case, while  $\hat{E}_{z_h} = \begin{pmatrix} \hat{E}_{z_h}^x \\ \hat{E}_{z_h}^y \end{pmatrix}$  and  $\hat{H}_{z_h} = \begin{pmatrix} \hat{H}_{z_h}^x \\ \hat{H}_{z_h}^y \end{pmatrix}$  for the 2D array case. The general problem thus requires matrix formulation to solve for the matrix  $\mathbf{M}$  to evaluate the fields in terms on the transfer matrix  $\mathbf{T}$ .

### 6.2.3 Generalized Matrix formulation for 1D and 2D arrays

Recalling some basic matrix rules, if  $\mathbf{M}$  is diagonalizable such that  $\mathbf{M} = \mathbf{M}_D \times \nu \times \mathbf{M}_D^{-1}$  with  $\nu$  a diagonal matrix, then we can write  $e^{\mathbf{M} \times h} = \mathbf{M}_D \times e^{\nu h} \times \mathbf{M}_D^{-1}$ . To find the matrices  $\mathbf{M}_D$  and  $\nu$  we can use the relation  $\frac{d^2}{dz^2} \hat{E} = (\mathbf{A}\mathbf{B}) \hat{E}$  which can be found directly from equation 6.14. Considering  $\nu_p^2 = (\mathbf{A}\mathbf{B})$  as the eigenvalues of this relation and  $\hat{H} = \mathbf{A}^{-1} \frac{d\hat{E}}{dz}$  we can write the Fourier coefficients of the fields as

$$\begin{aligned}\vec{E} &= Vc^+e^{\nu_p z} + Vc^-e^{-\nu_p z} \\ \vec{H} &= A^{-1}[\nu_p Vc^+e^{\nu_p z} - \nu_p Vc^-e^{-\nu_p z}]\end{aligned}$$

or

$$\begin{pmatrix} \hat{E}_{z_h} \\ \hat{H}_{z_h} \end{pmatrix} = \begin{pmatrix} V & V \\ A^{-1}\nu_p V & -A^{-1}\nu_p V \end{pmatrix} \begin{pmatrix} e^{\nu_p h} & 0 \\ 0 & e^{-\nu_p h} \end{pmatrix} \begin{pmatrix} c^+ \\ c^- \end{pmatrix} \quad (6.25)$$

and

$$\begin{pmatrix} \hat{E}_{z_0} \\ \hat{H}_{z_0} \end{pmatrix} = \begin{pmatrix} V & V \\ A^{-1}\nu_p V & -A^{-1}\nu_p V \end{pmatrix} \begin{pmatrix} c^+ \\ c^- \end{pmatrix}$$

Comparing the above relation with equation 6.16 and the fact that  $(AB) = V\nu_p^2 V^{-1}$ , where  $V$  is the matrix used to diagonalize  $(AB)$  we can write

$$\begin{aligned}M &= \begin{pmatrix} 0 & A \\ B & 0 \end{pmatrix} = \begin{pmatrix} Q & Q \\ P & -P \end{pmatrix} \begin{pmatrix} \nu_p & 0 \\ 0 & -\nu_p \end{pmatrix} \begin{pmatrix} Q^{-1}/2 & P^{-1}/2 \\ Q^{-1}/2 & -P^{-1}/2 \end{pmatrix} \\ &= M_D \times \nu \times M_D^{-1}\end{aligned} \quad (6.26)$$

where

$$\begin{aligned}Q &= V\nu_p \\ P &= BV\end{aligned}$$

On developing the matrix  $T = e^{M \times h} = M_D \times e^{\nu h} \times M_D^{-1}$  we get the transfer matrix as

$$T = \begin{pmatrix} Q \cosh(\nu_p h) Q^{-1} & Q \sinh(\nu_p h) P^{-1} \\ P \sinh(\nu_p h) Q^{-1} & P \cosh(\nu_p h) P^{-1} \end{pmatrix} \quad (6.27)$$

To have stable solutions, the eigenvalues  $\nu_p$  must satisfy the relation  $\text{Re}(\nu_p) \leq \text{Im}(\nu_p)$ . It has been seen that transfer matrix formulation is relatively unstable for large values of  $\text{Re}(\nu_p)$ . To solve this problem another matrix called the scattering matrix ( $S$ ) is more commonly used.  $S$  can be found easily from  $T$  and is related to the fields at  $z = z_0$  and  $z = z_h = z_0 + h$  as

$$\begin{aligned}\begin{pmatrix} \hat{E}_{z_h} \\ \hat{H}_{z_0} \end{pmatrix} &= S \times \begin{pmatrix} \hat{E}_{z_0} \\ \hat{H}_{z_h} \end{pmatrix} \\ S &= \begin{pmatrix} Q \frac{1}{\cosh(\nu_p h)} Q^{-1} & Q \tanh(\nu_p h) P^{-1} \\ -P \tanh(\nu_p h) Q^{-1} & P \frac{1}{\cosh(\nu_p h)} P^{-1} \end{pmatrix}\end{aligned} \quad (6.28)$$

We can use a more general relation between the Fourier coefficients by defining what we call the  $G$  matrix starting from the  $T$  matrix.

$$\begin{pmatrix} e^{-\nu_p h} & 0 \\ 0 & 1 \end{pmatrix} \begin{pmatrix} Q^{-1}/2 & P^{-1}/2 \\ Q^{-1}/2 & -P^{-1}/2 \end{pmatrix} \begin{pmatrix} \hat{E}_{z_h} \\ \hat{H}_{z_h} \end{pmatrix} = \\ \begin{pmatrix} 1 & 0 \\ 0 & e^{-\nu_p h} \end{pmatrix} \begin{pmatrix} Q^{-1}/2 & P^{-1}/2 \\ Q^{-1}/2 & -P^{-1}/2 \end{pmatrix} \begin{pmatrix} \hat{E}_{z_0} \\ \hat{H}_{z_0} \end{pmatrix} \quad (6.29)$$

or

$$G_h \begin{pmatrix} \hat{E}_{z_h} \\ \hat{H}_{z_h} \end{pmatrix} = G_0 \begin{pmatrix} \hat{E}_{z_0} \\ \hat{H}_{z_0} \end{pmatrix}$$

Using this relation to solve for the fields in the grating we need to solve for each slice the matrices defined by  $P$ ,  $Q$  and  $\nu_p$ , as shown in figure 6.4. For more complex geometries we can either decompose them in slices or use other numerical methods to derive the Toeplitz matrices as defined by equation 6.13 and thus the  $S$  and  $T$  matrices. One of such methods, the Finite element method will be described in brief in the next section. The complete method of combining FMM and FEM, that we have used to calculate the fields in this work will be described in chapter 7.

## 6.3 Finite element method (FEM)

Finite element methods (FEM) is a powerful tool to have approximate solutions of partial differential equations that arise in mathematical modeling of various physical phenomenon. Symmetric Maxwell's equations as described in equation 6.7 are one of such partial differential equations and thus can be solved using FEM [156, 157, 158]. The advantages of FEM are that it can be used for solving complex geometries, non linear problems, with possibilities of temporal, harmonic or modal solutions and can be hybridized with other analytical or numerical methods. In this section we will describe in brief the FEM and the formulation we have used in this work.

The starting point of FEM is describing a problem in terms of partial derivatives. Once such formulation is done, the domain under study is chosen based on symmetry or periodicity. The materials of each section of the domain can be described in terms of permittivity or permeability vectors. Suitable boundary conditions must be imposed at the boundary of the domain. These conditions are used while describing the symmetry of the system and help to reduce the domain of calculation. The domain is then discretized for 2D by dividing the surface in triangular or quadrangular elements and for 3D by sectioning the volume in cubic, tetrahedral or pyramidal elements.

### 6.3.1 The elements of Whitney

The domain under study  $\Omega$  is discretized by a mesh consisting of finite elements, where the electromagnetic field is described by approximate elementary matrices. Such matrices are assembled to generate to complete global matrix for the system. A simple system consisting of a circular domain is shown in figure 6.5 along with the defined symmetry, the boundary conditions and the mesh.

Each element of the mesh is identified by the nodes ( $n$ ), edge ( $a$ ), face ( $f$ ) or volume ( $v$ ). A simplicial mesh is when  $\Omega$  is discretized in such a way that any two elements can intersect only along a common

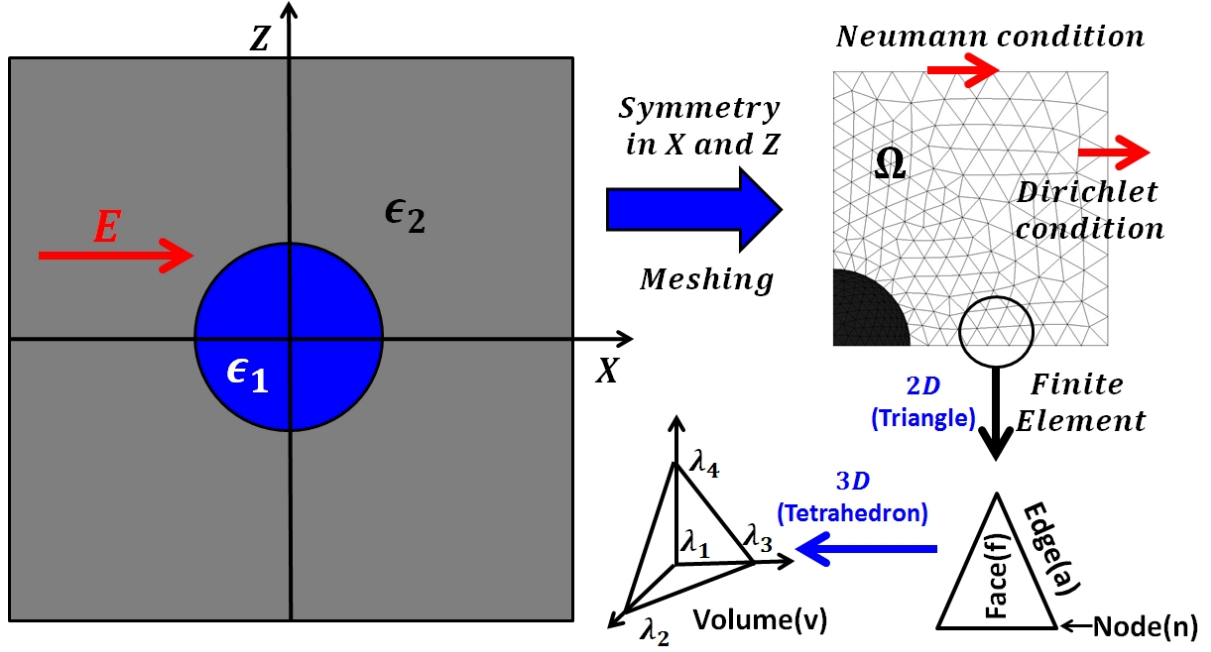


Figure 6.5: Basics of Finite element methods. The 3D structure consists of a sphere of permittivity  $\epsilon_1$  in a homogeneous medium of permittivity  $\epsilon_2$  with an incident electric field ( $E$ ) along  $X$ . The domain of study  $\Omega$  is chosen with respect to the periodicity in  $X$  and  $Z$ . The boundary conditions are applied at the boundary of the domain and then a 2D mesh (in  $X - Z$  plane) consisting of triangles or a 3D mesh for the entire volume is chosen.

node, edge or face. We denote  $N, A, F, V$  to the set of simplices of dimensions 0 to 3 respectively for nodes, edges, faces and volumes of the elements. We associate a function  $\lambda_i$  called the barycentric coordinates with each node  $i$  such that  $\lambda_i(\mathbf{k}) = 1$  if  $i = \mathbf{k}$  and  $\lambda_i(\mathbf{k}) = 0$  for all other nodes ( $\mathbf{k}$ ) with  $i \neq \mathbf{k}$ .

The element of Whitney is a differential vector field which relates the all the simplices of the mesh. For the lowest order (dimension of simplex) Whitney element which is associated to a node (order 0,  $W^0$ ) we can write  $w_n = \lambda_i$  for node  $i = n$ . In this case a scalar function  $\phi$  which can be defined as  $\phi = \sum_{n \in N} w_n \phi_n$  with  $\phi_n$  being the values of  $\phi$  at the node  $n$ , is continuous across the edge of the elements.

The next higher order of Whitney elements (order 1,  $W^1$ ) is defined for the edge  $\{i, j\}$  between nodes  $i$  and  $j$ . The vector field for the Whitney field in this case is defined as  $w_a = \lambda_i \nabla \lambda_j - \lambda_j \nabla \lambda_i$ . The field is non existent for the elements without the edge  $\{i, j\}$  in common and the circulation of the vector  $w_a = 1$  for that edge and zero for the others.  $w_a$  is discontinuous across the face of the elements, however the tangential component is continuous. The approximate field in terms of Whitney elements of order 1 can be written as  $\mathbf{h} = \sum_{a \in A} w_a \mathbf{h}_a$ . The degrees of freedom of  $\mathbf{h}_a$  are the circulation of  $\mathbf{h}$  along the edges.

Similarly for the Whitney elements of order 2 ( $W^2$ ) on the face  $\{i, j, k\}$  we can write  $w_f = 2(\lambda_i \nabla \lambda_j \times \nabla \lambda_k + \lambda_j \nabla \lambda_k \times \nabla \lambda_i + \lambda_k \nabla \lambda_i \times \nabla \lambda_j)$ . The flux of  $w_f = 1$  across the face  $\{i, j, k\}$  and zero for the others. The flux density can be approximated as  $\mathbf{b} = \sum_{f \in F} w_f \mathbf{b}_f$  with  $\mathbf{b}_f$  being the flux trough face  $f$ . For the third order ( $W^3$ ) we can define  $w_v$  for the volume of the element and the integral of it is unity over the defined volume element.

For electromagnetics the scalar potentials (electric  $\Phi$ , magnetic  $\Psi$ ) are approximated by  $W^0$ , the fields (electric  $E$ , magnetic  $H$ ) and vector potentials (electric  $U$ , magnetic  $A$ ) by  $W^1$ , the flux (electric  $D$ , magnetic  $B$ ) and current densities ( $J$ ) by  $W^2$  and the volume charge densities ( $\rho$ ) by  $W^3$ . Table 6.1 summarizes the different physical components of electromagnetics and the corresponding Whitney element to be used to approximate.

Table 6.1: Electromagnetic quantities and corresponding Whitney elements

	Volt(V)	Weber (Wb)	Ampere (A)	Coulomb (C)	
$W^0$	$\Phi$		$\Psi$		Scalar potentials
$W^1$	$E = -\nabla\Phi - \frac{\partial A}{\partial t}$	A	$H = -\nabla\Psi - \frac{\partial U}{\partial t}$	U	Fields, Vector potentials
$W^2$	$0 = \nabla \times E + \frac{\partial B}{\partial t}$	$B = \nabla \times A$	$J = \nabla \times H - \frac{\partial D}{\partial t}$	$D = \nabla \times U$	Flux density, Current density
$W^3$		$0 = \nabla \cdot B$		$\rho = \nabla \cdot D$	Charge density

### 6.3.2 FEM formulation for 1D array

The set of Maxwell's equations that have to be solved is given in equation 6.9. The equations can be written as

$$TE \left\{ -\frac{\partial}{\partial x} \left( \frac{1}{\mu^z} \frac{\partial E^y}{\partial x} \right) - \frac{\partial}{\partial z} \left( \frac{1}{\mu^x} \frac{\partial E^y}{\partial z} \right) = k_0^2 \epsilon^y E^y \right\} \quad (6.30)$$

It must be noted that we have chosen to formulate the problem in terms of the electric field for TE. The same can be written for TM as suited to the application this work is based on. For it the magnetic field  $H$  must be permuted with  $E$  and  $\epsilon$  with  $\mu$ . For TE we have only one component of the electric field ( $E^y$ ) and thus can be solved by approximating the field with nodal elements ( $W^0$ ). For TM we have the rotation form of the equations ( $\nabla \times$ ) and so edge elements ( $W^1$ ) must be used to approximate the electric fields.

The Galerkin method is commonly used in FEM to solve differential equations by converting them to a discrete problem by weak formulation. For a problem which can be described as  $Lu = f$  with  $L$  being the differential operator,  $u$  the function to be solved and  $f$  the source term, we can write  $\int_{\Omega} w_i (Lu - f) d\Omega = 0$  over the domain  $\Omega$ . The function  $u$  can then be discretized in terms of the weight function  $w_i$  as  $u = \sum_i w_i u_i$  with  $u_i$  being the basis function of  $u$ . For our purpose we would chose the weight function to be the elements of Whitney of zero or first order and describe the fields in terms of a basis function as  $E = e_i e^{i\gamma z}$  and  $H = h_i e^{i\gamma z}$ .

Using the Galerkin method for equation 6.30 and ignoring the source term we can write for TE polarization in terms of the fields  $\mathbf{E} = \begin{bmatrix} 0 & E^y & 0 \end{bmatrix}$  and  $\mathbf{H} = \begin{bmatrix} H^x & 0 & H^z \end{bmatrix}$  by weak formulation after integration by parts as

$$\begin{aligned} & - \int_{\Omega} \left[ \nabla w_n^* \cdot \begin{pmatrix} \mu^z & 0 \\ 0 & \mu^x \end{pmatrix}^{-1} \nabla E^y \right] d\Omega - k_0^2 \int [w_n^* \cdot \epsilon^y E^y] d\Omega \\ & = \pm \oint_{\Gamma_x} \left[ w_n^* \cdot \frac{1}{\mu^z} \frac{\partial E^y}{\partial x} \right] d\Gamma_x \pm \oint_{\Gamma_z} \left[ w_n^* \cdot \frac{1}{\mu^x} \frac{\partial E^y}{\partial z} \right] d\Gamma_z \end{aligned} \quad (6.31)$$

with  $w_n$  being the nodal elements with domain  $\Omega$  and surface of the domain  $\Gamma$ . For periodic structures the fields at the boundaries of the domain must be approximated to zero. The fields can be treated in the same manner for TM polarization using the edge elements ( $w_a$ ) and the tangential components for  $\mathbf{E} = \begin{bmatrix} E^x & 0 & E^z \end{bmatrix}$  and  $\mathbf{H} = \begin{bmatrix} 0 & H^y & 0 \end{bmatrix}$ .

Once such formulation is done and the fields are discretized in terms of nodal or edge elements we can use matrix formulation to solve for the field  $\mathbf{E}$  as  $[\mathbf{K}][\mathbf{E}] = [\mathbf{F}]$  with  $\mathbf{K}$  being the global matrix,  $\mathbf{F}$  the source term if any which are to be developed from the formulations. The boundary conditions at domain surface ( $\Gamma$ ) must be applied as  $[\mathbf{E}] = \mathbf{E}_0$  for Dirichlet or  $d[\mathbf{E}]/dn = \mathbf{H}_0$  for Neumann as applicable. It must be noted that  $\mathbf{K}$  is different from the scattering matrix described in section 6.2 for FMM and for FEM, it is a function of the barycentric coordinates of the Whitney elements ( $\lambda_i$ ). However we would use the same nomenclature and in the hybrid model used in this work we would combine the FMM and FEM methods in terms of the  $\mathbf{S}$  matrix to solve for the entire system, as described in the next chapter.

### 6.3.3 FEM formulation for 2D array

For 2D array all the 6 components of the fields must be treated. We would use the wave equation which can be solved by FEM. The wave equation was shown in equation 1.9. Ignoring external current densities, it can be written as

$$\nabla \times \frac{1}{\mu} \nabla \times \mathbf{E} - k_0^2 \epsilon \mathbf{E} = \mathbf{0} \quad (6.32)$$

Using the Galerkin method and Whitney elements as weight functions, as described in the previous section we can write

$$\begin{aligned} & \int_{\Omega} w_i \cdot \left[ \nabla \times \frac{1}{\mu} \nabla \times \mathbf{E}(r) - k_0^2 \epsilon \mathbf{E}(r) \right] d\Omega = \mathbf{0} \\ & \int_{\Omega} \left[ \nabla \times w_i \cdot \frac{1}{\mu} \nabla \times \mathbf{E}(r) \right] d\Omega + k_0^2 \int_{\Omega} [w_i \cdot \epsilon \mathbf{E}(r)] d\Omega \\ & - \oint_{\Gamma} \left[ w_i^* \cdot \mathbf{n} \times \frac{1}{\mu} \nabla \times \mathbf{E}(r) \right] d\Gamma = \mathbf{0} \end{aligned} \quad (6.33)$$

where we have used integration by parts and the relation  $\mathbf{A} \cdot \nabla \times \mathbf{B} = \mathbf{B} \cdot \nabla \times \mathbf{A} - \nabla \cdot (\mathbf{A} \times \mathbf{B})$ . Using  $\nabla \times \mathbf{E} = i\omega\mu\mathbf{H}$  we get

$$\begin{aligned}
& \int_{\Omega} \left[ \nabla \times \mathbf{w}_a \cdot \frac{1}{\mu} \nabla \times \mathbf{E} \right] d\Omega + k_0^2 \int_{\Omega} [\mathbf{w}_a \cdot \epsilon \mathbf{E}] d\Omega \\
& + i\omega\mu \oint_{\Gamma} [\mathbf{w}_a^* \cdot \mathbf{n} \times \mathbf{H}] d\Gamma = 0
\end{aligned} \tag{6.34}$$

We can create the global matrices by assembling the terms from the above relation in the form  $[\mathbf{K}][\mathbf{E}] = [\mathbf{F}]$  as in the case of 2D. Here for the formulation we have used the Whitney edge elements ( $\mathbf{W}^1$ ). To solve for the electromagnetic field we need to apply the boundary conditions

(a) Dirichlet boundary condition: The condition states that the tangential component of the electric field at the boundary must be continuous. Thus  $\mathbf{n} \times \mathbf{E} = \mathbf{0}$  for homogeneous boundary or  $\mathbf{n} \times \mathbf{E} = \mathbf{n} \times \mathbf{E}_{ex}$  for non-homogeneous boundary with external excitation  $\mathbf{E}_{ex}$  with  $\mathbf{n}$ , the vector normal to the boundary. For it we can consider a Perfect electric conductor (PEC) with vanishing tangential components of the electric fields at metallic boundaries, neglecting the skin depth.

(b) Neumann boundary condition: The condition is utilized for magnetic interfaces where the tangential component of the magnetic field is continuous. Thus  $\mathbf{n} \times \mathbf{H} = \mathbf{0}$  for homogeneous boundary ( $\mathbf{n} \times \nabla \times \mathbf{E} = \mathbf{0}$ ) or  $\mathbf{n} \times \mathbf{H} = \mathbf{n} \times \mathbf{H}_{ex}$  for non-homogeneous boundary with external excitation  $\mathbf{H}_{ex}$ . For it we consider a Perfect magnetic conductor (PMC) with vanishing tangential components of the magnetic fields at the boundary of the domain.

c) Absorbing Boundary conditions (ABC) also called the Silver-Muller method, where the unknown values at the boundary are chosen to be either the field diffracted by the domain or a plane wave at the domain boundary.  $\mathbf{E}^{tangent} - \sqrt{\frac{\mu_0}{\epsilon_0}} \mathbf{H} \times \mathbf{n} = \mathbf{0}$

d) Perfectly Matched Layers (PML) is an artificial absorbing layer where the fields are vanishing inside the layer. The major property for the formulation of the PML is that the fields incident on the PML from the domain do not reflect back into the domain.

In the next chapter we will describe the hybrid method used for this work where the fields inside the domain was calculated by FEM with proper boundary conditions and then the matrices solved by FEM were coupled to the FMM method to resolve for the entire extended system. This numerical model was developed in collaboration with Mondher Besbes of Laboratory Charles Fabry.



---

# Hybrid model for complex structures

---

The two numerical methods to solve the Maxwell's equations were described in the previous chapter. Both methods have their own advantages and disadvantages. The Fourier modal method (FMM) (section 6.2) using matrix formulation with propagation algorithm along a given direction can efficiently solve for most grating problems without large consumption of time or processor memory. However for complex geometries and particularly for metallic media, calculations with FMM leads to a convergence problem [159]. The Finite element methods (FEM) (section 6.3), using an appropriate mesh can overcome this problem. However, such calculations, for large computational domains compared to the wavelength of light, are time consuming and have high memory requirements. The time and memory requirements of such methods often become unreasonable even with the availability of commercial software and powerful computers. It is also redundant to use FEM for regions of the structure which comprise only of planar interfaces as such interfaces can accurately be solved by FMM. Thus the two methods are somewhat complementary and by coupling them we can effectively reduce the size of the computational domain and accurately solve for the electromagnetic fields over the complete geometry.

The structures presented in this work comprises of planar metallic or dielectric interfaces with a periodic arrays of metallic nano-structures. The basic approach of the hybrid model is to describe the electromagnetic problem (for example, in terms of the electric field  $\mathbf{E}$ ) for the complete system in matrix form as described in the previous chapter following the propagation algorithm (for example,  $[\mathbf{K}][\mathbf{E}] = [\mathbf{F}]$  with  $\mathbf{K}$  being the global matrix,  $\mathbf{F}$  the source term). The global matrix for the structured part of the system is solved by FEM formulations. The matrices for planar interfaces of the system and its far field response (total reflectivity or transmission of the system) is calculated by decomposition of the computational domain in layers and following FMM formulations. The structured zone is considered as one such layer of FMM formulation. The matrix obtained for that zone by FEM is coupled to the other matrices as obtained by FMM to calculate the response of the complete system. The schematic of this method for a 3D geometry comprising of an array of metallic nano-cylinders with underlying metallic planar film on a glass substrate is shown in figure 7.1. The global matrix for the schematic is considered to be the  $[\mathbf{K}]$  matrix described by equation 6.28 for FMM and in section 6.3.2 for FEM. For the structured zone, in this case the cylinder array, the matrix is computed by FEM. For the semi-infinite media on top and bottom of the array, the matrices are calculated by FMM and then the global matrix for the complete system is calculated by coupling all the individual matrices [160].

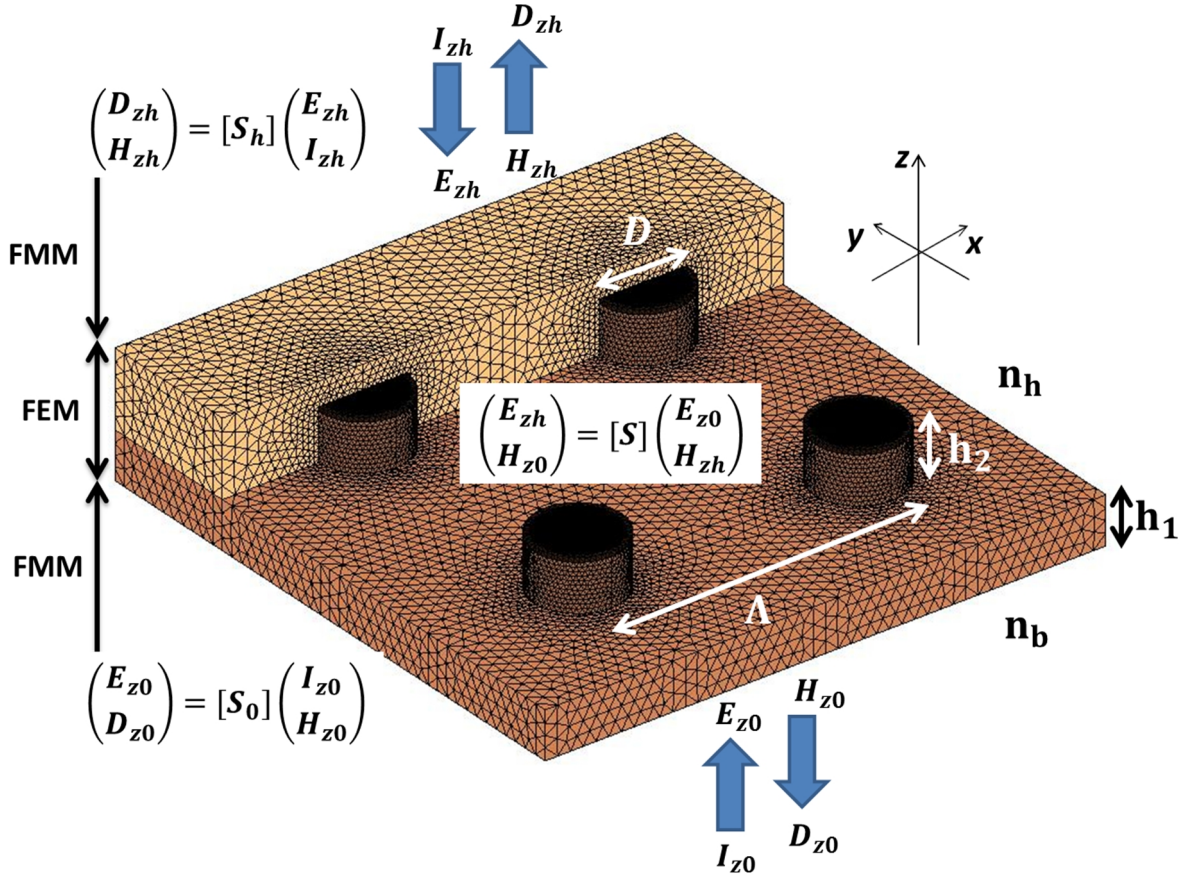


Figure 7.1: A sketch of the hybrid numerical method for a 3D geometry comprising of a metallic cylinder array on a metallic film, surrounded by homogeneous semi infinite media on both sides. The numerical method uses a mesh around the nano-structured region to calculate the  $[S]$  matrix by FEM, and then uses FMM to calculate the intensities diffracted by the system.

## 7.1 Formulations used for the hybrid numerical model

To compute the EM field in a diffraction grating problem, the domain is divided into multiple layers. By using Floquet theorem we can express the relationship between the harmonic coefficients of the fields  $\mathbf{E}$  and  $\mathbf{H}$  on the top of a layer to that at the bottom. This is done in terms of the  $\mathbf{G}$  matrix described in equation 6.29 of section 6.2.3. This matrix for the structured zone is determined by FEM, using the discretization of Maxwell's equations with Whitney elements to obtain an algebraic system relating the field  $\mathbf{E}$  at each position of the mesh to the field  $\mathbf{H}$  at the boundary.

For the simplest case, the nodal elements (Whitney elements  $\mathbf{W}^0$  with  $w_n = \lambda_i$  for node  $i = n$ ) are used for the formulation. The normal component of the electric field  $\mathbf{E}_z$  is determined by applying appropriate boundary conditions (section 6.3.3) at the limiting contours of the mesh towards top and bottom of the zone. For the  $x, y$  plane, the limiting contours of the mesh are related by pseudo-periodic conditions. To simplify the calculation, numbering of the nodes are chosen in a way to reduce the degrees of freedom within the mesh.

The algebraic system thus obtained can be written in matrix form as

$$\begin{pmatrix} \mathbf{K}_{N_0, N_0} & \mathbf{K}_{N_0, N} \\ \mathbf{K}_{N, N_0} & \mathbf{K}_{N, N} \end{pmatrix} \begin{pmatrix} \mathbf{E}_{N_0} \\ \mathbf{E}_N \end{pmatrix} = \begin{pmatrix} \mathbf{0} \\ \mathbf{H}_N^x \end{pmatrix} \quad (7.1)$$

where

$$\mathbf{K}_{i,j} = \int_{\Omega} \left[ \nabla w_i^* \cdot \begin{pmatrix} \mu^z & 0 \\ 0 & \mu^x \end{pmatrix}^{-1} \nabla w_j \right] d\Omega - k_0^2 \int_{\Omega} [w_i^* \cdot \epsilon^y w_j] d\Omega \quad (7.2)$$

This follows from the FEM formulations described in section 6.3.3 (equation 6.34) with  $\mathbf{E} = \sum_n w_n \mathbf{E}_n$  using the Galerkin method (section 6.3.2). The right hand side of equation 7.1 denotes the sources (considered zero for simplicity) and the field  $\mathbf{H}_N^x = \int_{\Gamma} [w_i^* \mathbf{H}^x] d\Gamma$ . The subscript  $N_0$  denotes the nodal elements (DOF numbers) inside the meshed domain. The subscript  $N$  denotes the elements at the boundaries with  $N = [N_h, N_b]$  where  $N_h$  denotes the DOF numbers for the top boundary and  $N_b$  for the bottom as shown in figure 7.2.

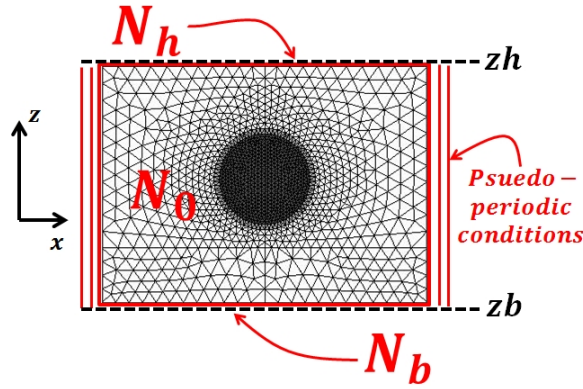


Figure 7.2: The nodal elements for the meshed zone of the calculation

The electric field inside the meshed zone can be written as  $\mathbf{E}_{N_0} = -(\mathbf{K}_{N_0, N_0})^{-1} \mathbf{K}_{N_0, N} \mathbf{E}_N^z$  while that at the boundary can be written as  $\mathbf{E}_N = (\mathbf{K}_{N, N} - \mathbf{K}_{N, N_0} (\mathbf{K}_{N_0, N_0})^{-1} \mathbf{K}_{N_0, N})^{-1} \mathbf{H}_N^x$ . Thus we can relate the  $\mathbf{E}_{N_0}$  at every node inside the mesh to the values at the boundaries  $\mathbf{E}_N$ . By appropriate numbering of the nodes and using the above matrix formulation we can find a relationship between the fields at the top ( $\mathbf{E}_{zh}$  at nodes  $N_h$ ) and bottom ( $\mathbf{E}_{zb}$  at nodes  $N_b$ ) boundaries to the sources and field  $\mathbf{H}$  in a matrix form given by

$$\begin{pmatrix} \mathbf{E}_{zh} \\ \mathbf{E}_{zb} \end{pmatrix} = \begin{pmatrix} \mathbf{M}_{h,h} & \mathbf{M}_{h,b} \\ \mathbf{M}_{b,h} & \mathbf{M}_{b,b} \end{pmatrix} \begin{pmatrix} \mathbf{H}_{zh} \\ \mathbf{H}_{zb} \end{pmatrix} \quad (7.3)$$

with

$$[\mathbf{M}] = (\mathbf{K}_{N, N} - \mathbf{K}_{N, N_0} (\mathbf{K}_{N_0, N_0})^{-1} \mathbf{K}_{N_0, N})^{-1}$$

where  $\mathbf{K}$  is the global finite element matrix and  $N$  are the DOF numbers at the top and bottom boundaries and  $N_0$ , the same inside the meshed domain.

### 7.1.1 Developing the G-matrix for the meshed domain

The relation between the fields at the top ( $z = z_h$ ) and bottom ( $z = z_b$ ) boundaries of the meshed domain are written in terms of the G-matrix to facilitate the coupling of FEM to FMM. This is done by transformation of the fields in terms of Floquet-Fourier series as described in equation 6.11 for FMM in section 6.2.1.

Such transformation together with Galerkin representation yield the following relations for the fields and their Fourier components.

$$\left\{ \begin{array}{l} \mathbf{E}^j = \sum_{m=1}^N \hat{\mathbf{E}}_m^j e^{i\beta_m x} \\ \hat{\mathbf{H}}_m^j = \frac{1}{\Gamma} \int_{\Gamma} [\mathbf{H}^j e^{i\beta_m x}] d\Gamma \\ j = x, y, z \end{array} \right\} \quad (7.4)$$

$$\left\{ \begin{array}{l} [\hat{\mathbf{E}}] = \frac{1}{\Gamma} \int_{\Gamma} [\mathbf{E} e^{i\beta_m x}] d\Gamma = [\mathbb{E}] [\mathbf{E}] \\ [\mathbf{H}] = \sum_{m=1}^N \hat{\mathbf{H}}_m e^{i\beta_m x} = [\mathbb{H}] [\hat{\mathbf{H}}] \end{array} \right\}$$

where

$$\beta_m = \beta_0 + mK_B$$

Using the above formulations we can relate the Fourier components of the fields at the top and bottom boundaries of the mesh to the corresponding fields as

$$\begin{pmatrix} \hat{\mathbf{E}}_{zh} \\ \hat{\mathbf{E}}_{zb} \end{pmatrix} = \begin{pmatrix} \mathbb{E}_h & \mathbf{0} \\ \mathbf{0} & \mathbb{E}_b \end{pmatrix} \begin{pmatrix} \mathbf{E}_{zh} \\ \mathbf{E}_{zb} \end{pmatrix} \quad (7.5)$$

$$\begin{pmatrix} \mathbf{H}_{zh} \\ \mathbf{H}_{zb} \end{pmatrix} = \begin{pmatrix} \mathbb{H}_h & \mathbf{0} \\ \mathbf{0} & \mathbb{H}_b \end{pmatrix} \begin{pmatrix} \hat{\mathbf{H}}_{zh} \\ \hat{\mathbf{H}}_{zb} \end{pmatrix}$$

Finally the above relation together with equation 7.3 can be rearranged to give the final relation for the fields at the two boundaries in terms of the Finite element G-matrix as

$$\begin{pmatrix} [\mathbf{I}] & -\mathbb{E}_h \mathbf{M}_{h,h} \mathbb{H}_h \\ \mathbf{0} & \mathbb{E}_b \mathbf{M}_{b,h} \mathbb{H}_h \end{pmatrix} \begin{pmatrix} \hat{\mathbf{E}}_{zh} \\ \hat{\mathbf{H}}_{zh} \end{pmatrix} = \begin{pmatrix} \mathbf{0} & -\mathbb{E}_h \mathbf{M}_{h,b} \mathbb{H}_b \\ [\mathbf{I}] & \mathbb{E}_b \mathbf{M}_{b,b} \mathbb{H}_b \end{pmatrix} \begin{pmatrix} \hat{\mathbf{E}}_{zb} \\ \hat{\mathbf{H}}_{zb} \end{pmatrix} \quad (7.6)$$

or

$$\mathbf{G}_h \begin{pmatrix} \hat{\mathbf{E}}_{zh} \\ \hat{\mathbf{H}}_{zh} \end{pmatrix} = \mathbf{G}_b \begin{pmatrix} \hat{\mathbf{E}}_{zb} \\ \hat{\mathbf{H}}_{zb} \end{pmatrix}$$

This relation is similar to the G-matrix formulation given by equation 6.29 derived by FMM. For the complete system under study, the G-matrices are calculated for the structured zones by FEM and for planar interfaces by FMM and the global matrix is then constructed and solved for the electric and magnetic fields for the entire computation domain by propagation algorithm as described earlier.

## 7.2 Conclusion

We have described in brief the formulations used to couple the two well known numerical methods, namely the FMM and FEM to solve the Maxwell's equations for a complete periodic system. This hybrid model so described was used for most of the numerical results presented in this work. Different periodic nano structures were studied in the course of this work with excitation wavelengths within the range of near UV to near IR. Almost all the structures comprise of either metallic nano-particle arrays or metallic films or the both. Different geometries such as infinite metallic strips, spherical nano-particles or cylindrical nano-particles with finite heights were considered. As this work is dedicated to bio-detection, molecular layers were simulated as thin dielectric layers with thickness of a few nanometers. For some calculations it was also necessary to simulate metallic layers of a few nanometers. As will be shown in this work, the hybrid model can be used to accurately calculate the far field reflectivity or transmission of such complex metallic systems and the results obtained almost have near perfect correspondence with the experimental results. To conclude we will list the basic advantages of the hybrid model when used for the purpose presented in this work.

- Possibility of reducing the computational domain by applying conditions for periodicity and considering the symmetry of the geometry
- Due to the formulation using the global matrix we can simultaneously calculate the EM fields and the intensities of diffraction for the structures.
- All the structures studied consists of metal and the hybrid model offers better convergence for metal.
- The hybrid model can be used for different complex geometries and was seen to give highly accurate results.



## **Part IV**

# **Plasmonics of Nano-structures**





---

# The concept of plasmonic mode

---

In this part, we will demonstrate the various plasmonic modes that can be supported by periodic structures with periodicity along a particular direction. All the results that will be demonstrated here were calculated using numerical methods described in part III. To understand the concept of plasmonic modes we will start with the very basic configuration that consists of a uniform metallic film on a glass substrate. The medium on the other side of the uniform film will be considered semi-infinite with refractive index  $n_h$ .

## 8.1 Uniform metallic film: the basic plasmonic mode

The propagating surface plasmon (PSP) was introduced in section 2.1 and its applications mentioned in chapter 3. The generalized Rouard method which is used to calculate the reflectivity of such planar surfaces was described in section 6.1. A calculated dispersion map of the PSP as a function of wavelength ( $\lambda$ ) and in-plane wave-vector ( $k_{//}/k_0$ ) =  $k_x/k_0$  was shown in figure 6.2 and the experimental map shown in figure 3.5. Here we will first describe the concept of a plasmonic mode and its analytical interpretation.

In the early part of the last century the concept of energy of light quanta was theoretically established. The well-known Planck–Einstein relation introduced the minimum energy required to create an electromagnetic field associated with an independent unit oscillating particle (photon) and is given as  $E = \hbar\omega$  with  $\omega$  being the angular frequency of the particle. The energy is related to the linear momentum ( $\mathcal{P}$ ) required to create the field as  $E = \mathcal{P}c$  for a photon with  $c$  being its linear velocity and thus we arrive at the de Broglie relation which holds for all particles as  $\mathcal{P} = \hbar k_0$  with  $k_0 = \omega/c$  in free space for a photon. The relation  $E = \mathcal{P}c$  which holds for a photon, can be generalized as  $\mathcal{P} = f(E)$  where the momentum associated with the electromagnetic field is a function ( $f$ ) of the energy of the field. Using Planck–Einstein relation and de Broglie relation we can write this in terms of a wave-vector  $\vec{k}$  (along a given direction) and angular frequency  $\omega$  as  $\vec{k} = f(\omega)$  and this relation signifies the dispersion of momentum along a given spatial direction with the angular frequency  $\omega$ .

First we would use this description of a photon to describe a plane wave incident on an optical system. Furthermore we will define a plasmonic mode as the function ( $f$ ) which can be used to describe this relation between momentum wave-vector ( $\vec{k}$ ) and the frequency of the associated electromagnetic field. In general the mode of a system is derived from the eigenvalues of the solution of Maxwell's equations without a source term. Such eigen values can be represented as the dispersion of the free-space

wave-vector ( $\mathbf{k}_0$ ) with the in-plane wave-vector ( $\mathbf{k}_{//}$ ) of the solution. We would follow a similar approach. Thus the function  $f$  denotes the dispersion of in plane wave-vector with the free space wave-vector of the plasmonic mode. For this work we will express the angular frequency in terms of the wave-vector of photons in free space  $\mathbf{k}_0 = \omega/c$  (let us call it the frequency wave-vector). Thus the major part of this work is to express the plasmonic effects in various media in terms of plasmonic modes or  $\vec{k} = f(\mathbf{k}_0)$ .

For an uniform metallic film, as shown in section 2.1.3 the dispersion of the PSP can be written as  $k_x = k_0 \sqrt{(n_h^2 n_m^2)/(n_h^2 + n_m^2)}$  where  $k_x$  denotes the momentum wave-vector of the plasmon along a given direction  $x$ . The physical aspect is that an uniform thin metallic film can support a wave whose momentum will change with its frequency as given by this relation. The relation itself is defined by the material properties and thus the propagating medium. With analogy to all the work published in the domain of guided optics, we can consider that a system comprising of a metal-dielectric interface can support a «mode» which satisfies the relation  $k_x = k_0 \times (k_{//}/k_0)$  with  $(k_{//}/k_0) = \sqrt{(n_h^2 n_m^2)/(n_h^2 + n_m^2)}$ , called the normalized in-plane wave-vector. It should be noted that the  $k_{//}$  denoted here gives the in-plane wave-vector that can be satisfied by the mode of the system, solved without considering any incident plane wave. This is similar to obtaining an eigen value by solving the Maxwell's equations without a source term. Thus the PSP so described is a mode that the specific system can support.

Now for a photon along a given direction  $x$ , the dispersion relation in a medium with refractive index of  $n_1$  is given by  $k_x = k_0 \times n_1$ . In analogy to this expression we can consider that a plasmonic system introduces a retardation to the momentum of the photon (considering plasmon-photon interactions) and thus can be effectively treated as  $(k_{//}/k_0)$  where the value of the normalized in-plane wave-vector depends on the geometry and physical properties of the plasmonic system. We will thus treat the plasmonic systems in terms of the frequency of electromagnetic field associated with the mode (written in terms of frequency wave-vector  $\mathbf{k}_0$ ) and the retardation it offers to an incoming photon, in terms of normalized in-plane wave-vector  $(k_{//}/k_0) = |\vec{k}|/k_0$ .

In most analytical studies we come across interfaces between two media. For an incident photon in medium 1 along a unit vector  $\hat{u}$ , the component of the momentum wave-vector parallel to the interface (unit vector parallel to the interface  $\hat{p}$ ) is thus  $\vec{k} \cdot \hat{p}$  with  $\vec{k} = k_0 n_1 \cdot \hat{u}$ . Defining  $(k_{//}/k_0)$  along the interface as  $(k_{//}/k_0) = \frac{\vec{k} \cdot \hat{p}}{k_0}$  we see that the maximum momentum possible for the incident photon is thus defined by its normalized in-plane wave-vector  $(k_{//}/k_0) = n_1$ .

For the interface  $1 \rightarrow 2$ , the momentum parallel to the interface is conserved, thus  $(k_0 n_1 \cdot \hat{u}) \cdot \hat{p} = (k_0 n_2 \cdot \hat{u}) \cdot \hat{p}$  which is the Snell's law for refraction. The critical condition when the incident photon has no positive momentum in the medium 2 is given by  $\vec{k} \cdot \hat{p} \geq k_0 n_2$  and thus in this situation  $(k_{//}/k_0) \geq n_2$ , when  $(k_{//}/k_0)$  is defined along the interface. This is a major advantage in treating systems in terms of  $(\mathbf{k}_0, (k_{//}/k_0))$  and we can directly relate the critical conditions for positive photon momentums while traversing various interfaces to the values of the  $(k_{//}/k_0)$  of the system. For all of the structures presented we will consider the interface in the  $x - y$  plane and  $(k_{//}/k_0)$  will be defined with respect to the momentum wave-vector parallel to the interface  $k_x$ .

The dispersion of the PSP in terms of the wave-vectors  $(\mathbf{k}_0, k_x)$  is shown in figure 2.2 and in terms of wavelength ( $\lambda$ ) in figure 3.1. In figure 8.1 the same dispersion is presented in  $(\mathbf{k}_0, (k_{//}/k_0))$  representation with the substrate of refractive index  $n_b = 1.72$  and medium of index  $n_h = 1.30$  on the other side. We would mention once again that in this treatment of the dispersion, we represent only the «mode» of the system without specifying any incident photon and thus without any photon-plasmon

interaction.

In such a system we can identify two modes that can be written as Mode  $PSP_h$  which satisfies  $(k_{//}/k_0) = \sqrt{(n_h^2 n_m^2)/(n_h^2 + n_m^2)}$  and Mode  $PSP_b$  which satisfies  $(k_{//}/k_0) = \sqrt{(n_b^2 n_m^2)/(n_b^2 + n_m^2)}$ . If a photon with appropriate  $(k_0, (k_{//}/k_0))$  is incident on the system, only then can it couple to a mode and create the electromagnetic field associated with the mode. For this particular geometry, a photon incident from medium  $n_h$  can have normalized in-plane wave-vector  $(k_{//}/k_0) < n_h$  and thus will not couple to any of the two modes. A photon incident from the medium  $n_b$  (where maximum possible normalized in-plane wave-vector is defined by  $(k_{//}/k_0) < n_b$ ) can however couple to Mode  $PSP_h$  but in that case as  $(k_{//}/k_0) > n_h$ , there will be no positive momentum in the medium  $n_h$  and thus the electromagnetic field caused by the photon should be considered as an evanescent field in medium  $n_h$ .

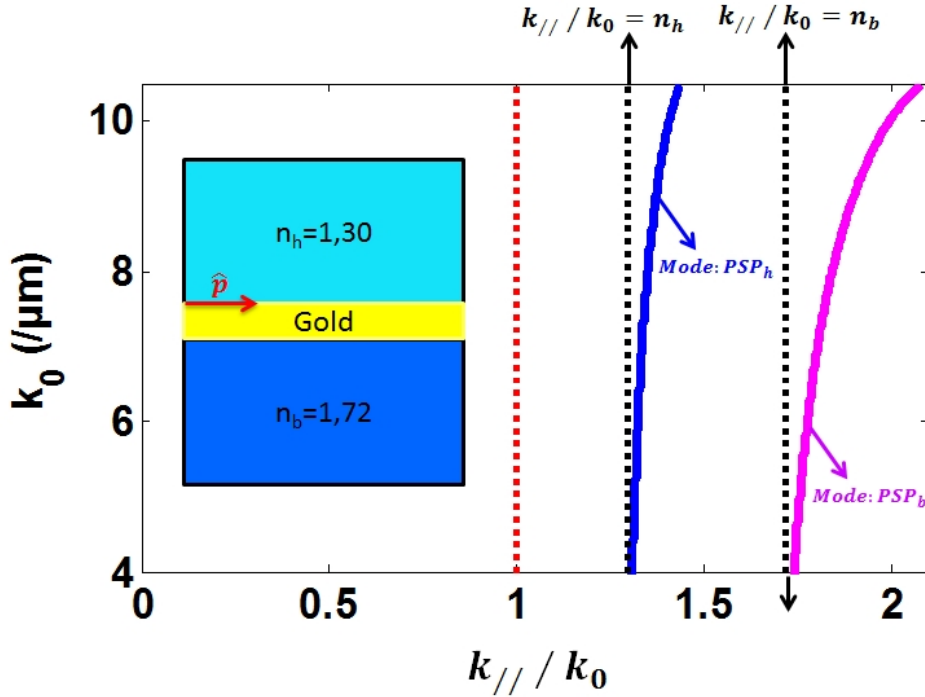


Figure 8.1: The propagating plasmon modes in an uniform gold film between two media with refractive indices  $n_h = 1.30$  and  $n_b = 1.72$ .

Considering that the retardation of a photon in a homogeneous medium is its refractive index, we can add vectorially the  $(k_{//}/k_0)$  values calculated along different directions. Thus for the direction perpendicular to the interface we can write  $(k_{//}/k_0)_z = \sqrt{n_d^2 + (k_{//}/k_0)_p^2}$  where  $n_d$  is either equal to  $n_h$  or  $n_b$ . This is similar to equation 2.5 where we derived the wave-vector of the PSP in the direction perpendicular to the interface. Using the values for gold and  $(k_{//}/k_0)$  along  $\hat{p}$  we see that for this configuration there exists no real value of  $(k_{//}/k_0)_z$ . Thus the field along  $z$  perpendicular to the interface is exponentially decaying.

By treating a geometry in terms of dispersion  $(k_0, (k_{//}/k_0))$  can directly give an insight of the basic modes supported by the system and the appropriate mechanism that can be used to couple an incoming photon to a corresponding mode.

Now we will describe the characteristics of the electromagnetic field associated with a mode. It must be noted that formulating modes in terms of frequency and momentum does describe the excitation

conditions of a particular mode but do not give any insight on the field distribution associated with it. This is because the mode is a property of the geometry of the system while the electromagnetic field associated is a property of the excitation mechanism or rather the coupling mechanism of the photon to the mode. For the modes presented in this work, they will have the same dispersion characteristics irrespective of the method of photon-plasmon coupling, however for the field distributions presented there may be a difference depending on the property of the incoming photon.

In the case of  $PSP_h$  it is simple to guess from the physical interpretation of the mode, that the electromagnetic field will be uniform along the interface gold- $n_h$  and exponentially decaying into the dielectric for a photon incident from the medium  $n_b$ . The penetration depth of the electromagnetic field was described in section 2.1.4. The propagation length of the plasmon was also defined using the wave-vector  $k_{sp}$ . We have now shown that the  $k_{sp}$  is basically proportional to the momentum of the photon that it can have when it couples to the Mode  $PSP_h$ . Thus the propagation length can be thought to be the length required for the photon to dissipate its momentum to the absorbing medium, in this case gold.

Now we will consider an incident photon from the medium  $n_b$  at an angle  $\theta$  with the normal to the interface. The normalized in-plane wave-vector for the photon is defined by  $(k_{//}/k_0) = \vec{k} \cdot \hat{p}/k_0 = n_b \sin\theta$  with its maximum  $(k_{//}/k_0) = n_b$  when  $\theta = 90^\circ$ . The reflectivity for such a geometry was calculated and shown in figure 8.2 as a function of frequency (represented by  $k_0$ ) and momentum (represented by  $(k_{//}/k_0)$ ). Reflectivity can be considered as ratio of the photons that retain the same momentum after reflection from the interface. Thus at the  $(k_0, (k_{//}/k_0))$  of the mode, the momentum was transferred to the  $PSP_h$  mode and thus we have a dip in reflectivity characteristic of PSP.

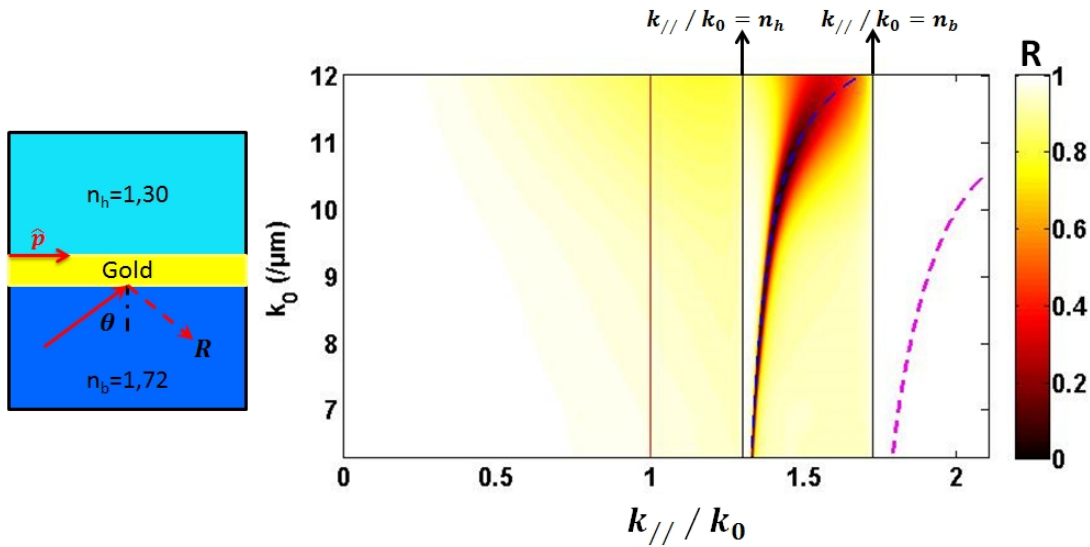


Figure 8.2: The calculated reflectivity from a uniform gold film between two media with refractive indices  $n_h = 1.30$  and  $n_b = 1.72$ .

An important feature to note in the reflectivity map is the broadening of the reflectivity dip for larger  $k_0$  and this gives an insight of the strength of the coupling between the incoming photon and the mode of the system. This is caused by the fact that the medium has a finite absorbance (given analytically by the imaginary component of the refractive index) and thus matching between the momentum of the mode and the incident photon is never perfect but occurs roughly over certain values of  $(k_0, (k_{//}/k_0))$ . We see

that the broadening is more for larger values of  $k_0$  and thus for smaller wavelengths and we can correlate this to the increase of the imaginary part of the refractive index of gold for smaller wavelengths (as shown in section 1.3).

We have now introduced the treatment of plasmonic modes with respect to the dispersion of  $(k_0, (k_{//}/k_0))$  and have shown the basic mechanism for coupling of a photon to such a mode. We will follow the same approach for different geometries and treat the plasmonic modes supported by the geometry and then demonstrate the effect of coupling of photons to the modes in terms of the electromagnetic field distribution and the far-field effects such as reflection and transmission.



---

# Plasmonics of a metallic grating on glass substrate

---

Following the approach described in the preceding chapter, we will describe the various modes that can be present in a periodic array of metallic structures on a glass substrate.

## 9.1 Plasmonic modes for binary metallic grating

We will start with a very basic metallic structure. Here we will consider a binary metallic grating with width ( $w_1$ ) and periodicity ( $\Lambda$ ) placed on a glass substrate. The schematic of the structure and the orientation of the unit vector  $\hat{p}$  defined for the calculation of  $(k_{//}/k_0)$  is shown in figure 9.1. For the calculations we would define the momentum of the modes in terms of the normalized in-plane wave-vector as  $(k_{//}/k_0) = \frac{\vec{k} \cdot \hat{p}}{k_0}$ .

Gratings have intrigued research in optics ever since Robert Woods demonstrated the phenomenon which bears his name as the Wood's anomaly. This was mentioned in brief in the beginning of chapter 2. The system studied here is in principle the same as the phenomenon observed by Woods and thus the consequent theories developed to explain a grating can directly be related to the plasmonic modes of the system.

Let us first consider a homogeneous medium with refractive index  $n_d$ . The mode of the system following the description of the previous chapter can be defined by the dispersion of the energy in the system with respect to a given frequency of the electromagnetic field and thus  $(k_{//}/k_0) = n_d$  and  $k_0 = \omega/c$ . The change in momentum due to a periodic structure can be denoted by the normalized in-plane wave-vector  $(k_{//}/k_0) = n_P$  and the total normalized in-plane wave-vector of the system can be represented by  $(k_{//}/k_0) = n_d \pm n_P$ .

To evaluate  $n_P$  let us consider the energy distribution of a periodic lattice. This is categorically described by the Bloch theorem [161]. According to the theorem named after Felix Bloch, the wavefunction ( $\Psi$ ) of any particle in a periodic environment can be given as

$$\Psi(\mathbf{r}) = e^{i\vec{k} \cdot \mathbf{r}} u(\mathbf{r}) \quad (9.1)$$

where  $u(\mathbf{r})$  is a function which denotes the periodicity of the environment.

In fact similar formulations to study a periodically repeating systems was formulated many times, notably the Floquet theory for periodic linear differential equations or the Kronig-Penney model for an electron in a 1D periodic potential [162, 163]. The basis of all such formulations is that the events within a given unit cell of the system repeats itself after a certain interval, denoted by its periodicity. This translational effect is denoted by the vector  $\vec{k}$  in equation 9.1. In solid state physics (for which Bloch theorem was originally developed) this vector is called the crystal wave vector and denotes the momentum associated with electrons in a crystal lattice,  $p_{crystal} = \hbar\vec{k}$ . The solution of the Bloch equation is not unique in the sense that it can be defined by all wave-vectors having the form  $\vec{k} + m\mathbf{K}_B$  where  $m$  is an integer and  $\mathbf{K}_B$  the reciprocal lattice vector [164, 165, 166]. Thus the maximum change in the momentum wave-vector  $\vec{k}$  is given by  $\pm\mathbf{K}_B = \pm 2\pi/\Lambda$  with  $\Lambda$  being the periodicity of the lattice.

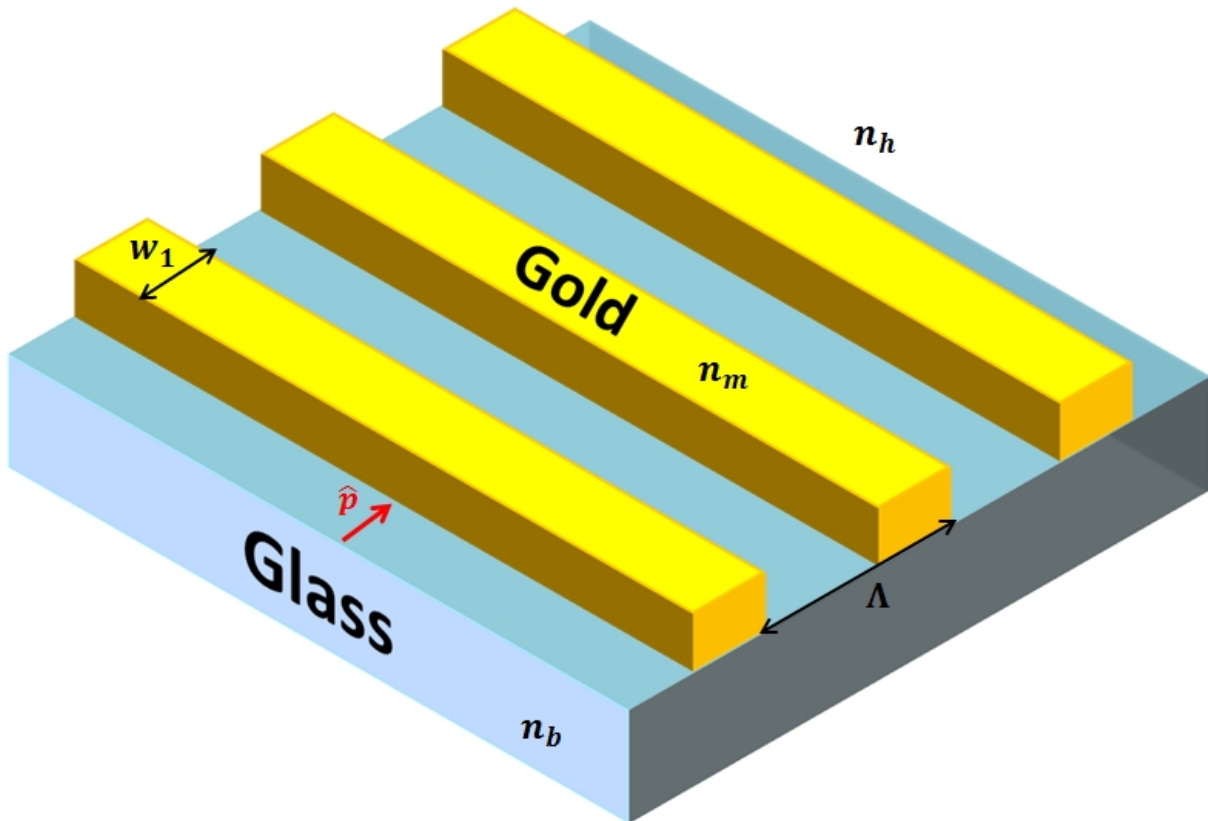


Figure 9.1: A binary grating of width  $w_1$  and periodicity  $\Lambda$  placed on a glass substrate with refractive index  $n_b$ . The medium surrounding the grating has a refractive index  $n_h$  and the metal with an index  $n_m$ .  $\hat{p}$  defines the unit vector in the plane of the interface perpendicular to the grating ridges.

### 9.1.1 The Wood-Rayleigh anomaly (WRA)

We can use this theorem to describe the possible modes in our periodic structure. The normalized in-plane wave-vector of a mode in a periodic structure can thus be written as  $(k_{//}/k_0) = n_d \pm n_P$  with  $n_P$  having values between 0 and  $m\mathbf{K}_B/k_0$ . The minimum of  $n_P = 0$  is when  $\hat{p}$  is defined perpendicular to the grating periodicity and the maximum  $n_P = m\mathbf{K}_B/k_0$  when  $\hat{p}$  is considered parallel to the grating periodicity with the intermediary values varying as a sinusoidal function depending on the direction of definition of  $\hat{p}$ .



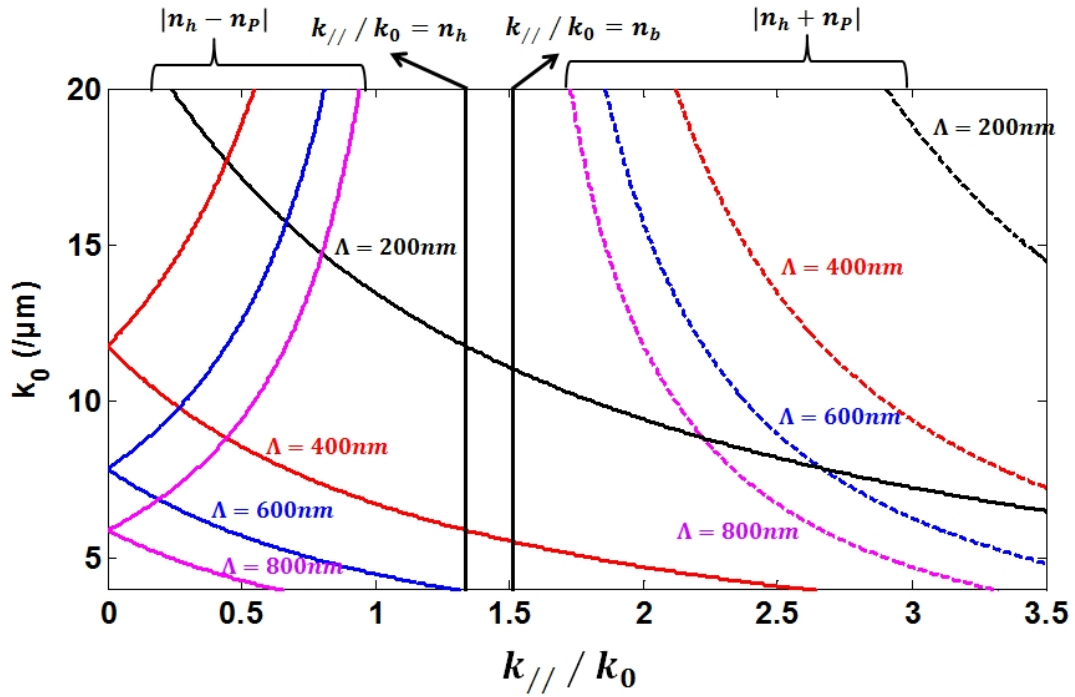


Figure 9.2: The calculated dispersion of the WRA  $((k_{//}/k_0)_h)$  for different periods ( $\Lambda$ ) with  $m = 1$ . The dotted curves represent  $(k_{//}/k_0)_h = |n_h + n_p|$  while the solid curves represent  $(k_{//}/k_0)_h = |n_h - n_p|$ . The refractive indices were  $n_h = 1.333$  and  $n_b = 1.513$ .

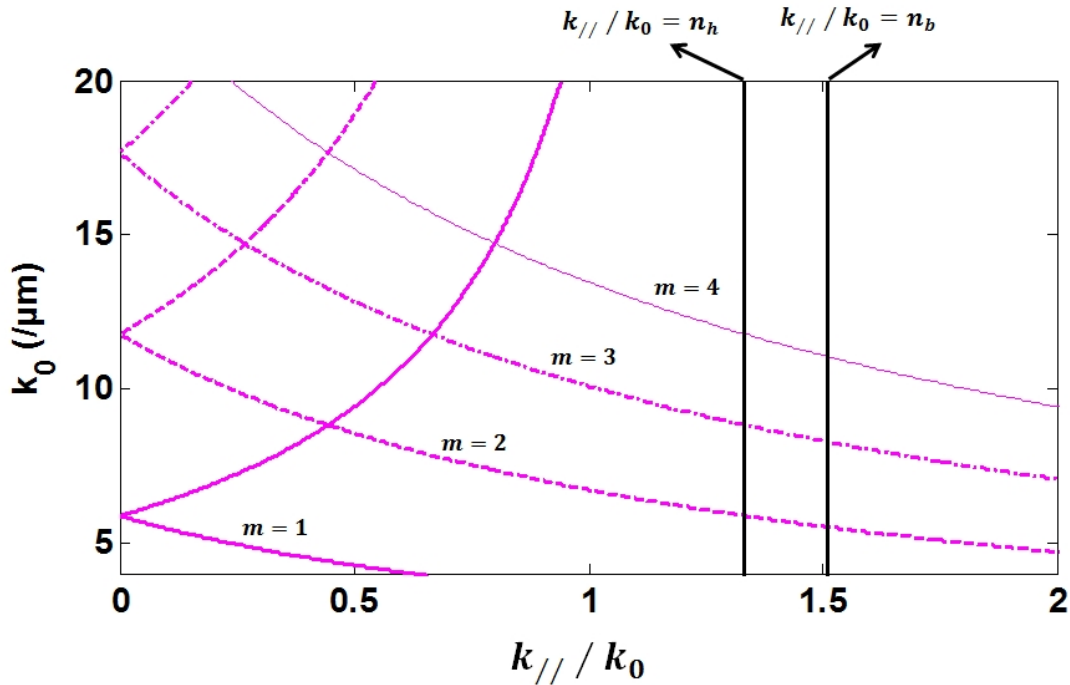


Figure 9.3: The calculated dispersion of the WRA  $((k_{//}/k_0)_h)$  for  $\Lambda = 800nm$  for different orders  $m$ . Here we show the calculated curves for  $(k_{//}/k_0)_h = |n_h - n_p|$ . The refractive indices were  $n_h = 1.333$  and  $n_b = 1.513$ .

In figure 9.1 we have defined the unit vector for  $(\mathbf{k}_{//}/\mathbf{k}_0)$  parallel to the grating periodicity and thus we can expect two different modes in the system given as

$$\begin{aligned}(\mathbf{k}_{//}/\mathbf{k}_0)_h &= |\mathbf{n}_h - \mathbf{n}_P| \\(\mathbf{k}_{//}/\mathbf{k}_0)_b &= |\mathbf{n}_b - \mathbf{n}_P|\end{aligned}\tag{9.2}$$

where  $(\mathbf{k}_{//}/\mathbf{k}_0)_h$  denotes the mode in the medium with refractive index  $n_h$  and  $(\mathbf{k}_{//}/\mathbf{k}_0)_b$  the mode in the medium with index  $n_b$ .

We will not consider the  $n_d + n_P$  term as it is not physically possible to excite this mode by a photon which would require increasing the photon momentum than what it has in a homogeneous medium. Such modes were reported in the literature for binary gratings, including the famous Wood-Rayleigh anomaly [167] and more recently in plasmonic structures such as Gao et al [168] where they named this mode the Rayleigh Anomaly (RA). We will follow the same nomenclature and call them the Wood-Rayleigh anomaly (WRA).

We must note that the WRA depend purely on the periodicity and is independent of the structure shape and dimensions. We also see from the equation that  $(\mathbf{k}_{//}/\mathbf{k}_0)$  is proportional to the energy of the modes as  $1/k_0$ . The dispersion of the WRA  $((\mathbf{k}_{//}/\mathbf{k}_0)_h)$  calculated by equation 9.2 for  $m = 1$  is shown in figure 9.2. We see that the  $(\mathbf{k}_{//}/\mathbf{k}_0) = 0$  for  $n_d = n_P$  and at this condition the normalized in-plane wave-vector for the homogeneous medium  $n_d$  is cancelled by the effect of the grating. In guided optics this condition is generally referred to as the cut-off condition. Writing  $k_0 = 2\pi/\lambda$  we can write this condition as  $m\lambda = n_d\Lambda$ . For the values of  $\lambda$  below this condition ( $k_0 \geq 2m\pi/n_d\Lambda$ ), the wave-vector of the WRA is in the direction of  $\hat{p}$  while for  $\lambda$  values above this condition ( $k_0$  values below this condition)) the direction of the wave-vector is opposite to  $\hat{p}$ .

### 9.1.2 Far and near field characteristics of the WRAs

Having described the possible modes in a simple grating structure let us now introduce the photon in the system and study the effect of these modes on the physical properties such as reflectivity or transmission. For this calculation we have used the rigorous numerical methods as described in chapter 7.

For light incident from the medium with refractive index  $n_h$  the normalized in-plane wave-vector for the photon can have values lying between  $(\mathbf{k}_{//}/\mathbf{k}_0) = 0$  to  $(\mathbf{k}_{//}/\mathbf{k}_0) = n_h$  while that incident from the medium with refractive index  $n_b$  will have normalized in-plane wave-vector values up to  $(\mathbf{k}_{//}/\mathbf{k}_0) = n_b$ . We will first consider light to be incident from the medium  $n_b$ .

Let us consider an incident plane wave perpendicular to the grating interface. In this case the momentum wave-vector of the photon along  $\hat{p}$  is zero. Considering the electric field of the photon along  $\hat{p}$  we can excite the WRA at the cut-off condition when  $m\lambda = n_d\Lambda$  where  $\lambda$  is the wavelength of the incident light. In this case  $(\mathbf{k}_{//}/\mathbf{k}_0)$  of the modes is zero and thus we expect the modes to be symmetric in the direction of  $\hat{p}$ . Since the wave-vector of the mode along  $\hat{p}$  is null, the field distribution would resemble the form of a standing wave with a periodicity equal to  $\Lambda/m$ .

The electric field for the structure with an incident plane wave from the medium with index  $n_b$ , perpendicular to the grating-substrate interface was calculated using the hybrid numerical model. In figure 9.4 the electric field intensity distribution of the structure for the WRAs is shown. For the calculation a 2D mesh was used in the  $X - Z$  plane. The electric field components along  $X$  and  $Z$  axes were

calculated and then the total intensity was evaluated as  $I = E_x^2 + E_z^2$ . The total calculated field was finally normalized to the incident field intensity  $I_0$ .

The period was taken as  $\Lambda = 1000nm$  and thus the cut off condition for  $(k_{//}/k_0)_h$  with  $n_h = 1.333$  is given by  $\lambda = 1333/m$  nm for the order  $m$ . The same for  $(k_{//}/k_0)_b$  with  $n_b = 1.513$  is given by  $\lambda = 1513/m$  nm. We see that for the mode  $(k_{//}/k_0)_h$  the field is more intense in the medium with index  $n_h$  while for  $(k_{//}/k_0)_b$  the field is distributed mainly in the medium  $n_b$ . We also see that for  $m = 1$  we have one standing wave (two spatial maxima for intensity distribution) within one period of the structure while for  $m = 2$  we have two standing waves. Thus we can define a so called wavelength of the WRA, being equal to  $\Lambda/m$  and this value is same for both  $(k_{//}/k_0)_b$  and  $(k_{//}/k_0)_h$ .

The field intensity distribution was also calculated for the same modes but with the light incident from the medium with refractive index  $n_h$  and shown in figure 9.5. We see that the distribution of the electric field intensity is similar to the case when light is incident from the medium  $n_b$ . Thus the WRAs can be excited with light incident from any side of the structures.

Now for the same configuration, the plane wave is considered to be incident at an angle  $\theta$  with  $\hat{p}$ . Thus the photon now has a momentum along  $\hat{p}$  and couple to the WRAs for the values when the incident momentum (in terms of normalized in-plane wave-vector  $(k_{//}/k_0)$ ) matches the dispersion of the WRA given by equation 9.2. Such coupling causes a change in the reflectivity which was calculated using the hybrid numerical method. We will consider light to be TM polarized and thus having a component of the electric field along  $\hat{p}$ .

First let us consider light to be incident from the medium  $n_h = 1.333$ . The width of the grating is taken as 200nm. The period of the grating was changed to study its effect on the reflectivity dispersion of the structure. This is shown in figure 9.6. First let us define the filling factor of the structures as  $f = w_1/\Lambda$  which the ratio of the surface covered by gold to the  $n_b - n_h$  interface. Considering the metal to have a reflectivity  $R_m$  and the interface to have a reflectivity  $R_d$  we can linearly approximate the total reflectivity of the structure to be

$$R_{tot} = f \times R_m + (1 - f) \times R_d \quad (9.3)$$

The reflectivity for  $n_h - n_b$  interface at  $\theta = 0^\circ$  is given by the Fresnel equation and is equal to  $\left(\frac{n_h - n_b}{n_h + n_b}\right)^2 = 0.004$ . The reflectivity drops with the incident angle  $\theta$  and is equal to zero at the Brewster's angle for TM polarization. So we can approximate the reflectivity  $R_d$  in this case to be almost zero. If we consider the reflectivity of the metal ( $R_m$ ) to be unit we can write  $R_{tot} = f$ .

For the gross reflectivity of the structures as shown in figure 9.6, we see that it decreases as we increase the period  $\Lambda$  and thus as we increase  $f$ . However apart from the gross reflectivity we also have some regions in the dispersion map where the reflectivity drops or increases sharply. These reflectivity minima correspond to the dispersion of the WRAs.

At the values of  $(k_0, (k_{//}/k_0))$  when the photon can couple to the  $(k_{//}/k_0)_h$  mode, the energy of electric field is confined in the medium  $n_h$  as can be see from the electric field intensity distribution of figure 9.5. This causes an increase of reflectivity when considering incidence from  $n_h$ . The inverse is true for the  $(k_{//}/k_0)_b$  mode and we expect a drop in reflectivity when the mode is excited. We clearly see the existence of the two WRA at each order. The mode with higher frequency wave-vector ( $k_0$ ) corresponds to  $(k_{//}/k_0)_h$  and we see an increase of reflectivity for that mode, while those at lower frequencies correspond to  $(k_{//}/k_0)_b$  and manifest in a drop of reflectivity.

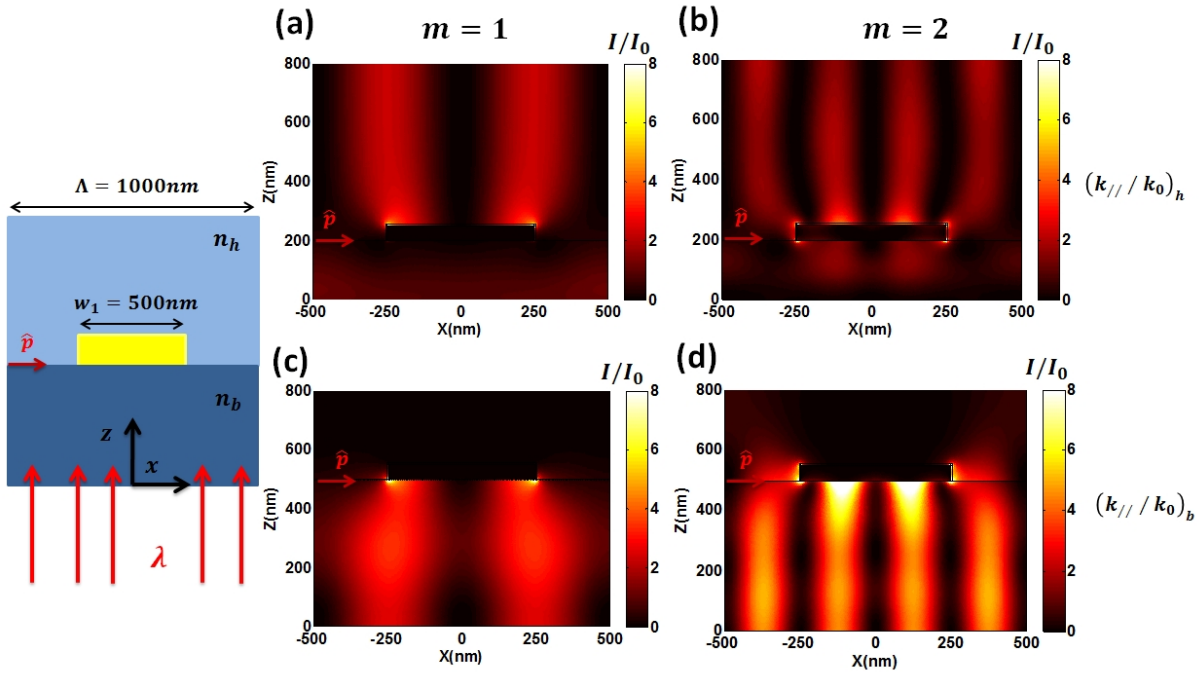


Figure 9.4: The electric field intensity for a grating of period 1000nm and width 500nm. A plane wave is incident along  $z$  axis from the medium  $n_b$  and linearly polarized with the electric field along  $x$  axis. The intensity was calculated at (a)  $\lambda = 1333\text{nm}$ :  $(k_{//}/k_0)_h$  mode with  $m = 1$ . (b)  $\lambda = 666.5\text{nm}$ :  $(k_{//}/k_0)_h$  mode with  $m = 2$ . (c)  $\lambda = 1513\text{nm}$ :  $(k_{//}/k_0)_b$  mode with  $m = 1$ . (d)  $\lambda = 756.5\text{nm}$ :  $(k_{//}/k_0)_b$  mode with  $m = 2$ . The gold-substrate interface is shown with solid lines and the vector  $\hat{p}$ . The height of the grating is taken as 50nm.

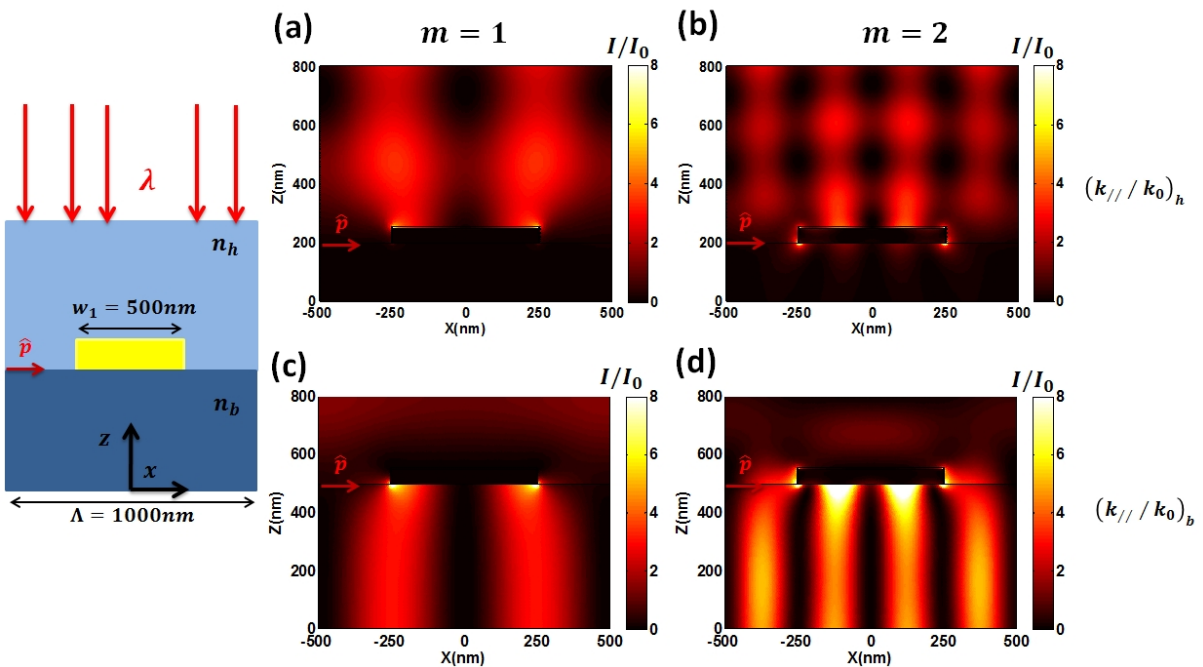


Figure 9.5: The same structure with a plane wave is incident along  $z$  axis from the medium  $n_h$  and linearly polarized with the electric field along  $x$  axis. The intensity was calculated at (a)  $\lambda = 1333\text{nm}$ :  $(k_{//}/k_0)_h$  mode with  $m = 1$ . (b)  $\lambda = 666.5\text{nm}$ :  $(k_{//}/k_0)_h$  mode with  $m = 2$ . (c)  $\lambda = 1513\text{nm}$ :  $(k_{//}/k_0)_b$  mode with  $m = 1$ . (d)  $\lambda = 756.5\text{nm}$ :  $(k_{//}/k_0)_b$  mode with  $m = 2$ .

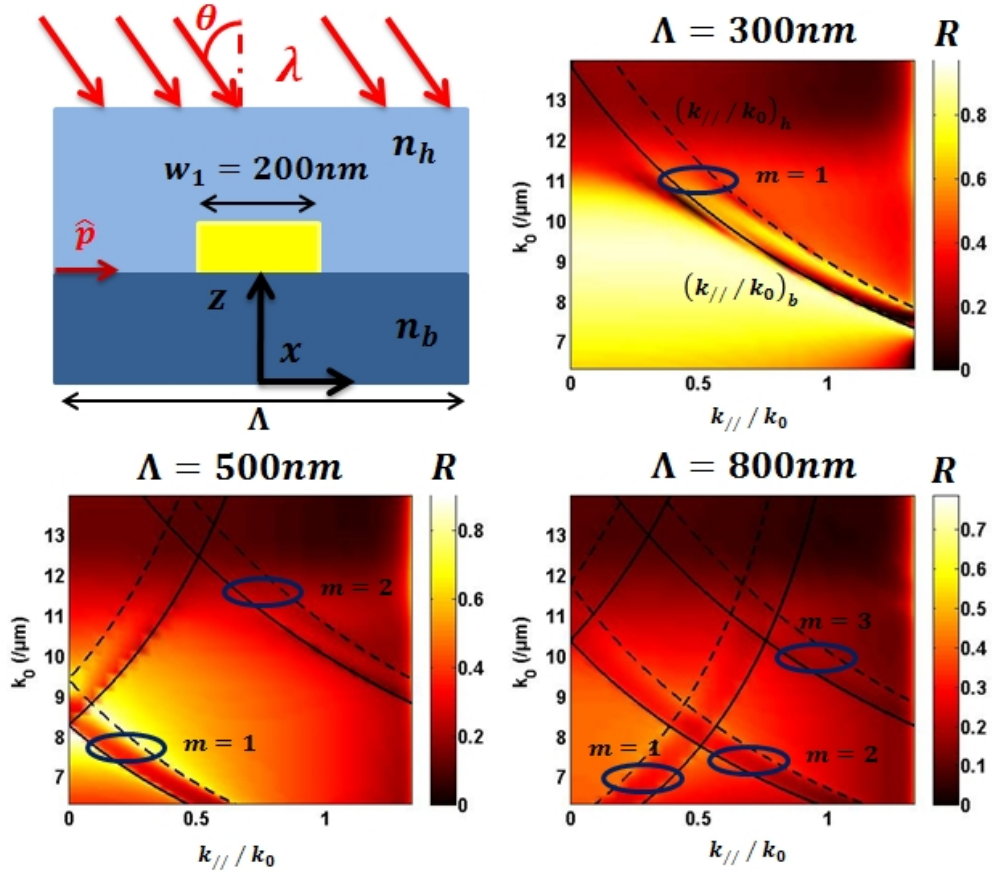


Figure 9.6: The reflectivity ( $R$ ) of the structure for different periods ( $\Lambda$ ) as a function of  $k_0 = 2\pi/\lambda$  and  $(k_{//}/k_0) = n_h \sin(\theta)$  for incident plane wave from the medium  $n_h$  at an angle  $\theta$ . The calculated values for WRAs are also shown in the figure ( $(k_{//}/k_0)_h$ :dashed and  $(k_{//}/k_0)_b$ :solid)

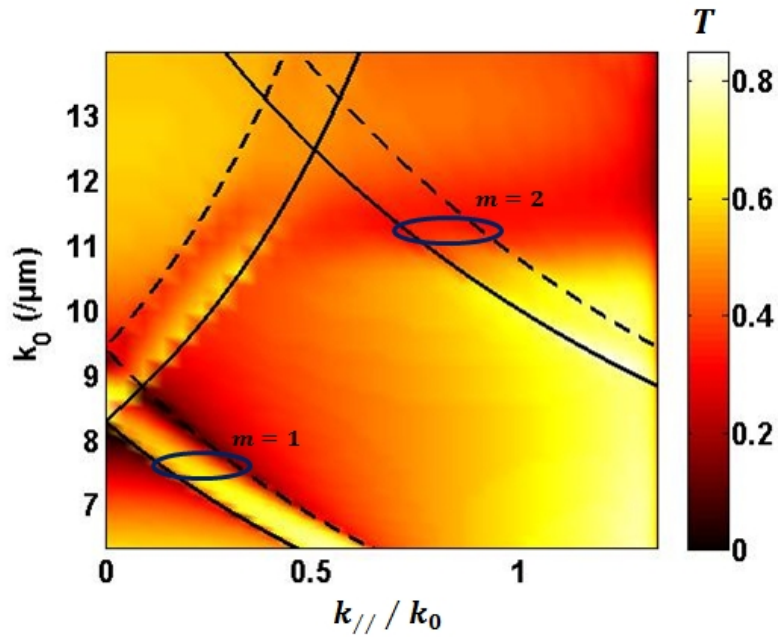


Figure 9.7: The transmission ( $T$ ) of the structure for  $\Lambda = 500nm$  as a function of  $k_0 = 2\pi/\lambda$  and  $(k_{//}/k_0) = n_h \sin(\theta)$  for incident plane wave from the medium  $n_h$  at an angle  $\theta$ . The calculated values for WRAs are also shown in the figure ( $(k_{//}/k_0)_h$ :dashed and  $(k_{//}/k_0)_b$ :solid)

The same understanding applies for the transmission and neglecting absorption (A) in the metal we can consider the transmission (T) equal to 1-R. We see from figure 9.7 a drop in T at the frequencies where  $(k_{//}/k_0)_h$  modes are excited and an enhanced transmission when  $(k_{//}/k_0)_b$  is excited.

The WRAs modes results from simple diffraction at the grating and thus is not confined in nano-metric scales as we expect plasmonic modes to be. We will call them the «Extended Modes». The energy of such extended modes is distributed into the far field and the type of mode dictates the characteristics of reflectivity or transmission of the structures. For this work we are rather interested in plasmonic modes which help to confine the electromagnetic field within nano-metric scales. We will call those modes the «Confined Modes». For various other geometries we will show the existence of different types of Extended or Confined modes.

For incident plane wave from the medium  $n_b = 1.513$  the normalized in-plane wave-vector for the photon can have access to all the values of  $(k_{//}/k_0)$  between 0 and  $n_b$ . Above  $(k_{//}/k_0) = n_h = 1.333$  we have total internal reflection and thus the reflectivity will be expected to be unit. The reflectivity dispersion map is for this configuration is shown in figure 9.8 for a grating width of 200nm and different periodicities.

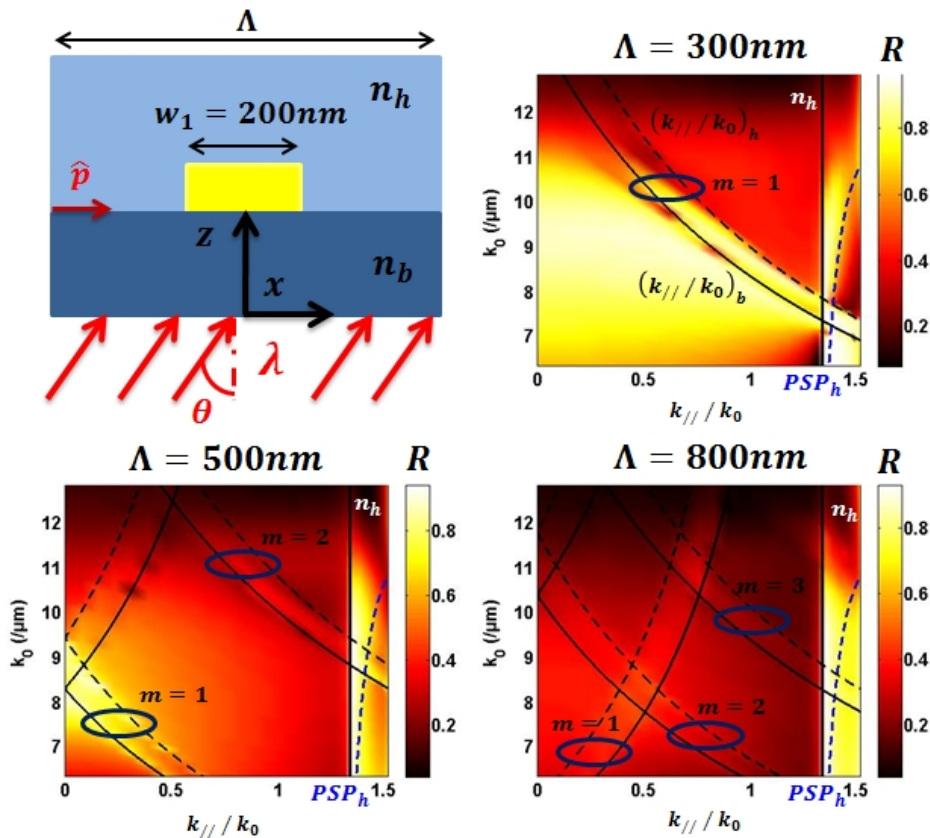


Figure 9.8: The reflectivity (R) of the structure for different periods ( $\Lambda$ ) as a function of  $k_0 = 2\pi/\lambda$  and  $(k_{//}/k_0) = n_h \sin(\theta)$  for incident plane wave from the medium  $n_b$  at an angle  $\theta$ . The calculated values for WRAs are also shown in the figure ( $(k_{//}/k_0)_h$ :black dashed and  $(k_{//}/k_0)_b$ :black solid). The calculated dispersion of the PSP mode ( $PSP_h$ ) is also shown (blue dashed)

The modes are not prominent in the reflectivity map. This is because of the high reflectivity above the critical angle ( $(k_{//}/k_0) = n_b$ ) due to the total internal reflection which overshadows the WRAs. This is

more so for larger periods when the filling factor decreases. However what is interesting to note is for a filling factor of  $f = 0.67$  which corresponds to  $w_1 = 200nm$  and  $\Lambda = 300nm$  we have a prominent mode above the critical angle. The reflectivity drops sharply for certain values of  $(k_{//}/k_0) > n_h$ . This drop of reflectivity for  $\Lambda = 300nm$  corresponds closely to the calculated dispersion of the mode  $PSP_h$  as described in section 8.1. Thus we see that for these structures there is a possibility of exciting the PSP mode, however for this particular configuration with  $w_1 = 200nm$  the PSP mode is not strong enough to have a distinct resonance dip in reflectivity.

Interpreting the results physically we can consider the WRAs as those conditions which are satisfied when one of the diffracted orders lie in the plane of the grating. Comparing the condition for the WRAs as given by equation 9.2 to the basic grating equation we can easily verify this notion.

For the modes as described in this work, we will define «Wavelength of the mode» ( $\lambda_{mode}$ ) as  $\lambda_{mode} = \lambda/(k_{//}/k_0)$  where  $\lambda = 2\pi/k_0$ . This is basically derived by writing the wave-vector of the mode as  $\vec{k} = 2\pi/\lambda_{mode}$ . This parameter will be useful to give an idea of the spatial magnitude of the mode along the defined vector  $\hat{p}$ . We can assume that for each mode of a structure to be excited efficiently by a photon, we need the feature length to be at least larger than the wavelength of the mode ( $\lambda_{mode}$ ). The wavelength of the  $PSP_h$  and  $PSP_b$  as a function of  $\lambda$  is shown in figure 9.9.

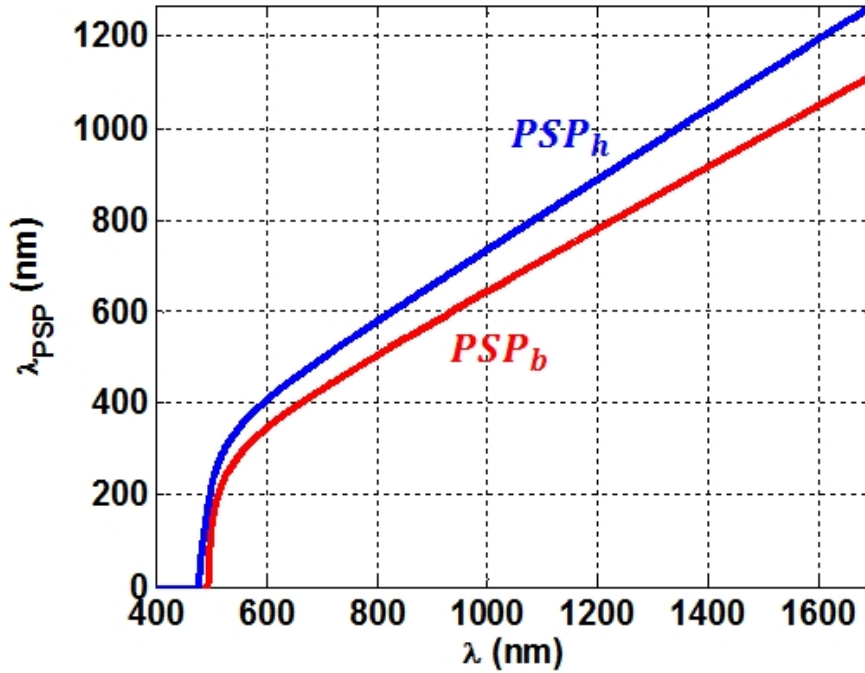


Figure 9.9: The wavelength of the PSP modes as a function of  $\lambda$ .

For the metallic ridges, the electric field of the incident light along the  $Z$  axis excite the PSP. However the coupling of the photon momentum to the momentum of the PSP mode is not strong enough given that the width of the grating ridge is  $300nm$  which is much smaller than the wavelength of the the PSP mode. However for larger ridge widths the PSP modes can be excited and the reflectivity dips are expected to be more prominent.

For the configuration with the photon incident from the medium with index  $n_b$ , we studied the effect of the width of the grating on the dispersion of the modes. The WRAs depend purely on the periodicity

and thus with a constant period we do not expect any change in the dispersion of the WRAs. For the study we will choose a period of  $\Lambda = 1400nm$  thus offering a larger range for the widths of the grating. The analytical dispersion of the structure is shown in figure 9.10. We have all the various orders ( $m$ ) of the two WRAs (only  $(k_{//}/k_0)_b$  shown in the figure) and thus over most of the  $(k_0, (k_{//}/k_0))$  space we expect sharp loss of reflectivity. But what is interesting to note is the zone above the critical angle where both the PSP and the WRAs are excited. This is where we expect mode coupling between the two modes. We will explain this phenomenon and it plays a principle role in understanding the plasmonic modes present in this work.

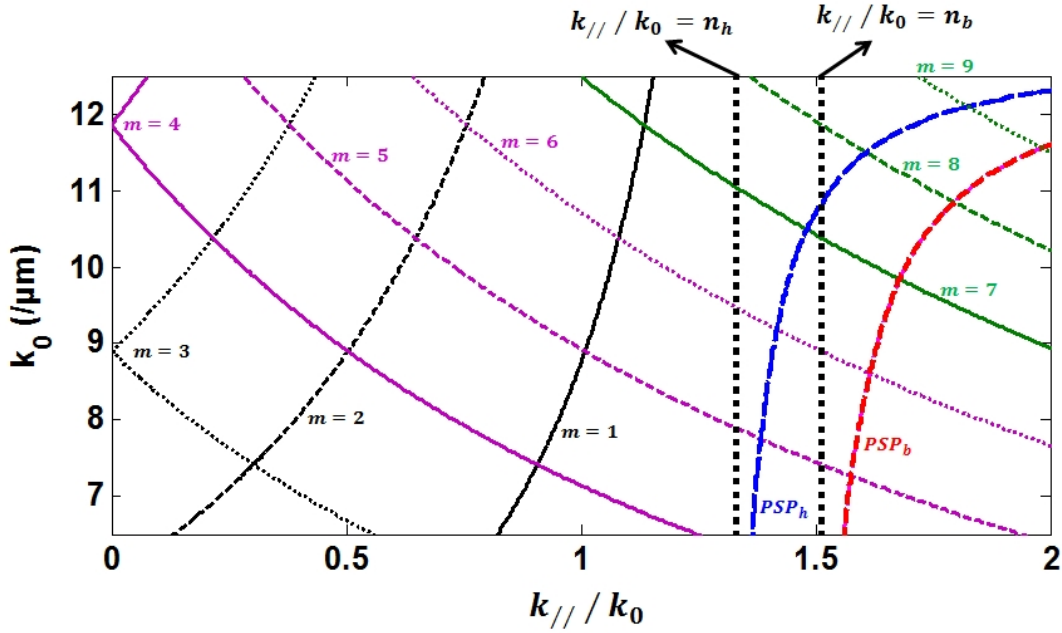


Figure 9.10: The calculated dispersion of the WRA ( $(k_{//}/k_0)_b$ ) for  $\Lambda = 1400nm$  for different orders  $m$ . The refractive indices were  $n_h = 1.333$  and  $n_b = 1.513$ . We have also shown the dispersion of the  $PSP_h$  (blue) and  $PSP_b$  (red).

### 9.1.3 Plasmonic Band Gaps in periodic structures

As we have mentioned in section 9.1.1 the momentum wave-vector for the condition that gives rise to the WRA is in the direction of  $\hat{p}$  for values of  $k_0$  above the cut off frequency while the momentum wave-vector is in the direction opposite of  $\hat{p}$  for  $k_0$  below the cut-off. We see from figure 9.10 that for the WRA condition that intersect the dispersion curve of the  $PSP_h$ , the values of  $k_0$  are below the cut-off. The momentum wave-vector of the  $PSP_h$  by definition lies in the direction of  $\hat{p}$ . Thus for values of  $(k_0, (k_{//}/k_0))$  where the WRA condition intersect the  $PSP_h$  we have the same normalized in-plane wave-vector  $((k_{//}/k_0))$  values for both the modes however oriented in opposite directions. Thus both the wave-vectors cancel each other and we have no positive wave-vector in the system. This manifests itself in the reflectivity or transmission map in the form of a «band-gap».

The band-gap in solid state physics signifies energy ranges where no particle states can exist. In analogy to that definition we can consider a plasmonic band-gap as the frequency ranges where several plasmonic modes with their respective wave-vector dispersion would have existed separately, however



owing to the geometry of the structure the resulting wave-vectors cancel each other and thus for the resulting configuration there exists no positive wave-vector [169, 170].

We must mention here that the basic definition of a plasmonic modes is the possibility of a photon with a particular momentum and frequency to couple to that mode of the system. Thus a plasmonic band-gap can be defined as the frequency and momentum of a photon which has no possibility to couple to a plasmonic mode of the system.

For the structure with  $\Lambda = 1400nm$  we have calculated the reflectivity dispersion map in figure 9.11. We see that at the frequencies of the  $PSP_h$ , we have a drop in reflectivity. This is the expected characteristic of a PSP mode. However close to the values of  $(k_0, (k_{//}/k_0))$  where the WRAs cross the PSP, we can see a band-gap. This is more evident in the absorption map. The absorption was calculated as  $A = 1 - R - T$  where  $R$  and  $T$  are the reflection and transmission respectively.

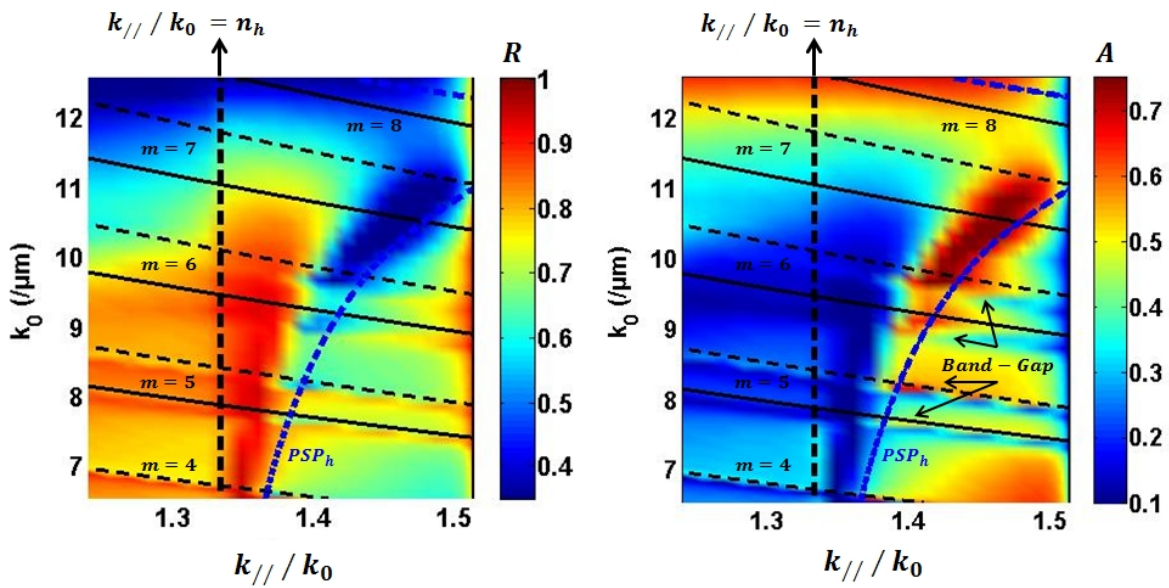


Figure 9.11: The reflectivity ( $R$ ) and the absorption ( $A$ ) for  $\Lambda = 1400nm$ ,  $w_1 = 1200nm$ . The refractive indices were  $n_h = 1.333$  and  $n_b = 1.513$ . We have also shown the calculated dispersion of the  $PSP_h$  (blue) and the WRAs ( $(k_{//}/k_0)_b$ ) (black solid) ( $(k_{//}/k_0)_h$ ) (black dashed).

We see absorption maximum for the PSP mode. Such an absorption maximum indicates that the energy of the incoming photon is not transferred to the far field (reflection and transmission) and thus is confined in the near field. This is not the case for the WRAs where we have reflection minima at the positions of the transmission maxima and vice versa. Thus a mode which has high absorption will be called the «Confined Modes» and should in principle be different from the Extended modes such as that satisfied at the condition for the WRAs. At the position of the band-gaps the absorption of the PSP drops sharply and thus indicating that the mode is non-existent.

The field intensity distribution ( $I/I_0$ ) for the different modes at  $(k_{//}/k_0) = 1.45$  was calculated. A plane wave from the medium with index  $n_b$  was incident at  $\theta = 73^\circ$ . The field intensity distribution in log scale is shown in figure 9.12. For all the modes we see the field intensity is confined within a few hundred nano-meters from the grating surface. The field intensity of the  $PSP_h$  is higher than the WRAs. However the field distribution shows the standing wave pattern as expected for the WRAs. This is a result of the coupling between the PSP and the WRA. It should be noted that for the standing wave pattern for

the WRAs the number of maxima in the intensity distribution directly indicates the order  $m$  of the modes.

Whenever we have a coupling between two modes the electric field distribution sustains some of the characteristics of both the modes. In this case the field is confined which is a characteristic of the PSP, however manifests a standing wave pattern which is the characteristic of the WRA. Thus such modes resulting from coupling are not in principle the same as the parent modes which couple and thus we will call them the hybrid modes. This will be described in later sections with much detailed examples.

To summarize the results, an incident photon having its momentum wave-vector perpendicular to the grating ridges can excite the WRAs which are extended modes with a very low electric field intensity confined close to the metal surface. For ridge widths larger than the wavelength of the PSP, the photon can excite the PSP which is a confined mode with intense electric field close to the metal surface and exponentially decaying within a few hundreds of nano-meters. The PSP and WRAs can couple given their dispersion has the same values of  $(k_0, (k_{//}/k_0))$ , giving rise to band-gaps and hybrid field distribution patterns.

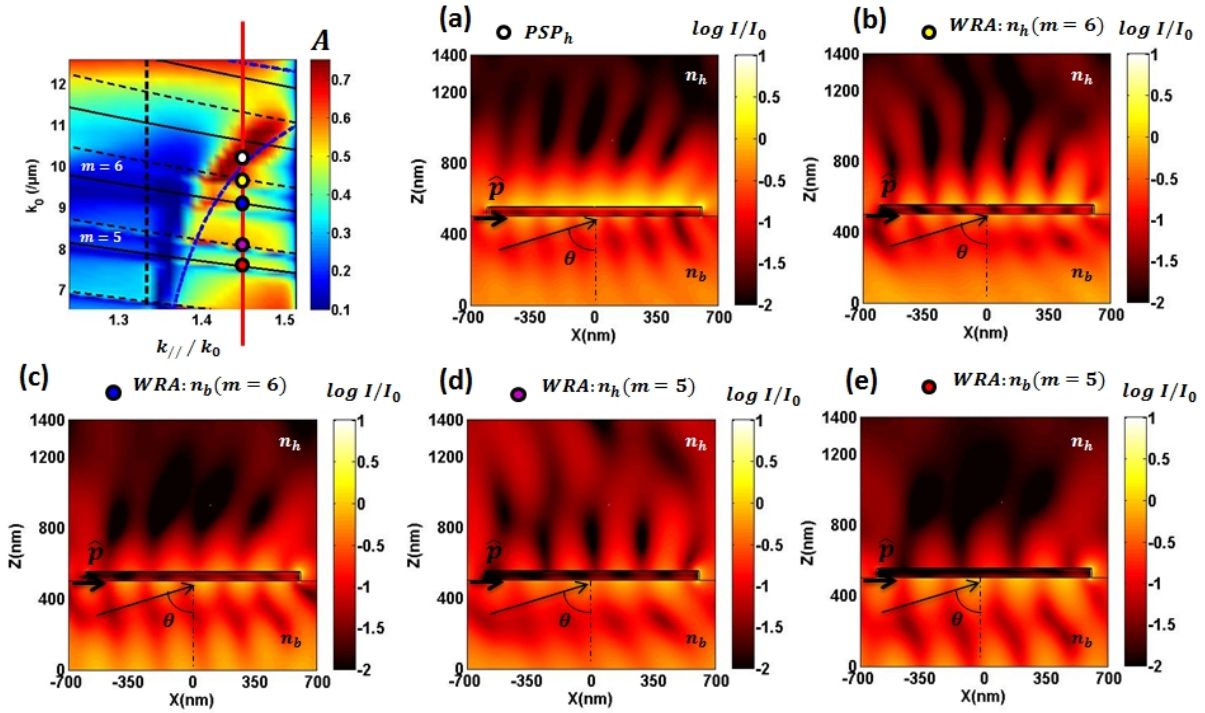


Figure 9.12: The electric field intensity distribution in log scale for the different modes (values of  $(k_0, (k_{//}/k_0))$ ) as shown in the dispersion map (top left) for  $\Lambda = 1400nm$ ,  $w_1 = 1200nm$ . For all the calculations  $(k_{//}/k_0) = 1.45$  ( $\theta = 73^\circ$ ). (a)  $\lambda = 612nm, k_0 = 10.3/\mu m$  (b)  $\lambda = 655nm, k_0 = 9.6/\mu m$  (c)  $\lambda = 694nm, k_0 = 9.0/\mu m$  (d)  $\lambda = 776nm, k_0 = 8.1/\mu m$  (e)  $\lambda = 828nm, k_0 = 7.6/\mu m$

In the next section we will describe the modes that can be excited by an incident photon with its momentum wave-vector parallel to the grating ridges.

## 9.2 Plasmonic modes in periodic metallic strips

We will consider the same binary grating structure as described in the last section (9.1) with width  $w_1$  and period  $\Lambda$ . But here to calculate the dispersion of the plasmonic modes we will define the unit vector

$\hat{p}$  parallel to the grating ridges. The schematic is shown in figure 9.13.

In the last section we introduced the wavelength of PSP. We mentioned that we need an uniform metal layer of length larger than  $\lambda_{PSP}$  along a defined  $\hat{p}$  to effectively excite the PSP mode. Thus the PSP was shown to be excited only for gratings with larger widths. By defining  $\hat{p}$  along the grating ridges however removes this constraint and thus we can expect to excite the PSP for smaller grating widths as well. However for efficient excitation of the PSP, the length of the metal layer perpendicular to the direction of propagation of the plasmon ( $\hat{p}$ ) also plays a major role. We will follow the same normalized in-plane wave-vector ( $(k_{//}/k_0)$ ) approach as mentioned earlier to express the modes of the system. Apart from the conventional PSP we will also introduce other modes that can be excited in such a geometry.

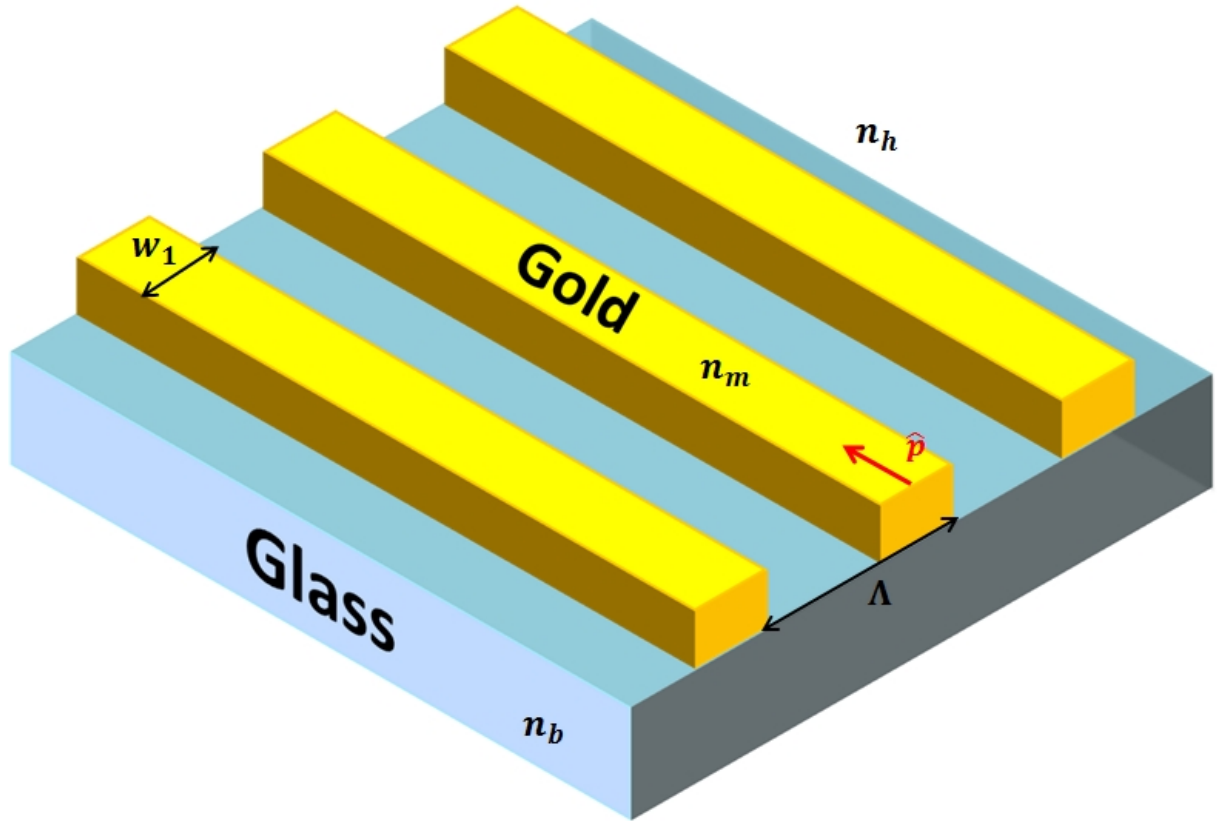


Figure 9.13: A binary grating of width  $w_1$  and periodicity  $\Lambda$ .  $\hat{p}$  defines the unit vector in the plane of the interface parallel the grating ridges.

In such a geometry the basic mode that we expect is the PSP and the  $(k_{//}/k_0)$  for the  $PSP_h$  and  $PSP_b$  can be written as

$$(k_{//}/k_0)_{PSP_h} = \sqrt{\frac{(n_h^2 n_m^2)}{(n_h^2 + n_m^2)}} \quad (9.4)$$

$$(k_{//}/k_0)_{PSP_b} = \sqrt{\frac{(n_b^2 n_m^2)}{(n_b^2 + n_m^2)}}$$

These modes would be expected to propagate on the top (interface of gold and medium  $n_h$ ) and the bottom (interface of gold and medium  $n_b$ ) of the strips respectively. The WRAs explained in the previous section appear solely when we have a periodicity in the direction of propagation of the modes. In this case

the strips are considered infinite and thus we would not have grating modes. However due to the finite width of the strips we expect something similar to the modes that exist in rectangular waveguides. Thus we should draw an analogy with the wave-guide modes in this section.

### 9.2.1 The Confined Propagating Plasmons (CPP)

To solve for the modes we will follow the approach used for rectangular waveguides. The geometry is shown in figure 9.14. The electric field along the propagation direction ( $y$ ) can be written as  $E_y(x, z) = E_0(x, z)e^{i\beta y}$  where  $\beta$  is the propagation vector of the guided mode. Considering the time-independent wave-equation (Helmholtz equation) we can write

$$\left(\frac{\partial^2}{\partial x^2} + \frac{\partial^2}{\partial z^2} + \beta^2\right)E_0(x, z) = 0 \quad (9.5)$$

By using the method of separation of variables and writing  $E_0(x, z) = E_x(x)E_z(z)$  we get

$$\frac{d^2 E_x}{dx^2} + k_x^2 E_x = 0$$

$$\frac{d^2 E_z}{dz^2} + k_z^2 E_z = 0 \quad (9.6)$$

where  $k_x$  and  $k_z$  are the wave-vectors along  $x$  and  $z$  respectively.

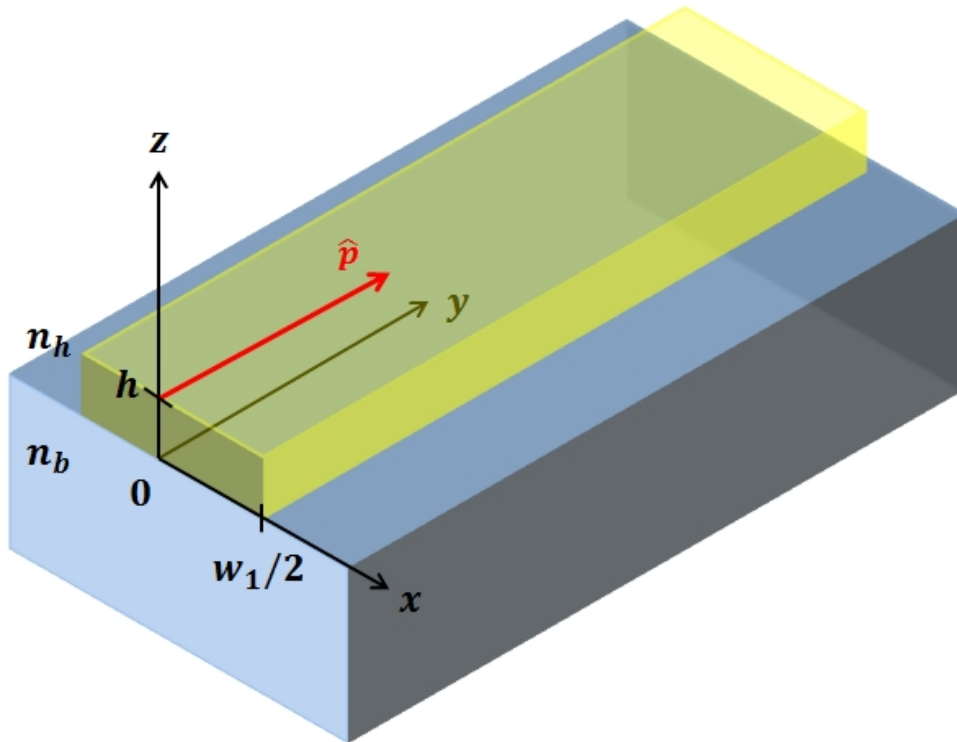


Figure 9.14: The geometry for a metallic strip

We will first approximate that the gold film is semi infinite along  $z$  and thus the solution will be derived for a gold-dielectric interface truncated along  $x$ . To solve for  $E_x$  we need to consider the following boundary conditions for the  $x - y$  plane with  $z = h$ .

$$\begin{aligned} E_0(x, z) &= 0 : x = w_1/2 \\ E_0(x, z) &= 0 : x = -w_1/2 \end{aligned} \quad (9.7)$$

Thus we can derive  $E_x$  of the form  $E_x(x) = \sin(k_x x)$  with  $k_x = m\pi/w_1$  where  $m$  is an odd integer. Thus the electric field is expected to have a standing wave pattern along  $x$  with odd number of lobes and a maxima at  $x = 0$  and zeros at  $x = w_1/2$  and  $x = -w_1/2$ . The wave-vector of guided mode  $\beta$  is related to  $k_x$  by the relation  $k_y^2 = \beta^2 - k_x^2$ . This is the result that we are interested in to classify the modes in terms of  $(k_{//}/k_0)$ . We defined our  $(k_{//}/k_0)$  along  $y$  and thus for our purpose  $(k_{//}/k_0)_{CPP} = k_y/k_0$ .

So far we have solved for the  $x$ -dependence of a guided mode in the system. For our configuration the mode which is guided along the strip is none other than the PSP that can be excited at a metal-dielectric interface. Thus the  $\beta$  in this case is simply the wave-vector of a propagating plasmon and can be given as  $\beta = k_0(k_{//}/k_0)_{PSP}$ . Now considering the real system with two metal-dielectric interfaces we can thus write the modes of the system as

$$\begin{aligned} (k_{//}/k_0)_{CPP_h} &= \sqrt{((k_{//}/k_0)_{PSP_h})^2 - (m\pi/k_0 w_1)^2} \\ (k_{//}/k_0)_{CPP_b} &= \sqrt{((k_{//}/k_0)_{PSP_b})^2 - (m\pi/k_0 w_1)^2} \end{aligned} \quad (9.8)$$

for order  $m=1,3,5...$  These modes are simply propagating plasmon modes that result due to the truncation of the uniform metal film along  $x$ . Thus we would call these modes the Confined Propagating Plasmons (CPP). The  $CPP_h$  mode results from the  $PSP_h$  which is guided along the metal- $n_h$  interface while the  $CPP_b$  is caused by  $PSP_b$  guided along metal- $n_b$  interface.

From equation 9.8 we see that the CPP modes depend only on the width ( $w_1$ ) of the metallic strips. The dispersion of the CPP (1st order) for widths  $w_1 = 500nm, 1000nm, 1500nm, 2000nm$  are shown in figure 9.15. The refractive indices are taken as  $n_b = 1.513$  and  $n_h = 1.333$ . The dispersion follows closely the PSP when we increase the width. This is expected as for an infinite width we have only the PSP in the system.

The dispersion of the different orders of the  $CPP_b$  is shown for  $w_1 = 2000nm$  in figure 9.16. The shift of the resonance frequencies of the CPP with width was also calculated and shown in the same figure. We must note here that unlike the WRAs, the CPP dispersion do not depend on the periodicity of the structure. The resonance frequencies of the CPP modes at a given  $(k_{//}/k_0)$  undergoes a red-shift with the width of the strips and approaches its corresponding PSP for larger widths (figure 9.15).

Confined modes guided along metallic structures have been reported previously [171, 172, 173, 174, 175, 176] and in our recent publication [177]. The modes described in such publications can be identified with the CPP mode described here.

### 9.2.2 Near-field and Far-field properties of the CPP

Having analytically expressed the dispersion of the CPP modes we will now present the coupling of an incoming photon to the CPP. In this case and as before, we can either introduce the photons from the medium  $n_h$  or the medium  $n_b$ . We will choose the later to have access to the values of  $(k_{//}/k_0) > n_h$ . It should be noted that whenever we have modes where the  $PSP$  plays a major role, it is always more interesting to study the properties for  $(k_{//}/k_0) > n_h$ . Thus we will consider a plane wave incident

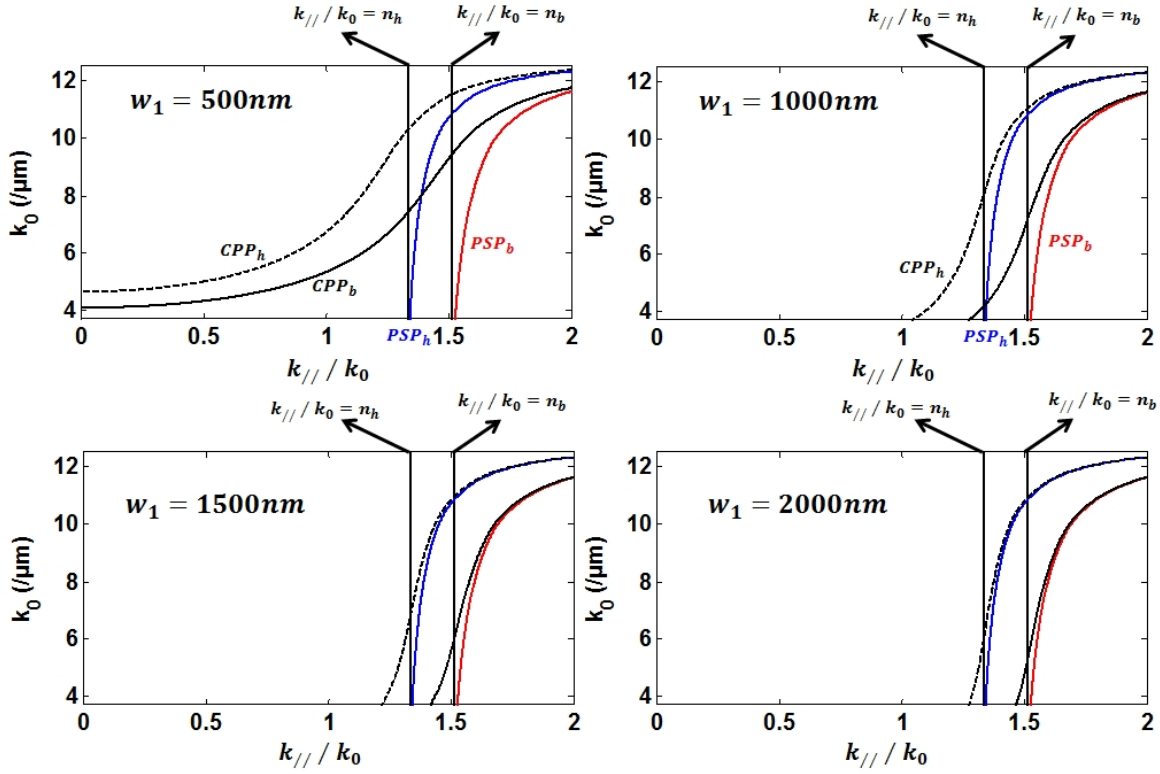


Figure 9.15: The calculated dispersion of the CPP modes for widths  $w_1$  of 500nm, 1000nm, 1500nm and 2000nm. The  $CPP_h$  and  $CPP_b$  are shown as black dashed and black solid respectively. The  $PSP_h$  (blue) and  $PS P_b$  (red) are also shown in the dispersion map.

from the medium with index  $n_b$  at an incident angle of  $\theta$  with the gold-dielectric interface. The direction of incidence is now along the length of the strips. Thus the  $(k_{//}/k_0)$  defined along the length of the strips ( $\hat{p}$ ) can be written as  $(k_{//}/k_0) = n_b \sin(\theta)$ . This configuration can be considered similar to the configuration shown in figure 9.8, however with the direction of incidence in this case being parallel to the grating ridges. We will study the properties of TM incident light as the PSP do not exist for TE polarization.

The reflectivity dispersion map was calculated for the structure with  $w_1 = 5\mu m$  and varying periodicity as shown in figure 9.17. Here we will consider  $(k_{//}/k_0)$  to be greater than  $n_h$  and thus the angle was varied from  $63^\circ - 85^\circ$ . Since the incident angle is greater than the critical angle for  $n_b - n_h$  interface we expect total internal reflection. However as already mentioned in chapter 8 we have a drop in reflectivity at the  $(k_0, (k_{//}/k_0))$  values where the plasmon modes are excited.

The major reflectivity dip corresponds to the dispersion of the  $PSP_h$ . We see that the dispersion of the modes in reflectivity do not change with period as expected from the discussion above. The only change is in the contrast of the reflectivity which decreases with increasing period. This phenomenon was explained in equation 9.3 and can be attributed to the fact that with increasing period we reduce the ratio of the surface covered by gold where the PSP is excited and the  $n_b - n_h$  interface (thus the filling factor  $f$ ). The analytical reflectivity was calculated using the linear approximation as  $R_{tot} = fR_m + (1 - f)R_d$ . Here in this case  $R_d$  is the reflectivity at the metal- $n_h$  interface and is equal to unit.  $R_m$  is the reflectivity calculated for an uniform metal film of 50nm. The reflectivity spectra at  $(k_{//}/k_0) = 1.46$  ( $\theta = 75^\circ$ ) is shown in figure 9.18. We see the minimum of reflectivity and thus the contrast of the reflectivity spectra

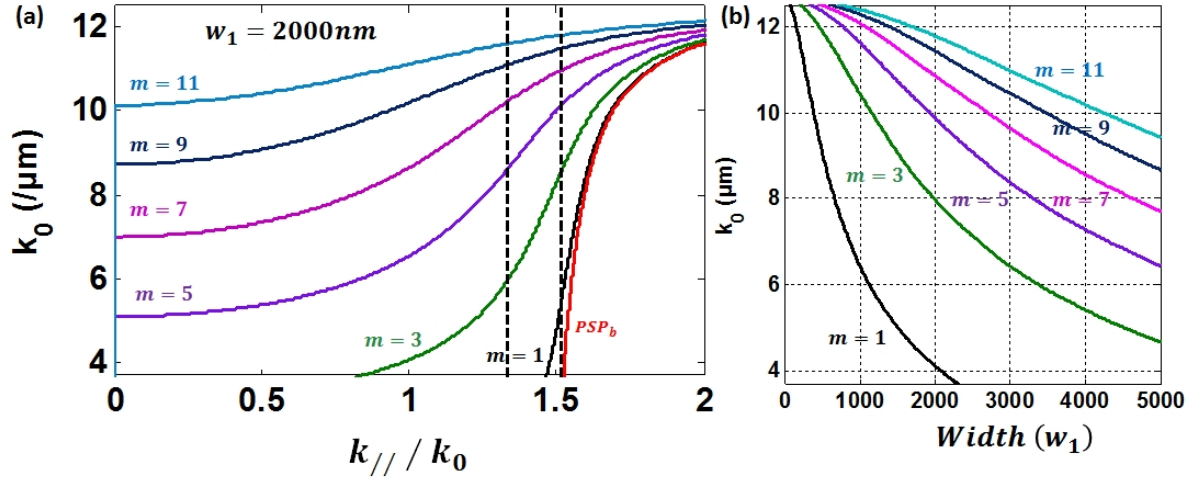


Figure 9.16: (a) The dispersion of the  $CPP_b$  modes for  $w_1 = 2000nm$  for different orders  $m$ . (b) Variation of resonance frequencies of the  $CPP_b$  with width of the strips for  $m=1,3,5,7,9,11$ . The value of  $(k_{//}/k_0)$  was taken to be 1.48.

fits closely with the calculated  $R_{tot}$ .

In figure 9.17 and 9.18 we see other dips in the reflectivity apart from the classical  $PSP_h$ . These can be attributed to the CPP modes. With the photon incident from the medium  $n_b$  it can couple to the  $CPP_b$  modes at the corresponding  $(k_0, (k_{//}/k_0))$  values. The energy of the photon then propagates along the length of the strips and thus causes dips in the reflectivity spectra at those  $(k_0, (k_{//}/k_0))$  values.

Keeping a constant filling factor  $f = 0.5$  ( $\Lambda = 2w_1$ ) we have calculated the reflectivity dispersion for different widths and periods of the structure. This is shown in figure 9.19. The dispersion of the  $CPP_b(m)$  and  $CPP_h(m)$  for the  $m^{th}$  order, calculated by equation 9.8 is also shown in the figure. We see a drop in reflectivity at the  $(k_0, (k_{//}/k_0))$  values associated with the CPP modes. The reflectivity dip is less pronounced for higher orders of the CPP. This can be explained by the fact that to excite the higher orders we need to increase the width of the grating. For larger widths, the incoming photon is coupled more strongly to the PSP and thus the CPPs of higher orders become less prominent.

In figure 9.20 we have plotted the frequencies of such reflectivity dips as a function of the structure width for  $(k_{//}/k_0) = 1.49$  ( $\theta = 80^\circ$ ). We see that the reflectivity minima undergo a redshift with increasing width. The dependence of the  $CPP_b(m)$  mode as a function of strip width was also calculated and plotted in the same figure. We see a very close correspondence between the numerically calculated reflectivity minima and the analytically calculated orders of the CPP. This confirms that the multiple reflectivity modes we have in this system are the different CPP modes.

The transmission of the structure in this configuration was also studied and no substantial transmission modes were observed. However for the WRAs in a previous section (9.1.1) we had observed transmission modes. This is not surprising because it must be noted that the WRAs were «Extended modes» while the CPPs are «Confined modes» and thus do not radiate energy into the far field. Thus in this case the reflectivity dip can be considered purely as the absorption of the structure where the energy remains confined to the near field.

Now we will present the near field characteristics of the CPP modes. While deriving the  $(k_{//}/k_0)$  for the CPPs we mentioned the boundary conditions that we applied for the guided modes. Thus the

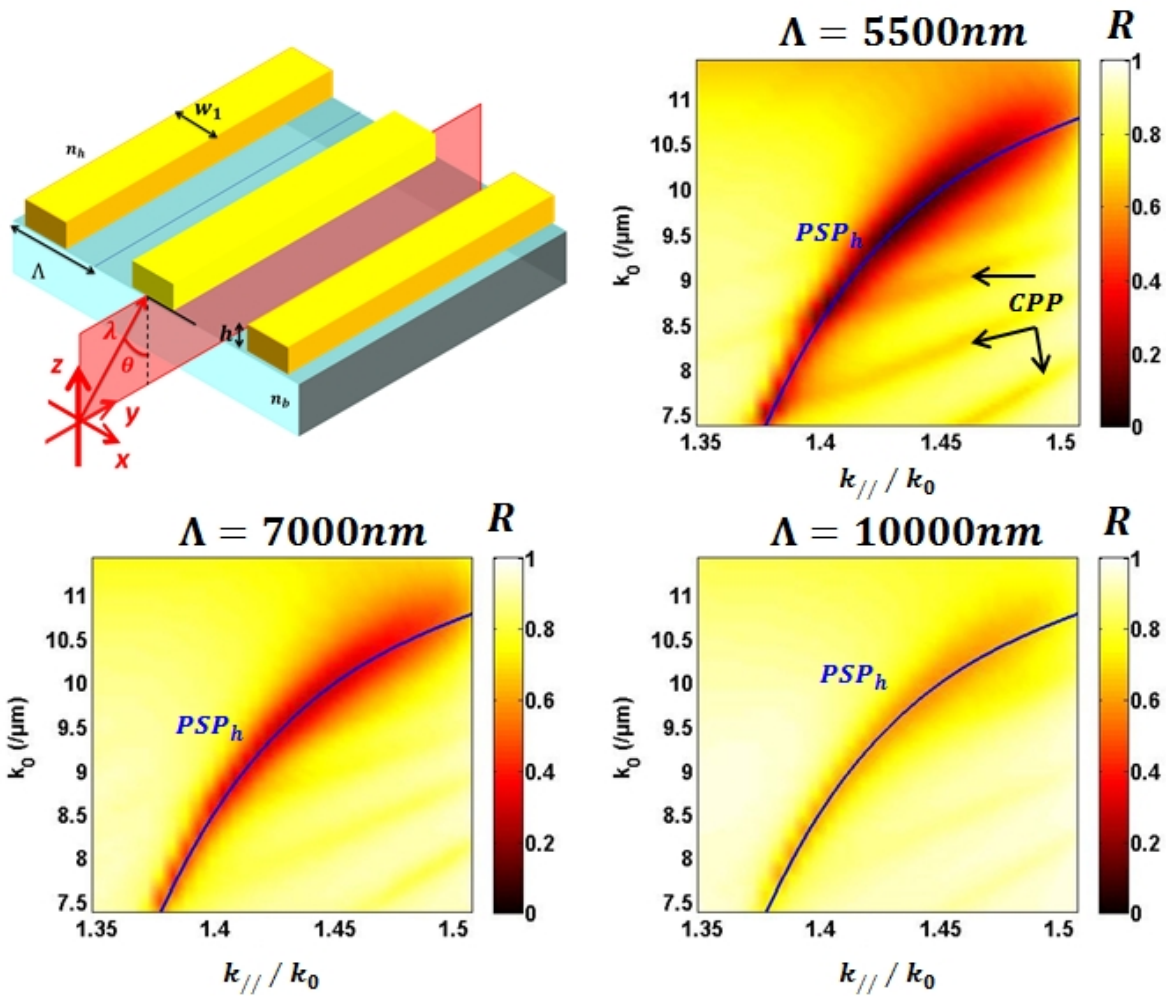


Figure 9.17: The reflectivity ( $R$ ) for metallic strips for width  $w_1 = 5000nm$  and periods ( $\Lambda$ ) of 5500nm, 7000nm and 10000nm thus a gap between the strips of 500nm, 2000nm and 5000nm respectively. The height of the strips ( $h$ ) was taken to be 50nm. The dispersion of the  $PSP_h$  is shown in blue.

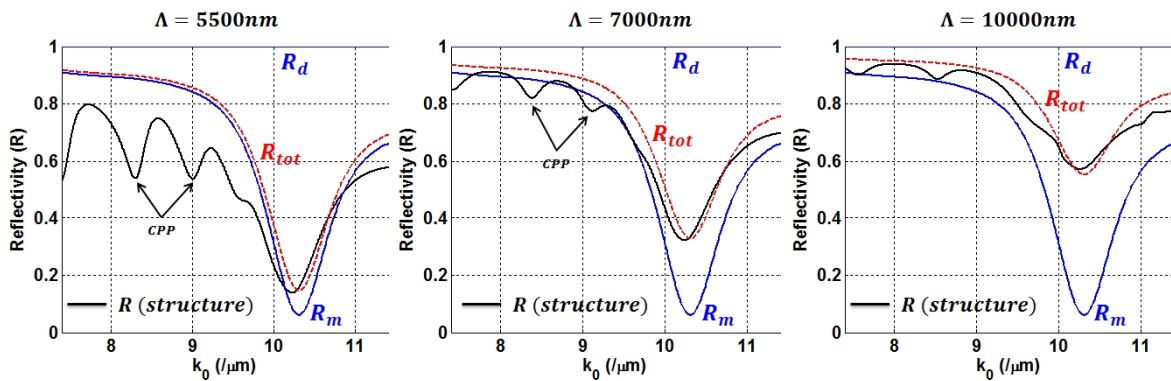


Figure 9.18: The reflectivity ( $R$ ) for the structure at  $(k_{//}/k_0) = 1.46$  for the three periods (black solid). Reflectivity of an uniform gold film of 50nm ( $R_m$ ) is shown in blue and  $R_d = 1$  for gold- $n_h$  interface. The linear approximated reflectivity ( $R_{tot}$ ) is shown in red dashed.



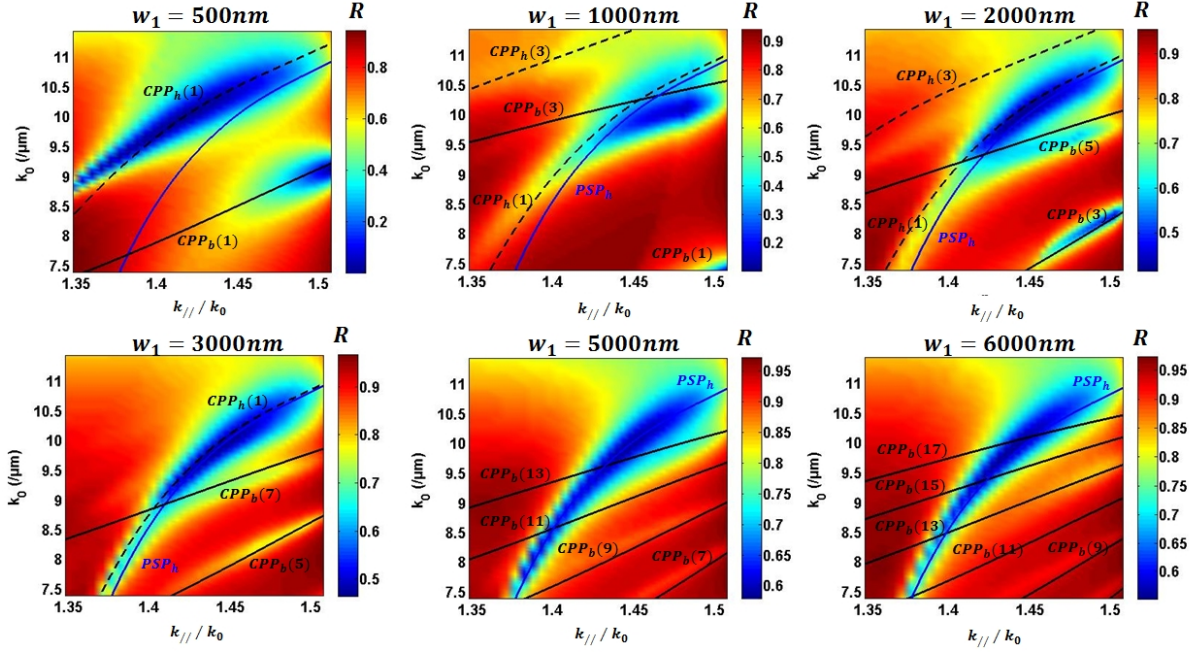


Figure 9.19: The reflectivity ( $R$ ) for metallic strips for width  $w_1$  of 500nm, 1000nm 2000nm and 3000nm. The period is taken as  $\Lambda = 2w_1$ . The strips ( $h$ ) was taken to be 50nm. For the analytical dispersion of the modes  $CPP_h(m)$  is shown as black dashed and  $CPP_b(m)$  as black solid for order  $m$ . The  $PSP_h$  dispersion is also shown as blue solid.

distribution of energy of the CPP modes would follow the same spatial profile. The electric field intensity would thus have a maxima at the center of the strips and decay towards the edges. The number of lobes of the standing wave pattern is equal to the order of the modes ( $m$ ).

We calculated the electric field using the hybrid numerical method for a quasi-3D period mesh. In this case the structure periodicity was taken in the  $x - z$  plane and a small width was considered along  $y$ . The periodicity condition was also applied along  $y$ , to simulate an infinite length of the strips. The electric field components were calculated along all the 3 directions and the total intensity evaluated as  $I = E_x^2 + E_y^2 + E_z^2$ . As before the field thus calculated was normalized to the incident intensity  $I_0$ .

The field distribution was calculated for  $w_1 = 2750nm$ . Within the calculated wavelength range of  $\lambda = 550nm - 900nm$  for this width we have 3 CPP modes of the orders 3,5 and 7. The reflectivity dispersion map for  $w_1 = 2750nm$  and  $\Lambda = 2w_1$  is shown in figure 9.21. We see reflectivity drops at the positions of the calculated  $CPP_b$  dispersion. The electric field intensity for the 4 modes namely the PSP and the 3 orders of CPPs at  $(k_{//}/k_0) = 1.49$  is also shown in the figure.

We see for the PSP ( $k_0 = 10.72/\mu m : \lambda = 586nm$ ) the electric field intensity is uniformly distributed along  $x$  at the metal- $n_h$  interface. This is the characteristic field distribution of the  $PSP_h$ . For the CPPs we have a standing wave pattern along  $x$  with  $(m + 1)/2$  lobes for the  $m$ th order. For example  $CPP_b(3)$  having 2 lobes and so on.

An interesting feature to note in the field distribution of the  $CPP_b$  is that they have a significant field intensity at the sides of the strips. The height of the ribbons ( $h$ ) was taken as 50nm. Thus we have a propagating plasmon mode confined to a few tens of nanometers. This can prove to be very useful for bio-sensing when detecting molecules at low concentrations. This feature will be described in details with respect to bio-sensing in later chapters (Part V).

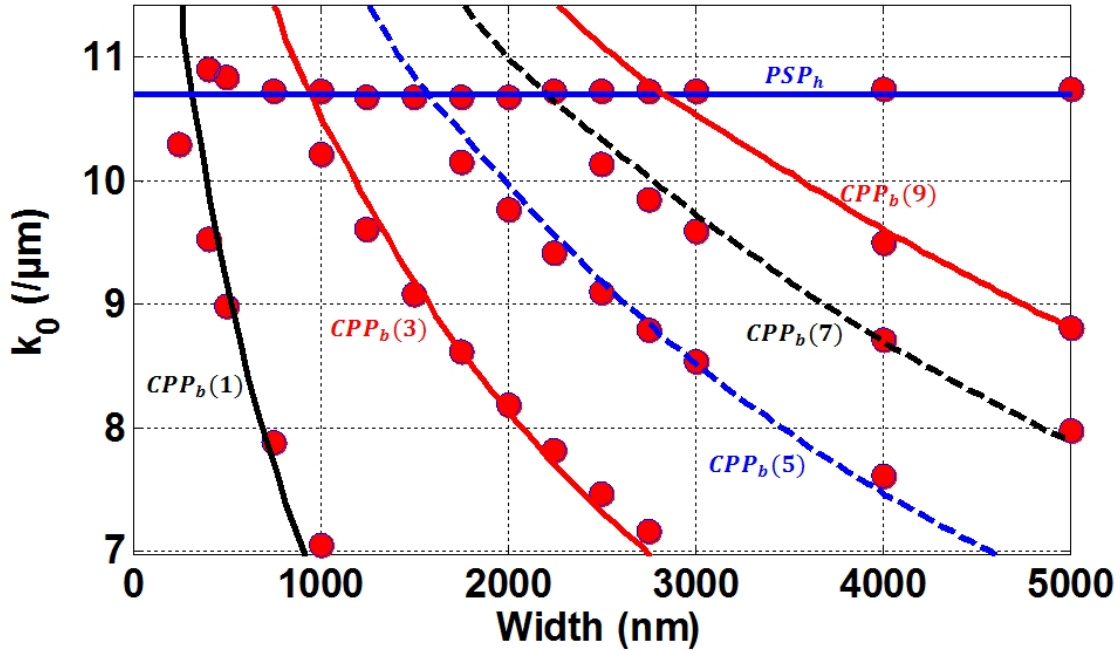


Figure 9.20: The frequencies ( $k_0$ ) of reflectivity minima as a function of strip width ( $w_1$ ) (red dots). The value of  $(k_{//}/k_0) = 1.49$  thus an incidence angle of  $\theta = 80^\circ$ . The calculated resonance frequencies of the  $CPP_b(m)$  modes for order  $m$  is also shown as a function of  $w_1$ .

The same structure was illuminated with the photons incident from medium  $n_h$ . In this case we will not excite the PSP. The normalized in-plane wave-vector for the incident photon ( $(k_{//}/k_0)$ ) will be less than  $n_h$ . From figure 9.15 we see that for  $(k_{//}/k_0) < n_h$  we can excite only the CPPs for small widths and more prominently the  $CPP_h$  mode. For incidence from  $n_h$ , there is not total internal reflection and thus a study of the transmission of the system would be more interesting. For the modes we can expect a dip in transmission. The transmission dispersion map for  $w_1 = 500nm$  and  $\Lambda = 1000nm$  is shown in figure 9.22. The analytical calculation of the dispersion of the CPPs is also shown. We see transmission dips at the  $(k_0, (k_{//}/k_0))$  values which correspond to the 1st orders of  $CPP_h$  and  $CPP_b$ . Another weak drop in reflectivity is also observed which corresponds to the  $CPP_h(2)$ . Thus in such a configuration the even orders of the  $CPP_h$  may also be excited.

The field distribution for the  $CPP_h(1)$  and  $CPP_b(1)$  was also calculated and is shown in figure 9.22. As expected we see one maxima for both the modes, confined at the interface of metal with  $n_h$  and  $n_b$  for  $CPP_h$  and  $CPP_b$  respectively.

An important point to note here is that the field distribution of the  $CPP_h$  is somewhat similar to the  $PSP_h$  however it can be excited with a plane wave incident from the medium  $n_h$ . This is not possible for the conventional  $PSP_h$ . This provides an advantage if we require to excite a quasi-conventional propagating plasmon mode without the Kretschmann configuration and total internal reflection setup. In the literature this is sometimes explained in a cursory manner as simple grating coupling. However the modal analysis present in this work gives a more subtle explanation of the phenomenon and helps in a complete understanding of its excitation.

We have presented different modes such as the WRAs and the CPPs that can be excited in metallic strips (gratings) by light incident either perpendicular or parallel to the strips. In the next chapter we

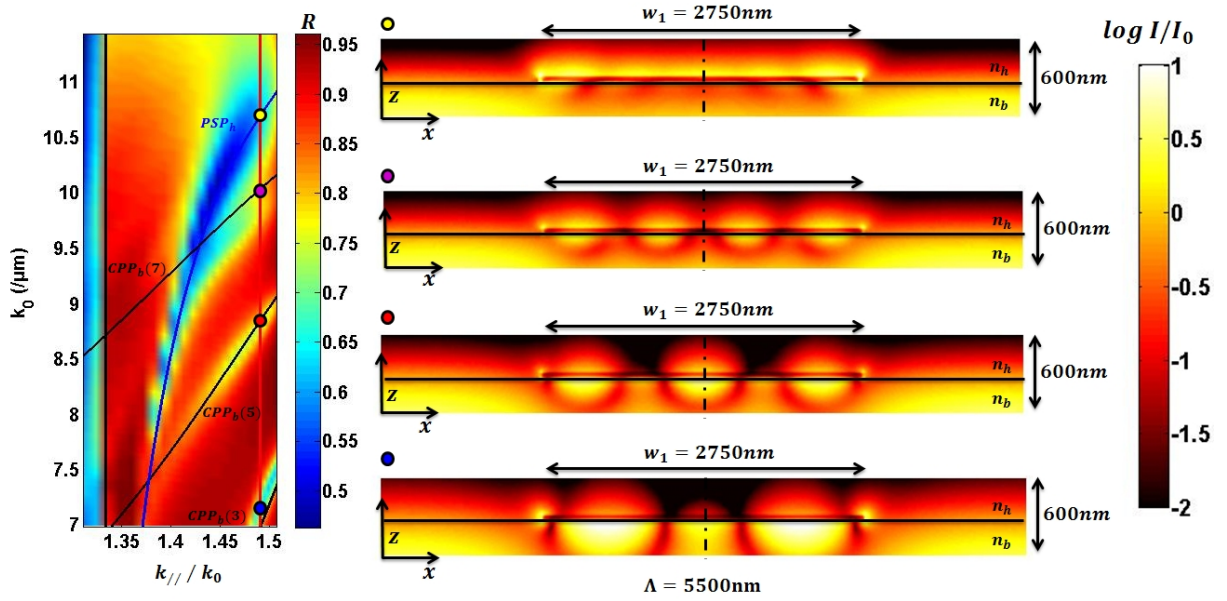


Figure 9.21: Left: The reflectivity dispersion map for  $w_1 = 2750nm$  and  $\Lambda = 5500nm$ . The height of the strips was taken as  $50nm$ . The analytical calculations for the dispersion of the PSP (blue solid) and the CPP modes (black solid) together with the light line in the dielectric medium  $(k_{//}/k_0) = n_h$  are also shown. Right: The electric field intensity in logarithmic scale for different  $k_0$  values corresponding to the different modes at  $(k_{//}/k_0) = 1.49$ . (Top-bottom):  $k_0 = 10.72/\mu m : \lambda = 586nm$ ,  $k_0 = 9.86/\mu m : \lambda = 637nm$ ,  $k_0 = 8.81/\mu m : \lambda = 713nm$ ,  $k_0 = 7.17/\mu m : \lambda = 875.5nm$ .

will describe the plasmonic modes that can be excited in a periodic 3D array consisting of metallic nano-particles.

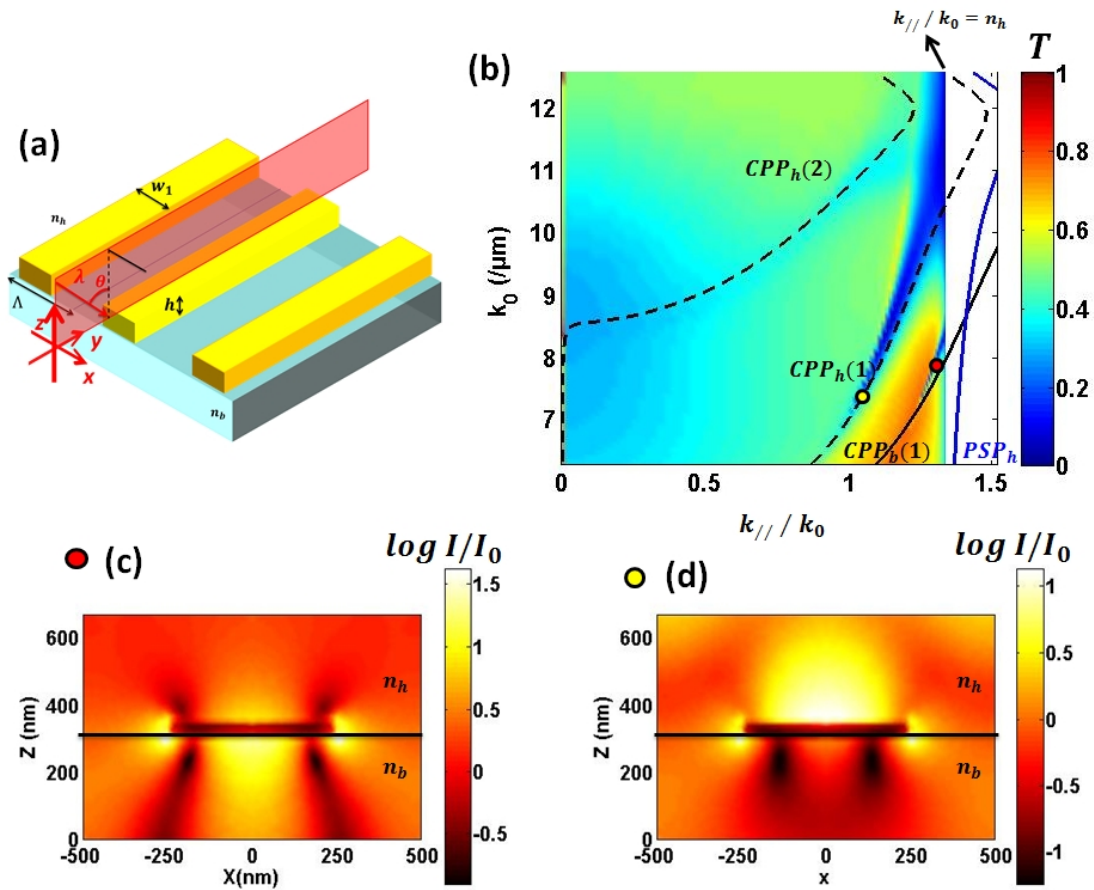


Figure 9.22: (a) The geometry of the configuration with an incident plane wave from the medium  $n_h$  at an angle  $\theta$  and the plane of incidence parallel to the strips (b) The transmission dispersion map for  $w_1 = 500\text{nm}$  and  $\Lambda = 1000\text{nm}$ . The height of the strips was  $h = 50\text{nm}$ . The analytical calculation for the  $(k_0, (k_{//}/k_0))$  of the different modes is shown. The electric field intensity in logarithmic scale for (c)  $k_0 = 8.03/\mu\text{m}$  ( $\lambda = 782\text{nm}$ ) and  $(k_{//}/k_0) = 1.31$  ( $\theta = 78.5^\circ$ ) (d)  $k_0 = 7.82/\mu\text{m}$  ( $\lambda = 803\text{nm}$ ) and  $(k_{//}/k_0) = 1.11$  ( $\theta = 56^\circ$ ).

---

# Plasmonics of nano-particles on glass substrate: The LSP resonance

---

So far we have discussed the modes which are either extended or confined caused by the propagating plasmon mode (PSP) and its confinement by the structures. In plasmonics there exists another fundamental type of resonance, namely the localized surface plasmon (LSP). In this chapter we will introduce the conditions for the LSP resonance in metallic nano-particles.

## 10.1 The LSP resonance condition

We will now study a complete 3D structure which consists of an array of gold cylinders in square packing placed on a glass substrate (medium with index  $n_b$ ). The medium surrounding the cylinders will be considered semi infinite with a refractive index  $n_h$ . The structure geometry is shown in figure 10.1.

So far we have described the confined plasmonic modes such as the PSP or the CPP and the extended modes such as the WRAs. In this structure with nano-particles, there exists another fundamental plasmonic mode, the Localized surface plasmon (LSP). The basic principle of the LSP was described in section 2.2 and the application of LSP for bio-detection was introduced in section 4. The LSP results from local electron oscillations in metallic nano-particles. However such oscillations are confined to the surface of the particles and thus do not cause energy to propagate along the structure. So our momentum-energy approach that we have used to describe the plasmonic modes so far is not directly applicable to the LSP as for them the momentum wave-vector does not have any physical meaning. Thus the LSP is not a «mode» of the system by our definition. It however follows a resonance condition and can be excited by photons having a certain particular energy or frequency. Thus for the LSP we will describe the resonance condition at which we expect them to be excited.

### 10.1.1 Theoretical models for LSP resonance

For a nano-particle of a given shape, it undergoes a LSP resonance at certain frequencies. This is generally explained by a term called the polarization of the particle. In fact, in any medium, an incident electromagnetic field can cause a displacement of the charges. This displacement creates surface charges in the medium which in turn counteracts the applied electric field. This is what we call the polarization of

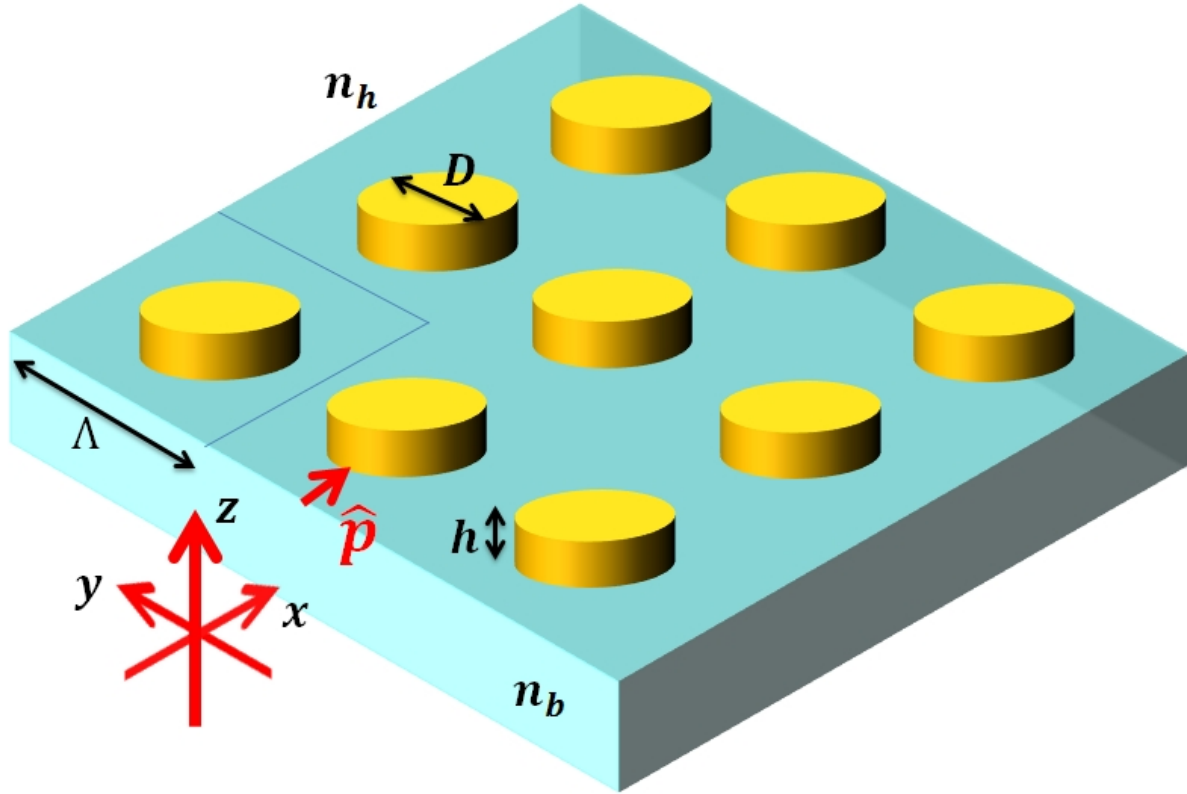


Figure 10.1: An array of gold cylinders of diameter  $D$  and periodicity  $\Lambda$  placed on a glass substrate with refractive index  $n_b$ . The medium surrounding the cylinders has a refractive index  $n_h$  and the metal with an index  $n_m$ .  $\hat{p}$  defines the unit vector in the plane of the interface.

the applied field. The amount of polarization offered by the particle depends primarily on the particle shape and properties. Such properties in electromagnetism is described by the polarizability ( $\alpha$ ).

For metallic nano-particles this polarization is caused by the presence of free electrons in the metal. At certain frequencies the free electrons undergo resonant oscillation causing the LSP. This resonant condition depends primarily on the shape of the particle and thus the distribution of the surface charges at the metal edges. The basic formulation for such polarization of metallic nano-particles was introduced in section 2.2 where the generalized equation for polarizability was given as

$$\alpha \propto \frac{\epsilon_m - \epsilon_d}{\epsilon_d + \chi(\epsilon_m - \epsilon_d)} \quad (10.1)$$

The poles of the polarizability gives the resonance condition for the LSP when the particle polarization to an incident field is maximum. Thus the plasmonic property of the nano-particle according to this approach is described purely by the factor  $\chi$  which is called the depolarization factor. However this model has a major drawback as it cannot be used for particles with complex geometry.

The basic principle of modeling the polarization offered by a particle by  $\alpha$  stems from replacing the extended particle by a dipole and thus approximating the response of the particle by a dipole response. Thus the simplest method is to solve the Laplace equation for a scalar electric potential ( $\nabla^2 \Phi = 0$ ) with  $E = -\nabla \Phi$ . Using the boundary conditions at the surface of the particle we calculate the polarization of the particle. For a spherical metallic particle with dimensions much smaller than the wavelength of light, it has been shown elsewhere that the depolarization factor is given as  $\chi = 1/3$  [178]. Using equation 10.1

with a spherical nano-particle surrounded by a homogeneous medium with refractive index  $n_h = 1.333$  we can calculate the resonance wavelength for the LSP as  $\lambda_{LSP} = 552nm$ , ( $k_0 = 11.38/\mu m$ ).

However this approach does not include the effect of diameter of the sphere on the resonance wavelength. However, as have been shown in numerous articles and reviews, the LSPR condition depends on the particle size for particles with dimensions of the order of the wavelength of light [179, 180, 181, 126].

Several other formulations have been used to calculate the resonance conditions for simple particle geometries [182, 183, 184, 185, 186]. Such theories are mostly based on using multipolar expansions to calculate the polarization offered by the particle to an incoming electric field. But there are very few geometries where the Mie scattering theory can be solved analytically and are only applicable for dimensions much smaller than the wavelength of light [187, 188].

In this work for the LSP, we will use a rigorous numerical approach to calculate accurately the resonance condition of the nano-particles. Let us consider a metallic nano-particle (refractive index  $n_m = \sqrt{\epsilon_m}$ ) with arbitrary shape present inside a homogeneous medium of refractive index  $n_h = \sqrt{\epsilon_h}$ . The field (electric  $\mathbf{E}$  or magnetic  $\mathbf{H}$ ) in the medium  $n_h$  can thus be written as a sum of the incident field ( $\mathbf{E}_{(i)}$ ) and the field scattered by the particle  $\mathbf{E}_{(s)}$ . Thus the average energy flow which is represented by the Poynting vector ( $\mathbf{S} = \mathbf{E} \times \mathbf{H}$ ) can be written as

$$\langle \mathbf{S} \rangle = \langle \mathbf{S}_{(i)} \rangle + \langle \mathbf{S}_{(s)} \rangle + \text{Re} \left\{ \mathbf{E}_{(i)} \times \mathbf{H}_{(s)}^* + \mathbf{E}_{(s)} \times \mathbf{H}_{(i)}^* \right\} \quad (10.2)$$

where  $\langle \mathbf{S}_{(i)} \rangle = \text{Re} \left\{ \mathbf{E}_{(i)} \times \mathbf{H}_{(i)}^* \right\}$  and  $\langle \mathbf{S}_{(s)} \rangle = \text{Re} \left\{ \mathbf{E}_{(s)} \times \mathbf{H}_{(s)}^* \right\}$ . The rate of energy flow is represented by the integral of the radial component  $\langle \mathbf{S} \rangle$ . In case of a dielectric nano-particle it is zero. However for a metallic particle, the integrals of the radial components of the three terms of equation 10.2 gives the rate at which energy is absorbed by the particle. Considering the medium  $n_h$  to be dielectric and thus the integral of the radial component of  $\langle \mathbf{S}_{(i)} \rangle$  to be zero we can write the total rate of energy absorbed and scattered by the particle as

$$W_{ext} = \text{Re} \left\{ \int_{\Omega} \left( \mathbf{E}_{(i)} \times \mathbf{H}_{(s)}^* + \mathbf{E}_{(s)} \times \mathbf{H}_{(i)}^* \right) \cdot \mathbf{n} d\mathbf{S} \right\} \quad (10.3)$$

where  $\Omega$  denotes the surface bounding the particle and  $\mathbf{n}$  being the normal to that surface. Using matrix formulation we can write  $\mathbf{E}_{(i)} \times \mathbf{H}_{(s)}^* + \mathbf{E}_{(s)} \times \mathbf{H}_{(i)}^* = \Phi_{(i)} \times \Phi_{(s)}$  with  $\Phi_{(i)} = \begin{pmatrix} \mathbf{E}_{(i)} \\ \mathbf{H}_{(i)} \end{pmatrix}$  and  $\Phi_{(s)} = \begin{pmatrix} \mathbf{E}_{(s)} \\ \mathbf{H}_{(s)} \end{pmatrix}$ . Using the divergence theorem and considering the media to have constant permeability ( $\mu$ ) we can write  $W_{ext}$  as

$$W_{ext} = \text{Re} \left\{ \int_V \left( \Phi_{(i)}^T (\epsilon_m - \epsilon_h) \Phi_{(s)} \right) dV \right\} \quad (10.4)$$

We will call this the extinction caused by the metallic particle to the incident electric field. Using FEM we have calculated the electric and magnetic fields without the metallic nano-particle ( $\Phi_{(i)}$ ) and then the total field with the particle ( $\Phi_{(s)}$ ). Then volume integral was carried out over the calculation domain as according to equation 10.4.

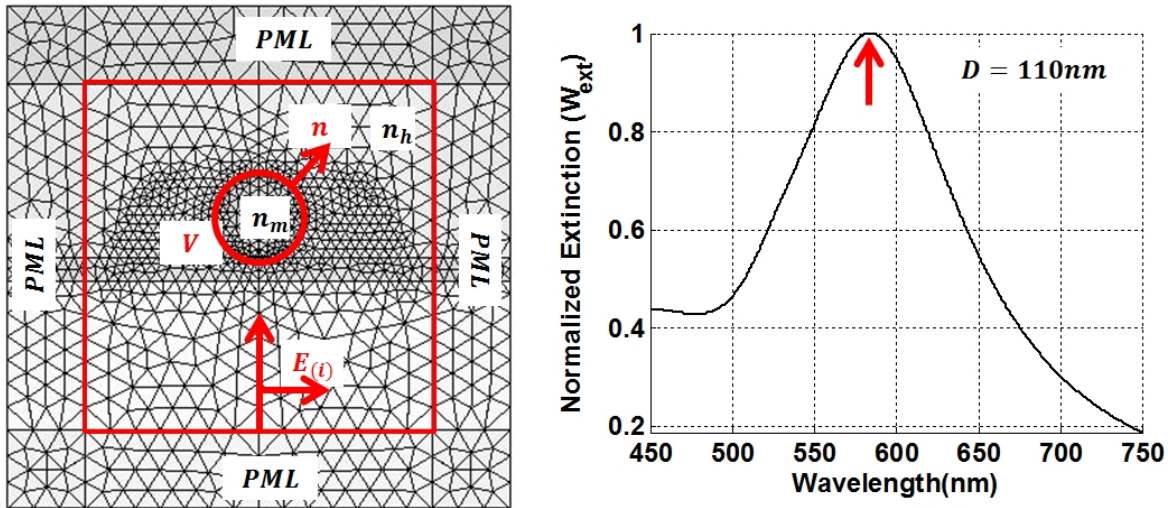


Figure 10.2: The calculated extinction ( $W_{ext}$ ) of a gold sphere of diameter ( $D$ ) 110nm in a homogeneous medium of refractive index  $n_h = 1.333$ . The computational domain for the FEM is shown in red.

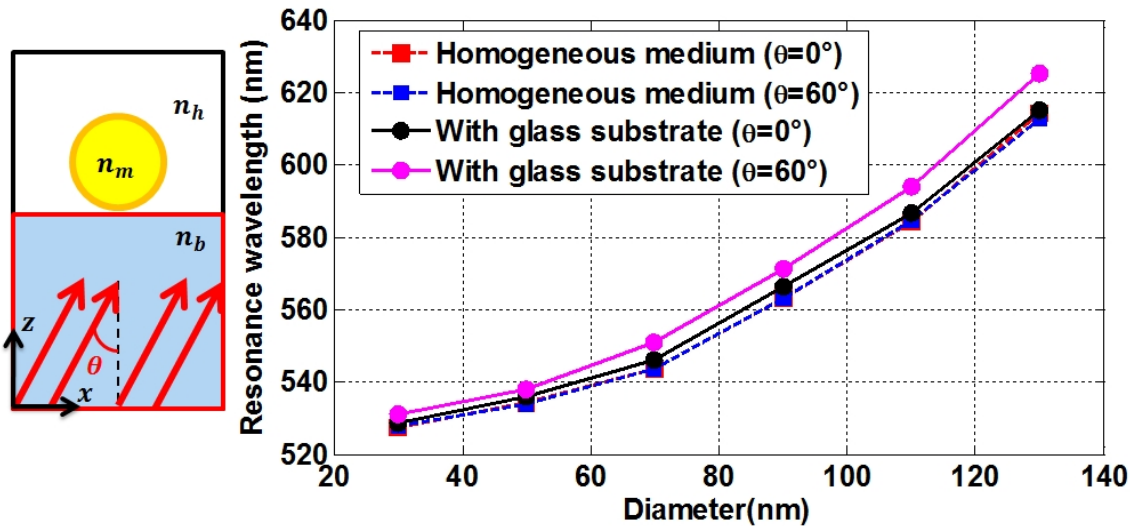


Figure 10.3: Resonance wavelength ( $\lambda_{LSP}$ ) for a gold sphere in a homogeneous medium with refractive index  $n_h = 1.333$  for two different angle of incidence  $\theta$ . (red and blue squares) The same calculation was done by considering the incident medium to have a refractive index  $n_b = 1.513$  (glass substrate).  $\lambda_{LSP}$  with a glass substrate is also shown (black and magenta circles). The incident light is TM polarized with its electric field oriented along  $x$  and  $z$  axes.

Such an extinction spectrum is shown in figure 10.2. A gold sphere of diameter 110nm was considered in a homogeneous medium of refractive index  $n_h = 1.333$ . The normalized  $W_{ext}$  is plotted as a function of incident wavelength  $\lambda$ . We see an extinction peak at  $\lambda_{LSP} = 584.4nm$ . This is not the same as the resonance wavelength calculated by considering the pole of polarizability. In fact using the FEM to calculate the extinction shows that the resonance condition depends on the diameter of the sphere unlike that predicted by equation 10.1.

The variation of the extinction peak and thus the LSP resonance wavelength ( $\lambda_{LSP}$ ) as a function of diameter of the sphere is shown in figure 10.3. We observe a red shift of the LSPR condition with the diameter of the sphere.



For the calculation an angle of incidence was considered as shown in the figure and thus the incident electric field can be separated into its  $x$  and  $z$  components (TM polarization). For a sphere in a homogeneous medium this distinction does not have a physical sense (as the dimensions of the sphere is same along  $x$  and  $z$ ) and thus as shown in the result, the resonance wavelengths found for two different angles of incidence are identical ( $\theta = 0^\circ$  and  $\theta = 60^\circ$ ). But this will be important when considering a more unsymmetrical geometry as in the case of a metallic cylinder.

The extinction for the sphere placed on a substrate with refractive index  $n_b = 1.513$  was also calculated and shown in figure 10.3. We see that with normal incidence ( $\theta = 0$ ) and thus for the electric field oriented along the interface ( $x$  axis) there is negligible difference of  $\lambda_{LSP}$ . Thus the presence of the substrate has little effect on the LSP resonance of a gold sphere when excited parallel to the interface.

However for  $\theta = 60^\circ$  when there exists a component of the electric field along  $z$  axis (perpendicular to the interface), the  $\lambda_{LSP}$  shifts towards slightly higher wavelengths. This shift is higher for larger diameters. We will present some analytical approximate theories that can help to predict the resonance wavelengths of such nano-particles.

### 10.1.2 Effect of particle dimensions on LSPR

Myroshnychenko et al in their publication [189] presented the retardation effects caused by a particle of finite size. In the calculations therein the phase delay between the charge distribution on two opposite sides of a particle was taken into account. A simplified analytical equation for the polarizability of a gold sphere was presented. Taking retardation effects into consideration the polarizability ( $\alpha$ ) can be written as

$$\alpha \propto \frac{1 - (\epsilon_m + \epsilon_d) \frac{X^2}{40}}{\frac{\epsilon_m + 2\epsilon_d}{\epsilon_m - \epsilon_d} - (\frac{\epsilon_m}{10} + \epsilon_d) \frac{X^2}{4} - i \frac{2}{3} \epsilon_d^{3/2} X^3} \quad (10.5)$$

where  $X = k_0 D/2$  defines a shape factor with diameter  $D$ . Thus in effect the second and the third term of the denominator represents the dipolar plasmon shift and the broadening of the resonance line-width respectively. This relation can be used to approximate the resonance condition of the LSP in the case of a gold sphere in a homogeneous medium. However the calculation using 10.5 does not fit accurately the calculated LSPR using the FEM.

The extinction caused by a spherical particle in a homogeneous medium can also be calculated directly using the Mie theory. We will describe the theory in brief and present the results we obtained by solving the Maxwell's equations using Mie theory [11].

For the solution of the Maxwell's equations as proposed by G.Mie, a spherical particle is considered in a homogeneous, isotropic medium. Both the particle and the medium are non-magnetic and the medium is dielectric. At the surface of the sphere the tangential components of  $\mathbf{E}$  and  $\mathbf{H}$  are continuous and the radial components of  $\epsilon \mathbf{E}$  and  $\mathbf{H}$  are also continuous. The total field of the system is considered to be a linear sum of the incident field, the fields within the sphere and the scattered field in the surrounding medium. Since the required solution applies only to spherical particles, the field vectors are transformed from Cartesian coordinates to spherical polar coordinates.

It can be shown that the vector fields  $\mathbf{E}$  and  $\mathbf{H}$  written in spherical polar coordinates can be derived from two independent scalar potentials known as Debye's potentials which satisfy the wave equation. Such a wave equation with the Debye's potentials can be represented as a series expansion. Integrating the corresponding equation reduces to a Bessel equation which can be solved by a linear combination of

Bessel and Neumann functions. These functions were used to obtain solutions for the field components. Detailed mathematical formulation used in this work for the Mie theory can be found in the following reference [190]. Once the field components  $E$  and  $H$  were calculated using Mie theory, the extinction of the spherical particle was calculated in the same method as described in equations 10.2 to 10.4.

The  $W_{ext}$  calculated by Mie theory and by FEM is shown for a sphere with two different diameters ( $D = 50nm$  and  $D = 150nm$ ) in figure 10.4. The medium around the sphere is considered to be water with index  $n_h = 1.333$ . We see that the FEM and Mie results fit closely to each other.

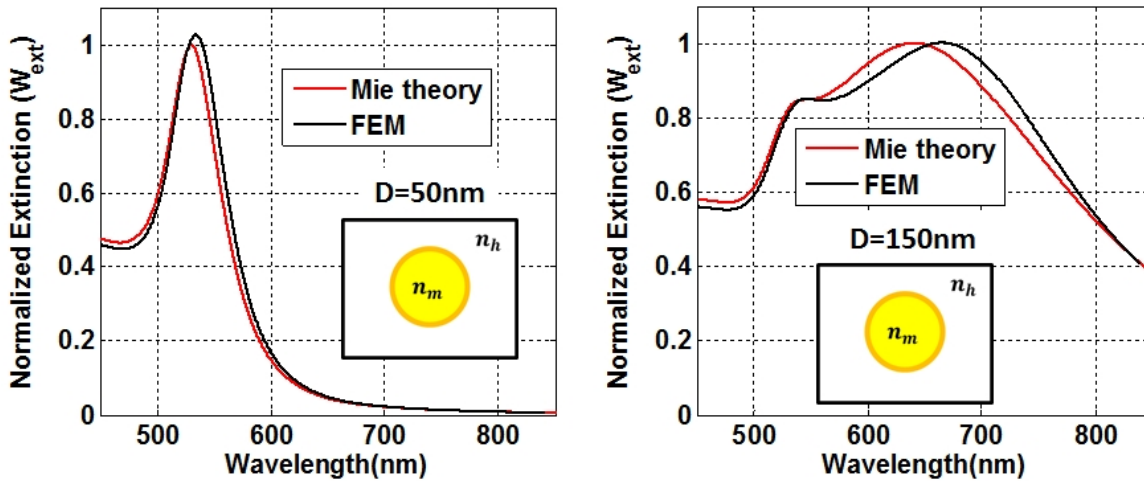


Figure 10.4: The extinction ( $W_{ext}$ ) of a gold sphere of diameter ( $D$ ) 50nm and 110nm in a homogeneous medium of refractive index  $n_h = 1.333$ . The calculation of the field components were done by Mie theory (red) and FEM (black)

A comparison of the three methods described above, the FEM, Mie theory and the calculation of polarizability by Myroshnychenko et al for a sphere in homogeneous medium with varying diameters is shown in figure 10.5. Two different media with  $n_h = 1.0$  and  $n_h = 1.333$  is shown. The peak of  $W_{ext}$  was calculated for the Mie theory and FEM which gives the resonance wavelength for the LSP ( $\lambda_{LSP}$ ). For the polarizability calculation the pole of  $\alpha$  denotes the resonance wavelengths. We see that for  $\lambda_{LSP}$  the Mie theory and FEM calculations give similar results.

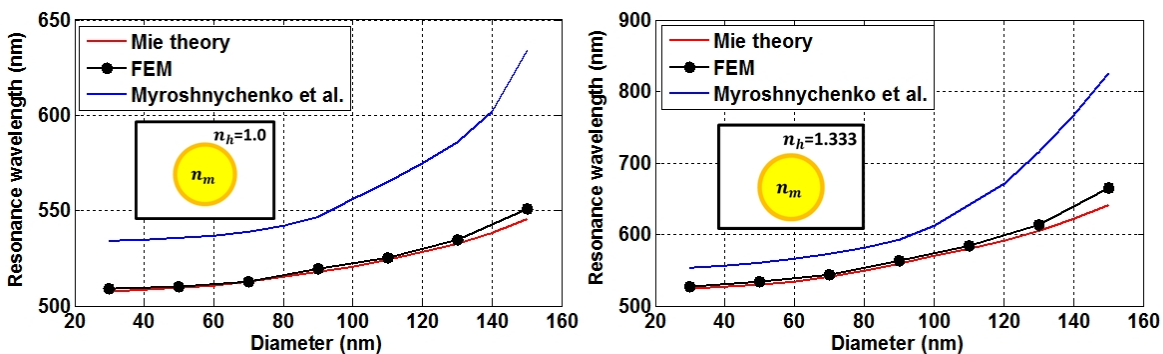


Figure 10.5: Resonance wavelength ( $\lambda_{LSP}$ ) for a gold sphere in a homogeneous medium with refractive index  $n_h = 1.0$  and  $n_h = 1.333$  as a function of sphere diameter. The calculations were done by Mie theory (red), FEM (black) and the polarizability calculation reported by Myroshnychenko et al.

The Mie theory is restricted to spherical particles, however the FEM method can be used for particles with complex geometry. So we will use the FEM method to find  $\lambda_{LSP}$  for the nano-particles used in this work.

For a sphere we aim to find a simple equation for the polarizability which can fit the FEM (and Mie theory) results. The polarizability can be generalized for different particles simply with equation 10.1. It may be a gross approximation, however it can be shown to fit rigorous results. The only free parameter in the equation is the depolarization factor  $\chi$ . By finding suitable analytical equations for  $\chi$  we can obtain approximate values for  $\lambda_{LSP}$ . We will call this method the  $\chi$  formulation.

For most plasmonic structures the resonance wavelength is an important parameter when applying them for various applications. Thus even though the  $\lambda_{LSP}$  may be an approximate value, it can help to characterize plasmonic structures. For verification of the results found by the  $\chi$  formulation we can use FEM calculations which in turn are validated by experimental results. To find an approximate value for  $\chi$  in the case of a metallic sphere in a homogeneous medium with index  $n_h$  we start from equation 10.5 where a shape factor  $X = k_0 D/2$  is used as a correction to the calculation of  $\alpha$ . We have seen that the resonance wavelength undergo a red shift with increasing diameter and with index  $n_h$ . So  $\chi$  should decrease with both diameter and  $n_h$ . We choose to express the depolarization factor as

$$\chi = \frac{\sqrt{\pi}}{n_h^2} (1 - \sqrt{X}) \quad (10.6)$$

$$X = \frac{k_0 D}{2}$$

Using the  $\chi$  formulation as shown in figure 10.6 the resonance wavelengths for the sphere in a homogeneous medium fits closely with Mie theory and rigorous FEM numerical calculations.

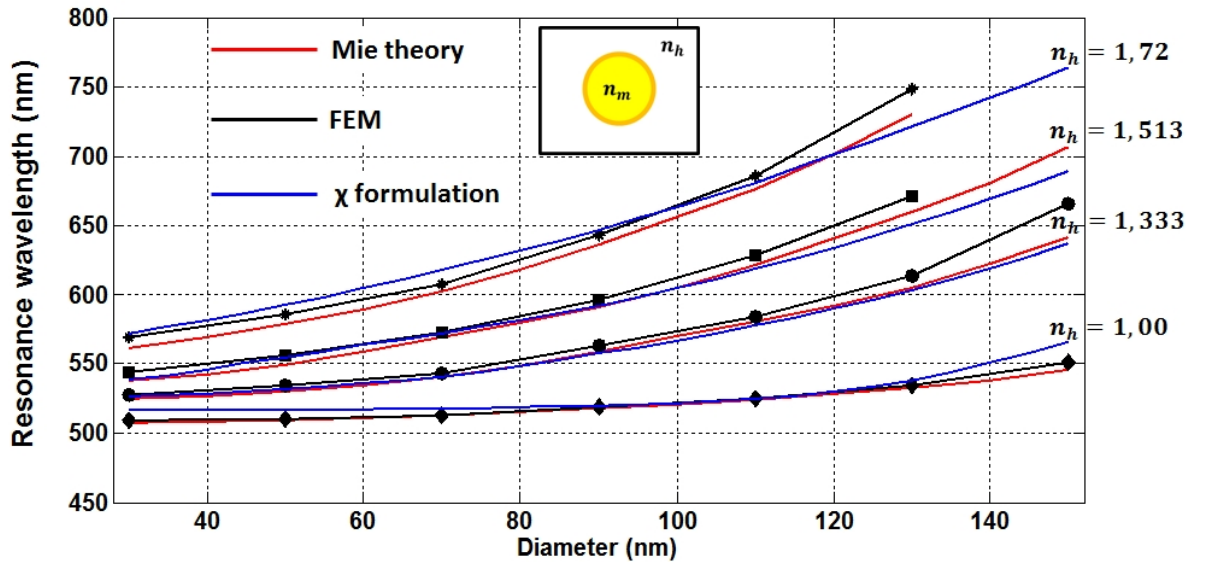


Figure 10.6: Resonance wavelength ( $\lambda_{LSP}$ ) for a gold sphere in a homogeneous medium with refractive index  $n_h$ . The calculations were done by Mie theory (red), FEM (black) and the polarizability calculation with  $\chi$  formulations (blue).

### 10.1.3 Effect of substrate on LSPR

Presence of a substrate is known to shift the resonance frequency of LSPR [191, 192, 193, 194]. Once we have obtained a simplified approximate formulation for the LSP resonance wavelength of a sphere in homogeneous medium, we can proceed to describing the effect of a substrate on  $\lambda_{LSP}$ . Particle-substrate interaction is generally treated by the concept of image charges. Such a treatment was reported by Vernon et al [195] and we will use the approach presented therein.

The theory simply calculates the polarizability of a particle in a homogeneous medium with an normalized in-plane wave-vector which accounts for the substrate. Without going into the details of the formulations, it can be shown that for particle of permittivity  $\epsilon_m$  in a homogeneous medium of  $\epsilon_h$  placed on a substrate with permittivity  $\epsilon_b$ , the polarizability can be written as

$$\alpha \propto \frac{\epsilon_m - \epsilon_{eff}}{\epsilon_{eff} + \chi(\epsilon_m - \epsilon_{eff})} \quad (10.7)$$

where the normalized in-plane wave-vector is given by

$$\epsilon_{eff} = \epsilon_h \frac{1 + \eta T / (1 + \gamma_\chi)}{1 + \eta T / (1 - \gamma_\chi)} \quad (10.8)$$

$$\text{with}$$

$$\eta = \frac{\epsilon_h - \epsilon_b}{\epsilon_h + \epsilon_b}$$

$$\gamma_\chi = \frac{1}{1 - 2\chi}$$

The factor  $T$  includes the effect of the substrate on the LSP of the nano-particle. To calculate  $\alpha$  for a particle in a homogeneous medium, the surface charges induced by an exciting electromagnetic field is taken into account. In the presence of a substrate, the electric field of the surface charges created on the particle, polarize the surface of the substrate and induces additional surface charges at the interface. Such induced surface charges are modeled by the method of image charges described above. In this model the mirror image of the particle acts as a pseudo-particle and its effect on the LSP of the particle is treated by a electrostatic coupled theory. This interaction of the electric field of the image charges with the dipole of the particle is represented by the factor  $T$ .  $T$  depends primarily on the distribution of the surface charges and thus on shape and dimensions of the particle.  $T$  also depends on the orientation of the surface charges with respect to the substrate interface. It can be approximated to

$$T = \frac{\gamma_\chi}{2\pi} \frac{3(\vec{p} \cdot \hat{d}_p)^2 - \vec{p} \cdot \vec{p}}{d_p^3} \quad (10.9)$$

where  $\hat{d}_p$  represents the unit vector pointing from the image to the nanoparticle with a separation  $d_p$  between the two and  $\vec{p}$  being proportional to the dipole moment.

The first important point to note here is that  $T$  depends on the component of the dipole moment of the pseudo-particle along the unit vector pointing from the image to the particle ( $\hat{d}_p$ ). So the value of  $T$  is negligible when the effective dipole of the particle is oriented perpendicular to  $\hat{d}_p$ . Thus for a particle polarized along the interface (thus for an incident electric field along the interface) the substrate can be considered to have less effect on the polarizability of the particle. We can see this from figure 10.3 where

for an incident electric field polarized along  $x$  the LSPR wavelengths are the same for the sphere in a homogeneous medium and when a glass substrate is introduced.

Now the second term in equation 10.9 represents the interaction of the dipole moments of the particle and its image. For an extended particle we can expect this term to depend strongly on the shape and the aspect ratio of the particle. Such interaction also depends on the homogeneous medium surrounding the dipole. The depolarization of the particle was approximated by  $\chi$  presented in the previous section. We will try to replace the term representing the dipole term in 10.9 with  $\chi$  and expect to have an approximation on the trend of the shift of  $\lambda_{LSPR}$  due to the presence of a substrate. Thus we can approximate  $T = -\frac{\gamma\chi}{2\pi}(\pi\epsilon_h)\chi$  to follow the effect of a substrate on the LSPR of a nano-particle.

The effect of a substrate with refractive index  $n_b$  (permittivity  $\epsilon_b$ ) is shown in figure 10.7. The calculation was done by rigorous FEM calculation as described in section 10.1.1 and with the analytical model. We see that the LSP resonance wavelength undergoes a slight red shift when the substrate is introduced with a component of the incident electric field along  $z$  axis (perpendicular to the interface and thus parallel to  $\hat{d}_p$ ). We checked that this shift is negligible for the field polarized along  $x$  as expected ( $\theta = 0$ ).

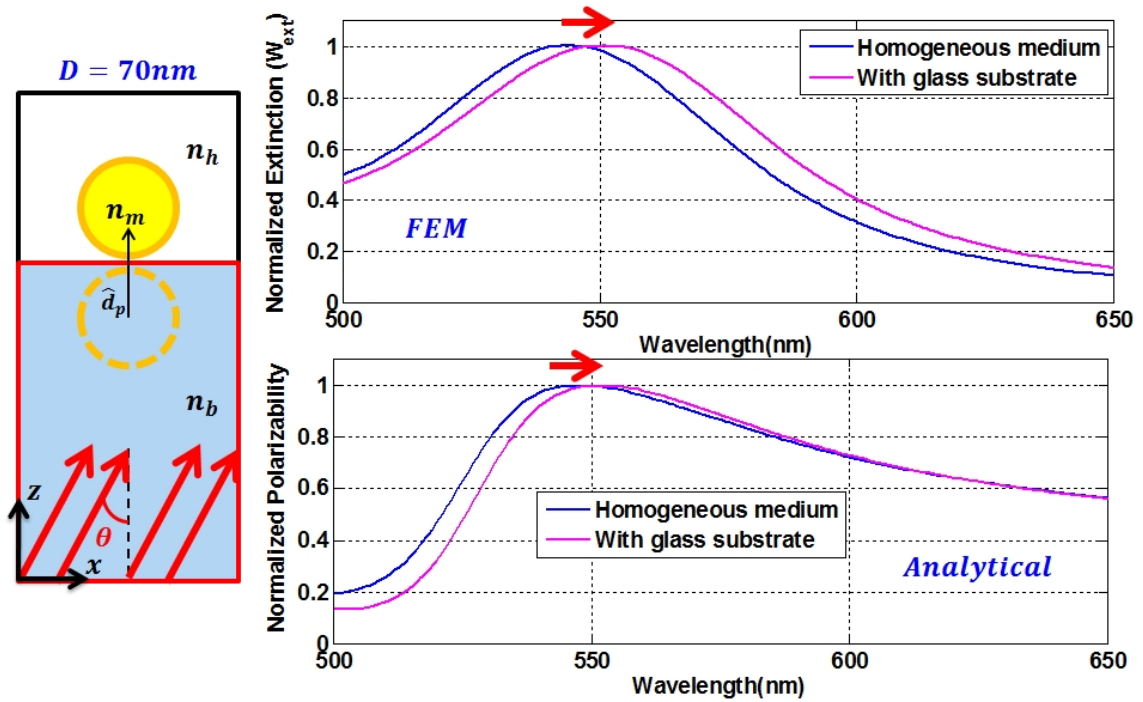


Figure 10.7: The calculated  $W_{ext}$  using FEM for a sphere in a homogeneous medium of refractive index  $n_h = 1.333$  and that with a glass substrate of index  $n_b = 1.513$ . The diameter of the sphere was  $D = 70nm$  and the incident light was TM polarized with an angle of incidence of  $60^\circ$ . Thus the incident electric field has both  $E_x$  and  $E_z$  components. The analytical calculation of polarizability ( $\alpha$ ) using the  $\chi$  formulation and the formulation for effect of substrate is also shown.

Thus to formulate the LSPR condition for metallic nano-particles we can use FEM to calculate precisely the extinction ( $W_{ext}$ ) of the particle. This method gives accurate results for complex geometries such as particles of various shapes and the presence of a substrate. The results for a sphere in a homogeneous medium match closely the solution obtained by Mie theory. However to explain the various effects of geometry and environment we developed an analytical model by using appropriate relations for the

depolarization factor  $\chi$  and thus approximating the LSPR condition by  $\chi$  formulations.

The effect of a substrate can also be analytically approximated by the pseudo-particle image theory and the results obtained for the LSPR condition follows a similar trend to the results obtained by FEM. Having described such numerical and analytical models we will now describe the LSPR condition in the case of a metallic cylinder.

## 10.2 LSPR condition for metallic nano-cylinders

For a nano-cylinder we will follow the same approach as described for a sphere in the last section. The Mie theory in this case is not applicable. The extinction spectrum ( $W_{ext}$ ) for a single cylinder in a homogeneous medium (with refractive index  $n_h$ ) was calculated by FEM. A plane TM polarized wave was considered to be incident on the cylinder at an angle  $\theta$ . The calculation is shown in figure 10.8 for two diameters of the cylinders ( $D = 50nm$  and  $D = 150nm$ ). Contrary to a sphere there is clearly a difference in the LSPR condition with  $\theta$ .

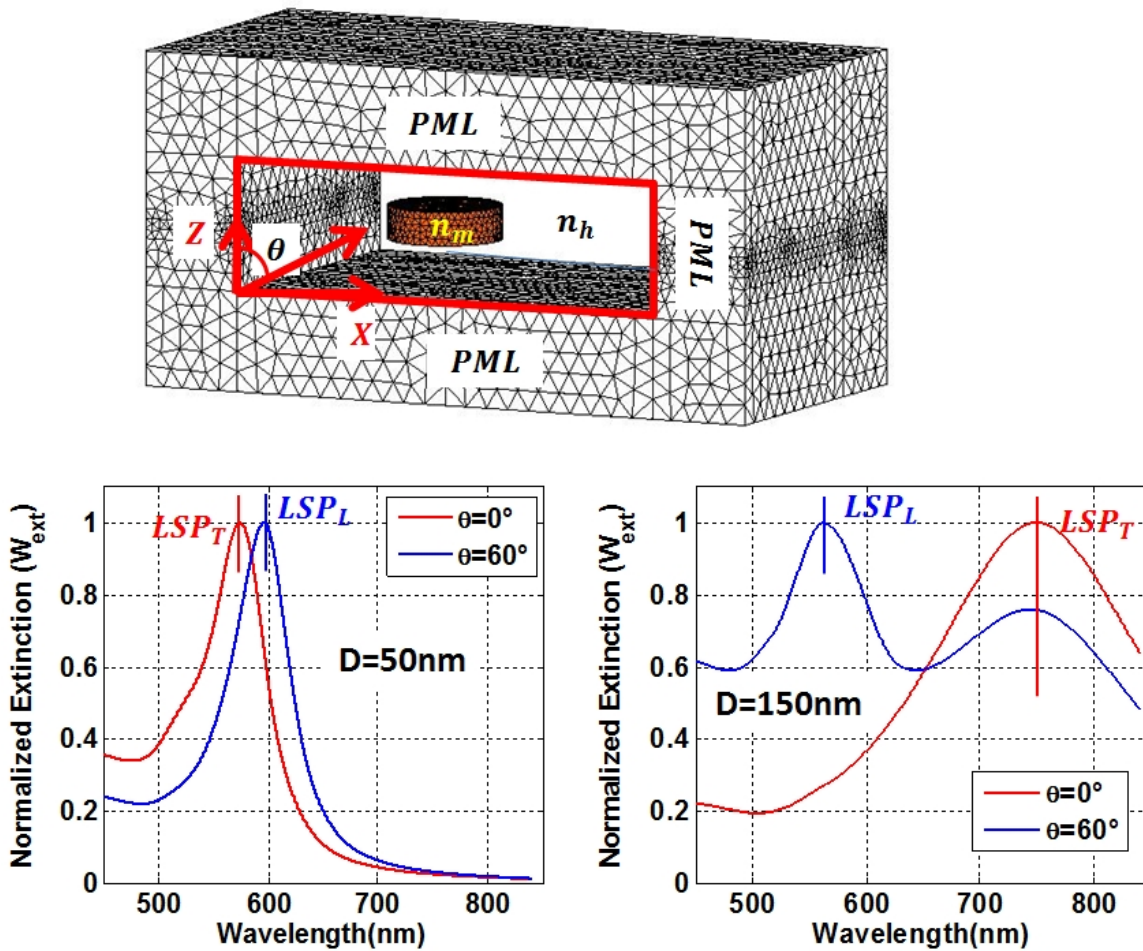


Figure 10.8: The calculated  $W_{ext}$  using FEM for a nano-cylinder in a homogeneous medium of refractive index  $n_h = 1.333$ . The height of the cylinder was  $h = 50nm$  and the incident light was TM polarized with an angle of incidence of  $\theta$ . The calculated value is shown for two diameters of the cylinders  $D = 50nm$  and  $D = 150nm$ .

To explain the results, we must first realize what the angle of incidence  $\theta$  implies in this case. The

incident field is TM polarized and thus at incidence of  $\theta = 0^\circ$  the incident electric field is polarized only along the  $x$  axis. So the LSP excited in the cylinder in this case is oriented only along  $x$ . For  $\theta = 60^\circ$  we have both the  $x$  and  $z$  components of the incident electric field. So in this case a LSP oriented along  $z$  is also excited. This is more evident from the calculation of the extinction for  $D = 150\text{nm}$  where for  $\theta = 0^\circ$  we have only one peak while for  $\theta = 60^\circ$  we have two peaks. We will call them the  $LSP_T$  and  $LSP_L$  for the one along  $x$  and  $z$  respectively where the subscripts  $L$  and  $T$  stand for longitudinal and transverse respectively.

From figure 10.8 we also see that  $LSP_T$  undergoes a red shift with increasing diameter. This is similar to a sphere in a homogeneous medium. However the  $LSP_L$  undergoes a blue shift with increasing diameter. The variation of  $\lambda_{LSP}$  with diameter for the two incident angles  $\theta$  was also calculated by FEM and is shown in figure 10.9. We see that at  $\theta = 0^\circ$  the extinction peak and thus  $LSP_T$  undergoes a red shift with diameter. The maximum of extinction at  $\theta = 60^\circ$  for  $LSP_L$  undergoes a blue shift.

We can simply explain this by the fact that  $LSP_L$  is oriented along the axis of the cylinder and thus it has opposite trend to  $LSP_T$  which is oriented perpendicular to the axis of the cylinder. As we will show in the following numerical model, the resonance wavelength of the LSP depends on the aspect ratio of the nano-particles along the direction of its orientation which is orthogonal for  $LSP_T$  and  $LSP_L$ .

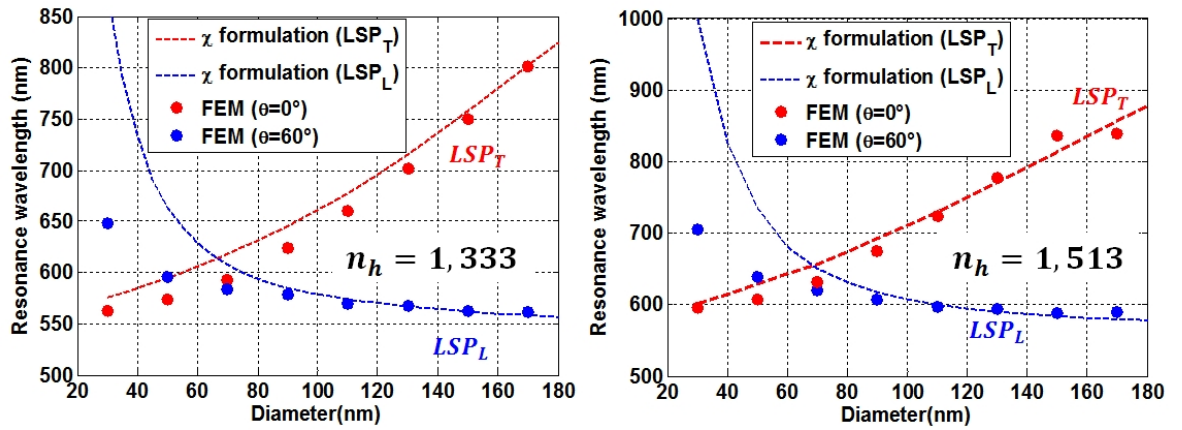


Figure 10.9: Resonance wavelengths ( $\lambda_{LSP}$ ) using FEM as a function of nano-cylinder diameter for incident light at  $\theta = 0^\circ$  ( $LSP_T$ ) and  $\theta = 60^\circ$  ( $LSP_L$ ). Two different media with  $n_h = 1.333$  and  $n_h = 1.513$  were calculated. The calculated  $\lambda_{LSP}$  obtained by  $\chi$  formulation for  $LSP_T$  and  $LSP_L$  are also shown. The height of the cylinder was taken as  $h = 50\text{nm}$ .

To quantify the LSPR condition for the two LSPs we will use the  $\chi$  formulation and use approximate equations for  $\chi$  to calculate the polarizability  $\alpha$  of the cylinder. For the analytical calculation the  $\chi$  for the two cases is given as

$$\chi_{T/L} = \frac{\sqrt{\pi}}{2n_h^2} \left(1 - \sqrt{X_{T/L}}\right)$$

$$X_T = \frac{k_0 D}{2} \tag{10.10}$$

$$X_L = \frac{h^2}{h^2 + D^2}$$

We see that the relation is similar to that obtained for a sphere. The shape factor  $X$  for  $LSP_T$  is the same as that for the sphere and this is because of the rotational symmetry of the cylinder in the transverse ( $x - y$ ) plane. The shape factor for  $LSP_L$  however is different and this relation was derived from various expressions for the depolarization factor of cylindrical structures found in the literature [196, 197].

The results shown for two different media with indices  $n_h$  follow closely the trend as calculated by FEM. However there are some discrepancies for  $D < 50nm$  for  $LSP_L$ . This is because the height of the cylinder was taken as  $h = 50nm$  and the formulation for  $\chi_L$  does not work for the case when  $D < h$ . It should be noted that for  $\chi$  formulation, it is the aspect ratio of the particles that play a major role and the calculations must be done with keeping the aspect ratio in consideration.

The effect of the substrate on the LSPR of the cylinders can be analytically calculated using the same formulation described in section 10.1.3. The result obtained for the resonance wavelengths with FEM calculations and  $\chi$  formulation is shown in figure 10.10. We see that  $LSP_T$  undergoes a red shift when a substrate is introduced as obtained for the case of a spherical nano-particle. However a dielectric substrate has negligible effect on the  $\lambda_{LSP}$  for  $LSP_L$ . The results obtained by FEM calculations also match closely the results obtained by  $\chi$  formulation for  $D > h$ .

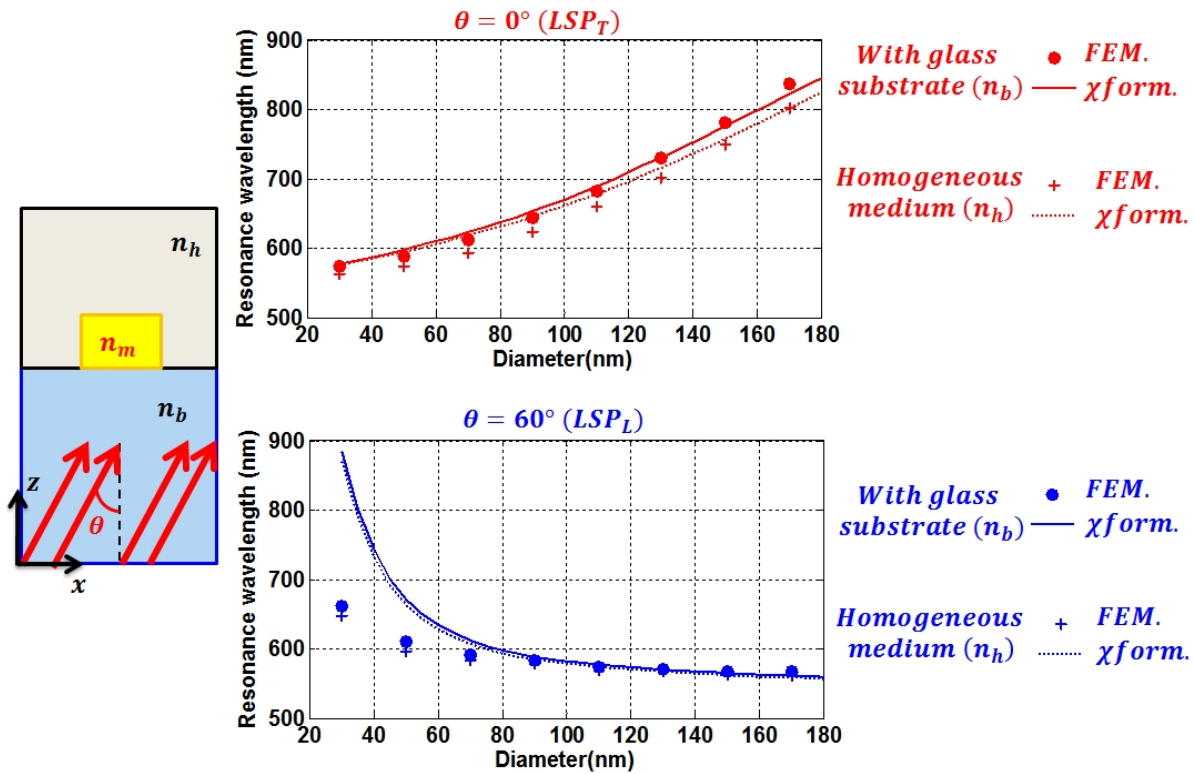


Figure 10.10: Resonance wavelengths ( $\lambda_{LSP}$ ) using FEM as a function of nano-cylinder diameter for incident light at  $\theta = 0^\circ$  ( $LSP_T$ ) and  $\theta = 60^\circ$  ( $LSP_L$ ) (scatter plots). The same is shown with  $\chi$  formulation (lines). The height of the cylinder was  $h = 50nm$ . The calculations were done with the cylinder in a homogeneous medium of index  $n_h = 1.333$  and also with a glass substrate ( $n_b = 1.513$ ).

To conclude, the dimensions of the nano-particle plays a major effect on the LSPR condition and the shift of  $\lambda_{LSP}$  depends on the type of localized plasmon excited in the sample. Presence of a substrate generally causes red shift of  $\lambda_{LSP}$ . However this effect is not very prominent for dielectric substrates. In later sections (Chapter 11) we will show that a metallic substrate has a major effect on the LSPR condition



of the nano-particles and it can be treated with similar pseudo-particle concept and  $\chi$  formulation.

### 10.3 Array of metallic cylinders on a glass substrate

Having described the LSPR condition for a single nano-particle with an underlying substrate we will now study an array of metallic nano-cylinders placed on a glass substrate.

We will describe the plasmonic characteristic of the array of metallic nano-cylinders in terms of plasmonic modes as done in the case of 2D gratings in chapter 9. In the case of a metallic nano-particle array on a glass substrate we do not expect propagating plasmons as the dimensions of the particles are much smaller than the wavelength of the PSP modes. The only possible modes that can be excited in such structures are the WRAs. But the far field characteristics of the WRA are not very prominent.

The reflectivity and transmission as a function of  $(k_0, (k_{//}/k_0))$  was calculated for the structure ( $D = 70nm, h = 30nm, \text{period } \Lambda = 200nm$ ) and shown in figure 10.11. An incident plane wave from a medium with refractive index  $n_b = 1.513$  was incident of the structure at an angle  $\theta$ . The incident light was considered to be TM polarized. The refractive index of the medium surrounding the cylinders was taken as  $n_h = 1.333$ . In this case as explained earlier, we can excite the structure with the photon normalized in-plane wave-vector values of  $(k_{//}/k_0) = n_b \sin\theta$  from 0 to  $n_b$  with the critical angle for  $n_b - n_h$  interface being  $(k_{//}/k_0) = n_h$ .

The analytically calculated curves for the WRAs ( $(k_{//}/k_0)_h$  and  $(k_{//}/k_0)_b$ ) are also shown in the figure. We see that the reflectivity drops at the  $(k_0, (k_{//}/k_0))$  values where the WRAs are excited. Apart from this there are not much features of interest in the study of reflectivity or transmission. The LSPR condition ( $\lambda_{LSP}$ ) for  $LSP_L$  and  $LSP_T$  as calculated by the  $\chi$  formulation with a glass substrate is also shown. Here the condition was plotted in  $(k_0, (k_{//}/k_0))$  map with  $k_0 = 2\pi/\lambda_{LSP}$ . Though  $(k_{//}/k_0)$  has no significance for the LSP such a representation is useful to visualize and for comprehension. We see a slight increase of reflectivity and a drop in transmission around the wavelengths where the LSPR condition is satisfied.

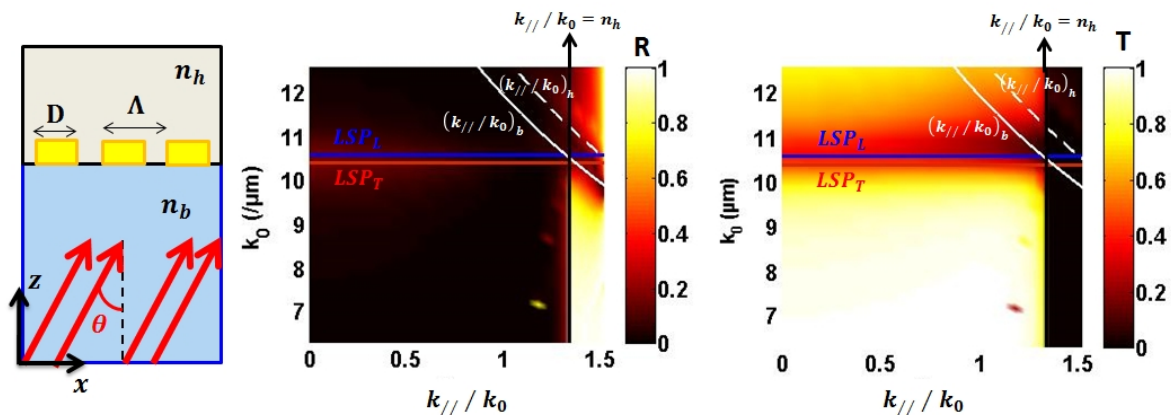


Figure 10.11: The reflectivity (R) and transmission (T) of an array of metallic cylinders on a glass substrate as a function of  $(k_0, (k_{//}/k_0))$ . The cylinder diameter (D) was 70nm, of height (h) of 50nm. The periodicity of the array was taken as 200nm. The calculated values for the WRAs ( $(k_{//}/k_0)_h$  and  $(k_{//}/k_0)_b$ ) and the LSPR conditions for  $LSP_T$  and  $LSP_L$  are also shown. The incident plane wave was TM polarized and the indices were  $n_h = 1.333$  and  $n_b = 1.513$ .

The most important property of the LSP is that at the resonance frequencies of the LSP the electromagnetic field is strongly confined at the surface of the nano-particles. Due to low dispersion of the LSP it is not very efficient for sensor based applications as will be discussed in later (Part V). However the field confinement that results from the LSP has paved its use for several applications. The electric field intensity was calculated using a 3D periodic mesh. In this case the plane wave was considered to be incident along the  $x - z$  plane. The incident field was TM polarized so as to assure the excitation of both  $LSP_L$  and  $LSP_T$  along  $z$  and  $x$  axes respectively. We must mention here that for TE polarization the  $LSP_T$  can be excited along  $y$  axis and at the same  $\lambda_{LSP}$  as the  $LSP_T$  excited for TM polarization. However the  $LSP_L$  which requires an incident field component along  $z$  axis cannot be excited for TE polarization.

The near field of the structure was calculated by FEM along  $x$ ,  $y$  and  $z$  axes by applying periodicity conditions in the  $x - y$  plane. The total electric field intensity was evaluated for each node ( $n$ ) of the 3D mesh as  $I_n = (E_x^2 + E_y^2 + E_z^2)/I_0$  where  $I_0$  is the incident field intensity. We are mainly interested in the field confined at the surface of the nano-cylinders, and such a high intensity of the confined field indicates the excitation condition of the LSPs.

To quantify such confinement it is more useful to calculate the surface integral of the field intensity over the surface of interest. In this case, the integral was calculated over the surface of the nano-cylinders ( $S_{cyl}$ ) as.

$$I_{surf} = \frac{1}{S_{cyl}} \iint_{S_{cyl}} I(S) dS \quad (10.11)$$

For the 3D mesh, first the mean field intensity ( $I_f$ ) is calculated from the values of  $I_n$  for each face ( $f_{cyl}$ ) of the tetrahedral meshing elements that lie on the surface of the cylinder. Then the surface area ( $S_f$ ) of those faces are also calculated. The total surface area of the cylinder was thus  $S_{cyl} = \sum_{f_{cyl}} S_f$ . Finally to evaluate the above integral, a discrete sum was carried out as shown below.

$$I_{surf} = \frac{1}{S_{cyl}} \sum_{f_{cyl}} (I(f) \times S_f) \quad (10.12)$$

$I_{surf}$  was calculated as a function of  $(k_0, (k_{//}/k_0))$  for each incident wavelength  $\lambda$  and angle of incidence  $\theta$ . Figure 10.12 shows the calculated field intensity for an incidence from the medium with index  $n_h$ . This is effectively same in terms of the LSPR condition, as the incidence from the medium  $n_h$ . However the field around the cylinders is somewhat more enhanced with an incidence from  $n_h$  as in this case we can directly excite the cylinders with the incident field.

We see clearly the presence of the two LSP. The  $LSP_L$  is more intense for larger  $(k_{//}/k_0)$  and thus for larger angle ( $\theta$ ) when the  $z$  component of the incident field is stronger. The LSPR condition ( $k_0 = 2\pi/\lambda_{LSP}$ ) as obtained by  $\chi$  formulation is also shown in the figure and matches closely to the  $(k_0, (k_{//}/k_0))$  values where we have strong field intensity enhancement on the cylinder surface. As can be seen from figure 10.9 the two LSPR condition cross for some particular cylinder dimensions. We can expect a much higher field confinement when the two LSPR conditions are satisfied simultaneously as in the case of  $D = 50nm$ . This explains the higher  $I_{surf}$  value for  $D = 50nm$  as compared to  $D = 110nm$ .

The spatial field intensity distribution for the two LSPs is shown in figure 10.13. We see that the field intensity for  $LSP_L$  is asymmetric along the  $x$  axis as it is excited by the electric field component

along  $z$ . For  $LSP_T$  which is excited by the field along  $x$  axis, the field distribution is symmetric in the  $x - y$  plane. We must mention here that we see a very high field intensity at the edges of the metallic structures. This is true for all field calculations presented in this work. This is a well-known phenomenon which rises due to the inability to calculate exactly the fields (thus showing a much higher amplitude of the fields) at a sharp discontinuity (edges) and the effect is more pronounced when such a discontinuity involves metals.

For both fields we see that the electric field is strongly confined close to the cylinder surface. Thus the LSP can be considered as a confined plasmonic mode which has no dispersion and undergoes a resonance with an enhancement of near-field intensity at certain frequencies when the LSPR condition is satisfied. Having described the confined plasmons such as the LSP and the PSP, in chapter 11, we will describe the coupling between the two, assured by adding a metallic substrate to the nano-particle array.

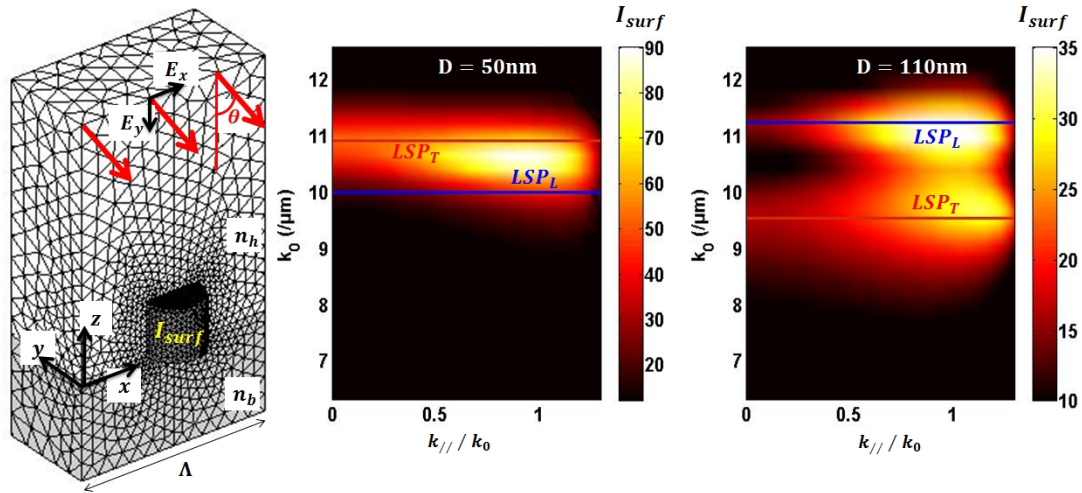


Figure 10.12: Integrated electric field intensity ( $I_{surf}$ ) over the surface of the cylinder of height 50nm for two different diameters ( $D = 50\text{nm}$  and  $D = 110\text{nm}$ ) as a function of  $(k_0, (k_{//} / k_0))$ . The periodicity of the array was taken as 200nm. The calculated LSPR condition for  $LSP_T$  and  $LSP_L$  for the structure is also shown.

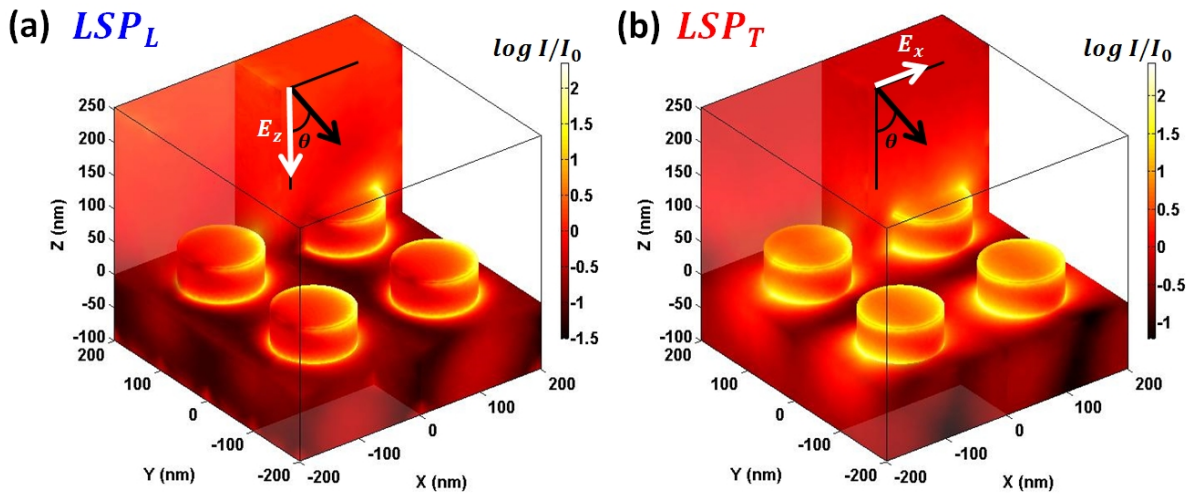


Figure 10.13: The electric field intensity in logarithmic scale for the two LSPs for cylinders of diameter 110nm and height 50nm with a periodicity of 200nm. The angle of incidence was  $\theta = 60^\circ$  (a) for  $LSP_L$  at  $k_0 = 11.02 / \mu\text{m}$  ( $\lambda = 570\text{nm}$ ) (b) for  $LSP_T$  at  $k_0 = 9.70 / \mu\text{m}$  ( $\lambda = 648\text{nm}$ )

---

# Plasmonics of a metallic array on metallic film

---

In the previous chapters we have described the various plasmonic modes and LSPR conditions of array of metallic nano-structures on glass substrate. In this chapter we will follow the same approach to describe the plasmonic modes of an array with a thin metallic film inserted between it and the glass substrate.

In such a structure the LSPR condition can be satisfied for the nano-particles. Owing to the thin metallic film the PSP can also be excited in such structures. This provides the opportunity to obtain new hybrid plasmonic modes that result from the coupling of the LSP and the PSP. Coupling of plasmonic modes was described in brief in section 9.1.3. Any coupling of plasmonic modes results in band-gaps just as in the case of the coupling of WRA and PSP (in this case it is a coupling of an extended mode and a confined mode). However the coupling between two confined plasmons as in the case of LSP and PSP also results in the phenomenon of anti-crossing and hybrid modes which retain some of the characteristics of both the modes. Such plasmonic modes in similar structures were the basis of some of our recent publications [198, 199]. They will be discussed in details in this work.

## 11.1 Metallic grating on gold substrate

Before going into the details of coupling between PSP and LSP, we will first describe another type of plasmonic mode that can be excited in a metallic array with a gold film. The structure geometry is shown in figure 11.1. The modes will be defined in terms of  $(\mathbf{k}_{//}/k_0)$  along the unit vector  $\vec{p}$  as shown in the figure.

The WRAs were described in section 9.1.1 and were shown to be the result of the change of momentum wave-vector owing to the periodicity of the grating. In a periodic array with analogy to a crystal lattice in solid state physics we can consider that the momentum of a photon ( $n_{inc}$ ) can undergo a maximum change of  $n_p = \pm mK_B/k_0$  where  $K_B = 2\pi/\Lambda$ . Based on this concept, the relation for the WRAs as given by equation 9.2 is derived.

The grating placed on a thin metallic film can support modes similar to the WRAs. However in this case the plasmonic modes result from the modification of the normalized in-plane wave-vector of the PSP mode of the thin film. For the PSP, the normalized in-plane wave-vector is defined as  $(\mathbf{k}_{//}/k_0)_{PSP_d} = \sqrt{\frac{(n_d^2 n_m^2)}{(n_d^2 + n_m^2)}}$  when it propagates in a medium of refractive index  $n_d$ . Thus the change

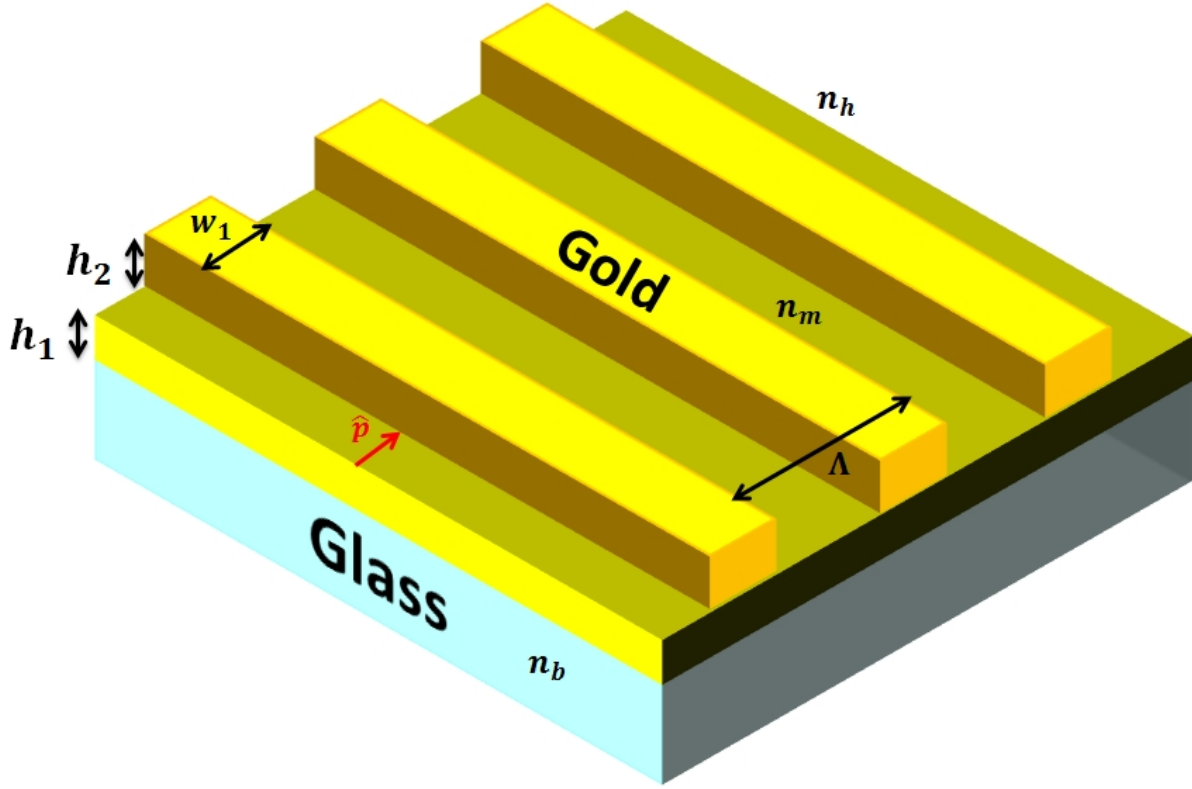


Figure 11.1: A grating of width  $w_1$ , height  $h_2$  and periodicity  $\Lambda$  placed on a thin metallic film of height  $h_1$ . The medium surrounding the grating has a refractive index  $n_h$  and the metal with an index  $n_m$ .  $\hat{p}$  defines the unit vector in the plane of the interface perpendicular to the grating ridges.

in normalized in-plane wave-vector of the PSP due to the periodicity of the structure can be written as  $(k_{//}/k_0)_d = |(k_{//}/k_0)_{PSP_d} - n_P|$ .

We can define a cut-off condition for the modes when  $(k_{//}/k_0)_{PSP_d} = n_P$ . Writing in terms of PSP wavelength  $\lambda_{PSP}$ , the cut off condition is given by  $\lambda_{PSP:d} = m\Lambda$  where the PSP is considered at the metal- $n_d$  interface. At the cut-off the value of the normalized in-plane wave-vector of the mode is zero.

The physical significance of the excitation of the modes can be explained with an analogy to the Bragg diffraction condition for crystalline solids. In such crystals, the Bragg diffraction condition is satisfied when there is a constructive interference between the light scattered by the periodic atomic lattice. For plasmonic modes the condition can be considered as a constructive superposition of the PSP, which propagate in each unit cell of the periodic array. The value of the PSP wavelength in this case is thus an integer multiple of the optical path length between adjacent unit periods. We will call these modes the Bragg Modes (BM) to differentiate them from the WRAs.

Such plasmonic modes have been reported before for different other structures such as nano-holes or corrugated gratings [200, 201, 202]. We must mention here that to excite the BM we only need a thin metallic film and a periodicity. The shape of the structures do not have any influence on the BMs. In spite of the analogy presented above, it should be noted that in reality the BMs (like the WRAs) are strictly not the result of interference. These are rather plasmonic modes that can be supported by the periodic structure.

### 11.1.1 The Bragg Modes

For the structure shown above the Bragg Modes can be represented in  $(\mathbf{k}_0, (\mathbf{k}_{//}/k_0))$  space as

$$\begin{aligned} (\mathbf{k}_{//}/k_0)_{BM_h} &= |(\mathbf{k}_{//}/k_0)_{PSP_h} - n_P| \\ (\mathbf{k}_{//}/k_0)_{BM_b} &= |(\mathbf{k}_{//}/k_0)_{PSP_b} - n_P| \end{aligned} \quad (11.1)$$

where  $(\mathbf{k}_{//}/k_0)_{PSP_h}$  and  $(\mathbf{k}_{//}/k_0)_{PSP_b}$  are the PSP modes at the interface of the gold film and medium with index  $n_h$  and  $n_b$  respectively. The dispersion of the BM for  $\Lambda = 800nm$  for different orders  $m$  is shown in figure 11.2. We see from comparing this with figure 9.3, that the trend of dispersion of the BMs are similar to the WRAs. Physically the BMs and the WRAs are similar modes, the former being a result of diffraction of the PSP while the later is a result of diffraction of the incident photon.

The resonance frequencies of the BMs at  $(\mathbf{k}_{//}/k_0) = 0$  which are the cut off frequencies for the BMs with respect to the array period is shown in figure 11.3. The BMs like the WRAs depend purely on the periodicity of the array. There is a red shift of the resonance frequencies of the BM with period of the array.

Having described the dispersion of the BMs in terms of  $(\mathbf{k}_0, (\mathbf{k}_{//}/k_0))$  we will now discuss their near field and far field characteristics. The electric field intensity ( $I = E_x^2 + E_z^2$ ) distribution was calculated using a 2D mesh, for a TM polarized plane wave incident from the medium with index  $n_h$ , perpendicular to the grating-substrate interface. The BMs cannot be excited for TE polarization as in that case the PSP is not excited.

The electric field was calculated for the resonance frequencies at cut-off for each BM and is shown in figure 11.4. The field intensity is normalized to the incident intensity  $I_0$  and is represented in logarithmic scale. We see that the distribution of field is similar to the WRAs as shown in figure 9.5. However the field intensity is much more enhanced (up to an order of magnitude) with respect to  $I_0$  for the BM than in the case of the WRAs. This is due to the fact that though the BMs are extended modes, they are derived from the PSP which in turn is a confined plasmonic mode.

As the PSP component of the BMs serve to confine the field somewhat close to the metal surface, the far field effects of the BM are more prominent in this case than for the WRAs. For the WRAs, a large part of the energy is radiated into the far field even at the excitation condition of the modes and thus there is not much observable difference at the resonance frequencies ( $(\mathbf{k}_0, (\mathbf{k}_{//}/k_0))$  values) as compared to other non-resonant conditions. However for the BM a considerable amount of electric field energy is confined within a few hundreds of nano-meters from the metal-substrate interface and thus we observe the difference directly at the resonance  $(\mathbf{k}_0, (\mathbf{k}_{//}/k_0))$  values of the modes.

The reflectivity and transmission of the structure, with a plane wave incident from the medium  $n_h$  at an angle  $\theta$  is shown in figure 11.5 and figure 11.6. Due to the presence of the gold film we expect high reflectivity for the structure. However at the  $(\mathbf{k}_0, (\mathbf{k}_{//}/k_0))$  values where the BMs are expected to be excited we see a drastic loss of reflectivity. The analytically calculated dispersion of the BMs ( $(\mathbf{k}_{//}/k_0)_{BM_h}$  and  $(\mathbf{k}_{//}/k_0)_{BM_b}$ ) are also shown in the figures. We see an almost perfect correspondence between the numerical and analytical calculations.

An interesting feature to note is in the transmission dispersion map. Due to the gold film we expect low transmission from the structure. This is seen in the map where we have a transmission of less than 10% for most of the  $(\mathbf{k}_0, (\mathbf{k}_{//}/k_0))$  space. However the transmission is drastically enhanced more than 60% at the  $(\mathbf{k}_0, (\mathbf{k}_{//}/k_0))$  values where the  $BM_h$  is excited. This can be explained by the fact that

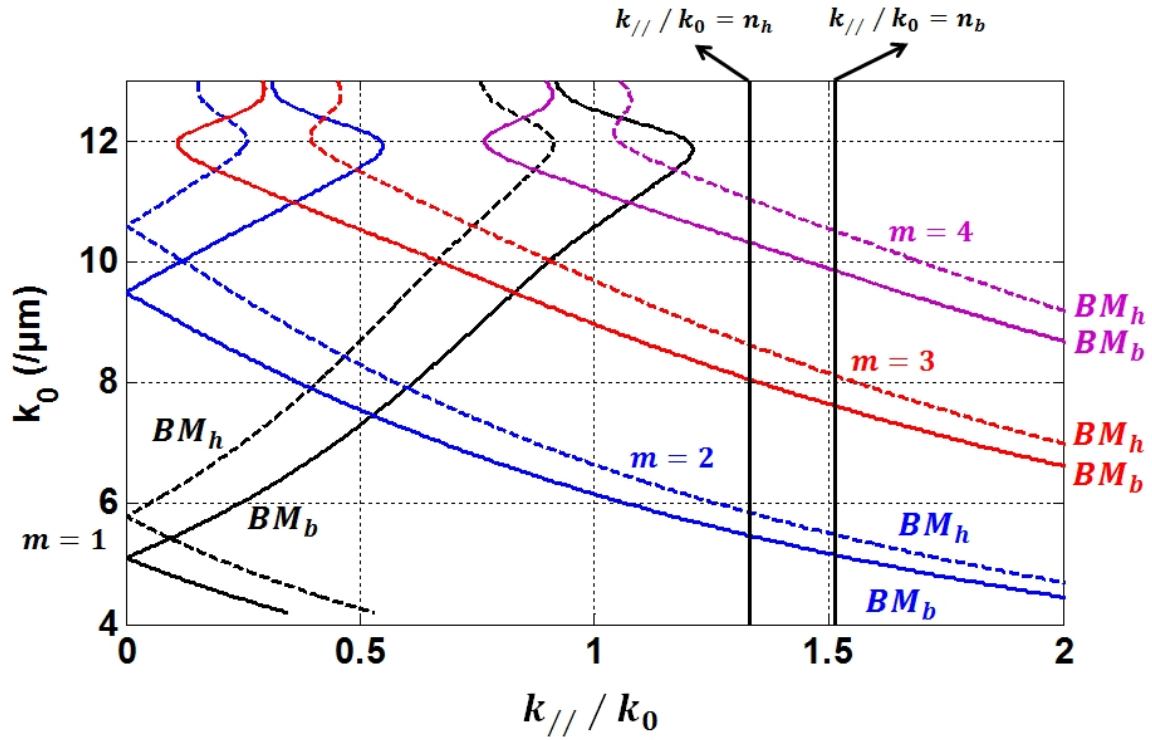


Figure 11.2: The calculated dispersion of the BM ( $(k_{//}/k_0)_{BM_h}$  dotted and  $(k_{//}/k_0)_{BM_b}$  solid) for  $\Lambda = 800nm$  for different orders  $m$ . The refractive indices were  $n_h = 1.333$  and  $n_b = 1.513$ .

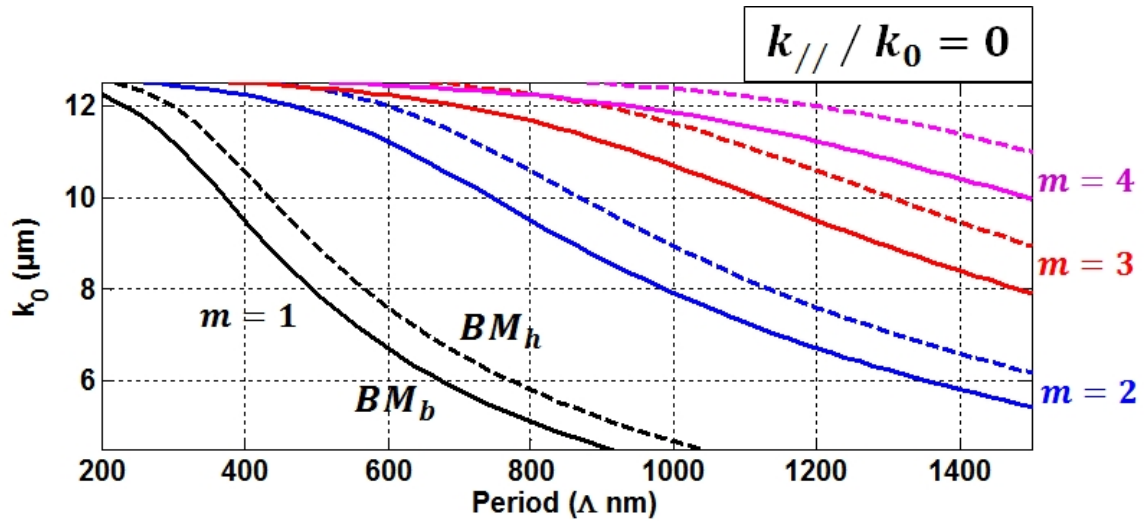


Figure 11.3: The cut off frequencies of the BMs (resonance frequencies  $k_0$  at  $(k_{//}/k_0) = 0$ ) as a function of array period. The BM on  $n_h$  ( $(k_{//}/k_0)_{BM_h}$ ) side is shown as dashed and BM on  $n_b$  side is shown as solid lines.

the BMs are extended modes with the energy radiated to the far field. The  $BM_b$  is excited by the PSP propagating on the  $n_b$  side and thus the BM resulting from them do not interact directly with the grating ridges. However the  $BM_h$  can directly interact with the ridges and this may cause an enhanced scattering of the energy to the far field resulting in the enhanced transmission. Such transmission will be further observed for other plasmonic modes and structures in this work. We will show that the transmission occurs whenever there is a  $BM_h$  involved in the excitation of the plasmonic modes.



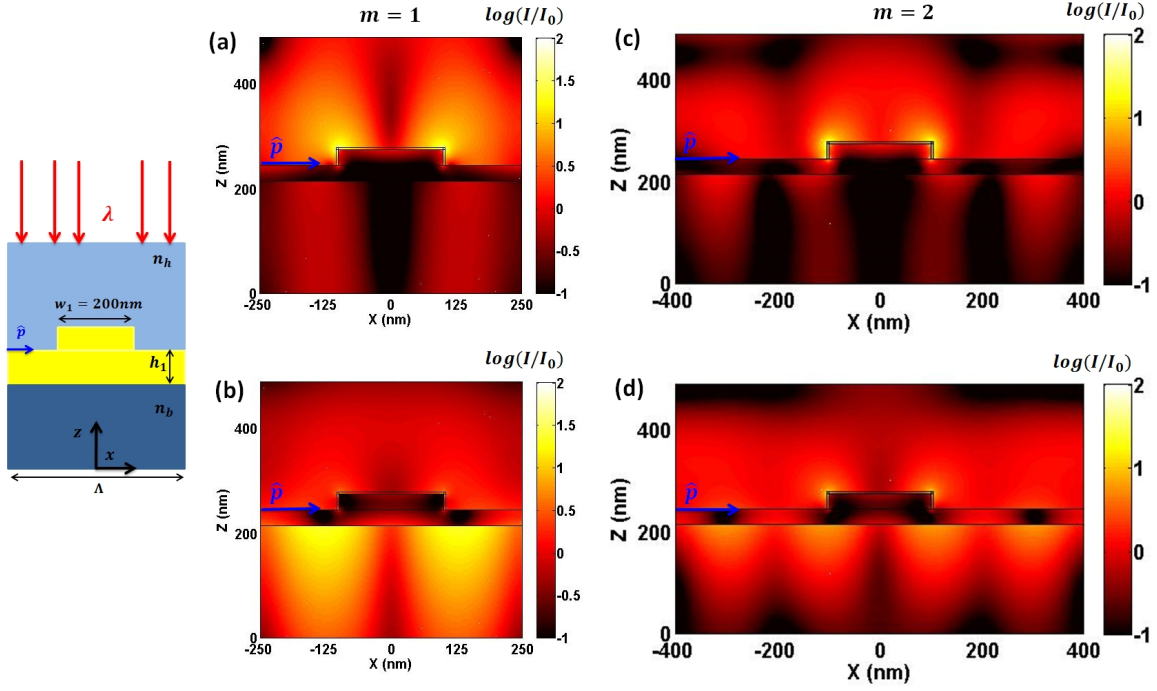


Figure 11.4: The electric field intensity for a grating of width 200nm and height 30nm with a metallic film of  $h_1 = 30\text{nm}$ . Plane wave is incident along z axis from the medium  $n_h = 1.333$  and linearly polarized with the electric field along x axis (TM). The intensity was calculated at (a)  $\lambda = 717\text{nm}$  ( $k_0 = 8.7/\mu\text{m}$ ):  $BM_h$  mode with  $m = 1$ . (b)  $\lambda = 810\text{nm}$  ( $k_0 = 7.7/\mu\text{m}$ ):  $BM_b$  mode with  $m = 1$ . The period of the array was  $\Lambda = 500\text{nm}$ . (c)  $\lambda = 610\text{nm}$  ( $k_0 = 10.3/\mu\text{m}$ ):  $BM_h$  mode with  $m = 2$ . (d)  $\lambda = 700\text{nm}$  ( $k_0 = 8.9/\mu\text{m}$ ):  $BM_b$  mode with  $m = 2$ . The period of the array for (c) and (d) was  $\Lambda = 800\text{nm}$ . The gold-substrate interface is shown with solid lines and the vector  $\hat{p}$ .

We can also note that the analytical calculation for the BM dispersion does not fit perfectly with the reflectivity or transmission extrema for higher frequencies ( $k_0 > 9/\mu\text{m}$ ). This is because of the presence of the LSPR condition which is satisfied around such frequencies for the metallic ridges. The excitation of the LSP alters the dispersion of the BM. The result of the LSPR condition on the different plasmonic modes of the system will be explained in details in the case of a metallic grating and with exact analytical solutions for an array of metallic nano-particles with an underlying gold film.

## 11.2 The hybrid plasmonic modes: Basic introduction

With incidence from the medium of index  $n_h$  we have access to the modes that have the normalized in-plane wave-vector  $(k_{//}/k_0) < n_h$ . But the PSP cannot be excited in this situation. With a plane wave incident from the medium of index  $n_b$  we can excite the modes that have  $(k_{//}/k_0)$  values between the light line in the two media  $n_h$  and  $n_b$ . In this situation we can observe very interesting features in the dispersion map.

The reflectivity and transmission for the same structures as shown in figure 11.5 and 11.6 respectively was calculated with the incident plane wave from the medium with index  $n_b = 1.513$ . The incident field was TM polarized as the PSP cannot be excited for TE polarization.

The reflectivity for three different periods is shown in figure 11.7. The dispersion for  $(k_{//}/k_0) < n_h$  is effectively the same as in the case of excitation from the medium  $n_h$ . Here in this zone we can excite

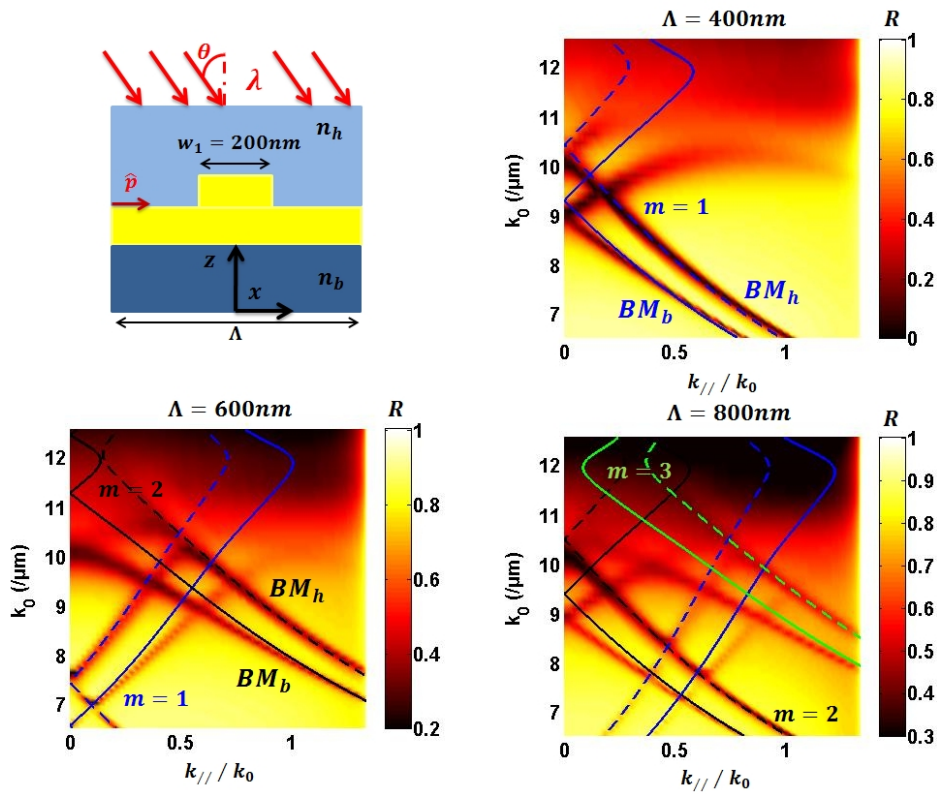


Figure 11.5: The reflectivity ( $R$ ) of the structure for different periods ( $\Lambda$ ) as a function of  $k_0 = 2\pi/\lambda$  and  $(k_{//}/k_0) = n_h \sin(\theta)$  for incident plane wave from the medium  $n_h = 1.333$  at an angle  $\theta$ . The calculated dispersion for BMs are also shown in the figure ( $(k_{//}/k_0)_{BM_h}$ :dashed and  $(k_{//}/k_0)_{BM_b}$ :solid) for different orders  $m$ . The height of the grating ridges and the thin film was taken as 30nm and  $n_b = 1.513$ .

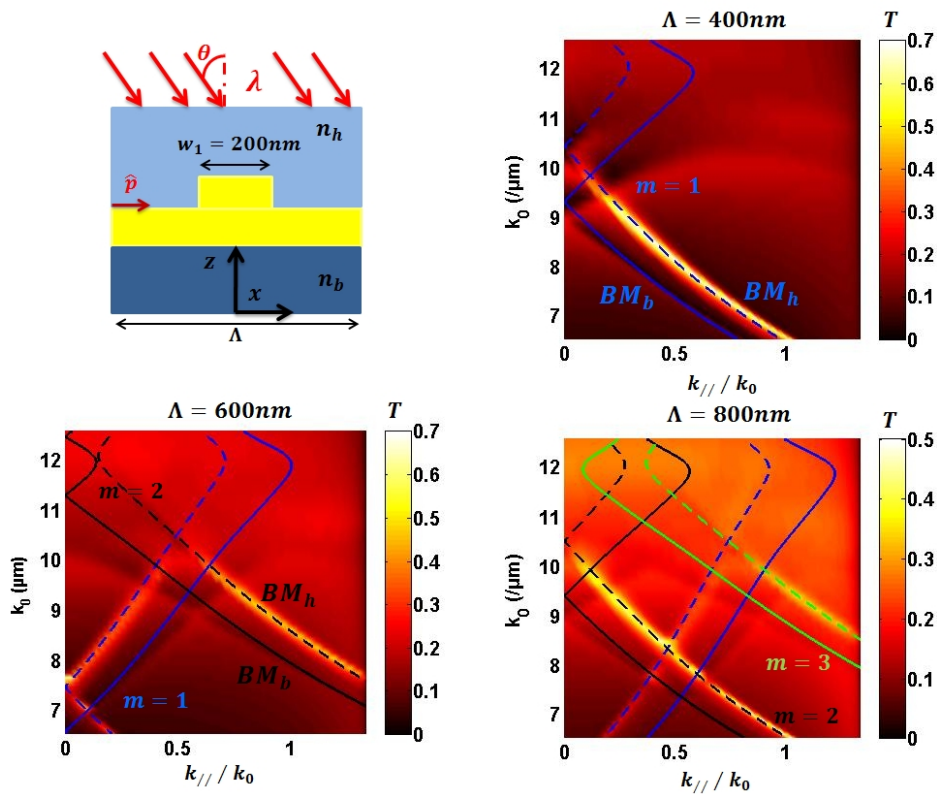


Figure 11.6: The transmission ( $T$ ) of the same as in figure 11.5

only the Bragg modes. However one must note here that the BMs excited in this configuration is much weaker than those excited with incident light from the medium  $n_h$ . This has important implications when using the BMs for various applications. The BMs are always stronger, with higher values of electric field intensity, when they are excited from the side of the particle arrays.

The interesting feature to note for excitation from the medium with higher refractive index  $n_b$  is for the values of  $(k_{//}/k_0) > n_h$ . This is the zone where the PSP can be excited in a metallic film. The PSP is a confined and propagating mode and thus has the opportunity to couple with other modes of the system over its propagation length. The propagation length of the PSP as shown in section 2.1.4 is of the order of a few tens of micrometers. For efficient coupling we thus need array sizes larger than this length. One such coupling of the PSP with the WRAs was described in section 9.1.3. We have shown that in arrays on glass substrate the PSP can couple directly to the WRAs excited in such structures with the occurrence of plasmonic band-gaps. In figure 9.11 the dispersion map of such a structure was shown, however for width of the grating ridge as large as  $w_1 = 1200nm$ .

With the metal film below the grating, we can excite the PSP in the film irrespective of the grating widths. We have shown the calculations in this case for a grating width of  $w_1 = 200nm$ . We see a drastic drop of reflectivity close to the dispersion of the PSP. However in contrary to the grating on glass substrate where the drop in reflectivity coincided with the PSP dispersion, in this case there is a slight shift of the dispersion of the reflectivity minima from the  $PSP_h$  dispersion. Thus the plasmonic mode in this situation is not directly the PSP but another plasmonic mode which happens to have similar dispersion characteristics as the  $PSP_h$ . We will call this more the Hybrid Lattice Plasmon (HLP) and it will be explained in details throughout this work.

The coupling of the HLP with the BM results in plasmonic bandgaps as mentioned for the coupling of HLP and WRA. Thus we can generalize that such band-gaps occur whenever there is a coupling of a confined plasmonic mode (PSP or HLP) and an extended plasmonic mode (BMs or WRAs). The occurrence of band-gaps can be clearly observed in the reflectivity dispersion maps of figure 11.7 at the positions of the BM dispersion.

To analyze the properties of the HLP we have shown the reflectivity (R), transmission (T) and absorption ( $A=1-R-T$ ) map for a grating of width  $w_1 = 200nm$  and period  $\Lambda = 300nm$  in figure 11.8. For the BMs we see a weak drop in reflectivity and transmission as expected. We must recall that for the excitation from the medium  $n_h$  we had observed an increase in transmission for  $BM_h$  and thus energy was radiated in the medium  $n_b$ . In this case (incident from  $n_b$ ) however we do not have such increase in transmission as for this configuration, transmission signifies the energy radiated in the medium  $n_h$ .

For absorption dispersion map, we do not observe much difference for the BMs. This is because the BMs do not actually confine the electromagnetic field but redistribute it, in either reflection or transmission. This retribution of energy to the far field is an important characteristic of extended modes (section 9.1.1). For the HLP we also observe such transmission (and low absorption) for certain  $(k_0, (k_{//}/k_0))$  where it behaves as an extended mode. This is discussed in details in section 12.3.

The HLP dispersion resembles that of the  $PSP_h$ , but for nano-structures there also exists the LSP which undergoes resonance at certain frequencies. The LSPR condition as obtained by FEM calculations for metallic strips is given in Appendix A. For the configuration under study with  $(k_{//}/k_0) > n_h$ , we consider oblique incidence ( $\theta > 45^\circ$ ) and TM polarization, so the incident electric field component is stronger along  $z$  axis than along  $x$ . So the LSPR condition satisfied in this case will be that for  $LSP_L$

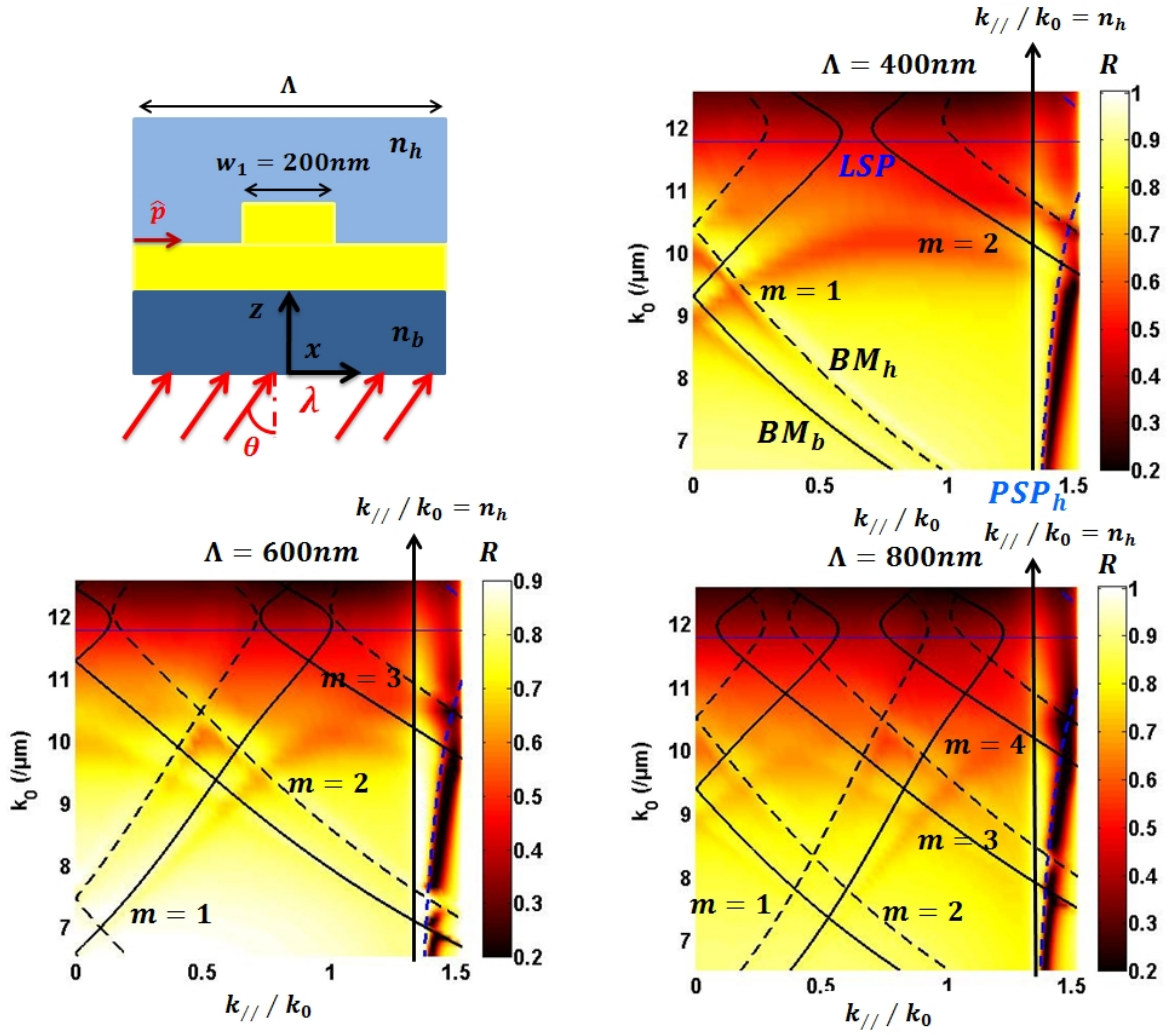


Figure 11.7: The reflectivity ( $R$ ) of the structure for different periods ( $\Lambda$ ) as a function of  $k_0 = 2\pi/\lambda$  and  $(k_{//}/k_0) = n_h \sin(\theta)$  for incident plane wave from the medium  $n_b = 1.513$  at an angle  $\theta$ . The calculated dispersion for BMs are also shown in the figure (black,  $(k_{//}/k_0)_{BM_h}$ :dashed and  $(k_{//}/k_0)_{BM_b}$ :solid) for different orders  $m$ . The height of the grating ridges and the thin film was taken as  $30\text{nm}$  and  $n_h = 1.333$ . The dispersion of the  $PSP_h$  is shown in blue dashed and the LSPR condition for metallic strip in homogeneous medium ( $n_h$ ) is shown as blue solid.

excited along the height of the grating ridges. For a ridge of width  $w_1 = 200\text{nm}$  in a homogeneous medium of index  $n_h = 1.333$ , we expect this condition to be satisfied at around  $\lambda = 530\text{nm}$  ( $k_0 = 11.9/\mu\text{m}$ ). We will neglect the effect of metallic substrate on the LSPR condition. The LSPR condition in this case is shown in figure 11.7 and 11.8. We note the dispersion of the HLP bends away (further from  $PSP_h$  dispersion) close to this LSPR condition. So the HLP can be considered as a result of harmonic coupling between the PSP and the LSP. Before going into the details of such a coupling between two confined plasmons, we would describe in brief the fundamentals of coupling in plasmonic systems.

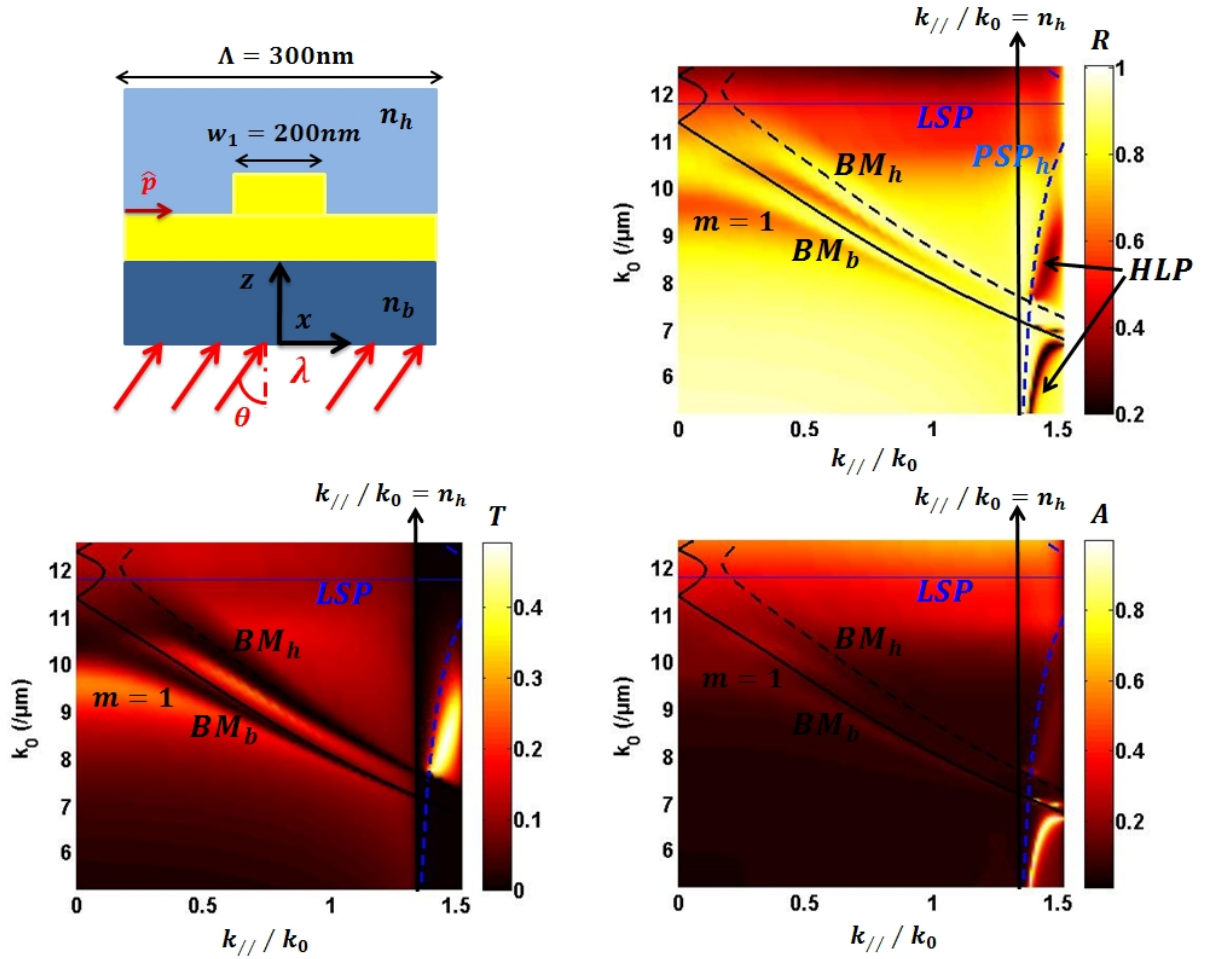


Figure 11.8: The reflectivity (R), transmission (T) and absorption (A) of the structure for  $\Lambda = 300\text{nm}$  and width  $w_1 = 200\text{nm}$  as a function of  $k_0 = 2\pi/\lambda$  and  $(k_{//}/k_0) = n_h \sin(\theta)$  for incident plane wave from the medium  $n_b = 1.513$  at an angle  $\theta$ . The calculated dispersion for BMs are also shown in the figure (black,  $(k_{//}/k_0)_{BM_h}$ :dashed and  $(k_{//}/k_0)_{BM_b}$ :solid) for order  $m = 1$ . The height of the grating ridges and the thin film was taken as  $30\text{nm}$  and  $n_h = 1.333$ . The dispersion of the  $PSP_h$  is shown in blue dashed and the LSPR condition for metallic strip in homogeneous medium ( $n_h$ ) is shown as blue solid.

### 11.2.1 Mode coupling in plasmonic systems: Fano resonance or not?

Plasmonic systems in principle can be defined as resonant systems. Such systems undergo an enhancement at certain resonant frequencies in response to an external excitation. The resonant frequencies depend on the system itself and on the environment. So far in this work we have defined such resonance frequencies for

- the PSP which confines the external excitation along a metal-dielectric interface with the energy propagating along the surface,
- the LSP for which at certain frequencies of the external excitation, a resonant oscillation of the electrons at metallic surfaces takes place.

Classically resonant systems are described as harmonic oscillators which undergo a resonant enhancement of their amplitude when the driving excitation frequency lies close to the eigen-frequency of the oscillator. Such a description is applicable for plasmonic systems [203, 204, 205].

The coupled modes in plasmonic systems exhibit asymmetric lineshapes and recently such coupling have been described for different structures as Fano-resonances [127, 206]. However the coupling of PSP and LSP to result in the HLP mode cannot be explained by the method described by Ugo Fano. We will first describe the basics of Fano resonances and then proceed to explain the actual process of coupling that results in the HLP mode.

The theory was developed by Ugo Fano to explain the narrow dark and bright bands from a metallic diffraction grating which is described earlier in this work as Woods anomaly, and thereafter explained for metallic gratings in terms of the WRAs [207, 8, 208, 209]. Fano explained the bands observed in metallic gratings as the interference between the incident plane wave and the resonant excitation of "leaky" surface waves near the surface of the gratings. The formulation presented for the WRAs in this work is effectively a simpler approach to the same physical phenomenon.

The Fano resonance or interference thus described have been shown to be present in different other configurations which involve a metallic structure and the excitation of surface plasmons [210, 211, 212, 144, 213]. However the basic mechanism of the Fano resonances in all the structures remains the same: an interference between the incident excitation which is generally termed as the "Continuum" state and leaky, evanescent waves excited in the structure which is termed as the "Discrete" state.

A classical approach to Fano resonances was reported by Joe et al [214] in terms of coupled harmonic oscillators. Considering a system consisting of two coupled harmonic oscillators with eigen-frequencies  $\omega_1$  and  $\omega_2$  respectively. The equation of motion ( $x_1$  and  $x_2$ ) of the two coupled oscillators can be written as

$$\begin{aligned} \ddot{x}_1 + \gamma_1 \dot{x}_1 + \omega_1^2 x_1 + \Gamma_{12} x_2 &= a_1 e^{i\omega t} \\ \ddot{x}_2 + \gamma_2 \dot{x}_2 + \omega_2^2 x_2 + \Gamma_{12} x_1 &= 0 \end{aligned} \quad (11.2)$$

where  $\gamma_1$  and  $\gamma_2$  are the damping parameters,  $a_1 e^{i\omega t}$  is the external driving excitation and  $\Gamma_{12}$  is the coupling parameter. The amplitudes  $c_1$  and  $c_2$  of the two oscillators can then be solved as

$$\begin{aligned} c_1 &= \frac{\omega_2^2 - \omega^2 + i\gamma_2 \omega}{(\omega_1^2 - \omega^2 + i\gamma_1 \omega) (\omega_2^2 - \omega^2 + i\gamma_2 \omega) - \Gamma_{12}^2} a_1 \\ c_2 &= \frac{\Gamma_{12}}{(\omega_1^2 - \omega^2 + i\gamma_1 \omega) (\omega_2^2 - \omega^2 + i\gamma_2 \omega) - \Gamma_{12}^2} a_1 \end{aligned} \quad (11.3)$$

We must note that here in this example, the first oscillator  $c_1$  is considered to be driven by the external excitation. This in turn drives the second oscillator at its eigen-frequency  $\omega_2$ . The schematic of such a coupled oscillator system where one acts as the forced oscillator and drives the other is shown in figure 11.9. Keeping the same notation as used elsewhere in this work to describe plasmonic modes, we will write the resonance frequencies of the oscillators in terms of  $k_0 = \omega/c$ . The two oscillators were considered to have the resonance frequencies at  $k_1 = 7/\mu m (\lambda = 897.6nm)$  and  $k_2 = 9/\mu m (\lambda = 698.1nm)$ . For the coupled system, oscillator 1 undergoes two resonances close to the individual resonances  $k_1$  and  $k_2$  of the two separate oscillators. Due to the destructive interference of the oscillations of the external excitation and the second oscillator (driven oscillator 2), there is a complete suppression of the amplitude of the first oscillator at the eigen frequency  $k_2$  of the second oscillator. This is the characteristic fingerprint of Fano resonances.

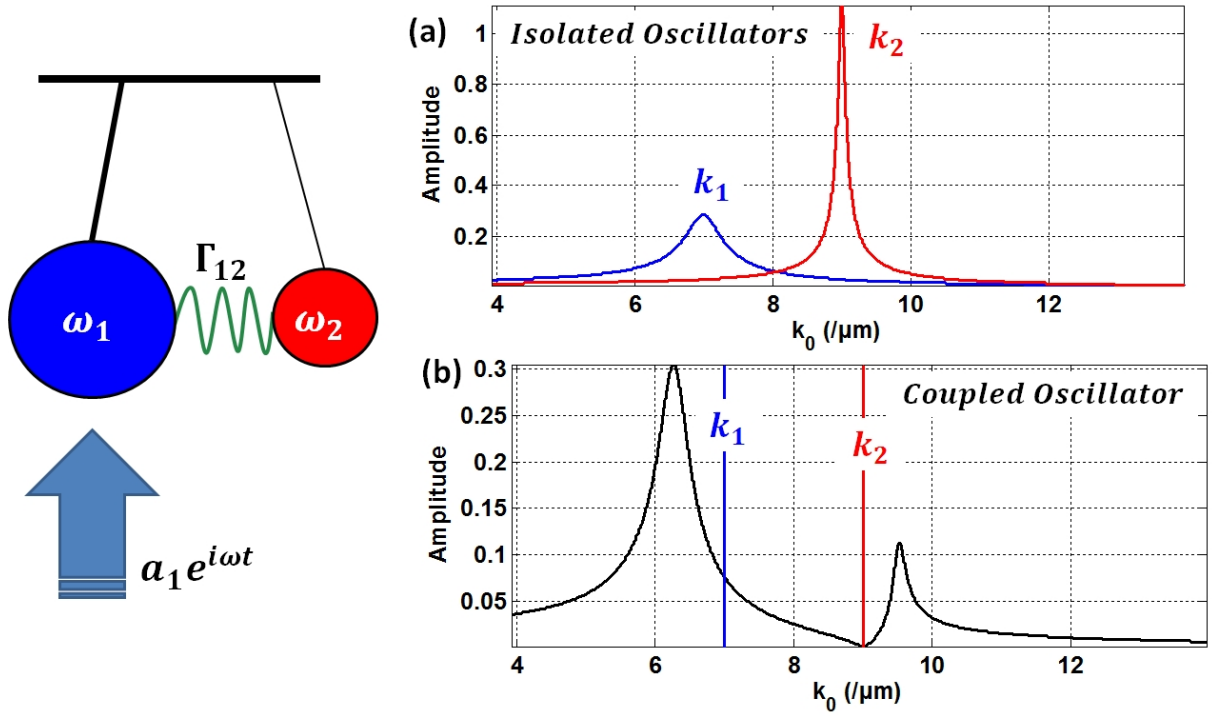


Figure 11.9: Fano resonance: Schematic for the coupling of two harmonic oscillators with eigen frequencies  $k_1 = \omega_1/c = 7/\mu\text{m}$  and  $k_2 = \omega_2/c = 9/\mu\text{m}$ . (a) The amplitude of the two separate systems can be calculated as  $c_1 = a_1/(\omega_1^2 - \omega^2 + i\gamma_1\omega)$  with the amplitude of the external excitation  $a_1 = 1$ . The damping parameters were taken as  $\gamma_1 = 0.5$  and  $\gamma_2 = 0.1$  (b) The amplitude of the forced oscillator ( $c_1$ ) when coupled to the driven oscillator with the coupling parameter  $\Gamma_{12} = 20$ .

As can be seen from the above example, Fano resonance occurs for two systems where the external excitation drives only one of the resonances, while the other is forced by the first resonant system. These two resonant systems, the continuum and discrete states respectively are also commonly termed as "Bright" modes, for the one which can be excited by the external excitation and "Dark" modes for the one indirectly driven by the bright mode.[215, 216, 217, 218] Another trademark feature of Fano resonance is the asymmetric line shape of the two resonances, more prominently the one close to the eigen frequencies of the driven oscillator. A detailed description of Fano resonances in nano-structures was presented in the review by Miroschnichenko et al.[210]

The fundamental question that is important for understanding the HLP mode is that if it is a result of Fano resonances. We have mentioned before that the HLP mode results from the coupling of the PSP and the LSP. The absorption (A) of the structure as shown in figure 11.8 with period  $\Lambda = 150\text{nm}$  and grating width  $w_1 = 50\text{nm}$  is shown in figure 11.10. A small period was taken to avoid the appearance of the BMs. Thus the mode present in the  $(k_0, (k_{//}/k_0))$  map is only the HLP mode.

The dispersion of the PSP is shown in figure. The height of the grating ridges was 30nm. We will assume that the LSPR condition for a strip of height 30nm and width 50nm is satisfied at  $k_0 = 9.0/\mu\text{m}$  with  $\lambda_{LSP} = 698\text{nm}$ . The calculated LSPR condition for metallic strips of such dimensions in a homogeneous medium was found to be  $\lambda_{LSP} = 535\text{nm}$  as shown in Appendix A. However a red shift of the LSPR condition is expected when the nano-structures are placed on a metallic substrate as mentioned in section 10.1.3. The value assumed here was found analytically for metallic cylinders of

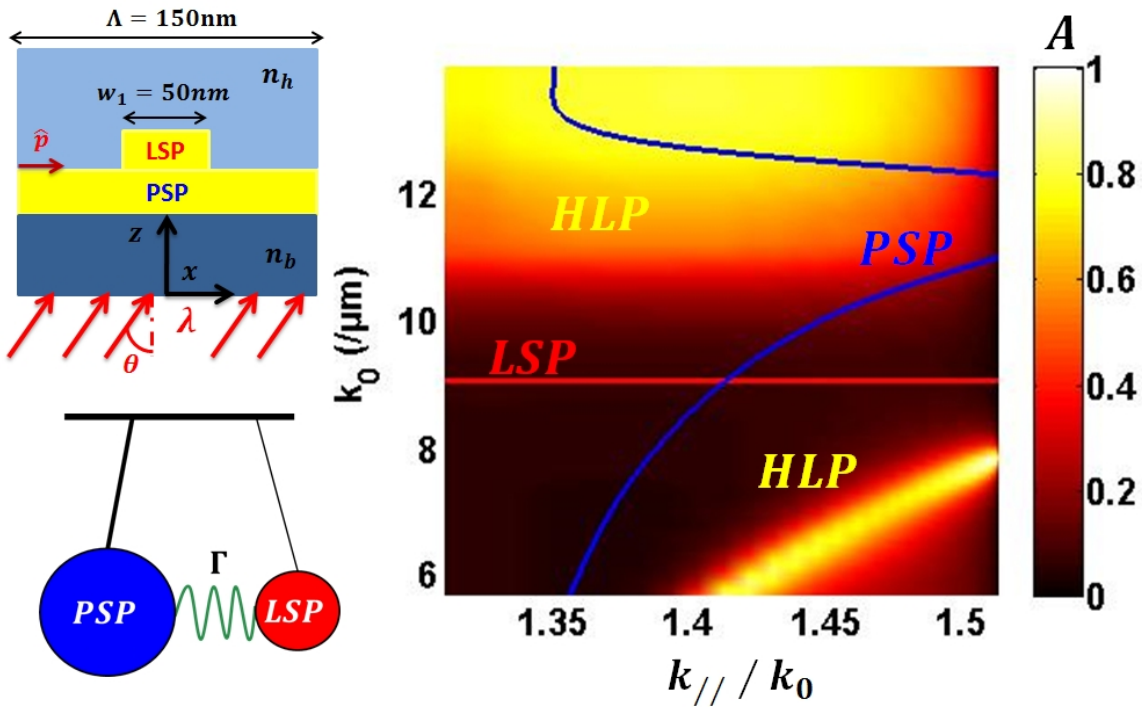


Figure 11.10: The absorption ( $A$ ) of the structure for  $\Lambda = 150\text{nm}$  and width  $w_1 = 50\text{nm}$  as a function of  $k_0 = 2\pi/\lambda$  and  $(k_{//}/k_0) = n_h \sin(\theta)$  for incident plane wave from the medium  $n_b = 1.513$  at an angle  $\theta$ . The calculated dispersion of the PSP (blue) and the assumed LSPR condition (red) is also shown in the figure.

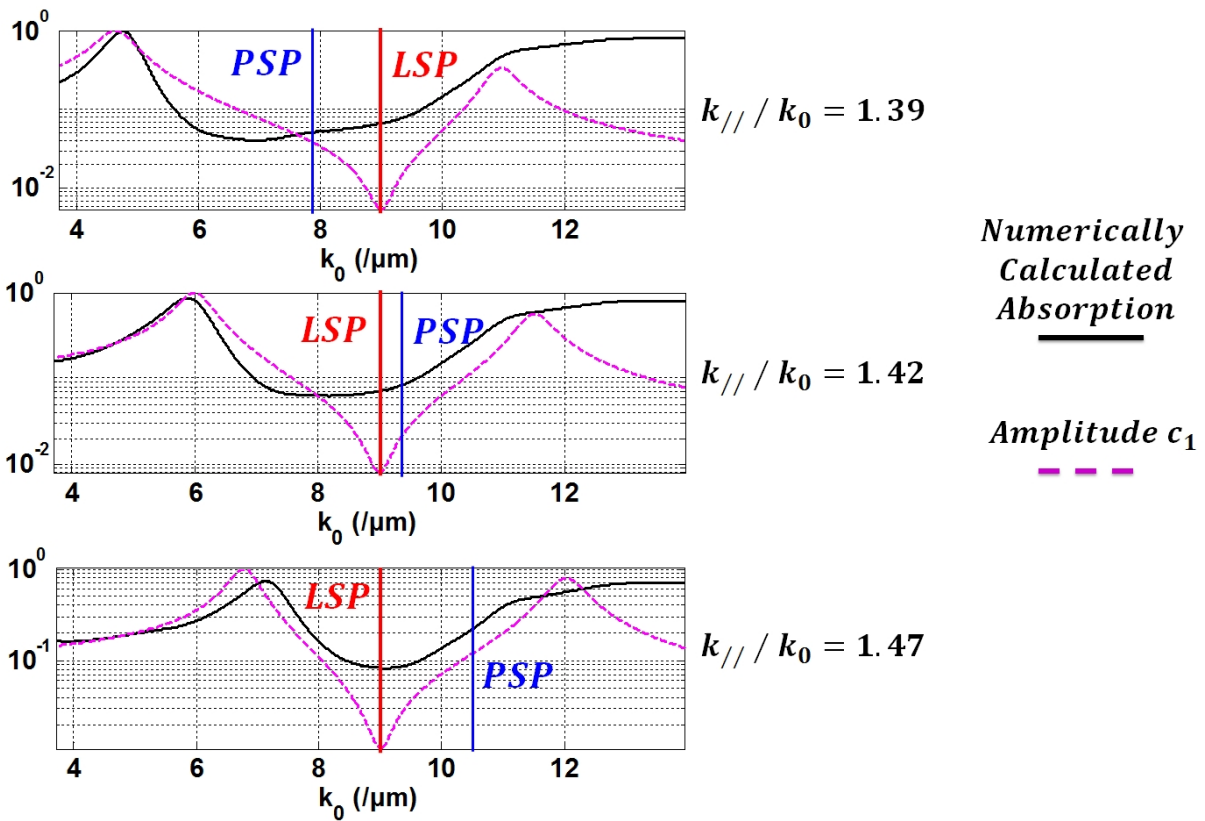


Figure 11.11: The absorption ( $A$ ) spectra in log scale of the same structure shown in figure 11.10 at three different values of  $(k_{//}/k_0)$  (black). The LSPR condition and PSP resonance frequencies are shown for each plot (red and blue respectively). The calculated amplitude of coupled oscillator undergoing Fano resonance is shown (in logscale) for each with  $k_1 = \omega_1/c$  for the PSP and  $k_2 = \omega_2/c$  for the LSP.



diameter  $D = 50nm$  and height  $h = 30nm$  and is shown in a later section (12.1). Thus for a basic understanding we can assume this value.

In the dispersion map shown in figure 11.10 we do not observe a sharp suppression of absorption close to the LSPR condition or rather at any particular value of  $k_0$ . Absorption spectra at three different values of  $(k_{//}/k_0)$  is shown in figure 11.11. We have fitted equation 11.3 for the absorption curve at  $(k_{//}/k_0) = 1.39$ . The values for the fit were  $\Gamma/c^2 = 48$ ,  $\gamma_1/c = 0.8$  and  $\gamma_2/c = 0.3$ . The PSP was considered as the driven oscillator with its resonance frequency  $\omega_1 = k_1c$  following the PSP dispersion curve for each  $(k_{//}/k_0)$  and the LSP was considered the discrete state with LSPR condition at  $\lambda_{LSP} = 698nm$  being considered for  $\omega_2$ . We see that the amplitude  $c_1$  as calculated for the coupled oscillator model (magenta in figure 11.11) has a sharp minima at the resonance frequency of the LSP while the absorption spectra do not show any particular minima. The peak of  $c_1$  follow closely the absorption peak for lower frequencies, however there exists marked discrepancy between the absorption maxima and the maxima calculated by the oscillator model.

Such close resemblance of the absorption spectra of those coupled plasmonic structures to the formulation of Fano resonances has prompted several reports in the literature to identify this coupling between plasmonic modes as Fano resonances or Fano-like resonances [219, 220, 221, 222, 209] and more recently in [223]. However most of these resonances are not at all Fano resonances. Furthermore the surface lattice resonance (SLR) mentioned in [219, 128, 224, 225] can be identified as the WRAs described in this work.

The reason that coupling between the PSP and LSPR is not a Fano resonance can be found in the very basic condition for Fano resonances. Such resonances are necessarily a result of coupling between a bright mode (continuum state) and a dark mode (discrete state). Plasmonic modes that can be excited by an incoming photon are bright modes. Thus both PSP and LSP can be termed as bright modes. Dark modes are such resonances which cannot be directly excited by an incoming photon, such as multipole oscillations in metallic nano-particles or discrete states in photonic crystals [226, 227, 228]. Thus the HLP is not a result of fano resonances or fano-like resonances.

However the same harmonic oscillator model, can be used to describe the coupling between two bright plasmonic modes. In quantum systems, coupling is generally defined in terms of strong and weak coupling [229]. In such a description we identify one of the components involved in the coupling as the donor and the other as the acceptor. For weak coupling regime, there is energy transfer from the donor to acceptor but no reversible energy transfer back to the donor from the acceptor can take place. This occurs when the rate of energy coupling between the acceptor and donor is much smaller than the damping rate of the donor. When the coupling increases and its rate becomes stronger than that of the damping rate of the donor we have back flow of energy from the donor to the acceptor. This regime is called the strong coupling regime and in this regime, the two resonators are indistinguishable. The characteristic resonance of the coupled system must be evaluated considering that the two resonators are inseparable and as a single resonant system.

A simple classical approach to strong coupling using the harmonic oscillator model was presented by Lukas Novotny [230] and we will use the same approach to explain the harmonic coupling between the PSP and LSP modes that result in the HLP. For the model let us assume as before, two coupled harmonic oscillators with eigen frequencies  $\omega_1$  and  $\omega_2$  and damping parameters of  $\gamma_1$  and  $\gamma_2$  and a coupling parameter of  $\Gamma_{12}$ . Since the two oscillators are considered indistinguishable they will feel the same forces

and thus have identical equations of motion. Here unlike the previous system, we will not introduce an external excitation to solve for the amplitude. Using this model we are interested in finding solutions for the eigen-frequencies of the system as a whole and thus no external excitation is necessary. The equation of motions can be written as

$$\begin{aligned}\ddot{x}_1 + \gamma_1 \dot{x}_1 + \omega_1^2 x_1 + \Gamma_{12}(x_1 - x_2) &= 0 \\ \ddot{x}_2 + \gamma_2 \dot{x}_2 + \omega_2^2 x_2 + \Gamma_{12}(x_2 - x_1) &= 0\end{aligned}\quad (11.4)$$

The resulting characteristic equation can be solved to obtain the resonance frequencies of the combined system as

$$\omega_{\pm}^2 = \frac{1}{2} \left[ \omega_1^2 + \omega_2^2 \pm \sqrt{(\omega_1^2 - \omega_2^2)^2 + 4\Gamma_{12}^2} \right] \quad (11.5)$$

Writing in terms of wave-vector  $k_0 = \omega/c$  we can write the resonance frequencies of the HLP modes ( $k_{HLP\pm}$ ) as

$$k_{HLP\pm} = \sqrt{\frac{1}{2} \left[ k_{PSP}^2 + k_{LSP}^2 \pm \sqrt{(k_{PSP}^2 - k_{LSP}^2)^2 + 4\frac{\Gamma_{12}^2}{c^4}} \right]} \quad (11.6)$$

The amplitude of the resonant system with an external excitation  $a_1 e^{i\omega t}$  can thus be written in terms of  $k_0 = \omega/c$  as

$$c_{HLP} = \frac{a_1/c^4}{\left( k_{HLP+}^2 - k_0^2 + i\frac{\gamma_1}{c} k_0 \right) \left( k_{HLP-}^2 - k_0^2 + i\frac{\gamma_2}{c} k_0 \right)} \quad (11.7)$$

The amplitude of resonance calculated using the harmonic coupling model was fitted to the absorption spectra obtained for  $\Lambda = 150nm$  and width  $w_1 = 50nm$ . The conditions are identical to that of figure 11.10 and figure 11.11. The absorption spectra for three different values of  $(k_{//}/k_0)$  are shown in figure 11.12. The values for the fit were taken as  $\Gamma/c^2 = 46, \gamma_1/c = \gamma_2/c = 0.4$  and  $a_1 = 1$ . We see a close fit of the amplitude thus calculated and the absorption of the structure. We will use this harmonic coupling model to find the resonance-frequencies of the HLP. The only free parameter in the model is the coupling constant  $\Gamma_{12}$  which will be evaluated for different structures.

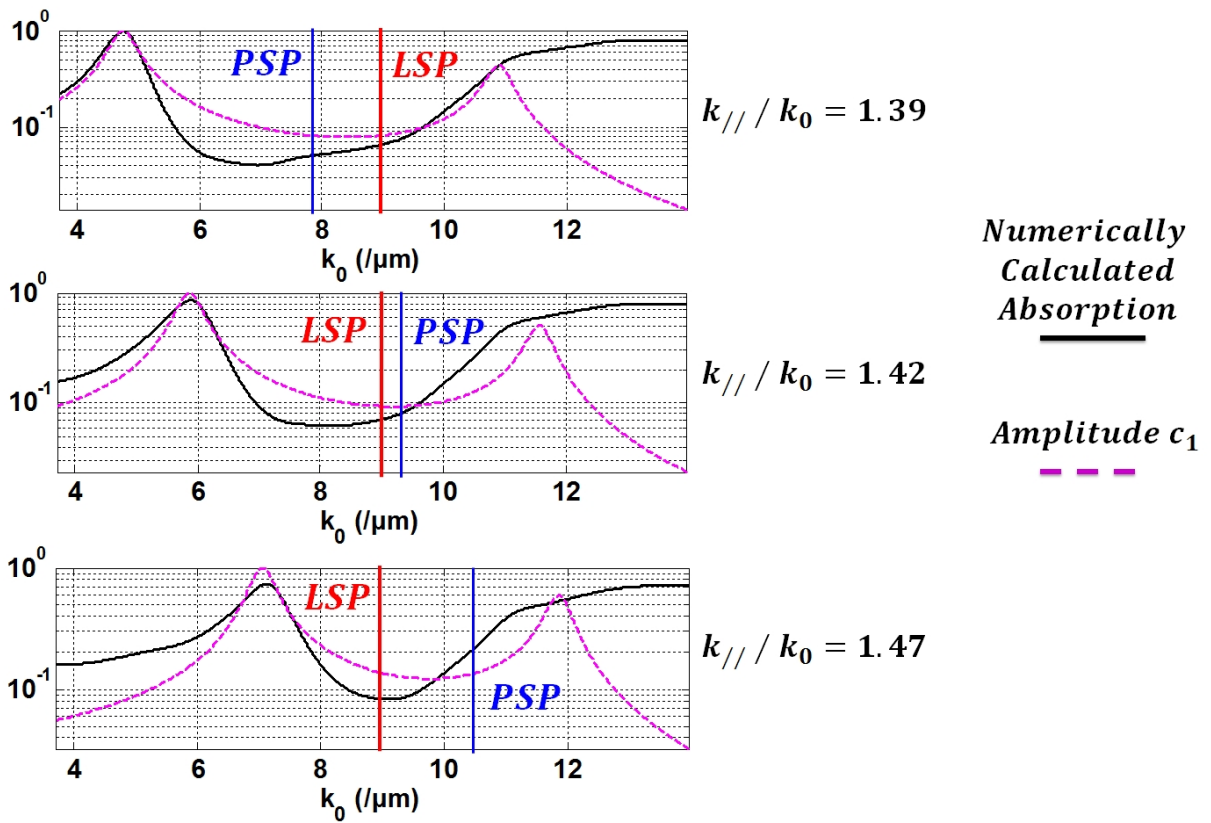


Figure 11.12: The absorption (A) spectra in log scale of the same structure shown in figure 11.11 at three different values of  $(k_{//} / k_0)$  (black). The calculated amplitude of harmonic coupling is shown (in log scale) for each with  $k_{HLP}$  calculated using equation 11.6 and  $\lambda_{LSP} = 698\text{nm}$ .



---

# The Hybrid lattice plasmon (HLP)

---

The hybrid lattice plasmon (HLP) mode was introduced in the last section (section 11.2.1). We have shown that the HLP is a result of harmonic coupling between the PSP and the LSP. In this chapter we will present the plasmonic modes that can be excited for an array of metallic cylinders with an underlying thin metallic film. The structure is similar to the grating structure presented in chapter 11. Thus the plasmonic modes we expect in this structure will also be similar to the grating. Due to the periodicity of the structure we will expect the BMs and also the HLP due to the coupling of the LSP of the cylinders and the PSP of the thin metallic film. We will show that the harmonic oscillator model for such a coupling can be used to describe the characteristics of the HLP mode.

## 12.1 Array of metallic cylinders on gold substrate

The structure geometry is shown in figure 12.1. The plasmonic modes of the structure will be defined along the vector  $\hat{p}$ . The dispersion of the PSP in the structure is given by  $(k_{//}/k_0)_{PSP}$  in equation 9.4. The dispersion of the BMs in the structure can be defined by  $(k_{//}/k_0)_{BM}$  in equation 11.1.

For the LSPR condition we can use the analytical equations presented in section 10.2. We will use the  $\chi$  formulation with the value of  $\chi$  given by equation 10.10. It should be noted that the resonance wavelength obtained by this formulation is the  $\lambda_{LSP}$  when the cylinders is considered in a homogeneous medium. In the actual situation we have an underlying gold film and the LSPR condition must be modified to take into account the effect of a gold substrate. The skin depth as presented in section 1.3 is less than  $30nm$  for wavelengths higher than  $\lambda = 550nm$ . Thus if the thickness of the gold film is equal to or more than  $30nm$  we can safely assume it to be a semi-infinite substrate in terms of the analytical calculations. We see from figure 1.2 in section 1.3 that gold has a high absorption coefficient for wavelengths less than  $520nm$  ( $k_0 > 12/\mu m$ ). So for the calculations we will consider the excitation wavelengths higher than this value.

To analytically calculate the LSPR condition for the metallic cylinders on gold substrate we will use the formulation presented in section 10.1.3. Once the  $\lambda_{LSP}$  is thus calculated we can calculate  $k_{LSP} = 2\pi/\lambda_{LSP}$ . Then the dispersion of the HLP mode can be calculated using equation 11.6. It should be noted that in the cylinders we have two possible LSPR conditions namely the  $LSP_T$  along the plane perpendicular to the axis of the cylinders and  $LSP_L$  along the axis of the cylinders. For the HLP and the BMs we will consider only TM polarized incident as they are dependent on the PSP which cannot

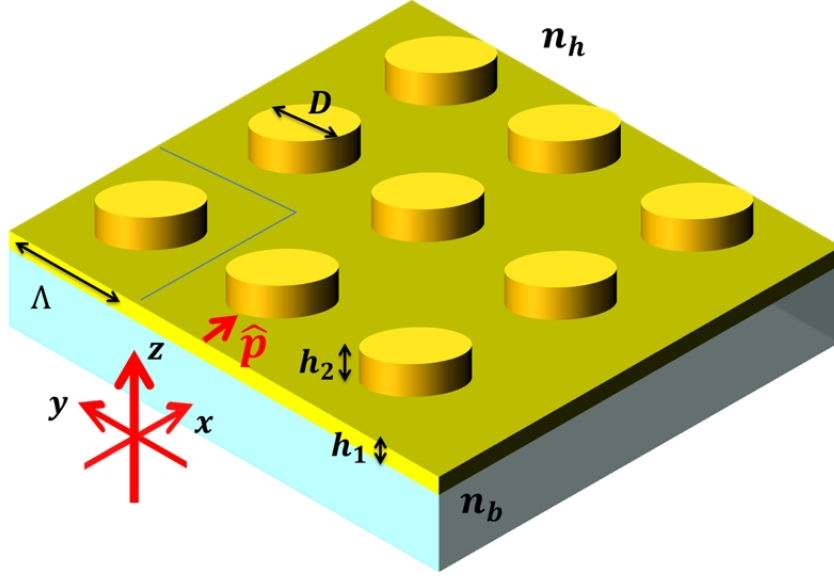


Figure 12.1: An array of metallic cylinders of diameter  $D$ , height  $h_2$  and square packing with period  $\Lambda$ . A thin metallic film of height  $h_1$  is placed below the array. The substrate has a refractive index of  $n_b$  and the medium surrounding the cylinders has an index  $n_h$ . The modes are defined along the vector  $\hat{p}$ .

$$\begin{aligned}
 & \text{PSP} \\
 (k_{//}/k_0)_{PSP(b/h)} &= \sqrt{\frac{(n_{(b/h)}^2 n_m^2)}{(n_{(b/h)}^2 + n_m^2)}} \\
 & \text{LSP} \\
 \alpha &\propto \frac{\epsilon_m - \epsilon_{eff}}{\epsilon_{eff} + \chi(\epsilon_m - \epsilon_{eff})} \\
 \epsilon_{eff} &= \epsilon_h \frac{1 + \eta T / (1 + \gamma_\chi)}{1 + \eta T / (1 - \gamma_\chi)} \\
 \eta &= \frac{\epsilon_h - \epsilon_b}{\epsilon_h + \epsilon_b} \\
 \gamma_\chi &= \frac{1 - 2\chi}{1} \\
 T &= -\frac{\gamma_\chi}{2\pi} (\pi \epsilon_h) \chi \\
 \chi &= \frac{\sqrt{\pi}}{2n_h^2} (1 - \sqrt{X_L}) \\
 X_L &= \frac{h_2^2}{h_2^2 + D^2} \\
 & \text{BM} \\
 (k_{//}/k_0)_{BM(b/h)} &= \left| (k_{//}/k_0)_{PSP(b/h)} - n_p \right| \\
 n_p &= \pm m(K_B)/k_0 \\
 K_B &= 2\pi/\Lambda \\
 & \text{HLP} \\
 (k_{//}/k_0)_{HLP\pm}^2 &= \frac{1}{2} \left[ (k_{//}/k_0)_{PSP_h}^2 + (k_{//}/k_0)_{LSP}^2 \right] \\
 & \pm \frac{1}{2} \left[ \sqrt{\left( (k_{//}/k_0)_{PSP_h}^2 - (k_{//}/k_0)_{LSP}^2 \right)^2 + 4 \frac{\Gamma_{12}^2}{c^4 k_0^4}} \right]
 \end{aligned}$$

be excited for TE polarized light. Also the PSP is excited only for incidence from the medium of index  $n_b$  for angles of incidence  $\theta$  that lie above the critical angle of  $n_b - n_h$  interface ( $(k_{//}/k_0) > n_h$ ). In this configuration the  $LSP_L$  is more intense and we will only consider the LSPR condition for it for the calculations of the HLP dispersion.

Thus we have all the calculation tools needed to analytically solve for the modes of the system. As a recapitulation, we have presented the analytical equations used for modeling the modes of the system along with figure 12.1. To use the same notation we will define  $(k_{//}/k_0)_{LSP} = 2\pi/(k_0\lambda_{LSP})$  which, however, do not have any physical significance.  $\lambda_{LSP}$  is calculated from the pole of  $\alpha$ .

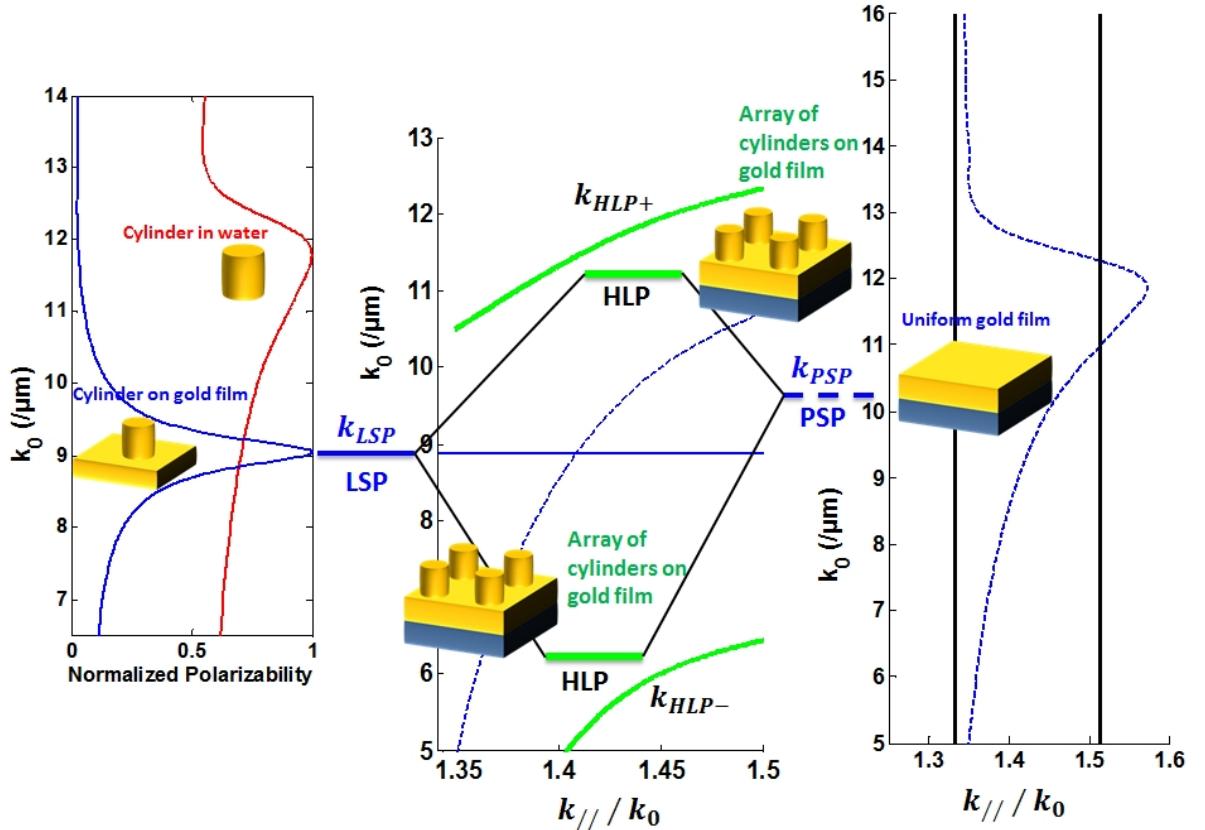


Figure 12.2: Left, the analytically calculated polarizability  $\alpha$  for a nanocylinder of 30nm height and 50nm diameter in a homogenous medium  $n_h$ (in red). The same for the cylinder placed on a semi-infinite gold medium (in blue). The calculated LSP frequency for the later configuration is  $k_0 = 8.87/\mu\text{m}$ . Center, the HLP mode (green) dispersion ( $k_0, (k_{//}/k_0)$ ), which results from the harmonic coupling of the LSP and PSP. Right, the calculated dispersion for the PSP in a gold film with plasmons propagating in the medium  $n_h$ . The resonance frequencies of the LSP (blue solid) and the PSP (blue dotted) are also shown. For this scheme, the period of the array was taken as 180 nm.

To calculate the modes of the system in terms of  $(k_0, (k_{//}/k_0))$  the only free parameter in the model is the coupling parameter  $\Gamma_{12}$ . The scheme of the coupling is shown in figure 12.2. The coupling parameter  $\Gamma_{12}$  has a dimension of  $1/\tau^2$  where  $\tau$  has a unit of time. By rigorous simulations of the far field characteristics of the structure (thus by following the dispersion of the HLP mode and fitting it to the analytical results) we have found that the coupling parameter is inversely proportional to the period of the structure and directly proportional to the diameter and height of the cylinders. By considering  $\Gamma_{12} = (1/\tau^2) \times (h_2 + D)/\Lambda$  we will show that the calculated analytical dispersion of the HLP

fits closely the numerical calculations of the far field characteristics. The value of the free parameter  $\tau = 0.37 \pm 0.03 fs$  was found by fitting the analytical calculations to numerical results and was found to be constant and independent of structural parameters.

We must mention here that the modes presented for the structure is not restricted only to nano-cylinders. In fact we have presented the same modes for an array of metallic strips on a gold substrate. Thus the calculation can be used for any arrayed structure on a metallic substrate. The only difference for different shapes of the nano-structures is in the LSPR condition and thus the accurate calculation of  $\lambda_{LSP}$ . Once we have the value for the LSPR condition of the metallic particle with an underlying metallic film, we can use the model to calculate the dispersion of all the other plasmonic modes of the system.

## 12.2 Far field characteristics of the HLP

The absorption (A) of the structure with a plane wave incident from the medium with index  $n_b$  is shown in figure 12.3 for two different period ( $\Lambda$ ) of the array. (For other periods see Appendix B). We see a strong absorption for the  $(k_0, (k_{//}/k_0))$  values close to the dispersion of the HLP. Thus the HLP is a confined plasmonic mode in this regime. We see appearance of plasmonic band gaps at the  $(k_0, (k_{//}/k_0))$  values which correspond to the dispersion of the BMs. This is in effect similar to what we observed for the coupling of the PSP with the WRAs in section 9.1.3. Here in this case these band gaps are a result of the coupling of the HLP with the BMs.

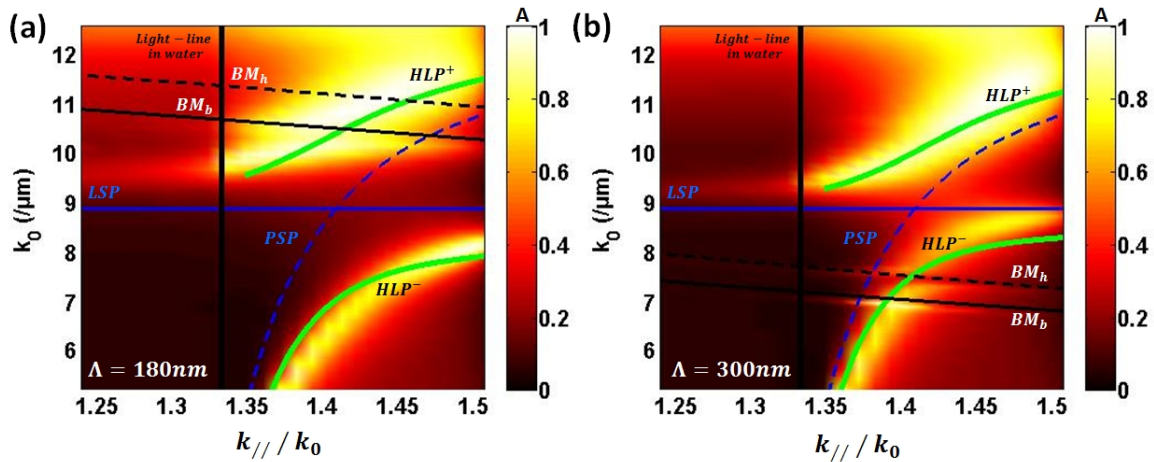
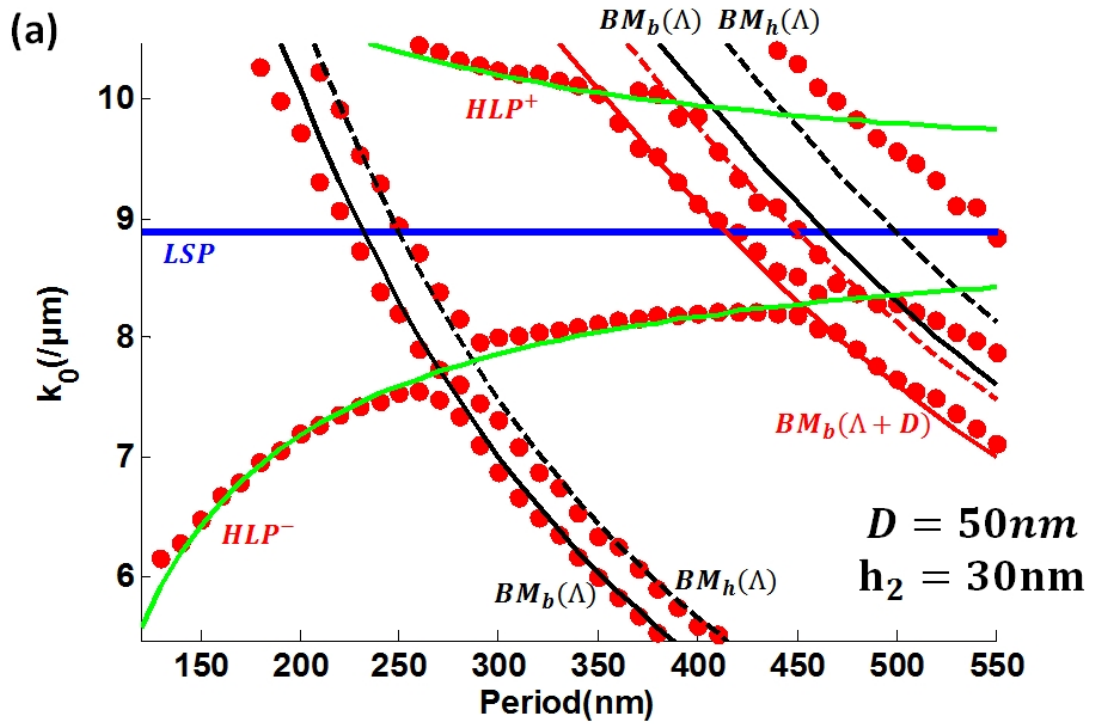


Figure 12.3: (a) The absorption (A) dispersion map as a function of  $(k_0, (k_{//}/k_0))$  for  $h_2 = 30\text{nm}$ ,  $D = 50\text{nm}$ , and period  $\Lambda = 180\text{nm}$  with the medium around the nanocylinders of refractive index  $n_h = 1.333$ . Plane wave is incident from the medium with index  $n_b = 1.513$ . The analytical calculation of the dispersion of different modes of the system are also shown: LSP (blue solid), PSP (blue dashed), HLP (green), and BMs (black solid and dashed). (b) Same as (a) for period  $\Lambda = 300\text{nm}$ .

From the expression of  $\Gamma_{12}$  we expect the coupling to be weaker for larger periods. The width of plasmonic band gaps (the spectral separation of the two branches of the HLP at the resonance position of the LSP) is proportional to the coupling parameter [230, 202]. Thus the dispersion curves of the HLP will be expected to approach the resonance frequencies of the LSP and PSP as the coupling parameter decreases for larger periods. This is exactly what we see in figure 12.3.





$\Lambda = 350\text{nm}$

$D = 50\text{nm}$

$D = 90\text{nm}$

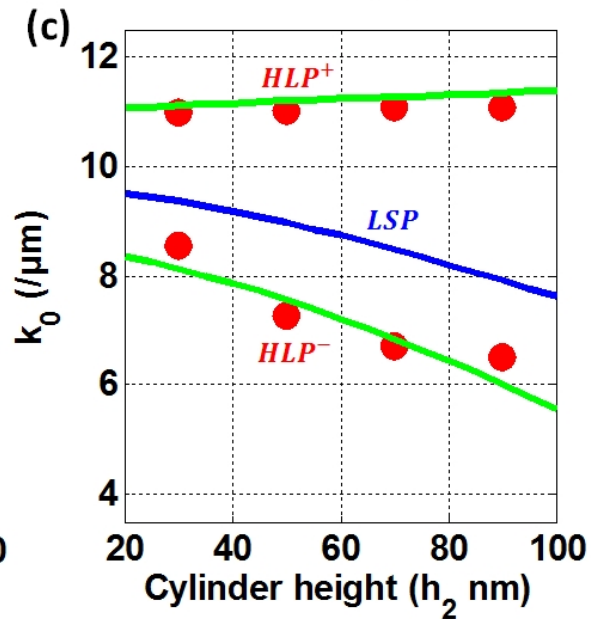
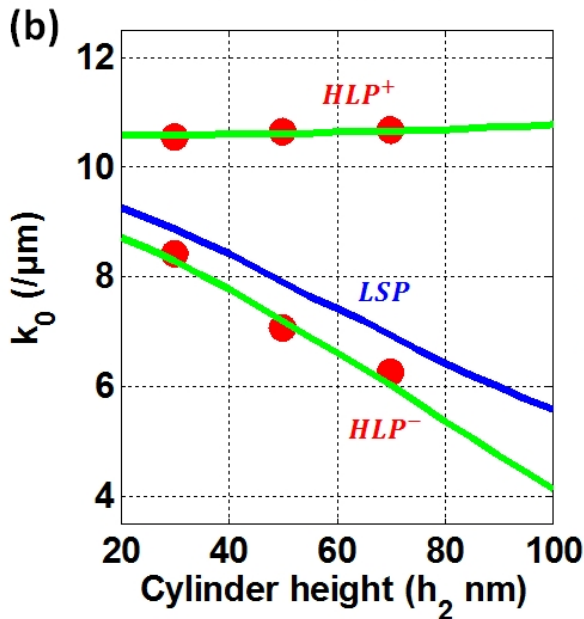


Figure 12.4: (a) Dependence of  $\Lambda$ : The resonance frequencies ( $k_0$ ) of all the modes in the structure ( $D = 50\text{nm}$ ,  $h_2 = 30\text{nm}$ ) manifest as absorption maxima in the dispersion map calculated by rigorous numerical method (red dots) as a function of array period for  $(k_{//}/k_0) = 1.42$ . We have superposed the analytically calculated frequencies of the modes as a function of period: LSP (blue), HLP (green), BMs calculated for  $K_B = 2\pi/(\Lambda)$  (black solid and dashed) and BMs for  $K_B = 2\pi/(\Lambda + D)$  (red dashed and solid). (The first and the second orders ( $m$ ) of the BMs is shown in the figure) (b) Dependence of  $h_2$ : The same for  $\Lambda = 350\text{nm}$ , and  $D = 50\text{nm}$  for  $(k_{//}/k_0) = 1.45$ . (c) The same for  $\Lambda = 350\text{nm}$ , and  $D = 90\text{nm}$  for  $(k_{//}/k_0) = 1.45$ .

The dependence of the resonance frequencies of the modes with the structural parameters such as the periodicity, height and diameter of the cylinders is shown in figure 12.4. For the figure the maxima of absorption as a function of  $k_0$  (calculated by numerical simulations) was traced for each structural parameter at a given value of  $(k_{//}/k_0)$ . (see Appendix B). These absorption maxima denotes the resonance frequencies of the structures. The analytically calculated resonance frequencies of the BMs and the HLP is also shown in the figure. For larger periods  $\Lambda > 300nm$  we also see the appearance of a BM which can be calculated using  $K_B = 2\pi/(\Lambda + D)$ . We see that each absorption maxima can be represented by one of the plasmonic modes (BMs or HLP) as per calculated by the analytical model thus validating the model.

Another important feature to note in the far field characteristics of the HLP is that at certain range of values of  $(k_0, (k_{//}/k_0))$  the structure transmits a portion of the incident flux. This is shown in figure 12.5. This is not generally expected as for the configuration we have a plane wave incident at angles greater than the critical angle of  $n_b - n_h$  interface and moreover we have a thin metal film. This feature can also be noted for metallic grating on metallic film as shown in figure 11.8.

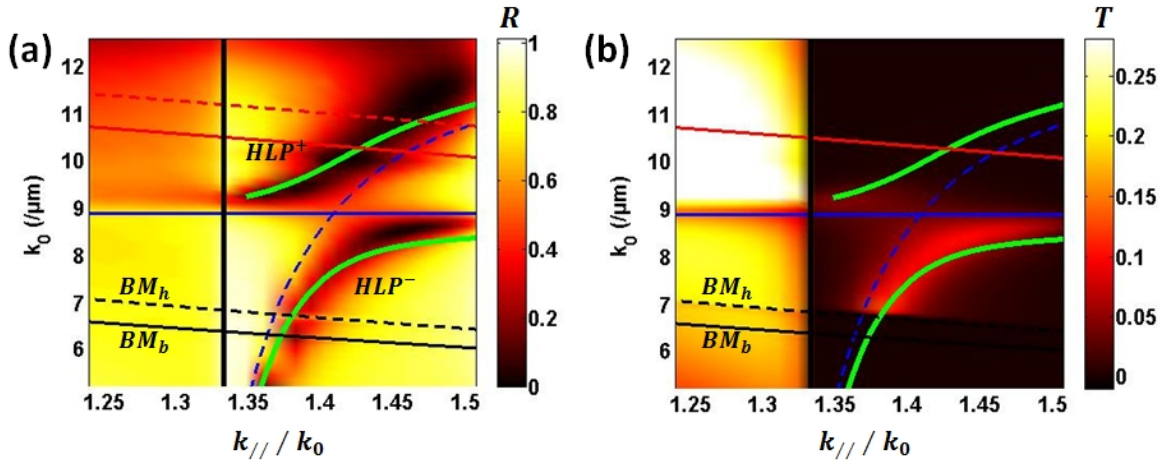


Figure 12.5: The reflectivity (R) dispersion map as a function of  $(k_0, (k_{//}/k_0))$  for  $h_2 = 30nm$ ,  $D = 50nm$  and period  $\Lambda = 340nm$  with an incident plane wave from medium with index  $n_b = 1.513$ . The analytical calculation of the dispersion of different modes of the system are also shown: LSP (blue solid), PSP (blue dashed), HLP (green) and BMs (black and red solid and dashed same as figure 12.3). (b) The transmission (T) for the same parameters.

The explanation of this phenomenon can be found in the very description of the plasmonic modes. We have defined the modes either as confined (PSP, CPP, HLP) or as extended (WRA, BM). The extended modes have such transmissions as shown in figure 11.6 for the BMs (section 11.1.1). In the present configurations we see that we have transmission for the values of  $(k_0, (k_{//}/k_0))$  when the  $BM_h$  dispersion cross that of the HLP. In this range there is a coupling of the HLP with  $BM_h$  and thus the characteristics of the HLP resembles more that of an extended mode than confined.

Such transmission has been reported for periodic arrays of various geometries and is termed as extraordinary transmission [231, 232, 233, 234, 235, 236]. The explanation in terms of coupling of an extended mode to a confined mode is also applicable for such reported extraordinary transmissions. This same phenomenon will be revisited when studying the near field characteristics of the HLP.

Below  $(k_{//}/k_0) < n_h = 1.333$  we expect high transmission. However a drop in T is observed

for the  $k_0$  values corresponding to the analytically calculated LSPR condition thus validating the  $\chi$  formulation.

### 12.3 Near field characteristics of the HLP

To calculate the near field characteristics of the modes we will follow the approach described in section 12.1. The field intensity confined around the cylinders was calculated as  $I_{surf}$  given by equation 10.12. An incident plane wave from the medium  $n_b$  was considered at an angle of incidence  $\theta$ . The  $I_{surf}$  as a function of  $(k_0, (k_{//}/k_0))$  is shown in figure 12.6 for  $\Lambda = 300nm$  and  $D = 50nm$ . The far field absorption (A=1-R-T) is also shown in the figure to compare the distribution of the field intensity with the various modes. A plot of the field intensity as a function of  $k_0$  for two different values of  $(k_{//}/k_0)$  is shown in figure 12.7.

First at the value of  $k_0$  where the LSPR condition is satisfied we see a weak maxima. The value of the field intensity for the LSP at  $(k_{//}/k_0) = 1.32$  and  $k_0 = 9.2/\mu m (\lambda = 683nm)$  is  $I_{surf} = 85.72$ . This value is similar in magnitude to the value of field intensity obtained for the  $LSP_L$  in an array of metallic cylinders on a glass substrate (figure 10.12). However the LSPR wavelength is red shifted as compared to the cylinders on a glass substrate owing to the metallic film.

The two small peaks that can be seen at  $(k_{//}/k_0) = 1.32$  for lower values of  $k_0$  in figure 12.7 are due to the BMs. We see that the confined field intensity is much lower for the BMs than the LSP and this is expected as the BMs are extended modes.

However the field confined around the cylinders for the HLP is even higher than the LSP with a value of  $I_{surf} = 168.85$  for  $(k_{//}/k_0) = 1.42$  and  $k_0 = 8.38/\mu m (\lambda = 750nm)$ . Thus the HLP has far field characteristics similar to the PSP with high dispersion, but can also confine the electric field intensity close to metallic nano-structures, a property similar to the LSP. This hybrid property of the HLP can prove to be very useful for bio-detection. As will be shown later, for SPR detection a high dispersion of the plasmonic modes is necessary for higher sensitivity. Thus the HLP mode can permit such high sensitivities but with a much higher localization of the electric field than the PSP.

Another important far field characteristic as shown in figure 12.5 is high transmission when the  $BM_h$  couples to the HLP. Thus the HLP for certain values of  $k_0$  which are greater than the  $k_0$  values of the  $BM_h$ , have the properties of an extended mode. Thus in the dispersion map of the HLP we can distinguish two regimes

- (a) Confined HLP: for values of  $k_0$  less than the that of  $BM_h$
- (b) Quasi-extended HLP : for values of  $k_0$  more than that of  $BM_h$ .

The two regimes are distinctly shown in figure 12.8 for a cylinder array of diameter 50nm, height 30nm and period  $\Lambda = 300nm$  and also for varying period. To define the regime in terms of period we have plotted absorption maxima for the structures with period  $\Lambda$  as a function of  $k_0$ . This is similar to figure 12.4(a) and on the same figure we have superimposed the transmission maxima as found by numerical methods. We see that for the HLP we have transmission maxima only for those values of  $(k_0, (k_{//}/k_0))$  which correspond to the situation described above as Quasi-extended HLP.

Finally, the near field intensity distribution as shown in figure 12.9 for the two regimes clearly shows the difference. The fields are shown for the same structure ( $\Lambda = 300nm, D = 50nm, h_2 = 30nm$ ) and for the same HLP mode but at two different values of  $(k_0, (k_{//}/k_0))$ . We see that the field in the

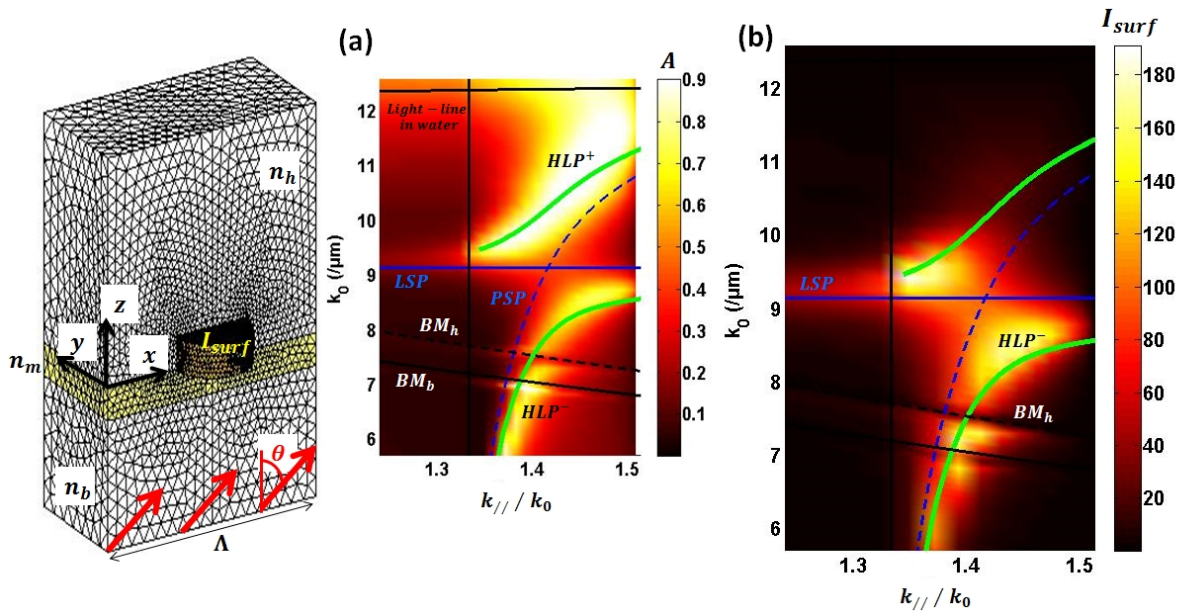


Figure 12.6: The absorption ( $A$ ) dispersion map as a function of  $(k_0, (k_{//}/k_0))$  for  $h_2 = 30\text{nm}$ ,  $D = 50\text{nm}$  and period  $\Lambda = 300\text{nm}$  with an incident plane wave from medium with index  $n_b = 1.513$ . The analytical calculation of the dispersion of different modes of the system are also shown: LSP (blue solid), PSP (blue dashed), HLP (green) and BMs (black and red solid and dashed same as figure 12.3). (b) Integrated electric field intensity ( $I_{surf}$ ) over the surface of the cylinder as a function of  $(k_0, (k_{//}/k_0))$ . The medium surrounding the cylinders has a refractive index of  $n_h = 1.333$  and the metal an index of  $n_m$ .

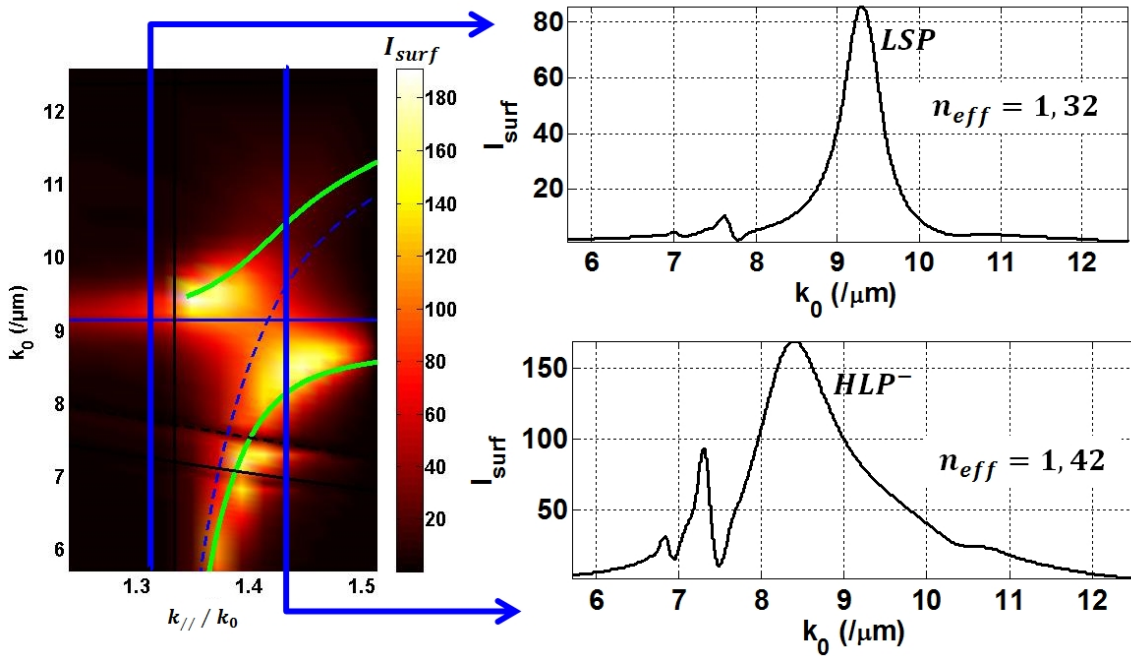


Figure 12.7: Integrated electric field intensity ( $I_{surf}$ ) over the surface of the cylinder as a function of  $k_0$  for  $(k_{//}/k_0) = 1.32$  and  $(k_{//}/k_0) = 1.42$ .

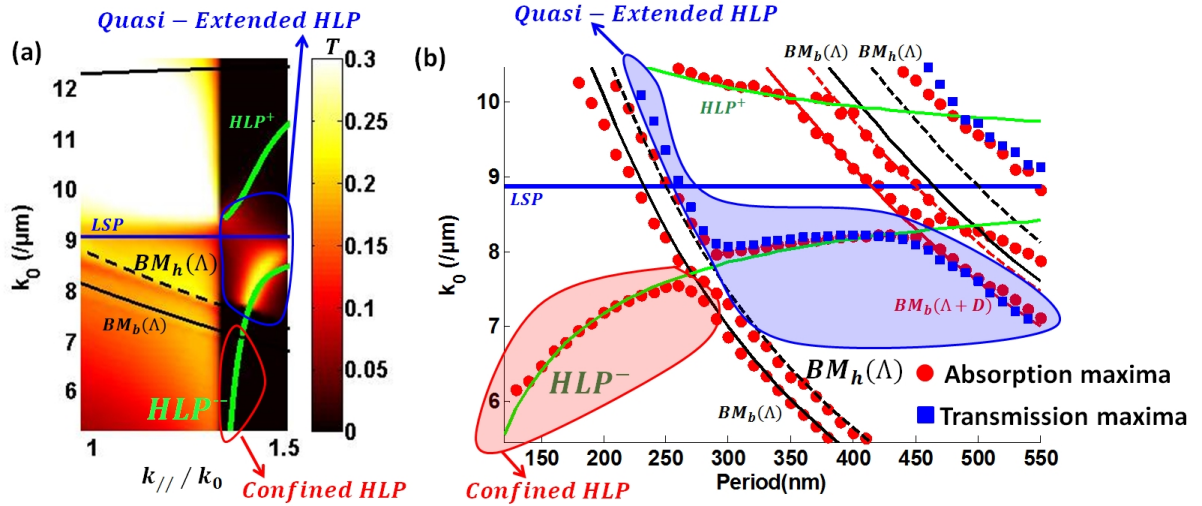


Figure 12.8: (a) The transmission ( $T$ ) dispersion map as a function of  $(k_0, (k_{//} / k_0))$  for  $h_2 = 30\text{nm}$ ,  $D = 50\text{nm}$  and period  $\Lambda = 300\text{nm}$  with an incident plane wave from medium with index  $n_b = 1.513$ . (b) The resonance frequencies ( $k_0$ ) of all the modes in the structure ( $D = 50\text{nm}$ ,  $h_2 = 30\text{nm}$ ) manifest as absorption maxima (red dots) and transmission maxima (blue squares) in the dispersion map calculated by rigorous numerical method as a function of array period for  $(k_{//} / k_0) = 1.42$ . The analytically calculated dispersion of the various modes namely the BMs, LSP and HLP are also shown

regime of confined HLP is more localized close to the cylinder surface, while that in the quasi-extended regime penetrates more into the dielectric medium  $n_h$ .

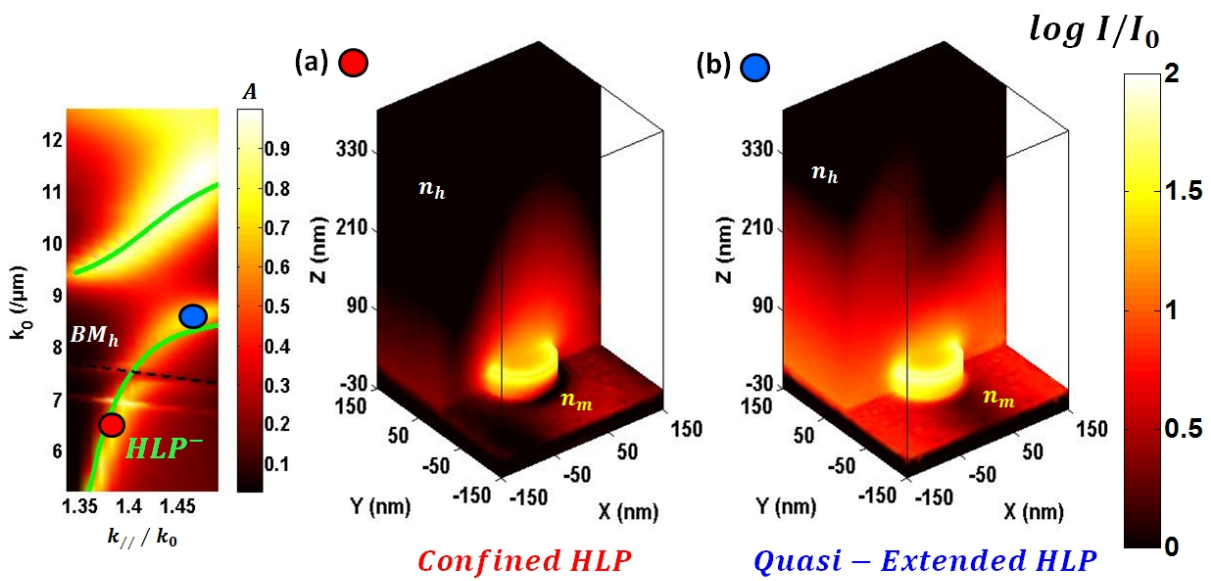


Figure 12.9: (a) The electric field intensity distribution for the BM for the two regimes (a) Confined HLP:  $(k_{//}/k_0) = 1.39$  ( $\theta = 67^\circ$ ),  $k_0 = 6.93$  ( $\lambda = 907\text{nm}$ ) (b) Quasi-Extended HLP:  $(k_{//}/k_0) = 1.46$  ( $\theta = 75^\circ$ ),  $k_0 = 8.54$  ( $\lambda = 736\text{nm}$ ). The structure dimensions are  $\Lambda = 300\text{nm}$ ,  $D = 50\text{nm}$ ,  $h_1 = h_2 = 30\text{nm}$ . Plane wave is incident from the medium  $n_b = 1.513$  at an angle  $\theta$  and  $n_h = 1.333$ . The structure geometry is shown in figure 12.6

---

# Conclusion of Part IV: Structures and Modes

---

In this part, we have introduced different plasmonic modes that we have used in this work to identify the dispersion characteristics of periodic structures. The structures are considered to be present in a medium with refractive index  $n_h$  and with an underlying substrate with index  $n_b$ . The dispersion is presented in terms of  $k_0 = 2\pi/\lambda$  and  $(k_{//}/k_0) = k_x/k_0$ . For a uniform metallic film we can excite the propagating surface plasmon (PSP) along the metal-dielectric interface and the dispersion relation can be written as

$$(k_{//}/k_0)_{PSP_{(b/h)}} = \sqrt{\frac{(n_{(b/h)}^2 n_m^2)}{(n_{(b/h)}^2 + n_m^2)}}$$

For a grating (or an array of metallic particles) with an incident light perpendicular to the grating ridges (period  $\Lambda$ ), the Wood's Rayleigh anomaly (WRAs) condition can be satisfied when the diffracted orders from the grating graze along the metal-dielectric interface. The dispersion relation is given as

$$(k_{//}/k_0)_{WRA_{(b/h)}} = |n_{b/h} - n_p| \text{ with } n_p = \pm m(2\pi/\Lambda)/k_0$$

For incident light parallel to the grating ridges, the Confined propagating plasmons (CPP) can be excited effectively due to a truncation of the metallic film along the grating ridges (width  $w_1$ ). For these modes the dispersion is given as

$$(k_{//}/k_0)_{CPP_{b/h}} = \sqrt{((k_{//}/k_0)_{PSP_{b/h}})^2 - (m\pi/k_0 w_1)^2}$$

For an array of metallic particles with an underlying metallic film, modes similar to the WRAs can be excited, which in this case is caused by the diffraction of the PSP excited at the thin film surface. These were called the Bragg modes (BMs) and were represented as

$$(k_{//}/k_0)_{BM_{(b/h)}} = \left| (k_{//}/k_0)_{PSP_{(b/h)}} - n_p \right|$$

Plasmonic modes were defined as (a) «Confined» modes where the electric field is confined close to the metallic surface such as the PSP, CPP and the localized surface plasmon at its resonance condition

(LSP) (b) «Extended» modes for those that do not have confined electric field distribution, but help to redistribute the incident energy as reflection, transmission and diffraction. The WRAs and BMs belong to the later type. All the above mentioned plasmonic modes are «Bright» modes or «Continuum» states. Thus they cannot undergo Fano resonances when there is a coupling among them. However the coupling of an extended mode with a confined modes gives rise to plasmonic band-gaps. This was shown for the coupling of PSP with the WRAs and BMs.

The coupling of two confined modes gives rise to hybrid plasmonic modes which can be described by harmonic coupling of two oscillators. One such coupling between the PSP and the LSP gives rise to the Hybrid Lattice plasmon (HLP) mode which can be described as

$$(k_{//}/k_0)_{HLP_{\pm}} = \frac{1}{2} \left[ (k_{//}/k_0)_{PSP_h}^2 + (k_{//}/k_0)_{LSP}^2 \right] \pm \frac{1}{2} \left[ \sqrt{\left( (k_{//}/k_0)_{PSP_h}^2 - (k_{//}/k_0)_{LSP}^2 \right)^2 + 4 \frac{\Gamma_{12}^2}{c^4 k_0^4}} \right]$$

with appropriate coupling parameters. The hybrid modes can behave both as confined or extended modes depending on the excitation conditions. In effect, the coupling of the LSP and PSP gives rise to a confined HLP. However due to a secondary coupling of the HLP with the BMs, the HLP was shown to have the characteristics of an extended mode with high transmission into the far-field and less confinement of the incident electric field (quasi-extended HLP).

The resonance condition for the LSP ( $\lambda_{LSP}$ ) was calculated by the extinction of metallic particles using FEM calculations. An approximate analytical model was developed called the  $\chi$  formulation to calculate the resonance conditions for nano-particles and the results were shown to fit closely to the numerical methods. The effect of a substrate (metallic or dielectric) on the LSPR resonance condition can also be calculated by the model.

The near and far field characteristics of the various modes were presented with incident plane wave from either the medium  $n_h$  or  $n_b$ . Such field distributions are of paramount importance when using various modes for applications in bio-detection. In the next part we will introduce the different bio-detection techniques and the process of optimizing the structures based on the modal representation presented in this part.



## **Part V**

# **Plasmonic modes for biodetection**



# Intrinsic sensitivity of plasmonic modes for bulk refractive index changes

---

SPR detectors were introduced in chapter 3 and their limitations were discussed in section 5.1.1. We have shown that when using surface plasmons to detect refractive index changes in the bulk medium or local molecular binding kinetics, the absolute resolution that can be achieved is limited by response of the particular plasmonic mode to such refractive index changes. This was quantified by the term  $\left[\frac{d(k_{sp}/k_0)}{dn}\right]^{-1}$ . Following the description of the various plasmonic modes in the previous part (part IV) we can simply identify this term for each plasmonic mode as  $\left[\frac{d((k_{//}/k_0))}{dn}\right]^{-1}$ . In this chapter we will first discuss the characteristics of various modes in terms of their sensitivity to bulk (and local) refractive index changes. Then we will introduce some criterion and also optimization of the structured bio-chip surface for SPR affinity biosensing.

The response of the various structures (and modes) described in part IV to change of bulk refractive index was calculated using rigorous numerical methods. For the calculations the light was considered to be incident from the medium with higher refractive index ( $n_b = 1.513$ ) and the refractive index of the medium surrounding the nano-structures ( $n_h$ ) was changed to mimic a step of bulk refractive index. This configuration is effectively same as the conventional Kretschmann configuration used for SPR detectors.

In section 3.2.1 the various interrogation methods for SPR detection were described. In brief one can either measure the change in reflectivity or measure the shift in the plasmon wavelength due to bulk refractive index changes. The wavelength interrogation method is generally more robust as the wavelength shift is less sensitive to the inhomogeneity over the biochip surface. This was explained in the publication of Sereda et al [35] and the measurements therein were done on a similar SPR setup as used in this work. The reflectivity interrogation method is also strongly dependent on the absolute reflectivity value of the plasmon dip and the line-width of the resonance. However the wavelength shift due to refractive index changes is independent of these parameters can thus can be quantified purely by the drift of  $(k_0, (k_{//}/k_0))$  of each mode.

### 13.1 Bulk index sensitivity for the PSP

We will start with the simple uniform thin gold film. In such a structure we can excite the PSP. We are interested in calculating the shift of the plasmon wavelength with respect to the refractive index changes in the bulk medium. To quantify such shift we will measure the response in terms of reflectivity change ( $\Delta R$ ) or wavelength shift ( $\Delta\lambda$  in  $nm$ ) due to a shift in bulk index ( $\Delta n_h$  in  $RIU$ ). The sensitivity of the system can then be written as  $S_R = \Delta R / \Delta n_h$  ( $/RIU$ ) or  $S_\lambda = \Delta\lambda / \Delta n_h$  ( $nm/RIU$ ).

So far in this work, we have described the modes in terms of  $(k_0, (k_{//}/k_0))$  to have a better understanding of the physical aspects of the modes in terms of wave-vectors. However for practical realization of bio-detectors a representation, in terms of  $(\lambda, (k_{//}/k_0))$  is more direct in terms of experimental configurations. Thus the response of the systems will be characterized in terms of  $\Delta\lambda$ ,  $\Delta\theta \propto \Delta(k_{//}/k_0)$  and so on. A simple conversion between the quantities can be carried out as  $k_0 = 2\pi/\lambda$  and  $(k_{//}/k_0) = n_{inc} \sin(\theta)$  with  $n_{inc}$  being the index of the incident medium.

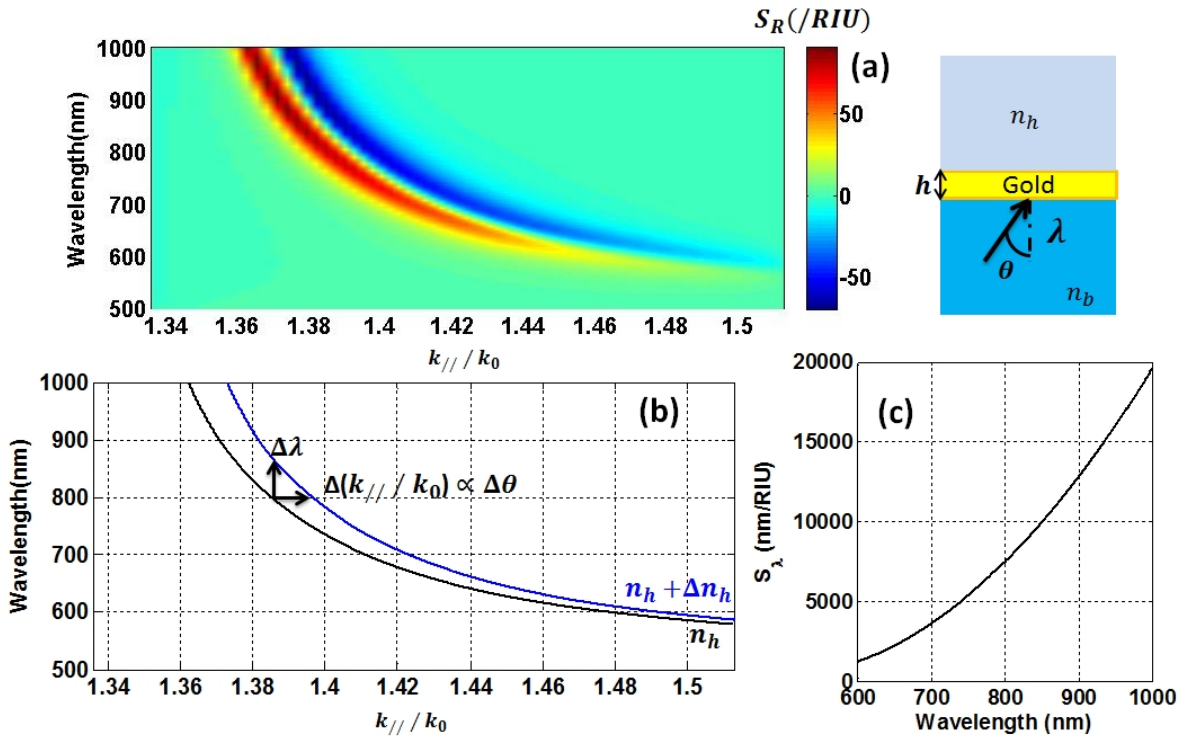


Figure 13.1: (a) The reflectivity variation ( $S_R$ ) as a function of  $(\lambda, (k_{//}/k_0))$  for a thin metallic film in Kretschmann configuration of height  $h = 50nm$ . (b) The analytically calculated dispersion of  $PSP_h$  with a change of bulk refractive index  $\Delta n_h = 10^{-2}RIU$ : The dispersion in medium  $n_h = 1.333$  is shown in black, the calculated dispersion  $(k_{//}/k_0) + \frac{\partial(k_{//}/k_0)}{\partial n_h} \Delta n_h$  is shown in blue. (c) The sensitivity  $S_\lambda$  as calculated analytically from (b) as a function of incident wavelength. The refractive index of the substrate was  $n_b = 1.513$ .

The reflectivity change ( $S_R$ ) as a function of  $(\lambda, (k_{//}/k_0))$  for a thin gold film of height 50nm is shown for a refractive index change  $\Delta n_h = 10^{-2}RIU$  in figure 13.1. The calculation was done with Rouard method for  $n_h = 1.333$  and  $n_b = 1.513$ . The reflectivity change is strongly dependent on the line width of the plasmon mode. For detectors that use reflectivity interrogation, a conventional figure of merit (FOM) can be defined as [237, 238, 239]

$$FOM = S/FWHM \quad (13.1)$$

where  $S$  is the sensitivity of the system in terms of change of reflectivity or wavelength shift per unit refractive index change. However for spectral interrogation, the FWHM of the plasmon dip do not play a major role and the intrinsic sensor response can be analytically calculated and depends purely on the dispersion characteristics of the mode.

The dispersion of the  $PSP_h$  mode is given by  $(k_{//}/k_0)_{PSP}(\lambda) = \sqrt{\frac{n_d^2 n_m^2}{n_d^2 + n_m^2}}$  with  $n_d = n_h$  or  $n_d = n_h + \Delta n_h$ . The shift of  $(k_{//}/k_0)$  with change in refractive index is given as

$$\frac{\partial(k_{//}/k_0)_{PSP}}{\partial n_h} = \frac{(k_{//}/k_0)_{PSP}}{n_h} - \frac{(k_{//}/k_0)_{PSP}^3}{n_h n_m^2} \quad (13.2)$$

Thus for a refractive index change of  $\Delta n_h$  the dispersion of the PSP mode can be written as  $(k_{//}/k_0)_{PSP} + \frac{\partial(k_{//}/k_0)_{PSP}}{\partial n_h} \Delta n_h$ . This relation is directly related to the response  $S_\theta$  for a SPR detector in angular interrogation mode with

$$\frac{\partial \theta}{\partial n_h} = \frac{\partial(k_{//}/k_0)}{\partial n_h} \frac{1}{n_{inc} \cos \theta} \quad (13.3)$$

However the relation for  $S_\lambda$  is not trivial but can be calculated from the relation for  $\frac{\partial(k_{//}/k_0)}{\partial n_h}$ . The analytical calculation of the dispersion of the  $PSP_h$  for  $n_h = 1.333$  and for a medium with a refractive index shifted by  $\Delta n_h = 10^{-2} RIU$  is also shown in figure 13.1. We see that for all the three interrogation methods, the sensitivity ( $S_R, S_\lambda, S_\theta$ ) increases with incident wavelength. We also note that the intrinsic sensitivity in spectral or angular interrogation can be directly calculated and is related to  $\frac{\partial(k_{//}/k_0)}{\partial n_h}$ . This is also applicable for all the other plasmonic modes presented in this work. This is one of the major reasons for using  $(k_{//}/k_0)$  representation to describe the plasmonic modes. The variation of the sensitivity to bulk index changes with other parameters such as  $\Delta n_h$  and film height ( $h$ ) is shown in Appendix C. The variation of  $S_\theta$  is also shown in in Appendix C.

## 13.2 Bulk index sensitivity for the WRAs

For the WRAs, the dispersion is given as  $(k_{//}/k_0)_{WRA} = n_h - n_P$  for the mode caused by the diffraction in the medium  $n_h$ . We will consider only this mode and not  $WRA_b$  as the later does not depend on the drift of  $n_h$ . Thus for the WRAs the shift in dispersion for a drift of  $n_h$  is given as

$$\frac{\partial(k_{//}/k_0)_{WRA}}{\partial n_h} = 1 \quad (13.4)$$

Thus the sensitivity of the WRAs to bulk index changes is independent of the excitation wavelength. The sensitivity of the structure presented in section 9.1.3 was calculated for  $\Delta n_h = 10^{-2} RIU$ . The reflectivity variation was calculated using numerical methods for a metallic grating of period  $\Lambda = 1400nm$ , ridge height  $h = 50nm$  and ridge width  $w_1 = 1200nm$ . The dispersion of the WRAs due to the shift of refractive index was calculated as  $(k_{//}/k_0)_{WRA} + \frac{\partial(k_{//}/k_0)_{WRA}}{\partial n_h} \Delta n_h$  and is shown in figure 13.2. We see that the analytically calculated shift of resonance wavelength ( $\Delta \lambda$ ) is almost negligible for the WRAs as compared to that for the PSP. This is also reflected in the value of  $\Delta R$  calculated numerically and shown in figure 13.2. The WRA orders  $m = 4, 5, 6$  are shown. We also see

that the reflectivity change is lower when there is coupling between the PSP and the WRAs. The spectral shift of the WRAs was calculated analytically and the sensitivity  $S_\lambda$  was derived from it. The values are independent of  $\lambda$  and was found to be  $350\text{nm}/\text{RIU}$ ,  $280\text{nm}/\text{RIU}$  and  $233.34\text{nm}/\text{RIU}$  for the orders 4,5 and 6 respectively. This is much lower than the sensitivity for the  $PSP_h$ , almost by an order of magnitude. We also see that the sensitivity of the WRAs decreases with increasing orders and this is because, even though the shift of  $(k_{//}/k_0)$  is independent of  $m$ , the values of  $(k_{//}/k_0)$  depends on  $m$  and thus the shift when translated to wavelength depends slightly on  $m$ . The same dependence on the order ( $m$ ) is also seen for the reflectivity sensitivity  $S_R$ .

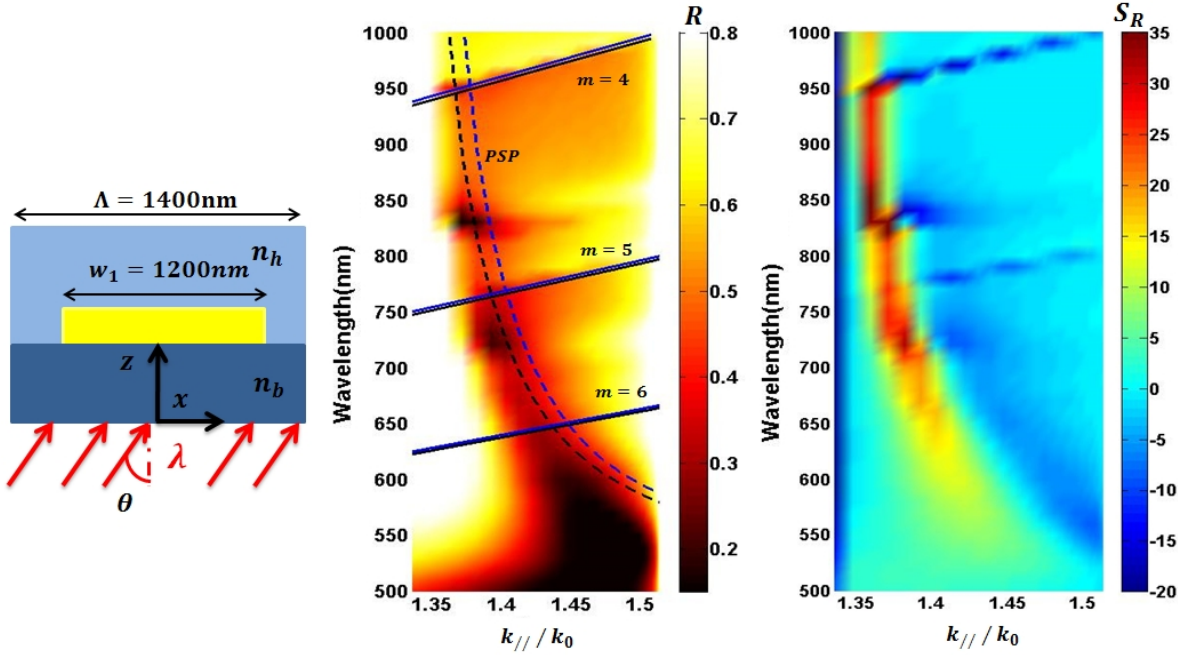


Figure 13.2: (Left) Reflectivity ( $R$ ) for  $\Lambda = 1400\text{nm}$  and  $w_1 = 1200\text{nm}$  as a function of  $(\lambda, (k_{//}/k_0))$ . The structure geometry and excitation in Kretschmann configuration is also shown. The analytical dispersion of the PSP (black dashed) and that of the  $WRA_h$  (black solid) for different orders  $m$  is calculated for  $n_h = 1.333$ . The same analytical calculation with a shift of index  $\Delta n_h = 10^{-2}\text{RIU}$  ( $n_h = 1.343$ ) is shown in the figure (blue dashed and solid). (Right) Sensitivity of the structure in reflectivity interrogation ( $S_R$ ) as a function of  $(\lambda, (k_{//}/k_0))$ . The refractive index of the substrate is  $n_b = 1.513$ .

### 13.3 Bulk index sensitivity for the CPP modes

The CPP modes were described in section 9.2. The dispersion of the CPPs is given as  $(k_{//}/k_0)_{CPP} = \sqrt{((k_{//}/k_0)_{PSP})^2 - (m\pi/k_0 w_1)^2}$  where the grating width is  $w_1$ . The shift of  $(k_{//}/k_0)$  for the  $CPP_h$  due to the confinement of the  $PSP_h$  propagating in the medium  $n_h$  is given as

$$\frac{\partial(k_{//}/k_0)_{CPP}}{\partial n_h} = \frac{(k_{//}/k_0)_{PSP}}{(k_{//}/k_0)_{CPP}} \frac{\partial(k_{//}/k_0)_{PSP}}{\partial n_h} \quad (13.5)$$

We expect no drift of  $CPP_b$  with  $n_h$  as it is caused by the confinement of the  $PSP_b$  which in turn is not sensitive to the change of the refractive index  $n_h$ .

The reflectivity dispersion for an array of metallic strips of width  $w_1 = 500nm$  and period  $\Lambda = 1000nm$  in the Kretschmann configuration with incident light from the medium  $n_b$  was calculated. The direction of incidence was considered to be along the length of the grating ridges, thus assuring the excitation of the CPPs. The reflectivity is shown in figure 13.3. The analytical calculation of the dispersion of the 1st order (m) of  $CPP_h$  and  $CPP_b$  are also shown and we see reflectivity dips corresponding to the two respective modes.

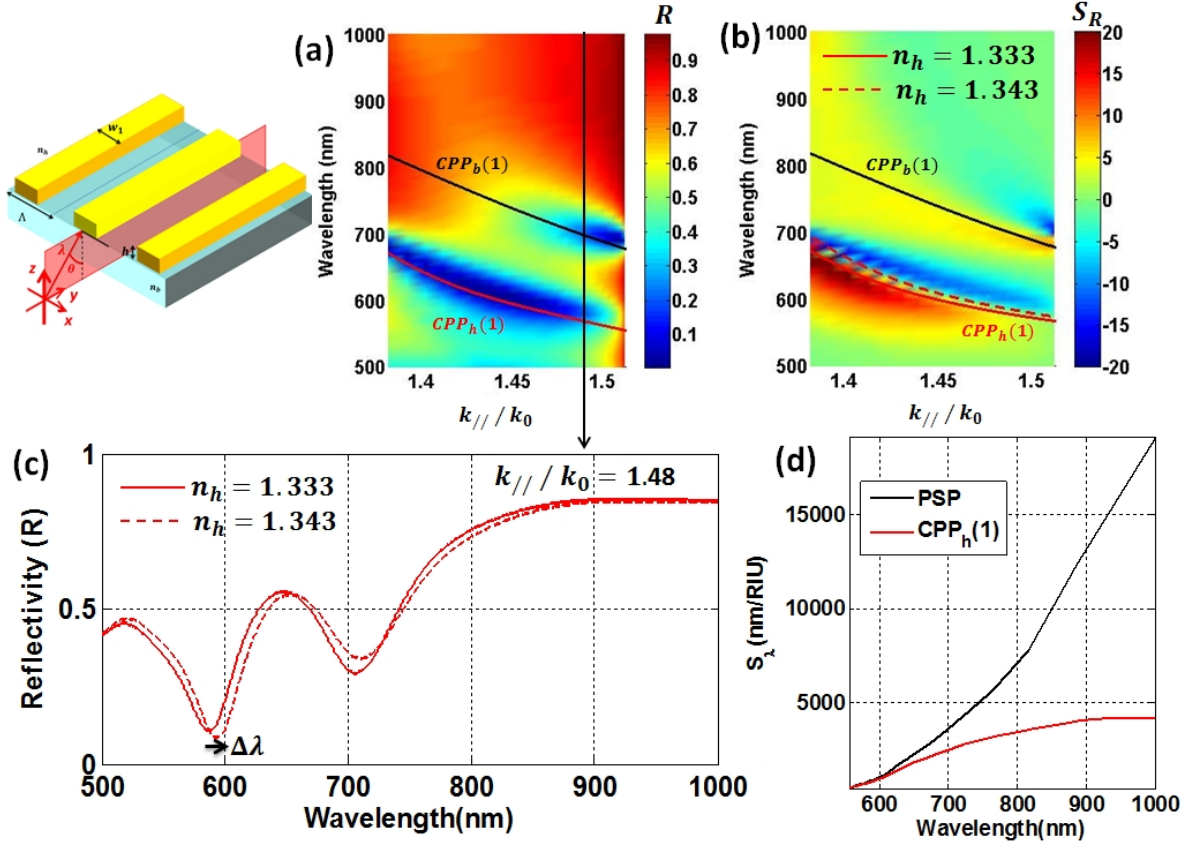


Figure 13.3: (a) The reflectivity ( $R$ ) for  $\Lambda = 1000nm$  and  $w_1 = 500nm$  as a function of  $(\lambda, (k_{//}/k_0))$ . The structure geometry and excitation in Kretschmann configuration is also shown. The analytical dispersion of the  $CPP_h(1)$  (red) and that of the  $CPP_b(1)$  (black) is calculated for  $n_h = 1.333$ . (b) Sensitivity of the structure in reflectivity interrogation ( $S_R$ ) as a function of  $\lambda - (k_{//}/k_0)$ . The analytical calculation with a shift of index  $\Delta n_h = 10^{-2}RIU$  ( $n_h = 1.343$ ) is shown in the figure for  $CPP_h(1)$  (red dashed). (c) Reflectivity as a function of wavelength for  $(k_{//}/k_0) = 1.48$  ( $\theta = 78^\circ$ ) for  $n_h = 1.333$  and  $n_h = 1.343$  calculated numerically. (d) Sensitivity  $S_\lambda$  as calculated analytically for  $CPP_h$  as a function of wavelength. The refractive index of the substrate was  $n_b = 1.513$ .

The dispersion of  $CPP_h$  due to a refractive index shift of  $\Delta n_h = 0.01RIU$  was calculated as  $(k_{//}/k_0)_{CPP} + \frac{\partial(k_{//}/k_0)_{CPP}}{\partial n_h} \Delta n_h$ . The sensitivity  $S_\lambda$  was also calculated and shown in figure 13.3. The calculation shows a much lower spectral sensitivity for the  $CPP_h$  to bulk refractive index changes as compared to the  $PSP_h$ . We also see that the reflectivity sensitivity calculated by numerical methods is lower for the  $CPP_h$  than the  $PSP_h$ .

For  $CPP_b$  we do not expect any intrinsic sensitivity to bulk refractive index changes as its  $(k_{//}/k_0)$  is not dependent on  $n_h$ . This is seen in the reflectivity spectrum of figure 13.3(c) where no substantial

shift of the spectrum is observed. The very slight shift of reflectivity observed, is because the  $CPP_b$  does confine a part of its electric field intensity in the medium  $n_h$ . This will be discussed in details in a later section.

### 13.4 Sensitivity of metallic array on metallic film to bulk index changes: BM and HLP

The modes of the structures consisting of an array of metallic nano-particles with an underlying thin metallic film were described in chapter 11. In brief, in such structures, the BMs are excited which are similar in principle to the WRAs but caused by the diffraction of the PSP by the array. Thus, we expect to have similar characteristics of the BMs to the WRAs with respect to bulk refractive index changes.

The dispersion of the BMs is given by  $(k_{//}/k_0)_{BM} = (k_{//}/k_0)_{PSP} - n_P$ . The drift of dispersion with change in the bulk refractive index  $n_h$  is given as

$$\frac{\partial(k_{//}/k_0)_{BM}}{\partial n_h} = \frac{\partial(k_{//}/k_0)_{PSP}}{\partial n_h} \quad (13.6)$$

However unlike the WRAs, the sensitivity of the BMs are dependent on  $\lambda$  as can be seen from equation 13.6. In fact, for  $BM_h$ , we expect the same sensitivity to refractive index changes as for  $PSP_h$ . The drift of  $(k_{//}/k_0)$  of the BM is same and therefore only the sensitivity in angular interrogation ( $S_\theta$ ) is equal to that of the PSP. However the spectral sensitivity ( $S_\lambda$ ) is different and we expect it to be much lower for the BM than that of the PSP owing to the dispersion of the BM.

In such hybrid structures we can also excite the HLP which was described in details in chapter 12. The dispersion of the HLP is given by as

$$(k_{//}/k_0)_{HLP\pm} = \sqrt{\frac{1}{2} \left[ (k_{//}/k_0)_{PSP}^2 + (k_{//}/k_0)_{LSP}^2 \pm \sqrt{((k_{//}/k_0)_{PSP}^2 - (k_{//}/k_0)_{LSP}^2)^2 + 4 \frac{\Gamma_{12}^2}{c^4 k_0^4}} \right]}$$

The drift of the HLP with refractive index changes will thus depend on the drift of both the PSP and the LSP. The drift can be evaluated to be

$$\begin{aligned} \frac{\partial(k_{//}/k_0)_{HLP}}{\partial n_h} &= \frac{(k_{//}/k_0)_{PSP}}{2(k_{//}/k_0)_{HLP}} \frac{\partial(k_{//}/k_0)_{PSP}}{\partial n_h} + \frac{(k_{//}/k_0)_{LSP}}{2(k_{//}/k_0)_{HLP}} \frac{\partial(k_{//}/k_0)_{LSP}}{\partial n_h} \\ &\pm \left[ \frac{(k_{//}/k_0)_{PSP}}{4C_\Gamma(k_{//}/k_0)_{HLP}} \frac{\partial(k_{//}/k_0)_{PSP}}{\partial n_h} - \frac{(k_{//}/k_0)_{LSP}}{4C_\Gamma(k_{//}/k_0)_{HLP}} \frac{\partial(k_{//}/k_0)_{LSP}}{\partial n_h} \right] \end{aligned} \quad (13.7)$$

$$\text{where } C_\Gamma = \sqrt{((k_{//}/k_0)_{PSP}^2 - (k_{//}/k_0)_{LSP}^2)^2 + 4 \frac{\Gamma_{12}^2}{c^4 k_0^4}}.$$

The term  $\frac{\partial(k_{//}/k_0)_{PSP}}{\partial n_h}$  is given by equation 13.3. However the derivation of the term  $\frac{\partial(k_{//}/k_0)_{LSP}}{\partial n_h}$  which is not trivial signifies the shift of the resonance condition of the LSP with a change of refractive index of the surrounding medium. To calculate this value analytically, we can use the notation  $(k_{//}/k_0)_{LSP} = 2\pi/(\mathbf{k}_0 \lambda_{LSP})$ .  $\lambda_{LSP}$  is calculated from the pole of  $\alpha$  as found analytically by  $\chi$  formulation or numerically by FEM as described in chapter 10.



We will consider an array of nano-cylinders of height  $h_2 = 30nm$  and diameter  $D = 50nm$ . The resonance condition for such a nano-cylinder placed on a gold substrate is given by  $\lambda_{LSP} = 693nm$  with  $n_h = 1.333$  and  $\lambda_{LSP} = 703nm$  with  $n_h = 1.343$ . Thus for such a cylinder the spectral sensitivity is  $S_R = 1000nm/RIU$  assuming that the shift in LSP condition is linear with  $n_h$  which is quite acceptable for small refractive index changes. In this case, the drift of  $(k_{//}/k_0)_{LSP}$  can be found to be equal to  $\frac{\partial(k_{//}/k_0)_{LSP}}{\partial n_h} = 12.9/k_0$ .

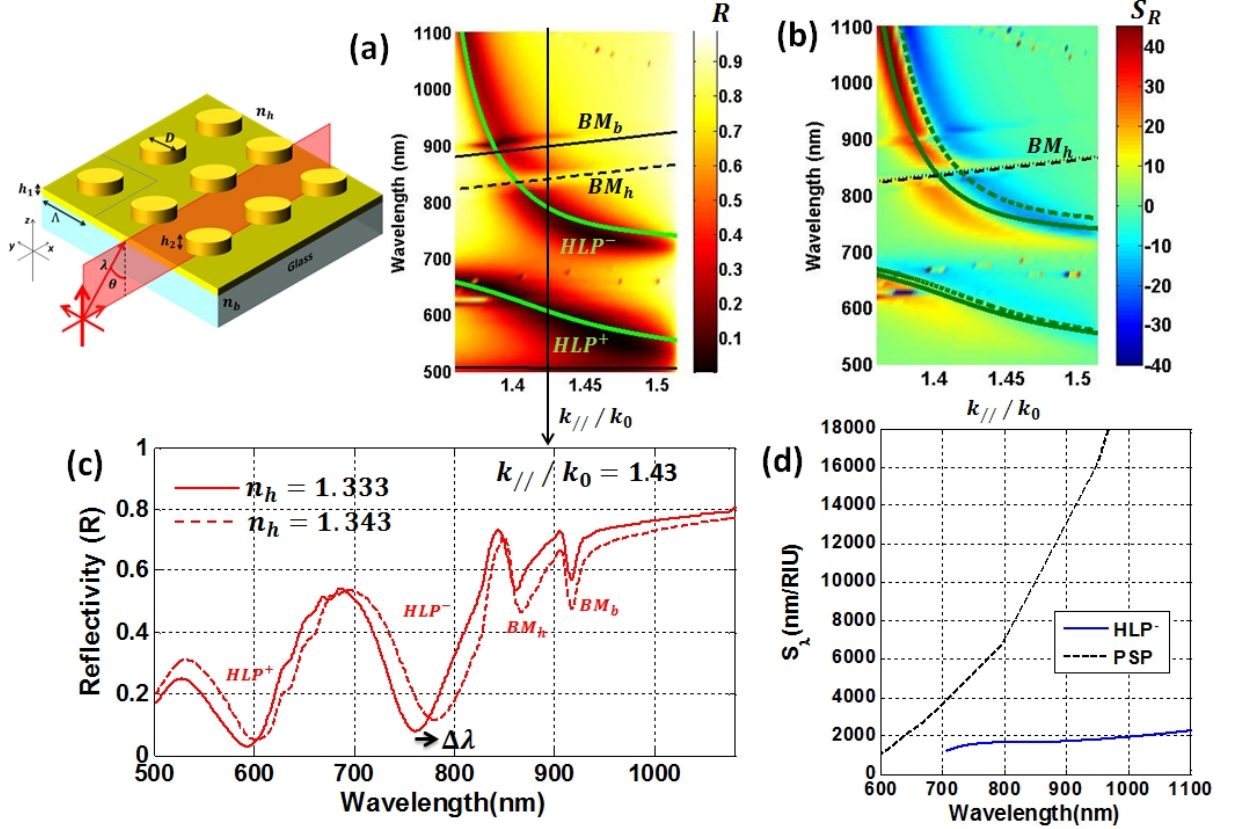


Figure 13.4: (a) The reflectivity ( $R$ ) for  $\Lambda = 300nm$  and  $D = 50nm$  as a function of  $(\lambda, (k_{//}/k_0))$ . The structure geometry and excitation in Kretschmann configuration is also shown. The analytical dispersion of the  $HLP$  (green), that of the  $BM_h$  (black dashed) and  $BM_b$  (black solid) is also shown for  $n_h = 1.333$ . (b) Sensitivity of the structure in reflectivity interrogation ( $S_R$ ) as a function of  $(\lambda, (k_{//}/k_0))$ . The analytical calculation with a shift of index  $\Delta n_h = 10^{-2} RIU$  ( $n_h = 1.343$ ) is shown in the figure for  $HLP$  (green dashed) and  $BM_h$  (black dotted). (c) Reflectivity as a function of wavelength for  $(k_{//}/k_0) = 1.43$  ( $\theta = 71.5^\circ$ ) for  $n_h = 1.333$  and  $n_h = 1.343$  calculated numerically. (d) Sensitivity  $S_\lambda$  as calculated analytically for  $HLP^-$  as a function of wavelength. The refractive index of the substrate was  $n_b = 1.513$ .

The reflectivity dispersion for the structure with the above mentioned array of cylinders placed on a thin gold film of height  $h_1 = 30nm$  in the Kretschmann configuration was calculated using numerical methods. The analytical calculation of the dispersion of the HLP and the BM is shown along with the reflectivity in figure 13.4 for  $n_h = 1.333$ . We can identify the various modes as described in chapter 12. The reflectivity shift was calculated with  $\Delta n_h = 10^{-2} RIU$ . In figure 13.4 the sensitivity in reflectivity interrogation ( $S_R$ ) is also shown. We see a significant sensitivity for the HLP with change of bulk refractive index but almost no appreciable sensitivity for the BMs.

It is clear that the sensitivity of the HLP for bulk refractive index changes is much smaller than that

of the PSP. This is because the HLP has a much confined field distribution as compared to the PSP. The spectral sensitivity  $S_\lambda$  for the  $HLP^-$  was calculated by equation 13.7 and we see that it is a bit higher than the LSP (which has a value of around  $1000nm/RIU$ ).  $S_R$  for the HLP is also smaller than that for the PSP.

This property of the HLP (and for most confined modes) is useful for affinity based biosensing. For it, we require a high sensitivity with respect to bound targets but low drift with changes in bulk refractive index. This is treated in the next section where this criteria will be considered to introduce appropriate figures of merit for such affinity based applications.

## Enhancing detection limit for affinity biodetection

Affinity biodetection was introduced in section 3.3. Though sensitivity of plasmonic modes to bulk index changes may be useful in certain applications, for most applications, such changes cause drift and noise in the signal owing to inhomogeneity or fluctuations of temperature for example. Thus affinity biosensors are better characterized by shift in the interrogation quantity with respect to the amount of target molecules bound to the substrate surface (for example to the size of the analyte molecules in nm) rather than to the change in RIU.

The evaluation of the spectral shift for the plasmonic modes in the presence of a layer of bio-molecules is not possible analytically. However for calculations using numerical methods, we can approximate the effect of the target molecules by considering a layer with refractive index close to that of the molecule in bulk. The effective scenario used to calculate the shift of the interrogation quantity in presence of an analyte is shown in figure 14.1. As an example, the direct detection condition shown in figure 3.8 of section 3.3 is considered.

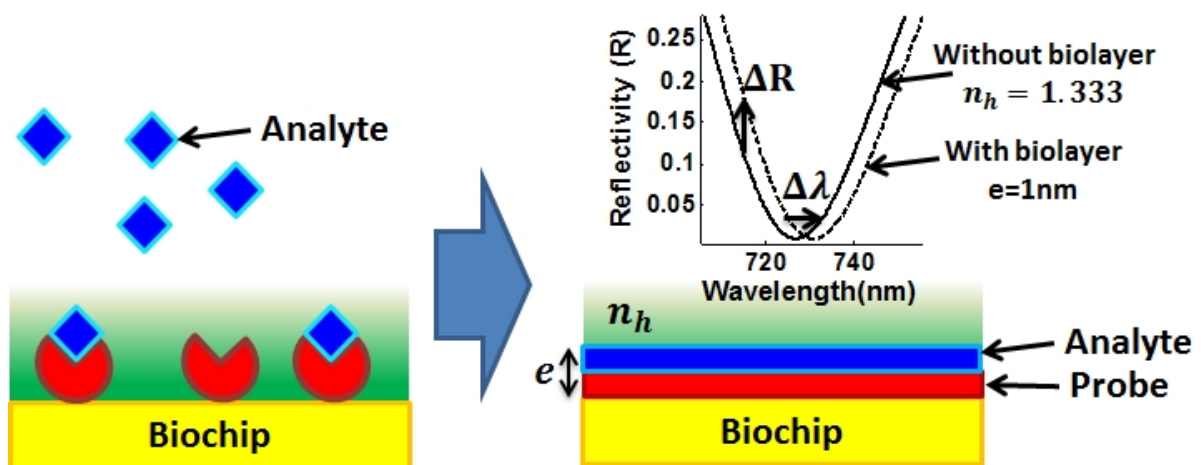


Figure 14.1: Representation of the binding probe and target molecules (analyte) for numerical calculations of reflectivity shift ( $\Delta R$ ) and spectral shift ( $\Delta \lambda$ ). For the inset the reflectivity of a gold film of height  $h = 50nm$  is shown with and without the biolayer at  $(k_{//}/k_0) = 1.4$ . The calculation was done by the Rouard method.

The reflectivity variation (in %) for 1nm of probe-analyte layer with a refractive index  $n_a = 1.48$  was calculated using the Rouard method. For this we have considered a thin gold film of height  $h = 50nm$  in the Kretschmann configuration. Thus here we calculate the properties of the PSP for affinity biosensing. We can define reflectivity sensitivity  $S_{mol:R}$  for affinity biosensors in terms of change of reflectivity ( $\Delta R$ ) due to thickness ( $e$ ) of bio-layer ( $S_{mol:R} = \Delta R/e$  in  $\%/nm$ ). In the same way the spectral sensitivity can be defined as  $S_{mol:\lambda} = \Delta\lambda/e$  in  $nm/nm$  for a spectral shift of  $\Delta\lambda$  in  $nm$ .

The sensitivity of the PSP for a gold film of  $h = 50nm$  is shown in figure 14.2. We will use these values as a reference to characterize the sensitivity of the various other modes. The variation of the sensitivity of the PSP with the height of the gold film is shown in Appendix C.

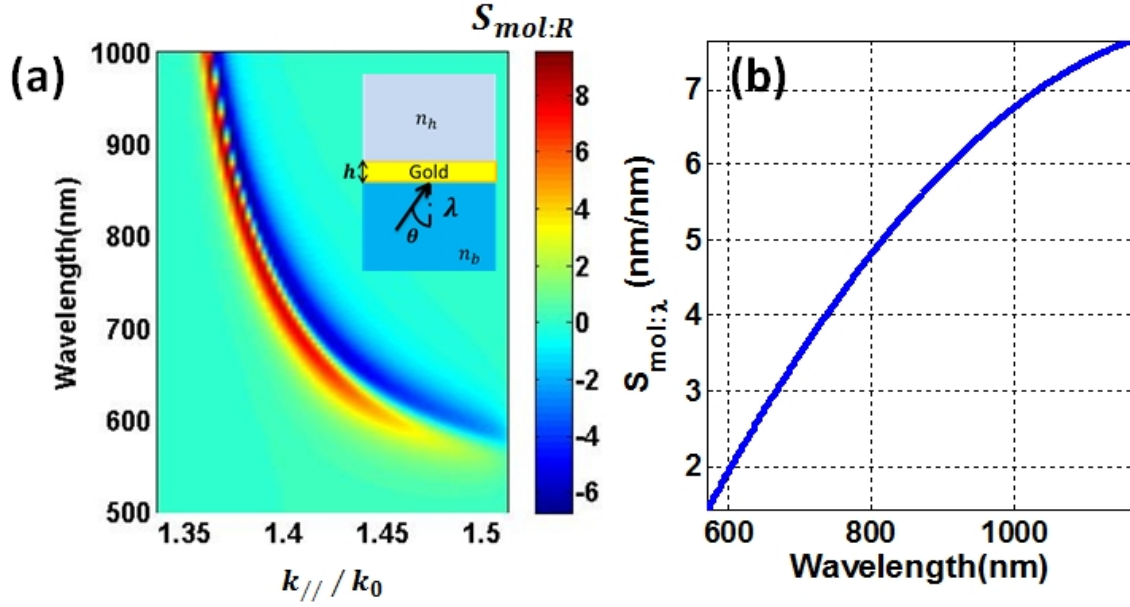


Figure 14.2: (a) The reflectivity sensitivity  $S_{mol:R}$  for 1nm of biolayer with refractive index  $n_a = 1.48$ . The height of the gold film was  $h = 50nm$ . (b) Spectral sensitivity ( $S_{mol:\lambda}$ ) as a function of wavelength ( $\lambda$ ). The refractive index of the substrate is  $n_b = 1.513$  and surrounding medium  $n_h = 1.333$ .

We can see from the results presented in Appendix C and the results for sensitivity for the plasmonic modes, the spectral interrogation (or angular interrogation) is more robust as a detection method than the reflectivity interrogation.

The sensitivity of a biochip depend directly on the amount of analyte bound to the biochip surface. We have defined our sensitivities with respect to the biolayer thickness. However the volume of the biolayer bound to the surface and thus the surface coverage plays a major role in the actual sensitivity of the biochip.

To demonstrate this effect, calculations for an uniform gold film was done by changing the surface coverage of the target biological layer on the surface. This is not possible by the Rouard method because the method is suitable only for uniform layers in the  $x - y$  plane as shown in figure 14.3. However such a calculation of reflectivity is possible with the hybrid numerical method. The scheme of the calculation is shown in figure 14.3. A uniform gold film of height  $h = 50nm$  is considered in the Kretschmann configuration with refractive index of the substrate  $n_b = 1.513$  and the surrounding medium  $n_h = 1.333$ . The thickness of the biolayer is taken as  $e$  and refractive index of the analyte and probe is  $n_a = 1.48$ . We have considered the biolayer to cover a width of  $w$  on the surface and thus a

surface coverage (molecular filling factor) of  $f_{mol} = w_{mol}/\Lambda$  where  $\Lambda$  is the width of the gold film. The calculation was done by a 2D mesh of periodicity  $\Lambda$ . (It should be noted that here  $f_{mol}$  was defined for a 2D structure and is represented as a ratio of lengths, for 3D biochips  $f_{mol}$  is expressed as a ratio of areas.)

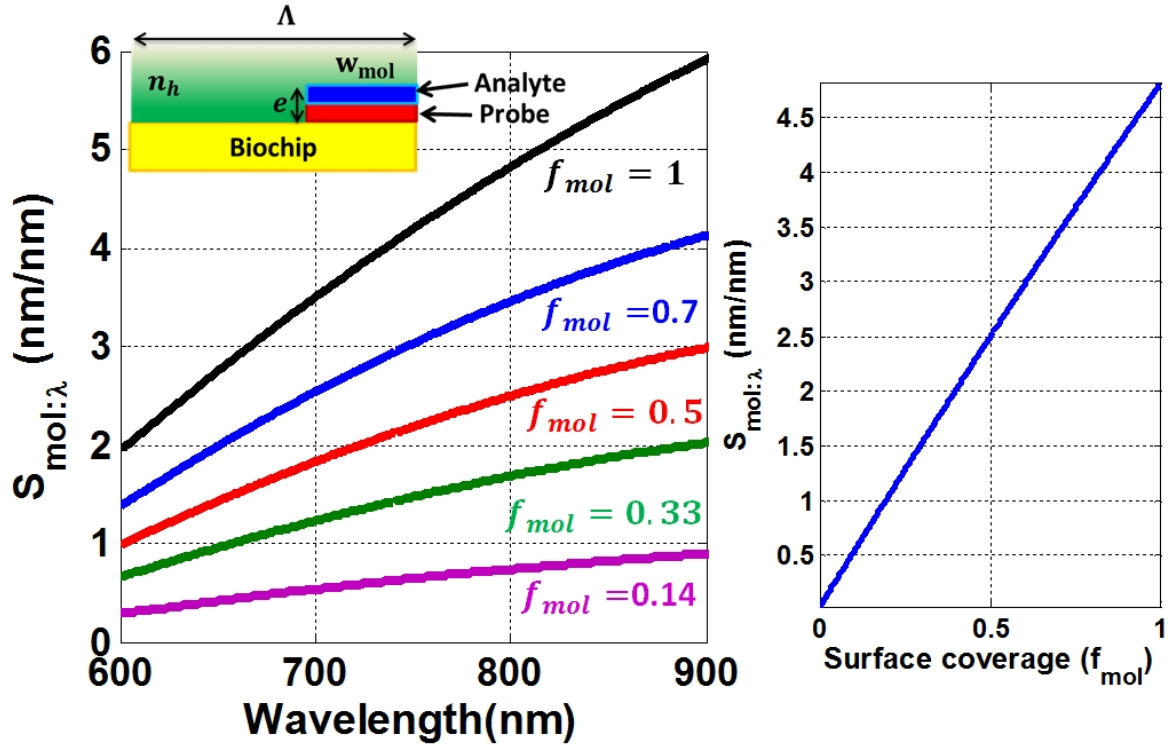


Figure 14.3: Dependence of the spectral sensitivity for target detection ( $S_{mol:\lambda}$ ) for a uniform gold film of height  $h = 50$  nm with a surface coverage of target molecules ( $f_{mol}$ ). (Left) Sensitivity is shown as a function of wavelength ( $\lambda$ ). The scheme of the calculation done by numerical methods is shown. The refractive indices were  $n_h = 1.333$ ,  $n_b = 1.513$  and probe-analyte index  $n_a = 1.48$ . The height of the biolayer was taken as  $e = 3$  nm. The values of sensitivity as a function of surface coverage for  $\lambda = 800$  nm is also shown (right).

The spectral shift in presence of the biological layer ( $\Delta\lambda$ ) was calculated as a function of  $\lambda$ . The plot for  $f_{mol} = 1$  is the same as that of figure 14.2(b). We see as expected, that the sensitivity to the molecules on the surface ( $S_{mol:\lambda}$ ), drops linearly as surface coverage of the target molecule is decreased. Generally the surface coverage is expressed in terms of mass (in  $pg/mm^2$ ). However we choose to express it as a dimensionless quantity and thus as ratio of lengths or areas given by  $f_{mol}$ .

Though this phenomenon is quite well known, however we present this calculation in this work because this is one of the most important limitations of using the PSP for affinity biosensors, that we aim to resolve using other plasmonic modes and nano-structures.

The sensitivity of the plasmonic modes to local refractive changes depends on the electric field distribution of the modes. For the PSP the electric field is uniformly distributed over the entire surface of the thin metallic film and decays exponentially far from the surface. Thus the sensitivity to molecules bound to the surface results from the contribution of all the molecules present on the surface. So a fall in filling factor of the molecules causes a drop in the sensitivity. However as we can see from part V, one can excite various plasmonic modes where the electric field distribution is not uniform but confined to certain

locations of the structured surface (electric field hotspots). Thus the sensitivity to bound molecules for these modes result purely from the molecules present in such locations of high field confinement. We can thus increase the overall sensitivity for affinity detectors by using such plasmonic modes and by selective localization of target molecules in such electric field "hotspots". This will be explained in the next section.

## 14.1 Sensitivity enhancement factor (SEF) for affinity biosensors

For a uniform gold film, the sensitivity is shown to be directly proportional to the volume of the bio-molecules functionalized on the biochip surface. Thus for such biochips we can normalize the sensitivities with respect to the volume of functionalized molecules as

$$S_{mol:Q:PSP} = S_{mol:Q} \times f_{mol} \quad (14.1)$$

where  $Q$  is the quantity measured,  $R$ ,  $\lambda$  or  $\theta$  and  $f_{mol}$  is the surface coverage of the molecules on the biochip. Let us consider that for a certain mode in a period structure, we have a sensitivity  $S_{mol:Q}^{mode}$  for an area  $A_{mol}$  of biomolecules functionalized on the surface and periodicity  $\Lambda$ . Thus we can define a relative sensitivity of the mode with respect to that of the PSP, considering the same surface coverage of the molecules as

$$SEF = \frac{S_{mol:Q}^{mode}/A_{mol}}{S_{mol:Q}^{PSP}/\Lambda}$$

or

$$SEF = \frac{S_{mol:Q}^{mode}}{S_{mol:Q:PSP}} \quad (14.2)$$

SEF (Sensitivity Enhancement Factor) so defined above relates the sensitivity of a plasmonic mode to the surface coverage of the molecules on the biochip surface. A mode which has higher sensitivity with less amount of molecules functionalized on the surface will thus have a higher SEF. For the PSP using an uniform gold film with complete surface coverage of molecules, the  $SEF = 1$ . Such a factor to characterize plasmonic affinity biosensors can be found in the literature [240, 241] and we will use this criteria to characterize the modes described in this work. To simplify the expression of the SEF we can write it as  $SEF = S_{fac}/f_{mol}$  where  $S_{fac}$  defines the ratio of the sensitivity of the mode to that of the PSP using an uniform metallic film.

The physical significance of the SEF for affinity biosensors lies in the fact that surface coverage of the analyte molecules depend on their concentration ( $C_a$ ) present in the solution. For trace concentrations of analyte, the surface coverage is expected to be lower as the amount of molecules present in the solution is not enough to fully cover the surface. Thus for an uniform gold film we expect the sensitivity to decrease for trace concentrations. For plasmonic modes with values of  $SEF > 1$  this decrease in sensitivity with concentration of the analyte will be less than the PSP which has  $SEF = 1$ . Thus SEF can be used to characterize the sensitivity of the system with respect to analyte concentrations.

The main advantage of SPR bio-sensors is the ability to follow the binding kinetics of probe-analyte molecules. For such sensors the evolution of the sensor signal ( $Q$ ) with injection time of the analyte in the fluidic cell is measured. Such a measurement can provide insight on the bio-molecular interactions between the probe and the analyte. For such detectors the evolution of the signal is fitted with a binding model, the simplest among them being the Langmuir model which follows a first-order kinetics [242, 243].

Assuming 1:1 interaction (one probe molecule interacts with one analyte), following the Langmuir model it can be shown that

$$Q(t) = \frac{Q_{max}C_a}{K_D + C_a} \left[ 1 - e^{-(k_a C_a + k_d)t} \right] \quad (14.3)$$

where  $Q_{max}$  is the maximum value of signal achieved at equilibrium with complete surface coverage of probe-analyte,  $C_a$  is the analyte concentration,  $k_a$  (in  $M^{-1}s^{-1}$ ) and  $k_d$  (in  $s^{-1}$ ) are the constants defining rates of association and dissociation of the probe-analyte respectively and  $K_D = k_d/k_a$  called the equilibrium constant. We can identify the term  $Q_{max}$  to be inversely proportional to the surface coverage of the molecules and thus directly proportional to  $SEF$ . Thus a high SEF can assure higher sensitivity for detectors following binding kinetics.

## 14.2 Increasing SEF by selective target localization

One important factor to note for the SEF is that it is inversely proportional to the area of the bio-chip covered by the molecules which cause the measurable signal. Thus to increase SEF, the plasmonic structures must have higher signal ( $\Delta R$  or  $\Delta\lambda$ ) however with less amount of bound target molecules. This is the main aim of using structured biochips and the calculations for their sensitivity would be carried out by covering only the hotspots of the structures with the target biological layers.

We will start with the basic binary grating structure with the incident plane wave parallel to the grating ridges. In such a structure we can excite the CPP as mentioned in sections 9.2.1 and 13.3. We have shown that for large ridge widths the  $PSP_h$  is excited however with a lower contrast owing to the lower surface coverage of the metal. The reflectivity of the structure for large ridge widths was shown in figure 9.17. In figure 14.4 the reflectivity of the same structure is shown for ridge width  $w_1 = 3500nm$ , height  $h = 50nm$  and period  $\Lambda = 7000nm$  and thus a filling factor of  $f = 0.5$ . The reflectivity is calculated at  $(k_{//}/k_0) = 1.46$  ( $\theta = 75^\circ$ ) which is same as figure 9.17. We see the reflectivity dips in the spectrum owing to the  $PSP_h$  and the  $CPP_b$ .

The reflectivity spectrum was also calculated by numerical methods for the same structure with a bio-layer of  $e = 15nm$  and refractive index  $n_a = 1.48$ . For the calculation the biological layer was considered to be present only around the grating ridge as shown in figure 14.4. Thus for the structure the molecular filling factor can be written as  $f_{mol} = (w_1 + 2h)/(\Lambda)$ . We see a spectral shift with the biological layer for all the modes, though the shift for the  $PSP_h$  is much larger than that for the CPPs. The spectral shift was calculated to be  $\Delta\lambda = 29nm$ . Thus the spectral sensitivity in this case is  $S_{mol:\lambda} = \Delta\lambda/e = 1.93nm/nm$  at the reference wavelength  $\lambda = 597.1nm$ . The spectral sensitivity for an uniform gold film using the  $PSP_h$  at  $\lambda = 597.1nm$  as shown in figure 14.2 is  $S_{mol:\lambda}^{PSP} = 1.87nm/nm$ . Thus the sensitivity factor of the mode in the structured biochip with respect to that of the  $PSP$  is  $S_{fac} = 1.93/1.87 = 1.03$ . The SEF can thus be calculated as  $SEF = S_{fac}/f_{mol} = 2.02$ .

Here in this example we see that the sensitivity of an affinity sensor can be enhanced by a factor of 2. The  $PSP$  mode excited in the structure has its electric field confined only around the grating ridges and almost negligible field in the gap between two ridges. This can be seen in the electric field distribution shown in figure 9.21. Thus the molecules functionalized between the grating ridges do not contribute to the overall sensitivity of the structure and almost the entire SPR signal ( $\Delta\lambda$ ) is caused by the molecules

bound to the grating ridges. Thus by selective localization of the molecules only in the locations where they contribute significantly to the SPR signal we can enhance the overall sensitivity of the system with respect to the amount of target molecules used.

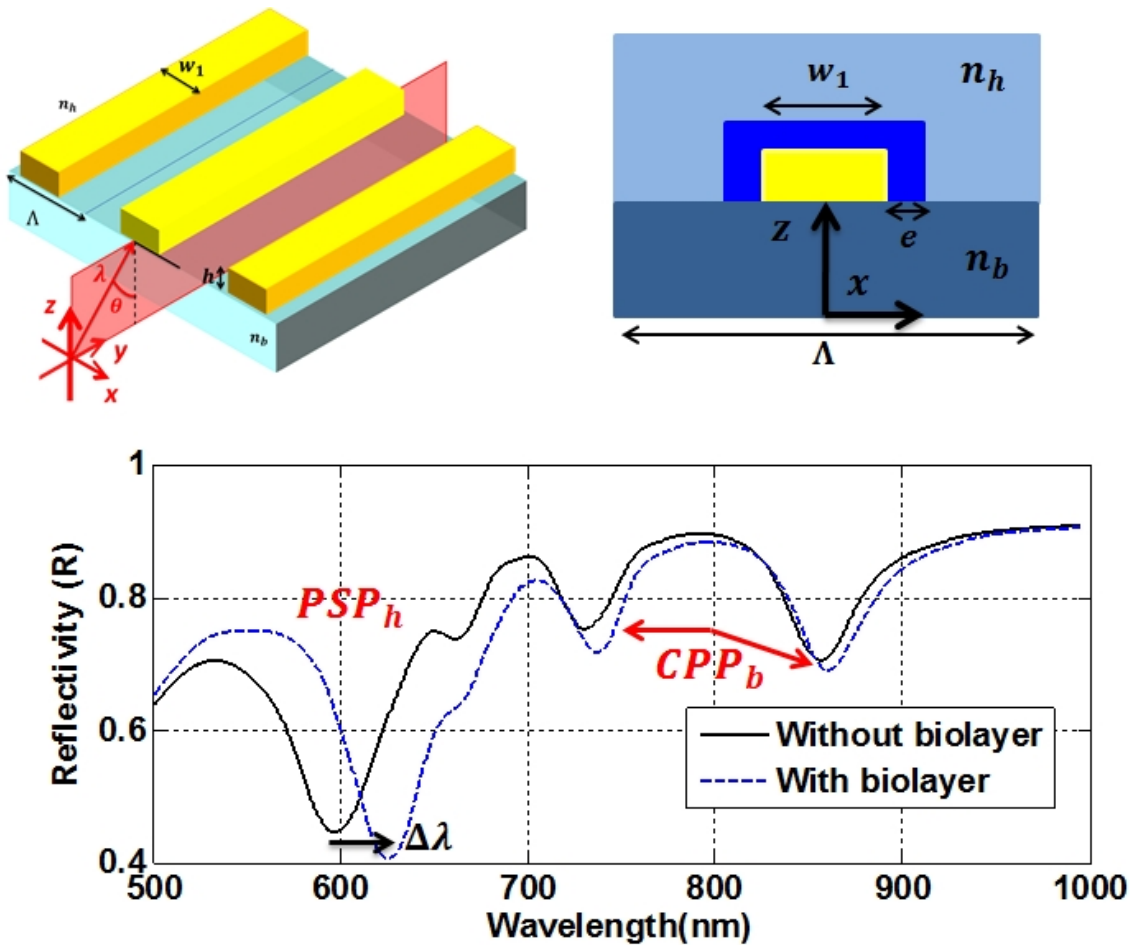


Figure 14.4: (Top) The schematic of the structure for the excitation of the  $PSP_h$  and the  $CPP$ . The biolayer is shown in blue and is considered to be of thickness  $e$  and localized around the grating ridges. (Bottom) The reflectivity of the structure with  $w_1 = 3750nm, h = 50nm, \Lambda = 7000nm$  at  $(k_{//}/k_0) = 1.46$  ( $\theta = 75^\circ$ ) and the refractive indices  $n_h = 1.333$  and  $n_b = 1.513$  (black). The same structure considering the biolayer with  $e = 15nm$  and  $n_a = 1.48$ .

### 14.2.1 The CPP modes for increasing SEF

From the same figure 9.21 we also see that for the  $CPP_b$  a major portion of the electric field is concentrated on the sides of the grating ridges. We can thus use the  $CPP$  mode with selective target localization on the grating sides to increase the SEF.

The reflectivity map for the structure with dimensions  $w_1 = 500nm$  and  $\Lambda = 1000nm$  is shown in figure 13.3 in section 13.3. The two modes  $CPP_h$  and  $CPP_b$  can be excited in the structure. The field distribution of the modes were discussed in section 9.2.2 for incidence from index  $n_h$ . The field distribution of the two modes in the Kretschmann configuration is shown in figure 14.5. The field was calculated using a 3D mesh and the electric field intensity  $I = E_x^2 + E_y^2 + E_z^2$  was normalized to the incident intensity  $I_0$ .



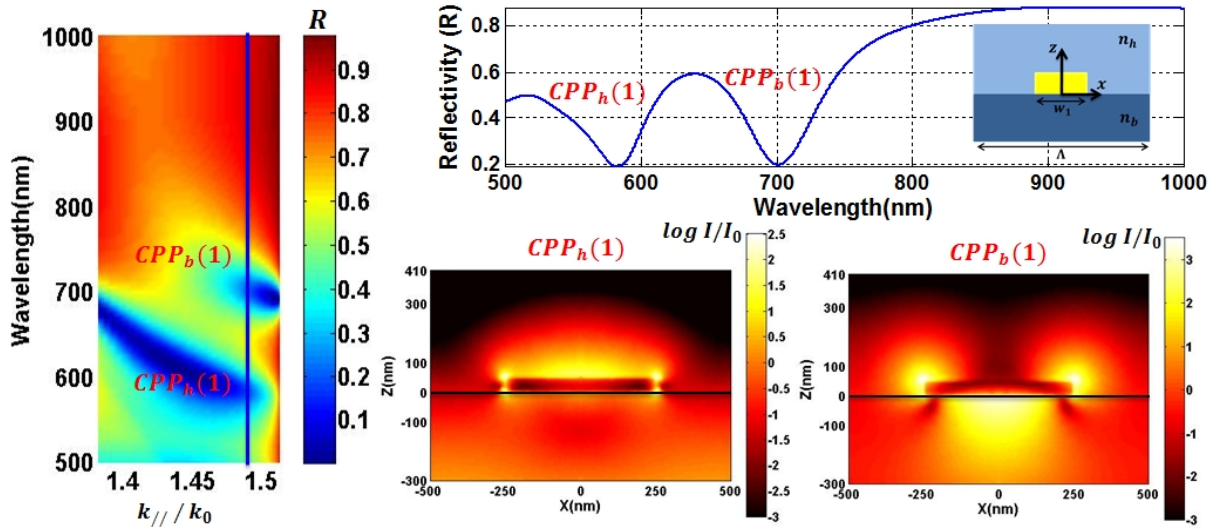


Figure 14.5: The reflectivity spectrum as  $(k_{//}/k_0) = 1.49$  ( $\theta = 80^\circ$ ) for the grating with incident plane wave parallel to the ridges. The dimensions are  $w_1 = 500nm$ ,  $h = 50nm$ ,  $\Lambda = 1000nm$  and the indices  $n_h = 1.333$  and  $n_b = 1.513$ . The electric field intensity in logarithmic scale is also shown for the two modes : $CPP_h(1)$  at  $\lambda = 583.4nm$  ( $k_0 = 10.77/\mu m$ ),  $CPP_b(1)$  at  $\lambda = 701.7nm$  ( $k_0 = 8.95/\mu m$ ).

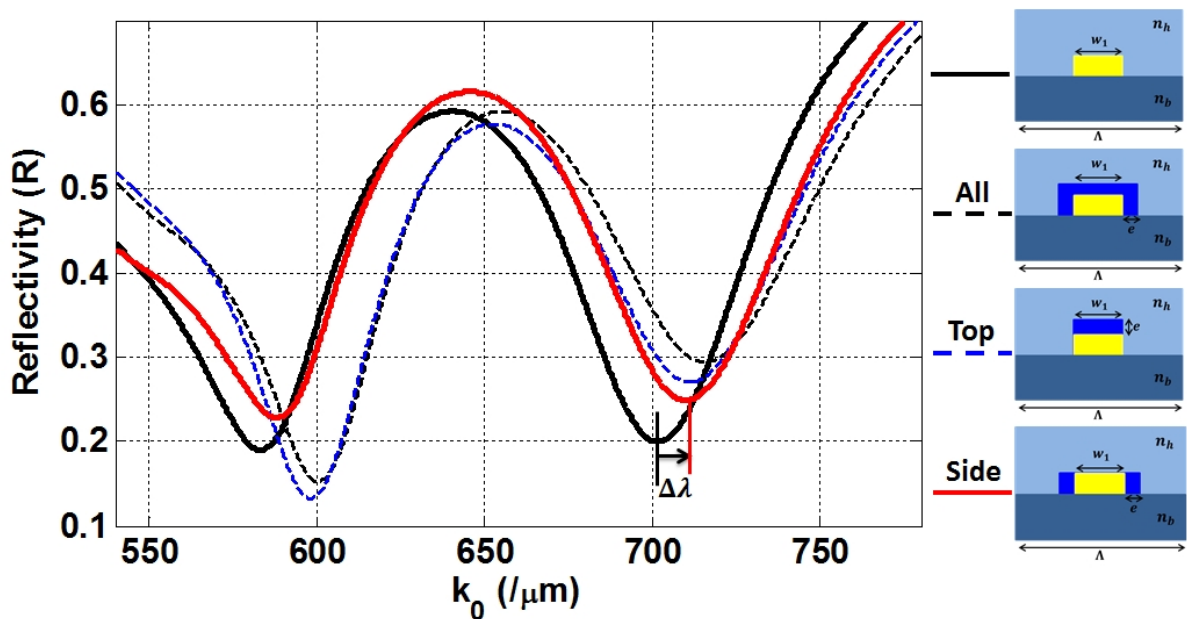


Figure 14.6: The reflectivity of a binary grating of height  $h = 50nm$ ,  $w_1 = 500nm$  and period  $\Lambda = 1000nm$  with incident plane wave parallel to the ridges in the Kretschmann configuration. The indices were  $n_b = 1.513$  and  $n_h = 1.333$ . The biological layer has a thickness  $e = 15nm$  and index  $n_a = 1.48$ . The different biolayer localizations are shown as 'All', 'Top' and 'Side'.

We see the field characteristic similar to figure 9.22 which had the incidence from  $n_h$ . We have one lobe for both the fields as they are both modes of the first order. We also see strong field confinement on the sides of the grating ridges for  $CPP_b$ .

The reflectivity spectrum with a biological layer of  $e = 15nm$  was calculated at  $(k_{//}/k_0) = 1.49$  ( $\theta = 80^\circ$ ) for the structure. The localization of the biolayer was selected as 'top' for the layer only on top of the ridges, 'side' for that on the ridge sides and 'all' for the layer covering the entire grating ridges. The schematic and the reflectivity spectra are shown in figure 14.6.

For all modes, the spectral shift with three biolayer localizations and the spectral sensitivity is shown in table 14.1. The calculation was done at  $(k_{//}/k_0) = 1.49$ . For the two wavelengths of the CPP modes, the sensitivity of the PSP from figure 14.2 is  $S_{mol:\lambda}^{PSP} = 1.63nm/nm$  at  $\lambda = 583.4nm$  and  $S_{mol:\lambda}^{PSP} = 3.55nm/nm$  at  $\lambda = 701.7nm$ . The SEF for the modes were calculated using these values for the  $CPP_h$  and  $CPP_b$  respectively.

Table 14.1: The spectral sensitivity of the CPP modes:  $w_1 = 500nm$ ,  $h = 50nm$ ,  $\Lambda = 1000nm$ . The thickness of the biological layer is  $e = 15nm$ .

$CPP_h$ :  $\lambda = 583.4nm$

Localization and $f_{mol}$	$\Delta\lambda$ nm	$S_{mol:\lambda}$ nm/nm	$S_{fac}$	SEF
All: $f_{mol} = 0.6$	17.1	1.14	0.70	1.16
Top: $f_{mol} = 0.5$	14.9	0.99	0.60	1.20
Side: $f_{mol} = 0.1$	4.2	0.28	0.17	1.70

$CPP_b$ :  $\lambda = 701.7nm$

All: $f_{mol} = 0.6$	14.2	0.94	0.26	0.43
Top: $f_{mol} = 0.5$	9.7	0.64	0.18	0.36
Side: $f_{mol} = 0.1$	8.6	0.57	0.16	1.6

From the table above, we see that for both the modes the SEF can be enhanced by a factor close to 1.6 by localizing the molecules only on the sides of the grating ridges and making use of the fact that the modes have a strongly confined field intensity within a height of 50nm of the ridges. It must be noted that though the SEF is higher for the structures, the signal  $\Delta\lambda$  and thus the sensitivity itself ( $S_{fac}$ ) remains quite low as compared to the PSP of an uniform thin film. This is a disadvantage of using the CPP modes for practical applications where for trace concentrations the signal itself may fall below the limit of detection of the system. In ideal situations we aim to have a  $S_{fac}$  close to 1 and then have high SEF, which was the case for  $PSP_h$  in a binary grating discussed in the last section (section 14.2).

The SEF was calculated with varying the structure period and width. The filling factor was kept as  $f = 0.5$ , thus period  $\Lambda = 2w_1$ . The biological layer was considered to be localized only on the sides of the grating ridges so  $f_{mol} = 2h/\Lambda$ . The variation of the CPP frequencies with the grating width was shown in figure 9.20. For the calculation of SEF, the structure width was changed from 500 – 1000nm.

The SEF as a function of width is shown in figure 14.7. The calculation was done at  $(k_{//}/k_0) = 1.49$ . The resonance frequencies of the CPP modes with  $w_1$  are also shown in the figure.

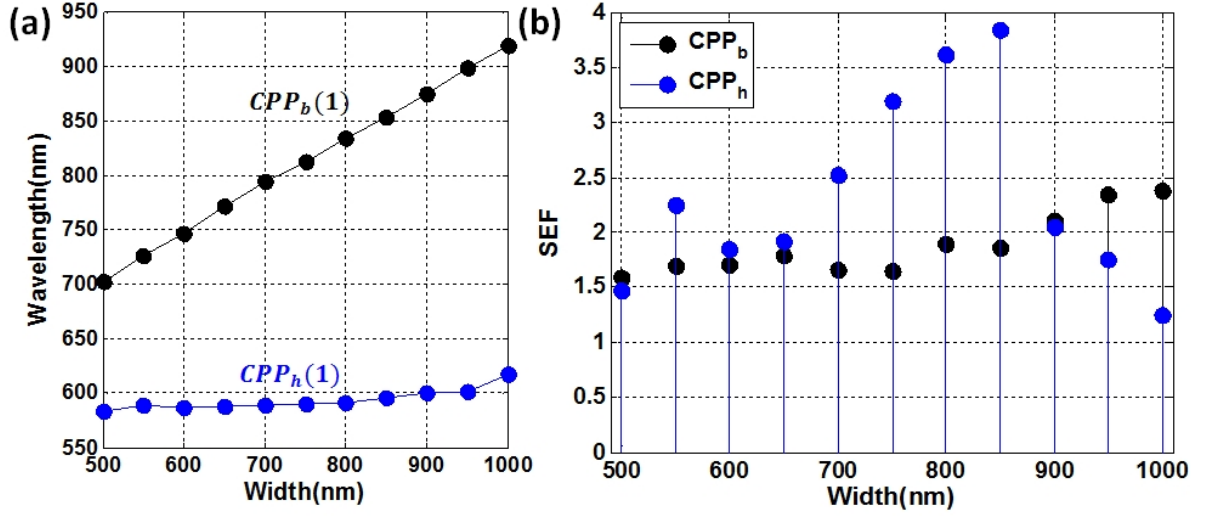


Figure 14.7: (a) The CPP excitation wavelength as a function of grating width  $w_1$  at  $(k_{//}/k_0) = 1.49$  ( $\theta = 80^\circ$ ). The two modes correspond to  $CPP_h(1)$  and  $CPP_b(1)$ . (b) The SEF for the two modes as a function of  $w_1$ . For the calculations period  $\Lambda = 2w_1$ .

We see that the SEF of  $CPP_b$  remains almost constant with  $w_1$ , even though for the structures,  $f_{mol} = 2h/\Lambda$  decreases with  $w_1$ , as we have considered  $\Lambda = 2w_1$ . This is because, the  $S_{fac}$  which is the ratio of the sensitivity of the mode to that of uniform gold film also decreases with increasing width.

We cannot simply increase the SEF just by increasing the periodicity of the structure (or decreasing the amount of localized molecules  $f_{mol}$ ). This is because the dispersion of the  $CPP$  mode depends on  $w_1$  and by changing it we also change the property of the mode, namely the field confinement and the effective sensitivity of the mode. Thus if we wish to increase SEF by increasing the geometrical dimensions of the structure (thus decreasing  $f_{mol}$ ) we must be careful to play with the dimensions that do not affect the intrinsic dispersion of the mode.

Now we will demonstrate that the sensitivity  $\Delta\lambda$  and thus  $S_{mol:\lambda}$  is however not directly proportional to the confined electric field intensity of the mode. This is shown in figure 14.8. The near field intensity ( $I$ ) normalized to the incident intensity, for the structures at the wavelength of the  $CPP_b$  was calculated using a 2D mesh for each  $w_1$ . Then the surface integral of the field intensity was calculated as  $I_{surf:side}$  by the method described in section 10.3. For the calculation the bio-layer was considered to be present only on the sides of the grating ridges and thus

$$I_{surf:side} = \frac{2}{h} \int_0^h I(l) dl \quad (14.4)$$

We see that the calculated  $S_{mol:\lambda} = \Delta\lambda/e$  for molecule localization on the sides do not follow the evolution of the electric field intensity on the sides of the cylinder. This is because the sensitivity is not proportional to the absolute electric field intensity of the mode at the position of the localized molecules, but rather is proportional to the change in the field intensity brought about by the localized molecules. This is shown experimentally in section 15.2.1.

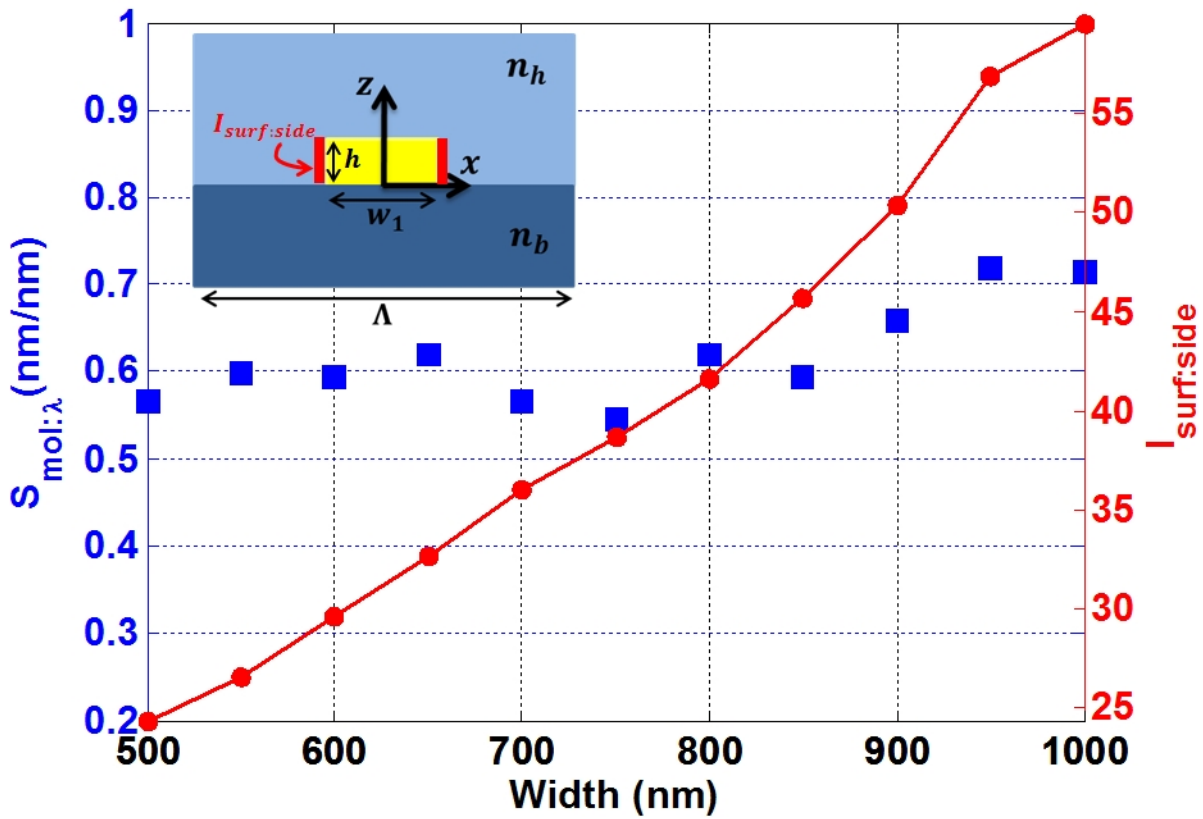


Figure 14.8: The variation of the spectral sensitivity with biolayer of thickness  $e = 15nm$  and localization on the sides of the gratings as a function of grating width  $w_1$ . The values were calculated for  $CPP_b(1)$  at  $(k_{//}/k_0) = 1.49$  and  $\Lambda = 2w_1$  (left axis). The corresponding integrated electric field intensity ( $I_{surf:side}$ ) was calculated at the wavelengths of the  $CPP_b(1)$  mode (shown in figure 14.7(a))(right axis).

Having said this, it is also true that field confinement plays a major role in sensitivity enhancement. As the sensitivity is proportional to the change of field intensity, selective target localization must assure that the target molecules are bound to the electric field "hotspots" so that they can affect the maximum possible change to the field intensity and thus assure higher sensitivity.

Another point to note from figure 14.7(b) is that the SEF increases for the  $CPP_h$  at certain  $w_1$ . This is because for higher  $w_1$  the  $PSP_h$  and the  $CPP_h$  overlap (see figure 9.19), thus the sensitivity obtained is different from both the  $PSP$  and  $CPP_h$  considered separately.

### 14.2.2 Increasing SEF using the HLP mode

We have shown in the last section that molecular localization help to enhance SEF owing to the fact that the signal is achieved using less amount of target molecules. For arrays of metallic structures on a thin metallic film, we have the possibility to confine the electric field close to the structures with the HLP mode. This was discussed in chapters 11 and 12. The field distribution of the HLP mode as discussed in section 12.3 shows a high field confinement close to the cylinders and almost negligible field on the surface of the underlying metallic film. Thus to enhance SEF, it is evident that we need to localize the target molecules around the cylinders.

The bulk index sensitivity for the HLP mode was shown in section 13.4. Such bulk sensitivity for the HLP mode is much less as compared to that of the PSP. This is because the electric field of the HLP, owing to its LSP component, is much more confined than that of the PSP. However this very property for the HLP can serve to be useful for target induced detection where the local field confinement plays the important role.

To characterize the spectral sensitivity of the HLP with target localization around the nanocylinders we will consider the same structure as presented in figure 13.4. The reflectivity dispersion was calculated using a bilayer of thickness  $e = 4nm$  of refractive index  $n_a = 1.48$ . The reflectivity sensitivity for the structure  $S_{mol:R} = \Delta R/e$  in  $\%/nm$  is shown in figure 14.9.  $S_{mol:R}$  is lower for the HLP than that for the *PSP*, the later shown in figure 14.2. However, the diameter of the cylinders is  $D = 50nm$ , with height  $h_2 = 30nm$  and periodicity of  $\Lambda = 300nm$ . Thus, with the bilayer considered only around the cylinders, the surface coverage of the molecules is much lower in this case than for an uniform metal film with complete coverage. The surface coverage (in this case defined as ratio of areas unlike the 2D case where it was a ratio of lengths) is given by

$$f_{mol} = \frac{\frac{\pi D^2}{4} + \frac{2\pi D h_2}{2}}{\Lambda^2} \quad (14.5)$$

For the chosen structure the surface coverage is  $f_{mol} = 0.074$ . We can define the reflectivity SEF in the same way as the spectral SEF as

$$\begin{aligned} SEF_R &= S_{fac}/f_{mol} \\ &\text{where} \\ S_{fac}(\lambda) &= \frac{S_{mol:R}^{mode}(\lambda)}{S_{mol:R}^{PSP}(\lambda)} \end{aligned} \quad (14.6)$$

For the calculation the  $S_{mol:R}$  for the uniform gold film (PSP) was evaluated for each excitation wavelength ( $\lambda$ ) and was used to normalize that of the structure. The  $SEF_R$ , as a function of ( $\lambda, (k_{//}/k_0)$ ) is shown in figure 14.9. We see that the SEF can reach values up to **12** using the HLP mode.

Similarly, the spectral shift ( $\Delta\lambda$ ) was calculated for the  $HLP^-$  mode as a function of period for  $(k_{//}/k_0) = 1.42$ . Cylinders of height  $h_2 = 30nm$  and diameter  $D = 50nm$  was used for the calculations. The bilayer layer thickness was considered to be  $e = 4nm$  and index of  $n_a = 1.48$ .

The excitation wavelength of the  $HLP^-$  mode (reflectivity dip for the structure) as a function of period is shown in figure 14.10. The analytical calculation for the dispersion of the HLP and the BMs are also shown in the figure (same as figure 12.4(a)). The spectral sensitivity ( $S_{mol:\lambda}$ ) for the corresponding reflectivity dip is shown in figure 14.10(b).

We must recall here the two regimes for the HLP modes introduced in section 12.3, namely the confined regime and the extended regime. The two regimes were shown as a function of period for  $(k_{//}/k_0) = 1.42$  in figure 12.8. For the present results, the periodicity was varied from  $\Lambda = 160 - 520nm$  with steps of  $40nm$ . For these periods the confined HLP is excited for  $\Lambda = 160 - 240nm$  and the extended HLP for  $\Lambda = 320 - 520nm$  with the  $BM(\Lambda)$  being excited for  $\Lambda = 280nm$  at the  $(k_{//}/k_0)$  used for the calculation. For periods  $\Lambda > 440nm$  in the present calculation, the HLP comes under the influence of the  $BM(\Lambda + D)$ .

We clearly see these trends in the calculation of  $S_{mol:\lambda}$ . As mentioned in the previous section, the spectral sensitivity depend on the change brought about to local electric field intensity by the bound

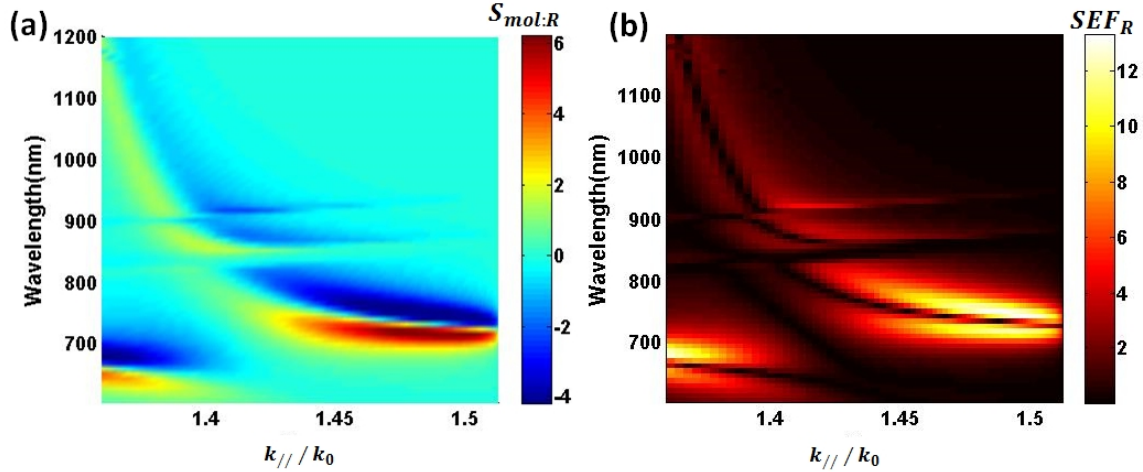


Figure 14.9: (a) The reflectivity sensitivity  $S_{mol:R}$  calculated for an array of gold cylinders of  $D = 50nm$ ,  $h_2 = 30nm$  and  $\Lambda = 300nm$  on an uniform gold film of height  $h_1 = 30nm$ . The refractive indices were  $n_h = 1.333$  and  $n_b = 1.513$ . A bilayer of thickness  $e = 4nm$  was considered around the cylinders with refractive index  $n_a = 1.48$ . (b) The calculated  $SEF_R$  for the structure as a function of  $(\lambda - (k_{//}/k_0))$ .

molecules. This field confinement and change to the field intensity is higher for the confined regime of the HLP. Thus we have higher spectral sensitivity for the smaller periods. For  $\Lambda = 240nm$  the spectral sensitivity is almost zero because of the BM, which is an extended mode. For higher periods we have lower  $S_{mol:\lambda}$  because the HLP excited for those periods at  $(k_{//}/k_0) = 1.42$  is extended. For  $\Lambda > 440$  the field intensity around the cylinders and thus the  $S_{mol:\lambda}$  is even lower because of the influence of  $BM(\Lambda + D)$ .

The SEF however is higher for larger periods because the surface coverage  $f_{mol}$  decrease as the square of the period (equation 14.5) thus increasing SEF rapidly with period. For effective affinity sensing both the SEF and  $S_{mol:\lambda}$  must be considered for optimizing the structures. Just a high SEF with very low spectral shift may not be useful as then the detectable signal ( $\Delta\lambda$ ) is too low for effective measurement. As an example, for this present structure geometry with cylinder diameter of  $50nm$ , the optimum period for effective detection is  $\Lambda = 400nm$  at incident angle  $\theta = 70^\circ$  ( $(k_{//}/k_0) = 1.42$ ). However it may well be different if other incident angle is considered. For such optimization the actual mode responsible for the reflectivity dip must be studied and thus the detailed understanding of the excitation of the modes presented in part IV is of paramount importance.

It is clear from the results that to have higher SEF we have to increase the periodicity of the structures and decrease the area over which the molecules are functionalized. For the current example of cylinder arrays we need to have smaller cylinder diameters and larger array periods. But with a square array, increasing the period in turn causes a shift of the resonance frequencies of the modes and thus changes the inherent sensitivity of the modes. As was stated in the previous section, if we need to increase the SEF by increasing the period, we need to play with the dimension which does not affect the dispersion of the HLP mode.

Recalling the concept of modes in terms of  $(k_0, (k_{//}/k_0))$  (chapter 8), the dispersion was characterized along a certain direction called the vector  $\vec{p}$ . For the HLP (chapter 12) this vector was defined along  $x$  axis of the structure. The dispersion of the BMs and the HLP are defined along this particular axis

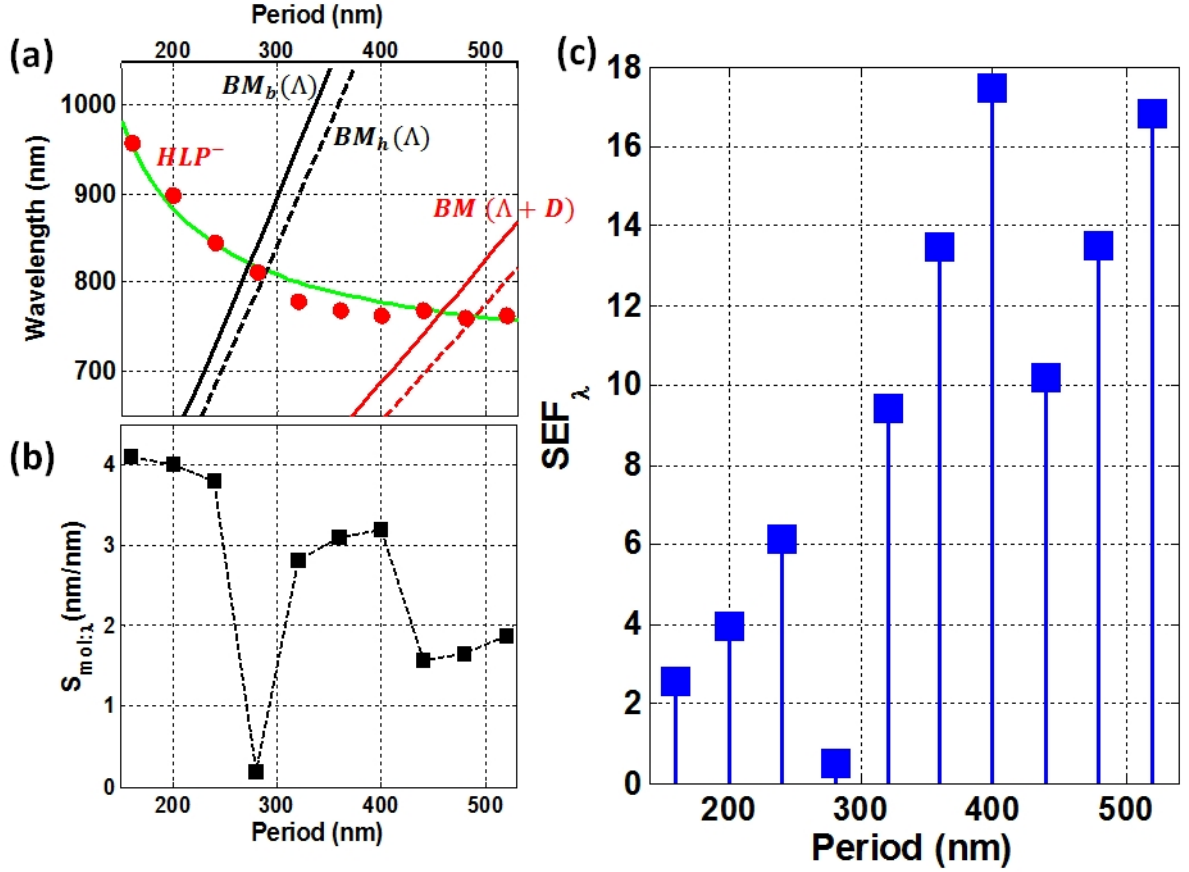


Figure 14.10: (a) The wavelength of the reflectivity minima for the HLP mode as a function of the array period ( $\Lambda$ ). The structure geometry is same as figure 14.9. The analytical calculation of the HLP and the BMs are also shown in the figure. (color code same as figure 12.4). (b) Spectral sensitivity of the corresponding reflectivity dip shown in (a) as a function of period. The biological layer was considered only around the cylinders and thickness  $e = 4nm$ . (c) The SEF of the same as a function of period.

and the period along the  $x$  axis plays the major role in the excitation condition of the modes. However the dispersion (mainly that of the BM) should be almost independent of the periodicity along an axis orthogonal to  $x$  (in this case  $y$  axis). We can then assume that an increase of the period along  $y$  ( $\Lambda_y$ ) will help to increase the SEF, however not affect the sensitivity ( $S_{mol:\lambda}$ ) of the modes.

The reflectivity was calculated with varying only the periodicity along  $y$  axis (rectangular array) and is shown in figure 14.11. As before the biolayer was considered only around the cylinders. The period along  $x$  was taken as  $\Lambda_x = 160nm$ .

The contrast of reflectivity and the resonance wavelengths of the BMs do not change with the period along  $y$ . We only notice a slight blue shift of the HLP wavelength. We must recall that the coupling parameter for the HLP was defined as  $\Gamma_{12} = (1/\tau^2) \times (h_2 + D)/\Lambda$  in section 12.1 for square array. In fact the dependence of the coupling parameter on the period is rather  $\sqrt{\Lambda_x \Lambda_y}$  for a rectangular packing when  $\Lambda_x \neq \Lambda_y$ . Thus as  $\Lambda_y$  is increased the coupling parameter decreases and thus there is blue shift of the  $HLP^-$  mode (the same trend for the  $HLP^-$  with period of the square array).

The sensitivity ( $S_{mol:\lambda}$ ) of the mode also does not change with  $\Lambda_y$ . However the surface coverage of the molecules which is now  $f_{mol} \propto 1/(\Lambda_x \Lambda_y)$  decreases with  $\Lambda_y$  and thus we can effectively increase the  $SEF$  of the structure. This is shown in figure 14.11(c) for  $\Lambda_x = 160nm$ .

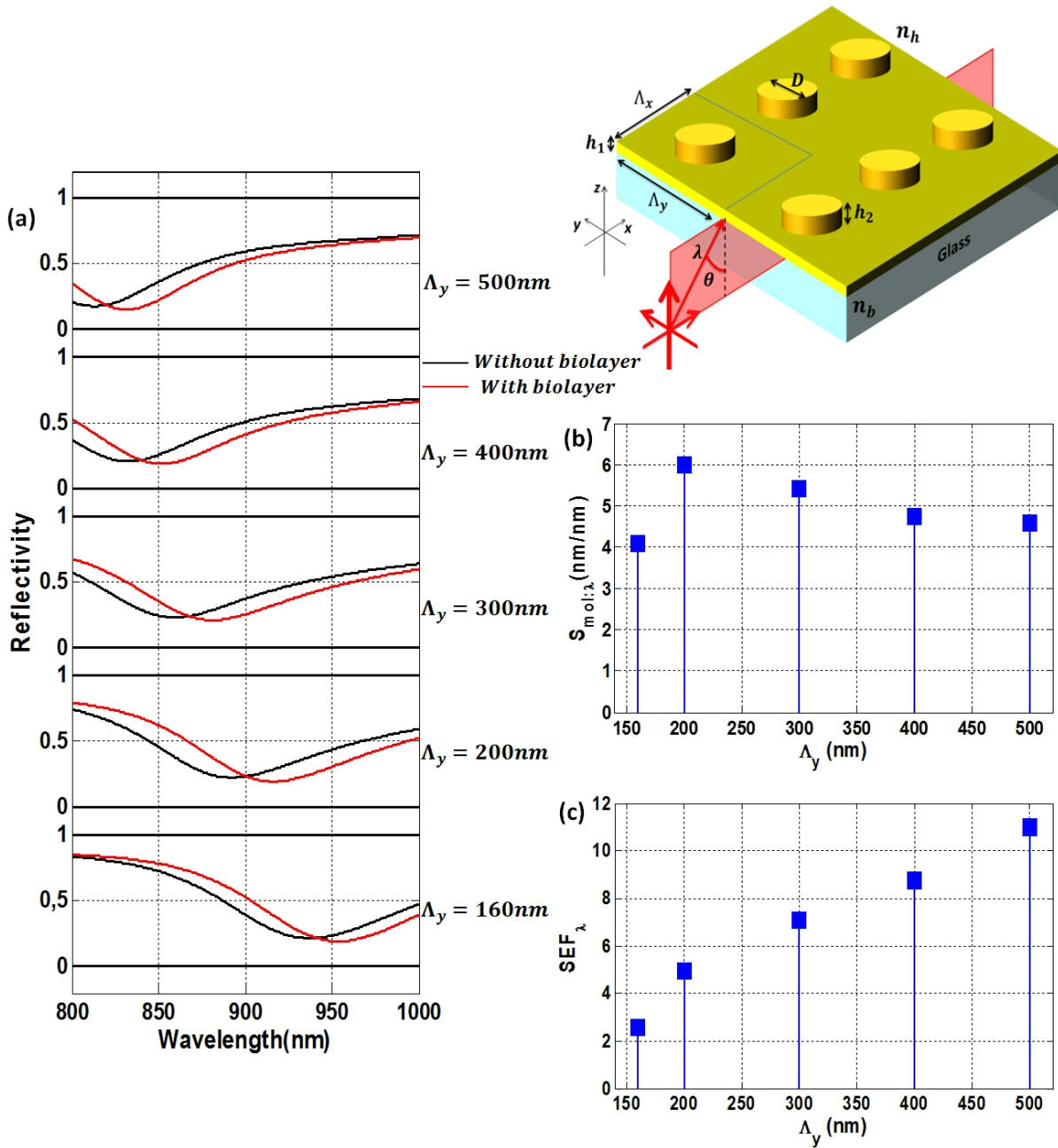


Figure 14.11: (a) Reflectivity as a function of wavelength  $\lambda$  for an rectangular array of cylinders with dimensions  $h_2 = 30nm$ ,  $D = 50nm$ ,  $\Lambda_x = 160nm$  for different periods along  $y$  ( $\Lambda_y$ ). The geometry is shown above. The curves with and without a biolayer of thickness  $e = 4nm$  localized around the cylinders is shown. (b) Spectral sensitivity  $S_{mol:\lambda} = \xi \Delta\lambda/e$  as a function of period along  $y$ . (c) The spectral  $SEF_\lambda$  in the same configuration.



To conclude on the SEF, an even higher SEF than those values shown here can be achieved by playing with the periods along the two axes and making certain that the working  $(\lambda, \theta)$  is chosen so that we excite the confined regime of  $HLP^-$ . It also assures a high enough signal  $S_{mol:\lambda}$  which is comparable to that of the PSP in a uniform metallic film with  $S_{fac}$  values close to 1.



---

# Experimental excitation of the modes in Kretschmann configuration

---

The SPR configuration used in this work was described in brief in section 3.2. In Kretschmann configuration, a glass prism is used to couple the incident light to the plasmons. A monochromator allows to scan the incident wavelength ( $\lambda$ ) and a motorized platform helps to scan the angle of incidence ( $\theta$ ) of the light. The incident light is collimated and polarized (TM or TE), thus we have an incident plane wave similar to the condition used in the numerical calculations.

The experimental bench is shown in figure 15.1. The various parts of the experimental setup will be described in brief.

**Light source:** A halogen lamp is used as the white light source. The lamp is coupled to a monochromator (iHR 320, HORIBA Scientific) to scan the incident wavelengths within the range 500-1500nm. The spectral width of the light can be adjusted by slits at the exit of the monochromator and was fixed to be 13nm to limit the speckle. The light from the monochromator is collected by an optical multimode fiber with a core diameter of 365  $\mu\text{m}$ .

**Collimating system:** The light from the fiber is collimated to obtain a beam of diameter 1cm and a residual angular divergence of  $0.23^\circ$ . A linear polarizer operated by a motor is used at the exit of the collimator to select TM or TE polarization of the incident beam with respect to the biochip-flow cell interface.

**Imaging system:** The light reflected from the biochip is collected by an objective and then imaged with a CCD camera (Pixelfly QE,  $1392 \times 1024$  pixels with a full well capacity of  $18000 e^-$ ). The objective has optical zoom to adapt to the size of the zone on the imaged biochip.

**Motorized angle scanning system:** The angle of incidence at the biochip-flow cell interface is scanned using a motorized platform to rotate the collimating system and the imaging system. The angle between the biochip-flow cell interface and the axis of the incident beam is considered to be the external angle of incidence ( $\theta_{ext}$ ). The internal angle of incidence  $\theta$  is defined as the angle between the incident beam and the axis perpendicular to the biochip-flow cell interface after refraction in the prism. The relation between the external angle and internal angle of incidence is given by  $\sin(\theta - A) = \sin((\pi/2 - A - \theta_{ext})/n_{pr})$  where  $A$  is the base angle and  $n_{pr}$  is the refractive index of the prism used.

The angle between the axis of the camera objective and the axis perpendicular to the biochip-flow

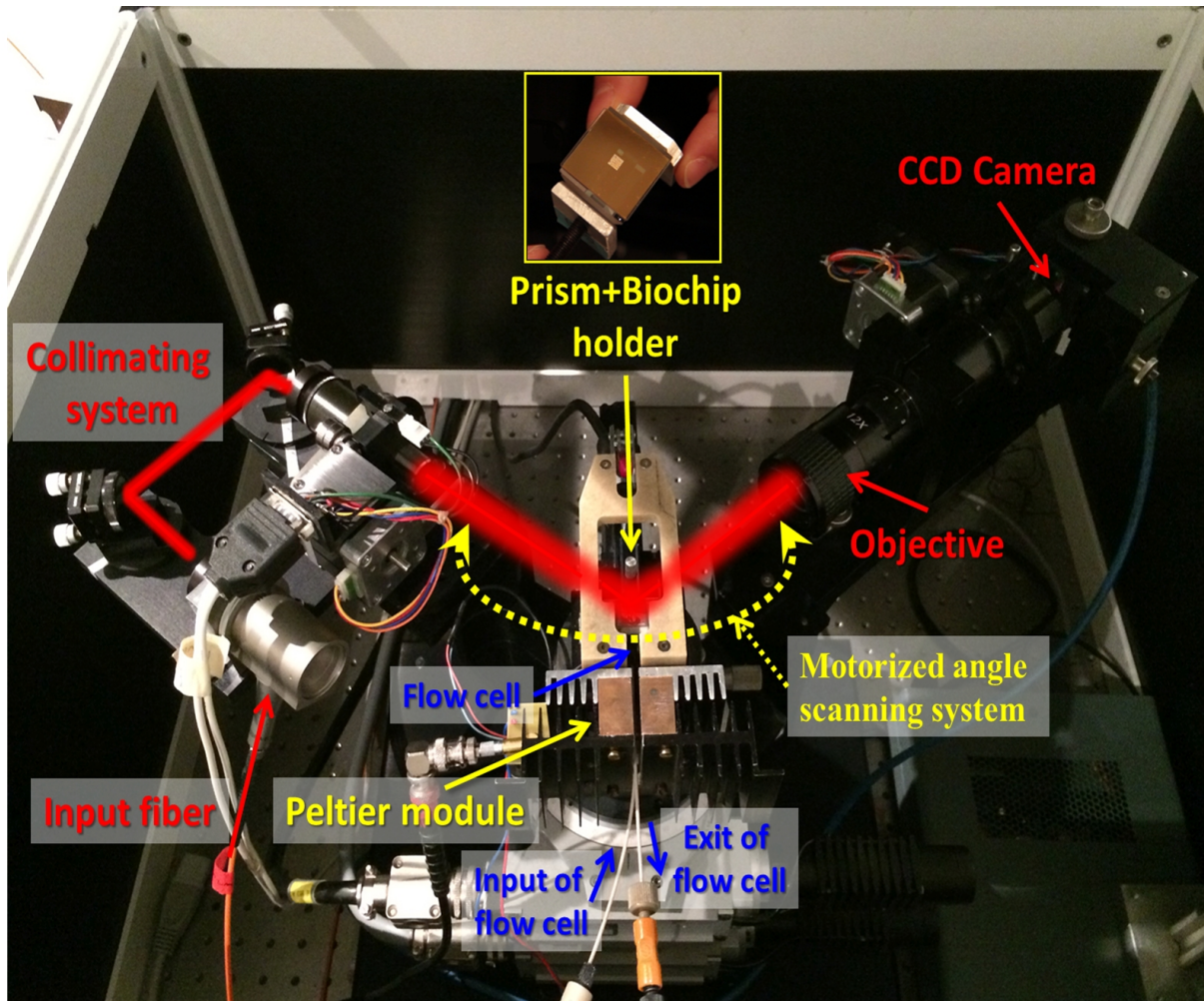


Figure 15.1: Picture of the SPR imaging system in Kretschmann configuration. The incident light from a monochromator is collected by a multimode fiber and then collimated and polarized. The biochip along with the prism is placed in the holder and the flow cell comprising of a Mylar film is attached to the biochip surface. Light reflected from the biochip-flow cell interface is collected by the imaging system comprising of an objective and a CCD camera.

The analyte solution is injected into the flow cell using a fluidic system. The temperature of the flow cell is stabilized by a Peltier module. The collimating system and the imaging system are placed on a motorized platform which permits the scanning of the incidence angle. Since for the setup, the angle of incidence and the angle of collection by the imaging system is fixed to be equal, the system can only record the specular reflection from the biochip.

cell interface gives us the imaging angle. For the motorized platform the external incident angle and the imaging angle are fixed to be equal and thus for the system only the specular reflection from the biochip surface can be imaged. Light backscattered by diffraction from the biochip is thus not collected by the camera. The external angle  $\theta_{ext} = 0$  ( $\theta = 79.29^\circ$  with a  $60^\circ$  BK7 prism), is defined when the collimator and the camera objection face each other. The scanning systems allows us to vary the angle of incidence within a range of  $0 - 45^\circ$  for the external angle ( internal angle  $\theta = 50.16 - 79.29^\circ$  with a  $60^\circ$  BK7 prism).

**Fluidic system:** A fluidic system is used to inject the solution of target analyte. The solution is fed into the flow cell by a peristaltic pump equipped with a degazer to avoid air bubbles in the flow cell. The fluid from the pump is pushed into a solid block of titanium into which two holes are drilled which serve as the entry and exit of the flow cell. A circle of 1cm diameter cut into a Mylar film of thickness  $90 \mu\text{m}$  serves as the flow cell and it is attached to the surface of the biochip.

For the measurements shown in this work, the water was injected into the flow cell and is the bulk medium. Sucrose solution was used to study the sensitivity of the biochip to bulk index changes. For affinity detection experiments the solution of the analyte was pumped into the flow cell for a fixed duration of time (as required for the analyte to attach to the biochip surface) and then water was injected to wash away the unbound analyte molecules.

**Peltier module:** The temperature of the flow cell is regulated with a precision of  $0.01^\circ\text{C}$  using a Peltier module. For the experiments shown in this work, the temperature was fixed at  $22^\circ\text{C}$ .

**Data processing:** An image of the biochip surface acquired by the system at a particular wavelength and incidence angle is shown in figure 15.2. Images taken with TM polarized are normalized to that taken with TE polarization. The angle of incidence for all the experiments shown, is larger than the critical angle of the prism-flow cell interface. Thus for TE polarization, considering that the plasmonic modes are not excited for this configuration, the image results from total internal reflection of the incident light. This normalization helps to correct the inhomogeneities caused by the illumination system.

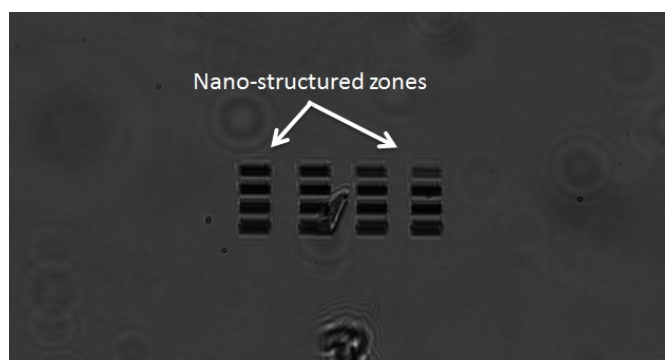


Figure 15.2: Image of a structured biochip as obtained by the CCD camera at a given incident angle and wavelength with TM polarized incidence.

Such value of reflectivity was calculated at the structured zone visible in figure 15.2. TM and TE images were acquired at each value of  $\lambda$  and  $\theta$  to obtain a complete dispersion map of the reflectivity as a function of  $\lambda$  and  $\theta$ . The acquisition was monitored by a home made Labview code.

## 15.1 Experimental characterization of the CPP modes

The Confined Propagating Plasmons (CPP) were described in section 9.2.1. Such plasmonic modes can be excited in a binary grating structure when light is incident parallel to the grating ridges. The dispersion of the CPPs with grating width was shown in figure 9.20. To confirm the numerical results, a binary grating was fabricated using e-beam lithography. The fabrication technique is briefly described in section 5.2. For this experiment, the structure was fabricated on a BK7 (borosilicate glass) slide, with grating height  $h = 50nm$  and width  $w_1 = 700nm$ . The period of the grating was taken as  $\Lambda = 1400nm$  and thus a filling factor of  $f = 0.5$ . The structure was fabricated by Anne-Lise Coutrot, Ingénieur de Recherche, CNRS at the clean-room of Thales Research and Technology, Palaiseau.

The biochip was characterized using the SPR imaging system described in the last section. The image of the biochip acquired is shown in figure 15.3. Multiple zones of the grating structure was fabricated on the same biochip so that different zones of the biochip can be studied simultaneously. Scanning electron microscope (SEM) images of the structured zone were acquired to verify the fabrication process. One such image is shown in figure 15.3. The grating fabricated was homogeneous in dimensions with a precision of about  $\pm 2nm$  on the width and period. An adhesion layer of  $2nm$  titanium was used between the glass and the grating ridges.

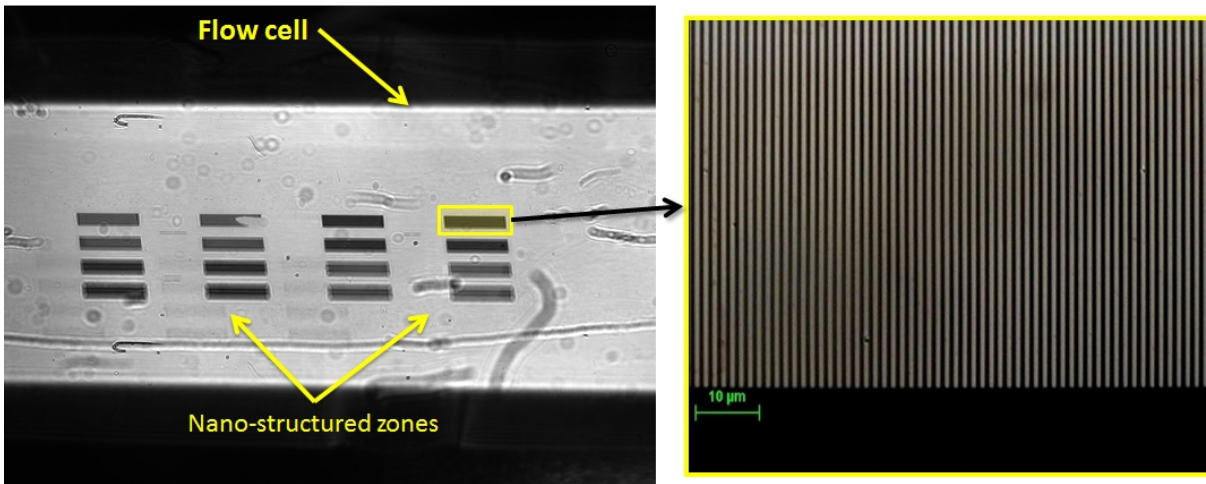


Figure 15.3: The image of a structured biochip as obtained by SPR imaging system. The edge of the flow cell is visible in the image. Multiple zones of the grating structure were fabricated on the biochip. The grating height was taken as  $h = 50nm$ , width of  $w_1 = 700nm$  and period  $\Lambda = 1400nm$ . The structure was fabricated on a BK7 glass substrate. An adhesion layer of  $2nm$  titanium was used. A SEM image of the structured zone is also shown (right).

Reflectivity value was extracted from the image obtained by the SPR setup for each wavelength and angle of incidence. The reflectivity dispersion map is shown in figure 15.4. As expected no reflectivity drop was observed for the TE polarized incidence. The angle of incidence was changed from  $\theta_{ext} = 1^\circ$  to  $\theta_{ext} = 30^\circ$  with a step of  $1^\circ$  which corresponds to the change of internal angle  $\theta = 60^\circ$  to  $\theta = 79^\circ$  with steps of  $0.6^\circ$ . The wavelength was changed from  $\lambda = 550nm - 900nm$  with steps of  $10nm$ . The reflectivity map is shown as a function of  $\lambda$  and  $\theta$ , which are the measured quantities. The existence of the two modes, namely the  $CPP_b(1)$  and the  $CPP_h(1)$  are clearly visible in the reflectivity map, which manifest as drops in reflectivity. The reflectivity calculated by numerical methods and shown

elsewhere in this work (figures 9.19,13.3 and 14.5) however has a much higher contrast (ratio of maximum and minimum of reflectivity) than that obtained in the experimental reflectivity.

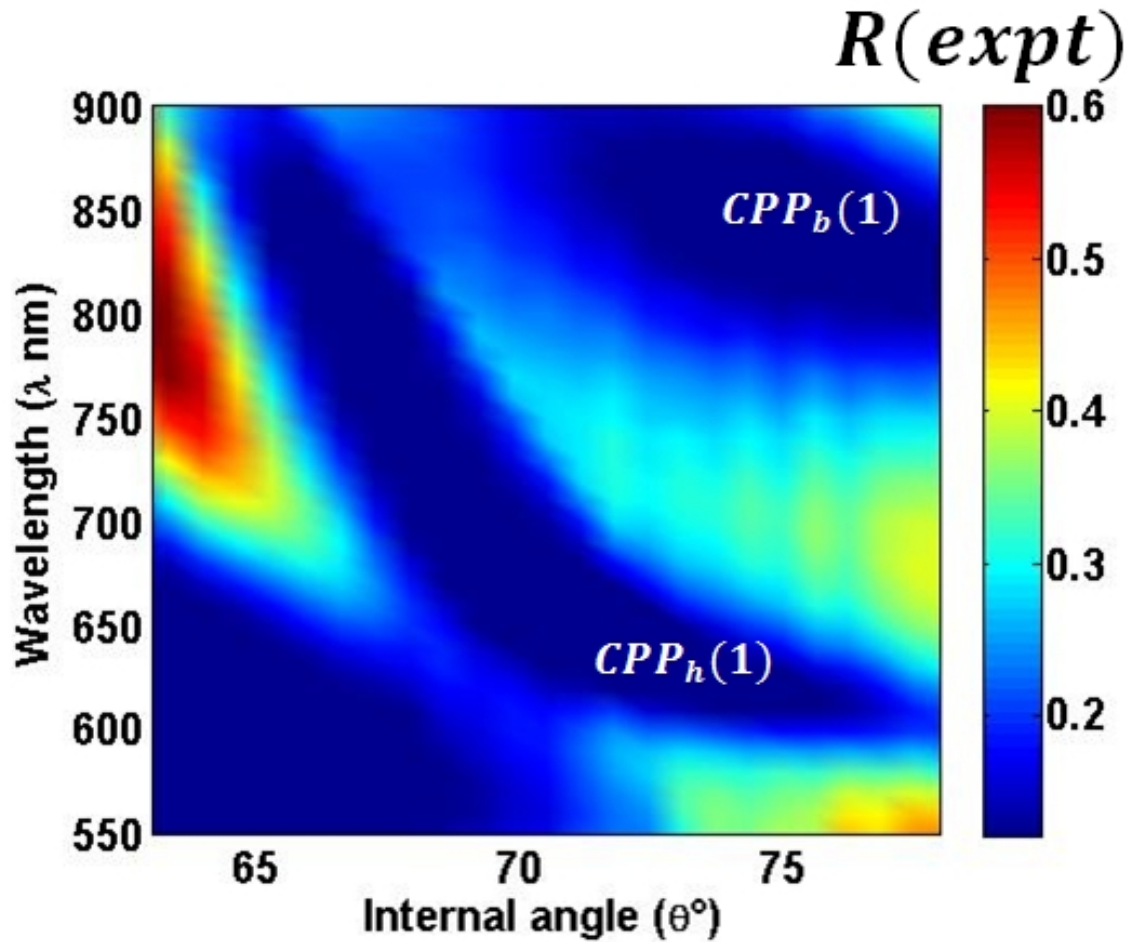


Figure 15.4: The experimental reflectivity ( $R(expt)$ ) of the binary grating structure as obtained by the SPR imaging system. The flow cell was filled with water.

For the numerically calculated dispersion, the total light flux reflected by a structure was considered. For the calculations of transmission, the total flux emitted on the side opposite to the incident side is considered. However, for the experiment, only the specularly reflected light is collected. Thus the experiment and the numerical calculations, match only when all the light from the biochip surface undergoes specular reflection. This is true for a thin metallic film but for binary gratings, only the 1st order of diffraction is reflected along an angle equal to the angle of incidence. But the higher orders, depending on the periodicity of the grating, are diffracted along other angles which are not collected by the objective and CCD camera used in the experimental setup. Thus, there is loss in intensity and the maximum reflectivity value in the reflectivity dispersion map is less than that calculated numerically.

With the numerical model used in this work, we have calculated the reflectivity with the contribution of different orders of diffraction (equation 6.5 of section 6.2 in terms of Rayleigh expansion). The first diffraction order for reflectivity ( $R_0$ ) corresponds to the specular reflection and represents the flux collected during the experiment.  $R_0$  for the structure is shown in figure 15.5 and we see that it matches closely the reflectivity map obtained in the experiment. An additional loss of reflectivity as compared to the calculated reflectivity shown elsewhere in this work is caused by the thin titanium adhesion layer used

for the experimental biochip. This Ti layer was considered for the numerical calculation shown in figure 15.5.

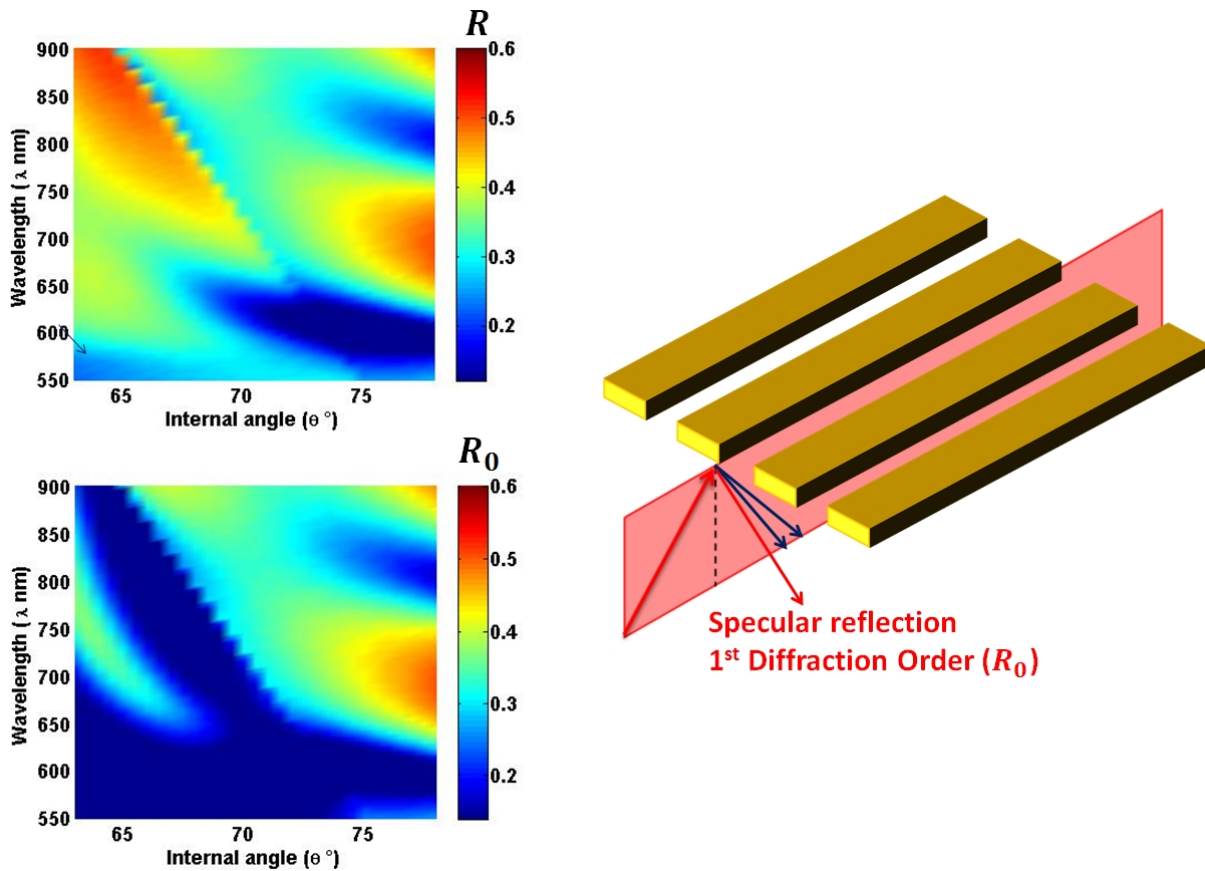


Figure 15.5: Reflectivity of the binary grating structure calculated numerically as a function of  $\lambda$  and  $\theta$ . The total reflected flux is shown as  $R$  (top) and that for the 1st diffracted order is shown as  $R_0$  (bottom). The refractive index of the medium surrounding the grating is  $n_h = 1.333$  and the substrate with index  $n_b = 1.513$ .

### 15.1.1 Measurement of bulk index sensitivity of CPP

Having validated the excitation of the CPP modes in the binary grating structure, we have measured the sensitivity of the modes to local refractive index changes.

The sensitivity for the CPP with respect to bulk refractive index changes was discussed in section 13.3. For the  $CPP_h$  the spectral sensitivity  $S_\lambda$  to bulk index changes is much lower than that of the PSP and  $CPP_b$  is not sensitive to such index changes. For the experiment, sucrose solution was injected in the flow cell to simulate the shift of bulk refractive index. Sucrose was dissolved in water in the ratio  $6.9mg$  of sucrose per  $ml$  of water. This causes a refractive index shift of water of  $10^{-3}RIU$ . The reflectivity spectrum was measured with the SPR imaging system with water in the flow cell and then by injecting the sucrose solution. The spectrum is shown in figure 15.6.

As expected, there is no shift of the  $CPP_b(1)$  wavelength with a change in bulk refractive index. For the  $CPP_h(1)$  the spectral shift is equal to  $\Delta\lambda = 1.6nm$ . Thus considering an index shift of  $\Delta n = 10^{-3}RIU$  the spectral sensitivity at  $\lambda = 587.5nm$  is  $S_\lambda = 1600nm/RIU$  which is similar to that obtained by numerical and analytical calculations for the  $CPP_h$  (figure 13.3d).



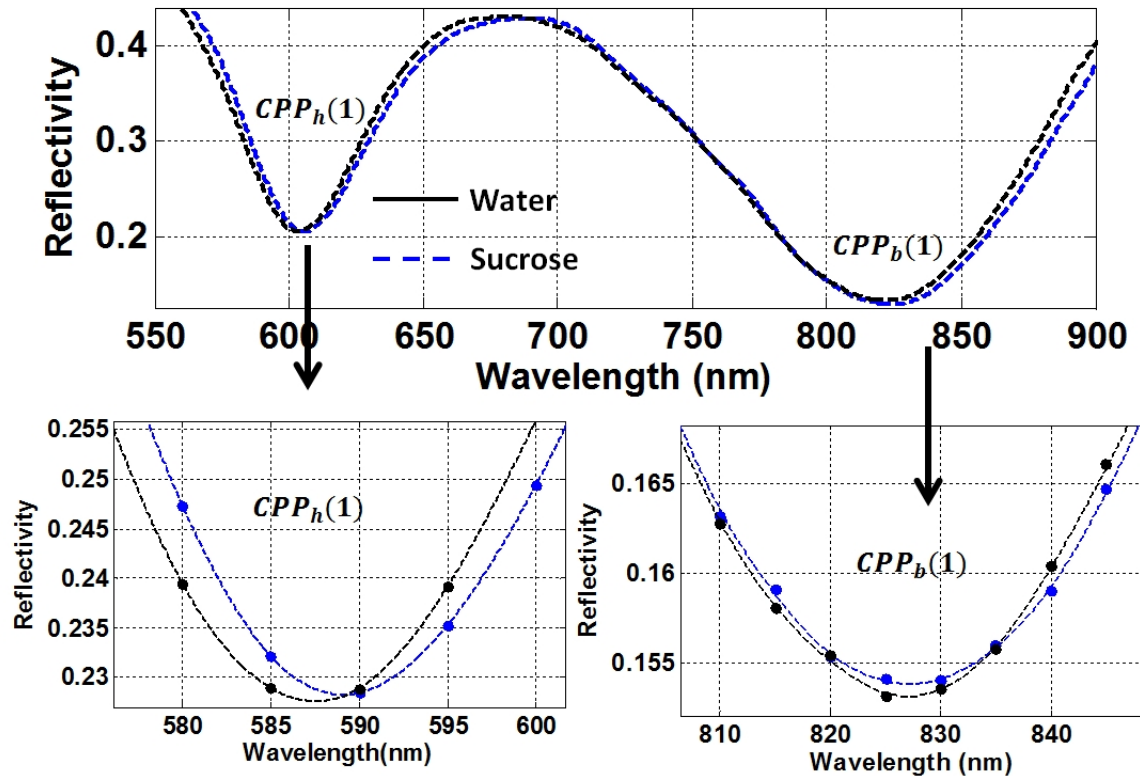


Figure 15.6: The reflectivity as a function of  $\lambda$  for angle of incidence  $\theta = 78.07^\circ$  obtained experimentally using the SPR imaging system. The reflectivity with water in the flow cell (black solid) and with the sucrose solution (blue dashed) is shown in the figure. A zoom at the positions of the two reflectivity dips which correspond to the modes  $CPP_h$  and  $CPP_b$  is shown (bottom).

### 15.1.2 Measurement of bio-molecular sensitivity of CPP

The sensitivity of CPP to the binding of a bio-layer was discussed in section 14.2.1. It was shown that to increase the sensitivity of the CPP for such detection in terms of SEF, one need to localize the analyte preferentially on the sides of the grating ridges. From figure 14.7 we see that such target localization results in a SEF of 2.5 for  $CPP_h$  and 1.7 for  $CPP_b$ .

To realize such target localization experimentally we need to passivate the regions of the biochip where we do not want the target to be adsorbed. This can be done by covering those regions with some material to which the target molecules will not bind. In this experiment, we have used Bovine serum albumin (BSA) molecules. Such protein molecules are known to bind on gold surfaces while it does not bind to dielectric layers such as silica. This principle can be used for selective target localization of the BSA molecules on the biochip to characterize the later in terms of SEF.

For selective binding of the BSA molecules to the sides of the grating ridges, the top of the grating was covered with silica. This was done by controlled sputtering of pulverized silica, along the direction perpendicular to the grating surface. Such method of selective silica deposition has already been reported [244]. The schematic of the principle is shown in figure 15.7. The thickness of the deposited silica was  $8 \pm 2nm$ . With such a deposition we expect the sides of the grating ridges to be free of silica and thus the BSA molecules to bind only to the sides.

The reflectivity of the biochip after silica deposition was measured using the SPR imaging system. The

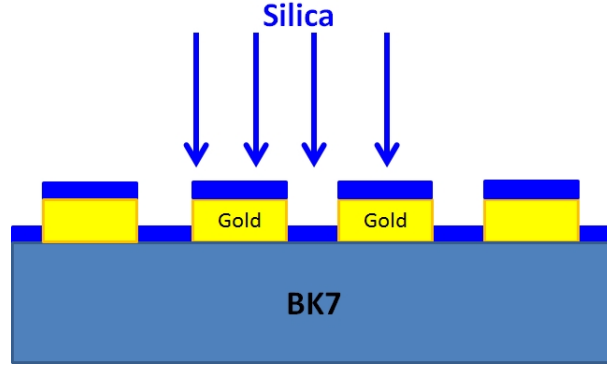


Figure 15.7: Schematic of silica deposition on the grating to cover the top of the ridges.

same structure characterized and shown in figure 15.6 was used with  $h = 50nm$ ,  $w_1 = 700nm$  and  $\Lambda = 1400nm$ . In figure 15.8 the reflectivity spectra for the two modes, before and after the deposition of silica is shown. The fluidic cell was filled with water. We clearly see a spectral shift of both the modes, the shift being much larger for  $CPP_h$  than  $CPP_b$ , where for the later the shift is almost negligible. For  $CPP_h$  the spectral shift was  $\Delta\lambda^{CPP_h} = 14.7nm$  for the spectral dip at  $\lambda = 588.3nm$ . On the same biochip a zone with a thin gold film of height 50nm was deposited to compare the sensitivity of the CPP modes with respect to that of the PSP. For the gold film, the spectral shift before and after silica deposition was found to be  $\Delta\lambda^{PSP_h} = 17.7nm$  for the spectral dip at  $\lambda = 600nm$ . Thus the  $S_{fac} = \Delta\lambda^{CPP} / \Delta\lambda^{PSP}$  was found to be  $S_{fac} = 0.8$  for the  $CPP_h$ .

The reflectivity spectra for  $h = 50nm$ ,  $w_1 = 700nm$  and  $\Lambda = 1400nm$  was calculated numerically and a spectral shift of  $1.05nm/nm$  for the  $CPP_h$  at  $\lambda = 589.6nm$  was seen for a layer of index  $n_a = 1.48$ , considered only on the top of the ridge. This gives a numerical  $S_{fac} = 0.63$  which is close to the value obtained experimentally.

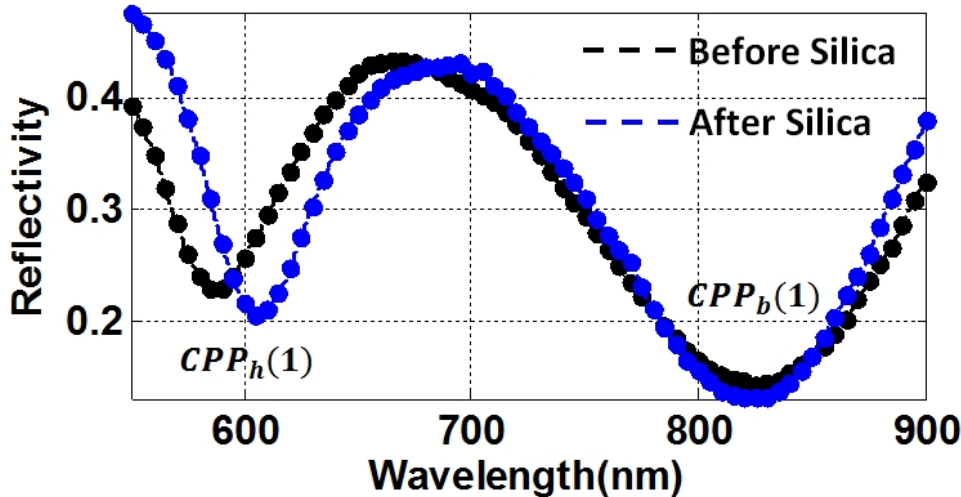


Figure 15.8: The reflectivity as a function of  $\lambda$  for angle of incidence  $\theta = 78.07^\circ$  obtained experimentally using the SPR imaging system before and after the deposition of 8nm silica layer perpendicular to the grating surface. The flow cell was filled with water.

The two experiments with and without the silica layer were done on different days and so with slightly

different experimental condition. The  $\Delta\lambda$  measured for the modes in this method are therefore not very accurate. However we have mentioned this result because it provides a gross indication that the silica layer was indeed deposited on the top of the grating, justified by the  $S_{fac}$  value being close to that found in the calculations with a layer of index  $n_a = 1.48$  deposited on the top of the ridges. We however did not notice appreciable spectral shift of the  $CPP_b$ . This can be explained by the fact that for  $CPP_b$ , the  $\Delta\lambda$  is very small (table 14.1) and thus such a small spectral shift may be unperceived when the same experimental conditions are not respected.

For accurate sensitivity measurement, BSA was used on the biochip with the deposited silica layer. The reflectivity spectrum was first measured in water, at the angle of incidence  $\theta = 78.07^\circ$ . The wavelengths of the plasmon dips for the  $CPP_h$  and  $CPP_b$  were found to be  $\lambda = 602.5nm$  and  $\lambda = 823.0nm$  respectively.

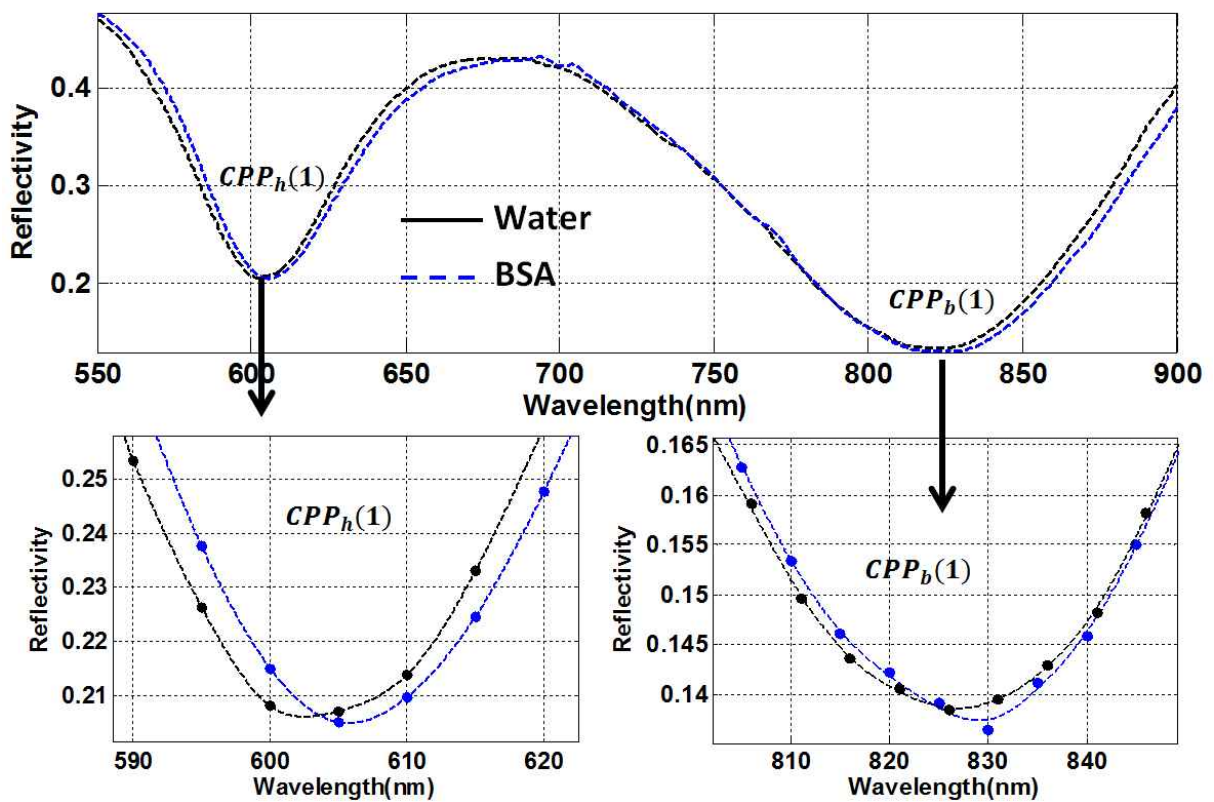


Figure 15.9: The reflectivity as a function of  $\lambda$  for angle of incidence  $\theta = 78.07^\circ$  obtained experimentally using the SPR imaging system. The reflectivity with water in the flow cell (black solid) and with bound BSA (blue dashed) is shown in the figure. A zoom at the positions of the two reflectivity dips which correspond to the modes  $CPP_h$  and  $CPP_b$  is shown (bottom).

The BSA solution was prepared by dissolving BSA in a phosphate-buffered solution (PBS) of pH 9 in the ratio of 1mg BSA per milliliter of PBS. The solution was then introduced into the flow cell and left to flow for 10-12 minutes, to assure that the BSA molecules were bound to the gold surface. Then water, was introduced into the flow cell and biochip rinsed for a few minutes. The reflectivity measurement was carried out with the flow cell filled with water. Thus any spectral shift observed is only due to the BSA molecules firmly bound to the biochip surface. The two reflectivity spectra, in water and with bound BSA are shown in figure 15.9.

The spectral shift with bound BSA molecules for the two modes are measured to be  $\Delta\lambda = 2.1nm$  for  $CPP_h$  and  $\Delta\lambda = 1.4nm$  for  $CPP_b$ . To normalize the spectral sensitivity to that of the PSP, the same experiment was carried out on a thin gold film of height  $h = 50nm$ . Although on the structured biochip, we had a zone with uniform thin gold film, it cannot be used for BSA binding measurements as no spectral shift was observed on that zone. This is because during the silica deposition the gold film was also covered with silica and thus the BSA molecules did not bind to that zone. This result also confirms that BSA molecules selectively bind to gold and not to silica.

For the reference gold film, the measurements were carried out at two values of the internal angles. For  $\theta = 78.1^\circ$  the spectral shift with BSA was measured to be  $\Delta\lambda = 7.0nm$  at  $\lambda = 595.25$ . For  $\theta = 65.9^\circ$  it was measured to be  $\Delta\lambda = 10.8nm$  at  $\lambda = 811.2$ . These two values were used to normalize the values obtained for  $CPP_h$  and  $CPP_b$  respectively. We obtain the experimental  $S_{fac} = 0.30$  for  $CPP_h$  and  $S_{fac} = 0.13$  for  $CPP_b$ . The values calculated numerically with "side" target localization for the two modes are  $S_{fac} = 0.18$  for  $CPP_h$  and  $S_{fac} = 0.12$  for  $CPP_b$ . The experimental value for  $CPP_b$  is thus consistent with the numerical calculation. However the experimental value for  $CPP_h$  is higher than the numerical result and this can be due to the fact that the silica layer was not considered for the numerical calculations, which affect the  $CPP_h$  more than the  $CPP_b$ .

For the grating of height  $h = 50nm$ , width  $w_1 = 700nm$  and period  $\Lambda = 1400nm$  with target localization on the sides of the ridges, the molecular filling factor is  $f_{mol} = (2h)/(\Lambda) = 0.07$ . Thus the SEF ( $= S_{fac}/f_{mol}$ ) for the structure in the experimental configuration presented above, can be calculated to be 4.2 for  $CPP_h$  and 1.85 for  $CPP_b$ . Referring to figure 14.7 and the calculated SEF of the two modes for width  $w_1 = 700nm$ , we see that the experimental results for the  $CPP_b$  match closely to the calculated values. As predicted by the numerical calculation, we see the SEF for  $CPP_h$  is higher than that for  $CPP_b$ .

## 15.2 Experimental characterization of the HLP and the BM modes

It was shown in chapter 12 that an array of metallic cylinders on a thin metallic film can support the Bragg modes (BM) and the hybrid mode HLP resulting from the coupling of PSP and LSP. To experimentally confirm these modes, arrays of gold nano-cylinders with an underlying gold film were fabricated using e-beam lithography. All the experimental samples mentioned here after, were fabricated by Jean-François Bryche as a part of his on-going PhD thesis at IEF, University Paris Sud and also within the framework of the project ANR Piranex.

The reflectivity of the structure, calculated numerically was shown in section 12.2 and the evolution of resonance frequencies of the modes with geometrical dimensions was shown in figure 12.4. Nano-cylinder arrays of varying periodicity were fabricated to study the variation of excitation wavelength of the different modes with period of the array.

For the fabricated structures the substrate was taken as BK7 glass and a gold film of height  $h_1 = 30nm$  was deposited on it by electron beam evaporation (EBE) and attached to the glass substrate by a 2nm layer of titanium. The cylinder array was then realized on the gold film using EBL with cylinder diameters of  $D = 50nm$  and height  $h_2 = 30nm$ . The film and cylinder heights were verified by ellipsometry-spectroscopy and X-ray measurements with a relative uncertainty of less than 10%. The mean diameters of the cylinders were measured by statistical analyses of SEM images treated with Otsu's method and the uncertainty was found to be less than 3nm.

On the same biochip, multiple zones with different periods ranging from  $\Lambda = 150nm$  to  $400nm$  were fabricated. This allows simultaneous reflectivity measurements of all the different periods with the SPR imaging system. Thus treatment of all the zones under the same experimental conditions is assured. The reflectivity from the biochip was recorded by the SPR imaging system with the flow cell filled with water.

The image of the biochip as recorded by the SPR experimental setup is shown in figure 15.10. The different zones with the corresponding periodicity is marked on the figure. SEM images of the zones with cylinder arrays are also shown in the figure.

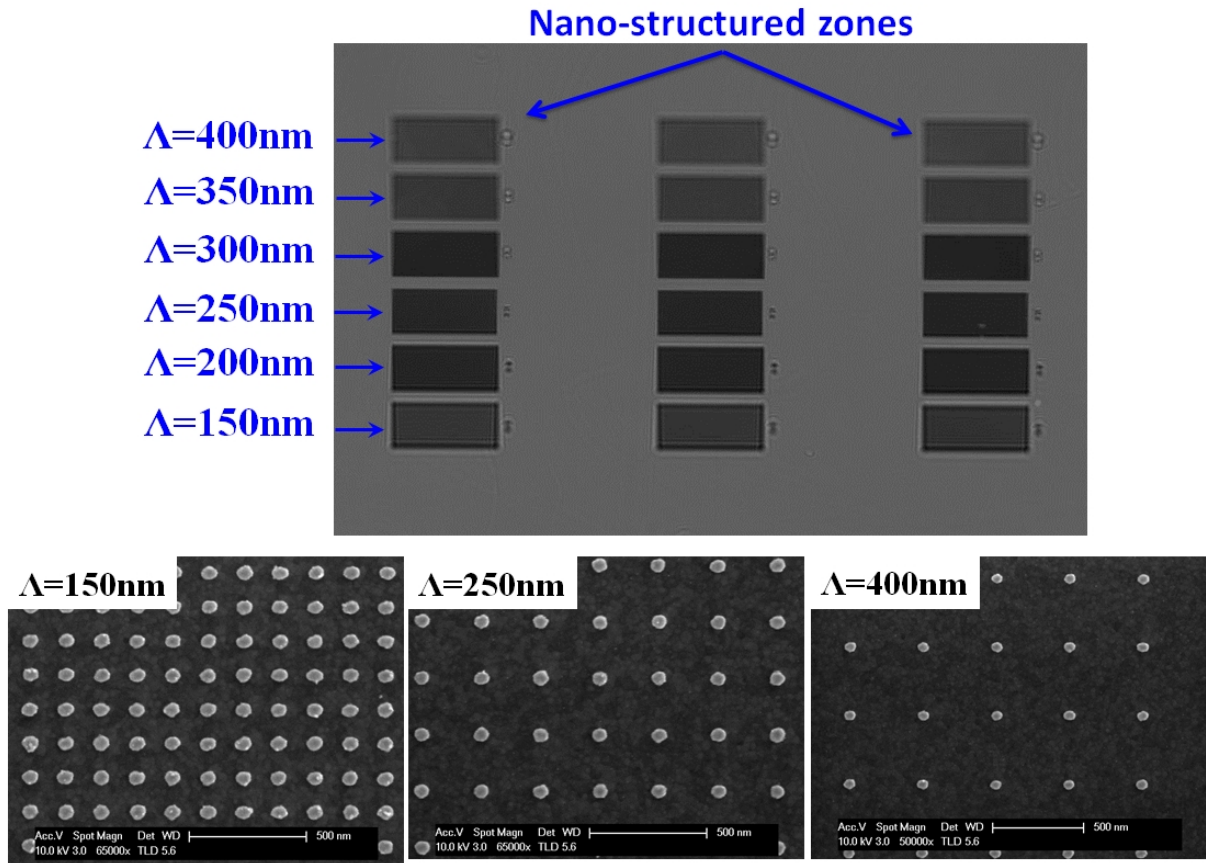


Figure 15.10: Image of the structured biochip as obtained by SPR imaging system (top). Multiple zones of cylinder arrays of different periodicities were fabricated on the biochip. The structure was fabricated on a BK7 glass substrate. An adhesion layer of  $2nm$  titanium was used. The gold film height was  $h_1 = 30nm$  and the cylinder dimensions of  $h_2 = 30nm$  and  $D = 50nm$ . The period was varied from  $150nm$  to  $400nm$ . SEM images of the structured zones for periods  $\Lambda = 150nm$ ,  $250nm$  and  $400nm$  is also shown (below).

The reflectivity as a function of the excitation wavelength and incident angle was recorded for each zone. Reflectivity obtained with TM polarized light was normalized to that obtained with TE polarized light. The result is shown in figure 15.11 for a period  $\Lambda = 200nm$ . In the same figure, the numerically calculated reflectivity of the same structure is also shown. We see a close match between the calculated and the experimental reflectivity map. For the calculated map, the titanium layer of  $2nm$  was considered. The numerical calculation shows the total reflectivity from the structure. Unlike the binary grating as shown in figure 15.5, for the structure with the underlying gold film, the total reflectivity results only from

the first diffracted order. Thus the total reflectivity ( $R$ ) is equal to the first diffraction order ( $R_0$ ). For such structures, no light intensity is lost in the higher diffraction orders even for larger periods.

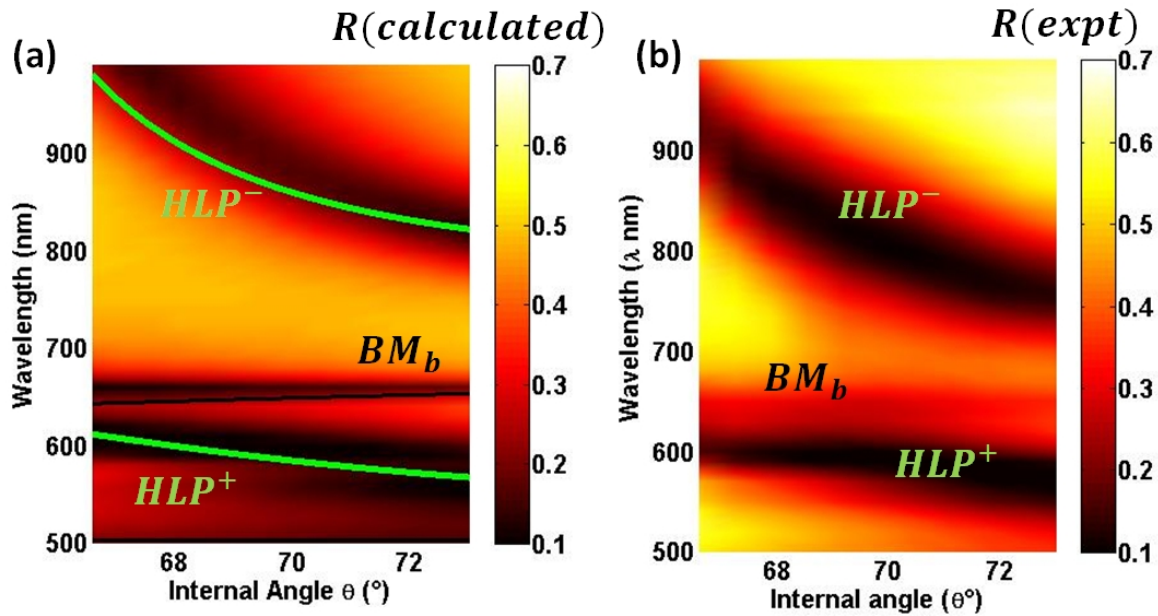


Figure 15.11: (a) Reflectivity ( $R$ ) for a cylinder array with dimensions  $h_1 = 30\text{nm}$ ,  $h_2 = 30\text{nm}$ ,  $D = 50\text{nm}$  and  $\Lambda = 200\text{nm}$  in a medium of refractive index  $n_h = 1.333$ . A titanium layer of  $2\text{nm}$  was considered between the substrate (index  $n_b = 1.513$ ) and the gold film. The analytical dispersion of the HLP (green) and the BM (black) for the structure is also shown. (b) The experimental reflectivity ( $R(\text{expt})$ ) of the structure as obtained by the SPR imaging system. The flow cell was filled with water.

The analytical calculation for the HLP and BM is also shown in the figure and thus we can identify the different reflectivity dips in the map with the corresponding modes. The experimental reflectivity maps for the other periods are shown as a function of  $k_0$  and  $(k_{//}/k_0)$  in Appendix B (figure B.2).

The dependence of the resonance wavelengths of the modes (reflectivity dips) with the period of the array were measured at incident angle  $\theta = 71.1^\circ$  and shown in figure 15.12. The reflectivity spectra at the given incident angle, for each period is shown, with the various reflectivity dips marked by arrows. The contrast (ratio of maximum and minimum of reflectivity) of all the dips is not the same: the dips corresponding to the BMs are much weaker than those for the HLP.

The dips in reflectivity as a function of array period is shown in figure 15.12(b) along with the analytical calculation for the dispersion of the various modes. This figure is comparable with the dispersion of the modes shown in figure 12.4(a). We see that all the modes as described in section 12.2 can be excited experimentally in the Kretschmann configuration.

Experimentally, the BM are generally not as strong in terms of reflectivity contrast as predicted by the numerical calculations. This is also evident from the complete reflectivity dispersion map shown in figure 15.11 and in figure B.2 of Appendix B. This can be explained by the fact that for the numerical calculations, a homogeneous array extending to an infinite distance was considered. Thus to be closer to the numerically predicted characteristics of the BM, the array needs to be homogeneous at-least up to the propagation length of the PSP which is around a few tens of micrometers (figure 2.3). The HLP however occurs due to the coupling of the PSP and the LSP and are thus results of a much more localized effect. So gross inhomogeneities of the array dimensions are not critical for their excitations. But the shape

and dimensions of the cylinders (or nano-particles in general) play a major role in the LSP resonance wavelength and thus in turn effect strongly the resonance wavelength of the HLP. These points should be noted during fabrication of the structures, in order to excite the different plasmonic modes.

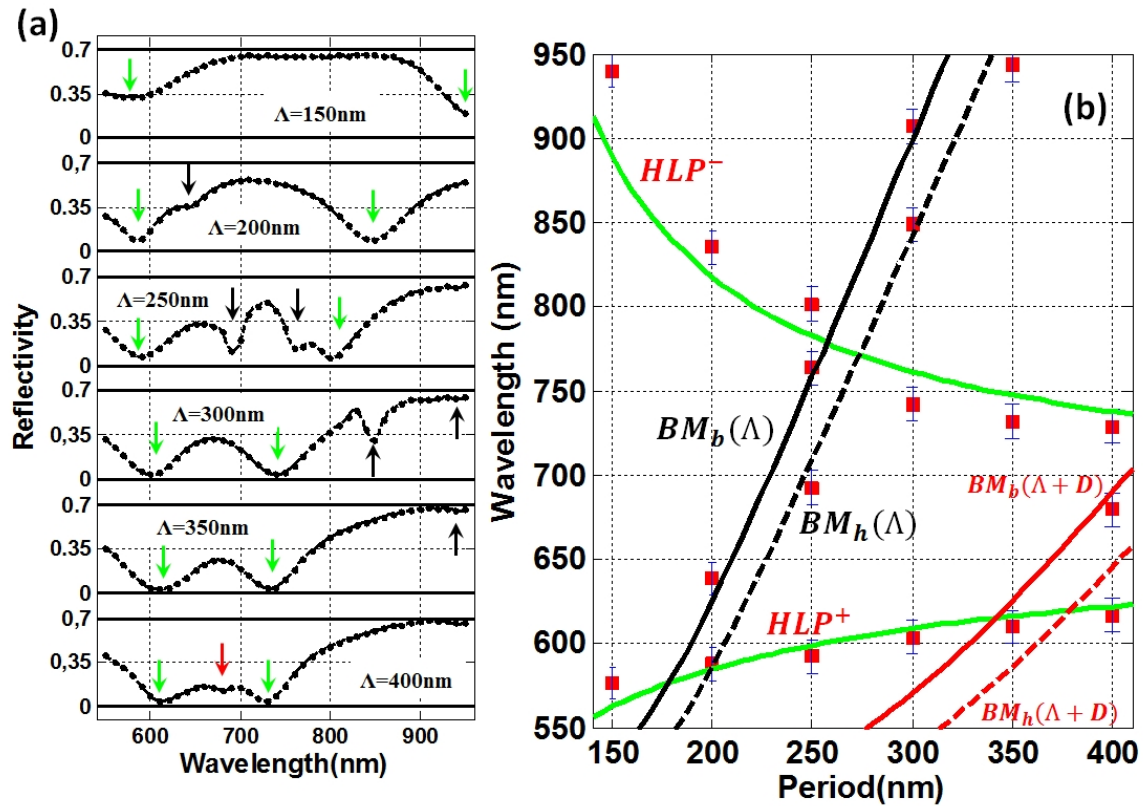


Figure 15.12: (a) Normalized reflectivity spectra at  $\theta = 71.14^\circ$  for different period ( $\Lambda$ ) of the structure. Arrows show the reflectivity minima, which correspond to the various modes excited in the structure. (b) The resonance wavelengths of all the modes (minima of reflectivity) are shown as red squares as a function of array period. The error bars correspond to the minimum step of incident wavelength (10 nm) used for the experiment. We have superposed the analytically calculated dispersion of the modes as a function of period: HLP (green), BMs calculated for  $k_B = 2\pi/(\Lambda)$  (black solid and dashed) and BMs for  $k_B = 2\pi/(\Lambda + D)$  (red dashed and solid).

### 15.2.1 Sensitivity measurements for the HLP

The sensitivity of the HLP for bulk index changes was discussed in section 13.4 and that for affinity biosensing was discussed in section 14.2.2. We have shown that by selective target localization the SEF for the HLP can be enhanced by more than an order of magnitude. However for such experiments, the biochip must be orthogonally functionalized by covering a portion of the biochip surface by a material to which the analyte cannot bind. This was successfully shown for the CPP in metallic grating structures in section 15.1.2. Fabrication techniques used allowed us to cover the top of the grating ridges with a thin silica layer and thus effectively enhance SEF. However to enhance SEF for the HLP mode, we need the silica layer to be deposited in the gaps between the cylinders and leave the top of the cylinders available for specific binding of the analyte. Current fabrication techniques and available methods were not able to achieve this orthogonal deposition of silica layer to cover only the uniform gold surface.

However in this section, we will present another very important experimental result for the HLP which is also applicable to plasmonic modes in general. We will show that the behavior of the same mode, with the same electric field distribution, in the presence of a molecular layer is very different from one another and this is evident in the sensitivity of the mode. This difference is brought about by the chosen interrogation method (choice of  $\lambda$  for spectral interrogation or  $\theta$  for angular interrogation). The difference is not observed by just a study of the field distribution of the mode, but is due to its inherent dispersion characteristics. In the following experimental verification, two different periods of the cylinder array was chosen to excite the HLP at the same wavelength ( $\lambda = 800nm$ ) but at two different incident angles. Fixing the wavelength also assures that the dispersion of the refractive index of the molecule used do not effect our measurement. This is shown in figure 15.13. We will show that for  $\Lambda = 200nm$  where the interrogation is done at a higher internal angle, the sensitivity is higher for smaller thickness of molecular layer than that for  $\Lambda = 300nm$  where the interrogation is done at a lower angle of incidence.

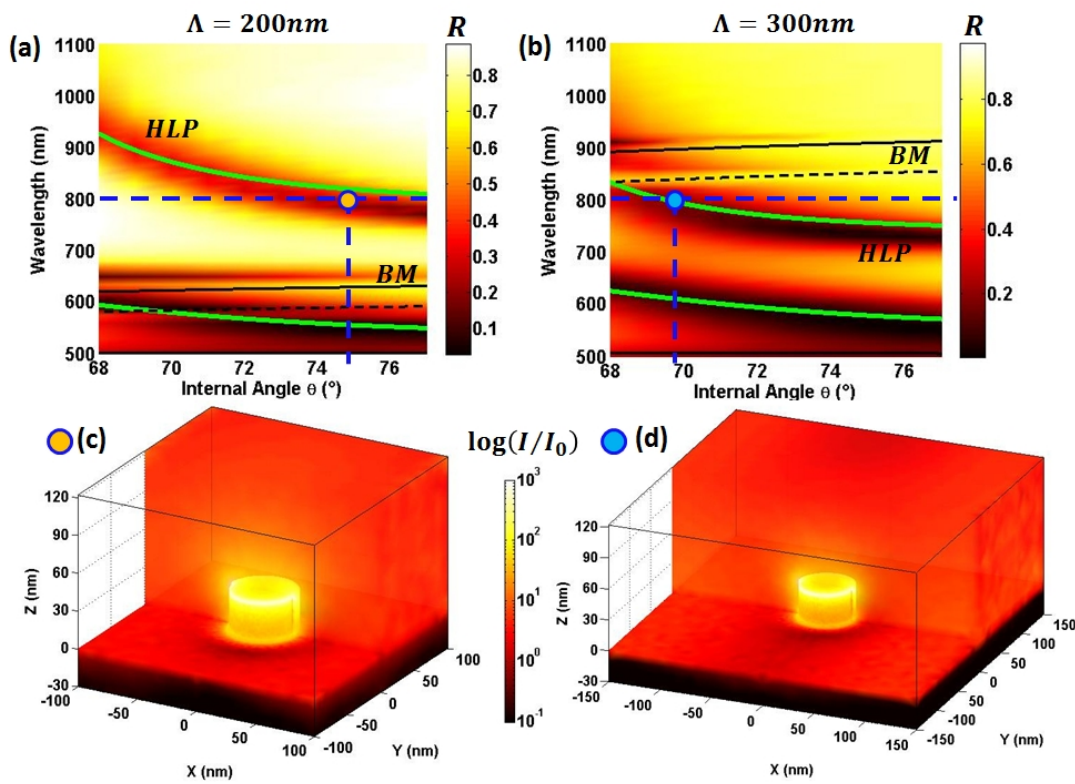


Figure 15.13: Reflectivity calculated numerically as a function of  $\lambda$  and  $\theta$  for cylinder arrays with period  $\Lambda = 200nm$  (a) and  $\Lambda = 300nm$  (b). The analytical calculation of dispersion for the BM (black solid for  $BM_b$  and dashed for  $BM_h$ ) and HLP (green) is shown. (c-d) The electric field intensity distribution for the HLP at  $\lambda = 800nm$  for the two periods. The refractive index of the medium around the cylinders was taken as  $n_h = 1.333$ . For the calculation the plane wave was incident from the substrate of index  $n_b = 1.513$

Arrays of nanocylinders of height  $h_2 = 30nm$  and diameter  $D = 50nm$  with an underlying gold film of height  $h_1 = 30nm$  with varying periods ( $\Lambda$ ) was used for the characterization. The fabricated biochip is similar to the one presented in the last section (figure 15.10). The reflectivity dispersion map as a function of wavelength and internal angle for  $\Lambda = 200nm$  and  $300nm$  is shown in figure 15.13. The analytical calculation for the BM and the HLP is also shown. For both the periods at  $\lambda = 800nm$ , the HLP mode is excited, at  $\theta = 75.1^\circ$  for  $\Lambda = 200nm$  and at  $\theta = 69.4^\circ$  for  $\Lambda = 300nm$ . The electric



field distribution for the two HLP modes is also shown in figure 15.13. We see that for both the periods, the electric near-field distribution is almost similar, confirming that the same plasmonic mode is excited in both the cases.

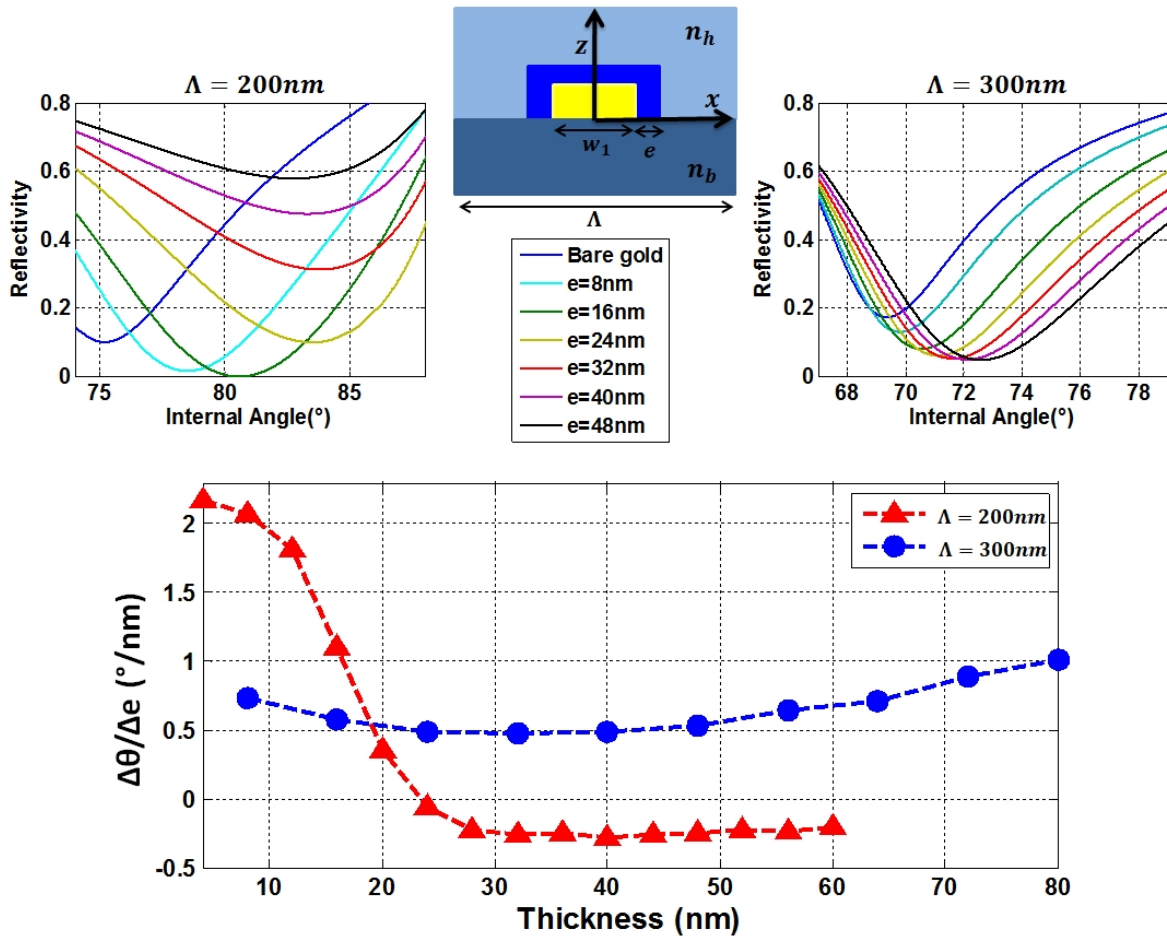


Figure 15.14: The numerically calculated reflectivity as a function of internal angle ( $\theta$ ) at  $\lambda = 800nm$  for two periods ( $\Lambda$ ) of the cylinder array with a molecular layer of thickness  $e$ . The schematic is also shown. The angular shift per nanometer increase of thickness ( $\Delta\theta/\Delta e$ ) for the two periods is shown below.

The reflectivity of the structure was then calculated numerically with a molecular layer around the cylinders of thickness  $e$  and refractive index  $n_a = 1.49$ . The thickness of the layer was varied and the reflectivity curves at  $\lambda = 800nm$  are shown in figure 15.14 for the two periods. We see that the reflectivity curves for  $\Lambda = 200nm$  rapidly decrease in contrast (ratio of minimum and maximum of reflectivity) while for  $\Lambda = 300nm$  the contrast remains the same and only an angular shift is observed with increase of thickness ( $e$ ). Thus the difference in behavior for the two periods is evident.

The angular sensitivity ( $\Delta\theta/\Delta e$ ) was calculated which represents the angular shift per nanometer of increase of the molecular layer. This is also shown in figure 15.14. For  $\Lambda = 200nm$  the sensitivity for small thickness  $e$  is higher than that for  $\Lambda = 300nm$  however we see a rapid loss in sensitivity for the smaller period while the sensitivity is almost constant for  $\Lambda = 300nm$ . Thus for larger values of  $e$  the sensitivity for  $\Lambda = 300nm$  becomes higher than that for  $\Lambda = 200nm$ . This can be explained by the fact that for  $\Lambda = 200nm$  the interrogation angle is higher and so the slope of dispersion of the mode

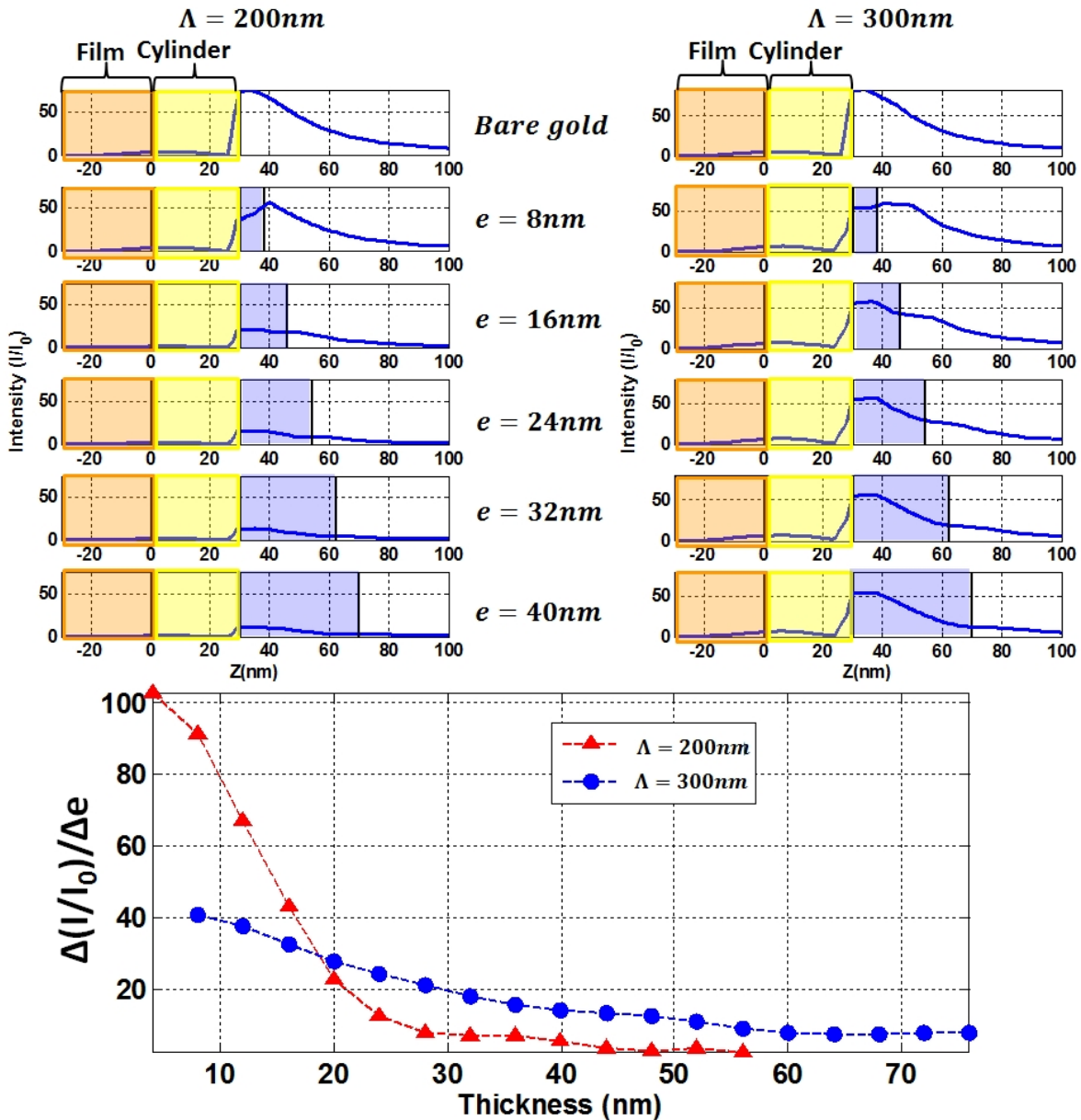


Figure 15.15: Electric field intensity ( $I/I_0$ ) with  $\Lambda = 200\text{nm}$  and  $\Lambda = 300\text{nm}$  at the center of the cylinders ( $x = 0, y = 0$ ) along the axis  $z$  for different molecular layer thickness  $e$ . The cylinders are placed as  $z = 0$  and are of height  $30\text{nm}$ . The uniform gold film of  $30\text{nm}$  was considered at  $z = -30\text{nm}$  to  $z = 0\text{nm}$ . The refractive index of the medium for  $z > 30\text{nm}$  was taken as  $n_h = 1.333$ . The molecular layer of thickness  $e$  is marked in the figure in blue. (Bottom) The variation of the total field intensity along  $z$  ( $\Delta(I/I_0)$ ) per nanometer increase of the thickness  $\Delta e$  as a function of  $e$ .

with respect to incidence angle (figure 15.13(a)) is also higher which results in a higher  $\Delta\theta$ . But with increasing molecular thickness, the interrogation angle approaches  $90^\circ$ , close to which the sensitivity drops rapidly.

We have shown in chapter 14 (figure 14.8) that the sensitivity (spectral shift) of the plasmon resonance is not proportional to the absolute electric field intensity. Here we will show that the sensitivity is rather proportional to the change in the field intensity caused by the deposited dielectric layer. This is an important point to note for biosensing. A mode with a very high field confinement may not always be as

efficient for biosensing, if the molecular layer cannot cause a significant change to the confined field.

To validate this fact, the near field intensity distribution for the confined and extended HLP at the two periods was calculated with increasing molecular layer thickness. This is shown in figure 15.15. The field intensity at the center of the cylinders ( $x = 0, y = 0$ ) along the axis of the cylinder ( $z$ ) is shown for the two periods. We see that the field distribution without the molecular layer (bare gold,  $e = 0$ ) is almost the same for the two periods confirming the fact that it is the same plasmonic mode (HLP). However by adding a molecular layer the field distribution for the interrogation at higher angle of incidence ( $\Lambda = 200nm$ ) decreases rapidly while that for the interrogation at lower angle of incidence has almost insignificant decrease. This is more evident in the curve showing the change of the total integrated intensity ( $\Delta I/I_0$ ) along  $z$  as a function of molecular layer thickness ( $e$ ). The trend of this curve with  $e$  follows closely the trend of the angular sensitivity evolution with thickness. The fact that the field intensity changes rapidly for higher incident angles, results in its higher sensitivity for lower values of  $e$  as compared to that at lower incident angle. However for higher values of  $e$  owing to the large intensity change, the field is almost negligible for  $\Lambda = 200nm$  and thus its sensitivity drops. This low field intensity for larger thickness  $e$  also explains the low contrast of the reflectivity dips observed for  $\Lambda = 200nm$ .

The angular sensitivity for the two periods was measured experimentally using the SPR setup. For this measurement the thickness of the molecular layer bound to biochip surface has to be changed in real time and the corresponding reflectivity as a function of internal angle needs to be measured. For this purpose two well known polyelectrolytes, Poly(allylamine hydrochloride) (PAH) and Poly(styrenesulfonate) sodium salt (PSS) were used and their binding to the biochip surface was studied [245, 246]. As gold is naturally electro-negatively charged, the positively charged PAH solution is first injected into the fluidic cell and it is expected to form a SAM on the gold surface. The second injection of PSS, whose charge is negative creates a PAH-PSS bilayer on the surface. The thickness of this PAH-PSS bilayer was measured by calibrated SPR measurement using an uniform gold film and the average thickness was found to be  $7.4nm$ . The refractive index of the bilayer was considered to be  $1.5$  at  $25^\circ C$ . The process is repeated multiple times and thus a change of molecular layer thickness ( $e$ ) was achieved with a step of  $7.4nm$ . In this work, we will not go into the details of the bilayer deposition procedure and this experiment was done as a part of the PhD thesis of Aurore Olivero at Laboratoire Charles Fabry. The results are summarized in figure 15.16.

The reflectivity as a function of angle of incidence shows the same trend as calculated numerically (figure 15.14). The loss of contrast for the reflectivity curves is observed for  $\Lambda = 200nm$  while for  $\Lambda = 300nm$  the minimum of reflectivity remains the same. The sensitivity was calculated as the change in the internal angle with each binding bilayer. This angular shift was normalized to that of the shift for an uniform gold film which was also fabricated on the same biochip and measured simultaneously. This was done to compensate for all the drifts and fluctuations during this long experiment. We see the sensitivity for the smaller period is higher by a factor of 2 as compared to that for higher period for the first bilayer. Then for consecutive bilayers the sensitivity for  $\Lambda = 200nm$  drops sharply and becomes less than that of  $\Lambda = 300nm$  for roughly  $e = 20nm$  (considering each bilayer to be  $7.4nm$ ). This same trend is observed for the numerically calculated sensitivity and the field intensity of the two modes.

This experiment thus validates that the sensitivity of a plasmonic mode depends on the change of electric field intensity brought about the molecular layer and not on the absolute electric field intensity confined by the mode. The same mode at different values of  $(\lambda, \theta)$  can behave differently owing to the

dispersion characteristics of the mode. Also the rapid drop in sensitivity for  $\Lambda = 200nm$  can be used for other applications such as optical switching.

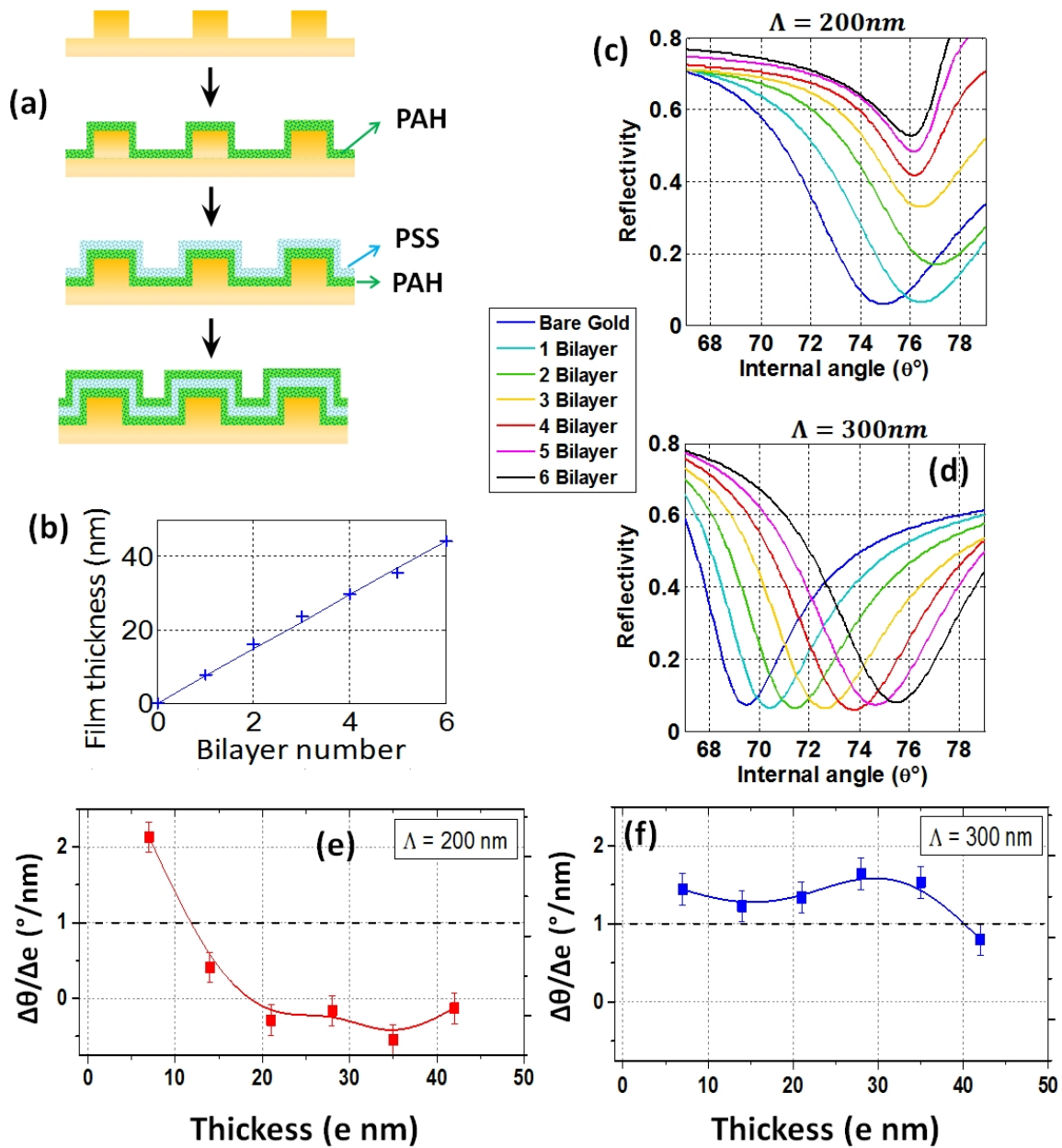


Figure 15.16: (a) The schematic for the binding of the polyelectrolytes bilayer to the biochip surface (b) The thickness of each bilayer as obtained by calibrated SPR measurement with an uniform gold biochip. (c) The experimentally measured reflectivity as a function of internal angle ( $\theta$ ) at  $\lambda = 800nm$  for  $\Lambda = 200nm$  with each PAH-PSS bilayer. (d) The same for  $\Lambda = 300nm$ . (e) The measured angular shift per nanometer increase of thickness ( $\Delta\theta/\Delta e$ ) for  $\Lambda = 200nm$  as a function of  $e$  (considering each bilayer to have an average thickness of 7.4nm) (f) The same for  $\Lambda = 300nm$ .

---

## Nano-structures for SERS detection

---

In section 5.4 the Piranex project to which this work was partially dedicated, was mentioned. The aim of the project is to develop a bimodal instrument combining SERS and SPRI detection. The nano-structures described in the preceding chapters and the consequent plasmonic modes can be used to enhance the sensitivity of the detectors for both SERS and SPRI. The sensitivity of the modes for SPRI have been explicitly discussed. The theoretical explanation of the phenomenon that leads to enhanced Raman spectroscopy (SERS) was described in section 4.2. In the section we have mentioned that the SERS enhancement results from two simultaneous enhancement processes,

(a) the enhancement of the incident field owing to excitation of plasmonic modes, occurring at the frequency of the excitation,  $M(\nu_i)$ .

(a) the enhancement of the raman scattered field re-radiated by the metallic structure at the frequency of emission,  $M(\nu_s)$

where  $\nu_i$  and  $\nu_s$  are the frequencies of excitation and emission respectively. The total enhancement of the SERS intensity can then be written as  $I_{SERS} \propto M(\nu_i)^2 \times M(\nu_s)^2$ .

The electromagnetic (EM) enhancement for the SERS intensity is thus proportional to the field intensity enhancement caused by excitation of various modes in the system. In this chapter we will briefly discuss with examples two such enhancements caused by the LSP in binary arrayed structures and by the BM in arrays with underlying thin metallic film. In both the case we will show with experimental data, that the SERS intensity is stronger by almost an order of magnitude whenever the excitation and Raman emission conditions satisfy the presence of the plasmonic modes in the structures.

For the SERS experiments shown in this work, the configuration presented in figure 4.7 of section 4.2.2 is used (Raman microscope XploRA ONE <sup>TM</sup> from Horiba Scientific). All SERS measurements and extinction spectra shown in this work were obtained by Raymond Gillibert as a part of his PhD thesis at CSPBAT, University Paris 13. The structured biochips used for characterization were realized on BK7 substrates by Jean-François Bryche at IEF, Orsay. For the SERS setup, the biochip is placed in the sample holder, with the surrounding medium being air, and the exciting laser light is incident on the biochip surface from air. SERS spectra of thiophenol obtained as a part of the PIRANEX project for gold nano-structured biochips is shown in figure 16.1. We do not observe the Raman scattered peaks with the molecules deposited on uniform glass or gold substrate. However strong peaks are recorded when the molecules are deposited on the gold nano-structures validating the enhancement of Raman scattering cross-section by metallic structures.

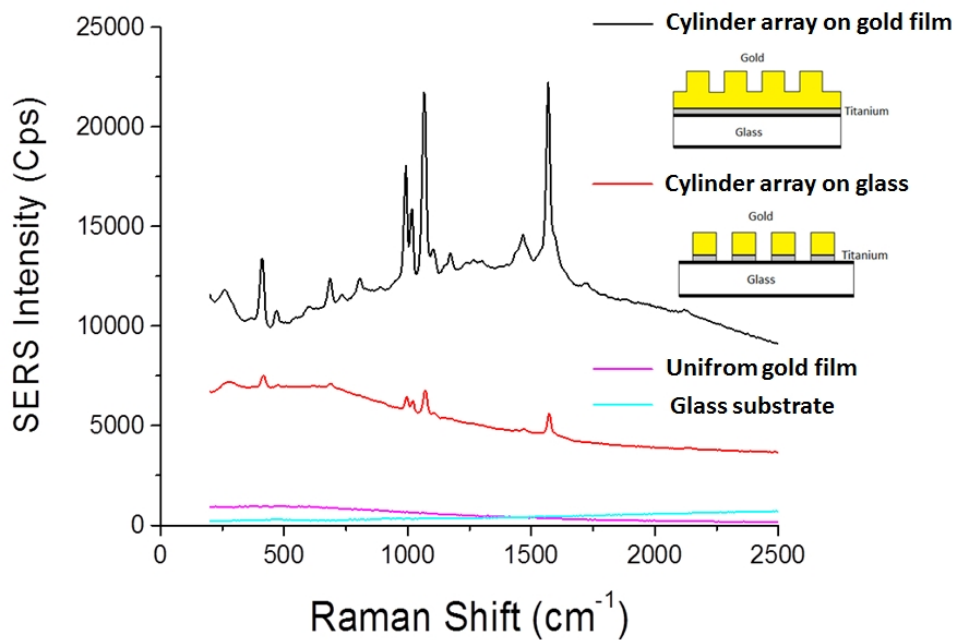


Figure 16.1: Adapted from J.F.Bryche et al [247]: SERS intensity spectra obtained for thiophenol molecules deposited on glass substrate; on a uniform gold film; on a cylinder array on glass; on a cylinder array with an underlying gold film.

The experimental configuration used for SERS measurements is different from the Kretschmann configuration presented so far in this part, in two important aspects as described below.

Recalling the concepts of plasmonic modes used in this work, (chapter 8), for describing the plasmonic modes in the structures we have used the notation  $k_0$  and  $(k_{//}/k_0)$  and the later depends index of the medium of incidence. For the biochip, we denote the index of the medium surrounding the structured surface by  $n_h$  and the index of the substrate by  $n_b$ . In this case  $n_h = 1$  while  $n_b$  can be approximated to 1.513 for BK7. Thus for the Kretschmann configuration with incidence from glass, we could excite the modes beyond  $(k_{//}/k_0) > n_h$  while in this case for SERS, with incidence from air we can access only the values of  $(k_{//}/k_0) < n_h$ . Thus the first major difference between the Kretschmann configuration and the SERS configuration used here is that in the later we cannot excite the PSP or the hybrid modes with result from the PSP such as the CPP or the HLP.

The second difference, though not a major one is that the medium surrounding the structures in the Kretschmann configuration was water while in this case it is air. Thus we may expect certain shifts of the resonance conditions for the modes mainly the LSP for the SERS experiments as compared to the SPRI experiments. Thus to analytically calculate the resonance conditions in terms of excitation wavelength and incident angle, the proper values of the indices must be used. It must also be noted that a structure optimized for a certain wavelength for SPRI may not have the same performance at that wavelength when used in the SERS experiment.

## 16.1 SERS enhancement by localized surface plasmons

To demonstrate the effect of field enhancement caused by excitation of the LSP in metallic particles on SERS intensity, arrays of gold nano-cylinders were used. The LSP resonance condition for such arrays was discussed in section 10.3.

The array of gold cylinders of height  $h = 50\text{nm}$  were fabricated on BK7 substrate using EBL. For the experiment the diameter of the cylinders were varied between  $D = 70\text{nm}$  and  $200\text{nm}$ . The spacing between adjacent cylinders were kept constant at  $200\text{nm}$  and thus the period of the array was  $\Lambda = D + 200\text{nm}$ . Zones with different diameters were fabricated on the same biochip to allow simultaneous measurements of the different structures. The SEM images of the fabricated structures are shown in figure 16.2.

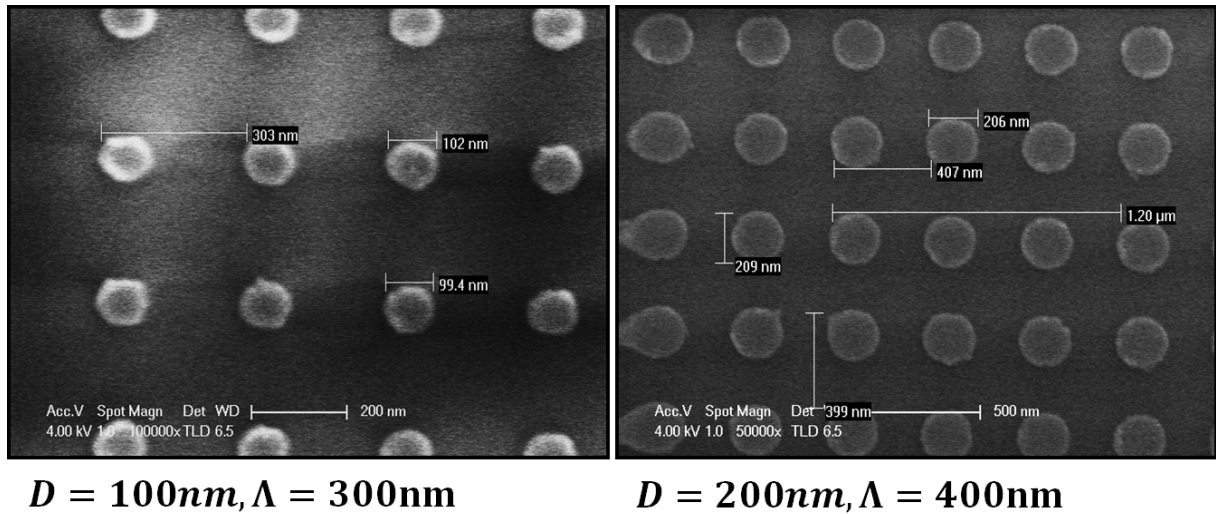


Figure 16.2: SEM images of gold nano-cylinder array on BK7 glass substrate. The cylinder heights were  $50\text{nm}$  and the period varied as  $\Lambda = D + 200\text{nm}$  where  $D$  is the diameter. Two zones of the same biochip are shown, with intended diameters  $D = 100\text{nm}$  and  $200\text{nm}$ . The uncertainty on the fabricated lengths was around  $\pm 5\text{nm}$ .

The Raman microscope XploRA ONE <sup>TM</sup> from Horiba Scientific also allows the measurement of the extinction spectra of the sample using a white light source and a spectrometer. Such extinction spectra were recorded for the different diameters and shown in figure 16.3.

The LSPR condition ( $\lambda_{LSP}$ ) corresponds to the peak of extinction. We see that there is a red shift of  $\lambda_{LSP}$  with diameter of the cylinders. This is the trend we expect for the  $LSP_T$  mode described in section 10.2. The LSPR resonance condition can be analytically calculated using the  $\chi$  formulation given by equation 10.10. The resonance condition thus obtained analytically for the cylinders and experimentally is also shown in figure 16.3. We see a small deviation of  $\lambda_{LSP}$  for the calculation and experiment and this is probably because the diameters of the cylinders in the fabricated structure are not precisely the values used for the calculation but have a uncertainty of around  $\pm 5\text{nm}$ .

To measure the SERS signal, thiophenol ( $C_6H_6S$ ) is used as the analyte because of its high Raman cross-section and due to the strong affinity of the thiol group to gold surfaces. The functionalization of thiophenol on the biochip surface was done first by preparing a  $0.1\text{mM}$  solution of thiophenol in ethanol and then dipping the biochip in the solution for about two hours. The biochip was then rinsed with ethanol and dried in nitrogen.

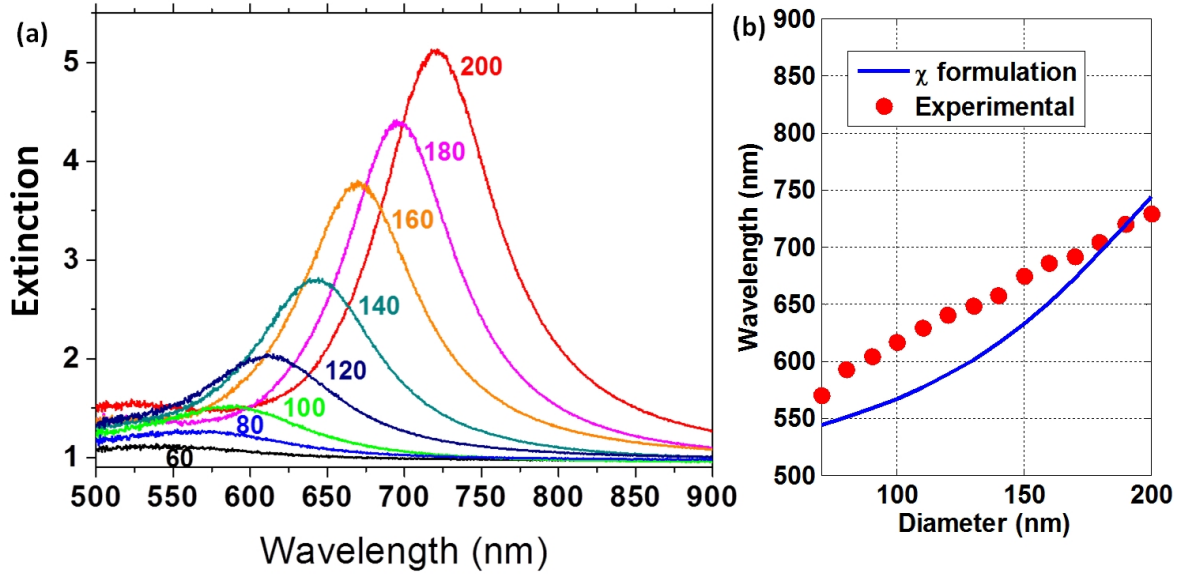


Figure 16.3: (a) The extinction spectra for the gold cylinder arrays on glass for different diameters. The diameters were varied from 60nm to 200nm and are marked on the figure for each curve. (b) The LSPR condition  $\lambda_{LSP}$  which corresponds to the peak of extinction as a function diameter (red dots). The analytical calculation for  $\lambda_{LSP}$  using  $\chi$  formulation is also shown (blue).

Raman shifts are measured in terms of wave-numbers and denoted by  $\Delta S_{Raman} = 1/\lambda_s - 1/\lambda_i$  in  $cm^{-1}$  where  $\lambda_i$  and  $\lambda_s$  are the excitation and emission wavelengths respectively. This shift is purely dependent on the type of molecule and independent of all experimental conditions. For Raman measurements, the scattered intensity at the shifted wavelength is recorded. For thiophenol there are several strong Raman peaks for shifts of  $419cm^{-1}$ ,  $1000cm^{-1}$ ,  $1024cm^{-1}$ ,  $1075cm^{-1}$  and  $1575cm^{-1}$ . The peak at  $1075cm^{-1}$  is the strongest and will be used for our measurements.

Three different lasers were used for the excitation with wavelengths  $\lambda_i = 633nm$ ,  $660nm$  and  $785nm$ . The corresponding Raman emission wavelengths for the peak at  $1075cm^{-1}$  are  $\lambda_s = 679nm$ ,  $710nm$  and  $857nm$ . The laser was focused on the biochip using a microscope objective ( $100\times$ ,  $N.A. = 0.9$ ) over a zone of around  $144\mu^2m$ . The backscattered light from the surface was collected by the same objective and recorded using a spectrometer with spectral resolution of  $4cm^{-1}$ . The recorded intensity spectra were normalized to the acquisition time and laser power. The intensity at  $1075cm^{-1}$  is used for the following discussions.

The measured SERS intensity for each cylinder diameter as a function of the corresponding experimental  $\lambda_{LSP}$  for the array, is shown in figure 16.4 for the three excitation wavelengths. The values are normalized to the maximum value for each curve. From the figure, we see that the SERS intensity undergoes an enhancement with varying diameters and have an optimum value. This value corresponds to the diameter of the cylinders for which we have  $\lambda_{LSP}$  close to the excitation wavelength of the measurement. Thus we can conclude that the SERS intensity is enhanced if the incident light can excite a plasmonic mode in the structure, in this case the LSP at the excitation wavelength.

For this configuration, the  $LSP_T$  is excited in the cylinders. The electric field intensity distribution of the mode with light incident from the medium surrounding the cylinders (which is true for our present



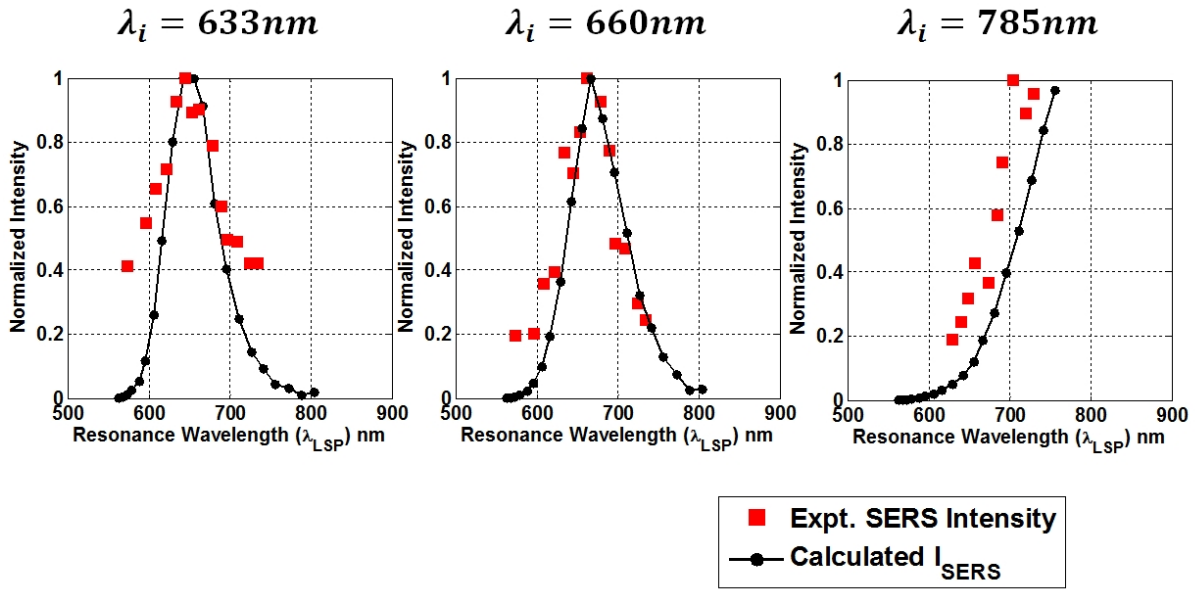


Figure 16.4: Experimental SERS intensity at raman shift of  $1075\text{cm}^{-1}$  for the arrays of varying diameters as a function of measured  $\lambda_{LSP}$  for the corresponding array (red squares). The calculated  $I_{SERS}$  given by equation 16.1 is also shown (black) as a function of  $\lambda_{LSP}$  calculated by  $\chi$  formulation for each given cylinder diameter.

SERS configuration) was shown in figure 10.13. The field is enhanced around the edges of the cylinders. To find a direct relation between the enhancement of SERS intensity and the electric field intensity around the cylinders we have numerically calculated the field intensity for each cylinder array at  $\lambda_i$  and  $\lambda_s$ . Plane wave with normal incidence from medium with index  $n_h = 1$  was considered for the calculation. The field intensity was then integrated around the cylinder surfaces ( $I_{surf}$ ) by the method described in section 10.3 (equation 10.11 and 10.12). Here the integral was calculated only around the cylinders because we expect the SERS intensity to result from only the thiophenol molecules bound on the gold surface.

As mentioned earlier, the SERS intensity is proportional to the product of the intensity enhancements at the excitation and emission wavelengths. Thus to calculate the electromagnetic contribution to the SERS intensity enhancement we will define

$$I_{SERS} = I_{surf}(\lambda_i) \times I_{surf}(\lambda_s) \quad (16.1)$$

This calculated  $I_{SERS}$  (normalized to the maximum value for each curve) is superposed in figure 16.4 for each pair of excitation and emission wavelengths. The calculated intensity is shown as a function of  $\lambda_{LSP}$  calculated analytically for each cylinder diameter by  $\chi$  formulation. The representation of the SERS intensity and the calculated intensity with respect to  $\lambda_{LSP}$ , assures that the uncertainty on the fabricated diameter values are avoided in the comparison.

We see a near perfect match for the variation of the SERS intensity and the calculated  $I_{SERS}$ . This result validates the principle of the two simultaneous processes for SERS enhancement described at the start of this chapter. The incident light excites the plasmonic modes (in this case the  $LSP_T$ ) in the structure, the confined EM field of the modes causes the a part of the enhancement. The re-radiated light from the molecules at Raman scattered wavelength re-excites plasmonic modes, the field confinement of

which causes another enhancement of the SERS intensity. Thus a mathematical product of electric field intensities at  $\lambda_i$  and  $\lambda_s$  can predict the tendency of the enhancement of SERS intensity.

We will now use the same principle and predict the SERS intensity enhancement with the excitation of another plasmonic mode, the Bragg mode in an array of metallic cylinders with an underlying metallic film.

## 16.2 SERS enhancement due to the Bragg Modes

The Bragg modes in a metallic array on a metallic film was described in details in chapter 11. The dispersion of the BMs was shown in figure 11.2. The resonance condition of the Bragg mode given by  $(k_{//}/k_0)_{BM(b/h)} = \left| (k_{//}/k_0)_{PSP(b/h)} - n_P \right|$  (equation 11.1) shows a strong dependence of the condition of the mode with angle of incidence. For the SERS experiment considering incidence from air, we can write the condition in terms of incidence angle as

$$\theta_{BM} = \sin^{-1} \left( \sqrt{\frac{(n_{b/h}^2 n_m(\lambda)^2)}{(n_{b/h}^2 + n_m(\lambda)^2)}} - m \frac{\lambda}{\Lambda} \right) \quad (16.2)$$

where the refractive indices of the substrate is  $n_b$  and the surrounding medium  $n_h$  is air. So for a given incident wavelength, there are two possible BMs ( $BM_h$  and  $BM_b$ ) excited at different angles of incidence, for the PSP in medium  $n_h$  and  $n_b$  respectively.

The experimental excitation of the BMs in the Kretschmann configuration was demonstrated in section 15.2. However in the Kretschmann configuration for values of  $(k_{//}/k_0) > n_h$  the BMs are generally eclipsed by the HLP mode. For the SERS experimental setup used in this work, the HLP are not excited and the strongest modes in terms of extinction that can be excited are the BMs. Thus this setup can help us study the dispersion characteristics of the BMs and also their performance for SERS.

We have shown before that the BMs do not depend on the shape of the structures comprising the array and thus can be excited in grating structures as well as nano-cylinder arrays. For this purpose, both the structures were fabricated using EBL. The array height (grating ridge height or cylinder height) was taken as  $h_2 = 30nm$  and the underlying gold film height as  $h_1 = 30nm$ . Gratings with width  $w_1 = 100nm$  and cylinders with diameter  $D = 220nm$  were fabricated. The period of the cylinder array was taken as  $\Lambda = 400nm$  while for the grating, three periods were fabricated,  $\Lambda = 300nm$ ,  $400nm$  and  $500nm$ . The SEM images for the fabricated grating structure and one of the cylinder arrays is shown in figure 16.5.

The Raman microscope was used to record the extinction spectra of the structures. To measure the spectra for different angles of incidence, the biochip was tilted precisely using the sample holder. The schematic of the experiment along with the extinction spectra of the grating structure is shown in figure 16.6. Both the excitation and collection are carried out with a  $10\times$  microscope objective ( $N.A. = 0.25$ ), the spectra recorded in transmission configuration using white light illumination. For all experiments, the excitation polarization was TM polarized with respect to the tilt of the biochip. This was assured by tilting the biochip about the axis of the grating ridges (as shown in figure 16.6(a)) and by linearly polarizing the incident light along the axis perpendicular to the grating ridges.

For the spectra shown in figure 16.6(b) we clearly see two peaks (a stronger one for lower wavelengths and a weaker peak for higher wavelengths) and both the peaks undergo a red-shift with increasing angle of

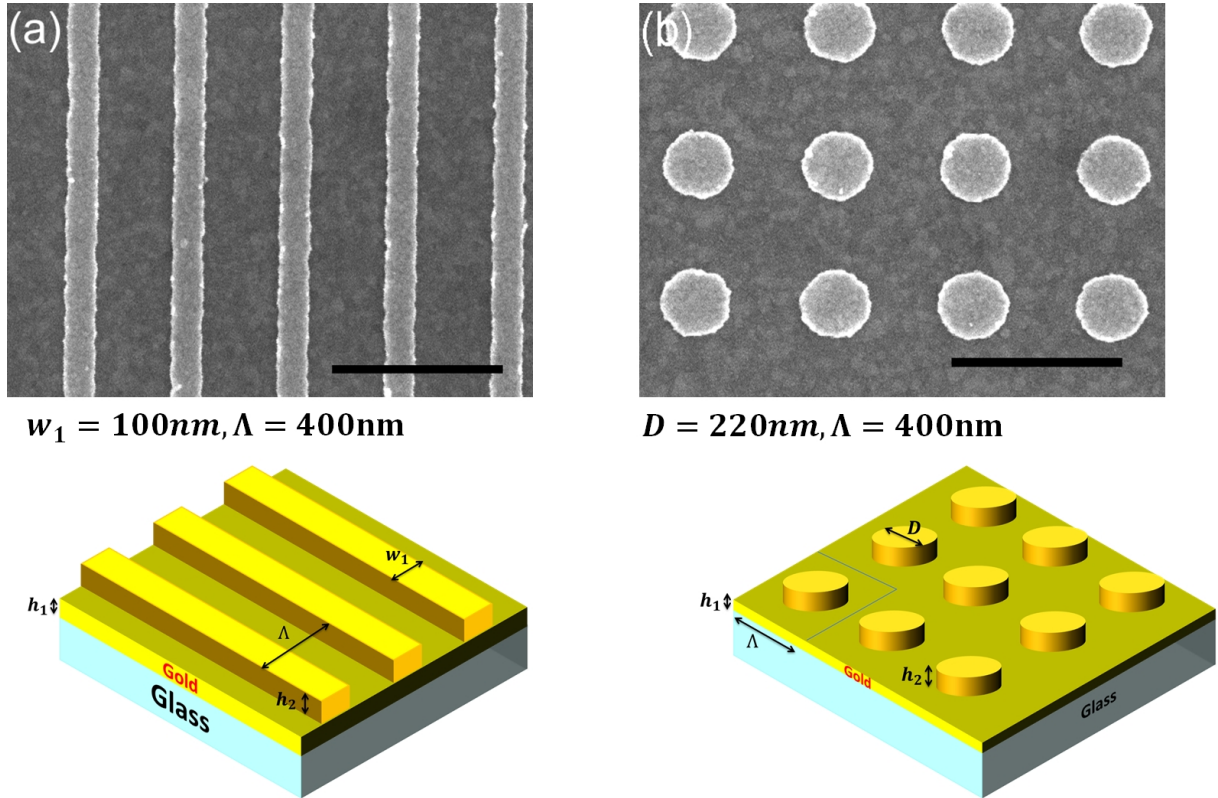


Figure 16.5: SEM image of (a) gold grating of width  $w_1 = 100\text{nm}$ , period  $\Lambda = 400\text{nm}$  and height  $h_2 = 30\text{nm}$  on a metallic film of height  $h_1 = 30\text{nm}$ . (b) array of metallic cylinders of diameter  $D = 220\text{nm}$  and period  $400\text{nm}$ . Both the structures are fabricated on BK7 glass substrate.

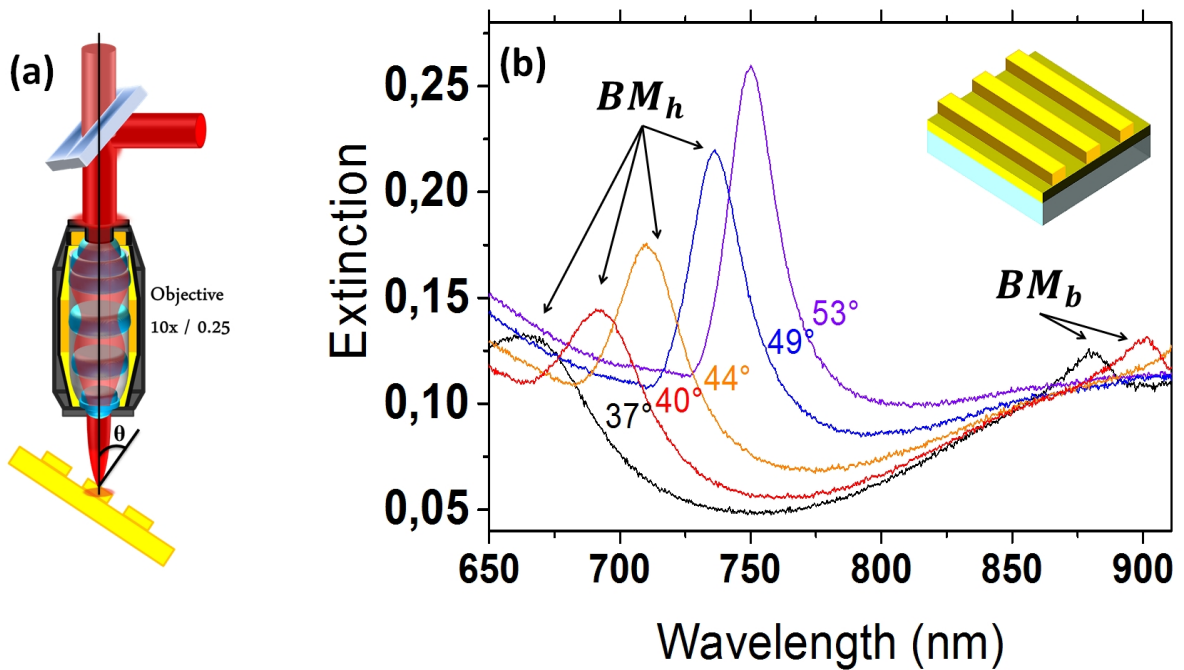


Figure 16.6: (a) Schematics of the experimental configuration to study the extinction spectra as a function of angle of incidence  $\theta$ . (b) The extinction spectra for different angles of incidence (marked for the curves) for the grating structure of width  $100\text{nm}$  and period  $400\text{nm}$ .

incidence. The two peaks can be identified as  $BM_h$  for the lower wavelengths and  $BM_b$  for the higher wavelengths.

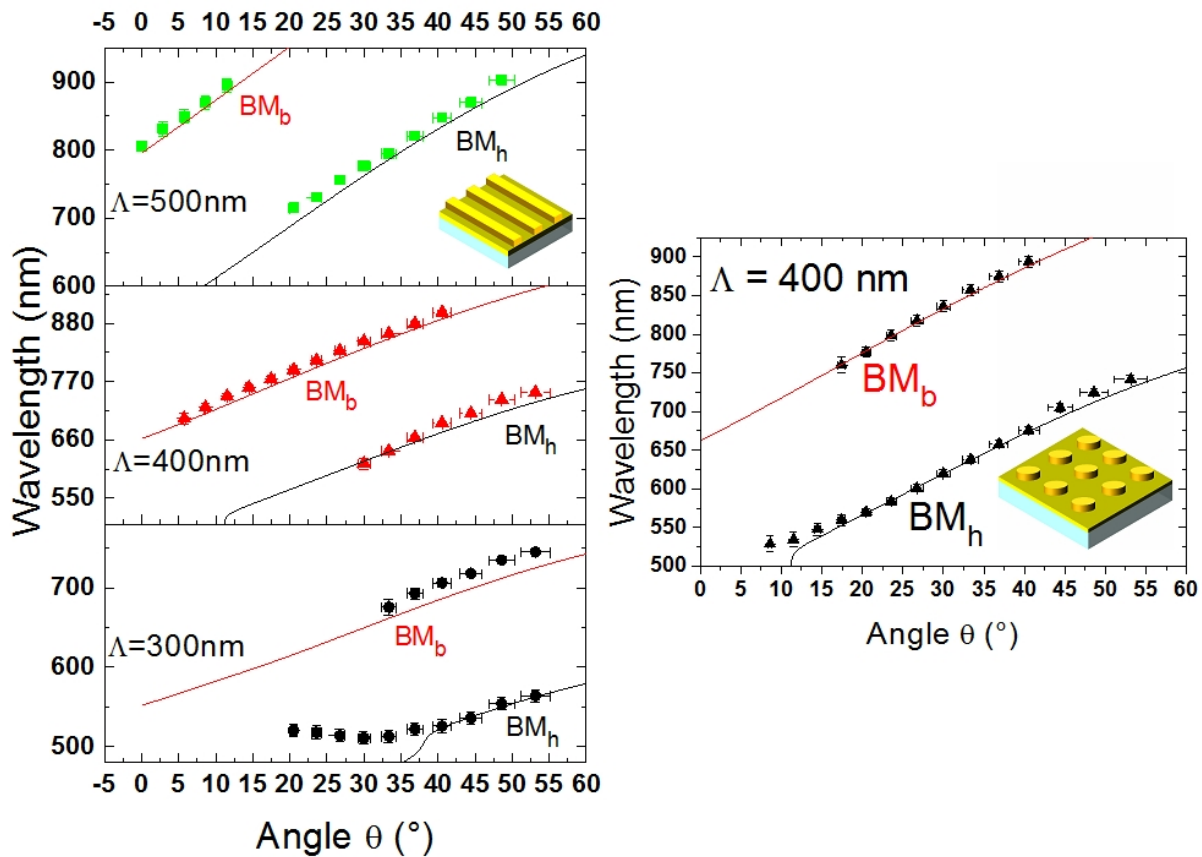


Figure 16.7: The wavelength of the extinction peaks as a function of incident angle  $\theta$  for the grating (three different periods) and the cylinder array (scatter plots). The analytical dispersion of the  $BM_b$  and  $BM_h$  are superposed on the plots (solid lines). For the analytical calculation the indices were taken as  $n_h = 1$  and  $n_b = 1.513$ .

The resonance wavelength of the two peaks as a function of angle of incidence is shown in figure 16.7 for the three periods of the grating and the cylinder array of period  $400nm$ . The analytically calculated dispersion of the BMs as a function of wavelength and angle of incidence is also superposed in the figure. We see that peaks for all the structures correspond to the excitation condition of the BMs. Another important aspect of this experimental result is that the wavelength of the extinction peaks (or the resonance condition of the BMs obtained experimentally) for  $\Lambda = 400nm$  is almost the same for the grating and the cylinder array. This confirms that indeed the BM condition does not depend on the structure shape but purely on the periodicity of the array.

### 16.2.1 Directional SERS intensity due to the Bragg modes

Conventionally the SERS substrates are excited and the emission from them are collected along the axis perpendicular to the substrate surface ( $\theta = 0$ ). A major motivation of our SERS experiment was to study the effect of excitation and collection of SERS signal at an oblique angle to the plane of the biochip. This in the literature is generally called the directionality of the SERS signal. Different reports have

demonstrated that the SERS signal undergoes an enhancement when such directional SERS signal is collected for various types of nano-particle arrays [248, 249, 250].

In this section we will show that this effect is mainly due to excitation of certain plasmonic modes (in our case the BM) for which the resonance condition is strictly dependent on the angle of incidence. It must be noted that using isolated nano-particles will not produce such an effect as the resonance condition of the LSP is not dependent on the angle of incidence.

The SERS intensity was measured using the same method as described in the preceding section. The biochip was tilted and SERS intensity was recorded for each incident angle at the three excitation wavelengths ( $633nm$ ,  $660nm$  and  $785nm$ ). One such SERS intensity spectrum is shown in figure 16.8 for the grating structure with period  $400nm$ . The SERS intensity for normal incidence ( $\theta = 0$ ) and for  $\theta = 34^\circ$  is shown. A clear enhancement of the SERS intensity at the oblique angle is observed for the Raman spectra. It can be seen from figure 16.7 that for this particular structure, the condition for  $BM_h$  at  $\lambda_i = 660nm$  is fulfilled around  $\theta = 34^\circ$ . This confirms that the enhancement of the SERS signal is due to the excitation of the BM.

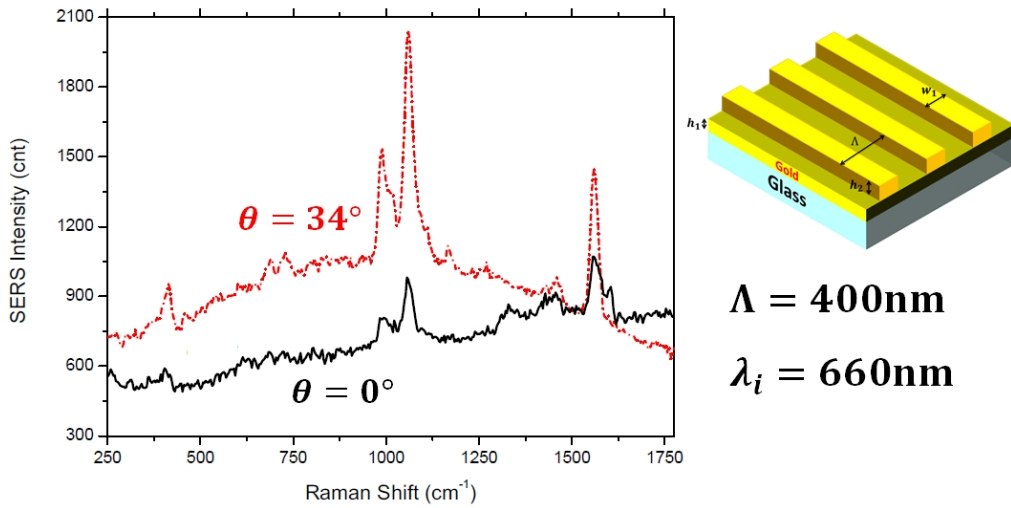


Figure 16.8: SERS intensity spectra of thiophenol recorded on the grating structure ( $w_1 = 100nm$  and  $\Lambda = 400nm$ ) with excitation wavelength  $\lambda_i = 660nm$ . Two excitation angles  $\theta = 0^\circ$  (black) and  $\theta = 34^\circ$  (red) are shown.

To validate the fact that the SERS enhancement observed at this particular angle of incidence is really due to the local EM field enhancement caused by the excitation of the BM, the field intensity for the structures were calculated using numerical methods. In the last section we have shown that the SERS intensity is proportional to  $I(\lambda_i) \times I(\lambda_s)$  where  $I$  is the near field intensity around the structures as a function of wavelength.

For the present calculation the field distribution for the structures were calculated at the given  $\theta$  for both the incident and emission wavelengths. Then the corresponding  $I_{SERS}$  was calculated as an integral over the entire metal surface ( $S_{cyl}$ ) as following

$$I_{tot}^2(\theta) = I(\lambda_i, \theta) \times I(\lambda_s, \theta_s)$$

$$I_{SERS}(\theta) = \frac{1}{S_{cyl}} \iint_{S_{cyl}} I_{tot}^2(S) dS \quad (16.3)$$

The above equation is a generalized expression when the incident excitation and the collection angle for the SERS emission are not the same ( $\theta$  and  $\theta_s$  respectively). However for our experiment the same objective is used to excite and collect the SERS intensity and so for the present experiment  $\theta = \theta_s$ . The calculated  $I_{tot}^2$  for the grating and the cylinder array (both of period  $400nm$ ) at  $\theta = 0^\circ$  and  $\theta = 34^\circ$  is shown in figure 16.9.

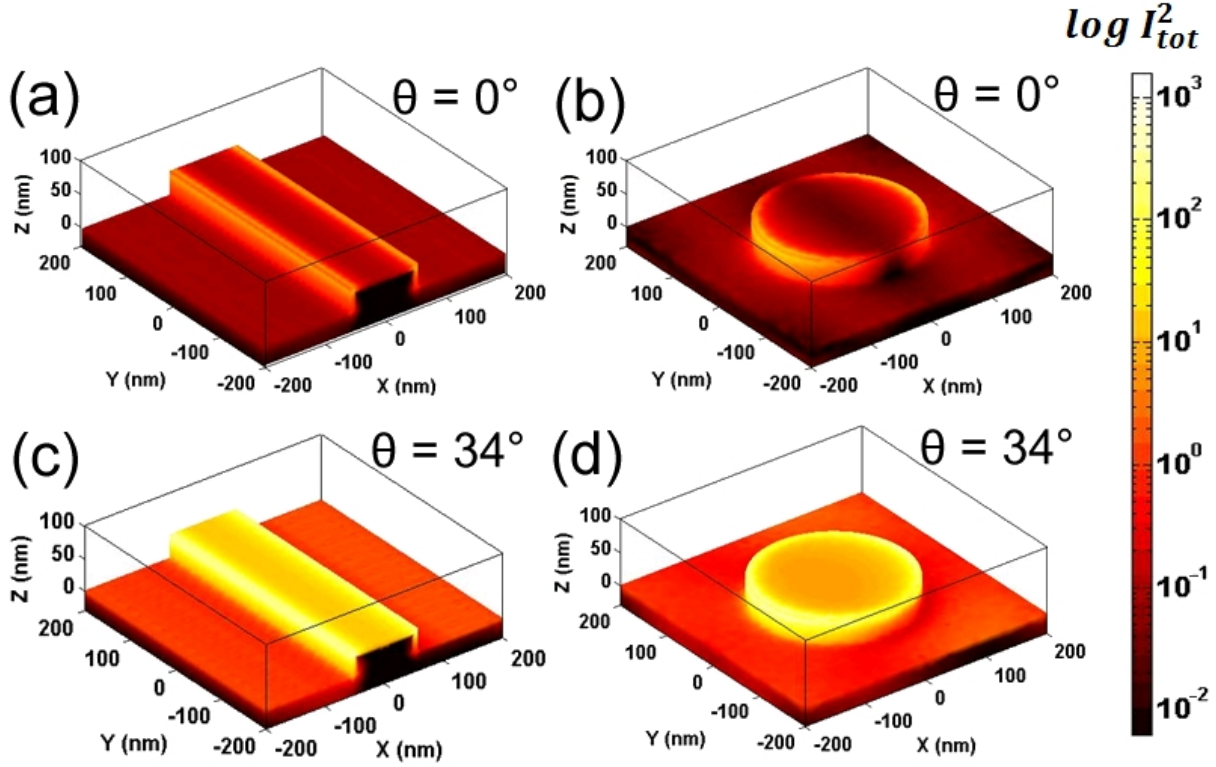


Figure 16.9: The calculated  $I_{tot}^2$  at  $\theta = 0^\circ$  for the (a) grating ( $w_1 = 100nm$ ,  $\Lambda = 400nm$ ) and the (b) cylinder array ( $D = 220nm$ ,  $\Lambda = 400nm$ ). (c,d) The same at  $\theta = 34^\circ$

A clear enhancement of the intensity distribution is observed at  $\theta = 34^\circ$  for both the structures. At  $\theta = 0^\circ$  the plasmonic modes do not satisfy a resonance condition and thus the field intensity is weak and concentrated only at the metallic edges. However when the BM undergoes resonance at  $\theta = 34^\circ$  the characteristic near field distribution of the BM is enhanced and thus results in a much stronger SERS signal. A minor point to note here is that as the BMs are extended modes, an appreciable portion of the electric field intensity is also distributed on the gold film surface away from the structures.

The SERS intensity as a function of incident angle for all the structures (gratings for three periods and the cylinder array of period  $400nm$ ) at the three excitation wavelengths for the Raman peak at  $1075cm^{-1}$  is shown in figure 16.10. On the same figure vertical lines are shown for the values of  $\theta_{BM}$  as calculated by equation 16.2. For each structure geometry these values correspond to the angles for  $BM_h$  and  $BM_b$  (also shown as a function of wavelength in figure 16.7) at the wavelengths of excitation  $\lambda_i$  and emission  $\lambda_s$ . For the experimental SERS intensity we see the presence of local maxima close to each of these values for almost all structure geometries and excitation wavelengths. This further validates that the excitation of the BMs enhance the recorded SERS intensity.

$I_{SERS}$  was calculated by equation 16.3 for all the structures for the pairs of excitation and emission wavelengths and the curves are superposed in each inset of figure 16.10. There are some interesting points

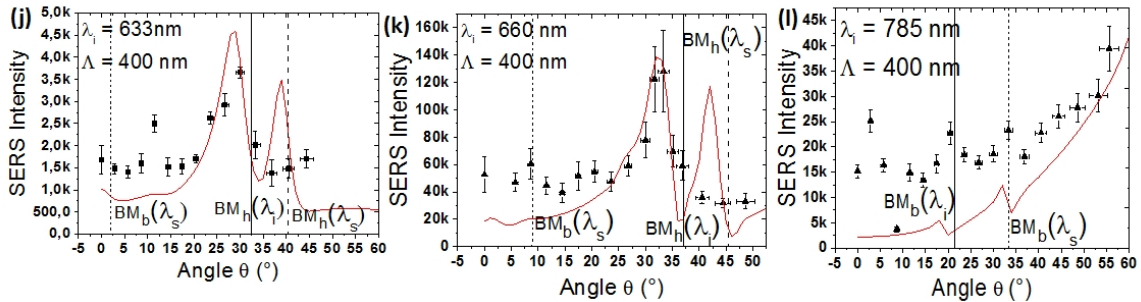
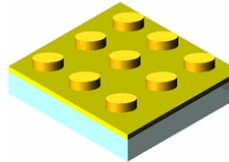
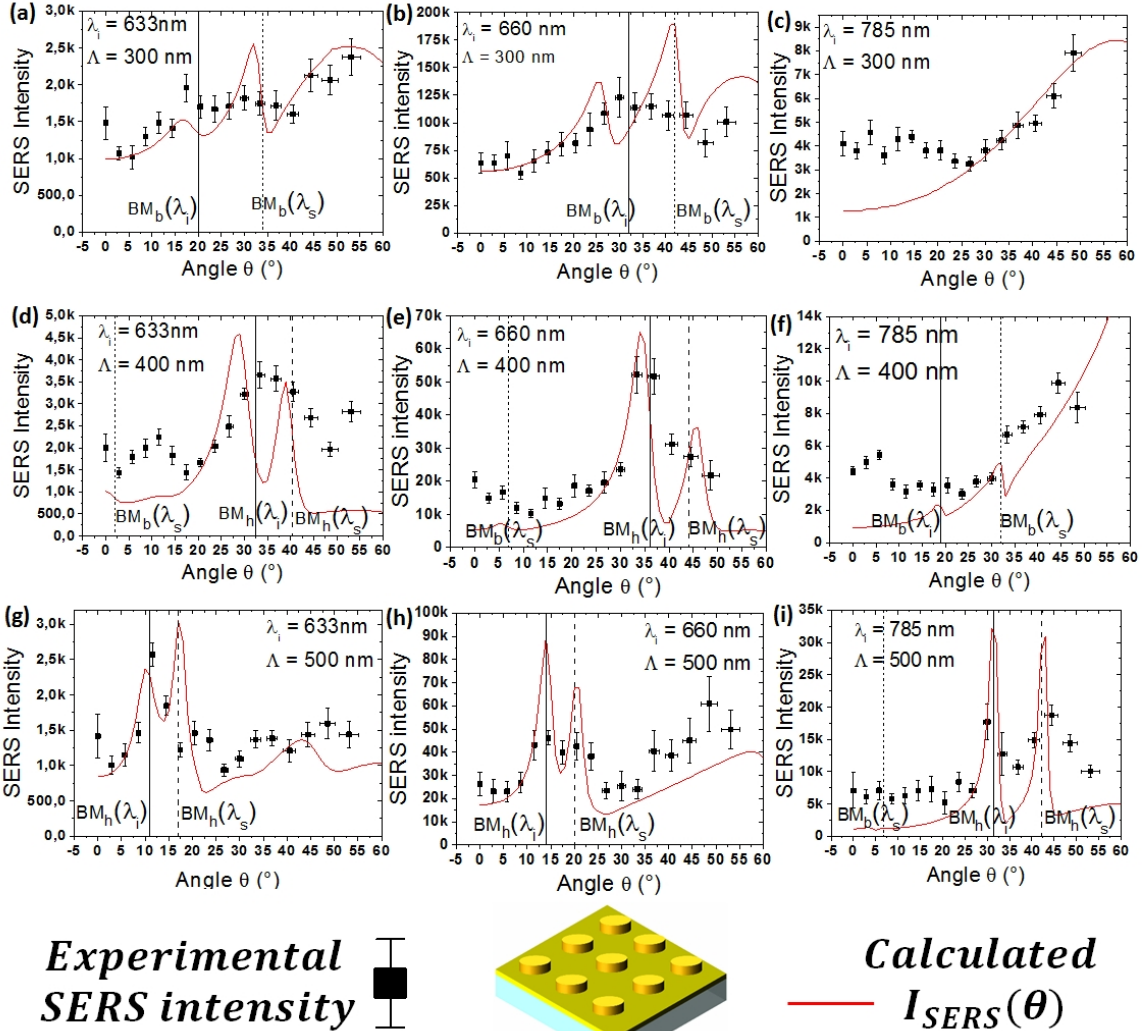
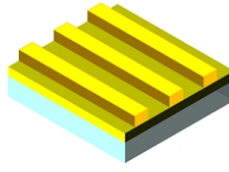


Figure 16.10: Experimental SERS intensities (dots) and calculated  $I_{SERS}$  (solid red lines) as a function of angle  $\theta$  for the three excitation wavelengths ( $\lambda_i = 633\text{nm}$  a,d,g,j,  $660\text{nm}$  b,e,h,k and  $785\text{nm}$  c,f,i,l) on gratings (a-i) with grating periods  $\Lambda = 300\text{nm}$  (a-c),  $400\text{nm}$  (d-f) and  $500\text{nm}$  (g-i). The same for the cylinder array (j-l) with period of  $\Lambda = 400\text{nm}$ . Vertical lines (black) indicate the analytically calculated angles of  $BM_h$  or  $BM_b$  excitation at  $\lambda_i$  (solid line) and  $\lambda_s$  (dashed).

to note from these results.

First, we see that the calculated  $I_{SERS}$  have local maxima close to  $\theta_{BM}$  for each structure. However the maxima are somewhat shifted from the analytically calculated resonance conditions of the BMs. This is because  $I_{SERS}$  is a measure of near-field confinement for the modes, while  $\theta_{BM}$  represents the far field excitation condition of the modes. Such shifts of the near field resonance condition and that for the far field has been observed and reported before [251, 252, 253]. We will not go into the details of this phenomenon.

The experimental SERS intensity follows the trend of  $I_{SERS}$  in terms of the maxima at the position of the calculated maxima for the BM excited at  $\lambda_i$ . However the linewidth of the peaks are much broader for the experimental SERS intensity and furthermore the peaks for the BM at  $\lambda_s$  are almost non-existent for the experiment. This can be attributed to the fact that the microscope objective used for the excitation and collection has a  $N.A. = 0.25$  and thus the angular divergence of the excitation beam and that of the collected light is around  $\pm 7^\circ$ . For the calculation such a large angular divergence was not taken into account. Due to the angular divergence the peaks tend to flatten out and this can explain the sharper peaks of the calculated value compared to the experimental ones. The broader experimental peaks for  $\lambda_i$  and  $\lambda_s$  almost overlap and thus we observe for most cases a single peak instead of the two peaks shown for  $I_{SERS}$ . However if the two peaks are sharp and well separated in terms of angle, as in the case of figure 16.10 (i) both the peaks can be observed in the experimental SERS intensity.

The last important aspect to note from figure 16.10 is that for  $\Lambda = 400nm$  we have almost the same angular dependence of both the experimental SERS intensity and the calculated  $I_{SERS}$  for the grating structure and the cylinder arrays. Thus we can conclude that the angular dependence of the SERS intensity is purely a result of the excitation and emission of the plasmonic modes in the structure (in this case the BM which only depends on the periodicity of the array).



## **General conclusion and perspectives**



## What has been done in this work : Conclusions

In this work we have described the various plasmonic modes that can be supported by metallic nano-structures. To study the resonance conditions in structures with complex geometries a numerical model was developed during the course of this work. This hybrid numerical model is a combination of two well-known methods namely the Fourier modal method (FMM) and the finite element methods (FEM). The model takes advantage of the two, rather complimentary numerical methods to reduce the computation times and memory requirements for near field calculations of structures with dimensions of the order of the wavelength of light. Furthermore combining FMM with FEM overcomes the convergence problem faced by FMM when metals are involved. We have shown in this work that the hybrid numerical model can give accurate results, for different complex geometries involving metal, which are verified by experiments.

Using the numerical method he have simulated the near and far field responses of various structures. Such simulations were useful to analytically calculate the resonance conditions of the different modes that can be excited in such structures. In this work we have described the resonance frequency ( $\omega$ ) of each plasmonic mode as a function of its momentum wave-vector in a given direction. This was quantified in terms of the wave-vector in free space ( $k_0 = \omega/c$  with  $c$  being the velocity of light in free space) and normalized in-plane wave-vector of the mode ( $k_{//}/k_0$ ). Such a description is useful to directly compute the dispersion relation of the different modes and understand categorically the excitation mechanism of the modes. The fundamental plasmonic mode is the propagating surface plasmon (PSP) which is excited in a uniform metal-dielectric interface. This plasmonic mode is well-known. In this work we have shown that by expressing the modes in terms ( $k_0 - (k_{//}/k_0)$ ) we can quantify the various other modes, originating from the PSP, that exist in nano-structures.

For metallic gratings on a glass substrate, owing to its periodicity, the Wood-Rayleigh anomaly (WRA) are excited when the incident photon lies along the axis perpendicular to the gratings. In this work we have analytically calculated the resonance condition for such modes. We have shown that the famous Wood's anomaly can be explained in terms of the WRAs.

When the photon is incident parallel to the grating ridges, the confinement of PSP by the finite width of the grating, give rise to the Confined Propagating plasmon (CPP) modes. These resonance condition for these modes, (as opposed to the WRAs which depend purely on the periodicity) depend purely on the grating width. Such modes were introduced in our publication Sarkar et al, Sensors and Actuators B, 2014. This mode to our knowledge has never been described before in any other publications.

The calculated electric field intensity for the CPP were shown to be confined around the grating ridges with a major portion on the sides of the gratings, which are a magnitude smaller in dimensions compared to the wavelength of light. Such a property is useful for applications in bio-sensing, as such strong confinement can effectively reduce the minimum amount of target molecules required to obtain a detectable signal. This is quantified as Sensitivity Enhancement Factor (SEF) which serves as a figure of merit for biosensors based on detection of probe-analyte binding events. We have shown that the CPP modes can increase SEF up to a factor of two. Experimental demonstration of the excitation of the CPP and their application in bio-sensing in the Kretschmann configuration is also shown.

The second fundamental plasmonic mode, the localized surface plasmon (LSP) is excited in nano-particles with dimensions much smaller than the wavelength of light. In this work we have introduced a novel analytical model called the  $\chi$  formulation to calculate the resonance condition for the LSP. This model is shown to give accurate results for spherical particles and close approximations for complex

geometries such as 3D nano-cylinders with or without the presence of a substrate. The electric field enhancement caused by the LSP is numerically calculated and such numerical results are used to justify the experimentally observed SERS intensity enhancement in arrays of gold nano-cylinders on glass substrate.

For arrays of metallic nano-particles with an underlying metallic film, modes similar to the WRAs, called the Bragg modes (BM) are excited. These modes are excited due to the diffraction of the PSP of the metallic film by the array of metallic particles. Complete analytical formulations for the excitation conditions of the BMs in different excitation configurations are presented in this work. The BMs are not useful for SPR detection, however the field enhancement caused by them are shown to enhance the SERS intensity recorded for hybrid structures comprising of arrays of gold nano-particles with an underlying gold film. The numerical calculations for the electric field intensity enhancement in such structures are shown to follow the trend of directional SERS intensity enhancement recorded experimentally.

In such hybrid structures, the LSP of the nano-particles can also couple to the PSP of the metallic film, to give rise to a new plasmonic mode, called the Hybrid Lattice Plasmon (HLP). This mode and its application to bio-sensing has never been reported before. We had introduced the presence of the HLP mode in Sarkar et al, ACS Photonics, 2015.

Though such coupling have been observed before and are generally termed as Fano-resonance or Fano-like resonances in the literature. However we believe that such a classification of the HLP as Fano resonance is erroneous. We have offered a complete description of the coupling mechanism of the LSP and the PSP and have justified the fact that such a coupling cannot be explained in terms of Fano resonances. It can rather be described as a harmonic coupling between oscillator systems and the resonance condition of the mode can be calculated by a classical approach to strong coupling using the harmonic oscillator model. This was the basis of our publication Sarkar et al, Optics Express, 2015.

This model along with the EM properties of the HLP is discussed in details for a 3D array of gold nano-cylinders on a gold film. However the description presented here is not only restricted to gold nano-cylinders and can be used to explain the plasmonic modes for metallic nano-particles with any shape and dimensions. The resonance condition for the LSP, BMs and the HLP as a function of geometrical parameters such as cylinder height or diameter and periodicity of the array is presented in details. The experimental excitation of the different modes (HLP and BMs) in such structures is demonstrated and shown to correspond closely to the numerical and analytically calculated results. With respect to bio-sensing the HLP mode is shown to increase SEF by an order of magnitude for certain geometries and excitation configurations with selective target localizations.

The sensitivity of the various modes to bulk refractive index change of the surrounding medium was also calculated by numerical methods. Appropriate analytical formulations for the same were also derived and shown in this work. The HLP mode is shown to have much lower bulk index sensitivity as compared to the PSP mode. This property of the HLP is useful for biosensors which detect specific bindings of target and probe molecules functionalized within a few nanometers from the metallic surface. For such biosensing applications a high sensitivity with respect to bound targets are required with low drift with changes in bulk refractive index.

Plasmonic modes are also classified as «Confined» modes such as the PSP, LSP and the CPP, or as «Extended» modes such as the WRAs and BMs. The HLP is shown to behave as confined modes as it results from the coupling of LSP and PSP. However when the  $(k_0, (k_{//}/k_0))$  values for the HLP lies close to that of the BMs, a secondary coupling of the HLP with the BM, causes the former to have certain

characteristics of extended modes. This same principle can explain the famous phenomenon of extraordinary transmission observed in nano-hole arrays, which is also seen for the HLP in its quasi-extended regime.

The sensitivity of the HLP mode is experimentally shown to have different behaviors depending on the interrogation angle of incidence, with respect to the thickness of the deposited molecular layer. For this purpose two well known polyelectrolytes, Poly(allylamine hydrochloride) (PAH) and Poly(styrenesulfonate) sodium salt (PSS) were used and their binding to the biochip surface was studied. Apart from the experimental validation of the two behavior for the HLP, this measurement also proved that the sensitivity in general for plasmonic modes is not proportional to the confined field intensity, but rather to the change of the field intensity of the mode, brought about by the molecular layer.

## **What can be done : Perspectives**

This work was done as a part of the ANR project PIRANEX which aims to combine SPR and SERS detection in the same instrument, using the same biochip. The HLP was shown to enhance the sensitivity of SPR detection. However such sensitivity enhancement is more useful when the target molecules can be selectively localized around the nano-cylinders. Such selective localization was somewhat achieved for the 2D metallic gratings by covering a portion of the structures by silica. But the same for 3D cylinder array, by covering the uniform gold film between the cylinders with silica, could not yet be achieved. Thus fabrication of such structures and the validation of an orthogonal chemistry have been done. The SEF, numerically calculated for the HLP, shows an increase by an order of magnitude. This remains to be validated experimentally.

Though the structures were optimized for SPR detection with a complete description and simple analytical models for the resonance wavelength and incident angles, such an optimization for SERS detection is still eluding. In this work a demonstration that certain modes (LSP and BM) can be used to enhance the SERS intensity was shown. However a complete description of the exact SERS enhancement and the role played by molecular localization on such enhancement must still be studied.

This work can be used to completely understand and analytically formulate the different plasmonic modes excited in nano-structures. The near and far field properties of the various plasmonic modes at resonance are harnessed for different applications. Though this work is based on applications to bio-sensing, such description of the electromagnetic properties of the plasmonic modes can also be useful for other domains where such modes are used. Metals owing to their high absorption, are often avoided for many such applications. But the theoretical models developed in the course of this work can be applied for other dielectric or meta-materials. Thus the application of the same theories of plasmonic modes can be tried for such materials and the characteristics can be optimized for them with respect to corresponding applications.

Finally the representation in terms of modes have been shown to be applicable for plasmon polaritons. It is now interesting to see if such theories can be applied for other quasi-particles such as phonons or excitons in hybrid nano-structures. That can then open new avenues for the theoretical basis presented in this work.



# Appendix





## Appendix A

# LSPR condition for metallic strips

The extinction spectrum ( $W_{ext}$ ) was calculated for a metallic strip in a homogeneous medium of refractive index  $n_h = 1.333$ . The width of the strip is  $w_1$  with the height  $h$ . The calculation was done by FEM using a 2D mesh. The incident light was considered to be a plane wave with an angle of incidence  $\theta$  with the  $z$  axis and TM polarized. We observe the presence of two LSPR condition depending on the angle of incident. The extinction peak ( $\lambda_{LSP}$ ) for  $\theta = 0^\circ$  undergoes a red shift with the width of the strips and a blue shift with the height. The trend is opposite for the extinction peak with  $\theta = 60^\circ$  with a slight blue shift with width and red shift with height. This can be explained as shown in section 10.2 by the fact that one LSPR condition is satisfied at  $\theta = 0^\circ$  with the plasmons excited along the width of the strips ( $x$  axis) while the other at  $\theta = 60^\circ$  with the plasmons excited along the height of the strips ( $z$  axis). The plasmons along the width will be called  $LSP_T$  while that along the height will be called  $LSP_L$ .

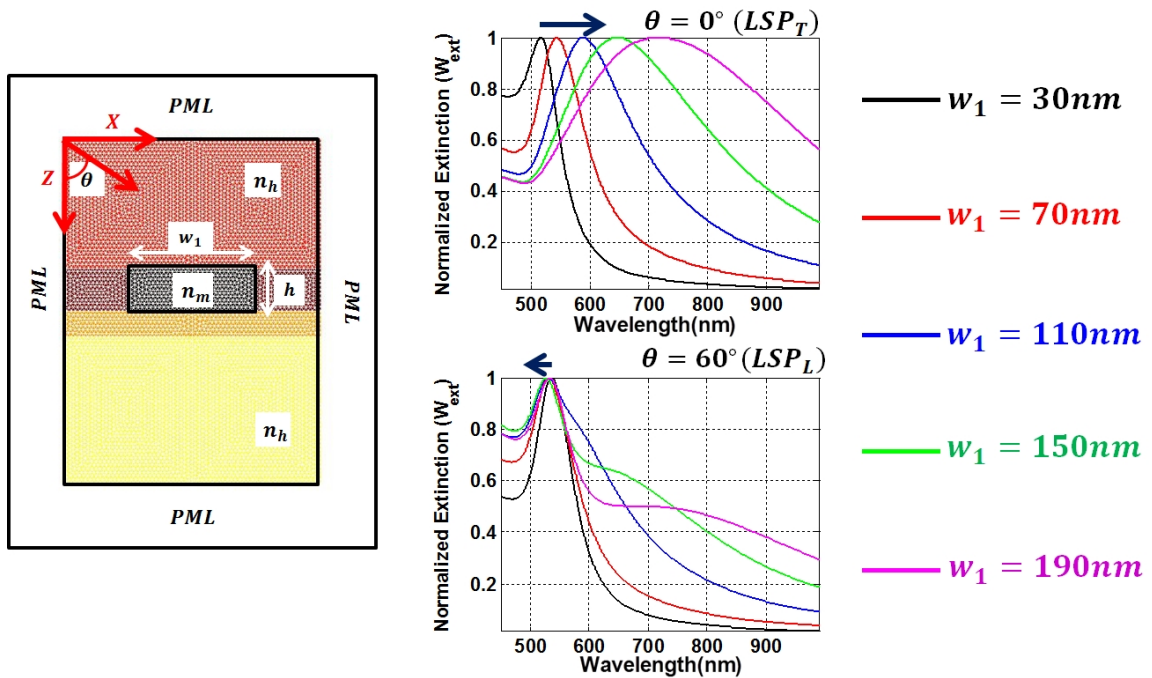


Figure A.1: The calculated  $W_{ext}$  using FEM for a metallic strip as a function of width  $w_1$  for height  $h$  in a homogeneous medium  $n_h = 1.333$ . The incident angle for the plane wave is  $\theta$ . At normal incidence the LSP along  $x$  is excited and undergoes a red shift with  $w_1$ . At  $\theta = 60^\circ$  the LSP along  $z$  is excited and undergoes slight blue shift with  $w_1$ .

The dependence of the resonance wavelength ( $\lambda_{LSP}$ ) on the width and height of the strip is shown in figure A.2. The electric field intensity ( $I = E_x^2 + E_z^2$ ) distribution normalized to the incident intensity ( $I_0$ ) was calculated and shown for the  $LSP_T$  ( $\theta = 0^\circ$ ) and  $LSP_L$  ( $\theta = 60^\circ$ ) for  $w_1 = 150nm$  and  $h = 50nm$ .

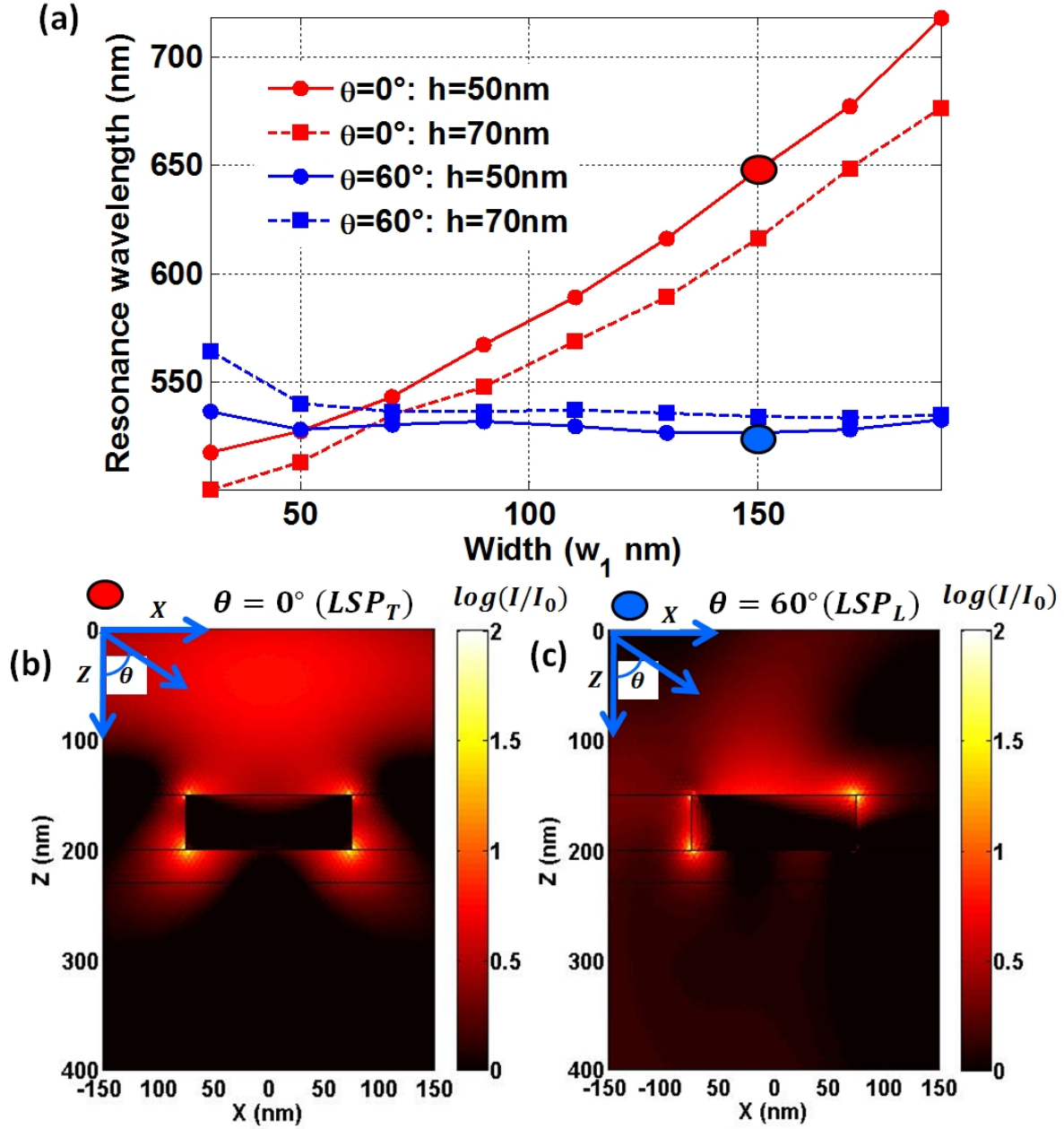


Figure A.2: (a) Resonance wavelengths ( $\lambda_{LSP}$ ) using FEM as a function of strip width ( $w_1$ ) for incident light at  $\theta = 0^\circ$  ( $LSP_T$ ) and  $\theta = 60^\circ$  ( $LSP_L$ ) for two heights  $h = 50nm$  and  $h = 70nm$ . (b-c) The electric field intensity in logarithmic scale for the two LSPs for strips of width 150nm and height 50nm. (b)  $\theta = 0^\circ$  ( $LSP_T$ ) at  $k_0 = 9.69/\mu m$  ( $\lambda = 648nm$ ) (c)  $\theta = 60^\circ$  ( $LSP_L$ ) at  $k_0 = 11.94/\mu m$  ( $\lambda = 526nm$ )

## **Dispersion maps for array of metallic cylinders on metallic film**

---

The model for the analytical calculation of the plasmonic modes in an array of metallic cylinders with an underlying metallic film was described in chapter 12. The reflectivity (R), transmission (T) and the absorption ( $A=1-R-T$ ) as a function of  $(k_0, (k_{//}/k_0))$  was also calculated using numerical methods. The analytical model was verified using these results as well as experimental reflectivity maps obtained using the SPR imaging setup working in Kretschmann configuration as described in part V. Here we present the different absorption and reflectivity maps thus obtained by numerical methods and by experiments. The dispersion of the various modes as obtained by the analytical model is also shown in the figures. We see a close to near perfect fit of the analytical model to such results.

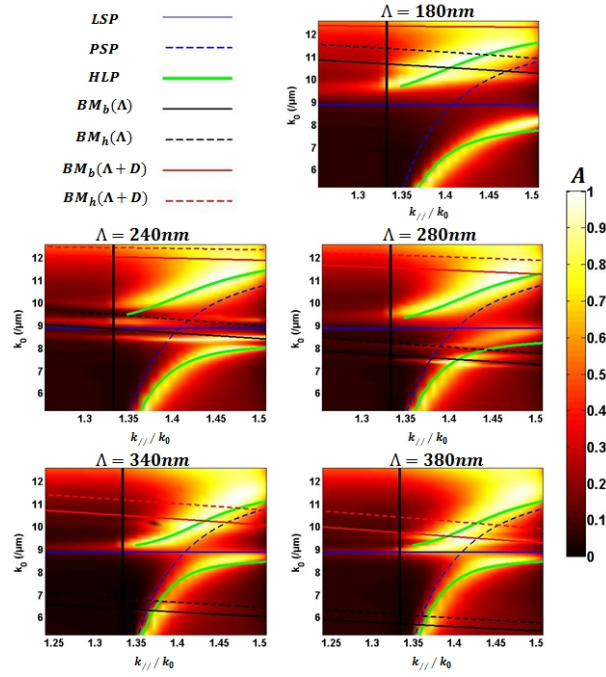


Figure B.1: The normalized absorption ( $A$ ) dispersion maps calculated by numerical methods with varying period ( $\Lambda$ ) as a function of  $(k_0, (k_{//}/k_0))$  for  $h_2 = 30nm$ ,  $D = 50nm$ . The analytically calculated dispersion of the various modes is also shown which fits accurately to the rigorously calculated numerical results.

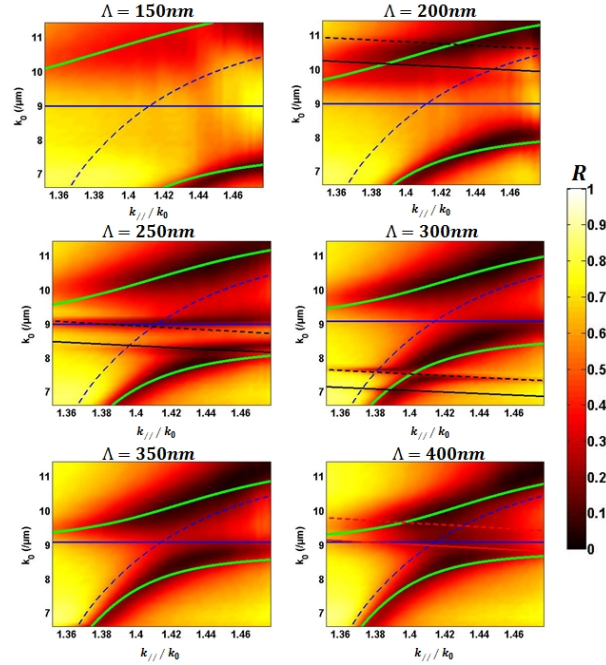


Figure B.2: The normalized reflectivity ( $R$ ) dispersion maps obtained experimentally with varying period ( $\Lambda$ ) as a function of  $(k_0, (k_{//}/k_0))$  for  $h_2 = 30nm$ ,  $D = 50nm$ . The analytically calculated dispersion of the various modes is also shown and the color legend is same as figure B.1.

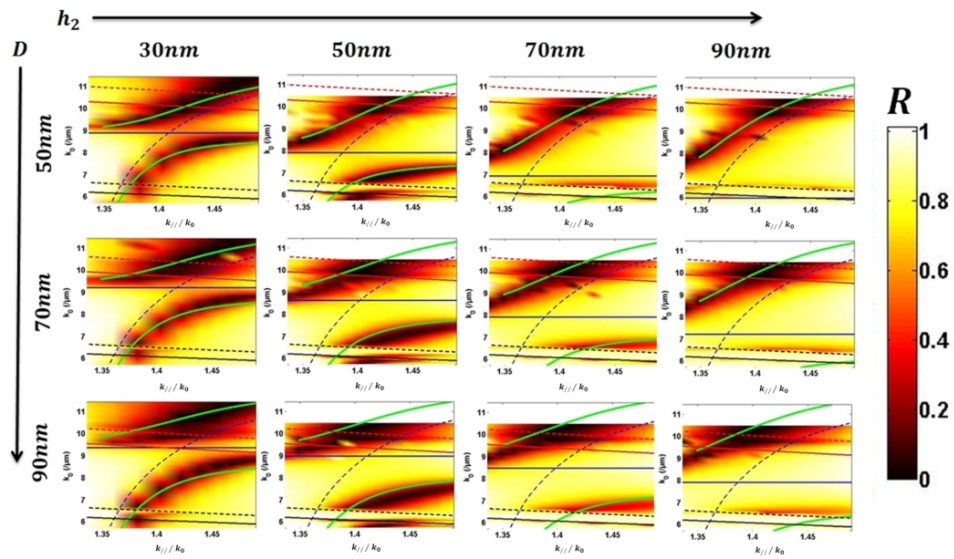


Figure B.3: The normalized reflectivity ( $R$ ) dispersion maps calculated by numerical methods with varying  $h_2$  and  $D$  as a function of  $(k_0, (k_{||}/k_0))$  for  $\Lambda = 350\text{nm}$ . The analytically calculated dispersion of the various modes is also shown and the color legend is same as figure B.1.



## Appendix C

# Sensitivity of gold film for bio-sensing

The sensitivity of a thin gold film in the Kretschmann configuration is defined as  $S_R = \Delta R / \Delta n_h$  (in  $/RIU$ ) for a change of bulk refractive index of  $\Delta n_h$  in reflectivity interrogation. In the same way for spectral interrogation the sensitivity to bulk refractive index changes is given by  $S_\lambda = \Delta \lambda / \Delta n_h$  (in  $nm/RIU$ ). Such values for a gold film of height  $h = 50nm$  was shown in figure 13.1 as a function of  $\lambda - (k_{//}/k_0)$ . The dependence of sensitivity on change in the bulk refractive index ( $\Delta n_h$ ) is shown in figure C.1. For the calculation done by the Rouard method, the film height of  $h = 50nm$  was considered and the plasmon excitation wavelength for  $n_h = 1.333$  was taken to be  $\lambda = 800nm$  (thus  $(k_{//}/k_0) = 1.39$  and  $\theta = 66.5^\circ$ ). The refractive index of the substrate was  $n_b = 1.513$ . We see that the sensitivity is not constant with change in  $\Delta n_h$ . For the calculations presented in section 13.1 the index change was taken as  $\Delta n_h = 0.01RIU$ .

We see that for large refractive index variations the sensitivity of the PSP decreases for reflectivity interrogation while increases for spectral interrogation. It should be noted that it is  $(k_{//}/k_0)$  which increases linearly with  $\Delta n_h$  and thus change of  $(k_{//}/k_0)/\Delta n_h$  is independent on  $\Delta n_h$ . However this is not true for  $\Delta \lambda$  which is not linear to  $\Delta n_h$  and thus the spectral sensitivity is not constant with  $\Delta n_h$  (see section 13.1).

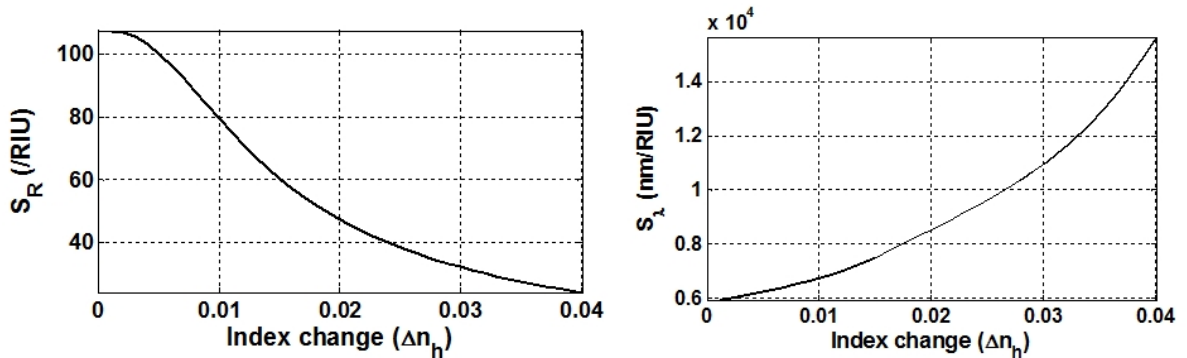


Figure C.1: The sensitivity of a thin gold film of height  $h = 50nm$  in reflectivity interrogation  $S_R$  and spectral interrogation  $S_\lambda$  as a function of the index shift. The reference refractive index was taken as  $n_h = 1.333$  and the wavelength of the plasmon dip for reference was  $\lambda = 800nm$ . The substrate refractive index was taken as  $n_b = 1.513$ .

The angular sensitivity  $S_\theta = \Delta \theta / \Delta n_h$  to bulk refractive index changes as a function of excitation

wavelength is shown in figure C.2. We see that angular sensitivity decreases with wavelength while the spectral sensitivity shown in figure 13.1 increases with wavelength. The angular sensitivity is almost independent of  $\Delta n_h$  as discussed above.

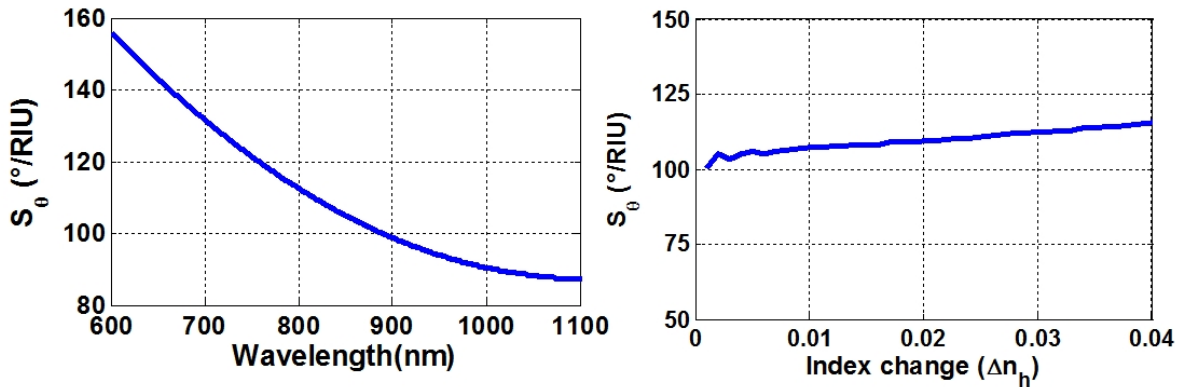


Figure C.2: (a) The sensitivity  $S_\theta$  as a function of incident wavelength for a gold film of height  $h = 50nm$ . The index change was taken as  $\Delta n_h = 0.01RIU$ . (b) The sensitivity as a function of index shift with excitation wavelength  $\lambda = 800nm$ .

The dependence of the sensitivity of the PSP to bulk refractive index as a function of the gold film height ( $h$ ) is shown in figure C.3. For the calculation a index shift of  $\Delta n_h = 0.01RIU$  was considered. The sensitivity as a function of excitation wavelength is shown in the figure. We see that there is an optimum height of the gold film which is required to have the maximum sensitivity for reflectivity interrogation ( $S_R$ ) and this optimum value depends on the excitation wavelength (the wavelength of the reference plasmon dip). However there exists no such optimum value in terms of height for sensitivity in spectral interrogation ( $S_\lambda$ ) and it increases with increasing wavelength. This is because  $\Delta R$  is dependent on the reference value of reflectivity while the spectral interrogation method is independent of it and is rather an intrinsic property of the plasmonic mode dispersion.

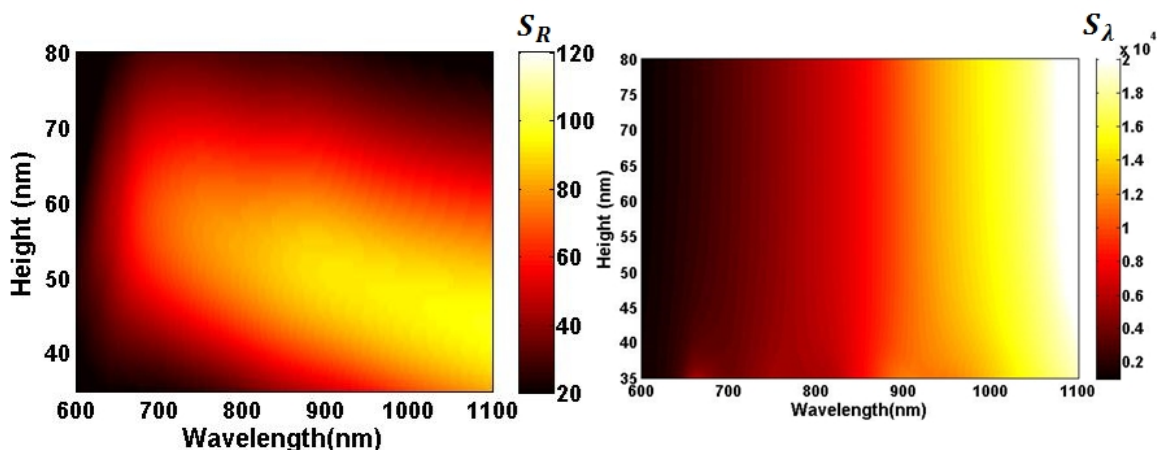


Figure C.3: The sensitivity of a thin gold film as a function of height ( $h$ ) in reflectivity interrogation  $S_R$  and spectral interrogation  $S_\lambda$ . The reference refractive index was taken as  $n_h = 1.333$  and index shift of  $\Delta n_h = 0.01RIU$  was considered.

For affinity biosensors the sensitivity is defined as  $S_{mol:R} = \Delta R/e$  (in  $\%/nm$ ) for reflectivity



interrogation and  $S_{mol:\lambda} = \Delta\lambda/e$  (in  $\%/nm$ ) for spectral interrogation for a bilayer thickness of  $e$  as described in section 14. The values for a gold film of height  $h = 50nm$  and a bio layer of  $e = 1nm$  and index  $n_a = 1.48$  is shown in figure 14.2.

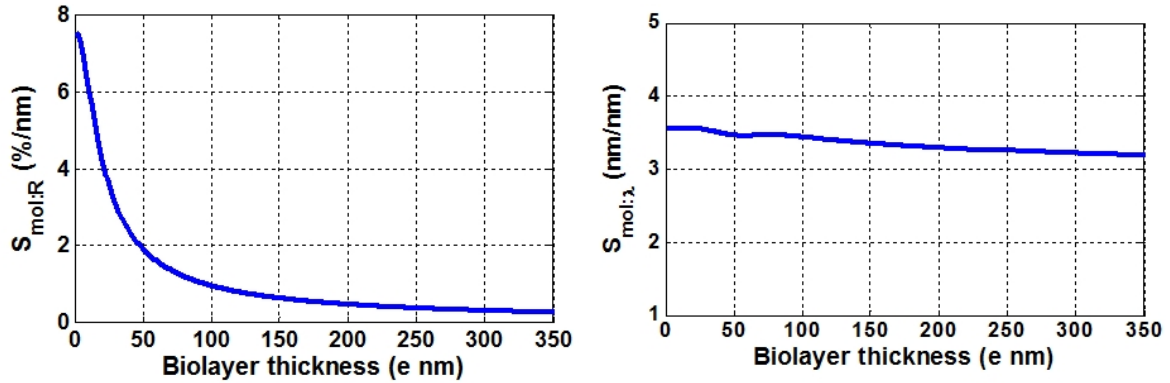


Figure C.4: The sensitivity of a thin gold film of height  $h = 50nm$  in reflectivity interrogation  $S_{mol:R}$  and spectral interrogation  $S_{mol:\lambda}$  as a function of bilayer thickness ( $e$ ). The reference refractive index was taken as  $n_h = 1.333$  and the wavelength of the plasmon dip for reference was  $\lambda = 700nm$  with bilayer index  $n_a = 1.48$ .

The dependence of sensitivity on the thickness of the bilayer ( $e$ ) is shown in figure C.4. For the calculation the film height of  $h = 50nm$  was considered and the plasmon excitation wavelength for  $n_h = 1.333$  was taken to be  $\lambda = 700nm$  (thus  $(k_{//}/k_0) = 1.41$  and  $\theta = 69^\circ$ ). We see that the reflectivity sensitivity  $S_{mol:R}$  decrease exponentially with the bilayer thickness. This is a characteristic feature of the PSP and the decay is related to the penetration depth of the PSP and described in section. The absolute value of reflectivity is dependent on the bilayer size and the contrast of reflectivity at the position of the plasmon dip decreases rapidly with the thickness of the bilayer. Thus the shift in reflectivity ( $\Delta R$ ) also decreases with the bilayer thickness. The spectral shift  $\Delta\lambda$  however is not dependent on the value of the absolute reflectivity and thus is not strongly dependent on bilayer thickness, decreasing less rapidly with the thickness.

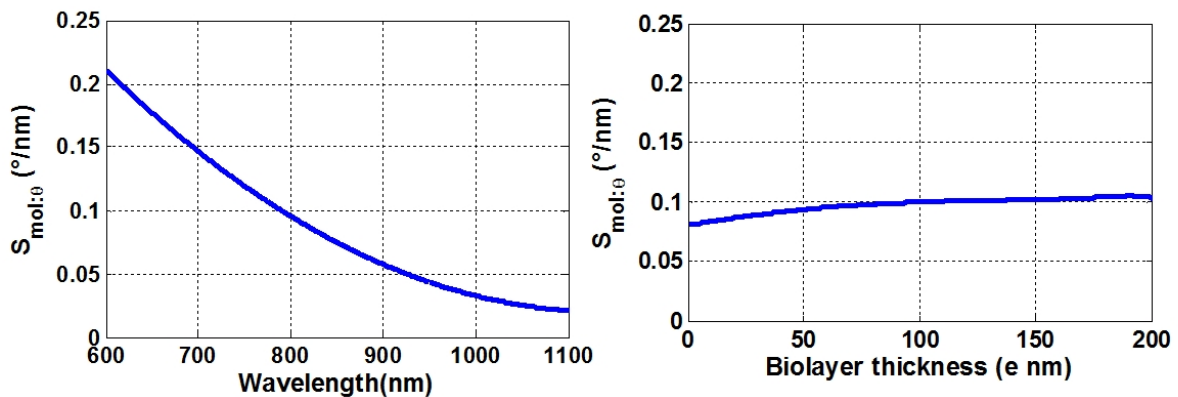


Figure C.5: (a) The sensitivity  $S_{mol:\theta}$  as a function of incident wavelength for a gold film of height  $h = 50nm$ . The thickness of the bilayer was taken as  $e = 1nm$ . (b) The sensitivity as a function of  $e$  at excitation wavelength  $\lambda = 800nm$ .

The angular sensitivity  $S_{mol:\theta} = \Delta\theta/e$  for affinity detection as a function of excitation wavelength

is shown in figure C.5. We see that angular sensitivity decreases with wavelength which is inverse to the trend of the spectral sensitivity as shown in figure 14.2 which increases with wavelength. The angular sensitivity is also independent of  $e$ .

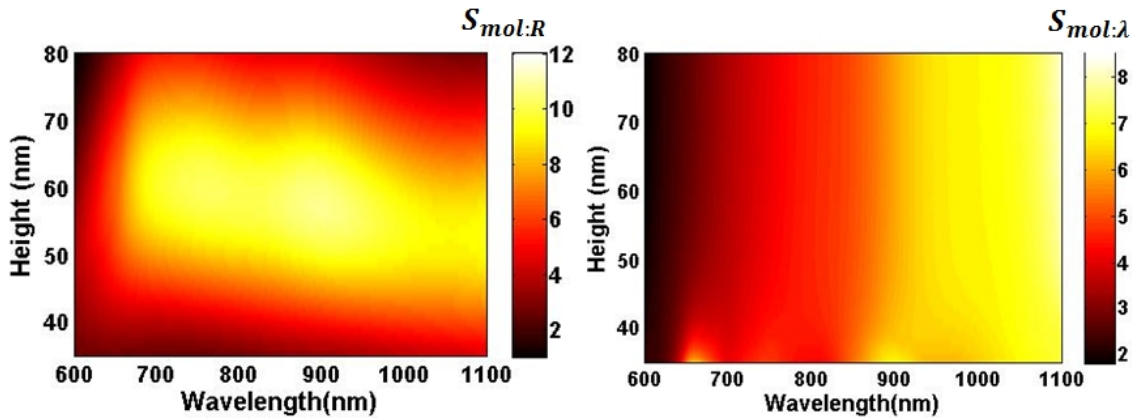


Figure C.6: The sensitivity of a thin gold film as a function of height ( $h$ ) in reflectivity interrogation  $S_{mol:R}$  and spectral interrogation  $S_{mol:\lambda}$ . The reference refractive index was taken as  $n_h = 1.333$  and bilayer thickness of  $e = 1nm$  of index  $n_a = 1.48$  was considered.

The dependence of the sensitivity of the PSP to target bio-layer as a function of the gold film height ( $h$ ) is shown in figure C.6. For the calculation a bio-layer of thickness 1nm was considered with an index of  $n_a = 1.48$ . The sensitivity was calculated as a function of the excitation wavelength  $\lambda$ . We see the variation of the sensitivity for target induced shift similar to that of the sensitivity for bulk index change. There is an optimum value of the sensitivity for reflectivity interrogation with respect to film height while no such dependence on the film height for the spectral shift caused by the target adsorption is observed.

---

# Bibliography

---

- [1] Stefan A. Maier. Surface plasmon polaritons at metal / insulator interfaces. In *Plasmonics: Fundamentals and Applications*, pages 21–37. Springer US, 2007.
- [2] P. Drude. Zur elektronentheorie der metalle. *Annalen der Physik*, 306(3):566–613, 1900.
- [3] P. B. Johnson and R. W. Christy. Optical constants of the noble metals. *Phys. Rev. B*, 6:4370–4379, Dec 1972.
- [4] Dominique Barchiesi and Thomas Grosjes. Errata: Fitting the optical constants of gold, silver, chromium, titanium and aluminum in the visible bandwidth. *Journal of Nanophotonics*, 8(1):089996, 2015.
- [5] P. G. Etchegoin, E. C. Le Ru, and M. Meyer. An analytic model for the optical properties of gold. *The Journal of Chemical Physics*, 125(16), 2006.
- [6] R W Wood. On a remarkable case of uneven distribution of light in a diffraction grating spectrum. *Proceedings of the Physical Society of London*, 18(1):269, 1902.
- [7] Lord Rayleigh. On the dynamical theory of gratings. *Proceedings of the Royal Society of London A: Mathematical, Physical and Engineering Sciences*, 79(532):399–416, 1907.
- [8] U. FANO. The theory of anomalous diffraction gratings and of quasi-stationary waves on metallic surfaces (sommerfeld’s waves). *J. Opt. Soc. Am.*, 31(3):213–222, Mar 1941.
- [9] J. C. Maxwell Garnett. Colours in metal glasses and in metallic films. *Philosophical Transactions of the Royal Society of London A: Mathematical, Physical and Engineering Sciences*, 203(359-371):385–420, 1904.
- [10] J. C. Maxwell Garnett. Colours in metal glasses, in metallic films, and in metallic solutions. ii. *Philosophical Transactions of the Royal Society of London A: Mathematical, Physical and Engineering Sciences*, 205(387-401):237–288, 1906.
- [11] Gustav Mie. Beiträge zur optik trüber medien, speziell kolloidaler metallösungen. *Annalen der Physik*, 330(3):377–445, 1908.

- [12] Daniel Maystre. Theory of wood's anomalies. In Stefan Enoch and Nicolas Bonod, editors, *Plasmonics*, volume 167 of *Springer Series in Optical Sciences*, pages 39–83. Springer Berlin Heidelberg, 2012.
- [13] Jean-Jacques Greffet. Introduction to surface plasmon theory. In Stefan Enoch and Nicolas Bonod, editors, *Plasmonics*, volume 167 of *Springer Series in Optical Sciences*, pages 105–148. Springer Berlin Heidelberg, 2012.
- [14] A. Archambault, T. V. Teperik, F. Marquier, and J. J. Greffet. Surface plasmon fourier optics. *Phys. Rev. B*, 79:195414, May 2009.
- [15] Jacob B. Khurgin. Ultimate limit of field confinement by surface plasmon polaritons. *Faraday Discuss.*, 178:109–122, 2015.
- [16] E. T. Arakawa, M. W. Williams, R. N. Hamm, and R. H. Ritchie. Effect of damping on surface plasmon dispersion. *Phys. Rev. Lett.*, 31:1127–1129, Oct 1973.
- [17] E. N. Economou. Surface plasmons in thin films. *Phys. Rev.*, 182:539–554, Jun 1969.
- [18] Edward S. Cai Wenshan Jun Young Chul White Justin S. Brongersma Mark L. Schuller, Jon A. Barnard. Plasmonics for extreme light concentration and manipulation. *Nature Materials*, 9(3):193–204, 2010.
- [19] Francisco Leary Rowan K. Holland Daniel J. Ducati Caterina Midgley Paul A. Nicoletti, Olivia de la Pena. Three-dimensional imaging of localized surface plasmon resonances of metal nanoparticles. *Nature*, 502(7469):80–84, 2013.
- [20] Eleonora Petryayeva and Ulrich J. Krull. Localized surface plasmon resonance: Nanostructures, bioassays and biosensing—a review. *Analytica Chimica Acta*, 706(1):8 – 24, 2011.
- [21] Y. Sonnefraud, A. Leen Koh, D.W. McComb, and S.A. Maier. Nanoplasmonics: Engineering and observation of localized plasmon modes. *Laser and Photonics Reviews*, 6(3):277–295, 2012.
- [22] Katherine A. Willets and Richard P. Van Duyne. Localized surface plasmon resonance spectroscopy and sensing. *Annual Review of Physical Chemistry*, 58(1):267–297, 2007. PMID: 17067281.
- [23] Eliza Hutter and Janos H Fendler. Exploitation of localized surface plasmon resonance. *Advanced Materials*, 16(19):1685–1706, 2004.
- [24] Weitao Singh David J. Fan, Xiaofeng Zheng. Light scattering and surface plasmons on small spherical particles. *Light Sci Appl*, 3:179, 2014.
- [25] E. Kretschmann and H. Raether. Radiative decay of nonradiative surface plasmons excited by light. *Z. Naturforsch. A*, 23:2135, 1968.
- [26] Heinz Raether. Surface plasmons on smooth surfaces. In *Surface Plasmons on Smooth and Rough Surfaces and on Gratings*, volume 111 of *Springer Tracts in Modern Physics*, pages 4–39. Springer Berlin Heidelberg, 1988.

- [27] I. Stemmler, A. Brecht, and G. Gauglitz. Compact surface plasmon resonance-transducers with spectral readout for biosensing applications. *Sensors and Actuators B: Chemical*, 54(1–2):98 – 105, 1999.
- [28] B.N. Feltis, B.A. Sexton, F.L. Glenn, M.J. Best, M. Wilkins, and T.J. Davis. A hand-held surface plasmon resonance biosensor for the detection of ricin and other biological agents. *Biosensors and Bioelectronics*, 23(7):1131 – 1136, 2008.
- [29] Marek Piliarik, Milan Vala, Ivo Tichý, and Jiří Homola. Compact and low-cost biosensor based on novel approach to spectroscopy of surface plasmons. *Biosensors and Bioelectronics*, 24(12):3430 – 3435, 2009.
- [30] Fabrice Bardin, Alain Bellemain, Gisèle Roger, and Michael Canva. Surface plasmon resonance spectro-imaging sensor for biomolecular surface interaction characterization. *Biosensors and Bioelectronics*, 24(7):2100 – 2105, 2009.
- [31] Alexandra Sereda, Julien Moreau, Marine Boulade, Aurore Olivéro, Michael Canva, and Emmanuel Maillart. Compact 5-LEDs illumination system for multi-spectral surface plasmon resonance sensing. *Sensors and Actuators B: Chemical*, 209:208 – 211, 2015.
- [32] Julia A. Ruemmele, W. Paige Hall, Laura K. Ruvuna, and Richard P. Van Duyne. A localized surface plasmon resonance imaging instrument for multiplexed biosensing. *Analytical Chemistry*, 85(9):4560–4566, 2013. PMID: 23560643.
- [33] Zheng Zheng, Yuhang Wan, Xin Zhao, and Jinsong Zhu. Interrogation of surface plasmon resonance sensors using temporally stretched ultrashort optical pulses. *Sensors and Actuators B: Chemical*, 133(2):671 – 676, 2008.
- [34] Soichi Otsuki and Mitsuru Ishikawa. Wavelength-scanning surface plasmon resonance imaging for label-free multiplexed protein microarray assay. *Biosensors and Bioelectronics*, 26(1):202 – 206, 2010.
- [35] A. Sereda, J. Moreau, M. Canva, and E. Maillart. High performance multi-spectral interrogation for surface plasmon resonance imaging sensors. *Biosensors and Bioelectronics*, 54:175 – 180, 2014.
- [36] Peter Schuck. Reliable determination of binding affinity and kinetics using surface plasmon resonance biosensors. *Current Opinion in Biotechnology*, 8(4):498 – 502, 1997.
- [37] S. Scarano, S. Mariani, and M. Minunni. SPR-based affinity biosensors as innovative analytical devices. *Lightwave Technology, Journal of*, 33(16):3374–3384, Aug 2015.
- [38] Jolanda Spadavecchia, Julien Moreau, Jérôme Hottin, and Michael Canva. New cysteamine based functionalization for biochip applications. *Sensors and Actuators B: Chemical*, 143(1):139 – 143, 2009.
- [39] Kathryn M. Mayer and Jason H. Hafner. Localized surface plasmon resonance sensors. *Chemical Reviews*, 111(6):3828–3857, 2011. PMID: 21648956.

- [40] James Spivey. *Metal Nanoparticles for Catalysis*. RSC Catalysis Series. The Royal Society of Chemistry, 2014.
- [41] Na Liu, Thomas Weiss, Martin Mesch, Lutz Langguth, Ulrike Eigenthaler, Michael Hirscher, Carsten Sönnichsen, and Harald Giessen. Planar metamaterial analogue of electromagnetically induced transparency for plasmonic sensing. *Nano Letters*, 10(4):1103–1107, 2010. PMID: 20017551.
- [42] Moyu Barrera Alejandra Donoso Zhou Dejian Vogtli Manuel Batchelor Matthew Cooper Matthew A. Strunz Torsten Horton Mike A. Abell Chris Rayment Trevor Aeppli Gabriel McKendry Rachel A. Ndieyira, Joseph Wafula Watari. Nanomechanical detection of antibiotic-mucopeptide binding in a model for superbug drug resistance. *Nat Nano*, 3(11):691–696, 2008.
- [43] Jason M. Tucker-Schwartz, Kelsey R. Beavers, Wesley W. Sit, Amy T. Shah, Craig L. Duvall, and Melissa C. Skala. In vivo imaging of nanoparticle delivery and tumor microvasculature with multimodal optical coherence tomography. *Biomed. Opt. Express*, 5(6):1731–1743, Jun 2014.
- [44] Jesse Aaron, Nitin Nitin, Kort Travis, Sonia Kumar, Tom Collier, Sun Young Park, Miguel José-Yacamán, Lezlee Coghlan, Michele Follen, Rebecca Richards-Kortum, and Konstantin Sokolov. Plasmon resonance coupling of metal nanoparticles for molecular imaging of carcinogenesis in vivo. *Journal of Biomedical Optics*, 12(3):034007–034007–11, 2007.
- [45] Maxim R. Shcherbakov, Anton T. Le, Natalia Dubrovina, Anatole Lupu, and Andrey A. Fedyanin. Plasmon ruler with gold nanorod dimers: utilizing the second-order resonance. *Opt. Lett.*, 40(7):1571–1574, Apr 2015.
- [46] A. Lupu, N. Dubrovina, R. Ghasemi, A. Degiron, and A. de Lustrac. Metal-dielectric metamaterials for guided wave silicon photonics. *Opt. Express*, 19(24):24746–24761, Nov 2011.
- [47] Clément Tardieu, Thomas Estruch, Grégory Vincent, Julien Jaeck, Nathalie Bardou, Stéphane Collin, and Riad Haïdar. Extraordinary optical extinctions through dual metallic gratings. *Opt. Lett.*, 40(4):661–664, Feb 2015.
- [48] T. Cesca, P. Calvelli, G. Battaglin, P. Mazzoldi, and G. Mattei. Local-field enhancement effect on the nonlinear optical response of gold-silver nanoplanets. *Opt. Express*, 20(4):4537–4547, Feb 2012.
- [49] Yunqing Wang, Bing Yan, and Lingxin Chen. Sers tags: Novel optical nanoprobe for bioanalysis. *Chemical Reviews*, 113(3):1391–1428, 2013. PMID: 23273312.
- [50] John Turkevich, Peter Cooper Stevenson, and James Hillier. A study of the nucleation and growth processes in the synthesis of colloidal gold. *Discuss. Faraday Soc.*, 11:55–75, 1951.
- [51] G. Frens. Particle size and sol stability in metal colloids. *Kolloid-Zeitschrift und Zeitschrift für Polymere*, 250(7):736–741, 1972.
- [52] G. Frens. Controlled nucleation for the regulation of the particle size in monodisperse gold suspensions. *Nature physical science*, 241:20–22, 1973.

- [53] Ralph A. Sperling, Pilar Rivera Gil, Feng Zhang, Marco Zanella, and Wolfgang J. Parak. Biological applications of gold nanoparticles. *Chem. Soc. Rev.*, 37:1896–1908, 2008.
- [54] Gonçalo Doria, João Conde, Bruno Veigas, Leticia Giestas, Carina Almeida, Maria Assunção, João Rosa, and Pedro V. Baptista. Noble metal nanoparticles for biosensing applications. *Sensors*, 12(2):1657, 2012.
- [55] W. Paige Lyandres Olga Shah Nilam C. Zhao Jing Van Duyne Richard P. Anker, Jeffrey N. Hall. Biosensing with plasmonic nanosensors. *Nature Materials*, 7(6):442–453, 2008.
- [56] Andreas Unger, Uwe Rietzler, Rüdiger Berger, and Maximilian Kreiter. Sensitivity of crescent-shaped metal nanoparticles to attachment of dielectric colloids. *Nano Letters*, 9(6):2311–2315, 2009. PMID: 19402652.
- [57] Julia M. Bingham, Katherine A. Willets, Nilam C. Shah, David Q. Andrews, and Richard P. Van Duyne. Localized surface plasmon resonance imaging: Simultaneous single nanoparticle spectroscopy and diffusional dynamics. *The Journal of Physical Chemistry C*, 113(39):16839–16842, 2009.
- [58] Yunliang Shao, Shuping Xu, Xianliang Zheng, Ye Wang, and Weiqing Xu. Optical fiber lspr biosensor prepared by gold nanoparticle assembly on polyelectrolyte multilayer. *Sensors*, 10(4):3585, 2010.
- [59] † Greg J. Nusz, † Stella M. Marinakos, † Adam C. Curry, ‡ Andreas Dahlin, ‡ Fredrik Höök, † Adam Wax, , and † Ashutosh Chilkoti\*. Label-free plasmonic detection of biomolecular binding by a single gold nanorod. *Analytical Chemistry*, 80(4):984–989, 2008. PMID: 18197636.
- [60] Jack J. Mock, David R. Smith, , and Sheldon Schultz. Local refractive index dependence of plasmon resonance spectra from individual nanoparticles. *Nano Letters*, 3(4):485–491, 2003.
- [61] Zehui Yong, Dang Lei, Chi Lam, and Yu Wang. Ultrahigh refractive index sensing performance of plasmonic quadrupole resonances in gold nanoparticles. *Nanoscale Research Letters*, 9(1):187, 2014.
- [62] Kathryn M. Mayer, Seunghyun Lee, Hongwei Liao, Betty C. Rostro, Amaris Fuentes, Peter T. Scully, Colleen L. Nehl, and Jason H. Hafner. A label-free immunoassay based upon localized surface plasmon resonance of gold nanorods. *ACS Nano*, 2(4):687–692, 2008.
- [63] Adam D. McFarland, , and Richard P. Van Duyne. Single silver nanoparticles as real-time optical sensors with zeptomole sensitivity. *Nano Letters*, 3(8):1057–1062, 2003.
- [64] Yadong Kunchakarra Siri Mukherjee Bipasha Gerion Daniele Jett Stephen D. Bear David G. Gray Joe W. Alivisatos A. Paul Lee Luke P. Chen Fanqing Frank Liu, Gang L. Yin. A nanoplasmonic molecular ruler for measuring nuclease activity and dna footprinting. *Nat Nano*, 1(1):47–52, 2006.
- [65] Mark W. Knight, Nicholas S. King, Lifei Liu, Henry O. Everitt, Peter Nordlander, and Naomi J. Halas. Aluminum for plasmonics. *ACS Nano*, 8(1):834–840, 2014. PMID: 24274662.

- [66] Leonor Soares, Andrea Csaki, Jacqueline Jatschka, Wolfgang Fritzsche, Orfeu Flores, Ricardo Franco, and Eulalia Pereira. Localized surface plasmon resonance (lspr) biosensing using gold nanotriangles: detection of dna hybridization events at room temperature. *Analyst*, 139:4964–4973, 2014.
- [67] Gerhard A. Berciaud Stéphane Heine Martin Groc Laurent Choquet Daniel Cognet Laurent Lou-nis Brahim Lasne, David Blab. Single nanoparticle photothermal tracking (snapt) of 5-nm gold beads in live cells. *Biophysical Journal*, 91:4598–4604, 2006.
- [68] Adolf Smekal. Zur quantentheorie der dispersion. *Naturwissenschaften*, 11(43):873–875, 1923.
- [69] C V Raman. A new radiation. *Indian J. Phys*, 2:387–398, 1928.
- [70] G. Landsberg. L. Imandelstam. Eine neue erscheinung bei der lichtzerstreuung in krystallen. *Naturwissenschaften*, 16(28):557–558, 1928.
- [71] G. Sun and J. B. Khurgin. Origin of giant difference between fluorescence, resonance, and nonresonance raman scattering enhancement by surface plasmons. *Phys. Rev. A*, 85:063410, Jun 2012.
- [72] Martin W. Howard, Ralph P. Cooney, and A. James McQuillan. The origin of intense raman spectra from pyridine at silver electrode surfaces: The role of surface carbon. *Journal of Raman Spectroscopy*, 9(4):273–278, 1980.
- [73] M. Fleischmann, P.J. Hendra, and A.J. McQuillan. Raman spectra of pyridine adsorbed at a silver electrode. *Chemical Physics Letters*, 26(2):163 – 166, 1974.
- [74] M. Grant Albrecht and J. Alan Creighton. Anomalously intense raman spectra of pyridine at a silver electrode. *Journal of the American Chemical Society*, 99(15):5215–5217, 1977.
- [75] David L. Jeanmaire and Richard P. Van Duyne. Surface raman spectroelectrochemistry. *Journal of Electroanalytical Chemistry and Interfacial Electrochemistry*, 84(1):1 – 20, 1977.
- [76] Martin Moskovits. Surface-enhanced spectroscopy. *Rev. Mod. Phys.*, 57:783–826, Jul 1985.
- [77] Alan Campion and Patanjali Kambhampati. Surface-enhanced raman scattering. *Chem. Soc. Rev.*, 27:241–250, 1998.
- [78] Paul L. Stiles, Jon A. Dieringer, Nilam C. Shah, and Richard P. Van Duyne. Surface-enhanced raman spectroscopy. *Annual Review of Analytical Chemistry*, 1(1):601–626, 2008. PMID: 20636091.
- [79] Eric D. Diebold, Nathan H. Mack, Stephen K. Doorn, and Eric Mazur. Femtosecond laser-nanostructured substrates for surface-enhanced raman scattering. *Langmuir*, 25(3):1790–1794, 2009. PMID: 19133764.
- [80] Shyh-Chyang Luo, Kundan Sivashanmugan, Jiunn-Der Liao, Chih-Kai Yao, and Han-Chi Peng. Nanofabricated sers-active substrates for single-molecule to virus detection in vitro: A review. *Biosensors and Bioelectronics*, 61:232 – 240, 2014.



- [81] Darya Radziuk and Helmuth Moehwald. Prospects for plasmonic hot spots in single molecule sers towards the chemical imaging of live cells. *Phys. Chem. Chem. Phys.*, 17:21072–21093, 2015.
- [82] Sameh Kessentini, Dominique Barchiesi, Cristiano D’Andrea, Andrea Toma, Nicolas Guillot, Enzo Di Fabrizio, Barbara Fazio, Onofrio M. Maragó, Pietro G. Gucciardi, and Marc Lamy de la Chapelle. Gold dimer nanoantenna with slanted gap for tunable lspr and improved sers. *The Journal of Physical Chemistry C*, 118(6):3209–3219, 2014.
- [83] Mohamad G. Banaee and Kenneth B. Crozier. Mixed dimer double-resonance substrates for surface-enhanced raman spectroscopy. *ACS Nano*, 5(1):307–314, 2011. PMID: 21162550.
- [84] Ashwin Gopinath, Svetlana V. Boriskina, W. Ranjith Premasiri, Lawrence Ziegler, Björn M. Reinhard, and Luca Dal Negro. Plasmonic nanogalaxies: Multiscale aperiodic arrays for surface-enhanced raman sensing. *Nano Letters*, 9(11):3922–3929, 2009. PMID: 19754067.
- [85] Holly J. Butler, Simon W. Fogarty, Jemma G. Kerns, Pierre L. Martin-Hirsch, Nigel J. Fullwood, and Francis L. Martin. Gold nanoparticles as a substrate in bio-analytical near-infrared surface-enhanced raman spectroscopy. *Analyst*, 140:3090–3097, 2015.
- [86] E. C. Le Ru, E. Blackie, M. Meyer, , and P. G. Etchegoin†. Surface enhanced raman scattering enhancement factors- a comprehensive study. *The Journal of Physical Chemistry C*, 111(37):13794–13803, 2007.
- [87] Daniel C. Rodrigues, Michele L. de Souza, Klester S. Souza, Diego P. dos Santos, Gustavo F. S. Andrade, and Marcia L. A. Temperini. Critical assessment of enhancement factor measurements in surface-enhanced raman scattering on different substrates. *Phys. Chem. Chem. Phys.*, 17:21294–21301, 2015.
- [88] Bin Wu De-Yin Tian, Zhong-Qun Ren. Surface-enhanced raman scattering—from noble to transition metals and from rough surfaces to ordered nanostructures. *The Journal of Physical Chemistry B*, 106(37):9463–9483, 2002.
- [89] De-Yin Wu, Sai Duan, Bin Ren, and Zhong-Qun Tian. Density functional theory study of surface-enhanced raman scattering spectra of pyridine adsorbed on noble and transition metal surfaces. *Journal of Raman Spectroscopy*, 36(6-7):533–540, 2005.
- [90] Eric C. Le Ru and Pablo G. Etchegoin. Quantifying sers enhancements. *MRS Bulletin*, 38:631–640, 8 2013.
- [91] E. C. Le Ru, S. A. Meyer, C. Artur, P. G. Etchegoin, J. Grand, P. Lang, and F. Maurel. Experimental demonstration of surface selection rules for sers on flat metallic surfaces. *Chem. Commun.*, 47:3903–3905, 2011.
- [92] Joel Gersten and Abraham Nitzan. Electromagnetic theory of enhanced raman scattering by molecules adsorbed on rough surfaces. *The Journal of Chemical Physics*, 73(7), 1980.
- [93] N. Guillot and M. Lamy de la Chapelle. The electromagnetic effect in surface enhanced raman scattering: Enhancement optimization using precisely controlled nanostructures. *Journal of*

*Quantitative Spectroscopy and Radiative Transfer*, 113(18):2321 – 2333, 2012. Electromagnetic and Light Scattering by non-spherical particles {XIII}.

- [94] Semion K. Saikin, Yizhuo Chu, Dmitrij Rappoport, Kenneth B. Crozier, and Alán Aspuru-Guzik. Separation of electromagnetic and chemical contributions to surface-enhanced raman spectra on nanoengineered plasmonic substrates. *The Journal of Physical Chemistry Letters*, 1(18):2740–2746, 2010.
- [95] Katrin Kneipp, Yang Wang, Harald Kneipp, Lev T. Perelman, Irving Itzkan, Ramachandra R. Dasari, and Michael S. Feld. Single molecule detection using surface-enhanced raman scattering (sers). *Phys. Rev. Lett.*, 78:1667–1670, Mar 1997.
- [96] Shuming Nie and Steven R. Emory. Probing single molecules and single nanoparticles by surface-enhanced raman scattering. *Science*, 275(5303):1102–1106, 1997.
- [97] Rebecca Halvorson Lahr and Peter J. Vikesland. Surface-enhanced raman spectroscopy (sers) cellular imaging of intracellularly biosynthesized gold nanoparticles. *ACS Sustainable Chemistry & Engineering*, 2(7):1599–1608, 2014.
- [98] Jeon Woong Kang, Peter T. C. So, Ramachandra R. Dasari, and Dong-Kwon Lim. High resolution live cell raman imaging using subcellular organelle-targeting sers-sensitive gold nanoparticles with highly narrow intra-nanogap. *Nano Letters*, 15(3):1766–1772, 2015. PMID: 25646716.
- [99] Elena Bailo and Volker Deckert. Tip-enhanced raman scattering. *Chem. Soc. Rev.*, 37:921–930, 2008.
- [100] Matthew D. Sonntag, Eric A. Pozzi, Nan Jiang, Mark C. Hersam, and Richard P. Van Duyne. Recent advances in tip-enhanced raman spectroscopy. *The Journal of Physical Chemistry Letters*, 5(18):3125–3130, 2014. PMID: 26276323.
- [101] Marek Piliarik and Jiří Homola. Surface plasmon resonance (spr) sensors: approaching their limits? *Opt. Express*, 17(19):16505–16517, Sep 2009.
- [102] Chien-Ming Wu and Ming-Chi Pao. Sensitivity-tunable optical sensors based on surface plasmon resonance and phase detection. *Opt. Express*, 12(15):3509–3514, Jul 2004.
- [103] C. Thirstrup and W. Zong. Data analysis for surface plasmon resonance sensors using dynamic baseline algorithm. *Sensors and Actuators B: Chemical*, 106(2):796 – 802, 2005.
- [104] Olivier R. Bolduc, Ludovic S. Live, and Jean-François Masson. High-resolution surface plasmon resonance sensors based on a dove prism. *Talanta*, 77(5):1680 – 1687, 2009.
- [105] Marek Piliarik, Lucie Párová, and Jiří Homola. High-throughput {SPR} sensor for food safety. *Biosensors and Bioelectronics*, 24(5):1399 – 1404, 2009. Selected Papers from the Tenth World Congress on Biosensors Shanghai, China, May 14-16, 2008.
- [106] Colin J. Alleyne, Andrew G. Kirk, Wei-Yin Chien, and Paul G. Charette. Numerical method for high accuracy index of refraction estimation for spectro-angular surface plasmon resonance systems. *Opt. Express*, 16(24):19493–19503, Nov 2008.

- [107] Yang Li, Ke Zhao, Heidar Sobhani, Kui Bao, and Peter Nordlander. Geometric dependence of the line width of localized surface plasmon resonances. *The Journal of Physical Chemistry Letters*, 4(8):1352–1357, 2013. PMID: 26282152.
- [108] Rupert F. Kivshar Yuri S. Liu, Wei Oulton. Geometric interpretations for resonances of plasmonic nanoparticles. *Scientific Reports*, 5:12148, 2015.
- [109] J.-X. Fu, A. Collins, and Y.-P. Zhao. Optical properties and biosensor application of ultrathin silver films prepared by oblique angle deposition. *The Journal of Physical Chemistry C*, 112(43):16784–16791, 2008.
- [110] Nan Zhang, Xiaodi Su, Paul Free, Xiaodong Zhou, Koon Gee Neoh, Jinghua Teng, and Wolfgang Knoll. Plasmonic metal nanostructure array by glancing angle deposition for biosensing application. *Sensors and Actuators B: Chemical*, 183:310 – 318, 2013.
- [111] G. Barbillon, J.-L. Bijeon, J. Plain, M. Lamy de la Chapelle, P.-M. Adam, and P. Royer. Electron beam lithography designed chemical nanosensors based on localized surface plasmon resonance. *Surface Science*, 601(21):5057 – 5061, 2007.
- [112] Luis Gutierrez-Rivera, Robert F. Peters, Steven K. Dew, and Maria Stepanova. Application of ebl fabricated nanostructured substrates for surface enhanced raman spectroscopy detection of protein a in aqueous solution. *Journal of Vacuum Science and Technology B*, 31(6), 2013.
- [113] Seung-Woo Lee, Kyeong-Seok Lee, Junhyoung Ahn, Jae-Jong Lee, Min-Gon Kim, and Yong-Beom Shin. Highly sensitive biosensing using arrays of plasmonic au nanodisks realized by nanoimprint lithography. *ACS Nano*, 5(2):897–904, 2011. PMID: 21222487.
- [114] Brandon D. Lucas, Jin-Sung Kim, Christine Chin, and L. Jay Guo. Nanoimprint lithography based approach for the fabrication of large-area, uniformly-oriented plasmonic arrays. *Advanced Materials*, 20(6):1129–1134, 2008.
- [115] Peixun Fan, Minlin Zhong, Lin Li, Ting Huang, and Hongjun Zhang. Rapid fabrication of surface micro/nano structures with enhanced broadband absorption on cu by picosecond laser. *Opt. Express*, 21(10):11628–11637, May 2013.
- [116] Tianrui Zhai, Yonglu Wang, Hongmei Liu, and Xinping Zhang. Large-scale fabrication of flexible metallic nanostructure pairs using interference ablation. *Opt. Express*, 23(2):1863–1870, Jan 2015.
- [117] Blake J. Plowman, Suresh K. Bhargava, and Anthony P. O’Mullane. Electrochemical fabrication of metallic nanostructured electrodes for electroanalytical applications. *Analyst*, 136:5107–5119, 2011.
- [118] Inès Massiot, Nicolas Vandamme, Nathalie Bardou, Christophe Dupuis, Aristide Lemaître, Jean-François Guillemoles, and Stéphane Collin. Metal nanogrid for broadband multiresonant light-harvesting in ultrathin gaas layers. *ACS Photonics*, 1(9):878–884, 2014.
- [119] Kyujung Kim, Dong Jun Kim, Seyoung Moon, Donghyun Kim, and Kyung Min Byun. Localized surface plasmon resonance detection of layered biointeractions on metallic subwavelength nanogratings. *Nanotechnology*, 20(31):315501, 2009.

- [120] Kyung Min Byun, M.L. Shuler, Sung June Kim, Soon Joon Yoon, and Donghyun Kim. Sensitivity enhancement of surface plasmon resonance imaging using periodic metallic nanowires. *Lightwave Technology, Journal of*, 26(11):1472–1478, June 2008.
- [121] Lidija Malic, Bo Cui, Maryam Tabrizian, and Teodor Veres. Nanoimprinted plastic substrates for enhanced surface plasmon resonance imaging detection. *Opt. Express*, 17(22):20386–20392, Oct 2009.
- [122] M G Manera, R Rella, J Spadavecchia, J Moreau, and M Canva. Real-time monitoring of carbonarius dna structured biochip by surface plasmon resonance imaging. *Journal of Optics A: Pure and Applied Optics*, 10(6):064018, 2008.
- [123] Ludovic S. Live, Anuj Dhawan, Kirsty F. Gibson, Hugo-Pierre Poirier-Richard, Duncan Graham, Michael Canva, Tuan Vo-Dinh, and Jean-François Masson. Angle-dependent resonance of localized and propagating surface plasmons in microhole arrays for enhanced biosensing. *Analytical and Bioanalytical Chemistry*, 404(10):2859–2868, 2012.
- [124] Liang-Ping Xia, Zheng Yang, Shao-Yun Yin, Wen-Rui Guo, Jing-Lei Du, and Chun-Lei Du. Hole arrayed metal-insulator-metal structure for surface enhanced raman scattering by self-assembling polystyrene spheres. *Frontiers of Physics*, 9(1):64–68, 2014.
- [125] P. Pastkovsky S. Hendren W. Wurtz G. A. Atkinson R. Pollard R. Podolskiy V. A. Zayats A. V. Kabashin, A. V. Evans. Plasmonic nanorod metamaterials for biosensing. *Nature Materials*, 8(11):867–871, 2009.
- [126] Xiaoli Wang, Philippe Gogol, Edmond Cambriil, and Bruno Palpant. Near- and far-field effects on the plasmon coupling in gold nanoparticle arrays. *The Journal of Physical Chemistry C*, 116(46):24741–24747, 2012.
- [127] Kristof Lodewijks, Jef Ryken, Willem Van Roy, Gustaaf Borghs, Liesbet Lagae, and Pol Van Dorpe. Tuning the fano resonance between localized and propagating surface plasmon resonances for refractive index sensing applications. *Plasmonics*, 8(3):1379–1385, 2013.
- [128] V. G. Kravets, F. Schedin, and A. N. Grigorenko. Extremely narrow plasmon resonances based on diffraction coupling of localized plasmons in arrays of metallic nanoparticles. *Phys. Rev. Lett.*, 101:087403, Aug 2008.
- [129] Wen-Di Li, Fei Ding, Jonathan Hu, and Stephen Y. Chou. Three-dimensional cavity nanoantenna coupled plasmonic nanodots for ultrahigh and uniform surface-enhanced raman scattering over large area. *Opt. Express*, 19(5):3925–3936, Feb 2011.
- [130] Stefan A. Meyer, Baptiste Auguié, Eric C. Le Ru, and Pablo G. Etchegoin. Combined spr and sers microscopy in the kretschmann configuration. *The Journal of Physical Chemistry A*, 116(3):1000–1007, 2012. PMID: 22175443.
- [131] P. I. Nikitin, A. A. Beloglazov, M. V. Valeiko, J. A. Creighton, and J. D. Wright. Silicon-based surface plasmon resonance combined with surface-enhanced raman scattering for chemical sensing. *Review of Scientific Instruments*, 68(6), 1997.

- [132] Yu Liu, Shuping Xu, Bin Tang, Ye Wang, Ji Zhou, Xianliang Zheng, Bing Zhao, and Weiqing Xu. Note: Simultaneous measurement of surface plasmon resonance and surface-enhanced raman scattering. *Review of Scientific Instruments*, 81(3):–, 2010.
- [133] Gérard Colas des Francs, Jonathan Grandidier, Sébastien Massenet, Alexandre Bouhelier, Jean-Claude Weeber, and Alain Dereux. Integrated plasmonic waveguides: A mode solver based on density of states formulation. *Phys. Rev. B*, 80:115419, Sep 2009.
- [134] Patrick Bouchon, Fabrice Pardo, Riad Haïdar, and Jean-Luc Pelouard. Fast modal method for subwavelength gratings based on b-spline formulation. *J. Opt. Soc. Am. A*, 27(4):696–702, Apr 2010.
- [135] Christopher G. Khoury, Stephen J. Norton, and Tuan Vo-Dinh. Plasmonics of 3-d nanoshell dimers using multipole expansion and finite element method. *ACS Nano*, 3(9):2776–2788, 2009. PMID: 19678677.
- [136] Benjamin Gallinet and Olivier J. F. Martin. *Ab initio* theory of fano resonances in plasmonic nanostructures and metamaterials. *Phys. Rev. B*, 83:235427, Jun 2011.
- [137] A. Manjavacas, F. J. García de Abajo, and P. Nordlander. Quantum plexcitonics: Strongly interacting plasmons and excitons. *Nano Letters*, 11(6):2318–2323, 2011. PMID: 21534592.
- [138] Romain Blanchard, Guillaume Aoust, Patrice Genevet, Nanfang Yu, Mikhail A. Kats, Zeno Gaburro, and Federico Capasso. Modeling nanoscale v-shaped antennas for the design of optical phased arrays. *Phys. Rev. B*, 85:155457, Apr 2012.
- [139] Emilie Sakat, Grégory Vincent, Petru Ghenuche, Nathalie Bardou, Christophe Dupuis, Stéphane Collin, Fabrice Pardo, Riad Haïdar, and Jean-Luc Pelouard. Free-standing guided-mode resonance band-pass filters: from 1d to 2d structures. *Opt. Express*, 20(12):13082–13090, Jun 2012.
- [140] Zhiwen Kang, Haixi Zhang, Haifei Lu, and Ho-Pui Ho. Double-layered metal nano-strip antennas for sensing applications. *Plasmonics*, 8(2):289–294, 2013.
- [141] C. Sauvan, J. P. Hugonin, I. S. Maksymov, and P. Lalanne. Theory of the spontaneous optical emission of nanosize photonic and plasmon resonators. *Phys. Rev. Lett.*, 110:237401, Jun 2013.
- [142] A. Sentenac, P. C. Chaumet, and G. Leuchs. Total absorption of light by a nanoparticle: an electromagnetic sink in the optical regime. *Opt. Lett.*, 38(6):818–820, Mar 2013.
- [143] J. Ctyroký, P. Kwiecien, and I. Richter. Analysis of hybrid dielectric-plasmonic slot waveguide structures with 3d fourier modal methods. *Journal of the European Optical Society - Rapid publications*, 8(0), 2013.
- [144] Andrea Lovera, Benjamin Gallinet, Peter Nordlander, and Olivier J.F. Martin. Mechanisms of fano resonances in coupled plasmonic systems. *ACS Nano*, 7(5):4527–4536, 2013. PMID: 23614396.
- [145] Mathieu Langlais, Jean-Paul Hugonin, Mondher Besbes, and Philippe Ben-Abdallah. Cooperative electromagnetic interactions between nanoparticles for solar energy harvesting. *Opt. Express*, 22(S3):A577–A588, May 2014.

- [146] F. Abeles. Recherches sur la propagation des ondes électromagnétiques sinusoïdales dans les milieux stratifiés, application aux couches minces. *Ann. Phys.(Paris)*, 5:596–640, 1950.
- [147] Pochi Yeh. In *Optical waves in layered media*, page 406. Wiley, 1988.
- [148] M. P. Rouard. Etudes des propriétés optiques des lames métalliques très minces. *Ann. Phys.(Paris) Ser. II*, 7:291–384, 1937.
- [149] Pierre Lecaruyer, Emmanuel Maillart, Michael Canva, and Jannick Rolland. Generalization of the rouard method to an absorbing thin-film stack and application to surface plasmon resonance. *Appl. Opt.*, 45(33):8419–8423, Nov 2006.
- [150] W. H. Bragg and W. L. Bragg. The reflection of x-rays by crystals. *Proceedings of the Royal Society of London A: Mathematical, Physical and Engineering Sciences*, 88(605):428–438, 1913.
- [151] J. Chandezon, M. T. Dupuis, G. Cornet, and D. Maystre. Multicoated gratings: a differential formalism applicable in the entire optical region. *J. Opt. Soc. Am.*, 72(7):839–846, Jul 1982.
- [152] Lifeng Li. Multilayer-coated diffraction gratings: differential method of chandezon et al. revisited. *J. Opt. Soc. Am. A*, 11(11):2816–2828, Nov 1994.
- [153] K. Knop. Rigorous diffraction theory for transmission phase gratings with deep rectangular grooves. *J. Opt. Soc. Am.*, 68(9):1206–1210, Sep 1978.
- [154] M. G. Moharam and T. K. Gaylord. Diffraction analysis of dielectric surface-relief gratings. *J. Opt. Soc. Am.*, 72(10):1385–1392, Oct 1982.
- [155] M. G. Moharam, T. K. Gaylord, Eric B. Grann, and Drew A. Pommet. Formulation for stable and efficient implementation of the rigorous coupled-wave analysis of binary gratings. *J. Opt. Soc. Am. A*, 12(5):1068–1076, May 1995.
- [156] Jianming Jin. *The Finite Element Method in Electromagnetics*. Wiley-IEEE Press, 3rd edition, 2014.
- [157] Dominique Cherouat Abel Grosge Thomas Borouchaki Houman Mezghani, Fadhil Barchiesi. Comparison of 3d adaptive remeshing strategies for finite element simulations of electromagnetic heating of gold nanoparticles. *Advances in Mathematical Physics*, 2015:12, 2015.
- [158] J P Webb. Application of the finite-element method to electromagnetic and electrical topics. *Reports on Progress in Physics*, 58(12):1673, 1995.
- [159] Philippe Lalanne. Convergence performance of the coupled-wave and the differential methods for thin gratings. *J. Opt. Soc. Am. A*, 14(7):1583–1591, Jul 1997.
- [160] J. P. Hugonin, M. Besbes, and P. Lalanne. Hybridization of electromagnetic numerical methods through the g-matrix algorithm. *Opt. Lett.*, 33(14):1590–1592, Jul 2008.
- [161] Felix Bloch. Über die quantenmechanik der elektronen in kristallgittern. *Zeitschrift für Physik*, 52(7-8):555–600, 1929.

- [162] G. Floquet. Sur les équations différentielles linéaires à coefficients périodiques. *Annales scientifiques de l'École Normale Supérieure*, 12:47–88, 1883.
- [163] Nagaraj and A. A. Krokhin. Long-range surface plasmons in dielectric-metal-dielectric structure with highly anisotropic substrates. *Phys. Rev. B*, 81:085426, Feb 2010.
- [164] Anne Sentenac, Patrick C. Chaumet, and Kamal Belkebir. Beyond the rayleigh criterion: Grating assisted far-field optical diffraction tomography. *Phys. Rev. Lett.*, 97:243901, Dec 2006.
- [165] Andrey G. Nikitin, Andrei V. Kabashin, and Hervé Dallaporta. Plasmonic resonances in diffractive arrays of gold nanoantennas: near and far field effects. *Opt. Express*, 20(25):27941–27952, Dec 2012.
- [166] A. Sentenac, J.-J. Greffet, and F. Pincemin. Structure of the electromagnetic field in a slab of photonic crystal. *J. Opt. Soc. Am. B*, 14(2):339–347, Feb 1997.
- [167] A. Hessel and A. A. Oliner. A new theory of wood's anomalies on optical gratings. *Appl. Opt.*, 4(10):1275–1297, Oct 1965.
- [168] H. Gao, J. M. McMahon, M. H. Lee, J. Henzie, S. K. Gray, G. C. Schatz, and T. W. Odom. Rayleigh anomaly-surface plasmon polariton resonances in palladium and gold subwavelength hole arrays. *Opt. Express*, 17(4):2334–2340, Feb 2009.
- [169] T. A. Kelf, Y. Sugawara, J. J. Baumberg, M. Abdelsalam, and P. N. Bartlett. Plasmonic band gaps and trapped plasmons on nanostructured metal surfaces. *Phys. Rev. Lett.*, 95:116802, Sep 2005.
- [170] Takayuki Okamoto, Janne Simonen, and Satoshi Kawata. Plasmonic band gaps of structured metallic thin films evaluated for a surface plasmon laser using the coupled-wave approach. *Phys. Rev. B*, 77:115425, Mar 2008.
- [171] Pierre Berini. Plasmon-polariton waves guided by thin lossy metal films of finite width: Bound modes of symmetric structures. *Phys. Rev. B*, 61:10484–10503, Apr 2000.
- [172] Pierre Berini. Plasmon-polariton modes guided by a metal film of finite width. *Opt. Lett.*, 24(15):1011–1013, Aug 1999.
- [173] Yinon Satuby and Meir Orenstein. Surface-plasmon-polariton modes in deep metallic trenches-measurement and analysis. *Opt. Express*, 15(7):4247–4252, Apr 2007.
- [174] David F. P. Pile, Dmitri K. Gramotnev, Rupert F. Oulton, and Xiang Zhang. On long-range plasmonic modes in metallic gaps. *Opt. Express*, 15(21):13669–13674, Oct 2007.
- [175] Georgios Veronis and Shanhui Fan. Guided subwavelength plasmonic mode supported by a slot in a thin metal film. *Opt. Lett.*, 30(24):3359–3361, Dec 2005.
- [176] Rashid Zia, Mark D. Selker, and Mark L. Brongersma. Leaky and bound modes of surface plasmon waveguides. *Phys. Rev. B*, 71:165431, Apr 2005.

- [177] Mitradeep Sarkar, Maha Chamtouri, Julien Moreau, Mondher Besbes, and Michael Canva. Introducing 2d confined propagating plasmons for surface plasmon resonance sensing using arrays of metallic ribbons. *Sensors and Actuators B: Chemical*, 191:115 – 121, 2014.
- [178] Alexander Moroz. Depolarization field of spheroidal particles. *J. Opt. Soc. Am. B*, 26(3):517–527, Mar 2009.
- [179] Dominique Barchiesi, Sameh Kessentini, Nicolas Guillot, Marc Lamy de la Chapelle, and Thomas Grosques. Localized surface plasmon resonance in arrays of nano-gold cylinders: inverse problem and propagation of uncertainties. *Opt. Express*, 21(2):2245–2262, Jan 2013.
- [180] Alexandre Vial and Thierry Laroche. Description of dispersion properties of metals by means of the critical points model and application to the study of resonant structures using the fdtd method. *Journal of Physics D: Applied Physics*, 40(22):7152, 2007.
- [181] J. Grand, M. Lamy de la Chapelle, J.-L. Bijeon, P.-M. Adam, A. Vial, and P. Royer. Role of localized surface plasmons in surface-enhanced raman scattering of shape-controlled metallic particles in regular arrays. *Phys. Rev. B*, 72:033407, Jul 2005.
- [182] Dominique Barchiesi and Thomas Grosques. Resonance in metallic nanoparticles: a rigorous formulation of the dipolar approximation. *European Journal of Physics*, 35(3):035012, 2014.
- [183] Jean Lermé. Plasmon hybridization model for a nanoparticle above a dielectric interface: Dielectric effects, comparison with the dimer system, range of applicability, and limits. *The Journal of Physical Chemistry C*, 119(36):21087–21104, 2015.
- [184] Timothy J. Davis, Kristy C. Vernon, and Daniel E. Gómez. Effect of retardation on localized surface plasmon resonances in a metallic nanorod. *Opt. Express*, 17(26):23655–23663, Dec 2009.
- [185] Isaak D. Mayergoyz, Donald R. Fredkin, and Zhenyu Zhang. Electrostatic (plasmon) resonances in nanoparticles. *Phys. Rev. B*, 72:155412, Oct 2005.
- [186] G. Pellegrini, G. Mattei, V. Bello, and P. Mazzoldi. Interacting metal nanoparticles: Optical properties from nanoparticle dimers to core-satellite systems. *Materials Science and Engineering: C*, 27(5–8):1347 – 1350, 2007. {EMRS} 2006 Symposium A: Current Trends in Nanoscience - from Materials to Applications.
- [187] Dominique Barchiesi and Thomas Grosques. Control of the applicability of the dipole approximation for gold nanoparticles. *Advanced Studies in Biology*, 7(9):403–412, September 2015.
- [188] Anuj Dhawan, Stephen J. Norton, Michael D. Gerhold, and Tuan Vo-Dinh. Comparison of fdtd numerical computations and analytical multipole expansion method for plasmonics-active nanosphere dimers. *Opt. Express*, 17(12):9688–9703, Jun 2009.
- [189] Viktor Myroshnychenko, Jessica Rodriguez-Fernandez, Isabel Pastoriza-Santos, Alison M. Funston, Carolina Novo, Paul Mulvaney, Luis M. Liz-Marzan, and F. Javier Garcia de Abajo. Modelling the optical response of gold nanoparticles. *Chem. Soc. Rev.*, 37:1792–1805, 2008.
- [190] M Born and E Wolf. *Principles of Optics*. Cambridge University Press, 6 edition, 1999.



- [191] Erik Martinsson, Marinus A. Otte, Mohammad Mehdi Shahjamali, Borja Sepulveda, and Daniel Aili. Substrate effect on the refractive index sensitivity of silver nanoparticles. *The Journal of Physical Chemistry C*, 118(42):24680–24687, 2014.
- [192] Mark W. Knight, Yanpeng Wu, J. Britt Lassiter, Peter Nordlander, and Naomi J. Halas. Substrates matter: Influence of an adjacent dielectric on an individual plasmonic nanoparticle. *Nano Letters*, 9(5):2188–2192, 2009. PMID: 19361166.
- [193] Michelle Duval Malinsky, K. Lance Kelly, George C. Schatz, , and Richard P. Van Duyne. Nanosphere lithography- effect of substrate on the localized surface plasmon resonance spectrum of silver nanoparticles. *The Journal of Physical Chemistry B*, 105(12):2343–2350, 2001.
- [194] Shunping Zhang, Kui Bao, Naomi J. Halas, Hongxing Xu, and Peter Nordlander. Substrate-induced fano resonances of a plasmonic nanocube—a route to increased-sensitivity localized surface plasmon resonance sensors revealed. *Nano Letters*, 11(4):1657–1663, 2011. PMID: 21410217.
- [195] Kristy C. Vernon, Alison M. Funston, Carolina Novo, Daniel E. Gómez, Paul Mulvaney, and Timothy J. Davis. Influence of particle-substrate interaction on localized plasmon resonances. *Nano Letters*, 10(6):2080–2086, 2010.
- [196] Abdelilah Mejdoubi and Christian Brosseau. Finite-element simulation of the depolarization factor of arbitrarily shaped inclusions. *Phys. Rev. E*, 74:031405, Sep 2006.
- [197] A.Zehe and A.Ramirez. The depolarization field in polarizable objects of general shape. *Rev Mex Fis*, 48:427, 2002.
- [198] Mitradeep Sarkar, Mondher Besbes, Julien Moreau, Jean-François Bryche, Aurore Olivéro, Grégory Barbillon, Anne-Lise Coutrot, Bernard Bartenlian, and Michael Canva. Hybrid plasmonic mode by resonant coupling of localized plasmons to propagating plasmons in a kretschmann configuration. *ACS Photonics*, 2(2):237–245, 2015.
- [199] Mitradeep Sarkar, Jean-François Bryche, Julien Moreau, Mondher Besbes, Grégory Barbillon, Bernard Bartenlian, and Michael Canva. Generalized analytical model based on harmonic coupling for hybrid plasmonic modes: comparison with numerical and experimental results. *Opt. Express*, 23(21):27376–27390, Oct 2015.
- [200] H. F. Ghaemi, Tineke Thio, D. E. Grupp, T. W. Ebbesen, and H. J. Lezec. Surface plasmons enhance optical transmission through subwavelength holes. *Phys. Rev. B*, 58:6779–6782, Sep 1998.
- [201] J. Dintinger, S. Klein, F. Bustos, W. L. Barnes, and T. W. Ebbesen. Strong coupling between surface plasmon-polaritons and organic molecules in subwavelength hole arrays. *Phys. Rev. B*, 71:035424, Jan 2005.
- [202] W. L. Barnes, T. W. Preist, S. C. Kitson, and J. R. Sambles. Physical origin of photonic energy gaps in the propagation of surface plasmons on gratings. *Phys. Rev. B*, 54:6227–6244, Sep 1996.
- [203] Na Liu and Harald Giessen. Coupling effects in optical metamaterials. *Angewandte Chemie International Edition*, 49(51):9838–9852, 2010.

- [204] P Törmä and W L Barnes. Strong coupling between surface plasmon polaritons and emitters: a review. *Reports on Progress in Physics*, 78(1):013901, 2015.
- [205] D. E. Gomez, K. C. Vernon, P. Mulvaney, and T. J. Davis. Surface plasmon mediated strong exciton-photon coupling in semiconductor nanocrystals. *Nano Letters*, 10(1):274–278, 2010. PMID: 20000744.
- [206] Carlo Forestiere, Luca Dal Negro, and Giovanni Miano. Theory of coupled plasmon modes and fano-like resonances in subwavelength metal structures. *Phys. Rev. B*, 88:155411, Oct 2013.
- [207] Ugo Fano. Some theoretical considerations on anomalous diffraction gratings. *Phys. Rev.*, 50:573–573, Sep 1936.
- [208] U. Fano. Effects of configuration interaction on intensities and phase shifts. *Phys. Rev.*, 124:1866–1878, Dec 1961.
- [209] A. Christ, T. Zentgraf, J. Kuhl, S. G. Tikhodeev, N. A. Gippius, and H. Giessen. Optical properties of planar metallic photonic crystal structures: Experiment and theory. *Phys. Rev. B*, 70:125113, Sep 2004.
- [210] Andrey E. Miroshnichenko, Sergej Flach, and Yuri S. Kivshar. Fano resonances in nanoscale structures. *Rev. Mod. Phys.*, 82:2257–2298, Aug 2010.
- [211] Nikolay I. Maier Stefan A. Halas Naomi J. Nordlander Peter Giessen Harald Chong Chong Tow Luk'yanchuk, Boris Zheludev. The fano resonance in plasmonic nanostructures and metamaterials. *Nature Materials*, 9:707–715, 2010.
- [212] Yan Francescato, Vincenzo Giannini, and Stefan A. Maier. Plasmonic systems unveiled by fano resonances. *ACS Nano*, 6(2):1830–1838, 2012. PMID: 22280066.
- [213] F. J. García de Abajo. *Colloquium* : Light scattering by particle and hole arrays. *Rev. Mod. Phys.*, 79:1267–1290, Oct 2007.
- [214] Yong S Joe, Arkady M Satanin, and Chang Sub Kim. Classical analogy of fano resonances. *Physica Scripta*, 74(2):259, 2006.
- [215] Jordi Sancho-Parramon and Salvador Bosch. Dark modes and fano resonances in plasmonic clusters excited by cylindrical vector beams. *ACS Nano*, 6(9):8415–8423, 2012. PMID: 22920735.
- [216] Peter Nordlander. Plasmonics: The dark side of the ring. *Nat Nano*, 8(2):76–77, 2013.
- [217] B. Gallinet, A. Lovera, T. Siegfried, H. Sigg, and O. J. F. Martin. Fano resonant plasmonic systems: Functioning principles and applications. *AIP Conference Proceedings*, 1475(1), 2012.
- [218] Mark I. Stockman, Sergey V. Faleev, and David J. Bergman. Localization versus delocalization of surface plasmons in nanosystems: Can one state have both characteristics? *Phys. Rev. Lett.*, 87:167401, Sep 2001.
- [219] S. R. K. Rodriguez, A. Abass, B. Maes, O. T. A. Janssen, G. Vecchi, and J. Gómez Rivas. Coupling bright and dark plasmonic lattice resonances. *Phys. Rev. X*, 1:021019, Dec 2011.

- [220] Xiao gang Yin, Cheng ping Huang, Qian jin Wang, Wan xia Huang, Lin Zhou, Chao Zhang, and Yong yuan Zhu. Fanolike resonance due to plasmon excitation in linear chains of metal bumps. *Opt. Express*, 19(11):10485–10493, May 2011.
- [221] AdnanDaud Khan, SultanDaud Khan, RehanUllah Khan, and Naveed Ahmad. Excitation of multiple fano-like resonances induced by higher order plasmon modes in three-layered bimetallic nanoshell dimer. *Plasmonics*, 9(2):461–475, 2014.
- [222] S Hayashi, D V Nesterenko, , and Z Sekkat. Waveguide-coupled surface plasmon resonance sensor structures: Fano lineshape engineering for ultrahigh-resolution sensing. *Journal of Physics D: Applied Physics*, 48(32):325303, 2015.
- [223] Nicolas Rana, Lévêque Gaëtan, Marae-Djouda Joseph, Montay Guillame, Madi Yazid, Plain Jérôme, Herro Ziad, Kazan Michel, Adam Pierre-Michel, and Maurer Thomas. Plasmonic mode interferences and fano resonances in metal-insulator- metal nanostructured interface. *Scientific Reports*, 5:14419, 2015.
- [224] A. I. Väkeväinen, R. J. Moerland, H. T. Rekola, A.-P. Eskelinen, J.-P. Martikainen, D.-H. Kim, and P. Törmä. Plasmonic surface lattice resonances at the strong coupling regime. *Nano Letters*, 14(4):1721–1727, 2014. PMID: 24279840.
- [225] Alastair D. Humphrey and William L. Barnes. Plasmonic surface lattice resonances on arrays of different lattice symmetry. *Phys. Rev. B*, 90:075404, Aug 2014.
- [226] D. E. Gómez, Z. Q. Teo, M. Altissimo, T. J. Davis, S. Earl, and A. Roberts. The dark side of plasmonics. *Nano Letters*, 13(8):3722–3728, 2013. PMID: 23802620.
- [227] Stefan A. Maier. Plasmonics- the benefits of darkness. *Nature Materials*, 8(9):699–700, 2009.
- [228] Ben Hopkins, Alexander N. Poddubny, Andrey E. Miroshnichenko, and Yuri S. Kivshar. Revisiting the physics of fano resonances for nanoparticle oligomers. *Phys. Rev. A*, 88:053819, Nov 2013.
- [229] K. R. Ozdemir S. K. Lee J. Maier S. A. Kim M. S. Tame, M. S. McEney. Quantum plasmonics. *Nature Physics*, 9:329–340, 2013.
- [230] Lukas Novotny. Strong coupling, energy splitting, and level crossings: A classical perspective. *American Journal of Physics*, 78(11), 2010.
- [231] H.F. Ghaemi T. Thio T.W. Ebbesen, H.J. Lezec and P. A. Wolff. Extraordinary optical transmission through sub-wavelength hole arrays. *Nature*, 391:667–669, 1998.
- [232] S. Carretero-Palacios, O. Mahboub, F. J. Garcia-Vidal, L. Martin-Moreno, Sergio G. Rodrigo, C. Genet, and T. W. Ebbesen. Mechanisms for extraordinary optical transmission through bulls eye structures. *Opt. Express*, 19(11):10429–10442, May 2011.
- [233] Haitao Liu and Philippe Lalanne. Microscopic theory of the extraordinary optical transmission. *Nature*, 452:728–731, 2008.

- [234] Weisheng Yue, Zhihong Wang, Yang Yang, Jingqi Li, Ying Wu, Longqing Chen, Boon Ooi, Xianbin Wang, and Xi-xiang Zhang. Enhanced extraordinary optical transmission (eot) through arrays of bridged nanohole pairs and their sensing applications. *Nanoscale*, 6:7917–7923, 2014.
- [235] F. Marquier, J.-J. Greffet, S. Collin, F. Pardo, and J.L. Pelouard. Resonant transmission through a metallic film due to coupled modes. *Opt. Express*, 13(1):70–76, Jan 2005.
- [236] Bin Sun, Ling-Ling Wang, Liu Wang, Xiang Zhai, Xiao-Fei Li, and Jian-Qiang Liu. Improved extraordinary optical transmission through single nano-slit by nano-defocusing. *Optics and Laser Technology*, 54:214 – 218, 2013.
- [237] A. Shalabney and I. Abdulhalim. Figure-of-merit enhancement of surface plasmon resonance sensors in the spectral interrogation. *Opt. Lett.*, 37(7):1175–1177, Apr 2012.
- [238] Ralf Ameling, Lutz Langguth, Mario Hentschel, Martin Mesch, Paul V. Braun, and Harald Giessen. Cavity-enhanced localized plasmon resonance sensing. *Applied Physics Letters*, 97(25):–, 2010.
- [239] Leif J. Sherry, Shih-Hui Chang, George C. Schatz, Richard P. Van Duyne, Benjamin J. Wiley, and Younan Xia. Localized surface plasmon resonance spectroscopy of single silver nanocubes. *Nano Letters*, 5(10):2034–2038, 2005. PMID: 16218733.
- [240] Kyung Min Byun, Seong Min Jang, Sung June Kim, and Donghyun Kim. Effect of target localization on the sensitivity of a localized surface plasmon resonance biosensor based on subwavelength metallic nanostructures. *J. Opt. Soc. Am. A*, 26(4):1027–1034, Apr 2009.
- [241] Maha Chamtouri, Anuj Dhawan, Mondher Besbes, Julien Moreau, Hassen Ghalila, Tuan Vo-Dinh, and Michael Canva. Enhanced spr sensitivity with nano-micro-ribbon grating—an exhaustive simulation mapping. *Plasmonics*, 9(1):79–92, 2014.
- [242] Fang Cheng, Ming-Yang Li, Han-Qi Wang, Dong-Qiang Lin, and Jing-Ping Qu. Antibody–ligand interactions for hydrophobic charge-induction chromatography: A surface plasmon resonance study. *Langmuir*, 31(11):3422–3430, 2015. PMID: 25734470.
- [243] D. S. Karpovich and G. J. Blanchard. Direct measurement of the adsorption kinetics of alkanethiolate self-assembled monolayers on a microcrystalline gold surface. *Langmuir*, 10(9):3315–3322, 1994.
- [244] Kyungjae Ma, Dong Jun Kim, Kyujung Kim, Seyoung Moon, and Donghyun Kim. Target-localized nanograting-based surface plasmon resonance detection toward label-free molecular biosensing. *Selected Topics in Quantum Electronics, IEEE Journal of*, 16(4):1004–1014, July 2010.
- [245] Peter Nestler, Stephan Block, and Christiane A. Helm. Temperature-induced transition from odd–even to even–odd effect in polyelectrolyte multilayers due to interpolyelectrolyte interactions. *The Journal of Physical Chemistry B*, 116(4):1234–1243, 2012. PMID: 22204702.
- [246] Matthias Cornelsen, Christiane A. Helm, and Stephan Block. Destabilization of polyelectrolyte multilayers formed at different temperatures and ion concentrations. *Macromolecules*, 43(9):4300–4309, 2010.

- [247] Jean-François Bryche, Raymond Gillibert, Grégory Barbillon, Philippe Gogol, Julien Moreau, Marc Lamy de la Chapelle, Bernard Bartenlian, and Michael Canva. Plasmonic enhancement by a continuous gold underlayer: Application to sers sensing. *Plasmonics*, pages 1–8, 2015.
- [248] H. Li, S. Xu, Y. Liu, Y. Gu, and W. Xu. Directional emission of surface-enhanced Raman scattering based on a planar-film plasmonic antenna. *Thin Solid Films*, 520:6001–6006, July 2012.
- [249] Yizhuo Chu, Wenqi Zhu, Dongxing Wang, and Kenneth B. Crozier. Beamed raman: directional excitation and emission enhancement in a plasmonic crystal double resonance sers substrate. *Opt. Express*, 19(21):20054–20068, Oct 2011.
- [250] Jeremy J. Baumberg, Timothy A. Kelf, Yoshihiro Sugawara, Suzanne Cintra, Mamdouh E. Abdelsalam, Phillip N. Bartlett, and Andrea E. Russell. Angle-resolved surface-enhanced raman scattering on metallic nanostructured plasmonic crystals. *Nano Letters*, 5(11):2262–2267, 2005. PMID: 16277465.
- [251] Jorge Zuloaga and Peter Nordlander. On the energy shift between near-field and far-field peak intensities in localized plasmon systems. *Nano Letters*, 11(3):1280–1283, 2011. PMID: 21319841.
- [252] Christoph Menzel, Erik Hebestreit, Stefan Mühlig, Carsten Rockstuhl, Sven Burger, Falk Lederer, and Thomas Pertsch. The spectral shift between near- and far-field resonances of optical nanoantennas. *Opt. Express*, 22(8):9971–9982, Apr 2014.
- [253] P. Alonso-González, P. Albella, F. Neubrech, C. Huck, J. Chen, F. Golmar, F. Casanova, L. E. Hueso, A. Pucci, J. Aizpurua, and R. Hillenbrand. Experimental verification of the spectral shift between near- and far-field peak intensities of plasmonic infrared nanoantennas. *Phys. Rev. Lett.*, 110:203902, May 2013.



# Epilogue

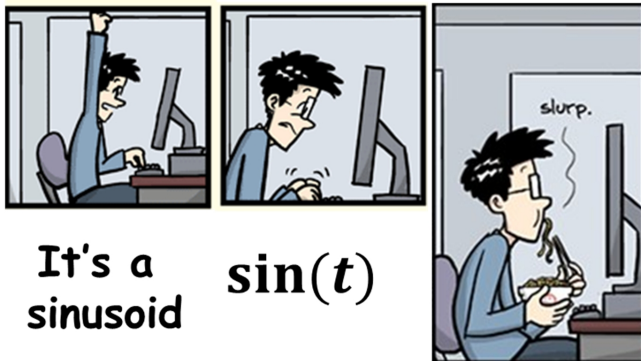




# THE BEST YEARS OF YOUR LIFE



WWW.PHDCOMICS.COM



It's a sinusoid

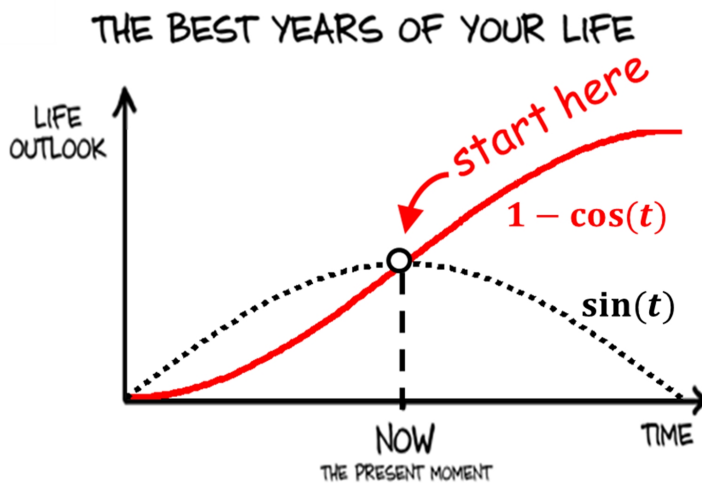
$\sin(t)$

$$\sin(t - \pi) = -\sin(t)$$

$$-\sin(t) + t$$

$$\frac{d(t - \sin t)}{dt} =$$

$$1 - \cos(t)$$



The PhD is only a milestone, the research is never complete



## Acknowledgments

I would like to thank you for reaching these last few pages of this long manuscript. This work that has been realized for the last three years (and a few months), is the longest work that I have produced till date and also probably the most important. Three years of discovery, of developing theories to explain different physical phenomena, three years of measurements and experiments to verify the obtained results finally culminated in this manuscript, but also everything obtained for the last three years, to realize this manuscript would not have been possible without the help of numerous other persons to whom I remain forever grateful.

First I would like to thank the President of the jury, Paul Charette, the two reviewers, Anne Sentenac and Dominique Barchiesi and the examiners, Anatole Lupu and Stephane Collin for their constructive remarks and judicial comments which helped immensely to improve this manuscript and above all the cordial discussions that followed the presentation of my thesis defense.

I would like to mention my eternal gratitude for the immense support over the last three years given by the director of my thesis, Michael Canva. I still remember the first time I walked into his office in the winter of 2012, looking for a PhD position. Ever since then his gentle smile, his gracious nature and his desire to explore new domains of science has inspired me to push the boundaries of my research. I would like to thank Michael for finding me worth of carrying out this work under his supervision and doing everything possible, sometimes even going out of the normal course of events to realize the research in a congenial and productive environment. In Michael, I found the ideal characteristics that every PhD student hopes for, to him the interests of the PhD student is an utmost priority. I would also mention that most of the fundamental foundations on which this manuscript is based would not have evolved without the judicious remarks of Michael. Throughout the last three years, it was Michael who came up with ideas, sometimes a bit unusual, and I have tried to develop on them, the best I could, always supported by his immense scientific know-how and experience. For this I will forever remain indebted to Michael.

This work would not also been possible without the support, scientific and non-scientific, of Julien Moreau who was also the supervisor of my thesis. His office was adjacent to mine and through out the last three years, I have often rushed into his office for discussing various ideas, weird results, even some not so intelligent remarks and questions from my part, and Julien has always treated them with immense interest and came up with solutions even if he was busy with loads of other works. His immense knowledge and experience for practical applications of the theories developed during this thesis, served to use them efficiently and make them presentable for a wider community of researchers. I would really like to thank him for his pedagogical approach to really tough scientific problems and his method to look at such problems in a much simplified and lucid manner. Apart from this work, I would also like to thank him for the amicable time that I spent in the group, all the jovial discussions we had on non-scientific topics, and for him serving as a beacon to lead my life as a doctorate student here at IOGS.

The third pillar that supports this work is Mondher Besbes. This work is a theoretical work based on loads of numerical simulations and frankly speaking this work is completely based on the numerical codes developed by Mondher. Thus without the developed numerical code, simply this work does not exist. In

this manuscript, I have presented only the results which worked perfectly and gave presentable results, however during the last three years, the simulations performed have stacked up to more than 80GB of raw data and Mondher has been there to help me understand and evaluate this gigantic amount raw data. He has always been calm and harmonious to solve the unique types of problems that I posed for him and have shown immense patience even when dealing with some of my silly errors in handling the numerical codes and treating some of the physically impossible problems that I postulated. I would mention here that early on in my thesis, I had discovered a grave error caused in the simulations, which was due to a carelessness on my part. But Mondher as well as Michael and Julien had treated it jovially and helped me regain my optimistic outlook and recover from the error within a few days. I am really grateful for having the opportunity to work with all the three of them and hope to continue collaborating with them.

A major part of the support for this work also came from the other PhD students who worked with me in related topics and the results obtained by them also form an important part of this manuscript.

First I would like to thank the two doctorates who worked on the same subject and finished their thesis before me from the same group.

Maha Chamtouri was in her final year when I started my thesis and the initial foundation of my thesis was based on the research performed by her and the ideas developed during the course of her thesis. I would like to thank Maha for the initial push to lay the base for my thesis.

Alexandra Sereda who successfully defended her thesis last year was a constant support for the first two years of my thesis. Apart from the experimental results which would not have been possible without her help, she had also been there to guide and help me adapt to the life of a PhD student here in the group.

At the time when I started my thesis I could hardly speak French and I must say that Alex has been my first teacher to master the language along with another PhD student from the same group Antoine Federici, who successfully defended his thesis last month. In fact, Antoine and me started our respective PhDs at the same time and I also shared my office with him. I would like to thank him for all the enjoyable time we had together during the course of our respective PhDs.

Aurore Olivero continued from where Alex had left. She started her PhD as an expert of the already existing experimental setup that we had here and she went on to develop the same and also a new experimental setup to suit the requirements of the project, which served immensely to the realization of the experimental part of this manuscript. Apart from being the sweet colleague, ever smiling and sometimes determined in terms of experimental manipulations, she has also been a loving friend. I would thank her for her patience shown in dealing with the demanding experiments that I wished to perform at certain times and that other demanding non-scientific questions that I may have posed mainly the tips on playing a piano (another domain in which she is an expert).

Jean Francois Bryche who started his PhD one year after me was almost a sort of working partner for this thesis. He worked on some of the simulations and helped me discover bugs in the code, but mainly he was there to fabricate all the nano-structured samples without which the experimental verification of the theories developed would not have been possible. We did not spend a lot of time physically because he was always busy in the clean room at IEF to fabricate perfectly such samples. I would thank him for the flawless samples that he accomplished during the last two years of his thesis. It was really remarkable the way he achieved these numerous samples in such a short span of time. I would also thank him for the

number of articles which we have co-authored during the last two years.

Raymond Gillibert has been the other working partner, mainly for the experiments concerning SERS. I was really amazed by the rapidity with which he came up with experimental results to correspond perfectly with the requirement of my thesis. He supplied some results which filled up the gaps in my approach to treat SERS, even before I had made my intentions clear to him. We used to spend hours (and literally hours) on the telephone to discuss the results between Palaiseau, the suburb in the south of Paris and Bobigny, the suburb in the north of Paris. I would like to mention that most of my know-how about the phenomenon of SERS were acquired with his help. It was also interesting the conversations between us which were carried out with me speaking in French and him in English which helped to master ourselves in the respective languages.

I would also like to thank the other researchers and PhD students with whom I worked during the course of my thesis, namely Anne-Lise Coutrot (LCF), Florent Collas (CSPBAT), Marine Boulade (LCF), Inga Tijunelyte (CSPBAT), Francisco Palazon (INL) and others.

A major part of this work was done as a part of the ANR project PIRANEX and I would like to thank all the different teams which participated in this project.

The team from IEF was primarily responsible for the fabrication of the nano-structured samples used in this work. I would like to thank Bernard Bartenlian for his help in this respect. Grégory Barbillon has helped immensely in the realization of the samples and I would like to thank Grégory also for the realization of the articles that we have co-authored. Philippe Gogol has also helped with certain theoretical aspects of the plasmonic modes described in this manuscript and I am grateful to the productive and pedagogical discussions that I had with him. I would also thank all the other members of the team of IEF who have participated in the PIRANEX project.

I would thank the team from CSPBAT mainly Marc Lamy de la Chapelle who have also provided important knowledge on the SERS phenomenon during the course of the PIRANEX project. I would also thank the other members of the CSPBAT team who have participated in this project.

I am grateful to Emmanuel Maillart and the other members of HORIBA Scientific who have participated in the realization of the experimental part of the PIRANEX project and my thesis.

I would also thank the team from INL (Lyon), Eliane Souteyrand, Yann Chevotot, Emmanuelle Laurenceau and others and the team from AGROParis, Douglas Rutledge and others for being a part of the PIRANEX project and helping me with certain aspects of my thesis.

During this thesis I have also conducted some courses as a teaching assistant and I would like to thank the team of Optical Labworks, Lionel Jacobowicz, Fabienne Bernard, Thierry Avignon and others and the team of Labview courses, Fredric Capmas and Pierre Krivosic. I would also like to thank Nicolas Dubreuil with whom I have participated in giving the tutorials for the course of Non-linear Optics.

I have also profited from the interesting and enriching scientific discussions which helped me to develop different aspects of this thesis. I am grateful to Jean-Jacques Greffet for all the advice that he has provided with respect to the approach that I have followed during the course of my thesis. I would also like to thank Henri Benisty, Buntha Ea-Kim, for the different scientific courses that I have followed

and Philippe Ben-Abdallah and Patrick Georges for their advices with respect to my research, during my thesis.

I would also like to thank all the members of LCF and IOGS, namely the teams of Optical and mechanical workshops, the library and informatics and the administration of IOGS. As a foreign student, I am grateful to the administration for all their help with the Visa procedures and the process of obtaining and the renewal of the Residence permit which were really handled in a smooth and effective manner.

I would also like to thank all my friends in the Paris region and also those who are almost in every corner of the globe. I would thank my family and parents who are in India, who have been a constant support not only during the last three years but for my life so far.

I have worked for the last three years at LCF and my scientific family during this period was in fact the Biophotonics group of which I was a member. I joined this group as a doctorate student almost at the same time as the formation of this group and now after three years I feel that I am completely inseparable from this family that we have created at work. The help and everything that we have shared in this group is not really possible to express in a few sentences but I will try.

Firstly Karen Perronet has been my guide to help me accustom with very French nature of things. She has been a constant support and teacher for the last three years for scientific and more for everything non-scientific ranging from the French food, to the requirement of eating five fruits and vegetables per day, to the way of life, to filling up administrative documents which I must say were rather difficult initially when I was not fluent in French and later even when I became fluent in the French language, for the very fact that they were just too demanding! I would like to thank Karen for always being there, ready to help and offer solutions for the slightest problem that I might have in the group.

I would like to thank Arnaud Dubois above all because it was him that I contacted three and a half years ago when I was looking for a PhD position. It is Arnaud that really introduced me to my director Michael. I would also thank him for the support he has provided during the course of my PhD as a permanent member of the Group Biophotonics. I would also thank Nathalie Westbrooke who helped me find the teaching position at IOGS during the course of my thesis and for all the other discussions that we had during the last three years.

I would like to thank the previous doctorate students of the group namely Masreshaw Demelash and Nicolas Fizzman who helped me to adapt to the life of a doctorate student in the initial few months of my thesis.

The other doctorate students of the group have also been there to help me relax and take the stress off the work and I thank them for the enjoyable time we had together at LCF.

Flavie Gillant has thrilled me with her straight to the point nature, strong determined attitude and sharp remarks which are really pleasing and takes away a lot of stress from time to time. If I try to really represent the discussions that we had then I must say that I have been like a helium filled balloon about to burst and she helped to pull me down and ground me with ease with her hilarious comments. I would like to thank Flavie for being there as a colleague and friend for the last two and a half years.

Jonas Ogien had recently joined the group but in the little time that we had spent together, I really cherish the discussions we had on French politics and ofcourse on music given Jonas is a skilled Alto player.

And Nathalie Barbier, thank you for being there. She had joined our group when I was half way through my thesis and for the last year and a half she has become a very close friend with whom I can discuss everything outside work, just as I would talk to myself. I would like to thank you for the discussions we had on topics ranging from ancient philosophy, to everything concerning life, to unintelligent tele-serials, to music, Cabrel (le PLUS préféré!!!) and Kendji and all other forms of music (must mention here that she has a marvelous singing voice) and of course world literature and trying to write some. Thank you for the long hours that we spent over coffee (café allongé au lait, matin, sans lait, apres midi!!!) and while going back home (the Berlingo). I don't know if these discussions helped me to develop the theories presented in this manuscript but they really helped me to develop a wide ideology which may have trickled down to the scientific knowledge, we will never know. I wish you all the best for your own thesis and I am sure we will continue our bizarre discussions (or disputes) in the future.

Finally and most importantly, Mitanti. You have been my support or rather my life for the last 9 years. It is not possible to write a few words to thank you, because for it I need to write a novel. Thank you for loving me and tolerating me for all these years and more so for the last three years when I believe I have been the most difficult. You have travelled and accompanied me through out these years to every part of the planet and helped me to remain constantly motivated in every thing that I do. I would also not be wrong if I say that my decision to pursue a thesis in the Paris region had been to some extent motivated by you. It is also a bit weird but though you are not from the scientific community (mainly given that you do not like Physics at all), you were the first with whom I discussed all the ideas I had relating my thesis. You were also the first to read the drafts of all scientific articles that I published and this manuscript and also came up with some really fruitful remarks regarding them. So it is apt that I dedicate this thesis to you. Your love has really been an inspiration to successfully realize everything that I have achieved for the last few years, your judicious arguments have helped me and will help me in the future to make critical decisions regarding my life and career. I hope you will continue to support me and be with me for the years to come.

# Hybrid surface plasmon modes in metallic nanostructures: Theory, numerical analysis and application to bio-sensing.

**Keywords** : Surface Plasmons, Biosensing, Numerical methods, Plasmonic modes, Metallic nanostructures

## Abstract

The surface plasmons on metallic surfaces are excited by the collective oscillations of free electrons. They satisfy certain resonance conditions and their dispersion can be considered as modes of the system. The plasmons at uniform metal-dielectric interfaces manifest as evanescent electromagnetic (EM) fields confined to a few hundreds of nanometers from the metallic surface and propagate along the interface. This mode is called the Propagating surface plasmon (PSP) and is a fundamental plasmonic mode. The other fundamental modes, which are non-propagative, results from collective oscillations of free electrons on curved surfaces of metallic nano-particles. They are called localized surface plasmon (LSP) modes. We have shown that the polarizability of complex geometries with an underlying substrate can be calculated analytically and the results obtained closely approximate the resonance conditions for such geometries.

In this work, various other plasmonic modes originating from the two fundamental modes were studied in details and described by their corresponding analytical formulation. In a binary metallic arrays on glass substrate, plasmonic modes are excited by diffraction orders, called the Wood-Rayleigh anomaly (WRA). In metallic strips the PSP is confined by the finite edges of the strips and propagate along the length of the strips, called the confined propagating plasmons (CPP).

For arrays of metallic nano-particles on a metallic film, the Bragg modes (BM) are excited by diffraction of the PSP. In such structures the LSP of the nano-particles and the PSP of the film can undergo a harmonic coupling to give rise to the hybrid lattice plasmon (HLP). The characteristics of the HLP mode for an array of metallic nano-cylinders on a metallic film is presented in details.

The effect of the surrounding medium on the plasmonic modes is used in surface plasmon resonance (SPR) detectors which probe the shift in resonance condition of the modes. Such shift is dependent on the intrinsic dispersion of the modes. The aim of this work is to optimize the SPR detectors for affinity biosensing where probe and analyte molecules are bound to the metallic surface. We have shown that by selective functionalization of the metallic biochip surface, an enhancement of the performance of such detection can be achieved in terms of the amount of analyte used. Also the near field enhancement plays a major role in surface enhanced Raman scattering (SERS). We have shown that the presence of certain modes in the system can enhance the recorded SERS intensity.

Rigorous numerical methods, adapted to the particular geometry under study, were developed to compute the near and far field characteristics of different structures. The experimental excitation of the



modes and their application in SPR detection was demonstrated using a setup based on a spectral scanning modality operating in the Kretschmann configuration. The various structures were fabricated on a biochip using e-beam lithography at IEF, University Paris Sud and the reflectivity dispersion from the biochip was recorded. Such experimental results were shown to be in close agreement with the theoretical results. SERS experiments were carried out in collaboration with CSPBAT at University Paris 13 and the results were seen to fit closely the theoretically predicted trends.

Such detailed description of plasmonic modes can offer a complete understanding of the surface plasmon resonance phenomenon in metallic structures and be optimized as per required for various applications. The theories presented in this work can be used to effectively describe the EM properties of different geometries and experimental configurations. From a comprehensive representation of plasmonic modes, different aspects of the photon-plasmon interactions can thus be elucidated.

# **Modes plasmoniques hybrides dans des nano-structures métalliques: Théorie, simulation numérique et application à la bio-capteurs.**

**Mots clés :** Plasmons de surface, Biocapteur, Method numerique, Mode plasmoniques, Nanostructures métalliques

## **Résumé**

Les Plasmons de surface à l'interface d'un métal et d'un diélectrique sont des oscillations collectives des électrons libres. Pour une interface plane, les plasmons se manifestent comme des champs électromagnétiques évanescents, confinée à quelques centaines de nanomètres de la surface métallique et se propagent le long de l'interface. Ce mode plasmonique, appelé plasmon propagatif de surface (PSP), est un mode fondamental. D'autres modes fondamentaux, non-propagatifs, sont appelé plasmons localisés (LSP) et apparaissent dans les nano-particules métalliques. Dans ce travail, nous avons calculé analytiquement la polarisabilité de géométries métalliques complexes et les résultats obtenus permettent d'expliquer les conditions de résonance des différents modes plasmoniques.

Parmi les divers modes plasmoniques, plusieurs modes fondamentaux ont été étudiés en détail et décrits par une formulation analytique. Tout d'abord, dans un réseau binaire de lignes métalliques, des plasmons propagatifs confinés par la dimension finie des lignes sont générés. Ce mode plasmonique est appelé plasmons propagatifs confinée (CPP). D'autre part, dans des réseaux périodiques de nano-particules métalliques, déposées sur un film métallique, des modes de Bragg (BM) sont excités par la diffraction des PSP. De plus, dans de telles structures, un couplage harmonique entre les LSP des nano-particules et le PSP du film métallique sous-jacent se traduit par l'apparition d'un mode hybride (HLP). Les caractéristiques de ce mode hybride pour un réseau de nano-cylindres métalliques sur un film métallique sont présentées en détails, en particulier son intérêt en bio-détection.

L'effet du milieu diélectrique environnant sur les modes plasmoniques est utilisé dans les détecteurs basés sur la résonance des plasmons de surface (SPR). Ces systèmes mesurent le décalage de la résonance d'un mode plasmonique, qui est fonction de l'indice de réfraction du milieu diélectrique. L'un des buts de ce travail est d'optimiser les détecteurs SPR pour des expériences typiques sondes-cibles ou les molécules sonde sont greffées à la surface du capteur. Nous avons montré que par une fonctionnalisation sélective de la surface métallique, une amélioration de la performance de détection peut être obtenue en terme de quantité de molécules cibles détectable. L'amélioration de champ proche joue aussi un rôle majeur dans les techniques de diffusion Raman exaltée de surface (SERS). La présence de certains des modes

plasmoniques étudiés dans les substrats nano-structurés permet d'augmenter significativement l'intensité du signal SERS.

Pour réaliser ce travail, des méthodes numériques adaptées à la géométrie particulière des structures étudiées ont été développés pour calculer les distributions des champs proches et lointains dans ces structures. Les caractéristiques de ces modes plasmoniques ont été mesurés expérimentalement et leurs performances en détection SPR ont été démontrées en utilisant une configuration basée sur une interrogation angulo-spectrale en configuration de Kretschmann. Des expériences de SERS ont également été réalisées en collaboration avec le CSPBAT à Paris 13. Les différentes structures ont été fabriquées par lithographie électronique à l'IEF à Paris 11. Les résultats expérimentaux concordent avec les résultats numériques et analytiques.

Cette description détaillée des modes plasmoniques offre une compréhension plus complète du phénomène de résonance des plasmons de surface dans les nanostructures métalliques et permet d'optimiser les structures selon l'application souhaitée. Le modèle présenté dans ce travail est relativement général et peut être utilisé pour décrire les propriétés électromagnétiques de différentes géométries et configurations expérimentales. De la représentation complète des modes plasmoniques, différents aspects des interactions photons-plasmons peuvent ainsi être étudiés.

## List of publications

### Publications included in this work

- **Generalized analytical model based on harmonic coupling for hybrid plasmonic modes: comparison with numerical and experimental results.** M.Sarkar, Jean-Francois Bryche, Julien Moreau, Mondher Besbes, Grégory Barbillon, Bernard Bartenlian, Michael Canva, **Optics Express**, Volume 23(21), Pages 27376, 2015.

- **Hybrid plasmonic mode by resonant coupling of localized plasmons to propagating plasmons in a Kretschmann configuration.** M.Sarkar, M Besbes, J Moreau, J.F. Bryche, A Olivéro, G Barbillon, A.L. Coutrot, B Bartenlian, M. Canva, **ACS Photonics**, Volume 2, Pages 237, 2015.

- **Introducing 2D confined propagating plasmons for surface plasmon resonance sensing using arrays of metallic ribbons.** M.Sarkar, M.Chamtouri, J.Moreau, M.Besbes, M.Canva, **Sensors and Actuators B**, Volume 191, Pages 115-121, 2014.

- **Directional Surface Enhanced Raman Scattering on gold nano-gratings.** Raymond Gillibert, M.Sarkar, Jean-Francois Bryche, Ryohei Yasukuni, Julien Moreau, Mondher Besbes, Grégory Barbillon, Bernard Bartenlian, Michael Canva, Marc Lamy de la Chapelle, **Nanotechnology**, 2016.

### Other publications

- **Field enhancement and target localization impact on the biosensitivity of nano-structured plasmonic sensors.** M.Chamtouri, M.Sarkar, J.Moreau, M.Besbes, H.Ghalila, M.Canva, **JOSA B**, Volume 31, Pages 1223-1231, 2014.

- **Waveguide structures for efficient evanescent field coupling to zero mode waveguides.** M Sarkar, A. J. H. Wachtters, H. P. Urbach, J. J. H. B. Schleipen, P. J. van der Zaag, R. Wimberger-Friedl, **JEOS:RP**, Volume 9, Pages 14019, 2014.

- **Biosensor Comprising Waveguide.** J. J. H. B. Schleipen, R. Wimberger-Friedl, P. J. van der Zaag, H. P. Urbach, M Sarkar, **Patent: WO/2015/082247 A1** , 2015.

- **Density effect of gold nanodisks on the SERS intensity for a highly sensitive detection of chemical molecules.** Jean-Francois Bryche, Raymond Gillibert, Grégory Barbillon, M Sarkar, Anne-Lise Coutrot, Frédéric Hamouda, Abdelhanin Aassime, Julien Moreau, Marc Lamy de la Chapelle, Bernard Bartenlian, Michael Canva, **Journal Of Materials Science**, Volume 50(20), Pages 6601-6607, 2015.

## Resumé en Français

### **Modes plasmoniques hybrides dans des nano-structures métalliques: Théorie, simulation numérique et application aux bio-capteurs.**

Ce travail est basé sur la compréhension des différents modes plasmoniques qui peuvent être excités dans les structures métalliques. L'application de ces modes plasmoniques pour le bio-détection a été étudiée. L'existence de plasmons de surface a été observée il y a plus d'un siècle par Robert Wood lors de son étude des réseaux métalliques. Depuis, la capacité des structures métalliques pour confiner les champs électromagnétiques a intrigué les chercheurs et cette capacité a trouvé son chemin dans diverses applications.

Il est bien connu que les métaux absorbent le rayonnement EM et elle est traitée mathématiquement par leur permittivité diélectrique complexe. Les plasmons de surface peuvent être décrits par le fait que les structures métalliques subissent une résonance dans cette absorption du rayonnement EM. Cette absorption de résonance est nommée comme les plasmons de surface parce que lorsque cette condition de résonance est satisfaite, le champ EM est confiné à des distances de sous-longueur d'onde sur les surfaces métalliques. La compréhension de base de plasmons de surface réside donc dans l'explication ou plutôt prédire cette condition de résonance.

La condition dépend évidemment de la type de métal qui à son tour est mathématiquement exprimée par la permittivité complexe du métal. Le premier chapitre est donc centré sur les différents modèles actuellement disponibles pour décrire la permittivité diélectrique complexe. Le premier modèle a été proposé par Paul Drude en 1900 basé sur des propriétés de gaz d'électrons libres. Ce modèle est considéré à donner des résultats précis pour les grandes longueurs d'onde, mais pour des longueurs d'onde visibles, l'effet des électrons liés doit être considéré et donc le modèle a ensuite été modifié par Arnold Sommerfeld. Dans le domaine visible du spectre, les photons d'énergie plus élevés peuvent exciter les électrons des couches inférieures de l'atome de métal au bande de conduction. Afin de répondre à cet effet, le modèle a été développé pour inclure des transitions inter bandes dans les métaux réels. Beaucoup plus tard, en 1972, Johnson et Christy mesuré expérimentalement les constantes optiques de divers métaux et ces valeurs sont largement utilisés pour décrire les propriétés électromagnétiques des métaux.

La condition dépend aussi fortement de la géométrie des structures métalliques. Ceci est évident du fait que les polaritons de plasmon sont confinés à la surface métallique et ainsi, les discontinuités dans la surface jouent un rôle majeur dans la condition de résonance. Cependant jusqu'à ce jour, les solutions analytiques pour de telles conditions ne sont disponibles que pour quelques géométries. Solutions analytiques sont utiles non seulement pour la prédiction de la résonance mais aussi pour une explication simple et intuitive du mécanisme d'excitation de plasmons de surface dans une géométrie donnée.

Le deuxième chapitre décrit brièvement les deux types de plasmons de surface qui sont excités dans les structures métalliques pour lesquelles la condition de résonance peut être calculé analytiquement. La géométrie très basique est une interface métal-diélectrique et les plasmons de surface sont connus pour se propager le long d'une telle interface. La formulation mathématique pour l'excitation de ces plasmons est décrite dans le chapitre. Le second type de plasmon de surface peut être supporté par des particules isolées de dimensions beaucoup plus petites que la longueur d'onde de la lumière. L'excitation de ces plasmons conduire à de forts champs électromagnétiques localisés près de la surface des particules métalliques. Cependant formulation analytique de la condition de résonance est disponible seulement pour sphérique ou dans une certaine mesure pour les particules elliptiques.

La condition de résonance dépend aussi du milieu diélectrique entourant la surface du métal. Ce facteur est utilisé dans le but de détection moléculaire. En fait, la condition de résonance de plasmons de surface dépend fondamentalement sur l'indice de réfraction du milieu environnant. Ainsi molécules liées à la surface du métal entraîne une modification de cet indice de réfraction et peuvent être détectées en mesurant le changement dans la condition de résonance. Se agit du principe de base pour capteurs de résonance de plasmons de surface qui sont décrits dans le chapitre 3. A la résonance, l'absorption de structures métalliques est brusquement augmentée et cela se manifeste dans la réflectivité ou l'extinction des spectres de ces structures, comme une chute ou le pic respectivement. Détecteurs SPR suivent le changement dans ce chute de réflectivité ou pic d'extinction pour mesurer la cinétique d'interaction des molécules sondes et analytes. Ainsi, afin d'optimiser la sensibilité de ces détecteurs, une compréhension de base de la condition de résonance de plasmons de surface est très importante.

Un autre type de technique de détection plasmonique, la Surface Enhanced Raman Scattering (SERS) décrit dans le chapitre 4, repose sur l'intensité du champ EM confiné autour des nanoparticules métalliques. Diffusion Raman a été démontré dans les années 1920 et offre une empreinte spectrale des molécules. Cependant technique d'identification de molécules n'a pas été pleinement exploité jusqu'à ce que les années 1970, quand il a été montré que Diffusion Raman sont grandement améliorée lorsque les molécules se trouvent à proximité de surfaces métalliques. Ce bien ouvert la voie à la SERS détectations, le mécanisme physique exacte derrière une telle amélioration est encore échappait.

Pour les deux techniques de détection mentionnées ci-dessus, SPR et la SERS, nano-structures métalliques à améliorer leurs performances en termes de sensibilité et de la limite de détection. Cette amélioration de la sensibilité est provoquée par les différents types de plasmons de surface qui peuvent être excités dans ces géométries. De nombreux rapports peuvent être trouvés dans la littérature qui décrit une telle amélioration de la performance et de nombreuses géométries de structures ont été étudiées à cet effet. Cependant, une description complète des mécanismes d'excitation de ces types de plasmons de surface sont presque rare. Dans le chapitre 5, les limitations de détecteurs SPR classiques et les différents types de biopuces nanostructurés étudiés afin de surmonter ces limitations sont discutées. Une grande partie de ce travail a été fait dans le cadre du projet ANR PIRANEX qui vise à développer un nouvel instrument combinant la SERS et la détection SPR.

Ainsi, nous avons démontré l'importance de comprendre l'excitation de plasmons de surface dans nanostructuré, destiné à leur application à biocapteurs. Comme déjà mentionné, la formulation analytique de la condition de résonance n'est pas disponible pour de nombreuses configurations d'excitation plasmon. Toutefois, les propriétés électromagnétiques de ces géométries peuvent être calculées en résolvant les équations de Maxwell par des méthodes numériques. Ces méthodes calculent les champs électromagnétiques dans un domaine de calcul donné. Une brève introduction à ces différents modèles numériques est présentée au chapitre 6. Dans ce travail, des simulations numériques rigoureuses ont été menées pour évaluer les caractéristiques des champs proches et lointains de diverses structures métalliques. De telles simulations une compréhension de l'excitation des plasmons de surface dans les structures métalliques a été atteinte.

Le modèle numérique utilisé pour ce travail est une combinaison de deux méthodes bien connues, la méthode de Fourier modale (FMM) et les méthodes d'éléments finis (FEM). Le champ électrique et magnétique peut être calculé pour des structures périodiques en utilisant la formulation de matrice de FMM. Un réseau à deux dimensions peut être découpé le long du plan parallèle au réseau, et les champs

électriques et magnétiques le long de chaque tranche peuvent être liés à la tranche adjacente, par la S-matrice en utilisant l'algorithme de propagation. Cependant, la formulation FMM ne convient pas à la géométrie complexe et celles impliquant métal pose un problème de la convergence. FEM peut surmonter ce problème en utilisant une maille fine pour représenter la géométrie de la structure, mais consomme énormément de mémoire et de temps de calcul. Le code développé en Matlab pour ce travail, calcule la matrice S (ou matrices liés qui concerne les champs électromagnétiques à différentes tranches) par FEM pour la section nanostructuré de la géométrie. Puis, en utilisant la formulation de matrice de FMM, nous pouvons relier les champs calculés autour des nano-structures, à la transmission (T) et de réflexion (R) de la structure complète en fonction de la longueur d'onde incidente et de vecteur d'onde. Ce modèle hybride est décrit dans le chapitre 7 peut être utilisé pour différentes géométries complexes impliquant métal et donner des résultats précis qui sont vérifiées par des expériences.

Après avoir décrit l'objectif de ce travail et l'outil numérique utilisé pour cela, nous avons ensuite décrit l'excitation de divers types de plasmons de surface dans un certain nombre de géométries périodiques. À notre connaissance, une telle description complète des mécanismes qui expliquent l'excitation plasmon dans les structures métalliques n'ont jamais été publiés. Avec de nouvelles explications pour les types déjà observés de plasmons de surface, dans ce travail, nous avons également introduit de nouveaux types de plasmons de surface qui peuvent être excités dans les structures périodiques. Elles sont couvertes dans la partie 4 de ce travail.

Pour expliquer le mécanisme de l'excitation des différents types de plasmons de surface dans les structures métalliques, nous les avons classés en termes de modes plasmoniques. Le principe de base réside dans la description de la fréquence de résonance ( $\omega$ ) pour les plasmons de surface en fonction de son vecteur d'onde dans une direction donnée. Cela a été quantifiée en termes de vecteur d'onde dans l'espace libre ( $k_0 = \omega/c$  ou  $c$  est la vitesse de la lumière dans l'espace libre) et le vecteur d'onde du mode ( $k_{//}/k_0$ ). L'indice est utilisé par analogie avec l'optique guidée. Le concept de modes plasmoniques a été décrit dans le chapitre 8.

Le mode fondamental appelé le plasmon propagatifs (PSP) peut être excité à une interface métal-diélectrique et se propage le long de l'interface avec un champ évanescent confinée à quelques centaines de nanomètres dans la direction perpendiculaire à l'interface. Pour nanostructures, en fonction de sa géométrie, le PSP peut se manifester aux diverses autres modes plasmoniques. Le mode PSP peut être excité uniquement pour la lumière polarisée TM qui a une composante du champ électrique perpendiculaire à l'interface. Ainsi, tous les modes plasmoniques étudiés dans ce travail, qui sont fondées sur la PSP sont excités seulement pour la lumière incidente polarisée TM.

Pour réseaux métalliques sur un substrat de verre, en raison de sa périodicité, les modes Wood-Rayleigh (WRM) sont excités lorsque le photon incident se trouve le long de l'axe perpendiculaire aux réseaux. La condition de résonance de ces modes peut être analytiquement calculée en utilisant le théorème de Bloch qui décrit la fonction d'onde d'une particule dans un réseau périodique. La dispersion du mode dépend uniquement de la périodicité des structures. Le célèbre anomalie de Wood peut être expliqué en termes de WRMS. Les propriétés électromagnétiques de ces modes sont décrites en détail dans la section 9.1 du chapitre 9. Pour des largeurs des lignes plus grandes que la longueur d'onde, la PSP excités sur les lignes peut se coupler aux WRMs pour provoquer des bandes interdites plasmoniques.

Lorsque le photon est incident parallèle aux lignes de réseau, le PSP peut se propager le long de la longueur des lignes. Cependant en raison de la largeur finie de la ligne, les modes plasmon propagatifs

confiné (CPP) peuvent être excités. La condition de résonance de ces modes, contrairement aux WRMS, dépend uniquement de la largeur des lignes. L'intensité de champ électrique calculé pour ces modes sont confinés autour des lignes de réseau avec une partie principale sur les côtés des lignes. Ces modes sont décrits dans la section 9.2 du chapitre 9.

Un autre mode plasmonique fondamentale est excité dans des nano-particules de dimensions beaucoup plus petites que la longueur d'onde de la lumière. Ces modes sont appelés modes de plasmons localisés (LSP) et les champs électriques sont fortement confinés à quelques dizaines de nanomètres de la surface métallique. La condition de résonance pour des particules sphériques peut être analytiquement calculée par la théorie de Mie. Dans ce travail, nous avons introduit un modèle analytique simple appelé le  $\chi$  formulation pour calculer la condition de résonance pour le LSP. Ce modèle est basé sur l'expression de la polarisabilité des charges de surface créées sur la surface métallique, en termes de facteur de dépolarisation  $\chi$  qui dépend de la forme des nano-particules. La condition de résonance est calculée par les pôles de la fonction de polarisabilité. Ce modèle est représenté à donner des résultats précis pour les particules sphériques et bonnes approximations pour des géométries complexes tels que 3D nano-cylindres avec ou sans la présence d'un substrat. Ce procédé et sa comparaison avec la théorie de Mie et résultats obtenus par calculs FEM est décrite dans le chapitre 10.

Pour des réseaux de nano-particules métalliques avec un film métallique sous-jacente, un mode similaire à la WRM, appelés les modes de Bragg (BM) sont excités. Ces modes sont excités en raison de la diffraction du PSP du film métallique par la matrice de particules métalliques. Elles sont décrites au chapitre 11. Dans une telle structure, le LSP de nanoparticules peut également se coupler à la PSP du film métallique, donner lieu à un nouveau mode plasmonique, dite Hybride Lattice Plasmon (HLP). Bien que ces couplage ont été observés avant et sont généralement qualifié de Fano résonance dans la littérature, une description complète de l'excitation de ce mode n'a jamais été rapportée. Cependant, nous croyons qu'une telle classification du HLP que la résonance de Fano est erronée.

Dans la section 11.2, nous avons démontré une description complète du mécanisme de couplage de la LSP et la PSP et avons justifié le fait qu'un tel couplage ne peut être expliqué en termes de résonances de Fano. Il peut plutôt être décrit comme un couplage harmonique entre les systèmes d'oscillateurs et la condition de résonance de la mode peut être calculée par une approche classique simple à couplage fort en utilisant le modèle de l'oscillateur harmonique.

Ce modèle ainsi que les propriétés électromagnétiques de la HLP est abordée au chapitre 12 pour un réseau 3D de nano-cylindres métalliques sur un film métallique. La condition de résonance pour le LSP, BM et le HLP en fonction de paramètres géométriques tels que la hauteur ou le diamètre du cylindre et de la périodicité du réseau a été étudiée par des méthodes numériques. La réflectivité et transmission du réseau pour configuration d'excitation différent ont également été calculées. Formulation analytique appropriée est introduite dans ce travail qui peut prédire avec précision la condition de résonance de tous les modes plasmoniques qui sont excités dans ces types de nano-structures.

Modes plasmoniques sont également classés comme « modes confinés » tels que la PSP, LSP, et le CPP, ou ceux de « modes étendus » tels que les WRM et BM. Le HLP est représenté de se comporter comme modes confinés car il résulte du couplage des LSP et PSP. Cependant, lorsque la condition de résonance pour le HLP se trouve proche de celle de la BM, un couplage secondaire du HLP avec la BM, amène le premier à avoir certaines caractéristiques des modes étendus. Ce même principe peut être utilisé pour expliquer le fameux phénomène de transmission extraordinaire observée dans des réseaux de



nano-trous, qui est également observée pour le HLP dans son régime quasi-étendue.

Enfin dans la partie 5, les modes plasmoniques ont été étudiés pour leur application dans la bio-détection. Tout d'abord la sensibilité des différents modes au changement d'indice de réfraction du milieu environnant a été calculée par des méthodes numériques. Les formulations analytiques appropriées pour les mêmes ont été dérivées et présentées dans le chapitre 13. Pour le mode HLP la sensibilité à l'indice est beaucoup plus faible par rapport au mode PSP, qui est classiquement utilisé pour les capteurs SPR réservés aux détectant les changements d'indice de réfraction. Cette propriété du HLP est utile pour les détecteurs SPR pour des expériences typiques sondes-cibles ou les molécules sonde sont greffées à la surface du capteur. Pour de telles applications une sensibilité élevée par rapport à cibles liées est requis avec une faible dérive avec les changements de l'indice de réfraction.

Dans le chapitre 14, la sensibilité des différents modes, pour bio détection sondes-cibles est calculée par des méthodes numériques. Pour ces calculs, la couche moléculaire est simulée par une couche uniforme homogène avec un indice de réfraction proche de celui de l'analyte. L'effet de la localisation des molécules cibles dans les zones des structures où l'intensité du champ EM est améliorée en raison de l'excitation des modes plasmoniques (appelés points chauds), a été calculée numériquement.

Pour la PSP en film métallique uniforme, la sensibilité décroît de façon linéaire avec la diminution de la couverture de surface de molécules cibles. Mais pour les modes plasmoniques confinés tels que le CPP ou le HLP, localisation sélective de molécules cibles à les points chauds peut produire une sensibilité élevée même avec une diminution de la couverture de la surface moléculaire. Pour quantifier ce pour les modes plasmoniques un facteur de mérite appelé SEF a été présenté comme le rapport de la sensibilité du mode plasmoniques à celle de la PSP compte tenu de la même quantité de la couverture de la surface moléculaire.

Les nano-structures ont été fabriqués par lithographie électronique pour valider les résultats numériques. Un système d'imagerie SPR, basé sur une modalité de balayage spectral a été utilisé pour exciter les modes plasmoniques expérimentalement dans les différents nano-structures. Ceci est couvert dans le chapitre 15. La longueur d'onde incidente a été fixée à l'aide d'une lampe halogène et d'un monochromateur et l'angle d'incidence a été modifié par une plate-forme motorisée. Un polariseur est utilisé pour basculer entre les polarisations TE et TM. La structure a été placée dans une micro-cellule contenant la solution qui agit comme l'indice du milieu environnant et également pour injecter des molécules cibles pour les expériences de détection moléculaire. La réflectivité de la surface de la biopuce structuré a été mesurée dans la configuration Kretschmann. Les calculs numériques pour les différentes structures et les calculs analytiques pour les différents modes plasmoniques correspond bien avec les résultats expérimentaux. La SEF pour le CPP a également été évaluée expérimentalement.

Les modes plasmoniques pour SERS a également été étudiées expérimentalement et calculs pour quantifier la contribution électromagnétique pour l'amélioration de l'intensité de la SERS ont été montré dans le chapitre 16. Cette amélioration a été montrée pour être proportionnelle au produit de l'intensité du champ à l'excitation et les longueurs d'onde d'émission Raman. Ceci est vérifié expérimentalement pour le LSP dans des réseaux nano-cylindres sur des substrats de verre et pour les BM dans des réseaux avec film métallique sous-jacente. Pour la BM, l'intensité de la SERS change avec l'angle d'incidence et ce phénomène est qualifié comme SERS directionnelles dans la littérature. Les calculs numériques pour les intensités de champs et des calculs analytiques pour la BM justifiées que cette SERS directionnelle est le résultat de l'excitation de la BM dans de telles structures.